MODELLING AND STABILITY ANALYSIS OF ELECTRO-MECHANICAL ACTUATION SYSTEM FOR MORE-ELECTRIC AIRCRAFT

A THESIS SUBMITTED TO THE UNIVERSITY OF SHEFFIELD FOR THE DEGREE OF DOCTORATE OF PHILOSIPHY IN THE FACULTY OF ENGINEERING

2020

ALI ELMAJDUB

DEPARTMENT OF ELECTRONIC AND ELECTRICAL ENGINEERING

Acknowledgment

I would like to sincerely thank my parents, Salma and Mohamed, for their encouragement and for everything they do for me. I also would like to thank my wife, Najwa, and my little daughter, Ruaa. Throughout my PhD, I have had many personal hardships in many aspects yet I managed to reach this stage. I also express my deepest thankfulness to my country, Libya, which has been supporting me all this time.

A special acknowledgment goes to my supervisors, Dr. Milijana Odavic and Prof. Kais Atallah for their guidance and assistance. I truly appreciate their help and support. They are inspiring and I have learned a lot from them indeed. I thank all my friends within EMD group and university in general who have been a great support.

Abstract

In modern electric aircraft, many conventional systems are replaced with their electrical equivalents. Actuation system is one system that is replaced by electromechanical actuators instead of hydraulic actuators. Electromechanical actuators are powered by electrical motor through a set of power electronic conversion interfaces. The actuator's main role is to provide actuation for flight control surfaces, which is subject to aerodynamic loads. The aerodynamic load along with the actuator dynamics have certain characteristics that could interact with the power system. This is because, in case of interactions, the overall system might destabilise but both electrical and mechanical components can wear down.

In this project, electromechanical interaction in the rudder electromechanical actuation system is investigated. Full model of the actuator is tested that highlights dynamics of which some are critical. Simplified models are suggested in attempt to include only the crucial actuator dynamics and neglect the unimportant ones. The proposed models show good matching with the full detailed model. Origin of anti-resonance is investigated due to its effect on system stability. It is shown that for closed speed loop and closed position loop, anti-resonance occurs due to different factors. To make sure that the suggested modelling methodology is generic, rudder actuation system is sized for a range of aircraft sizes. Using small signal sensitivity, interaction is proved to occur between electrical and mechanical systems. A test rig is used to emulate the actuation system using Hardware In the Loop technique. The experimental rig reproduces the actuation system behaviour and validates the simulated work.

Understanding of electromechanical interactions and their effects on the system stability will create opportunities to enhance the robustness of more electrical aircraft power system through improved design and/or control.

Contents

List of Figures

List of Tables

Table of abbreviations

AC	Alternating current
AEA	All-Electric Aircraft
BW	Bandwidth
CFRP	Carbon fibre-reinforced plastic
CLA	Conventional linear actuator
CPL	Constant power load
DC	Direct current
DHA	Distributed hydraulic actuator
DOF	Degree of freedom
EBHA	Electrical backup hydraulic actuator
ECS	Environmental Control System
EHA	Electro-hydrostatic actuator
EMA	Electromechanical actuator
EMF	Electromotive force
EPA	Electrically powered actuators
EPS	electrical power system
FEM	Finite Element Method
FFT	Fast Fourier Trasform
GCU	generator control unit
GFRP	Glass fibre-reinforced plastic
GHG	greenhouse gasses
HSR	High speed rotor
IAP	Intermediate Annular Pole Pieces
IFE	In-flight Entertainment
IFEP	Integrated full electric propulsion
IM	Induction machine
IPMA	Inner Permanet-Magnet Array
LPP	Lightning protection plates
LSR	Low speed rotor
LVDT	Linear variable differential transformed
MEA	More-Electric Aircraft
MTOW	maximum take-off weight
NCMGs	Non-Contacting Magnetic Gears
OPMA	Outer Permanent-Magnet Array

PDD	Pseudo Direct Drive
PI	Proportional-integral
PM	Permeant magnet
PMSM	Permanent magnet synchronous machine
SHA	Smart hydraulic actuator
SLP	Slotted Lamination Pack
SM	Synchronous machine
SM-Resolver	Solution-Module Resolver
SR	Switched reluctance machine
VSI	voltage source inverter
WAI	Wing Anti Icing

Table of Notation

symbol	*Description*	*unit*
$\overline{A_{servo}}$	*Complement of* A_{servo}	-
$\overline{B_{servo}}$	*Complement of* B_{servo}	-
$\overline{Z_{servo}}$	*Complement of* Z_{servo}	-
$\{v\}$	*vector of amplitudes*	-
A	*To indicate phase A*	-
a	*Rudder upper side dimension*	m
A_{enc}	*PDD encoder signal*	-
A_R	*Rudder surface area*	m^2
AR	*Aspect ratio*	-
A_{sc}	*Cross sectional area of screw shaft*	m^2
A_{servo}	*Servo motor encoder signal*	-
A_t	*Tail area*	m^2
A_u	*Matrix including stiffness and mass matrices*	-
A_θ	*Amplitude of* θ_{sc}	*rad*
B	*To indicate phase B*	-
b	*Rudder lower side dimension*	m
B_{enc}	*PDD encoder signal*	-
B_{servo}	*Servo motor encoder signal*	-
B_θ	*Amplitude of* θ_{LSR}	*rad*
C	*To indicate phase C*	-
c_{HSR}	*Viscous damping of the HSR*	$N.m.s.rad^{-1}$
c_{HSR_LSR}	*Viscous damping between HSR and LSR*	$N.m.s.rad^{-1}$
c_{LSR}	*Viscous damping of the LSR*	$N.m.s.rad^{-1}$

C_{LSR}	*Average circumference of the LSR*	*m*
D_1	*Diode 1*	-
D_2	*Diode 2*	-
D_3	*Diode 3*	-
D_4	*Diode 4*	-
D_5	*Diode 5*	-
D_6	*Diode 6*	-
D_i	*LSR inner diameter*	*m*
D_o	*LSR outer diameter*	*m*
D_{sc}	*Screw diameter*	*m*
$\boldsymbol{E}$	*Back EMF phasor*	*V*
e_a	*Phase A back EMF*	*V*
$\boldsymbol{E_{ag}}$	*Airgap induced voltage phasor*	*V*
e_b	*Phase B back EMF*	*V*
e_c	*Phase C back EMF*	*V*
e_i	*Eigenvalue matrix and also the i-th eigenvalue*	-
$\boldsymbol{E_L}$	*Stator windings induced voltage phasor*	*V*
E_p	*amplitude of back EMF*	*V*
E_{sc}	*Young's modulus of screw material*	*GPa*
f_1	*First resonant frequency (with respect to LSR)*	*Hz*
$f_{1\_reflected}$	*First resonant frequency (with respect to HSR)*	*Hz*
f_{1_rig}	*The 1st resonant frequency under influence of the rig*	*Hz*
f_{ar_tr}	*Anti-resonant frequency found in the transfer receptance*	*Hz*
f_{base}	*Base frequency*	*Hz*
f_c	*Current loop bandwidth*	*Hz*

f_{co}	*First order filter cut-off frequency*	*Hz*
F_d	*Disturbance force*	*N*
f_e	*Three-phase windings current frequency*	*Hz*
f_g	*Resonant frequency due to magnetic stiffness*	*Hz*
f_i	*The i-th natural frequency*	*Hz*
f_p	*Position loop bandwidth*	*Hz*
f_s	*Speed loop bandwidth*	*Hz*
F_{sc}	*Force produced by the ball-screw*	*N*
f_{sw}	*Switching frequency used in the switching model*	*kHz*
f_{sw_servo}	*Servo drive switching frequency*	*kHz*
f_{TF}	*Transfer function of the first order filter*	-
f_z	*Frequency of oscillation of root* s_z	-
g	*Row number of* $\alpha(\omega)$	-
G_1	Gain used to transfer v_{LSR} to ω_{LSR}	-
G_2	Gain used to transfer $\omega_{p.u.}^*$ to v_ω^*	-
G_r	*PDD Gear ratio*	-
G_{sc}	*Shear modulus of screw material*	*GPa*
h	*Aircraft tail height*	*m*
$\boldsymbol{I}$	*Stator current phasor*	*A*
i	*The number of the natural frequency*	-
$i_{\%}$	*Percentage of current demand to the rated current*	-
i_a	*Phase A current*	*A*
i_{active}	*Active current of the servo drive*	*A*
i^{Agk}	*Modal constant (residue)*	-
i_b	*Phase B current*	*A*

I_{base}	*PDD base current*	*A*
i_c	*Phase C current*	*A*
i_d	*d-axis current*	*A*
i_d*	*d-axis current demand*	*A*
I_{max}	*Servo machine maximum current*	*A*
I_p	*amplitude of phase current*	*A*
i_q	*q-axis current*	*A*
i_q*	*q-axis current demand*	*A*
i_r^*	*Current demand to the servo drive*	*A*
I_{sc}	*Area moment of inertia of screw*	m^4
I_{servo_rated}	*Rated current of the servo machine*	*A*
ISR_FREQUENCY	*Switching frequency used in the PDD drive test rig*	*Hz*
I_u	*Unity matrix*	-
J_c	*Inertia of coupling*	$kg.m^2$
$J_{coupling}$	Moment of inertia	$kg.m^2$
J_e	*Inertia of the extended triangular plate*	$kg.m^2$
J_{ep}	*End plates inertias*	$kg.m^2$
J_{HSR}	*Moment of Inertia of HSR*	$kg.m^2$
J_L	*Moment of inertia of the load (seen at LSR)*	$kg.m^2$
J_{LSR}	*Moment of Inertia of LSR*	$kg.m^2$
J_{pp}	*Inertia of pole-pieces fibre glass*	$kg.m^2$
J_R	*Sum of J_{LSR} and J_{sc}*	$kg.m^2$
J_r	*Rudder surface inertia*	$kg.m^2$
J_{R2}	*Sum of Sum of J_{LSR}, J_{sc}, and J_L*	$kg.m^2$
J_{rig}	*Sum of J_{servo} and J_{LSR}*	$kg.m^2$

J_s	*The single inertia*	$kg.m^2$
J_{sc}	*Moment inertia of the ball-screw*	$kg.m^2$
J_{servo}	*Servo machine inertia*	$kg.m^2$
J_v	*Inertia of the virtual plate*	$kg.m^2$
K	*Stiffness matrix*	-
k	*Column number of α(ω)*	-
K_a	*Aerodynamic stiffness*	*N/m*
K_{ar}	*Rotary aerodynamic stiffness*	*N.m/rad*
K_b	*Stiffness of the bearing*	*N/m*
K_c	*Stiffness of the coupling*	*N.m/rad*
$K_{coupling}$	*Stiffness of coupling between LSR and servo machine*	*N.m/rad*
K_e	*PDD EMF Constant*	*V.s/rad*
K_E	*Servo machine EMF constant*	$V/kmin^{-1}$
K_{eq}	*Equivalent stiffness of K_n and K_b in series*	*N/m*
K_{eq1}	*Equivalent stiffness of K_{eq} and K_a in parallel*	*N/m*
K_{eq2}	*Equivalent stiffness of K_n and K_b in parallel*	*N/m*
K_g	*Magnetic stiffness of the PDD*	*N.m/rad*
k_i	*Generalised stiffness matrix of mode i*	-
K_{ic}	*Current control integral gain*	-
K_{is}	*Speed control integral gain*	-
K_n	*Stiffness of the screw-nut interface*	*N/m*
K_{pc}	*Current control proportional gain*	-
K_{ps}	*Speed control proportional gain*	-
K_{rig}	*Sum of test rig torsional stiffness*	*N.m/rad*
K_{sa}	*Screw shaft axial stiffness*	*N/m*

K_{st}	*Screw shaft torsional stiffness*	$N.m.rad^{-1}$
K_t	*PDD Torque constant*	$N.m.A^{-1}$
K_T	*Servo machine torque constant*	$N.m.A^{-1}$
K_{t_LSR}	*PDD torque constant from LSR side*	$N.m.A^{-1}$
$K_{transducer}$	*Transducer torsional stiffness*	$N.m.rad^{-1}$
L	*Self-inductance*	H
L_a	*Link arm length*	m
L_{ax}	*LSR axial length*	m
L_d	*d-axis inductance*	H
L_{ls}	*Leakage inductance*	H
L_m	*Magnetising inductance*	H
L_{ns}	*Length of the pole-piece square shape*	m
$L_{ph\text{-}ph}$	*Servo machine phase to phase inductance*	H
L_q	*q-axis inductance*	H
L_s	*PDD synchronous inductance*	H
L_{sc}	*Length of the screw shaft*	m
M	*Mass matrix*	-
m	*Number of torque entry*	-
M_A	*Sum of M_{sc} and M_L*	kg
M_h	*Moment at hinge*	$N.m$
m_i	*Generalised mass matrix of mode i*	-
M_{JLSR}	*Equivalent mass of LSR inertia*	kg
M_{Jsc}	*Equivalent mass of screw inertia*	kg
M_L	*Equivalent load mass*	kg
M_R	*Rudder mass*	kg

M_{sc}	*Mass of screw shaft*	*kg*
M_{sl}	*Mass of the slide*	*kg*
N	*Aircraft tail upper side dimension*	*m*
n	*Star point of the PDD windings*	-
N_{bits}	*TI ADC number of bits*	*bits*
N_d	*Number of degrees of freedom*	-
n_{HSR}	*HSR speed in rpm*	*rpm*
n_{HSR_MAX}	*Maximum speed of HSR*	*rpm*
N_{int_MAX}	*Maximum number of discrete values over the input*	-
n_{LSR_MAX}	*Maximum speed of LSR*	*rpm*
N_n	*Neutral point in the inverter*	-
n_{rig}	*Speed of J_{rig} in rpm*	*rpm*
n_s	*Number of PDD pole-pieces*	-
N_t	*Number of PDD windings turns*	-
$N_{v\_interval}$	*Number of discrete values over the analogue input*	-
P	*Position control proportional gain*	-
P	*Aircraft tail lower side dimension*	*m*
p_h	*Number of PDD HSR pole-pairs*	-
P_{HSR}	*Mechanical power of the HSR*	*W*
p_l	*Number of stationary PM arrays in PDD*	-
P_{LSR}	*Mechanical power of the LSR*	*W*
P_{sc}	*Power of the slide on the ball-screw*	*W*
q	*State variable vector*	-
q_j	*State variable of the row j*	-
q_l	*State variables of the linearised system*	-

$R_{ph\text{-}ph}$	*Servo machine phase to phase resistance*	*Ω*
R_{Rt}	*Ratio of rudder surface area to tail area*	-
R_s	*PDD Phase resistance*	*Ω*
S	*Ball-screw stroke*	*m*
s	*Laplace operator*	-
s_i	*Laplace operator related to the i-th natural frequency*	$rad.s^{-1}$
s_z	*The z-th root of the linearised system*	$rad.s^{-1}$
T	*Torque matrix*	-
t	*time*	*s*
T_a	*Torque produced due to phase A current*	*N.m*
T_b	*Torque produced due to phase B current*	*N.m*
T_c	*Torque produced due to phase C current*	*N.m*
$T_{coupling}$	Torque	*N.m*
$T_{coupling\_peak}$	Peak torque	*N.m*
T_d	*Disturbance torque*	*N.m*
T_e	*Electromagnetic torque*	*N.m*
T_{ep}	*End plate thickness*	*m*
T_K	*Torque element of the column K*	-
T_L	*Load torque*	*N.m*
T_{LSR}	*LSR torque*	*N.m*
T_{LSR_MAX}	*Peak torque demand (Limit)*	*N.m*
T_{max}	*Pull out Torque*	*N.m*
T_R	*Rudder surface thickness*	*m*
T_r	*LSR radial thickness*	*m*
T_{ra}	*Taper ratio*	

T_{re}	*Reaction torque (demand from model to the servo drive)*	*N.m*
$T_{sampling}$	*Sampling time*	*s*
T_{sc}	*Screw torque*	*N.m*
T_{servo}	*Servo motor actual torque*	*N.m*
u	*Base of the extended triangular plate*	*m*
$\boldsymbol{V}$	*Applied voltage phasor*	*V*
v	*Vector of dimension N×1*	-
v_{an}	*Phase A voltage*	*V*
v_{an}^{*}	*Phase A voltage demand*	*V*
V_{base}	*PDD base voltage*	*V*
v_{bn}	*Phase B voltage*	*V*
v_{bn}*	*Phase B voltage demand*	*V*
v_{cn}	*Phase C voltage*	*V*
v_{cn}^{*}	*Phase C voltage demand*	*V*
v_d	*d-axis voltage*	*V*
v_d*	*d-axis voltage demand*	*V*
V_{dc}	*Nominal voltage of inverter DC bus*	*V*
$\boldsymbol{V_{drop}}$	*Voltage drop in the windings resistance*	*V*
$v_{i[1]}$	*First entry of $[v_v]$ corresponding to f_i*	-
$v_{i[2]}$	*Second entry of $[v_v]$ corresponding to f_i*	-
$v_{i[3]}$	*Third entry of $[v_v]$ corresponding to f_i*	-
$v_{i[4]}$	*Fourth entry of $[v_v]$ corresponding to f_i*	-
$v_{i[5]}$	*Fifth entry of $[v_v]$ corresponding to f_i*	-
$v_{i[6]}$	*Sixth entry of $[v_v]$ corresponding to f_i*	-
v_L	*Translational speed of M_L*	$m.s^{-1}$

v_q	*q-axis voltage*	*V*
v_q^*	*q-axis voltage demand*	*V*
V_r	*Excitation signal applied to the resolver*	*V*
V_{ref}	*ADC voltage reference*	*V*
V_{ref_MAX}	*ADC maximum voltage reference*	*V*
v_{sc}	*Linear speed of M_{sc}*	$m.s^{-1}$
v_v	*Eigenvector matrix*	-
v_{v_scaled}	*Scaled eigenvector matrix*	-
v_{vn}	*Mass normalised eigenvector matrix*	-
v_ω^*	*Voltage representing the HSR speed demand*	*V*
v_{ω_rig}	*Voltage representing ω_{rig}*	*V*
w	*Hypotenuse of the extended triangular plate*	*m*
x	*Position on the screw shaft*	*m*
x_1	*Displacements of masses contributing in f_1*	*m*
X_1	*Laplace transform of x_1*	-
x_L	*Load axial position*	*m*
x_L^*	*Load axial position demand*	*m*
$XL_{p.u.}$	*PDD per unit reactance*	*Ω*
x_s	*Position of nut on the screw shaft*	*m*
x_{sc}	*Screw axial displacement*	*m*
z	*The number of root of the linearised system*	-
Z_{base}	*PDD base impedance*	*Ω*
Z_{enc}	*PDD encoder index signal*	-
Z_{servo}	*Servo motor encoder index signal*	-
Z_{servo}	*Servo motor encoder index signal*	-

$\alpha(\omega)$	*Receptance matrix*	-
α_d	*Deflection angle*	°
$\alpha_{gk}(\omega)$	*The general element in* $\alpha(\omega)$	-
γ	*Transmission ratio*	$m.rad^{-1}$
δ	*Torque angle*	*rad*
Δx_{sc}	*Screw axial deformation*	*m*
$\Delta\theta_{sc}$	*Screw torsional deformation*	*rad*
ζ_z	*Damping ratio of root* s_z	-
θ_e	*HSR electrical position*	*rad*
θ_{HSR}	*HSR mechanical position*	*rad*
θ_{LSR}	*LSR mechanical position*	*rad*
θ_r	*Referred load angle between HSR and LSR*	*rad*
θ_R	*Displacement of* J_R	*rad*
θ_{R2}	*Displacement of* J_{R2}	*rad*
θ_{rig}	*Position of* J_{rig}	*rad*
θ_{sc}	*Screw angular displacement*	*rad*
θ_{servo}	*Position of servo machine shaft*	*rad*
Λ	*Screw pitch*	*m*
λ	*Screw lead*	*m*
ρ_A	*Density of rudder material*	$kg.m^{-3}$
ρ_{ep}	*Density of end plates material*	$kg.m^{-3}$
ρ_{LSR}	*Average density of the pole-pieces rotor*	$kg.m^{-3}$
ρ_{st}	*Density of the screw material*	$kg.m^{-3}$
σ	*Real part of s*	$rad.s^{-1}$
σ_i	*Real part of* s_i	$rad.s^{-1}$

σ_{LSR}	*Shear stress on LSR*	*Pa*
σ_z	*Real part of* s_z	$rad.s^{-1}$
Ψ_m	*Rotor flux phasor*	*Wb*
ω	*Imaginary part of s*	
ω_{base}	*PDD base speed*	$rad.s^{-1}$
ω_e	*PDD electrical speed*	$rad.s^{-1}$
ω_{HSR}	*HSR mechanical speed*	$rad.s^{-1}$
ω_{HSR}^*	*HSR mechanical speed demand*	$rad.s^{-1}$
ω_i	*The i-th natural frequency*	$rad.s^{-1}$
ω_{LSR}	*LSR mechanical speed*	$rad.s^{-1}$
$\omega_{p.u.}^*$	*Per unit speed demand*	
$\omega_{p.u.\_code}^*$	*Representing the value of* $\omega_{p.u.}^*$ *received by the code*	
ω_R	*Angular speed of* J_R	$rad.s^{-1}$
ω_{rig}	*Angular position of* J_{rig}	$rad.s^{-1}$
ω_{servo}	*speed of servo machine shaft*	$rad.s^{-1}$
ω_z	*Imaginary part of* s_z	$rad.s^{-1}$
τ_c	*Time constant of the current loop*	

Chapter 1 Introduction

1.1 Application background

1.1.1 Cost and environmental concerns

Aviation is a major transportation type and it grows by 5% every year [1]. 12% of the global greenhouse gasses (GHG) emissions come from aviation. By lessening fuel consumption, less gasses will be emitted and also more money can be saved [1]. Therefore, increasing aircraft efficiency is the key that makes aviation less costly and have less negative impact on environment. In consequence, efficiency increase has been a crucial target in aircraft industry [2] [1].

Fuel is burned in the aircraft engine to provide, mainly, thrust but also power is extracted for defined auxiliary systems called secondary power systems. Each form of the secondary power has its own distribution network forming an integral part of the airframe operation. Pneumatic power is used to operate the Environmental Control System (ECS) and Wing Anti Icing (WAI). Electrical power is required for systems such as lighting, flight control avionics, In-flight Entertainment (IFE) and aircraft galley. Mechanical power is extracted from the engine spool and employed to drive an electric generator and a hydraulic compressor [1]. Figure 1 shows the gas turbine energy conversion systems for traditional aircraft.

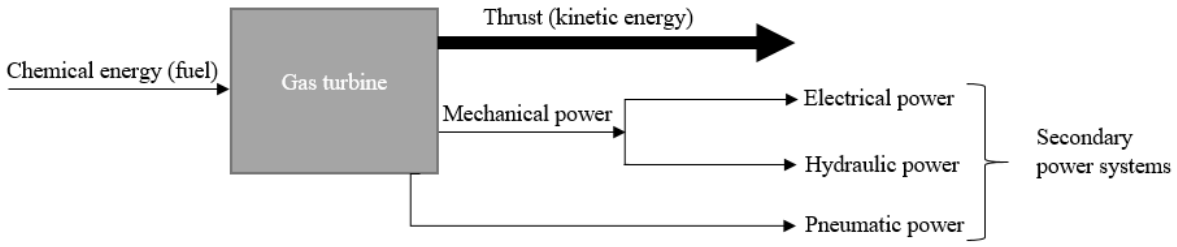

Figure 1. Gas turbine energy conversion systems for traditional aircraft [1]

One possible way to boost aircraft efficiency and decrease maintenance demands is to enhance the use of electrical power systems. This is to simplify engine and airframe. Further, although hydraulic systems have a high force to weight ratio, they are heavy since many pipes are placed along the wing length leading to more stress. This indeed increases weight, which in turn decreases lift capability. Moreover, hydraulic systems are of high cost and hydraulic fluids are corrosive and flammable. For such reasons, electrification of aircraft is of high benefit [1].

1.1.2 All-Electric aircraft

All electric aircraft (AEA) was the initial proposal. That means electric machines are the source to power all systems; include, propulsion system, wing anti-icing system, environmental control system, actuation systems. However, in large aircraft (such as Boeing 777 and Airbus A340), providing a

propulsion power of 60 MW is not within technical capabilities. This is owing to the fact that over-sized and over-weighted electric generators are needed. Besides, current energy storage technology has 50 times less energy density than aviation fuel. For those reasons, the trend was directed towards more electric aircraft (MEA) [3].

1.1.3 More electric aircraft (MEA)

It is challenging to make a dramatic improvement in the aero gas turbine efficiency since it is a mature technology [1]. Also, as mentioned above, implementing all electric aircraft for commercial aviation is not possible. The reasons highlighted above are due to power density issues associated with electrical machines and power storage technology. Therefore, MEA is concerned with electrifying secondary power systems. Mechanical power offtake is increased to supply the increase in electrical power demand [3]. Figure 2 shows the gas turbine energy conversion systems for MEA. Indeed, the increase in electrical power demand in MEA gives rise to an enlargement in electrical loads driven by power electronics including motor drive systems [2].

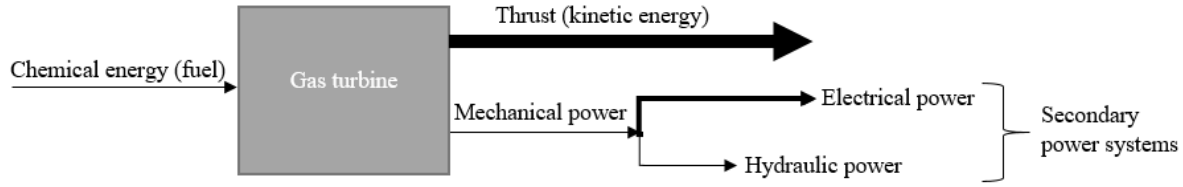

Figure 2. Gas turbine energy conversion systems for MEA [1]

Some systems on board, such as actuation systems, can be electrified [1]. Actuators are needed to actuate thrust reverser, landing gear, gear brakes, flight control surfaces and so on [3]. For example, thrust reverser functions to provide brake during landing, as seen in Figure 3 (a). It does so by managing the engine thrust and directing it to front to slow down aircraft hence it helps stop aircraft within shorter distance [4]. Figure 3 (b) illustrates the use of actuator for landing gear extension and retraction [3].

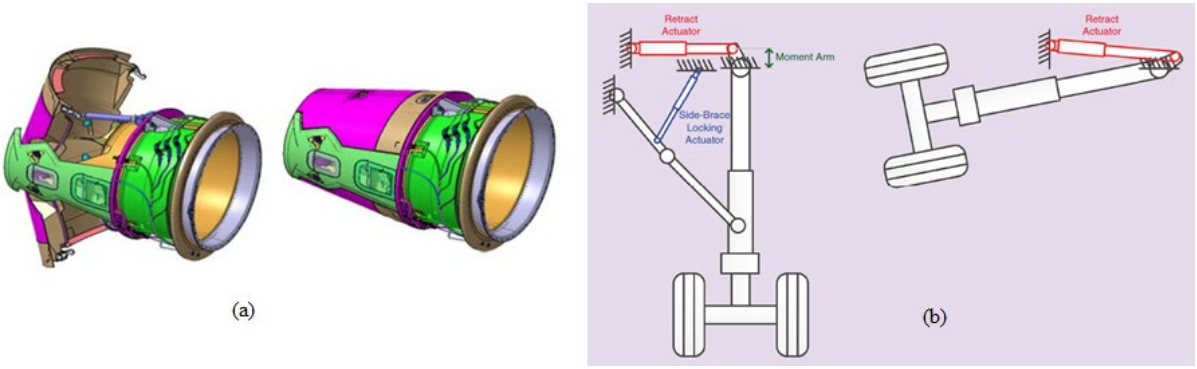

Figure 3. (a) the opening of thrust reverser [4] *(b) Extension and retraction of landing gear* [3]

1.1.4 Flight control surfaces

Figure 4 shows flight control surfaces, which can be divided into primary flight controls and secondary flight controls. The three primary flight control surfaces provide motions around three defined axes. The elevator functions to provide pitch. The aileron provides roll. The rudder is crucial to provide yaw. For secondary control surfaces, flaps are deployed during take-off and landing to maximise wing area and hence lift is increased. Slats are also deployed to increase wing area and thus assist in increasing lift. Spoilers are employed to decrease lift and increase drag and hence they assist in braking [5] [6].

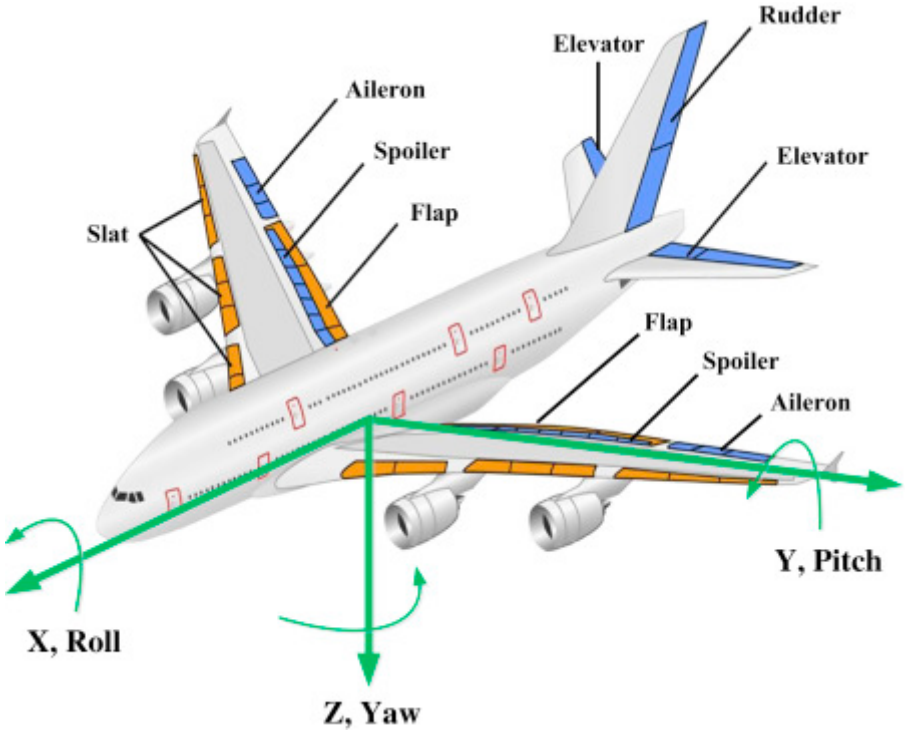

Figure 4: Flight control surfaces [5]

Flight control forces can be generated using a mechanical method. In such a method, force is mechanically produced by pilots (like old days small aircraft) and then actuators due to increased aircraft size. These actuators can be of any type such as hydraulic actuators.

1.1.5 Types of actuators

To actuate a flight surface according to demand, various types of actuators can be used [1]; such as, Conventional linear actuator (CLA), Smart hydraulic actuator (SHA), Distributed hydraulic actuator (DHA), Electro-hydrostatic actuator (EHA), Electrical backup hydraulic actuator (EBHA), and Electromechanical actuator (EMA).

In EHA, the actuation process is performed by a hydraulic actuator. However, the hydraulic fluid is controlled by an electric motor. The hybrid electrical/hydraulic actuator is the first approach towards MEA [4]. This type of actuators has been used in A320, A340, F16 and F18. F35 was the first to employ EHA on the primary flight control. A380 was the first civil aircraft to use EHA [7]. Electrical backup

hydraulic actuator (EBHA) is very similar to EHA but just it has an electrical backup [4]. EBHA was first used in A380 [7].

With the tendency to boost system efficiency, electrically powered actuators (EPA), such as electrohydraulic actuators or electromechanical actuators (EMA), are the new trend to substitute hydraulic actuators. Actuation is required to have a proper demand tracking property; accurate, swift, and rigid. The advancement in power electronics has shown the electric actuators as a favourable choice [7].

1.1.6 Electromechanical actuator

As mentioned in [7], many requirements and features of the aircraft actuation system must be met; such as, efficiency, thermal capability, stall load, maximum and rated power, weight, cost, power consumption, safety and reliability. Furthermore, many challenges are associated with primary flight control surface actuators. Most importantly is that primary flight surface is subjected to high power loads for a continuous period of time. This is considered as a thermal challenge for the PM motor and controller. Moreover, the surface position is moving fast within small distance. This imposes a high current demand to hold these loads and hence a thermal challenge. Another issue is the shortage of data ascribed to lack of aviation experience; therefore, probability of jamming, caused by failure of screw due to shock loads, such as winds or strikes, is unknown [8]. Further, no data of wear life is available since loads on primary flight control surface can be different to other types of loads [3].

EMA has become a competitive option as a result of technological advancements in fields such as machine design and power electronics. Further, because of recent improvements in electric machine drives, power to weight ratio has increased to become comparable to that of the EHA. Some issues are reported with this technology related to jamming during failure. Also, power to weight ratio is still less than conventional alternatives. However, many advantages are appreciated for the EMA; such as, lighter weight of electrical power distribution system, reductions in maintenance and better controllability. EMA is employed in secondary flight control surfaces (spoilers) in B787 [7].

The topology of actuator can be broadly classified into two categories, rotary and linear, as shown in Figure 5. In the rotary EMA, a resolver is employed to measure the degrees of rotation of the electric motor. In the linear EMA, the position of the nut actuating the load is measured by a linear variable differential transformed (LVDT). A high speed motor is employed, which is coupled to a reduction gear and a linear screw-nut system. The motor is controlled by a power electronic converter.

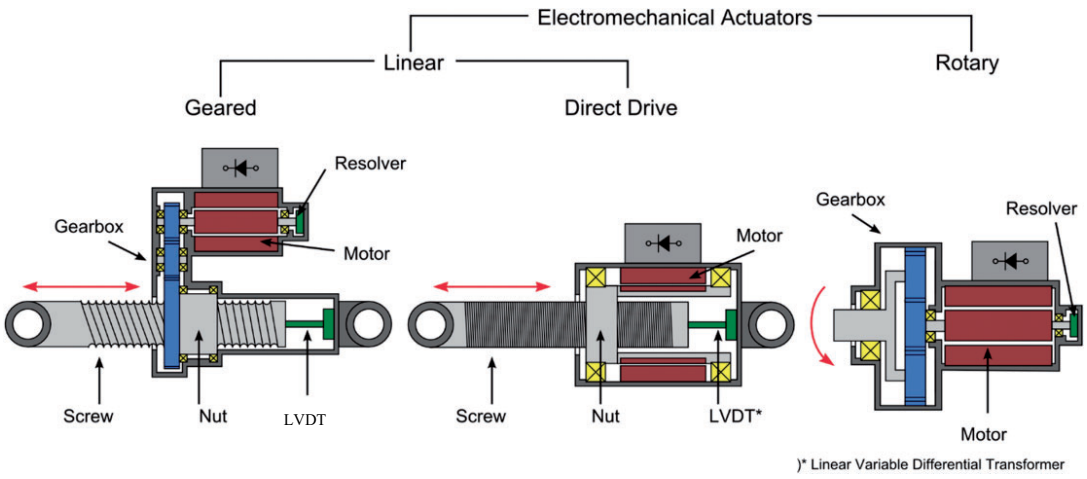

Figure 5: EMA topologies [9]

1.1.6.1 Screw-nut systems

Three types of screw are common; lead-screw, roller-screw, and ball-screw. Roller-screw is highly costly [10]. Instead of the sliding friction occurring in conventional lead-screw, ball screw replaces that with rolling friction [11]. Ball screw drive systems are accurate and cheap and screw has high mechanical stiffness [12] [13]. Further, high resolution and repeatability can be achieved by ball-screw [11]. Ball screw drive system provides wider displacement stroke. Moreover, it is more robust under work force (such as cutting force) and load inertia variations [13]. For such advantages, ball-screw is commonly used in industrial and precise applications [11]. Ball-screw drive system is used in 80% of machine tools [13].

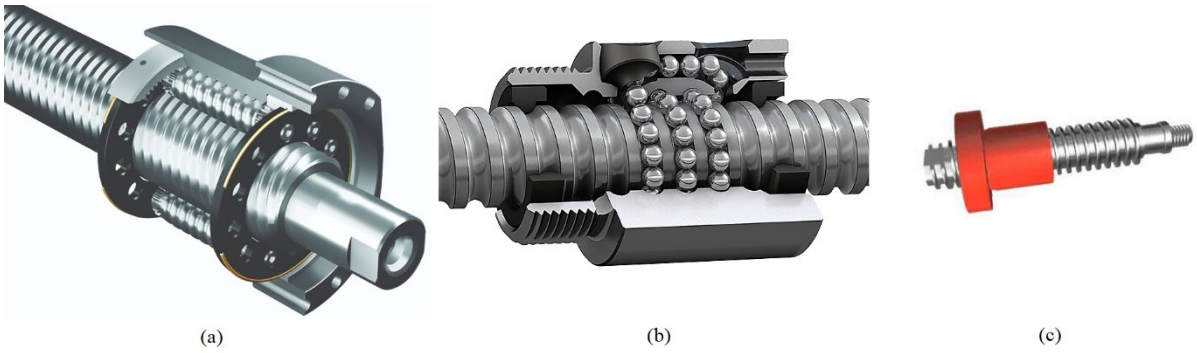

Figure 6. (a) Roller screw [10] *(b) ball-screw* [14] *(c) leadscrew* [15]

1.1.6.2 Motor topologies

With respect to [4], motoring in EMA system can be provided by several types of electrical machines, such as synchronous machine (SM), induction machine (IM), permanent magnet synchronous machine (PMSM) and switched reluctance machine (SR). The need of large amount of torque necessitates the need for a large size of motor. Therefore, a gear is used to minimise electric machine size. The use of a gearbox helps match the operating torque of the machine to the requirements of the load.

Mechanical gears can have a high torque density but have many disadvantages such as noise, vibration, reliability and the need of lubrication and cooling [16] [17] [18]. A solution of this issue is appreciated by the development of Non-Contacting Magnetic Gears (NCMGs), which use rare-earth magnets. A high torque density magnetic gear is presented in [18] [19] and torque density is mentioned to reach *100 kN.m/m^3*. The magnetic gearing relies on the principle of flux modulation, which is explained in detail in [20].

Many topologies are proposed to couple the magnetic gear with a PM machine [16]. A more compact topology is to mechanically and magnetically integrate a motor and a magnetic gear within a single unit; such configuration is known as pseudo direct drive (PDD). In accordance with [16] [17], a *60-110 kN.m/m^3* torque density can be reached by PDD, which provides high torque transmission capabilities. Also, a power factor of *0.9* can be reached with low cogging torque. Furthermore, the PDD has overload protection capability, which makes the PDD slip in case the load torque exceeds the pull-out torque. This will prevent damage to the drivetrain in the system. PDD offers a significant benefit since a gearing stage can be eliminated and hence a simpler configuration is adapted. In [8], PDD is proposed for aircraft primary flight control surface.

1.2 Literature review

It is stated above that as a way to improve aircraft efficiency, the use of electrical power systems is enlarged by electrifying certain systems. Upon electrification of the aircraft, more loads are driven by power electronics that tend to maintain constant power for a load, particularly motors. CPLs represents a challenge to aircraft electrical power system (EPS) since the load will start behaving like a negative impedance, which reduces the system stability margin [2]. As such, to benefit from this, it is crucial to ensure electrical power system stability to guarantee a safe flight operation. One of the crucial electrified systems is the EMA system used for rudder actuation.

To fully perceive the influence of EMA system on power system stability, such electromechanical system needs to be considered. The problem of interactions in electromechanical systems are documented in many systems. Literature review is given for, firstly, conventional methodology followed to model aero EMA systems. Then, dynamics of EMA systems used in non-aero system are introduced to underscore the importance of considering the mechanical system dynamics of EMA rather than the conventional simplified approach. Thirdly, the issue of electromechanical interaction in different systems are highlighted to be put into comparison with our aero EMA in question. This is expected to help understand the impact of mechanical system on electrical system and vice versa.

1.2.1 Aero electromechanical system

Figure 7 shows the schematic of aircraft electromechanical system. The three-phase voltage source generator is driven by a gas turbine engine through shafts and gears. The generator is regulated by a generator control unit (GCU). Transmission lines transfer AC from the generator to be rectified by a

six-pulse uncontrolled diode rectifier. Then a DC-link filter is employed to smoothen the rectifier output. For surface control actuation, a motor, a gear, and a ball-screw assembly are utilised. This general topology is introduced in [1] [2] [21].

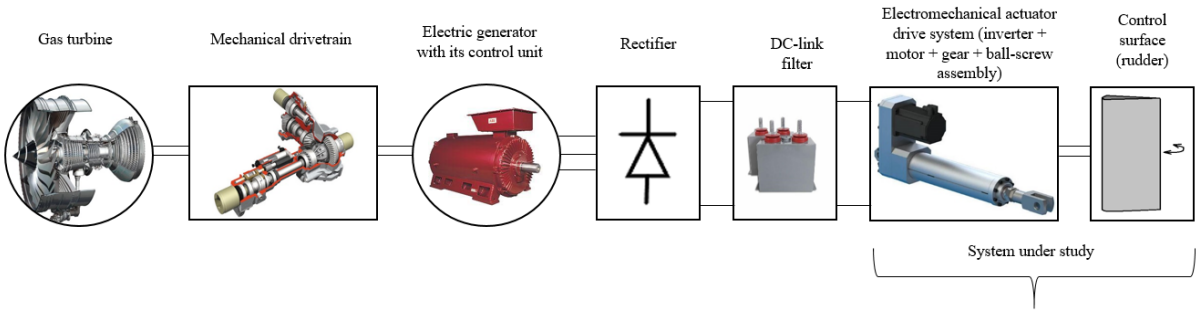

Figure 7. Schematic of EMA system in aero electromechanical system

1.2.2 Electromechanical actuator drive system

The system under study, briefed in Figure 7, is depicted in more details in Figure 8. It consists of a three-phase voltage source inverter used to drive the electromechanical conversion device, which is the PDD. A suitable coupling connects the PDD to the ball-screw, which actuates the rudder surface.

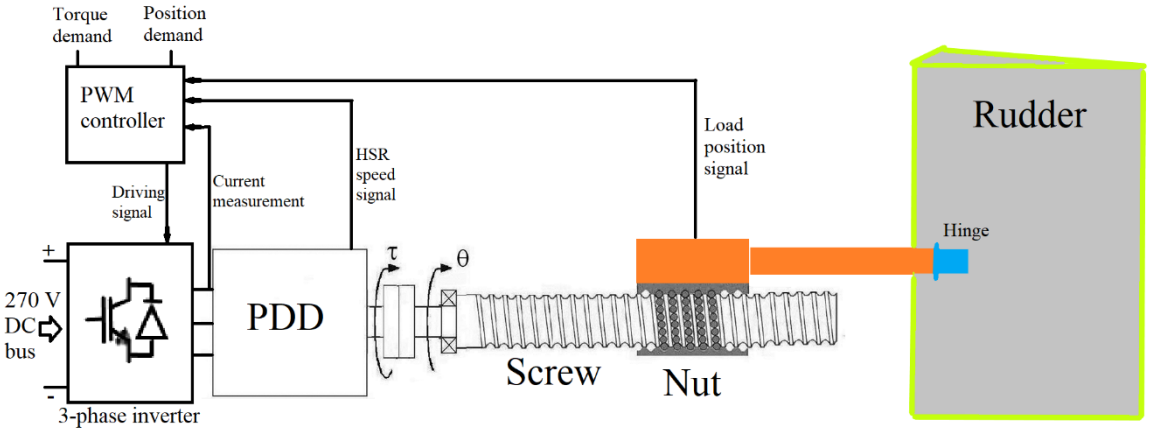

Figure 8. Aero control surface EMA system

1.2.2.1 Pseudo Direct Drive (PDD)

The electromechanical actuator, in this project, is used to actuate the rudder, which is the primary flight surface that produces yaw. A high actuation force is required against the aerodynamic load so a substantial amount of torque must be provided. Pseudo direct drive (PDD) offers a compact topology where a motor and a magnetic gear are mechanically and magnetically integrated within a single unit [16]. In [8], PDD is used for aircraft primary flight control surface.

1.2.2.1.1 Construction of PDD

PDD is a magnetic gear integrated with a PM motor in one package. Implementing a PDD will result in a simpler configuration due to removal of at least one mechanical gear stage [8]. In [8], the PDD is

employed to actuate the ball screw. The construction of PDD is presented in [17]. It is composed of three rings; high speed rotor (HSR), low speed rotor (LSR) and the permanent magnets ring segment. Figure 9 shows a schematic of the topology proposed for this project. In this topology, HSR and LSR rotate in the same direction [17].

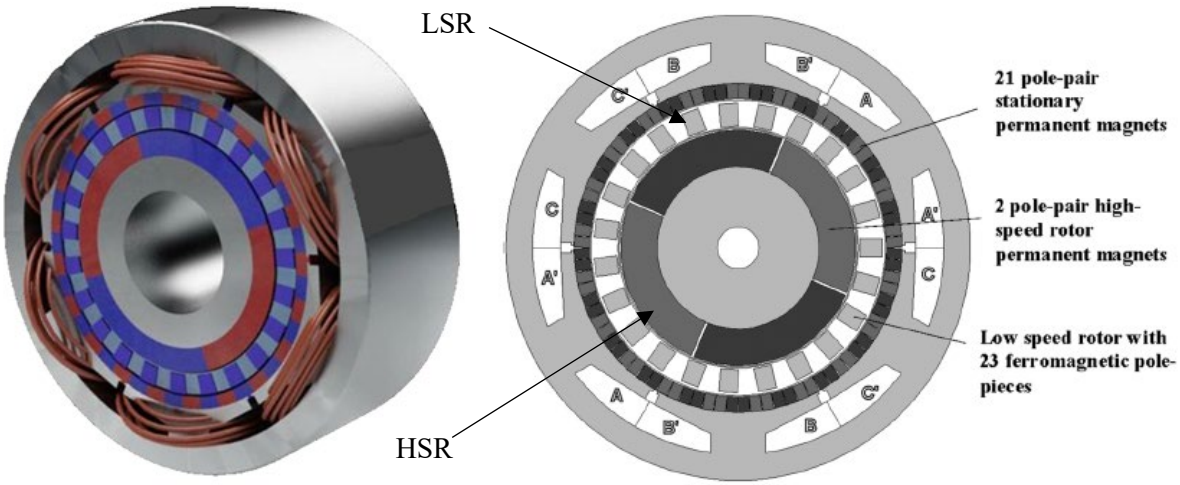

Figure 9. PDD cross-section view [16]

The inner ring (HSR) and the outer ring (stationary) are made of rare earth magnets. Lower number of magnets are used for the inner ring whilst a higher number of magnets are employed for the outer ring. The outer ring is joined to the inner side of the stator bore. The stator contains the windings that produce the stator flux as a result of stator windings current. Further, the middle ring (LSR) is composed of ferromagnetic pole-pieces. The HSR and LSR are supported by bearings [17].

1.2.2.1.2 PDD principle of operation

Principle of PDD operation is based upon two stages; torque production stage and torque transmission stage. Torque production stage contains two elements; stator windings and HSR PMs. This is shown in Figure 10 (a). The figure outlines the components in this stage as Inner Permanet-Magnet Array (IPMA) and Slotted Lamination Pack (SLP). On the other hand, torque transmission involves HSR PMs, outer PM segments array and ferromagnetic pole-pieces. This is shown in Figure 10 (b). The figure outlines the components in this stage as Outer Permanent-Magnet Array (OPMA), Intermediate Annular Pole-Pieces (IAP), and (IPMA) [20].

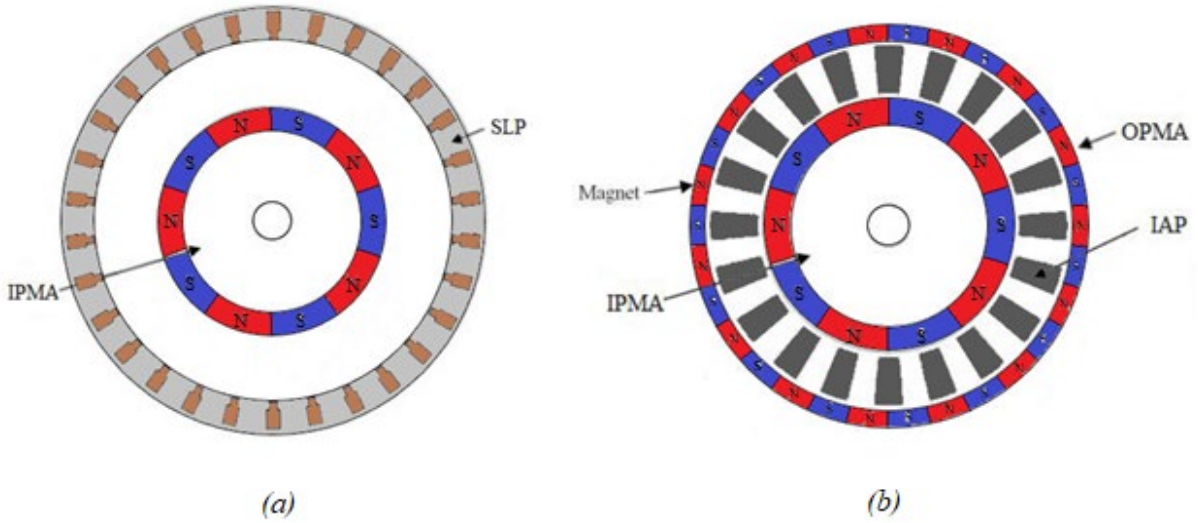

Figure 10. (a) Torque production stage (b) Torque transmission stage [20]

The stator windings are supplied with a three-phase current to produce a three-phase stator flux, which has its field axis. The inner ring (HSR) contains permanent magnets, which produces a purely radial sinusoidal flux in the air gap close to the stationary magnet array ring. The rotor flux also has its field axis. Electromagnetic torque is produced as a result of interaction between rotor and stator fields during their continuous efforts to line up. Torque is, therefore, proportional to the product of such field strengths and also is proportional to $sin(\delta)$. Where δ is known as the torque angle or the power angle, which is the angle between both fields [20].

Figure 11 provides a schematic of stator and rotor fields trying to line up and interact resulting in torque production. It is important to mention that the stator and HSR PMs contain the same number of pole-pairs [20].

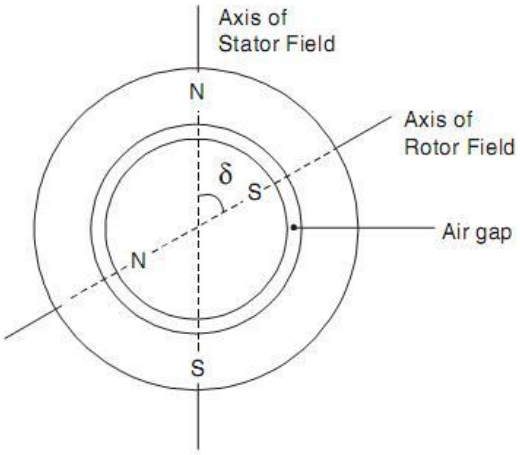

Figure 11. Stator and rotor fluxes [20]

To produce toque, number of pole-pairs on stator and rotor must be equal, otherwise net torque is zero [20]. From this particular concept, the idea of flux modulation becomes the responsible mechanism for creating flux densities harmonics [20].

Upon the rotation of the HSR PMs, a purely sinusoidal rotating flux is created, which becomes modulated by virtue of the ferromagnetic pole-pieces. The modulation, essentially, splits the flux and makes it look like as it is a flux that matches the number of stationary PMs array pole-pairs. The interaction between the modulated flux and the stationary PMs array flux yields in torque to be transmitted to the LSR [20].

The permeance of the ferromagnetic pole-pieces modulates the HSR PMs flux and results in other two space field harmonic components; beside the fundamental component. The fundamental component has the speed of the HSR and is the component that interacts with stator winding flux. The other two harmonic components have different angular speeds. Yet, one component produces a higher flux density than the other and hence it is chosen to be the one that interacts with the stationary PM array flux [20]. For instance, in this project, HSR pole-pairs are 4, number of pole-pieces is 31. The magnetic array within the stator bore can be either 35 or 27 but the 27 is chosen since it will interact with the higher flux density harmonic component. Therefore, number of stationary PM array, p_l, can be given by Equation (1) [20].

$$p_l = n_s - p_h = 27 \tag{1}$$

where p_l is the number of stationary PM array, n_s is the number of pole-pieces, and p_h is the number of HSR pole-pairs.

The magnetic gear ratio, G_r, can be calculated using Equation (2).

$$G_r = \frac{n_s}{p_h} \tag{2}$$

Figure 12 shows the HSR radial flux (modulated & unmodulated) [17].

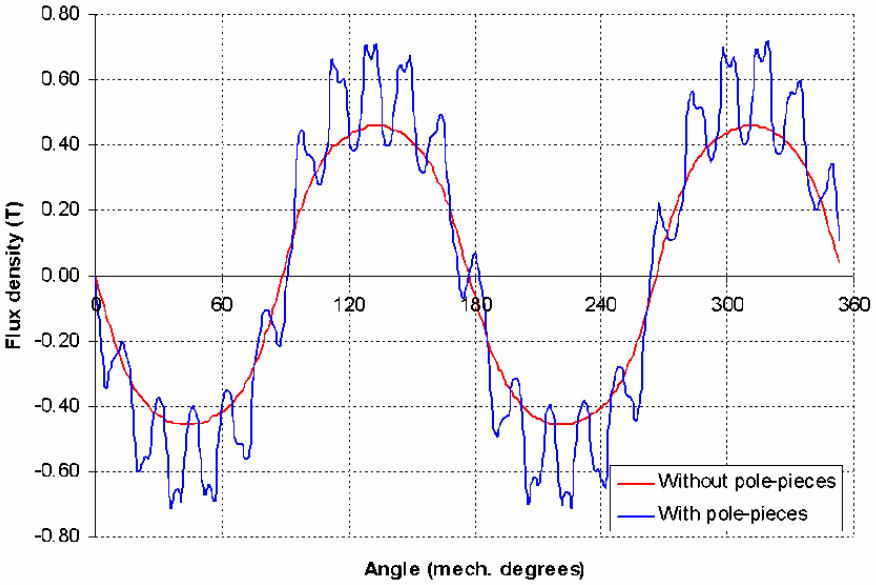

Figure 12. HSR radial flux [17]

Figure 13 shows the harmonic spectra of HSR radial flux density in the air gap with and without the insertion of the ferromagnetic pole-pieces. The two pole-pair fundamental component is the one that interacts with the stator winding flux to produce electromagnetic torque. But, the 21 pole-pair (presented according to parameters in [17]) is the component that interacts with the magnet array of the stationary ring to transmit torque from HSR to LSR [17].

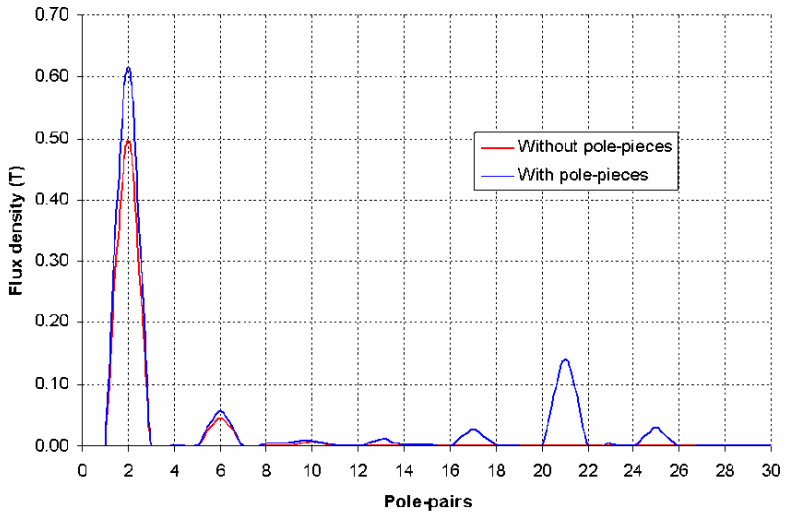

Figure 13. Harmonic spectra of HSR radial flux density [17]

1.2.2.2 Ball-screw

Ball-screws are essentially employed to convert a rotational motion of a motor, for example, into a linear motion. They are used in various applications, such as industrial automation, where ball-screws are used to move workpieces, and used as feed drives in machine tools [22], for example. Figure 14 illustrates a typical ball screw drive, where in this case the screw shaft is coupled to the driving motor

shaft via a coupling. The screw itself is supported by bearings. The rotation of the screw, results in the linear motion of the nut.

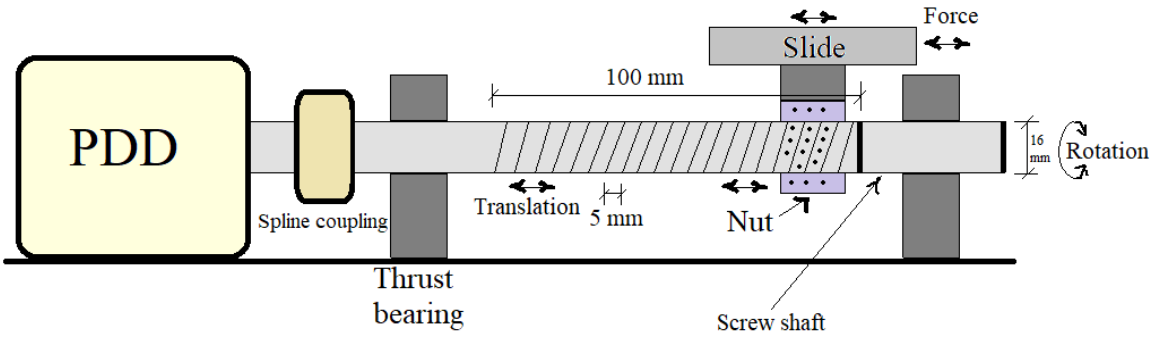

Figure 14. Schematic drawing of ball-screw drive

The amount of linear travel with respect to motor rotation is governed by transmission ratio, γ, which is defined by [22]:

$$\gamma = \frac{\lambda}{2\pi} \approx 0.0008\ m/rad \tag{3}$$

where, λ is known is the screw lead, which is the linear distance travelled for one revolution [23]. This is different to the screw pitch, Λ, which is the linear distance between two adjacent threads [23]. Figure 15 shows the difference between screw lead and pitch in a single-start screw and a triple-start screw. The screw implemented in this project has a single start and hence pitch equals lead.

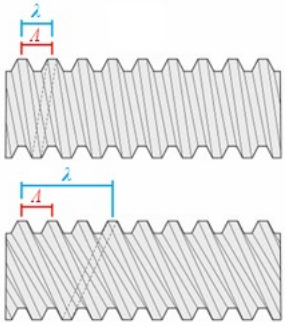

Figure 15. Lead vs pitch of screw [24]

1.2.3 Dynamics of EMA assembly

In ball-screw assembly, kinetic energy is stored in motor, slide and screw. On the other hand, potential energy is stored in screw, bearings and nut [25]. The energy is substantially dissipated in bearings and joints. Many issues emerge during operation of ball-screw drive system. An abstract issue is that system tends to vibrate during operation [26]. The influence of resonance on performance is a function of the damping within the system [25]. Also, it is reported that variation in slide position changes the screw effective length, which alters the screw stiffness. This, in turn, is said influences the system dynamics and may limit the required performance [26].

Resonant frequencies and mode shapes

For a ball-screw drive, system can be characterised by three main vibrational modes [26] [27] [28]. The axial mode is the translational oscillation of the table and load. This is significantly lower than the torsional mode for most technical applications [28] [26]. The torsional mode is the angular deformation of the rotational system. The flexural mode can be neglected provided proper mounting of the assembly is adopted. Flexural/lateral shape of vibration occurs only when very long and slender ball screws are used [22].

In fact, the mode of each resonant frequency comprises axial and torsional components [28]. For example, the first mode is mainly axial but the second is mainly torsional. The level of coupling between such components is largely affected by the transmission ratio [28]. Therefore, certain parameters affect a mode shape at a particular resonance. In addition to the dependency of a mode shape, at a particular resonance, on certain parameters, the resonant frequencies can also be affected by certain parameters, the axial and torsional resonances and screw dynamic behaviour are a function of system physical parameters and operating conditions [26] [28].

Operating conditions

As for operating conditions, two main variables stand out; nut position and load mass [26]. Load mass and position with respect to the motor end can influence the equivalent stiffness and inertia of the screw. Effects of nut position is discussed in literature, since the axial resonance shifts with nut position [11]. The resonant frequencies decrease to their lowest values when the load is placed at the farthest end from motor [22] [25]. This is because variation of load position causes variation in the effective loaded length of the screw, which in turn changes its effective torsional stiffness and axial stiffness. Furthermore, a change in load position results in variation in system mass/inertia distribution [22]. In fact, all resonant frequencies are dependent on nut position [22]. Furthermore, the equivalent mass is an important parameter since it is associated with actuated load and considerably affects the second resonant frequencies [22]. It is suggested that a model has to be validated for different operating conditions [22].

Design parameters

Geometrical dimensions of the screw shaft include diameter and length, which affect the rigidity of the screw. During operation, the friction between the screw and nut generates heat that causes an expansion in the screw. As a result of screw expansion in length, screw stiffness decreases and hence the total axial stiffness of the mechanism decreases [11]. In addition to screw rigidity, important parameters such as screw mass and inertia are also direct function of diameter and length (more detail can be found in Section 3.2.2.5 and Section 3.2.2.6.

Lead of the screw defines the transmission ratio, which describes the coupling between axial and rotational motions. Therefore, transmission ratio determines the degree of interaction between the axial

and torsional resonances. With a higher transmission ratio, the influence of rotational resonances on axial resonances increases [26]. On the other hand, lower transmission ratio shows decoupled axial and torsional resonances. In such a case, equivalent load mass has more significant impact on axial resonance [26]. According to [28], low transmission ratio is preferred if the position is fed back from the motor rotor, where a notch filter can be used to eliminate this negative effect.

The flexible modes of the system, particularly the first resonance, limit the bandwidth of the closed loop drive system and this causes speed limitations [13] [12] [29] [30] [27] [25] [26]. This limitation is specified to be strongly dependant on the first resonance if the axial positon of the carriage is fed back to close the control loop. For this reason, in such a case, adaptive control strategies are recommended to obtain a higher bandwidth [28].

1.2.4 Conventional modelling methodology in aero EMA system

Stability of aircraft power system is studied in [2]. This study is fully detailed in [21]. The study investigates actuator dynamics effects on power system stability under various system parameters and operating conditions. The investigated system parameters incorporate system frequency, dc-link voltage filter bandwidth, and speed loop natural frequency. Operating conditions comprise actuator load torque. Actuator load torque is increased in steps and it is estimated and observed that at a certain actuator load torque power system destabilises. Figure 16 illustrates instability in the DC-link.

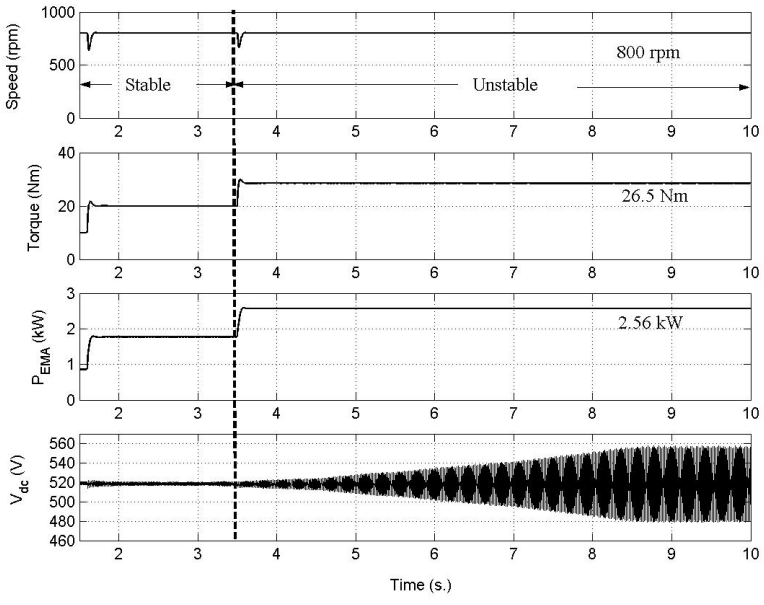

Figure 16. Power system instability due to increased actuator load torque [2]

It is concluded that actuator dynamics, such as actuator load torque, is capable of destabilising the power system. A relevant part here is that the actuator is modelled as a single inertia. This means that all the

actuator structure dynamics are neglected and thus actuator parts are lumped with the motor. Figure 17 shows how everything is lumped with the motor inertia.

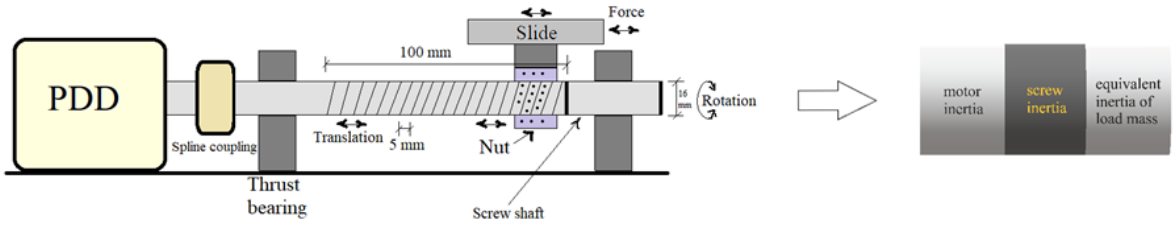

Figure 17. Lumping actuation system with motor inertia

MEA power system stability, under parameter uncertainties, is investigated in [31]. Since many changes may occur in load demand and environmental conditions, it is argued that such changes can affect other parameters of which system stability is dependent upon. Thus [31] proposes a robust model to be used in stability analysis. In a similar manner to [2] and [21], the actuator, in [31], is modelled as lumped single inertia. A similar study is presented in [32] that aims to develop a modelling technique to analyse MEA power system stability under unexpected operating conditions. Again in this paper, the actuator is modelled as a single inertia. Further, aircraft EMA models are suggested in [33]. The work is more focused on the electrical side in the power system but the mechanical part of the actuator is modelled as a single inertia and hence actuator structure dynamics are neglected.

In [8], a Pseudo Direct Drive (PDD) electrical machine is implemented, as an electromagnetic conversion device, for aircraft rudder actuation. Results are shown for various displacements and torque demands. However, the linear actuator is modelled to be lumped with the PDD low speed rotor inertia (LSR). Also, in [34], PDD is implemented for primary flight control surface actuation. Yet, the paper is rather focused on the design characteristics and performance of the PDD. More importantly, when the actuator is considered, it is assumed as a single inertia.

Reflecting load inertia and lumping it with motor inertia is a traditional method and a common practice, which has many drawbacks [35]. The behaviour of each component of the drivetrain cannot be separately examined hence their respective effects is not considered. Further, interaction between components is also neglected. Also, when one component is changed, the whole model needs to be altered accordingly [35]. For such reasons, it is thought that such technique of modelling is inaccurate [35].

For feed drives, the vibrational mode is mainly influenced by the ball-screw assembly [26]. A model describing the dynamics and vibrational modes of the screw assembly is needed to help in machine design and also controller tuning [28]. High control bandwidth requires higher order plant models as well as a better understanding of the system dynamics [27]. However, it should be always considered

that the number of inertia, spring-damper system increases the model computation time exponentially [1].

A model representing aircraft EPS behaviour, under various flight conditions, is a pre-requisite for securing a reliable EPS structure [2]. Further, to be able to efficiently implement advanced control strategies, the mechanical system must be fully appreciated and, in turn, an accurate model must be developed [26]. From all of the above, it can be emphasised that ball-screw dynamics must be known to design a controller that fulfils the specified requirements. Therefore, a point needs to be confirmed regarding the sufficiency of modelling the mechanical parts in EMA as a single inertia. The way to prove this is to look at ball-screw models and dynamics employed in other applications.

1.2.5 Models of ball-screw assembly

Two main qualities must be regarded when modelling any system; simulation time and accuracy. A high level of fidelity of a model will increase the computation time. Similarly, too short simulation time requires a too simple model that excludes many of the crucial dynamics and characteristics. Hence there should be a trade-off between the mentioned elements. Many publications are available for the model and control of ball-screw drives. The approach to model ball-screw can be broadly classified into three main categories.

- Finite Element Method (FEM).
- Discrete model; this is when all parameters are modelled as physically lumped parameters [26].
- Hybrid model; this is sometimes referred to as distributed-parameter model [22]. This model is where some parameters are physically lumped but other parameters are considered to be continuous [26]. In this type of modelling, a mixture of discrete and continuous formulation elements are used [26]. The term continuous is used to indicate that continuous deformation, rotation and torsion of the ball-screw shaft are approximated using some form of a finite series expansion. The process of approximation uses basic functions, which are continuous functions which are required to satisfy the geometric conditions of the system [22].

1.2.5.1 Finite element method

A model of the ball screw using FEM is presented in [36]. The paper considers the nut movement effect on the ball screw dynamic behaviour. FEM is also applied in [37] to model the entire machine frame including the drive structures and analyse the vibration behaviour of the entire mechanical system. Moreover, FEM is used in [26] to build Timoshenko beam to represent the screw shaft. FEMs are usually employed to observe parameter spatial distributions such as stresses and deformations and when the complex behaviour of the ball-screw is considered [26].

This method, according to [38], results in a large number of resonance modes, but it is relatively slow. To overcome such problems, simpler techniques are used to obtain simple models that highlight the

relevant characteristics and show the dominant effects of the ball-screw assembly, since the relevant dynamics are mainly influenced by the first axial and rotational modes [26].

1.2.5.2 Discrete models

The lumped-parameter model is referred to, in [35], as the traditional modelling method. Many research papers simplify the ball-screw model by lumping it with the load and motor inertia. For instance, [12] introduces some issues of ball-screw used in industrial applications. It also proposes fuzzy logic controller to overcome such issues. In the paper, the motor inertia, coupling inertia, ball screw inertia and load mass equivalent inertia are all lumped in to represent a single inertia. This is the same modelling approach used for aero EMA system, as mentioned above. In [25] second-order wave equations are employed to obtain a two-degree of freedom discretised model. Two ball-screws are tested here to account for two different sizes of load.

In [26], ball-screw as feed drive in machine tools application is modelled. The discrete model assigns two rigid bodies for the screw shaft; a screw inertia for rotational motion and a screw mass for translational motion. Both motions are coupled by the transmission ratio. The torsional stiffness of the shaft is lumped with the coupling stiffness whereas the axial stiffness of the screw shaft is lumped with the axial stiffness of the bearing. Different operating and coupling conditions are investigated. The load position variation is presented by introducing a screw axial stiffness that is a function of the effective length. Results show good agreement with the experiments. However, only transmission ratio, load position and load mass are changed whilst other parameters are kept constant. Figure 18 illustrates this lumped parameter model.

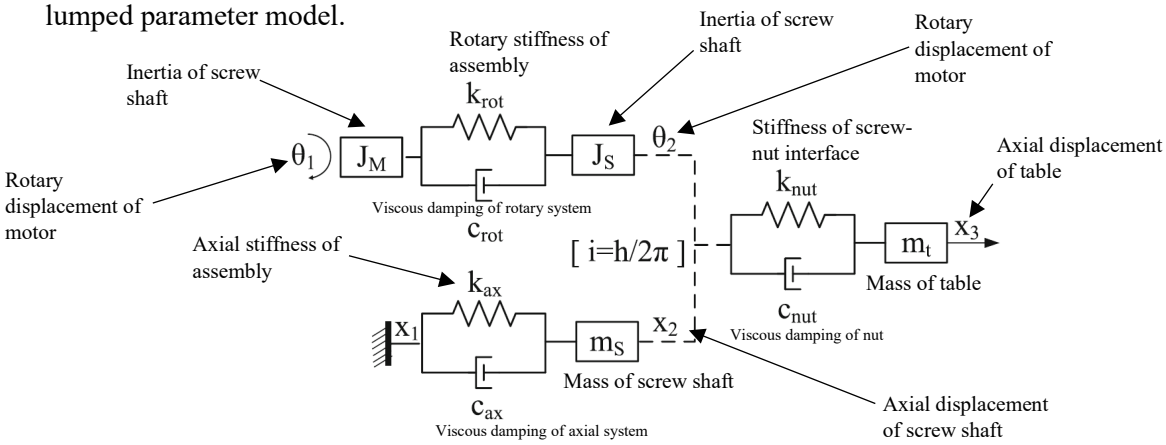

Figure 18. Lumped-parameter model [26]

Discrete models are normally simple but the hybrid models are normally more complex. Both model types are shown and compared in [26], where it is shown that both techniques yield in acceptable results, especially for the first axial resonant frequency.

1.2.5.3 Hybrid models

In this type of modelling, the screw shaft is considered a continuous element. This approach is useful when spatial distribution is important and has a significant effect on the vibrational modes. A hybrid

model assuming the screw as a continuous element and the rest of the components considered as discrete is presented in [26], as shown in Figure 19.

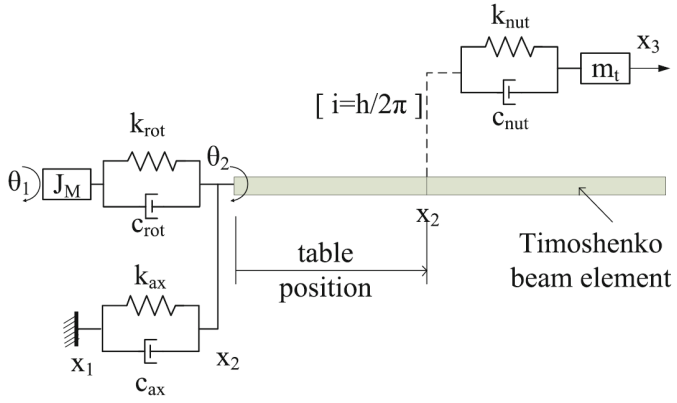

Figure 19. A hybrid model: the screw is continuous whereas other elements are discrete [26]

A similar model, has also been presented, for a ball-screw drive in machine tools applications [35]. The screw is modelled as distributed mass, inertias and stiffness while other elements are considered in a lumped form. The screw is divided into four rigid elements; three rotational and one translational. The three inertias are separated by screw torsional stiffness. One of the inertias is coupled to the translational mass through the transmission ratio. The screw translational stiffness is combined with the bearing stiffness under an equivalent stiffness. Reasonable approximation for the first two resonances are obtained. With respect to that, [35] uses a hybrid model and includes non-linear effects such as friction and backlash for the purpose of making the model more realistic.

Similar considerations, in terms of modelling the screw with distributed elements are presented in [27] [28] [22]. The distributed parameter screw dynamics are characterised using potential and kinetic energy equations. Predictions and experimental results are compared in time domain and also presented in [38], where model speed shows acceptable agreement with measured speed; with minimum error at higher speed and largest error at low speed since coulomb friction at low speed is difficult to compute precisely.

A hybrid model, introduced in [22], describes all the important dynamics of the ball-screw assembly. This hybrid model of with six-degrees of freedoms seems appropriate, since it is fairly simple to implement and exhibits sufficient accuracy. Indeed, good agreement between predictions and measurements are reported in [22], as shown in Figure 20.

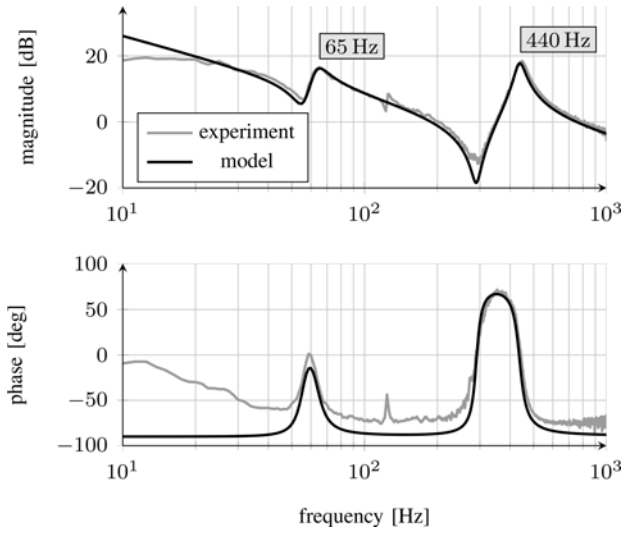

Figure 20. Frequency response of the ball-screw drive [22]

It is shown in this section, especially in Figure 20, that electromechanical actuator system has its own structure dynamics and also dynamics are closely related with system control. This forms an electromechanical system that could be affected by electromechanical interaction.

1.2.6 Electromechanical interaction

It is explained in previous sections, with respect to reported literature, that mechanical systems have structure properties. Similarly, electrical systems have their own dynamic properties. Useful power is transferred between electrical and mechanical systems using electrical machines. In reality, not only functional power is transferred but also unwanted disturbance can travel along, which may cause resonance excitation [39]. Excitation can be caused by internal or/and external means. Internal excitation may come from the acceleration and control signal [29] [27]. On the other hand, external excitation may be a result of load forces (external disturbances); such as cutting forces or unpredicted friction transients. Both excitations lead to undesired vibrations and compromise stability, which indicate the occurrence of electromechanical interaction.

Electromechanical interaction has a significant impact on mechanical elements and electrical power system stability. Additionally, the level of coupling and interaction is a function of two main factors; electrical machine power rating and controller design [39]. This study is focused on aero application. Yet, interaction is reported to involve various applications.

1.2.6.1 Interaction in land-based power systems

Electromechanical interaction occurs in land-based power systems. When series capacitors are employed for transmission system compensation, sub-synchronous currents are generated, within the generator stator windings, with a frequency that is lower than the power system frequency. Such currents cause alternating torques on the shaft, which may excite resonance frequencies of mechanical components [40]. Figure 21 shows the turbine-generator shafts which represent the mechanical system.

Subsequently, undesired excessive torques are resulted at couplings. The frequency of the alternating torques can be estimated by finding out the difference between the synchronous and sub-synchronous frequencies [40].

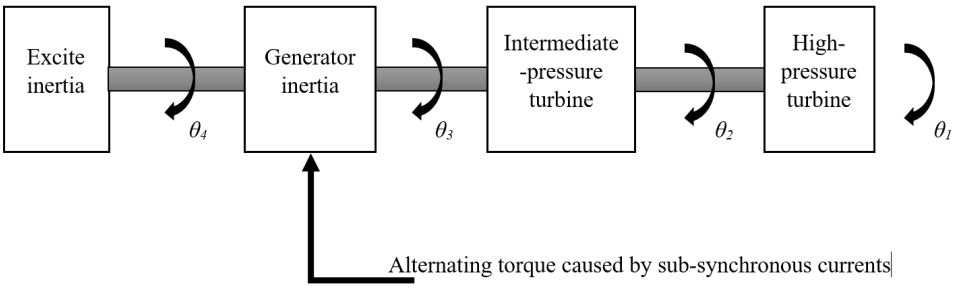

Figure 21. Model of turbine generator shaft

The bandwidth of the torque gain characteristic in this paper is defined as the range of frequencies around the resonant frequencies that when a disturbance signal is applied of a frequency that is encompassed within this range, torque gain increases to pass half the peak value. It is concluded that reinforcement of resonant frequencies, due to electrical disturbance, may occur over a large bandwidth about the resonant frequencies [40].

1.2.6.2 Interaction in wind power generation.

In [41] [42], an induction machine drive is used as a generator in wind power station. A flywheel is coupled to the generator via a shaft. The flywheel system with the generator are employed to smoothen wind farm power and also to prevent grid frequency runaway in case of a major power plant tripping. This makes the utilisation of the flywheel that has the ability to store and release kinetic energy.

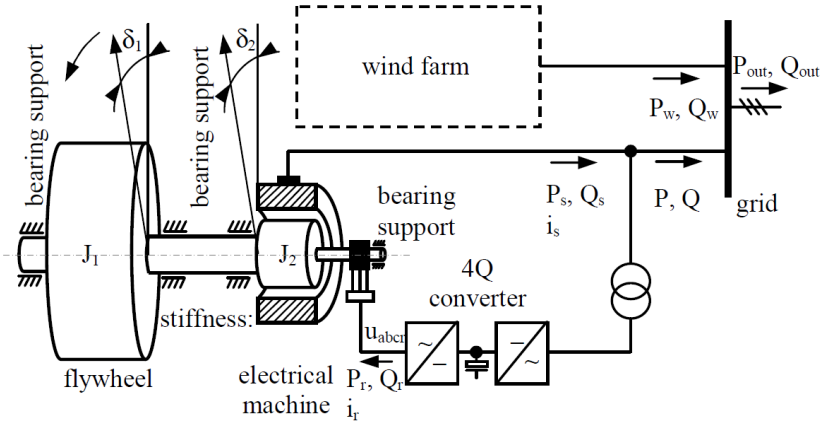

Figure 22. Flywheel in wind power generation system [41] [42]

The integrated system of the flywheel and the generator, with a shaft in between are shown in Figure 22. The formed mechanical system has its own torsional dynamics. If the generator controller is set considerably fast, negative damping may occur and lead to excitation of the torsional resonance, which cause electromechanical interaction [41] [42]. It is suggested that natural frequency of the mechanical

system and generator control bandwidth must be coordinated. The torsional vibration, in [41] [42], is mitigated by controller design and also mechanical system design. It is emphasised that shaft stiffness is increased to be distinct from the generator controller bandwidth.

1.2.6.3 Marine applications

Interaction is shown to be found in integrated full electric propulsion (IFEP) system [43] used in marine applications. A common set of generators are exploited to supply propulsion and auxiliary loads, as shown in Figure 23.

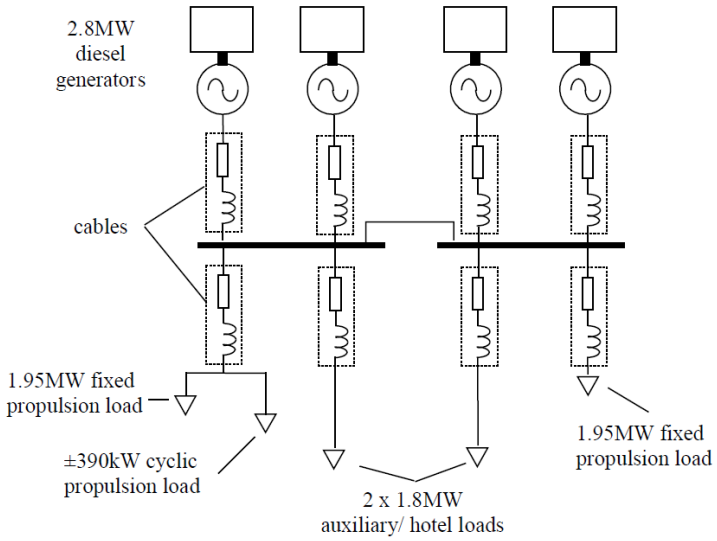

Figure 23. IFEP system model with varying propulsion load and also auxiliary loads [43]

Disturbance load with varying frequencies is applied, to present propeller movements and manoeuvring. Such disturbance excites resonances and cause oscillations in engine output power, electrical system frequency and voltage. This leads to deterioration in power quality hence it is concluded that electromechanical interaction is crucial to consider [43].

To avoid interactions, measures are proposed starting from properly modelling the mechanical system so important dynamics are defined. When disturbance with critical frequencies is expected, all generators should be operated to boost system inertia and robustness. However, this does not come in the favour of system efficiency [43]. Yet, this option is not preferred in aero applications since weight is a vital constraint.

1.2.6.4 Industrial applications

Electromechanical interaction issues are experienced in many industrial applications such as rolling mills. Various sections of paper machine is investigated in [44] [45]. Such a mechanical system consists, typically, of motor, a gear, jackshaft, and couplings (Figure 24). Elasticity of the system mainly result from jackshafts since they are the most elastic elements within the drivetrain. Therefore, torsional oscillations are in essence caused by them. This happens when changes occur at load or reference. Extra

elasticity is also added by the gear. In addition, gears may introduce backlash, which has effects at low load operation and may trigger torsional oscillations [44] [45].

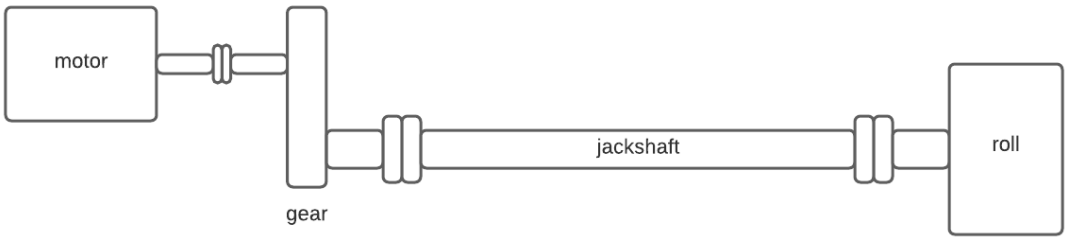

Figure 24. Typical rolling mill drive system

According to [44] [45], it is important to consider resonant and anti-resonant frequencies since they determine the speed controller bandwidth to prevent instability problems. Torsional resonance can be suppressed using mitigation techniques; drivetrain design and appropriately-tuned controller.

Jackshaft is suggested to be hollow to boost shaft stiffness, for a given weight, so associated resonance frequency is increased. Further, speed controller is suggested to be set to critically damped response to prevent overshoot that produces gear backlash. In addition, it is recommended to use ramp reference commands instead of step reference commands. This is because transient response to step demand usually contains oscillations. These oscillations die away promptly depending on the damping amount associating with a particular frequency. Improper setting of controller will cause these oscillations to persist [44] [45].

Interactions could also occur in many drives within cement industry drives; such as, single/tandem-motor fan drives and impact crusher drives [46]. Sources of resonance excitation can be classified, with respect to where they originate, into four categories; excitations due to electrical supply system, excitations due to motor drive system, excitations caused by mechanical system, and excitations caused by load system. Disturbance may occur at the interface variables, shown in Figure 25, leading to oscillations [46].

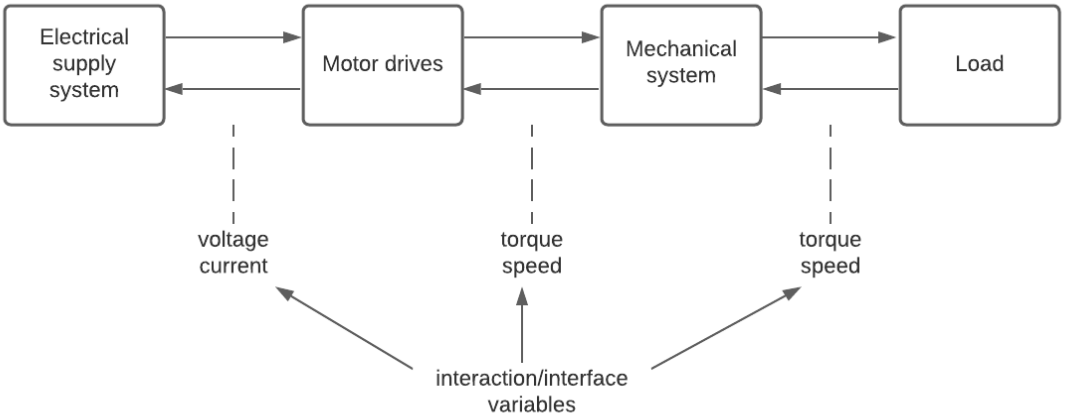

Figure 25. Major drive system components and interaction variables

Interaction occurs between electrical drive systems and its control with the mechanical structure, which has resonance characteristics. Further, the level of interaction is decided upon the relationship between the interface variables illustrated in Figure 25. Such relationship determines how electrical variables respond to mechanical speed oscillations. The magnitude and phase of such response are a function of certain components; such as, the frequency of oscillations, motor type, supply system parameters, and control system. Electromechanical interaction results in different sort of consequences. For instance, it may dampen speed oscillations and it may increase them. In certain circumstances, interaction could cause system instability by creating a continuous oscillations at a resonant frequency [46].

1.2.6.5 Aero applications

In [39], power is transferred from an aero gas turbine to an electric generator through series of shafts and gears, which make up natural frequencies. In turn, the generator supplies various electrical loads. The electromechanical system is shown in Figure 26.

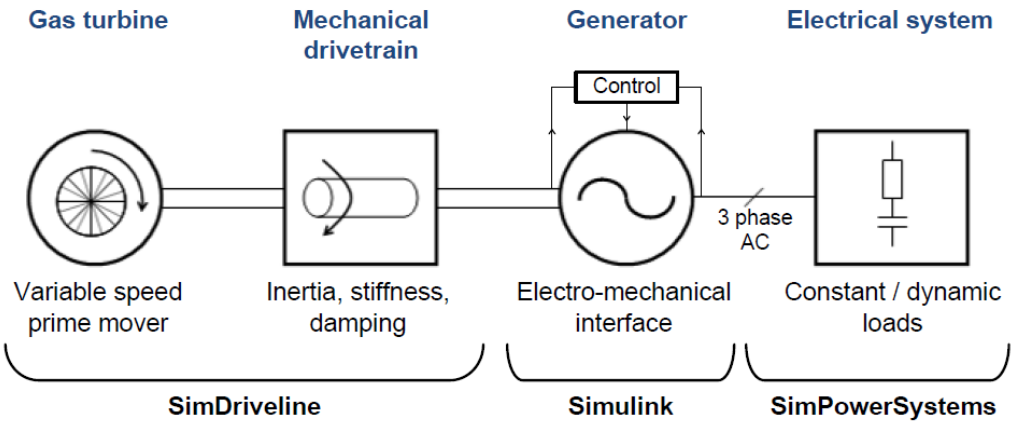

Figure 26. Schematic of aero electro-mechanical system

Variation in electrical load is seen from the mechanical drivetrain side as a torque disturbance that causes speed vibrations, which return to the electrical power network through the generator. Vibration continues unless system damping is sufficient. It is concluded in [39] that transients in the electrical network can excite resonances in the mechanical network. Also, low amplitude pulsating electrical load (like a radar) represents an electromagnetic torque, which causes continuous torsional oscillations.

According to [39], many challenges are associated with the aero generation system. For instance, weight limits lead to usage of lower stiffness shafts and that lowers the damping in the mechanical system. Also, the prime mover speed may vary over a certain range and, in turn, the generator frequency could also be affected by that.

For the case study, electrical power is converted into mechanical power by means of electrical motor, which is PDD in this case. So PDD represents the interface that couples electrical and mechanical domains, which are found to have resonance modes.

1.2.6.6 Electromechanical interaction suppression

To ensure safe operation of the system, system dynamics, expected disturbance frequencies and controller must all be considered concomitantly. Further, it is also recommended to ensure minimum backlash if gearboxes are employed. The influence of resonance on performance is a function of the damping within the system [25]. Measures taken to suppress electromechanical interaction can be said to fall into two categories, passive damping and active damping.

Passive damping

This method is based on repositioning of resonance modes through design [39] [41] [42]. That is, resonance modes are designed to be separated from disturbance frequencies. This effectively adds more mass and stiffness to the system. This can be effective. Yet, this is not welcomed in aero applications since weight is a constraint [39].

In the case of marine application presented in [43]. Some measures, which might be effective to reduce interactions, are proposed. Essentially, resonant frequencies must be well defined through developing an accurate model. When disturbance with critical frequencies are expected, all generators ought to be operated to boost system overall inertia. This enhances robustness against disturbance. Yet, this comes with a price of efficiency decrease.

Active damping

Control scheme disturbance rejection can be an effective way to suppress interaction. For instance, it is possible to provide positive damping by reducing control gains [41] [42]. Active damping through the generator controller can act like a frequency filter, which limits the transfer of disturbance between the

electrical and mechanical domain. This must be done carefully so as not to impair power quality on the electrical network [39].

It is reported in [29] that pre-filtering of trajectory commands or notch filtering control signals help reduce internal excitations. Filtering control signals help reduce internal excitations.

Moreover, energy storage system with practical converters and control systems might be used. The idea is, when system is subject to a varying load, to charge and discharge the storage system to increase stability and improve quality of electrical power (frequency and voltage) [43].

1.3 Scope, aims, objectives, contribution, and layout of the Thesis

In this section, thesis overview is briefly introduced along with aims and objectives.

This thesis extends the research study conducted on stability of aircraft power systems presented mainly in [33] and [2]. It is deduced that aircraft power system stability can be highly affected by actuator dynamics, such as load torque. Other actuator dynamics, such as structure resonance, are neglected. However, such EMA system is proved to have its own resonance dynamics [22] [47]. Incorporating the mechanical system with the electrical power system forms an electromechanical system, which may be susceptible to electromechanical interaction. An example is reported in [39] and [48] for aero generation system. In such a system, the aero gas turbine drives an electrical generator through a mechanical drivetrain, which has its own resonance dynamics. It is concluded in [39] and [48] that extreme electrical loads could excite mechanical resonance resulting in an electromechanical interaction and hence power system instability.

Therefore, it is important to investigate the effect of the EMA structure resonance as to anticipate the occurrence of electromechanical interaction, which, if passed to electrical network, could lead to power system instability. For those reasons, this study is to include such dynamics and extend the model presented before in [33], [2] and [8].

Previous investigation of electromechanical interaction in aero EMA system, considering mechanical parts, has not been identified in the literature. Although actuation system load mass estimation is mentioned, EMA system structure resonance dynamics for various aircraft sizes has also not been identified.

To bring advantage to an increased electrification the aircraft requires an uprated EMA system model. EMA system must be ensured stable to protect the electrical power network. Optimised functionality of EMA system is an integral part of a safe flight operation.

Scope of the Research

The research of the thesis discusses the modelling and stability analysis of the rudder EMA system used in MEA. The small signal stability analysis is performed assuming defined uncertainties in mechanical

components. The thesis presents simplification of effective models capable of representing EMA dynamic behaviour for stability studies. The proposed simplified model can be used to predict instability points for variations in system operating conditions or system parameters.

Aims and objectives

The aims of the study are:

- To suggest a way of modelling EMA that is accountable for predicting electromechanical interaction to be used when control is designed.
- To check the validity of the suggested generic modelling methodology for various aircraft sizes.

The objectives of the study are:

- To investigate mechanical system dynamics:
  - To model the ball-screw system with the load in full details.
  - To find out resonant modes.
  - To identify crucial dynamics and obtain a reduced-order model accordingly.
- To investigate dynamics in larger aircraft:
  - To estimate equivalent load masses.
  - To estimate the required sizes of EMA.
  - To identify dynamics across the various range of sizes.
- To identify interaction between electrical and mechanical domains:
  - To integrate the reduced order model with the electrical system.
  - To carry out small signal sensitivity analysis.
  - To identify how key mechanical system dynamics may interact with control.
  - To validate findings experimentally.

Contribution

This thesis proposes a modelling methodology for MEA EMA system, to be considered when control is designed. Emphasis is placed on the comparison between the proposed models and the conventional models, which neglects key components. The proposed modelling methodology is proved to be valid for a wide range of aircraft. This is confirmed by carrying out aircraft rudder and EMA sizing using curve fitting equations, which could be used by other researchers. Extensive analysis is carried out on the integrated electromechanical system. Significant findings are pointed out to show occurrence of electromechanical interaction between the mechanical structure of the actuation system and the position, speed, and current control loops. The impact of such interaction is shown to be propagated to the electrical system causing instability. An experimental test rig is used, employing Hardware In the

Loop (HIL) technique, to emulate the actuation system. Results validate the modelling techniques and electromechanical interaction analysis.

Thesis layout

Chapter 1 aims to provide an introduction about the importance of transitioning towards electric aircraft. EMA system elements are introduced. A literature review is presented to show connection to previous work and to point out the research gap. Also, previous work for modelling ball-screw systems is presented to show that such system has its own dynamics. Also, previous work is presented with respect to electromechanical interaction phenomenon occurring in various applications, and this enforced the need for the research.

Chapter 2 aims to suggest a way of modelling MEA EMA. System specifications are given and the conventional model of MEA EMA is implemented to be compared with the proposed models. To investigate the mechanical system dynamics, which are ignored in the conventional model, the ball-screw system is modelled in more detail. Eigenvalue and eigenvector analysis is carried out to determine the structure resonance properties; resonant and anti-resonant frequencies. Relevant dynamics are highlighted and based on that simplified models for the MEA EMA are proposed.

Chapter 3 aims to confirm whether the models proposed in Chapter 2 are generic and can be used for a wide range of aircraft. For a various aircraft sizes, rudder is sized to obtain the equivalent load mass. Further, EMA system is sized for the same aircraft types. Similar analysis carried out in Chapter 2 is performed for the larger aircraft to assess actuator dynamics. It is proved that the modelling methodology suggested in Chapter 2 is valid for big range of aircraft.

Chapter 4 aims to predict electromechanical interaction occurring in MEA EMA system. The reduced order model, suggested in Chapter 2 and proved to be generic in Chapter 3, is integrated with the electrical system. Small signal sensitivity analysis is carried out to see impact of mechanical system parameters upon system stability. Electromechanical interaction is identified, between electrical and mechanical domains, by highlighting the relationship between structure resonance and position, speed and current control loops. Time domain simulated work is carried out to prove frequency domain theoretical findings.

Chapter 5 aims to validate simulation results. PDD and its drive is used to represent the electrical motor and the gearing stage used to drive the ball-screw assembly. Servo motor drive is used to emulate the behaviour of the ball-screw and the load by applying a reaction torque on the PDD. The torque signal driving the servo motor is generated using dSPACE real time platform, which contains the reduced order model suggested in Chapter 2.

Chapter 6 aims to conclude the work done in previous chapters and to highlight significant findings and contribution.

Chapter 2 Modelling of aero EMA system

2.1 Introduction

Stability of aircraft power system is studied in [2]. It is found that certain actuator dynamics, such as excessive load torque, may destabilise the power system. Other important actuator dynamics such as actuator structure modes are not found to be reported. Literature reports that structure modes of mechanical systems could be excited, by various reasons, leading into instability. It is sensible to zoom into this to identify actuator structure modes. This helps decide how many degrees of freedom are adequate to model aero EMA system suitable for stability analysis.

The purpose of this chapter is to determine a modelling methodology of electromechanical actuators for aircraft rudder applications. Aim is achieved by analysis of existing model using eigenvalue problem with a view to reducing model order. This chapter is establishing the background for this thesis contribution.

In this chapter, a general overview of the system specifications is given and also how EMA system is conventionally modelled in aero application is presented. Simplification assumptions are stated. Further, abstract time simulation is presented to show whether such a simplified model is adequate subject to extreme loading conditions. Then, EMA is modelled in more details to highlight relevant dynamics. This is a key that allows model simplification.

2.2 System Configuration

2.2.1 System structure

This study is based on an actuator to be used in a business jet, which is light to medium aircraft. The business jet is specified in Electro-Mechanical Magnetic Actuator System (EMMAS) project, which is a project of which the University of Sheffield has carried out in cooperation with Magnomatics Ltd and Triumph Group. Many studies were presented on this business jet such as Development of Fault Tolerant Electronic Drives. The maximum take-off weight (*MTOW*) ranges from *7000* to *10000 kg*.

As mentioned in literature review, mechanical power is extracted into an electrical generator from a gas turbine engine. Three-phase electrical power is transmitted through three-phase transmission line. Three-phase is converted into dc by virtue of a rectifier. A dc link filter is then employed to smoothen the dc voltage.

The EMA drive system consists of a motor drive system, a gear, and a ball screw that actuates the rudder. For many advantages mentioned in literature review, the mechanical gear and electric motor are replaced with PDD. The PDD integrates the electric motor and a magnetic gear inside a single package. The PDD is driven by a three-phase voltage source inverter. The DC bus voltage is $\mp 270\ V\ DC$, which is shown at the inverter terminals. The configuration of the actuation system is shown in Figure 27.

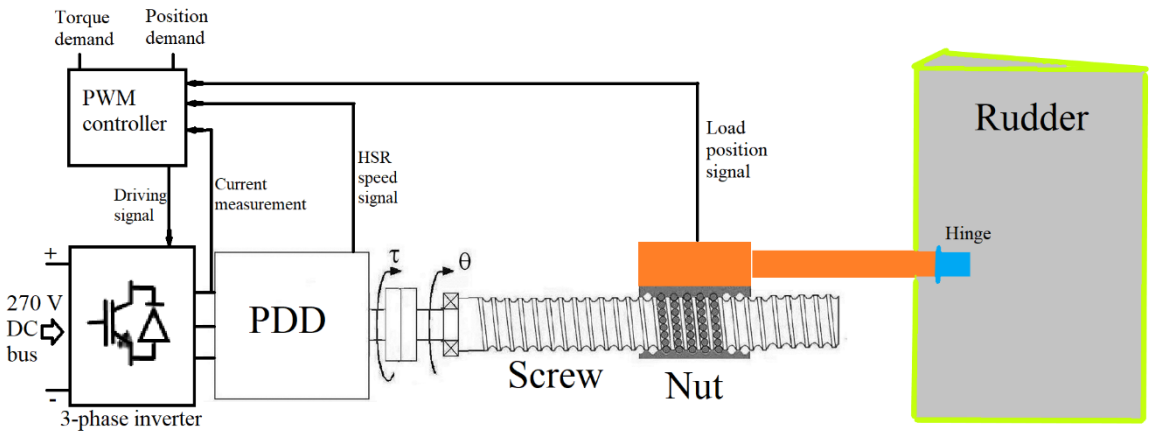

Figure 27. EMA drive system and aerodynamic load

The three-phase voltage source inverter (*VSI*) consists of three legs; each leg corresponds to a specific phase voltage and contains two switches of which each is in parallel with a freewheeling diode. The two switches on a leg can only have complementary switching status. The neutral point on the DC bus shown (*point* N_n), which represents the reference point of the output voltage for each phase. For example, the output voltage for phase A is v_{an} and it is measured from point A to the common point N and so on. Therefore, two main factors determine the output voltage of the inverter; namely, the DC voltage and the switching status [49]. In simulation, the switching is assumed ideal. However, in practice, there should be a dead time between the switching of the two transistors on each leg. Figure 28 shows three-phase VSI.

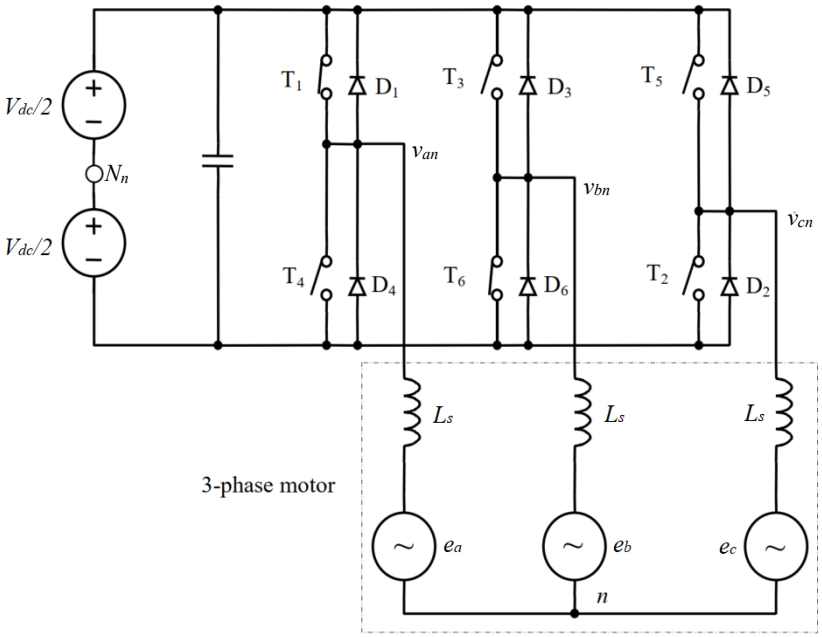

Figure 28. Three-phase voltage source inverter [49]

where *n* is the star point of the PDD stator windings, and *D* denotes the diode.

2.2.2 Parameters

The technical specification for the system requirements, electromechanical actuator and the PDD are given for the EMMAS project. All parameters are shown in Table 1, Table 2 and Table 3.

Key system requirements

Table 1. Key system requirements

parameter	*symbol*	*value*	*units*
Surface stall torque		*900*	*Nm*
Surface Max Stroke		*30*	*°*
Surface Min Stroke		*-30*	*°*
Nominal Voltage	V_{dc}	*270*	*V*
Max Voltage		*285*	*V*
Min Voltage		*235*	*V*
Link Arm Length	L_a	*0.1*	*m*
Surface Inertia	J_r	*0.2963*	kgm^2
Equivalent Load Mass	M_L	*29.63*	*kg*

EMA parameters

Table 2. EMA parameters

parameter	*symbol*	*value*	*units*
Actuator Stroke	S	*0.1*	*m*
Ball screw diameter		*0.0197*	*m*
Ball nut diameter		*0.024*	*m*
Screw lead	λ	5.00×10^{-3}	*m*
Moment of Inertia of the Ball screw	J_{sc}	2.44×10^{-5}	$kg.m^2$
Moment of Inertia of the Load (seen at LSR)	J_L	1.88×10^{-5}	$kg.m^2$
Inertia of coupling	J_c	*0*	$kg.m^2$
Mass of the slide	M_{sl}	*0.5*	*kg*
Shear modulus of screw material	G_{sc}	*79*	*GPa*
Area moment of inertia of screw	I_{sc}	1.49×10^{-8}	m^4
Density of the screw material	ρ_{st}	*7700*	$kg.m^2$
Young's modulus of screw material	E_{sc}	*207*	*GPa*
Cross sectional area	A_{sc}	3.06×10^{-4}	m^2
Stiffness of the bearing	K_b	2.00×10^{8}	*N/m*
Stiffness of the coupling	K_c	1.67×10^{4}	*N.m/rad*

Stiffness of the screw-nut interface	K_n	2.89×10^{8}	*N/m*
Transmission ratio	γ	7.96×10^{-4}	*m/rad*
Length of the screw shaft	L_{sc}	*0.213*	*m*

PDD parameters

Table 3. PDD parameters

parameter	*symbol*	*value*	*units*
Moment of Inertia on HSR	J_{HSR}	1.35×10^{-4}	$kg.m^2$
Moment of Inertia on LSR	J_{LSR}	1.08×10^{-4}	$kg.m^2$
LSR Peak Speed	n_{LSR_MAX}	*1200*	*rpm*
HSR Peak Speed	n_{HSR_MAX}	*9300*	*rpm*
Pole Pairs	p_h	*4*	*-*
Number of pole pieces	n_s	*31*	*-*
Gear ratio	G_r	*7.75*	*-*
Pull out Torque	T_{max}	*10.3*	*N.m*
Peak torque demand	T_{LSR_MAX}	*8.6*	*N.m*
PDD Torque Constant	K_{t_LSR}	*1.145*	*N.m/A*
Motor Phase Resistance	R_s	*0.7*	*Ω*
Motor Phase Inductance	L_s	*1.90E-03*	*H*
Number of Turns		*54*	*-*
EMF Constant	K_e	*0.102*	*V.s/rad*
Switching frequency	f_{sw}	*10*	*kHz*

2.3 Conventional mathematical model

All models in this thesis are implemented using Matlab Simulink.

DC voltage bus

Power converter systems can be modelled using methods such as state-space averaging (*SSA*), average-value modelling and dq transformation theory method [2]. SSA method is used in power converters in DC and AC distribution systems. It results in high order model when applied to three-phase systems. Furthermore, average-value modelling is used in 6 and 12 pulse diode rectifiers. No information from AC side is provided. Also, it cannot be usable for multi-converter power electronic systems. Moreover, dq transformation theory method is used for AC system analysis where power converters are looked at as time-varying transformers. This method provides lower order models for three-phase AC distribution systems. Additionally, it can be used to model power systems based on vector-controlled converters. In [2] and [21], dq transformation theory is used to represent the power system in the dq reference frame. Essentially, transmission line and the diode rectifier are transformed into dq frame [21].

In this research, the DC voltage bus is assumed ideal and modelled as a constant voltage DC source (V_{dc}=±270 *V*). This is because the study is mainly focused on propagation of mechanical system dynamics into electrical system. Also, the consideration of non-ideal voltage source is already considered in previous literature.

2.3.1 Control scheme

Control scheme used is illustrated in Figure 29. It consists of an inner current loop in the *dq* reference frame, an outer loop for speed control, and an utmost loop for position control. The symbol "*" indicates the signal demand. Speed control feedback is taken from PDD HSR whereas position control feedback is taken from the screw-nut position. The control scheme design is explained in [50] [6]. Note: symbols are defined in the table of notation.

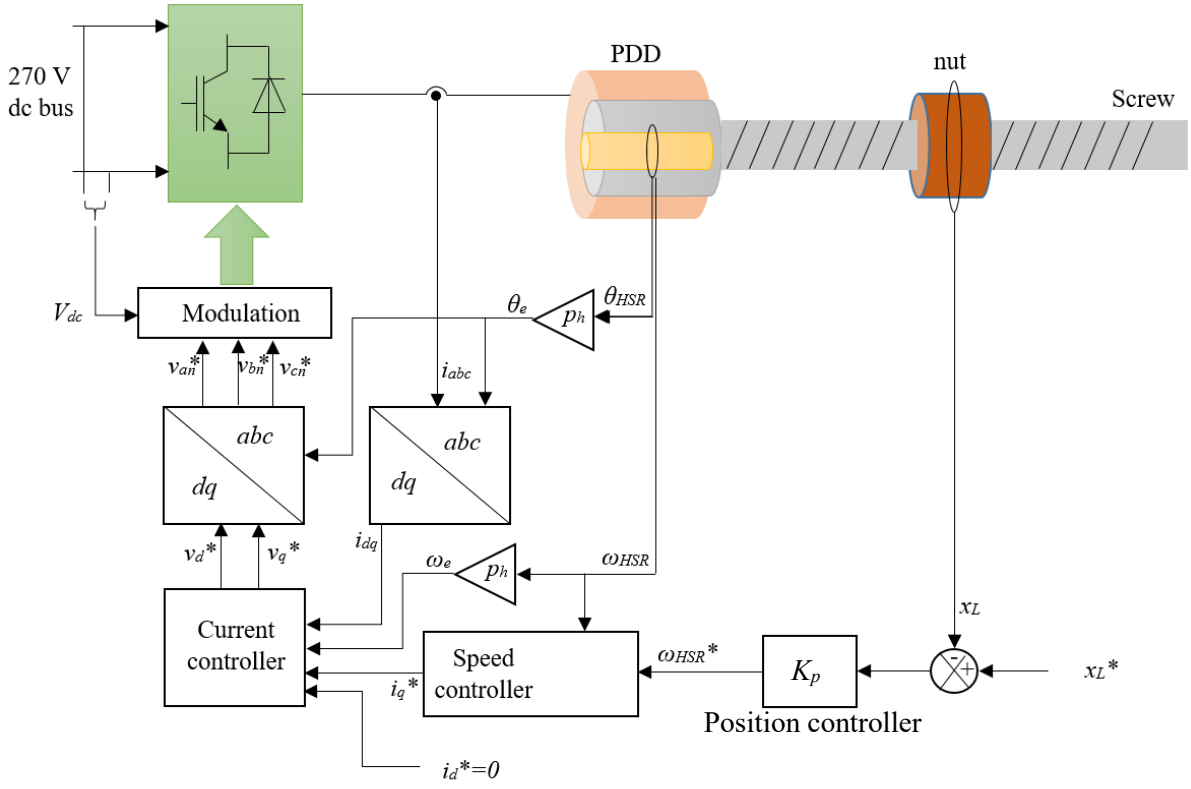

Figure 29. Control scheme in use

The measured three-phase stator currents, i_a, i_b and i_c are transformed into synchronously rotating *dq* reference frame, i_d and i_q, which are controlled using PI controllers. i_d^* and i_q^* are d-axis current demand and q-axis current demand, respectively. To ensure maximum torque per ampere operation, i_d^* is set to zero. To ensure independent control of torque and flux currents, decoupling term is added. This technique is known as field oriented control (FOC). The aim of this technique is to maintain i_d zero and independently regulate i_q, which is kept orthogonal to i_d and flux, according to torque demand. The

current controller outputs d-axis voltage demand, v_d^*, and q-axis voltage demand, v_q^*, which are then transformed to their equivalent three phase voltage demands, v_{an}^*, v_{bn}^*, and v_{cn}^*.

Figure 30 reveals current control scheme shown in Figure 29.

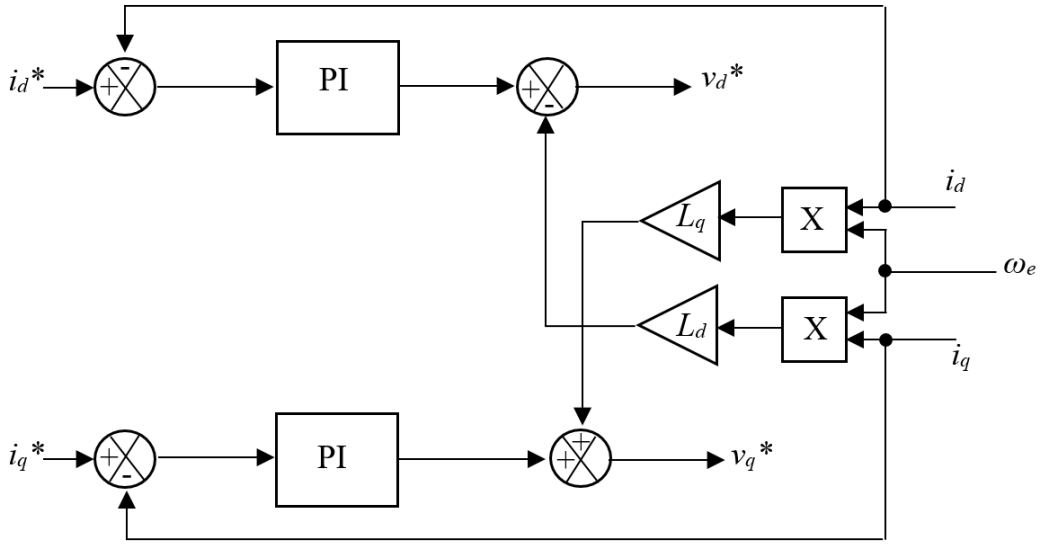

Figure 30. Current loop control

where L_d and L_q are d-axis and q-axis inductances, respectively. Both values are equal apart from when the rotor is salient. In the PDD, the rotor is non-salient and hence Equation (4) is true.

$$L_d = L_q \tag{4}$$

Also, L_d *and* L_q are related to the synchronous inductance, L_s, according to Equation (5) [49].

$$L_d = L_q = L_s \tag{5}$$

In a control system, inner loops have to be faster than outer loops, by a factor of 10 according to the rule of thumb. The main purpose of this is that the inner loop has to swiftly stabilise in response to any changes in outer loops. The current loop bandwidth is estimated with respect to mechanical system speed capabilities. Let us initially assume that the maximum axial displacement can be estimated to be achieved within 0.2 s. This makes the position loop bandwidth equal to 5 Hz. Speed loop bandwidth, therefore, can be suitably equal to 50 Hz. Subsequently, current loop bandwidth can be equal to 500 Hz.

Many methods are suggested to tune current controller. Pole-zero cancellations allows the estimation of the proportional gain, K_{pc}, and integral gain, K_{ic} [17]. The tuning is based on the required bandwidth of the current controller, f_c, which is *500 Hz*.

$$\tau_c = \frac{1}{2\pi f_c} = 0.000318 \tag{6}$$

$$K_{pc} = \frac{L_q}{\tau_c} = \frac{0.0019}{0.000318} = 5.97 \quad (7)$$

$$K_{ic} = \frac{R_s}{\tau_c} = \frac{0.7}{0.000318} = 2199.115 \quad (8)$$

where τ_c is the time constant of the current loop.

IP Speed control block diagram is shown in Figure 31. The same speed control scheme is used in [17] [8] since it provides a better performance than conventional PI by minimising oscillations. More explanation about this scheme is detailed in [51]. Note: symbols are defined in the table of notation.

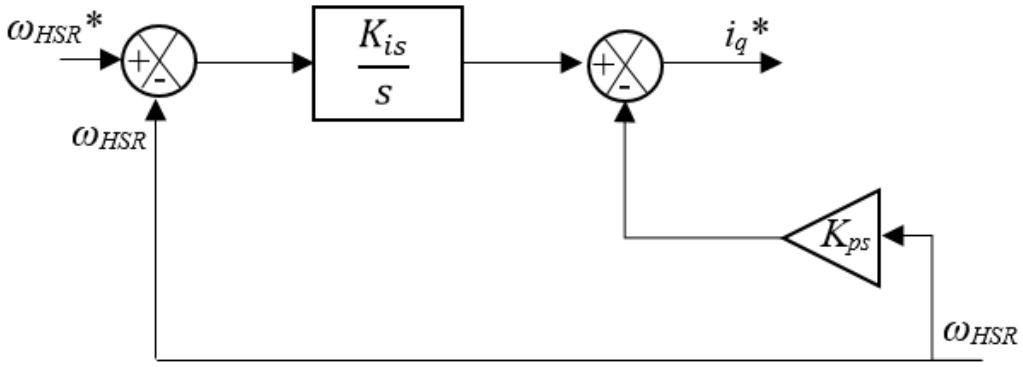

Figure 31. IP speed loop control

2.3.2 PDD model

A mathematical model of the PDD is available in literature [52] [17] [16] [8]. The model available is sufficiently accurate to provide the important dynamics of the PDD such as the magnetic stiffness and the torque dependence upon the load angle. In PDD, the electromagnetic torque is applied to the HSR and the torque is transmitted to the LSR via magnetic coupling. Thus, as mentioned in the Principle of Operation Section (1.2.2.1.2), two stages dominate the operation of the PDD; namely, torque production and torque transmission. Hence the modelling approach will be organised accordingly.

Torque production stage

In this section, the model will essentially be similar to that of PMSM. PDD performs conversion of electrical power into mechanical power. Torque is produced from the three-phase current supplied to the PDD three-phase windings. The model will begin with the differential equations of the three-phase stator windings. More details can be found in [50] [6].

The stator three phase currents can be given in Equation (9), Equation (10), and Equation (11).

$$i_a = I_p \sin(\omega_e t) \quad (9)$$

$$i_b = I_p \sin(\omega_e t - \frac{2\pi}{3}) \tag{10}$$

$$i_c = I_p \sin(\omega_e t + \frac{2\pi}{3}) \tag{11}$$

where I_p is the amplitude of phase current, and the quadrature current, i_q, is equal to this value, as shown in Equation (12).

$$i_q = I_p \tag{12}$$

Figure 28 shows the VSI connected with a three-phase motor. Per phase equivalent circuit and phasor diagram are shown in Figure 32.

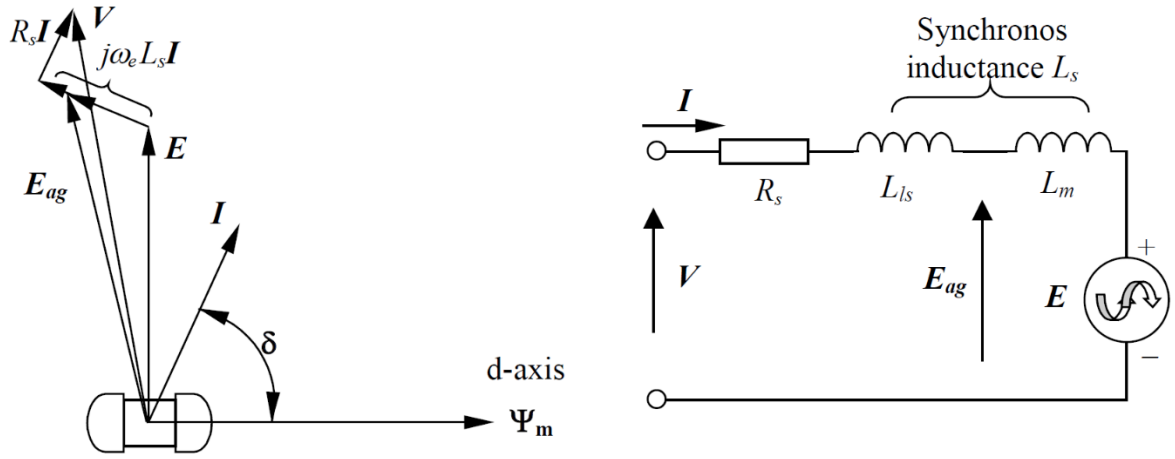

Figure 32. Per phase equivalent circuit [49]

where $\boldsymbol{I}$ is the stator current phasor, δ is the torque angle, $\boldsymbol{E}$ is the back EMF phasor, $\boldsymbol{V}$ is the applied voltage phasor, $\boldsymbol{\Psi_m}$ is rotor flux phasor, and ω_e is the electrical speed.

The flux linkage phasor, Ψ_m, is used as a reference phasor. Also, the amplitudes of voltage and current phasors are represented by their rms values. But the amplitude of flux linkage phasors are represented by their peak values. For example,

$$I_p = \sqrt{2}I \tag{13}$$

L_m is magnetising inductance of the PDD windings, and it is related to the self-inductance of the phase winding, L, according to Equation (14).

$$L_m = \frac{3}{2}L \tag{14}$$

The synchronous inductance, L_s, is the sum of the magnetising inductance, L_m, and the leakage inductance, L_{ls}, as shown in Equation (15).

$$L_s = L_m + L_{ls} \tag{15}$$

As a result of the alternating currents, voltages are induced in the stator windings. The induced voltage phasor is given by Equation (16).

$$\boldsymbol{E_L} = j\omega_e L_m \boldsymbol{I} \tag{16}$$

The stator currents produce voltage drops, $\boldsymbol{V_{drop}}$, in the winding resistance, R_s, and leakage inductance, L_{ls}, as shown in Equation (17).

$$\boldsymbol{V_{drop}} = (R_s + j\omega_e L_{ls})\boldsymbol{I} \tag{17}$$

The airgap induced voltage phasor, $\boldsymbol{E_{ag}}$, is given by Equation (18).

$$\boldsymbol{E_{ag}} = \boldsymbol{E} + \boldsymbol{E_L} \tag{18}$$

$\boldsymbol{V}$ is related to $\boldsymbol{E_{ag}}$ through Equation (19).

$$\boldsymbol{V} = \boldsymbol{V_{drop}} + \boldsymbol{E_{ag}} \tag{19}$$

Phase A voltage, v_{an}, phase B voltage, v_{bn}, and phase C voltage, v_{cn}, seen in the figure, can be given by Equation (20), Equation (21) and Equation (22), respectively.

$$v_{an} = R_s i_a + L_s \frac{di_a}{dt} + e_a \tag{20}$$

$$v_{bn} = R_s i_b + L_s \frac{di_b}{dt} + e_b \tag{21}$$

$$v_{cn} = R_s i_c + L_s \frac{di_c}{dt} + e_c \tag{22}$$

where t is time in second. The three-phase back EMFs can be given in Equation (23), Equation (24) and Equation (25), respectively.

$$e_a = E_p \cos(\omega_e t) \tag{23}$$

$$e_b = E_p \cos\left(\omega_e t - \frac{2\pi}{3}\right) \tag{24}$$

$$e_c = E_p \cos\left(\omega_e t + \frac{2\pi}{3}\right) \tag{25}$$

where Ep is amplitude of back EMF and it is given by,

$$E_p = \omega_{HSE} p_h \Psi_m = \sqrt{2}E \tag{26}$$

Note that the magnitude of the phase back EMF is the product of the HSR mechanical speed, ω_{HSR}, and the machine constant, K_e, as shown in Equation (27).

$$|e_a| = \omega_{HSE} p_h \Psi_m = \omega_{HSE} K_e \tag{27}$$

Each phase current produces flux that interacts with rotor flux to generate torque. Equation (28), Equation (29) and Equation (30) show the torque produced due to each phase, respectively.

$$T_a = i_a p_h \Psi_m \cos(\omega_e t) \tag{28}$$

$$T_b = i_b p_h \Psi_m \cos\left(\omega_e t - \frac{2\pi}{3}\right) \tag{29}$$

$$T_c = i_c p_h \Psi_m \cos\left(\omega_e t + \frac{2\pi}{3}\right) \tag{30}$$

The electromagnetic torque, T_e, is the sum of the contributions of the three phases as shown in Equation (31).

$$T_e = T_a + T_b + T_c \tag{31}$$

Equation (32) relates HSR mechanical angle, θ_{HSR}, to electrical angle, θ_e.

$$\theta_e = p_h \theta_{HSR} \tag{32}$$

where θ_e is the electrical angle between the d-axis (magnet or flux axis) and phase A winding axis, as shown in Figure 33.

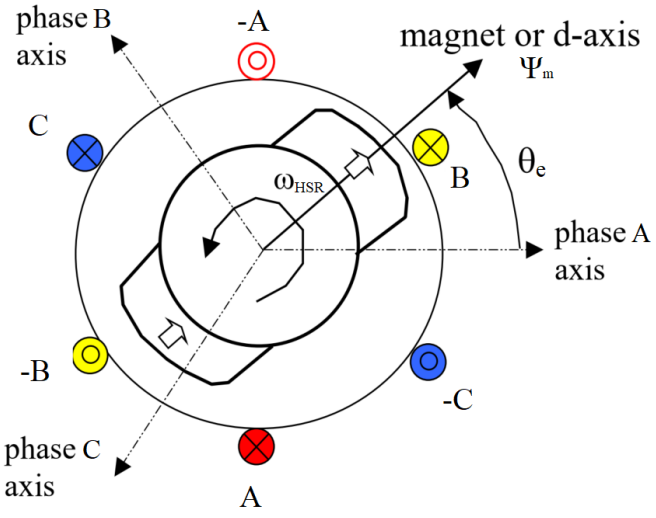

Figure 33. Three-phase windings and their axes [49]

Similarly, Equation (33) relates HSR mechanical speed, ω_{HSR}, to electrical speed, ω_e.

$$\omega_e = p_h \omega_{HSR} \tag{33}$$

Stator currents frequency, f_e, is given in Equation (34). In brushless AC PM motor drive, the stator is supplied with a set of balanced three-phase current whose frequency is controlled to be in synchronism with the rotor rotation.

$$f_e = \frac{\omega_e}{2\pi} = \frac{p_h \omega_{HSR}}{2\pi} \tag{34}$$

Torque transmission stage

Motion of the HSR can be expressed in Equation (35) [17].

$$T_e - \frac{T_{max}}{G_r}\sin(\theta_r) = J_{HSR}\ddot{\theta}_{HSR} \tag{35}$$

where T_{max} is pull out toque and J_{HSR} is the moment of inertia of HSR. Also, θ_r is known as the referred load angle between HSR and LSR and it is given by Equation (36).

$$\theta_r = p_h\theta_{HSR} - n_s\theta_{LSR} \tag{36}$$

where θ_{LSR} is the LSR mechanical position.

Similarly, motion of the LSR can be expressed in Equation (37) [17].

$$T_{max}\,sin(\theta_r) - T_L = J_{LSR}\ddot{\theta}_{LSR} \tag{37}$$

where, T_L is the load torque and J_{LSR} is the moment of inertia of the LSR. According to [17], for the system to be stable, $cos(\theta_r)$ must be positive. Figure 34 shows the load angle with respect to LSR torque, T_{LSR}. Stable regions and unstable regions are illustrated in the figure.

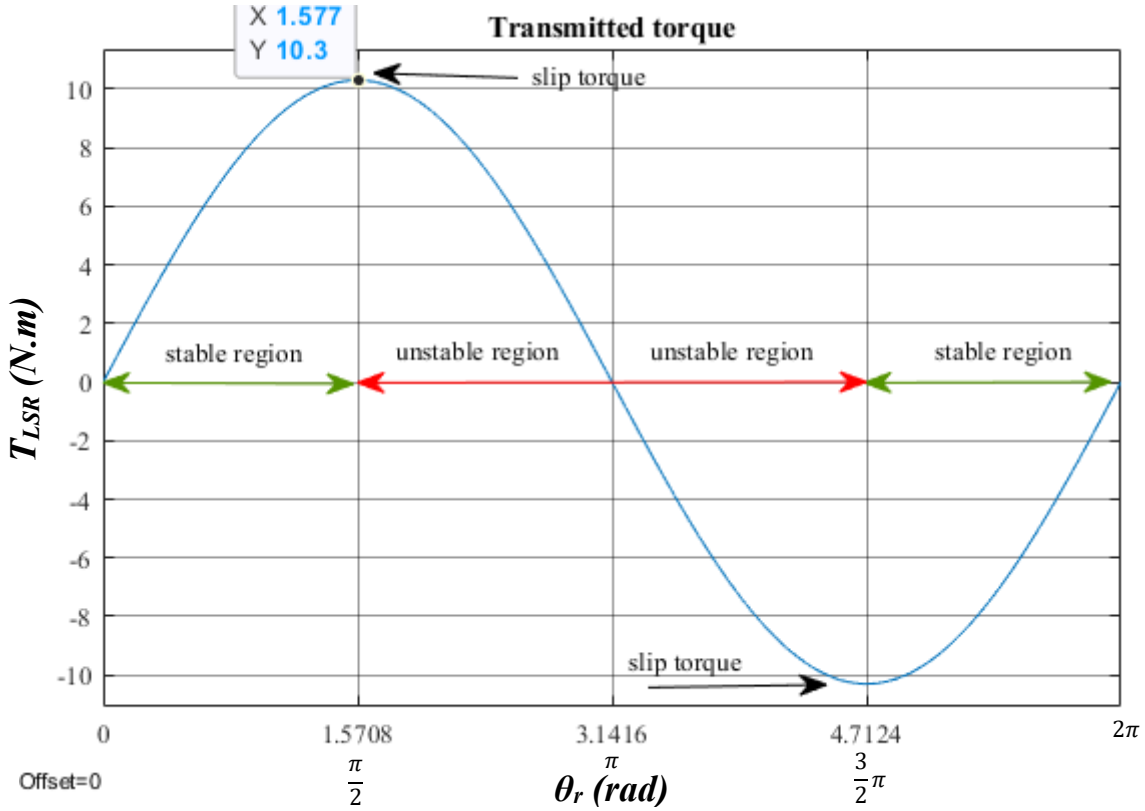

Figure 34. Transmitted torque with respect to referred angle

Equations of motions of the PDD rotors can be implemented in Simulink as shown in Figure 35.

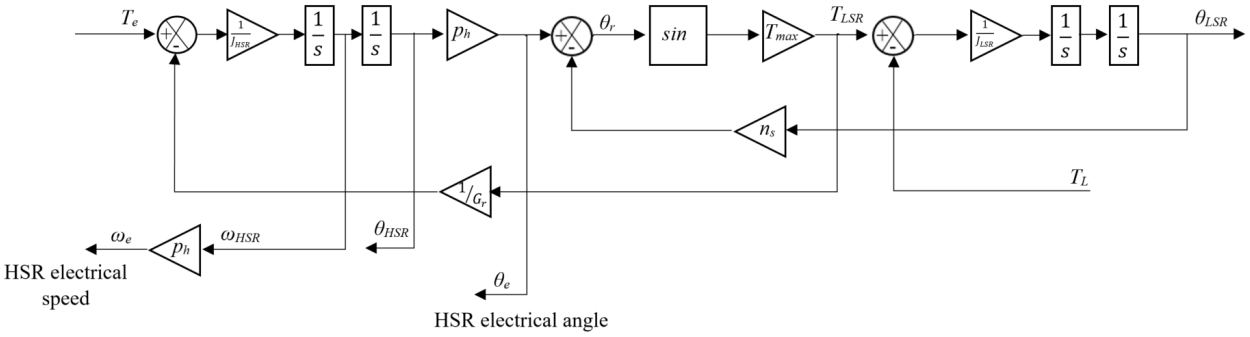

Figure 35. Model of equation of motion of PDD rotors

2.3.3 Conventional simplified model of aero EMA

The mechanical system consists of ball-screw assembly connected to the PDD LSR via coupling, as shown in Figure 36. The PDD transmitted torque is converted into a force of the screw nut that actuates the rudder according to demand. Equation (38) shows mechanical power conversion, which assumes zero losses in the power transmission. Practically, losses may be in a form of heat due to friction.

$$P_{HSR} = T_e \times \omega_{HSR} = P_{LSR} = T_{LSR} \times \omega_{LSR} = P_{sc} = F_{sc} \times v_L \quad (38)$$

where, P_{HSR} is the mechanical power of the PDD HSR, T_e is the electromagnetic torque produced by interaction between HSR permanent magnets and stator windings currents, ω_{HSR} is the HSR angular speed, P_{LSR} is the mechanical power of the PDD LSR, T_{LSR} is the transmitted torque to the LSR, ω_{LSR} is the LSR angular speed, P_{sc} is the power of the slide, F_{sc} is linear force of the slide, v_L is the translational speed of the slide.

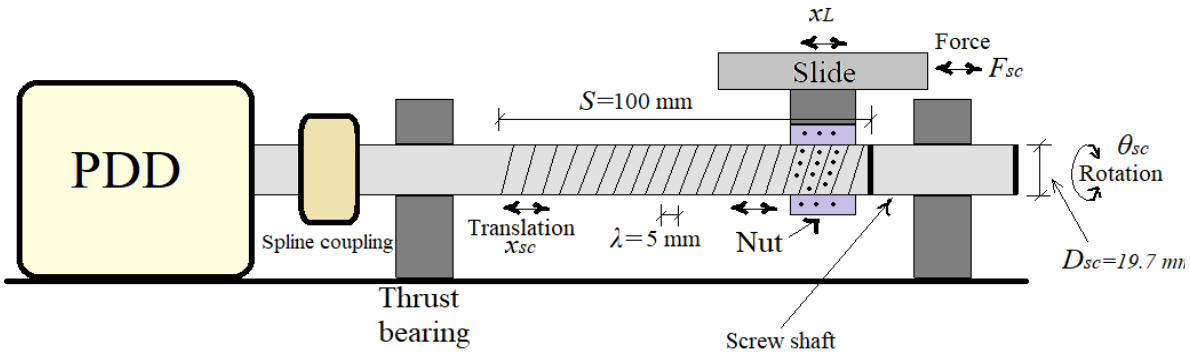

Figure 36. Ball-screw drive

As mentioned in the introduction of this chapter, EMA used in MEA is modelled as an inertia that is composed of inertias of motor, screw and load. For instance, [8] assumes an ideal screw connected to PDD. In fact, EMA in other applications may also be modelled as a simplified single inertia that is added with the load and motor. For example, in [12] compares between the performance of ball-screw drive under conventional PID controller and fuzzy logic controller. Initially, we shall use the conventional model so a comparison with a more-detailed model may be appreciated.

In accordance with [53], resonance analysis is conducted through three model stages. **Spatial model** describes the physical structure of the system in terms of mass/inertia, stiffness and damping properties. **Modal model** describes the structure's behaviour in terms of natural frequencies and corresponding mode shapes. This model is calculated using analytical model analysis on the spatial model. **Response model** describes the manner of which the structure vibrates in response to given excitation conditions; especially with what amplitudes. This model can have many solution since it depends on properties of structure and type and magnitude of excitation.

Equivalent single inertia calculation

In this case, screw is assumed ideal. Figure 37 shows this lumped parameter model.

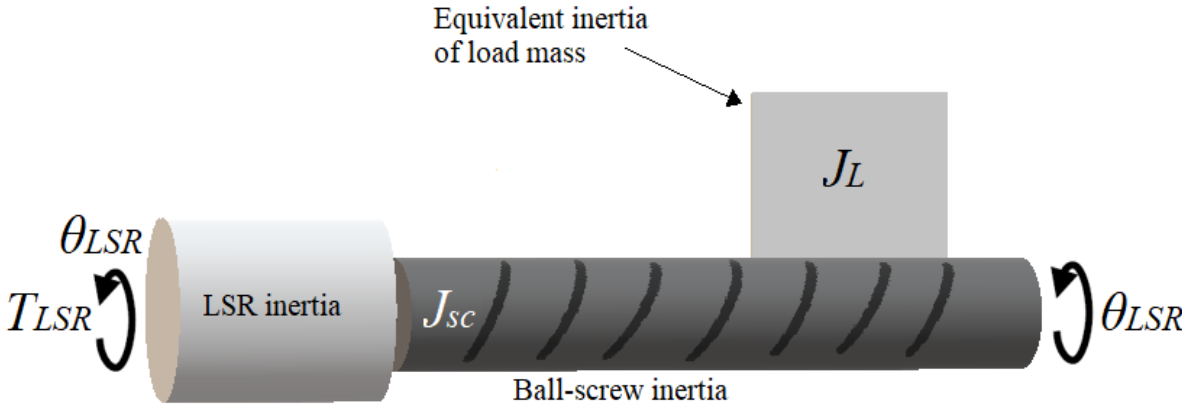

Figure 37. One-DOF model

LSR inertia, J_{LSR}, ball-screw inertia, J_{sc}, and load mass, M_L, are already given in Table 1, Table 2 and Table 3. Equivalent inertia of equivalent load mass, J_L, is calculated in Equation (39).

$$J_L = M_L \left(\frac{\lambda}{2\pi}\right)^2 = M_L \gamma^2 = 1.876 \times 10^{-5}\ kg.m^2 \tag{39}$$

The single inertia, J_s, can be determined using Equation (40).

$$J_s = J_{LSR} + J_{sc} + J_L = 1.51 \times 10^{-4}\ kg.m^2 \tag{40}$$

Aerodynamic stiffness calculation

Maximum load is reached at maximum deflection of the surface, which is $\pm 30°$. This corresponds to $\pm 50\ mm$ on the screw. If the screw lead is given as $5\ mm$, then the screw will make 10 rotations under maximum load torque on the machine. Figure 38 shows a top view of rudder actuation with respect to slide displacement on screw.

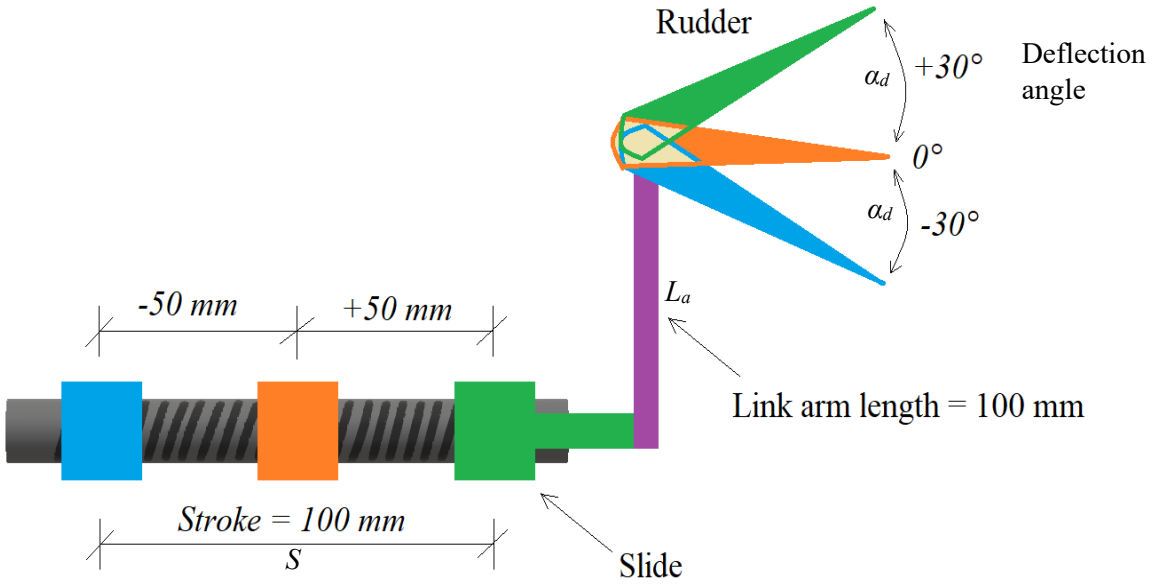

Figure 38. Rudder deflection angle vs slide displacement on screw

As the rudder angle, α_d, increases from $0°$ to $\pm 30°$, the aerodynamic pressure on the rudder increases. This pressure will reflect on the screw as a force. The relationship will be assumed linear, as shown in Figure 39.

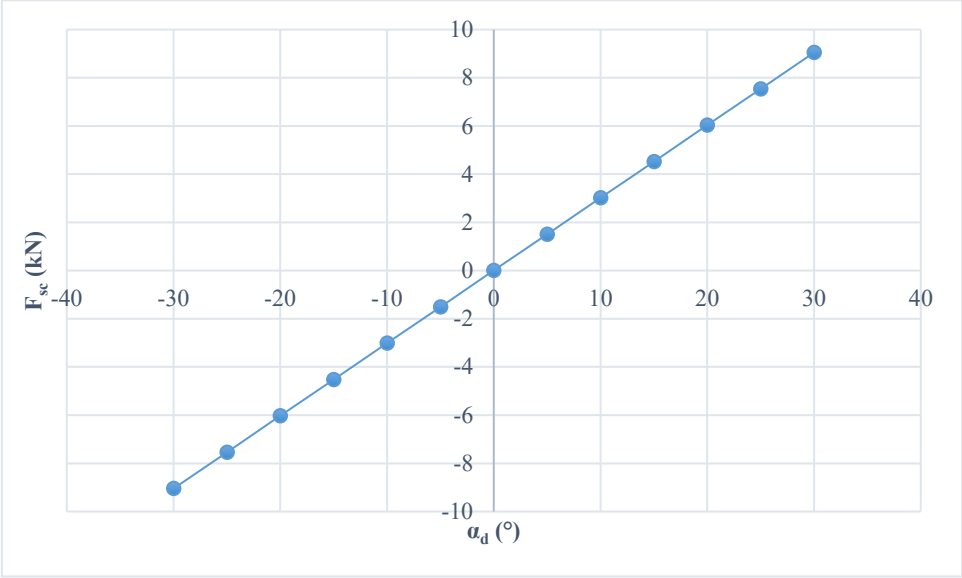

Figure 39. Screw force (F_{sc}) & rudder deflection angle (α_d)

10 rotations of the screw are converted into radians in Equation (41).

$$\theta_{sc} = 10 \times 2\pi = 62.83\ rad \tag{41}$$

where, θ_{sc} is the screw position.

Therefore, PDD LSR torque changes linearly with the screw angle as shown in Figure 40.

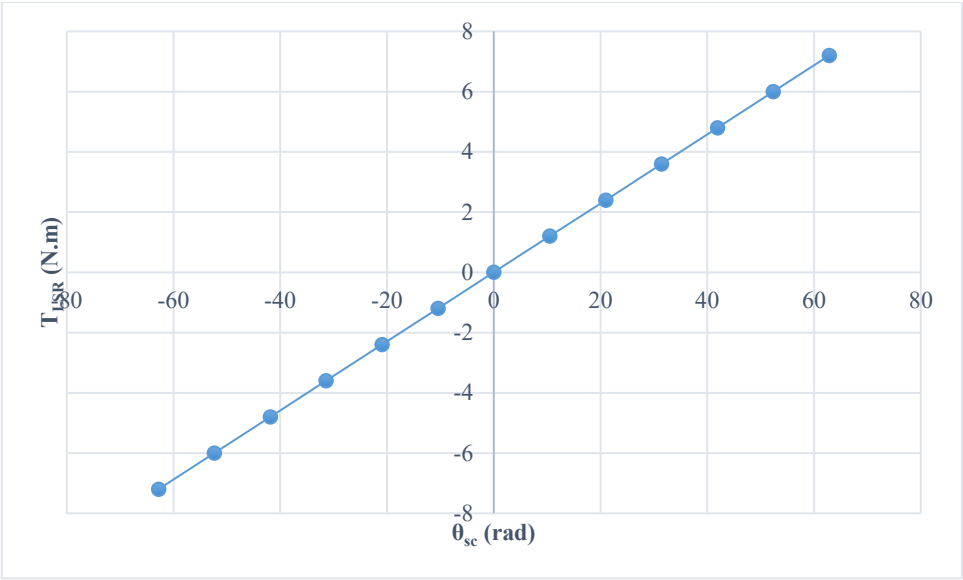

Figure 40. PDD torque and screw angle

From Figure 40, a linear relationship between a torque and an angular position can be seen, from which the slope of such relationship can be interpreted as stiffness. Hence, the rotary aerodynamic stiffness, K_{ar}, can be calculated as follows.

$$T_{LSR} = K_{ar}\theta_{sc} \rightarrow K_{ar} = \frac{T_{LSR}}{\theta_{sc}} = 0.115\ N.m.rad^{-1} \tag{42}$$

Considering the aerodynamic stiffness, it can be inserted into Figure 37, as shown in Figure 41.

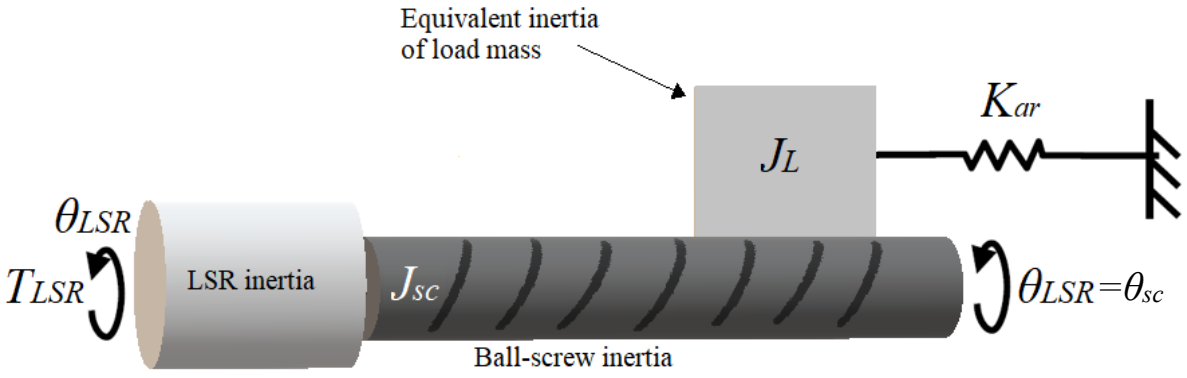

Figure 41. Spatial model of simplified one-DOF model with aerodynamic stiffness

This system block diagram is shown in Figure 42. The transfer function of the system is shown in Equation (43).

$$\frac{\theta_{sc}}{T_{LSR}} = \frac{1}{J_s s^2 + K_{ar}} \tag{43}$$

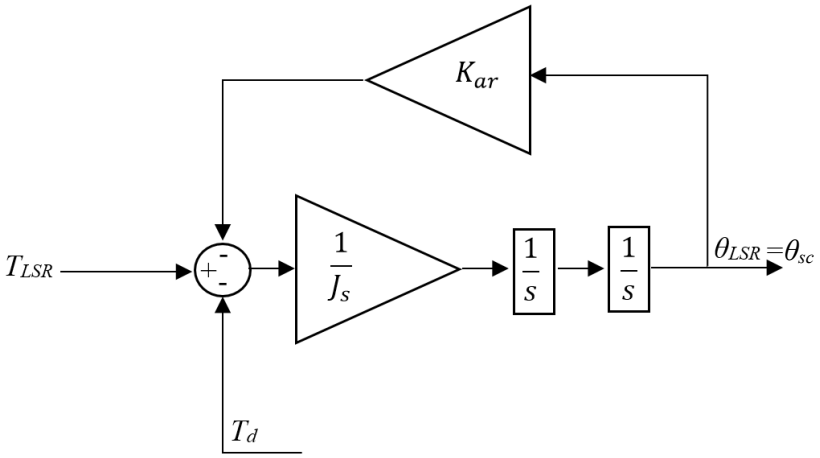

Figure 42. Simulink implementation of one-DOF model

where T_d is disturbance torque. The frequency response of the block diagram in Figure 42 is shown in Figure 67.

2.3.4 Simulation results

The block diagram in Figure 42 is inserted into Figure 35 and implemented in Simulink.

2.3.4.1 Frequency domain analysis

With the use of Matlab linear analysis tool, frequency response can be plotted as shown in Figure 43. Matlab linear analysis tool is a tool used to analysis the dynamics of linear systems; such as system behaviour in time domain and frequency domain. Electromagnetic torque, T_e, is the input whilst the angular displacement of the rotary system, θ_{sc}, is the output. This frequency response function (FRF) model is known as receptance, as stated in [53].

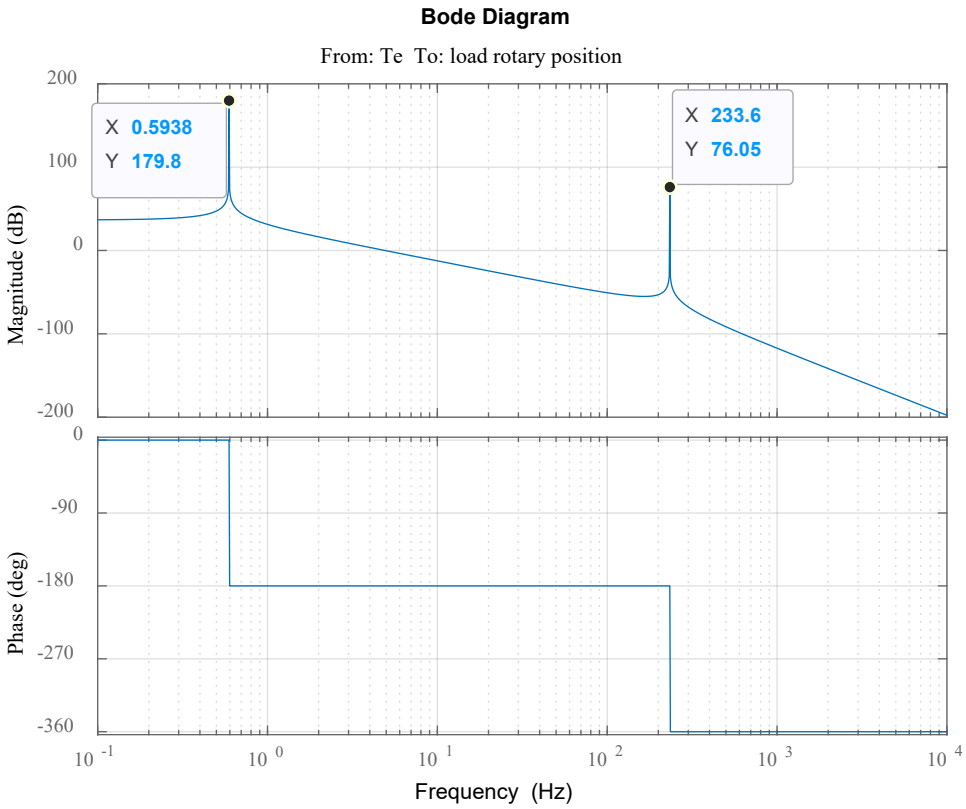

Figure 43. Bode plot (PDD electromagnetic torque to load rotary position)

The ball-screw assembly is a 1-DOF model and yields the natural frequency $f_{1\_reflected}$. Furthermore, magnetic stiffness, between HSR and LSR of the PDD, produces f_g. Table 4 summarises the frequencies observed in the bode plot, which construct part of the modal model.

Table 4. Summary of bode plot

	Resonance frequency (*Hz*)	rad.s^{-1}	Significant stiffness
$f_{1\_reflected}$	0.59	*3.73*	K_{ar}
f_g	234	*1470*	*Magnetic stiffness*

Matlab calculates the first resonant frequency ($f_{1\_reflected}$) with respect to the HSR. This value of reflected frequency can be mathematically calculated using Equation (44). This equation is used for fixed-free system and it can be derived as shown in Equation (65).

$$f_{1\_reflected} = \frac{\frac{1}{2\pi}\sqrt{\frac{K_{ar}}{J_s}}}{G_r} = \frac{\frac{1}{2\pi}\sqrt{\frac{0.115}{1.51\times10^{-4}}}}{7.75} = 0.57\ Hz \tag{44}$$

If this frequency is referred to the LSR, it is possible to estimate it using Equation (45).

$$f_1 = \frac{1}{2\pi}\sqrt{\frac{K_{ar}}{J_s}} = 4.39\ Hz \tag{45}$$

Regarding f_g, it can also be calculated analytically but, firstly, equation must be linearised so torque can be a function of magnetic stiffness, K_g. This is shown in Equations (219), (220) and (224) in Chapter 4.

Practically, the rudder is actuated in response to a pilot demand, which is translated into a position demand for the screw nut. The controller consistently obtains a position feedback signal, which could be the nut axial positon or PDD rotor rotary position. Then, the position feedback signal is compared with the position demand signal to produce the PDD HSR speed demand.

2.3.4.2 Time-domain analysis

To observe the inter-connected system response under various loading conditions, different tests are carried out, using the switching model explained.

A step position demand

A reference position step demand is set to a maximum displacement, which is 62.83 rad as explained by Equation (41). In response to the step demand, the rotary position can be seen in Figure 44.

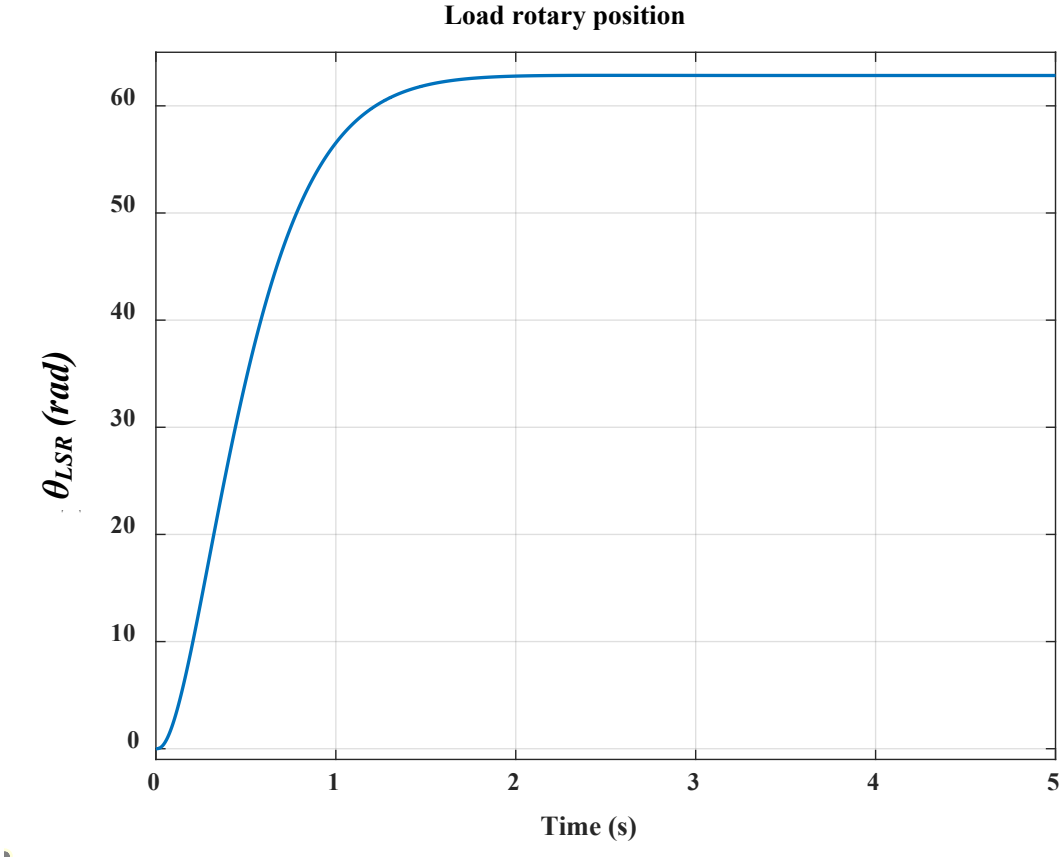

Figure 44. Load position

The electrical system is stable. This can be indicated in the PDD stator winding currents, as shown in Figure 45.

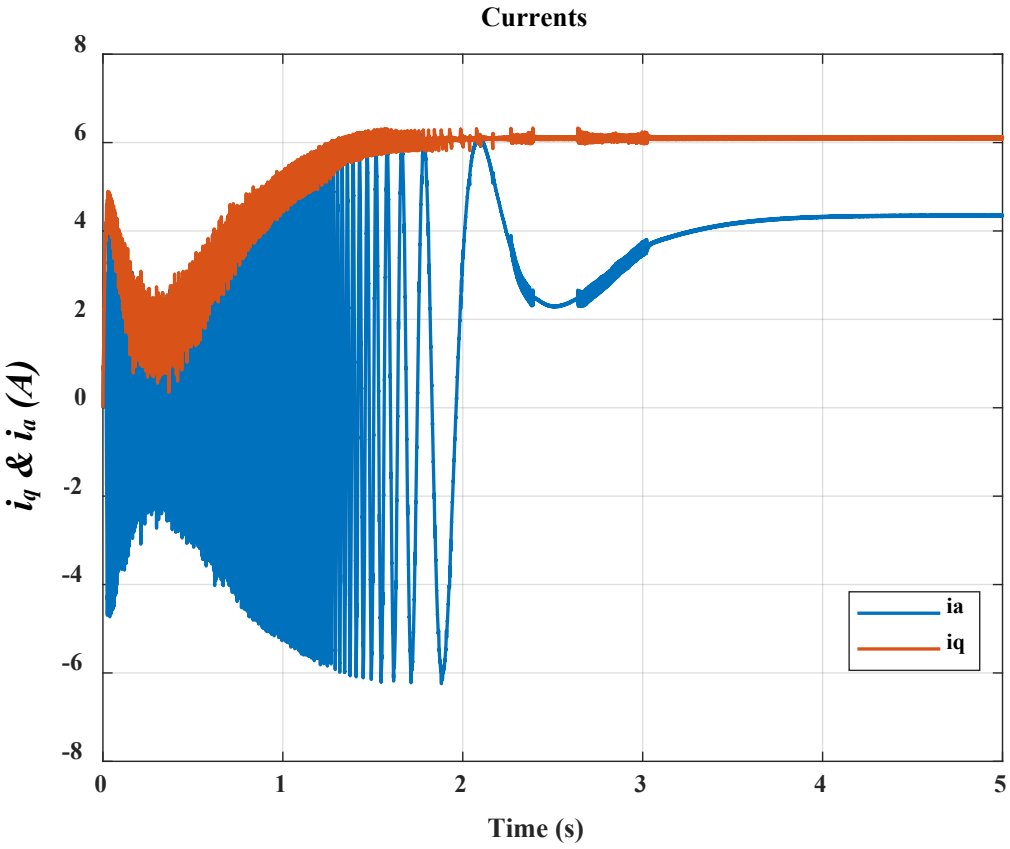

Figure 45, Phase A current and quadrature current

Disturbance torque with certain frequencies

A chirp signal is applied to represent a frequency varying disturbance torque. The amplitude of the disturbance is 0.8 N.m and the frequency range is between 1 Hz to 600 Hz.

Chirp signal (Amplitude = 0.8 N.m & frequency varies from 1 to 300 Hz)

A disturbance torque is applied with such a frequency range. No dynamics are spotted during the lower frequencies. As the disturbance frequency approaches f_g, a resonance becomes excited. The rudder starts to oscillate back and forth between the two maximum displacements. The frequency of such oscillation is 4.38 Hz, which is the frequency of the aerodynamic load. This can be seen in Figure 46.

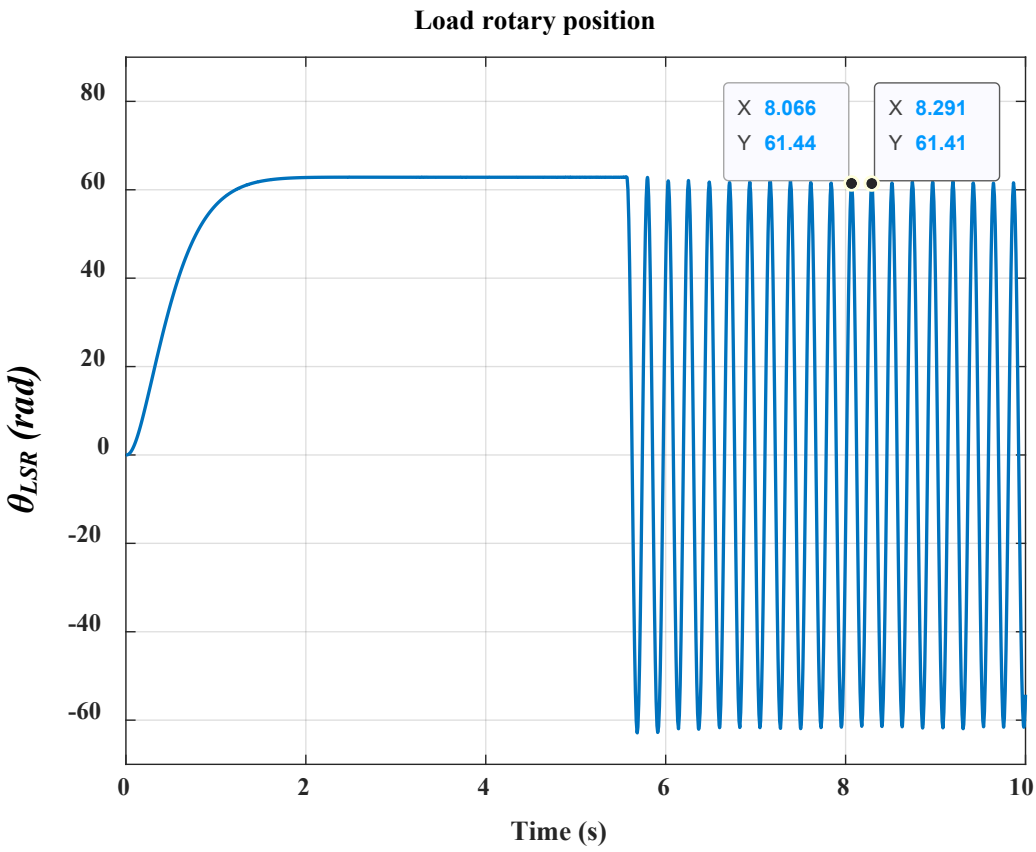

Figure 46. Load position (frequency of oscillations = 4.4 Hz)

f_g can be seen when disturbance is of other frequencies than f_g, as shown in Figure 47.

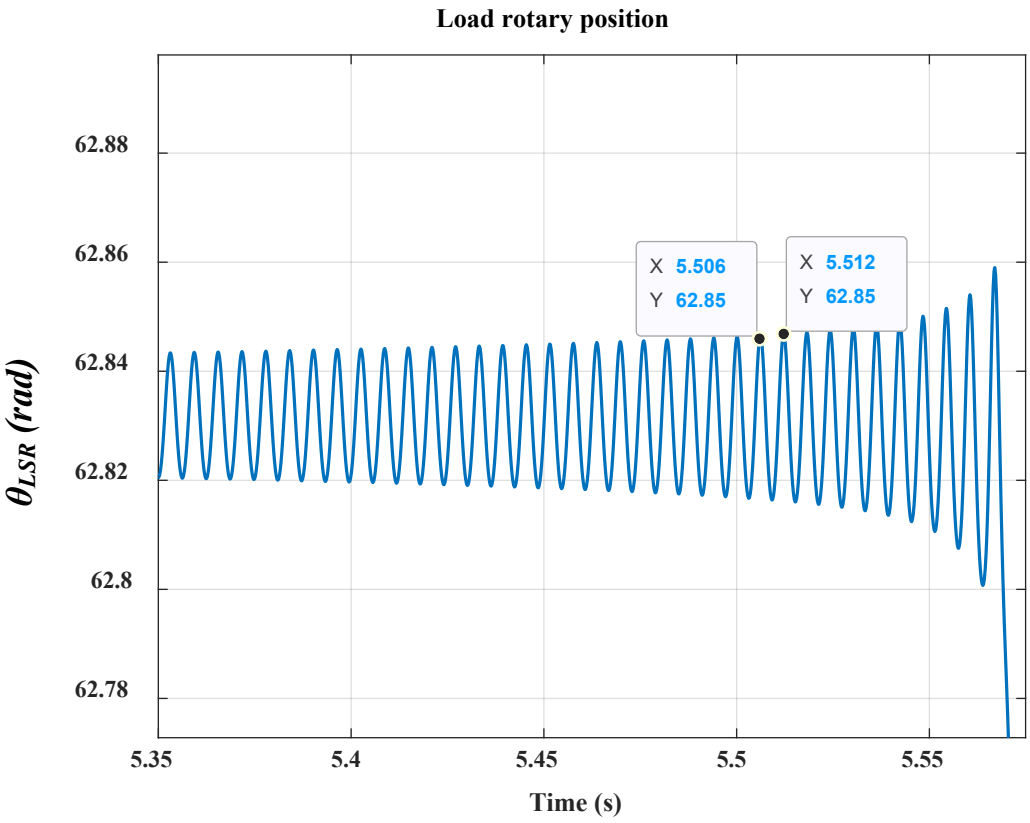

Figure 47. Load rotary position (frequency of oscillations = 167 Hz)

The resonance excitation is propagated into the electrical system and can be observed in the PDD stator winding current. As a result, the current oscillates in the way observed in Figure 48.

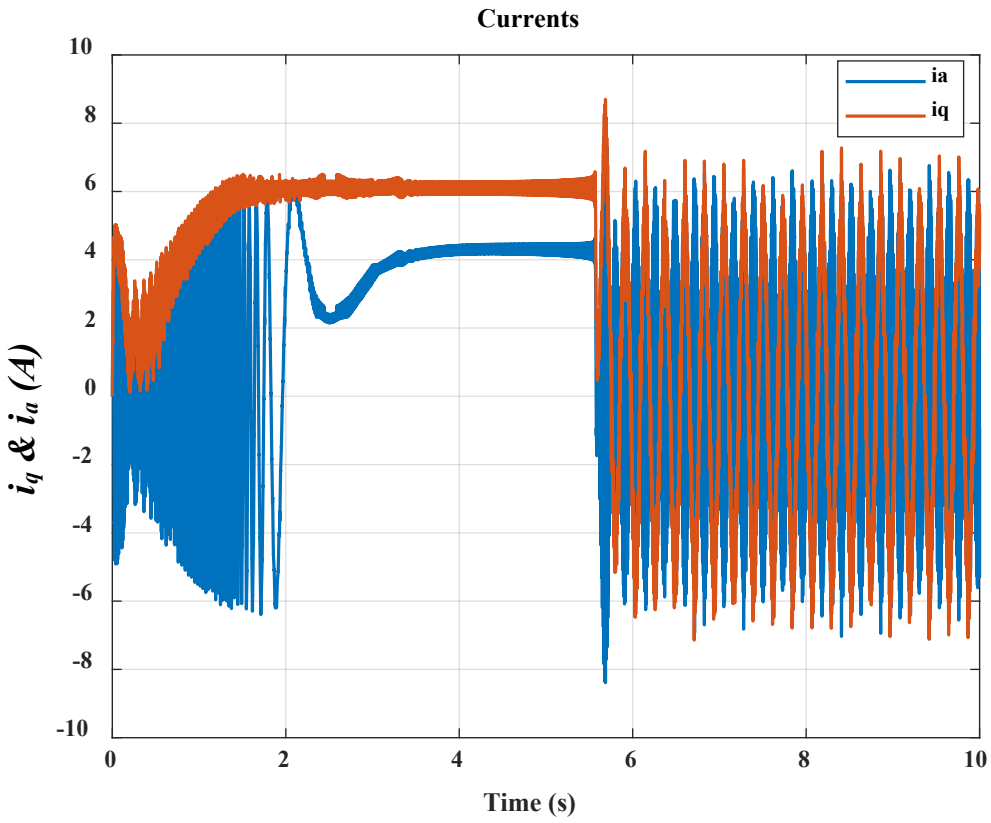

Figure 48. Phase A current and iq current

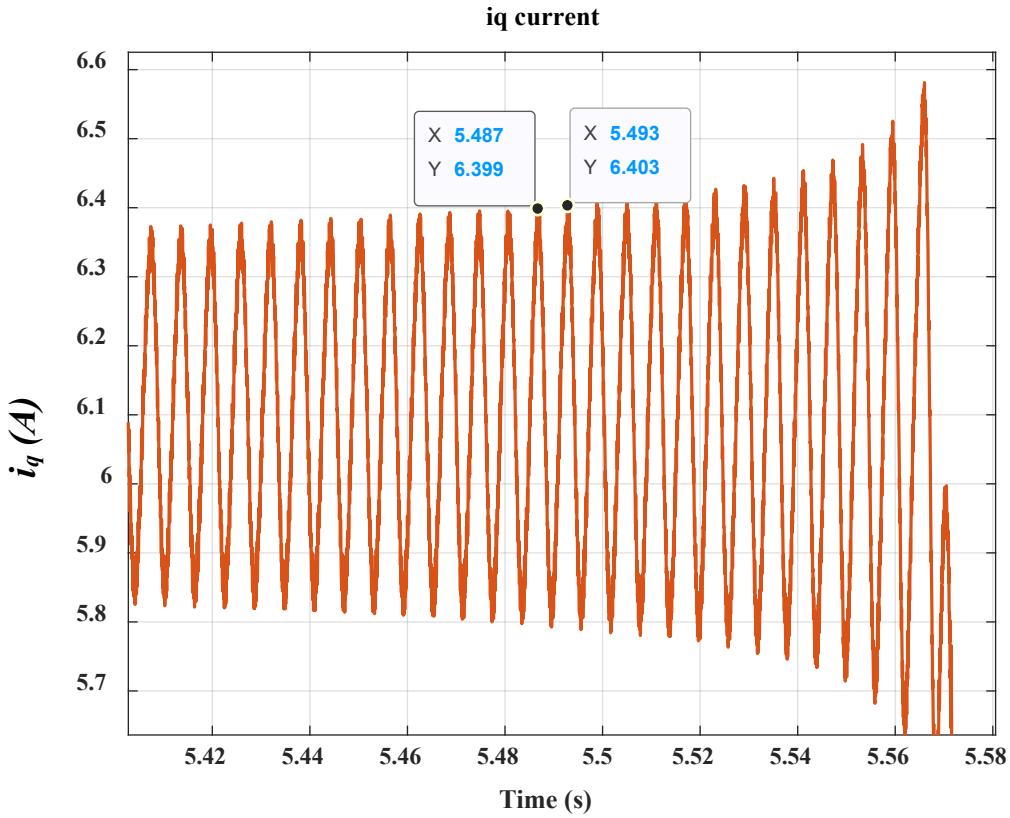

Figure 49. Frequency of oscillations = 167 Hz

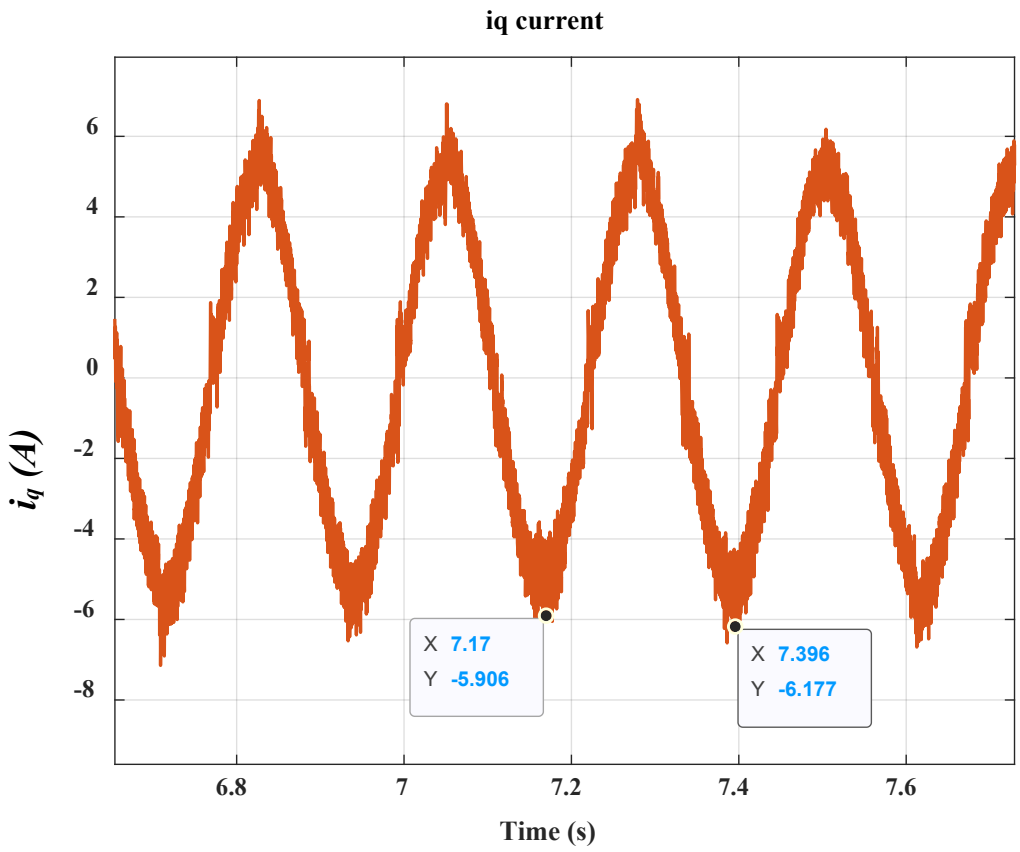

Figure 50. Frequency of oscillations = 4.4 Hz

Chirp signal (Amplitude = 0.8 N.m & frequency varies from 300 to 600 Hz)

A disturbance torque is applied with such a frequency range. No dynamics are spotted during all this range of frequencies, as can be seen in Figure 51.

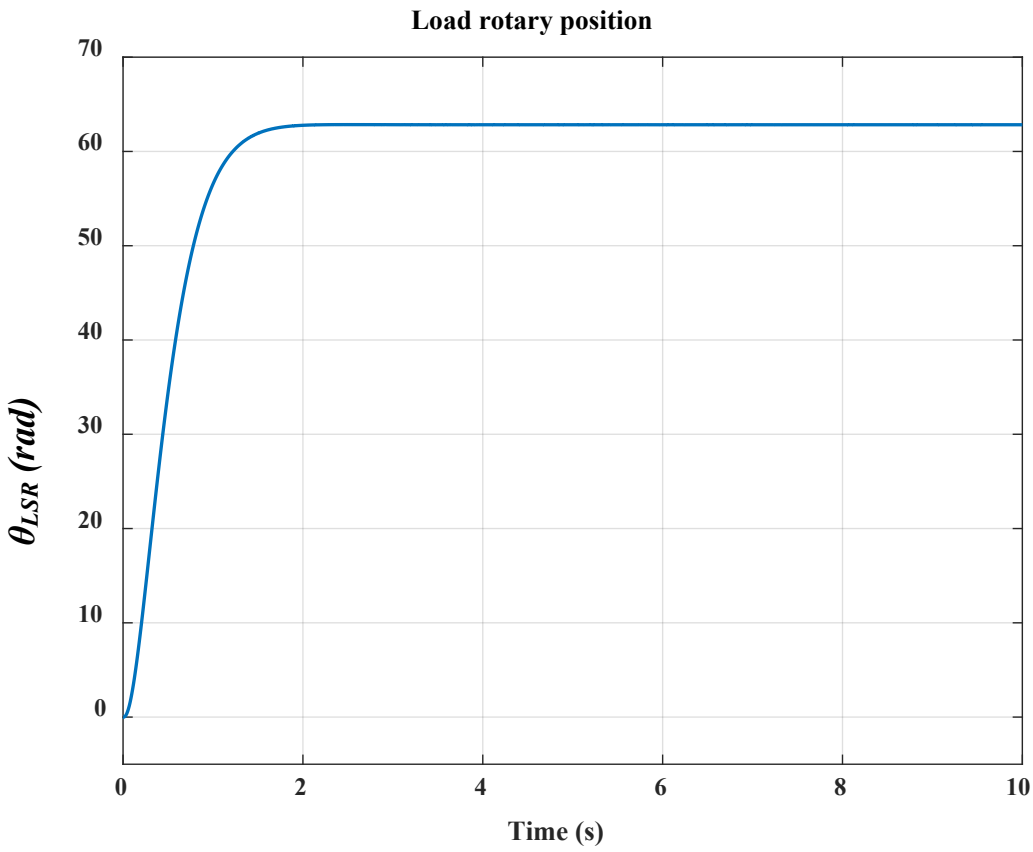

Figure 51. Load position

The current is stable, as shown in Figure 52.

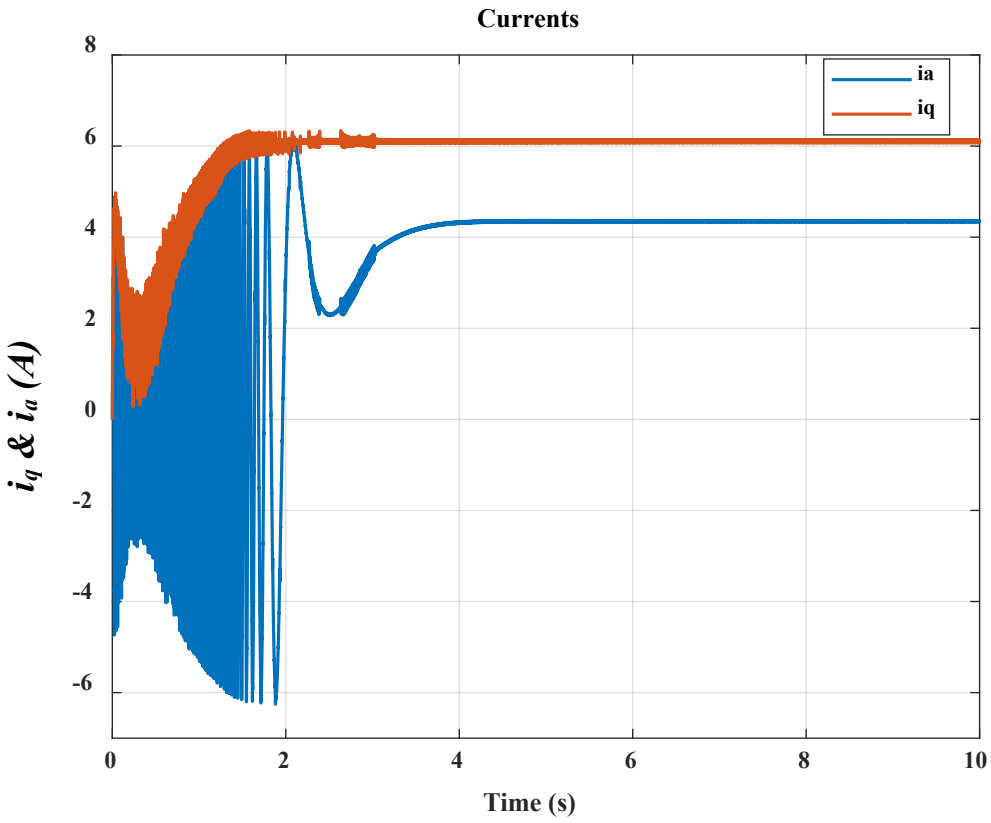

Figure 52. i_a and i_q

Resonance is excited due to magnetic stiffness of the PDD. Instability is clearly observed in the load position and propagated to the electrical system and can be seen in the winding currents. However, no dynamics are shown for the ball-screw system throughout the relevant frequency range (0 to 500 Hz). This might be due to neglecting important dynamics, which implies that the system model might be over simplified.

To recap up to this section**,** Bandwidths of the controllers (current, speed and position) are set to actuate the rudder according to demand within a required time. Various tests are performed to highlight any dynamics of the moving parts that occur within the bandwidth set. The frequency domain analysis of the mechanical system shows only one frequency of the aerodynamic load. Another resonance, which occurs due to PDD magnetic stiffness, is shown when the ball-screw simplified model is integrated with the PDD.

By carrying out time domain tests, the resonance associated with the PDD magnetic stiffness is excited. The load position oscillates between its maximum deflection points and instability is propagated into the electrical system and seen in the PDD winding currents. However, no dynamics of the mechanical system are shown throughout the frequency of interest (1-600 Hz). This either means that there are actually not relevant dynamics of the mechanical system or the significant dynamics are eliminated due

to model over-simplification. So, it is sensible to consider the mechanical system to see whether crucial dynamics are there that should be taken into account.

To sum up, sufficiency of modelling the EMA for MEA as a single inertia needs to be reconsidered. The way to prove this is to look at existing ball-screw models and apply them for this application. This is because modelling the mechanical system will assist in identifying the resonant frequencies and associated mode shapes.

2.4 Implementation of EMA models

In section 2.3, the mechanical drivetrain, which includes the ball-screw system was lumped with the PDD LSR. Reflecting load inertia and lumping it with motor inertia is a traditional method and a common practice, which has many drawbacks [35]. The behaviour of each component of the drivetrain cannot be separately examined hence their respective effects is not considered. Further, interaction between components is also neglected. Also, when one component is changed, the whole model needs to be altered accordingly [35]. For such reasons, it is thought that such technique of modelling is inaccurate [35].

For feed drives, the vibrational mode is mainly influenced by the ball-screw assembly [26]. A model describing the dynamics and vibrational modes of the screw assembly is needed to help in machine design and also controller tuning [28]. High control bandwidth requires higher order plant models as well as a better understanding of the system dynamics [27]. However, it should be always considered that the number of inertia, spring-damper system increases the model computation time exponentially [1].

Many publications are available for the modelling and control of ball-screw drives. By looking at previous publications, ball-screw models can be said to fall into three categories.

Finite element method

This method, according to [38], results in a large number of resonance modes, but it is relatively slow. Drawbacks associated with FEM are stated in literature review. To avoid such problems of FEM method, other simpler techniques are used, which result in simple models that show the dominant effects of the ball-screw assembly. In addition, it is reported that the relevant dynamics are mainly influenced by the first axial and rotational modes [26]. Therefore, discrete and hybrid models seem adequate.

Discrete model

This is when all parameters are modelled as physically lumped parameters [26]. The lumped-parameter model is referred to as the traditional modelling method in [35]. Discrete models are normally simple but the hybrid models are normally more complex. Both model types are shown and compared in [26], where it is shown that both techniques yield in acceptable results, especially for the first axial resonant.

Hybrid model

This is where some parameters are physically lumped but other parameters are considered to be continuous [26]. This is sometimes referred to as distributed-parameter model [22]. In this type of modelling, the screw shaft is considered a continuous element. This approach is useful when spatial distribution is important and has a significant effect on the vibrational modes. A hybrid model assuming the screw as a continuous element and the rest of the components considered as discrete is presented in [26].

A model introduced in [22] represents a low order hybrid model and is satisfactorily validated with practical experimentation.

For the purpose of the current research, a model is required which describes all the important dynamics of the ball-screw assembly. The hybrid model with six-degrees of freedoms, introduced in [22] seems appropriate, since it is fairly simple to implement and exhibits sufficient accuracy. Indeed, good agreement between predictions and measurements are reported in [22], Figure 53. We shall apply this model and decide whether simplification can be adequately made.

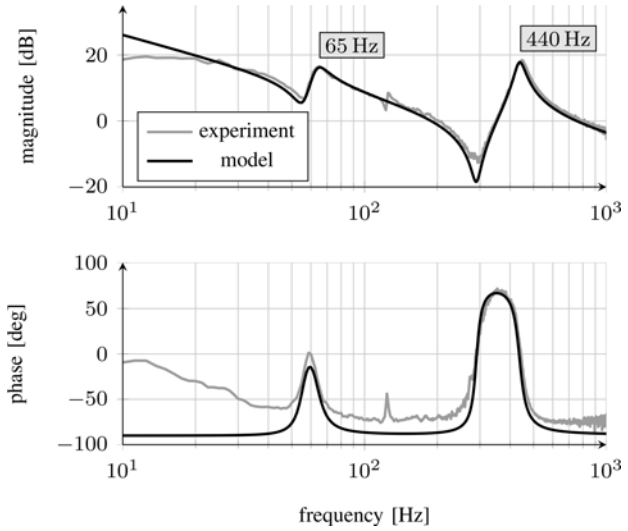

Figure 53. Frequency response from motor current to motor angular velocity [22]

2.4.1 Six-degree of freedom model

Since structure resonance is highly important characteristics of the mechanical system, mechanical structure is looked into in deeper details using vibration analysis. Vibration analysis is performed through three stages. **Spatial model** describes the physical structure of the system in terms of mass/inertia, stiffness and damping properties. **Modal model** describes the structure's behaviour in terms of natural frequencies and corresponding mode shapes. This model is calculated using analytical model analysis on the spatial model. **Response model** describes the manner of which the structure vibrates in response to given excitation conditions; especially with what amplitudes. This model can

have many solution since it depends on properties of structure and type and magnitude of excitation [53].

A six-degree of freedom model, which is introduced in [22], is employed. In the model, the screw is considered like a flexible straight bar that continuously deforms axially and torsionally. Hence, the torsional and translational flexibility properties of the screw shaft are introduced by adding spring stiffness (torsional and linear) terms to the system. Other elements are assumed in the lumped form. For example, bearing is modelled as a lumped linear stiffness, K_b, whereas the coupling between motor and screw is modelled as a lumped rotational stiffness, K_c. The spatial model, illustrating the degrees of freedom, is shown in Figure 54.

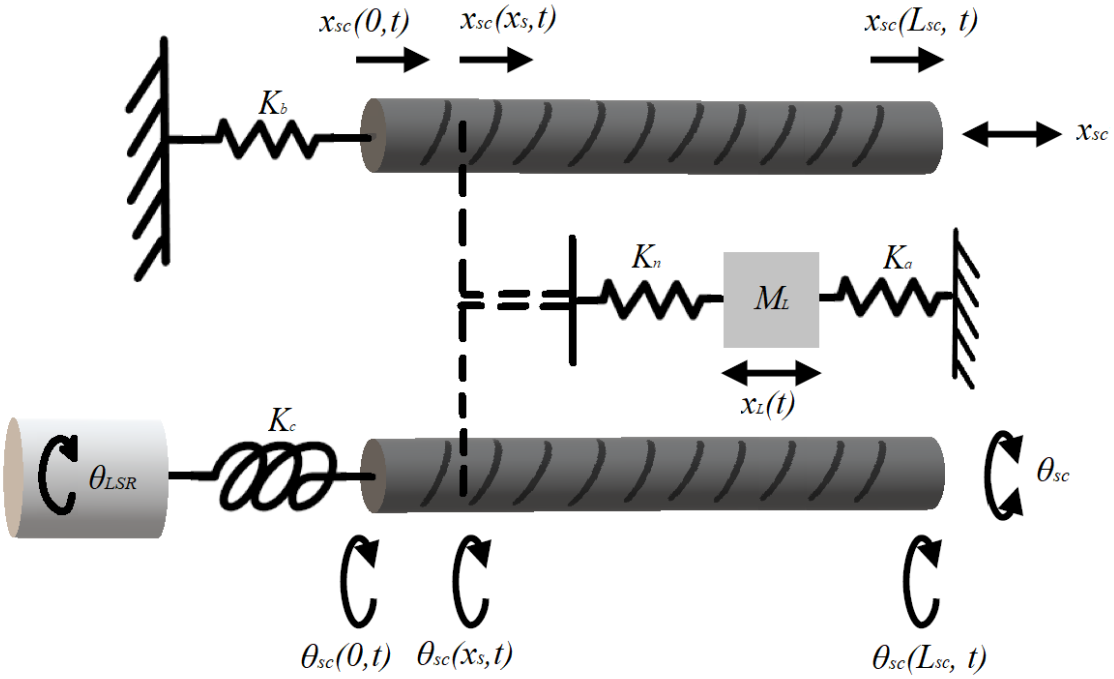

Figure 54. Rotational and axial degrees of freedoms [22]

where K_n is the screw-nut interface stiffness, L_{sc} is the length of the screw shaft, $x_{sc}(x,\ t)$ is the axial translation of the ball-screw shaft, and $\theta_{sc}(x,\ t)$ is the rotation of the ball-screw shaft. Further, positions on the screw shaft are specified using the variable x, where $x = 0$ denoting the position at the PDD end, $x = L_{sc}$ denoting the position at the far end, and $x = x_s$ denoting the position of the slide [22].

The state variables are: PDD LSR angular displacement, θ_{LSR}, axial translation of the load, x_L, screw angular displacement, θ_{sc}, torsion of screw shaft, $\Delta\theta_{sc}$, axial translation of the screw shaft, x_{sc}, and axial deformation of the screw shaft, Δx_{sc}. Four of such motions are rigid body motions whilst two of them are deformation motions. State variables and typed of motion are illustrated in Table 5.

Table 5. State variables and types of motion

State variables		*Type of motion*
θ_{LSR}	*PDD LSR angular displacement*	*rigid*
x_L	*Load axial position*	*rigid*
θ_{sc}	*Screw angular displacement*	*rigid*
$\Delta\theta_{sc}$	*Screw torsional deformation*	*deformation*
x_{sc}	*Screw axial displacement*	*rigid*
Δx_{sc}	*Screw axial deformation*	*deformation*

The continuous deformations are represented by displacements using field functions. Ritz series expansion uses basic functions to formulate the displacement fields. The number of terms in the Ritz series determine the number of degrees of freedom. Kinetic and potential energy equations are written to characterise the distributed-parameter screw dynamics. Lagrange equation, which is power balance equation, is used to derive equations of motion, given by [22]:

$$M\ddot{q} + Kq = T \tag{46}$$

with, q is the state variable vector and is given by:

$$q = [\theta_{LSR} \quad x_L \quad \theta_{sc} \quad \Delta\theta_{sc} \quad x_{sc} \quad \Delta x_{sc}]^T \tag{47}$$

Also, the mass *(M)*, stiffness *(K)* and torque *(T)* matrices are, respectively, given by [22]:

$$M = \begin{bmatrix} J_{LSR}+\frac{1}{2}J_c & 0 & 0 & 0 & 0 & 0 \\ 0 & M_L+M_{sl} & 0 & 0 & 0 & 0 \\ 0 & 0 & \rho_{st}I_{sc}L_{sc}+\frac{1}{2}J_c & \rho_{st}I_{sc}(L_{sc}-\frac{1}{2}x_s) & 0 & 0 \\ 0 & 0 & \rho_{st}I_{sc}(L_{sc}-\frac{1}{2}x_s) & \rho_{st}I_{sc}(L_{sc}-\frac{2}{3}x_s) & 0 & 0 \\ 0 & 0 & 0 & 0 & \rho_{st}A_{sc}L_{sc} & \rho_{st}A_{sc}(L_{sc}-\frac{1}{2}x_s) \\ 0 & 0 & 0 & 0 & \rho_{st}A_{sc}(L_{sc}-\frac{1}{2}x_s) & \rho_{st}A_{sc}(L_{sc}-\frac{2}{3}x_s) \end{bmatrix} \tag{48}$$

$$K = \begin{bmatrix} K_c & 0 & -K_c & 0 & 0 & 0 \\ 0 & K_n+K_a & -\gamma K_n & -\gamma K_n & -K_n & -K_n \\ -K_c & -\gamma K_n & K_c+\gamma^2 K_n & \gamma^2 K_n & \gamma K_n & \gamma K_n \\ 0 & -\gamma K_n & \gamma^2 K_n & \frac{G_{sc}I_{sc}}{x_s}+\gamma^2 K_n & \gamma K_n & \gamma K_n \\ 0 & -K_n & \gamma K_n & \gamma K_n & K_n+K_n & K_n \\ 0 & -K_n & \gamma K_n & \gamma K_n & K_n & \frac{A_{sc}E_{sc}}{x_s}+K_n \end{bmatrix} \tag{49}$$

$$T = [T_{LSR} \quad 0 \quad 0 \quad 0 \quad 0 \quad 0]^T \tag{50}$$

Note: symbols are defined in the table of notation.

As mentioned previously, upon the full deployment of the rudder for maximum load, the rudder deflects up to 30°, which is equivalent to a nut displacement of 50 mm. This aerodynamic load varies linearly

with displacement. The linear aerodynamic stiffness, K_a, may be calculated in Equation (51) and inserted to the stiffness matrix (49).

$$K_a = \frac{F_{sc}}{x_L} = 180000\ N/m \tag{51}$$

Furthermore, this model enables determination of natural frequencies as nut position changes on the screw shaft. The key parameter representing nut position is x_s, which is included in matrices (48) and (49). In this test, location of nut is assumed to be 0.05 m away from the motor. This approximates the position of nut at around 50 mm which corresponds to the rudder zero position.

By applying the model to first case study in the thesis, using parameters presented in Table 1, Table 2 and Table 3, eigenvalue and eigenvector analysis is performed to help obtain the system modal model. By taking the square root of the eigenvalues, natural frequencies can be determined in *rad/s*, which is then divided by 2π to convert it into *Hertz*.

Note that the mass of slide, M_{sl}, in Table 2, is small when compared with the equivalent mass of load, M_L and hence M_{sl} can be neglected. Also the inertia of coupling, J_c, is significantly small and therefore, it can be neglected.

Eigenvalue and eigenvector analysis

Free vibration solution can be considered to find out the natural modal properties. So,

$$T = 0 \tag{52}$$

A solution can be assumed to exist in the form

$$\{q(t)\} = \{v\}e^{j\omega_i t} \tag{53}$$

where $\{v\}$ is a vector of amplitudes and dimension of $N_d \times 1$, N_d is the number of degrees of freedom, ω_i is natural frequency (in rad/s), and i ranges from 1 to N_d and denotes the number of the natural frequency. It is clear that:

$$\{\ddot{q}\} = -\omega_i^2\{v\}e^{j\omega_i t} \tag{54}$$

Equations (53) and (54) can be substituted in Equation (46).

$$M\left(-\omega_i^2\{v\}e^{j\omega_i t}\right) + K\left(\{v\}e^{j\omega_i t}\right) = ([K] - \omega_i^2[M])\{v\}e^{j\omega_i t} = \{0\} \tag{55}$$

The only non-trivial solution is:

$$det\left|[K] - \omega_i^2[M]\right| = 0 \tag{56}$$

The determinant of the matrix yields a sixth degree polynomial. Using Matlab, it is possible to find the roots of the polynomial. In addition, it is possible to find eigenvectors for each eigenvalue considering the following equation:

$$\left([K] - \omega_i^2[M]\right)v = -\omega_i^2 v \tag{57}$$

The complete solution can be summarised in two $N_d \times N_d$ matrices, which are called the eigenmatrices.

$$[e_i], [v_v] \tag{58}$$

$[e_i]$ is known as the eigenvalue matrix, which is a diagonal matrix whose elements reflect the natural frequency (in rad/s) squared, as shown in Equation (59).

$$[e_i] = [\omega_i^2] \tag{59}$$

Also, e_i can also refer to the i-th eigenvalue in the matrix. For example, e1 refers to the 1st eigenvalue.

On the other hand, $[v_v]$ is called the eigenvector matrix, which describes the corresponding mode shape. The entries of the eigenvector matrix, $v_{i[1]}$ to $v_{i[6]}$, correspond to the entries of the state variable vector matrix represented in Equation (47), as shown in Table 6.

Table 6. Elements of the eigenvectors

Entry	Corresponding motion
$v_{i[1]}$	Rotation of motor
$v_{i[2]}$	Axial displacement of the nut
$v_{i[3]}$	Rigid rotation of the screw shaft
$v_{i[4]}$	Torsional deformation of the screw shaft
$v_{i[5]}$	Rigid axial displacement of the screw shaft
$v_{i[6]}$	Axial deformation of he screw shaft

Results

It is mentioned above that the model enables calculation with various nut position. To start with, calculations are to be performed for the nut at position 0.05 m, which reflects the 0º position rudder (Figure 38).

Eigenvalues

$$e_i = \begin{bmatrix} 753 & 0 & 0 & 0 & 0 & 0 \\ 0 & 4124769 & 0 & 0 & 0 & 0 \\ 0 & 0 & 5.3 \times 10^8 & 0 & 0 & 0 \\ 0 & 0 & 0 & 9.7 \times 10^8 & 0 & 0 \\ 0 & 0 & 0 & 0 & 2.4 \times 10^{10} & 0 \\ 0 & 0 & 0 & 0 & 0 & 4.4 \times 10^{10} \end{bmatrix} \tag{60}$$

Eigenvectors

$$v_v = \begin{bmatrix} 81 & 31 & 41 & 3.5 & -5 & 0.001 \\ 0.065 & -0.17 & -0.001 & 0.015 & 2.43 \times 10^{-5} & -0.0001 \\ 81 & 30 & -99 & -18 & 720 & -0.3 \\ 0 & -0.6 & -91 & -13 & -791 & 0.45 \\ -5.1 \times 10^{-5} & -0.106 & 0.187 & -1.268 & -0.0038 & -4.952 \\ -8.1 \times 10^{-6} & -0.017 & 0.025 & -1.142 & 0.0026 & 5.57 \end{bmatrix} \quad (61)$$

Scaling of eigenvectors

Since the eigenvectors refer to the mode shape, which include translational and rotational motions, scaling is needed to help interpret the results.

$$\begin{bmatrix} 1 & 0 & 0 & 0 & 0 & 0 \\ 0 & \frac{1}{\gamma} & 0 & 0 & 0 & 0 \\ 0 & 0 & 1 & 0 & 0 & 0 \\ 0 & 0 & 0 & 1 & 0 & 0 \\ 0 & 0 & 0 & 0 & \frac{1}{\gamma} & 0 \\ 0 & 0 & 0 & 0 & 0 & \frac{1}{\gamma} \end{bmatrix} \begin{bmatrix} 81 & 31 & 41 & 3.5 & -5 & 0.001 \\ 0.065 & -0.17 & -0.001 & 0.015 & 2.43 \times 10^{-5} & -0.0001 \\ 81 & 30 & -99 & -18 & 720 & -0.3 \\ 0 & -0.6 & -91 & -13 & -791 & 0.45 \\ -5.1 \times 10^{-5} & -0.106 & 0.187 & -1.268 & -0.0038 & -4.952 \\ -8.1 \times 10^{-6} & -0.017 & 0.025 & -1.142 & 0.0026 & 5.57 \end{bmatrix} \quad (62)$$

The results of the scaling yields in a clear version of the eigenvectors.

$$v_{v\_scaled} = \begin{bmatrix} 81 & 31 & 41 & 3.5 & -5 & 0.001 \\ 81 & -215 & -1.44 & 18 & 0.03 & -0.172 \\ 81 & 30 & -99 & -18 & 720 & -0.3 \\ 0 & -0.6 & -91 & -13 & -791 & 0.45 \\ 0 & -133 & 235 & -1593 & -4.8 & -6222 \\ 0 & -21 & 31 & -178 & 3.3 & 6997 \end{bmatrix} \quad (63)$$

Natural frequencies

Each eigenvalue and eigenvector describes a free vibration mode of the system structure. The i-th natural frequency, f_i, is related to the eigenvalue, e_i, via the following equation.

$$f_i = \frac{\omega_i}{2\pi} = \frac{\sqrt{e_i}}{2\pi} \quad (64)$$

Table 7 shows a summary of the natural frequencies.

Table 7. System natural frequencies

f_1	f_2	f_3	f_4	f_5	f_6
4.37	*323*	*3664*	*4950*	*24401*	*33438*

With respect to Table 7, it is clear that there are two significant frequencies, which are f_1 and f_2 being sufficiently low to be within the bandwidth of the current controller. All other frequencies are considerably high.

Influence of nut position

The previous results are obtained with the nut positioned at 0.05 m, which corresponds to 0º of rudder (Figure 38). Additionally, it is shown in Table 7 that only the first two frequencies are significant since they occur within the bandwidth of the current controller. Therefore, previous analysis is carried out again for different nut position to help decide whether nut position should be considered.

Figure 55 shows variation of f_1 with respect to nut position. It can be seen that the difference is minor and hence it can be said that nut position has no influence on f_1.

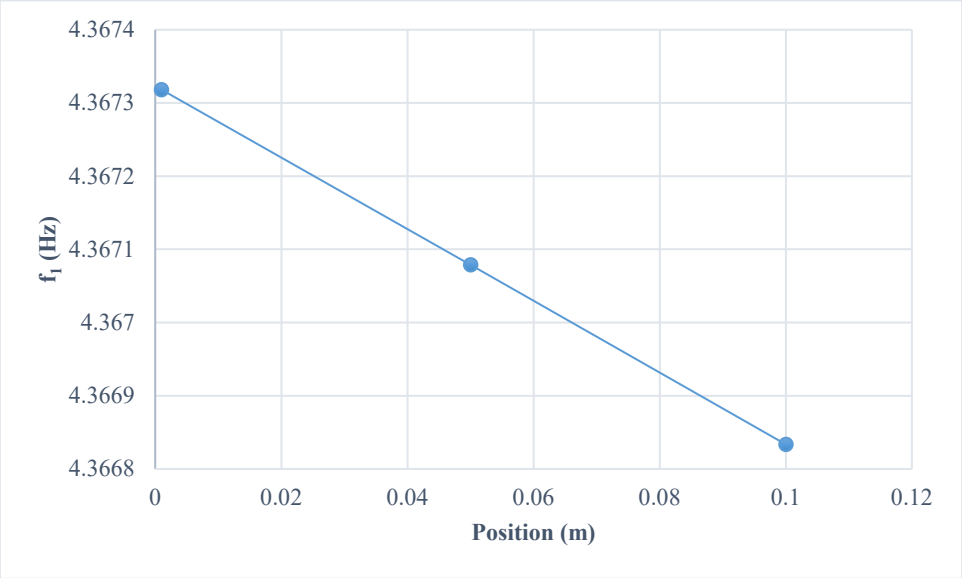

Figure 55. f_1 variation with nut position

Figure 56 shows variation of f_2 with respect to nut position. The difference between close end and far end is 28 Hz and that makes an error of 8 %, which is insignificant. For such a reason, it can be said that variation of nut position as rudder is actuated between ±30º can be neglected.

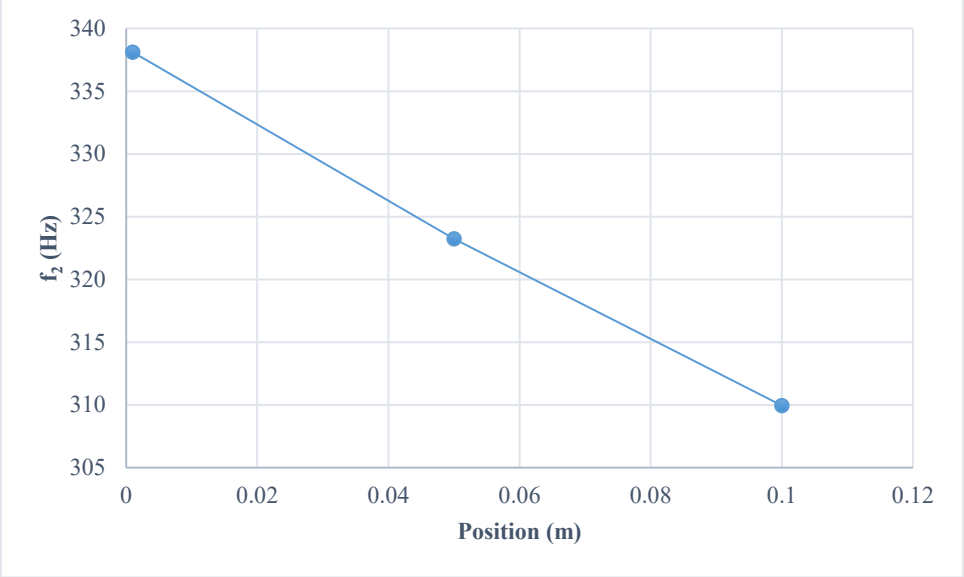

Figure 56. f_2 variation with nut position

Mode shapes of the natural frequencies

It is mentioned above that for each of the natural frequencies, presented in Table 7, free vibration occurs with the mode shape described by the eigenvectors, which are given in Equation (63).

The first column in Equation (63) shows the motion of the structure elements at f_1 (4.37 Hz). It can clearly be seen that the load equivalent mass, screw and motor are moving uniformly. They seem to move against the aerodynamic stiffness, K_a, which is the key factor here. Figure 57 illustrates this mode.

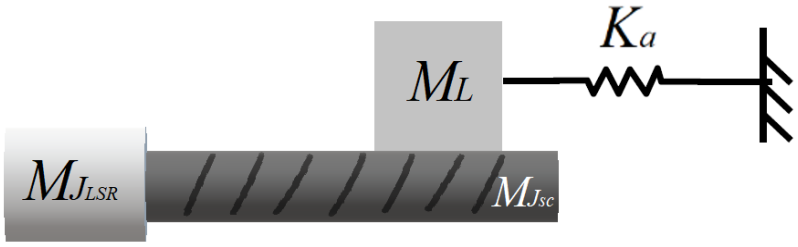

Figure 57. Mode shape at f_1

Since all rigid elements are vibrating against the aerodynamic stiffness, K_a, which is an axial stiffness, hence this mode can be classified to be an axial mode. It is possible to estimate this mode using a simple equation by carrying out the following analysis of the basic vibration theory.

Newton's equation is written for the masses, which states that the force applied by the spring on the masses is equal and opposite to the force exerted by the mass on the spring, as shown in Equation (65). Note that the inertias of the screw and the PDD LSR are converted into their equivalent masses, as $M_{J_{sc}}$ and $M_{J_{LSR}}$ respectively, since they are acting on the axial spring.

$$(M_L + M_{J_{sc}} + M_{J_{LSR}})\ddot{x_1} + K_a x_1 = (M_L + \frac{J_{sc}}{\gamma^2} + \frac{J_{LSR}}{\gamma^2})\ddot{x_1} + K_a x_1 = 0 \quad (65)$$

By taking Laplace transform of both sides with initial conditions equal to zero, the following equation can be obtained.

$$\mathcal{L}\{(M_L + \frac{J_{sc}}{\gamma^2} + \frac{J_{LSR}}{\gamma^2})\ddot{x_1} + K_a x_1\} = \mathcal{L}\{0\} \quad (66)$$

$$X_1\{s^2(M_L + \frac{J_{sc}}{\gamma^2} + \frac{J_{LSR}}{\gamma^2}) + K_a\} = 0 \quad (67)$$

From which,

$$s^2(M_L + \frac{J_{sc}}{\gamma^2} + \frac{J_{LSR}}{\gamma^2}) = -K_a \rightarrow s^2 = -\frac{K_a}{M_L + \frac{J_{sc}}{\gamma^2} + \frac{J_{LSR}}{\gamma^2}} \quad (68)$$

Also, s is given by:

$$s = \sigma + j\omega \quad (69)$$

where σ is the real part of s denoting the system stability, and ω is the imaginary part representing the frequency of oscillation. The previous equation can be made general to be used in any natural frequency analysis as follows.

$$s_i = \sigma_i + j\omega_i \quad (70)$$

Since analysis is carried out for undamped system,

$$s_i = j\omega_i \rightarrow s_i^2 = -\omega_i^2 \quad (71)$$

By equating Equations (68) and (71), it is possible to write for the first natural frequency that;

$$\omega_1^2 = \frac{K_a}{M_L + \frac{J_{sc}}{\gamma^2} + \frac{J_{LSR}}{\gamma^2}} \quad (72)$$

Considering Equation (64), it is then possible to write (71) as follows.

$$f_1 = \frac{1}{2\pi}\sqrt{\frac{K_a}{M_L + \frac{J_{sc}}{\gamma^2} + \frac{J_{LSR}}{\gamma^2}}} = 4.37\ Hz \quad (73)$$

Which analytically determines the first mode with 0% error.

The second column in Equation (63) shows the motion of the structure elements at f_2 (323 Hz). It can clearly be seen that the motion is dominant by, primarily, load mass and, secondarily, the screw mass. The most significant parameter is the stiffness of the bearing K_b. So, the load equivalent mass, M_L, and the screw mass, M_{sc}, move against the bearing. In addition, since the load mass is connected with the screw shaft through the screw-nut interface, its stiffness also affects this mode. Notice also, that the PDD LSR inertia , J_{LSR}, and screw inertia, J_{sc}, move in a similar magnitude with the same sign meaning that stiffness of coupling has nearly no contribution in this frequency. Figure 58 represents this motion, which suggests that this mode is an axial mode.

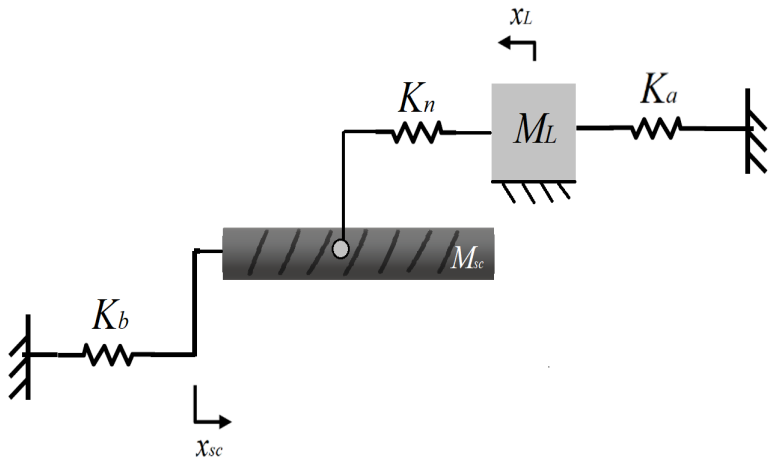

Figure 58. Mode shape at f_2

The value of load mass is highly greater than the screw mass (Table 2). Therefore, it is possible to consider this mode shape as the load mass oscillating against the equivalent linear stiffness, which can be evaluated using the spring-in-series Equation (74). Figure 59 illustrates a more simplified version of Figure 58.

$$\frac{1}{K_{eq}} = \frac{1}{K_n} + \frac{1}{K_b} \rightarrow K_{eq} = 118360715.7 \text{ N/m} \tag{74}$$

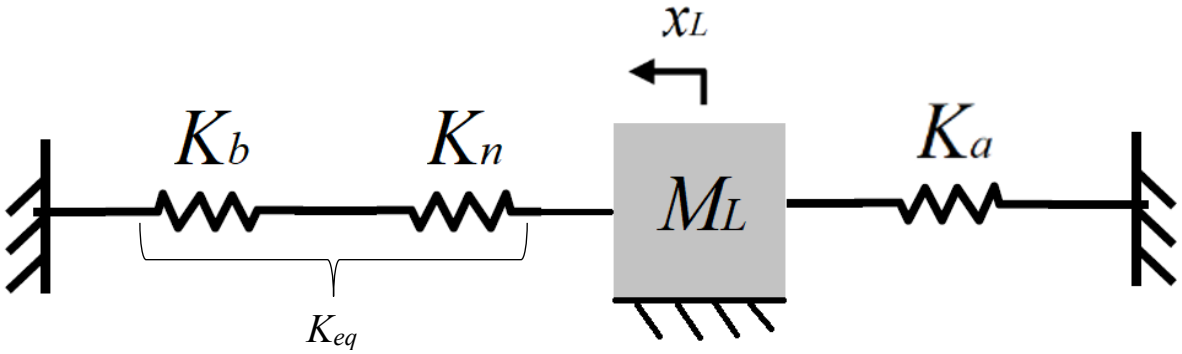

Figure 59. Mode shape at f_2 (simplified)

K_{eq} and K_a are connected in parallel. Equation (75) calculates the equivalent stiffness.

$$K_{eq1} = K_{eq} + K_a = 118540715.7 \text{ N/m} \quad (75)$$

Note the difference in the values of K_{eq} and K_{eq1} in Equation (74) and Equation (75), respectively. The impact of K_a is almost negligible. However, if K_a becomes greater than K_{eq}; that is, K_{eq} is reduced, then K_a will have the dominant effect.

Having simplified Figure 58 into Figure 59, then the natural frequency of the system, shown in Figure 59, can be analytically approximated using Equation (76), which represents the purely decoupled system; fixed-free system.

$$f_2 = \frac{1}{2\pi}\sqrt{\frac{K_{eq1}}{M_L}} = 318.3\ Hz \quad (76)$$

Considering the screw-nut interface stiffness is beneficial since the model applies a finite screw-nut interface stiffness. Also, the second column in Equation (63) shows some difference in magnitude between load and screw mass motions. If screw mass and load mass are assumed perfectly coupled implying that the screw-nut interface stiffness is infinite, then Figure 60 can be used to represent this resonance.

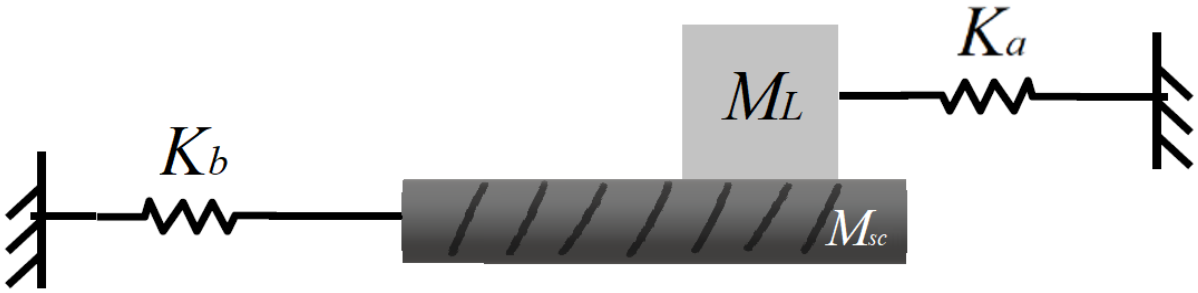

Figure 60. Mode shape at f_2 (simplified)

In this case, Equation (77) can be used.

$$f_2 = \frac{1}{2\pi}\sqrt{\frac{K_b + K_a}{M_L + M_{sc}}} = 410.2\ Hz \quad (77)$$

The result of Equation (76) (*318.3 Hz*) is closer to the model value (*323 Hz*), than the results of Equation (77). According to Equations (76) and (77), this frequency seems to increase with an increase in stiffness of screw-nut interface and stiffness of the bearing and a decrease in load mass and screw mass, which is expected. It is a translational vibration that occurs at this frequency, as seen above. This is a significant resonant frequency that can potentially cause instability when excited.

Effect of K_a

It is mentioned above that in the case of aero application, the load force is a function of the screw nut position, which is a function of the rudder position. This adds the aerodynamic stiffness, K_a. From Figure 58 and Figure 59, it can be seen that K_b and K_n are in series but this combination is connected with K_a in parallel, from which Equation (75) calculates the equivalent stiffness.

The load dependency on K_a has certainly an influence on system dynamics; especially at low values of K_b. Figure 61 shows the variation of f_2, as a result of altering K_b, with and without K_a. This illustrates the difference between normal feed drive systems, where load is only a mass load, and the aero EMA system, where load is a function of position.

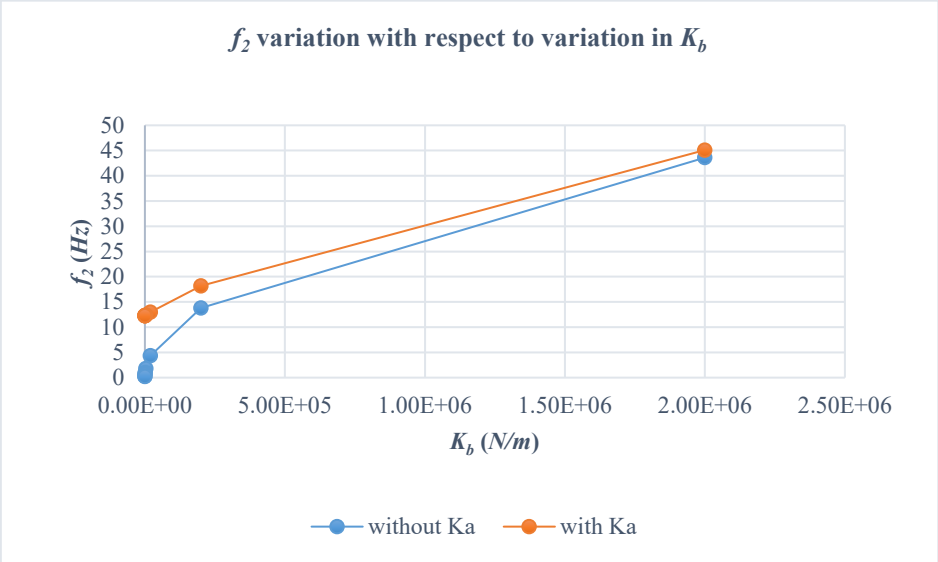

Figure 61. f_2 with respect to variation in K_b

As K_b decreases, Equation (75) becomes;

$$K_{eq1} \approx K_a \tag{78}$$

For example, in the nominal case, Equation (76) becomes,

$$f_2 = \frac{1}{2\pi}\sqrt{\frac{K_a}{m_L}} = 12.4\ Hz \tag{79}$$

Therefore, f_2 can never go below 12.4 Hz.

The third column in Equation (63) shows the motion of the structure elements at f_3 (3664 Hz). It can be observed that the highest amplitude of motion is that which refers to the axial translation of the screw. However, the screw inertia moves in opposite direction to the PDD LSR inertia with significant amplitudes. In this case, stiffness of the coupling, K_c, is the most compliant element. Therefore, at this frequency, it seems that as the screw inertia oscillates opposite to the LSR inertia due to coupling

compliance, the screw translates, back and forth, against the bearing simultaneously. This suggests that this mode is mainly a rotational mode. Figure 62 summarises this motion.

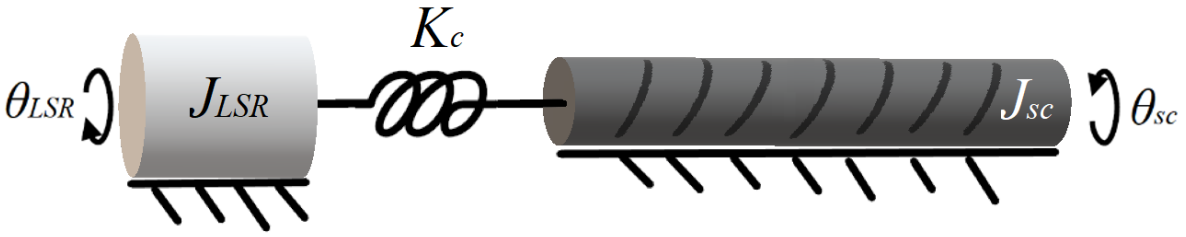

Figure 62. Mode shape at f_3

Such mode is represented by two inertias with a spring in between. Both inertias vibrate with a single frequency. To find out the suitable simplified equation, the following analysis is introduced.

Since both inertias vibrate with the same frequency, therefore, their displacements can be written according to the following two equations.

$$\theta_{sc} = A_\theta \cos(\omega_i t) \tag{80}$$

$$\theta_{LSR} = B_\theta \cos(\omega_i t) \tag{81}$$

where A_θ and B_θ are amplitudes of θ_{sc} and θ_{LSR}, respectively.

Newton's equation is written in a similar way to Equation (65) for θ_{sc} and θ_{LSR} as follows,

$$K_c(\theta_{sc} - \theta_{LSR}) = -J_{sc}\frac{d^2\theta_{sc}}{dt^2} \tag{82}$$

$$K_c(\theta_{sc} - \theta_{LSR}) = J_{LSR}\frac{d^2\theta_{LSR}}{dt^2} \tag{83}$$

Substituting Equations (80) and (81) into Equation (82) and Equation (83), respectively,

$$K_c(B_\theta \cos(\omega_i t) - A_\theta \cos(\omega_i t)) = -J_{sc}A_\theta\omega_i^2 \cos(\omega_i t) \tag{84}$$

$$K_c(B_\theta \cos(\omega_i t) - A_\theta \cos(\omega_i t)) = J_{LSR}B_\theta\omega_i^2 \cos(\omega_i t) \tag{85}$$

It can be noticed that,

$$J_{LSR}B_\theta\omega_i^2 \cos(\omega_i t) = -J_{sc}A_\theta\omega_i^2 \cos(\omega_i t) \tag{86}$$

Therefore,

$$J_{LSR}B_\theta = -J_{sc}A_\theta \rightarrow A_\theta = -\frac{J_{LSR}B_\theta}{J_{sc}} \tag{87}$$

It is possible to plug Equation (87) into Equation (84),

$$K_c\left(B_\theta\cos(\omega_i t)+\frac{J_{LSR}B_\theta}{J_{sc}}\cos(\omega_i t)\right)=J_{sc}\frac{J_{LSR}B_\theta}{J_{sc}}B_\theta\omega_i^2\cos(\omega_i t) \tag{88}$$

Simplify to get,

$$K_c\left(1+\frac{J_{LSR}}{J_{sc}}\right)=J_{LSR}\omega_i^2 \tag{89}$$

Which leads to,

$$\omega_3^2=K_c\frac{J_{LSR}+J_{sc}}{J_{LSR}J_{sc}} \tag{90}$$

Equation (91) shows how this resonant frequency can be estimated.

$$f_3=\frac{1}{2\pi}\sqrt{K_c\frac{J_{LSR}+J_{sc}}{J_{LSR}J_{sc}}}=4607\ Hz \tag{91}$$

which is a little different to the value calculated by the model (3664 Hz) since for this particular system and this particular specification, there is a translational component, beside the rotary one. This translational component is explained by the Equation (63) that the screw translates, back and forth, against the bearing.

The fourth column in Equation (63) shows the motion of the structure elements at f_4 (4950 Hz). It can be observed that the vibration of the screw mass is the dominant motion, yielding that this mode is axial. The screw mass moves in opposite direction to load mass making the screw-nut interface stiffness, K_n, a significant element. Furthermore, the stiffness of the bearing also has a significant contribution here since the screw mass can move with respect to K_b. Figure 63 depicts the mode shape in a form of mass-spring system.

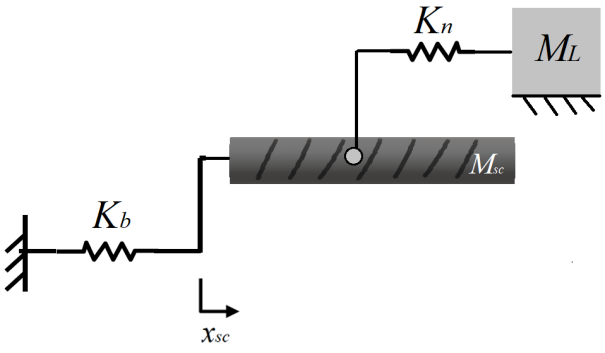

Figure 63. Mode shape at f_4

The amplitude of motion for the load mass is insignificant if compared with the amplitude of screw mass translation motion, as can be seen in Equation (63) (fourth column). Therefore, it is possible to neglect the load mass movement and assume it as a mechanical ground (Figure 64).

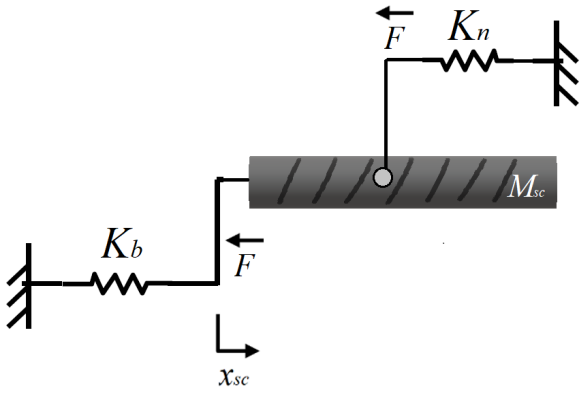

Figure 64. Mode shape at f_4 (simplified)

It is possible to consider this mode shape as the screw mass, M_{sc}, oscillating against the equivalent linear stiffness. This is a two-spring-one-mass system and the equivalent stiffness can be evaluated using Equation (92).

$$K_{eq2} = K_n + K_b = 489960199\ N/m \tag{92}$$

Having simplified the system in Figure 63 to the one in Figure 64, then the natural frequency of the system, shown in Figure 64, can be analytically approximated using Equation (95), which represents the purely decoupled system; fixed-free system (in a similar way to Equation (73)).

$$f_4 = \frac{1}{2\pi}\sqrt{\frac{K_{eq2}}{M_{sc}}} = 4972.2\ Hz \tag{93}$$

which is very close to the model calculated value (4950 Hz).

Table 8 summarises the resonances determined by the six-degree of freedom model and the ones estimated using simplified equations, where good agreements can be seen. The simplified equations clearly highlight the important parameters affecting a particular frequency. Figures are in Hertz.

Table 8. Summary of resonances (6-DOF model and simplified equations)

Resonance	*Model*	*Simplified equations*
$f_1\ (Hz)$	*4.37*	*4.37*
$f_2\ (Hz)$	*323*	*318.3*
$f_3\ (Hz)$	*3664*	*4607*
$f_4\ (Hz)$	*4950*	*4972.2*

By using a full model, frequencies are identified and two frequencies are found critical; f_1 and f_2. In order to justify the importance of modelling the EMA in more details, the findings are compared with the single-inertia model used in literature.

Simplified single inertia model

In this case, screw is assumed ideal. Figure 65 shows this lumped parameter model.

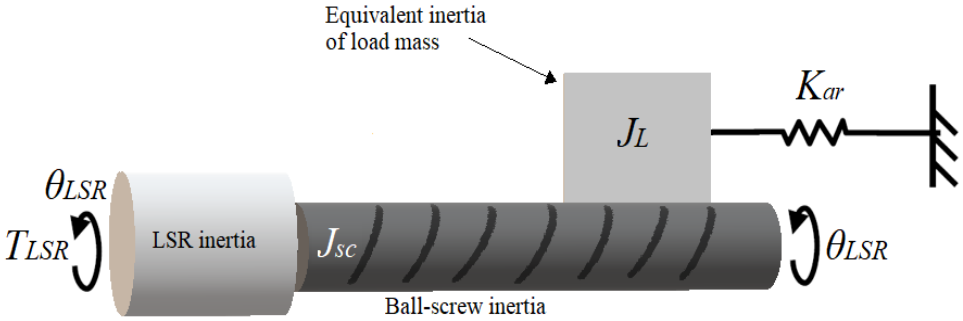

Figure 65. Spatial model of simplified one-DOF model

Newton's second law is applied as follows,

$$T_{LSR} - K_{ar}\theta_{LSR} = J_s\ddot{\theta}_{LSR} \tag{94}$$

By taking Laplace transform to both sides,

$$T_{LSR} - K_{ar}\theta_{LSR} = s^2 J_s \theta_{LSR} \tag{95}$$

The system model is implemented in Simulink as shown in Figure 66.

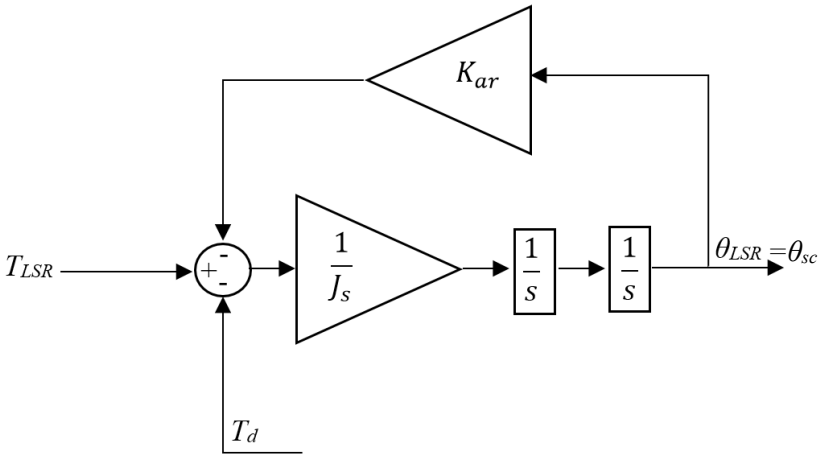

Figure 66. Simulink implementation of one-DOF model

Ignoring any disturbance, the system natural frequency can be analytically obtained according to the following analysis.

$$(T_{LSR} - K_{ar}\theta_{LSR})\frac{1}{J_s s^2} = \theta_{LSR} \tag{96}$$

By rearranging, transfer function can be determined,

$$\frac{\theta_{LSR}}{T_{LSR}} = \frac{1}{J_s s^2 + K_{ar}} \tag{97}$$

Considering Equation (69) and Equation (70), Equation (97) can be rewritten as,

$$\frac{\theta_{LSR}}{T_{LSR}} = \frac{1}{J_s s_i^2 + K_{ar}} \tag{98}$$

The poles are taken to be,

$$J_s s_i^2 + K_{ar} = 0 \rightarrow s_i^2 = -\frac{K_{ar}}{J_s} \tag{99}$$

Considering Equation (71),

$$\omega_1^2 = \frac{K_{ar}}{J_s} \rightarrow \omega_1 = \sqrt{\frac{K_{ar}}{J_s}} \tag{100}$$

Hence, the natural frequency is,

$$f_1 = \frac{1}{2\pi}\sqrt{\frac{K_{ar}}{J_s}} = 4.39\ Hz \tag{101}$$

Receptance is the ratio between torque and position [53]. When response is measured at the point of excitation, it is called **Point receptance** [53]. Frequency response is taken for the simplified model and the point receptance is shown in Figure 67. It can be observed that only one frequency can be seen, which is f_1. In contrary, f_2, which is determined using the six-DOF model, cannot be shown.

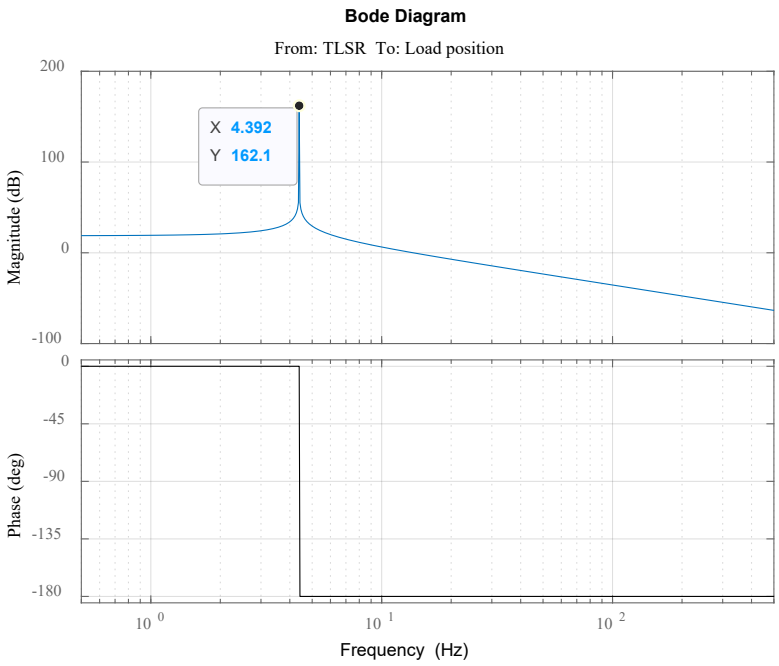

Figure 67. Bode plot (single inertia model)

It can be stated that the six-DOF model highlights an important frequency, whereas such a resonance is ignored using the single-DOF model. Therefore, the single-DOF model cannot be used due to oversimplification. Additionally, the six-DOF model unnecessarily shows high frequency resonances, which are damped by the controller. Therefore, some resonances can be neglected for control purposes. For such a reason, a model ought to be used that is simple and can adequately shows the crucial dynamics. In the following section, the six-DOF model is further simplified to include three and two degrees of freedom models, respectively.

Proposed modelling methodology

The fifth and sixth columns in Equation (63) confirm that the highest two frequencies, f_5 and f_6, are dominated by the torsional and axial deformations of the screw, respectively. Such deformations depend on the properties of the ball screw, as matrices (48) and (49) imply.

Furthermore, the effects of these two motions on the lower frequency modes, the first and second column in Equation (63), are negligible. Therefore, it can be stated that at f_1 and f_2 the contributions of screw translational and torsional compliances are negligible. From this, it can be deduced that torsional and translational compliances can be neglected and hence the screw shaft can be assumed and modelled as a rigid element.

We begin simplification process by eliminating these two frequencies, f_5 and f_6. But before we proceed, matrix is written in equation form to make mathematical manipulations easier. Furthermore, coupling inertia, J_c, and mass of slide, M_{sl}, are small and hence they can be neglected.

$$J_{LSR}\ddot{\theta}_{LSR} + K_c\theta_{LSR} - K_c\theta_{sc} = T_{LSR} \tag{102}$$

$$M_L\ddot{x}_L + K_n x_L - \gamma K_n\theta_{sc} - \gamma K_n\Delta\theta_{sc} - K_n x_{sc} - K_n\Delta x_{sc} + K_a x_L = 0 \tag{103}$$

$$\begin{aligned}\rho_{st}I_{sc}L_{sc}\ddot{\theta}_{sc} + \rho_{st}I_{sc}\left(L_{sc} - \frac{1}{2}x_s\right)\Delta\ddot{\theta}_{sc} - K_c\theta_{LSR} - \gamma K_n x_L + (K_c + \gamma^2 K_n)\theta_{sc} \\ + \gamma^2 K_n\Delta\theta_{sc} + \gamma K_n x_{sc} + \gamma K_n\Delta x_{sc} = 0\end{aligned} \tag{104}$$

$$\begin{aligned}\rho_{st}I_{sc}\left(L_{sc} - \frac{1}{2}x_s\right)\ddot{\theta}_{sc} + \rho_{st}I_{sc}\left(L_{sc} - \frac{2}{3}x_s\right)\Delta\ddot{\theta}_{sc} - \gamma K_n x_L + \gamma^2 K_n\theta_{sc} \\ + \left(\frac{G_{sc}I_{sc}}{x_s} + \gamma^2 K_n\right)\Delta\theta_{sc} + \gamma K_n x_{sc} + \gamma K_n\Delta x_{sc} = 0\end{aligned} \tag{105}$$

$$\begin{aligned}\rho_{st}A_{sc}L_{sc}\ddot{x}_{sc} + \rho_{st}A_{sc}\left(L_{sc} - \frac{1}{2}x_s\right)\Delta\ddot{x}_{sc} - K_n x_L + \gamma K_n\theta_{sc} + \gamma K_n\Delta\theta_{sc} \\ + (K_b + K_n)x_{sc} + K_n\Delta x_{sc} = 0\end{aligned} \tag{106}$$

$$\begin{aligned}\rho_{st}A_{sc}\left(L_{sc} - \frac{1}{2}x_s\right)\ddot{x}_{sc} + \rho_{st}A_{sc}\left(L_{sc} - \frac{2}{3}x_s\right)\Delta\ddot{x}_{sc} - K_n x_L + \gamma K_n\theta_{sc} + \gamma K_n\Delta\theta_{sc} \\ + K_n x_{sc} + \left(\frac{A_{sc}E_{sc}}{x_s} + K_n\right)\Delta x_{sc} = 0\end{aligned} \tag{107}$$

Note: symbols are defined in the table of notation.

From the arguments made above, screw torsional and axial deformations are to be neglected and hence set equal to *0*.

$$\Delta\theta_{sc} = 0 \tag{108}$$

$$\Delta x_{sc} = 0 \tag{109}$$

Additionally, it is useful to recall that,

$$I_{sc}L_{sc}\rho_{st} = J_{sc} \tag{110}$$

$$\rho_{st}A_{sc}L_{sc} = M_{sc} \tag{111}$$

Further, equations can be re-ordered so rotational motions are represented by the first two lines whereas the translational motions are shown in the third and fourth lines. Therefore, Equations (102) to (107) become:

$$T_{LSR} - K_c(\theta_{LSR} - \theta_{sc}) = J_{LSR}\ddot{\theta}_{LSR} \tag{112}$$

$$K_c(\theta_{LSR} - \theta_{sc}) - K_n((\gamma^2\theta_{sc} + \gamma x_{sc}) - \gamma x_L) = J_{sc}\ddot{\theta}_{sc} \tag{113}$$

$$-K_b x_{sc} - K_n((\gamma\theta_{sc} + x_{sc}) - x_L) = M_{sc}\ddot{x}_{sc} \tag{114}$$

$$K_n((\gamma\theta_{sc} + x_{sc}) - x_L) - K_a x_L = M_L \ddot{x}_L \tag{115}$$

Consequently, matrices of state variables, mass, stiffness and torque expressed by Equations (47), (48) and (49) and (50) are reduced to equations (116), (117), (118) and (119), respectively.

$$q = [\theta_{LSR} \quad \theta_{sc} \quad x_{sc} \quad x_L]^T \tag{116}$$

$$M = \begin{bmatrix} J_{LSR} & 0 & 0 & 0 \\ 0 & J_{sc} & 0 & 0 \\ 0 & 0 & M_{sc} & 0 \\ 0 & 0 & 0 & M_L \end{bmatrix} \tag{117}$$

$$K = \begin{bmatrix} K_c & -K_c & 0 & 0 \\ -K_c & K_c + \gamma^2 K_n & \gamma K_n & -\gamma K_n \\ 0 & \gamma K_n & K_n + K_b & -K_n \\ 0 & -\gamma K_n & -K_n & K_n + K_a \end{bmatrix} \tag{118}$$

$$T = [T_{LSR} \quad 0 \quad 0 \quad 0]^T \tag{119}$$

This becomes a discrete model of four degrees of freedoms. The equations above can be represented in Figure 68, where the ball-screw is assumed to be rigid.

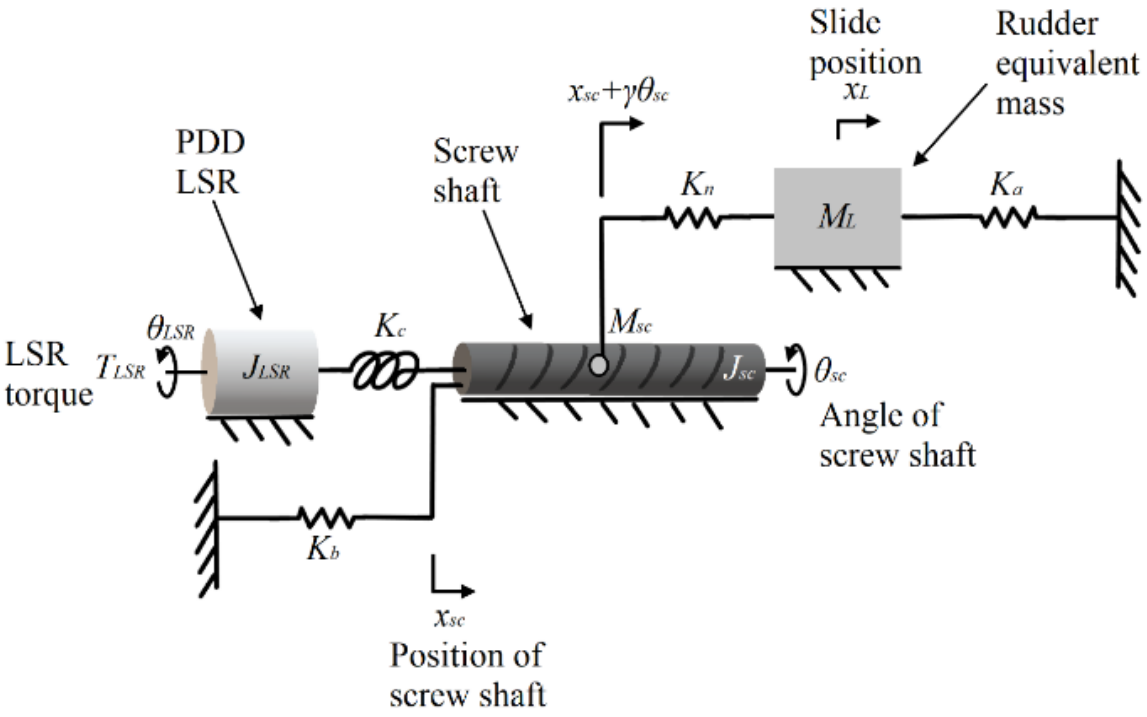

Figure 68. Four-degree of freedom model

Proposed three-degree of freedom model

The simplification reduces the order of the model to three degrees of freedom. It is based on the discrete four degree of freedom model. The way the simplification is introduced is essentially separating

motions into two axial motions, x_{sc} and x_L, and another rotational motion, θ_R. Figure 69 shows the spatial model of such a system.

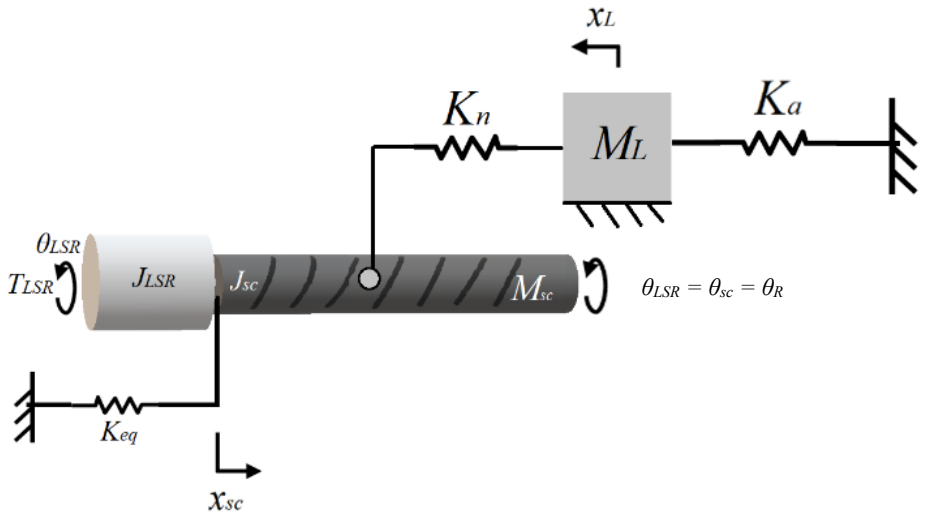

Figure 69. Three-degree of freedom model

The equations of motion represented from (112) to (115) are further reduced to include Equations (121), (122) and (123), which are for the system shown in Figure 69. Note that θ_R is adopted to help represent the change in the model but this symbol is the same as θ_{LSR}. This is because in the three-DOF model the screw inertia, J_{sc}, is lumped with the PDD LSR inertia, J_{LSR}, to form the only rotary inertia, J_R. Equation (120) defines θ_R for this particular model.

$$\theta_R = \theta_{LSR} = \theta_{sc} \tag{120}$$

The equations are as follows:

$$T_{LSR} - \gamma K_n((\gamma\theta_R + x_{sc}) - x_L) = J_R\ddot{\theta}_R \tag{121}$$

$$-K_b x_{sc} - K_n((\gamma\theta_R + x_{sc}) - x_L) = M_{sc}\ddot{x_{sc}} \tag{122}$$

$$K_n((\gamma\theta_R + x_{sc}) - x_L) - K_a x_L = M_L\ddot{x_L} \tag{123}$$

where:

$$J_R = J_{LSR} + J_{sc} \tag{124}$$

Consequently, matrices of state variables, mass, stiffness and torque expressed by Equations (116), (117), (118) and (119) are reduced to Equations (125), (126), (127) and (128), respectively.

$$q = [\theta_R \quad x_{sc} \quad x_L]^T \tag{125}$$

$$M = \begin{bmatrix} J_R & 0 & 0 \\ 0 & M_{sc} & 0 \\ 0 & 0 & M_L \end{bmatrix} \tag{126}$$

$$K = \begin{bmatrix} \gamma^2 K_n & \gamma K_n & -\gamma K_n \\ \gamma K_n & K_b + K_n & -K_n \\ -\gamma K_n & -K_n & K_n + K_a \end{bmatrix} \tag{127}$$

$$T = [T_{LSR} \quad 0 \quad 0]^T \tag{128}$$

The three-degree of freedom system is implemented in Simulink and it is shown in Figure 70.

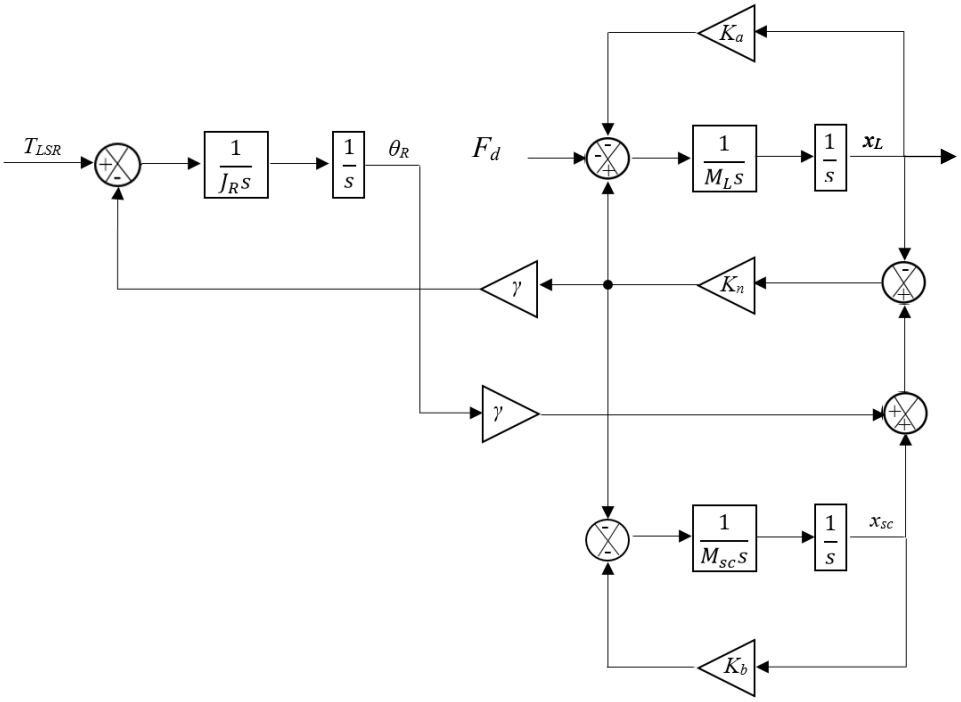

Figure 70. Three-degree of freedom model Simulink implementation

where F_d is disturbance force.

Frequency response is taken from the PDD LSR torque to load position. Since the response is measured from a different point to the excitation point, it is therefore called **Transfer receptance** [53]. Response model is plotted in Figure 71.

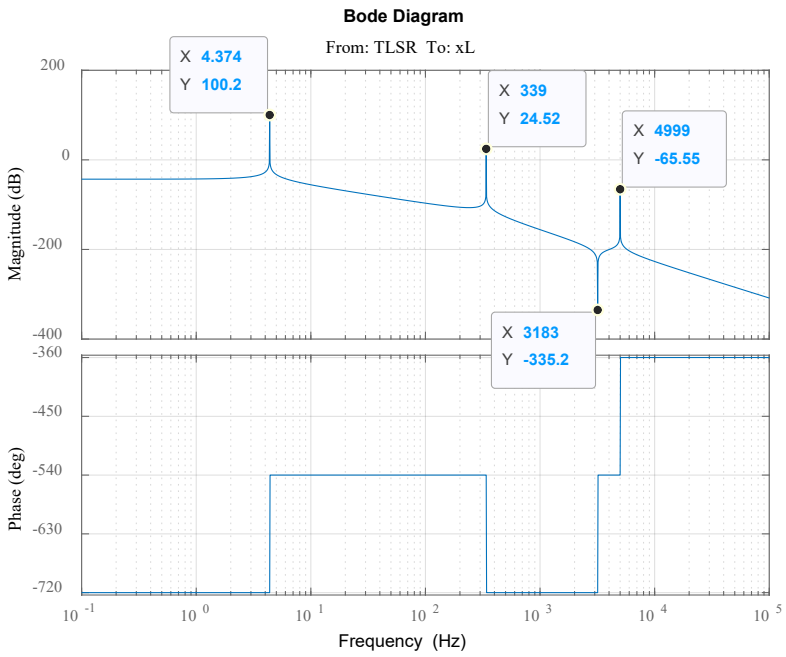

Figure 71. Bode plot (x_L/T_{LSR})

Resonant frequencies of the three-degree of freedom model are indicated in the bode plot shown in Figure 71. For f_1, which results from the aerodynamic stiffness, the three-degree of freedom model shows agreement with the six-degree of freedom model. Also, both models seem to agree with Equation (73). For f_2, good match between both models and Equation (76) can also be seen. The three-DOF approximates f_2 with a percentage error that is lower than 5%. Regarding f_4, it is also well approximated by the model.

It is evident that the three-DOF model determines f_1, f_2 and f_3 but not f_4. This is because f_3 is associated with the coupling stiffness, K_c, which is neglected in this case. Although f_4 is higher than f_3, maintaining K_n inevitably outcomes f_4 since the latter highly depends on K_n.

Table 9 provides a summary of results, which indicates that the simplified model is a good approximation of the relevant resonance frequencies.

Table 9. Comparisons of results

Resonance	*6-DOF model*	*Simplified equations*	*3-DOF model*
$f_1\ (Hz)$	*4.37*	*4.37*	*4.37*
$f_2\ (Hz)$	*323*	*318.3*	*339*
$f_4\ (Hz)$	*4950*	*4972.2*	*4999*

Proposed two-degree of freedom model

Literature mentions that higher accuracy and resistance to disturbance can be obtained when the position signal is fed back from the axial slide position rather than the motor position [11]. Since the application

of this actuation system is safety critical, then the feedback signal ought to be fed from the axial slide position.

In addition, literature also indicates that in the case of axial slide position is the feedback signal, the low resonance becomes relevant whereas higher resonance are relevant if motor position is the feedback signal [28]. Also, it is shown above that the lower resonances are mainly affected by translational masses and stiffnesses of bearing and screw-nut interface whereas, higher resonances can be due to coupling stiffness and rotational inertias. In an attempt to only highlight the relevant dynamics, the four degrees of freedom may be further reduced. Therefore, a further simplified model is proposed here.

The simplification reduces the order of the model to just two degrees of freedom. It is based on the discrete four degree of freedom model. The way the simplification is introduced is essentially separating motions into a one axial motion, x_{sc}, and another rotational motion, θ_{R2}. Figure 72 shows the spatial model, which illustrates how such motions are lumped.

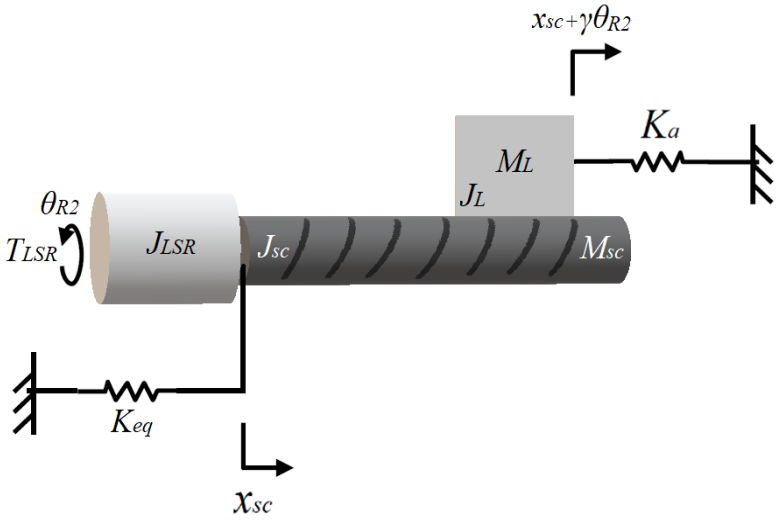

Figure 72. Two-degree of freedom model

The equations of motion represented from (112) to (115) are further reduced to include only (130) and (131), which are for the system shown in Figure 72. Note that θ_{R2} is adopted to help represent the change in the model but this symbol is the same as θ_{LSR}. This is because in the two-DOF model the screw inertia, J_{sc}, the PDD LSR inertia, J_{LSR}, and the equivalent inertia of the load mass, J_L, are all lumped together to form the only rotary inertia, J_{R2}. J_L is defined and calculated in Equation (39). Note that J_{R2} is equal to J_s calculated in Equation (40) and the change in the symbol is adopted to help represent the change in the model. Equation (129) defines θ_{R2} for this particular model.

$$\theta_{R2} = \theta_{LSR} = \theta_{sc} \tag{129}$$

The equations are as follows:

$$T_{LSR} - \gamma K_a(\gamma\theta_{R2} + x_{sc}) = J_{R2}\ddot{\theta}_{R2} \tag{130}$$

$$-K_{eq}(x_{sc}) - K_a(\gamma\theta_{R2} + x_{sc}) = M_A\ddot{x}_L \tag{131}$$

where:

$$J_{R2} = J_{LSR} + J_{sc} + J_L \tag{132}$$

and

$$M_A = M_{sc} + M_L \tag{133}$$

Consequently, matrices of state variables, mass, stiffness and torque expressed by Equations (116), (117), (118) and (119) are reduced to Equations (134), (135), (136) and (137), respectively.

$$q = [\theta_{R2} \quad x_{sc}]^T \tag{134}$$

$$M = \begin{bmatrix} J_{R2} & 0 \\ 0 & M_A \end{bmatrix} \tag{135}$$

$$K = \begin{bmatrix} \gamma^2 K_a & \gamma K_a \\ \gamma K_{eq} & K_a + K_{eq} \end{bmatrix} \tag{136}$$

$$T = [T_{LSR} \quad 0]^T \tag{137}$$

The two degrees of freedom system is implemented in Simulink and it is shown in Figure 73.

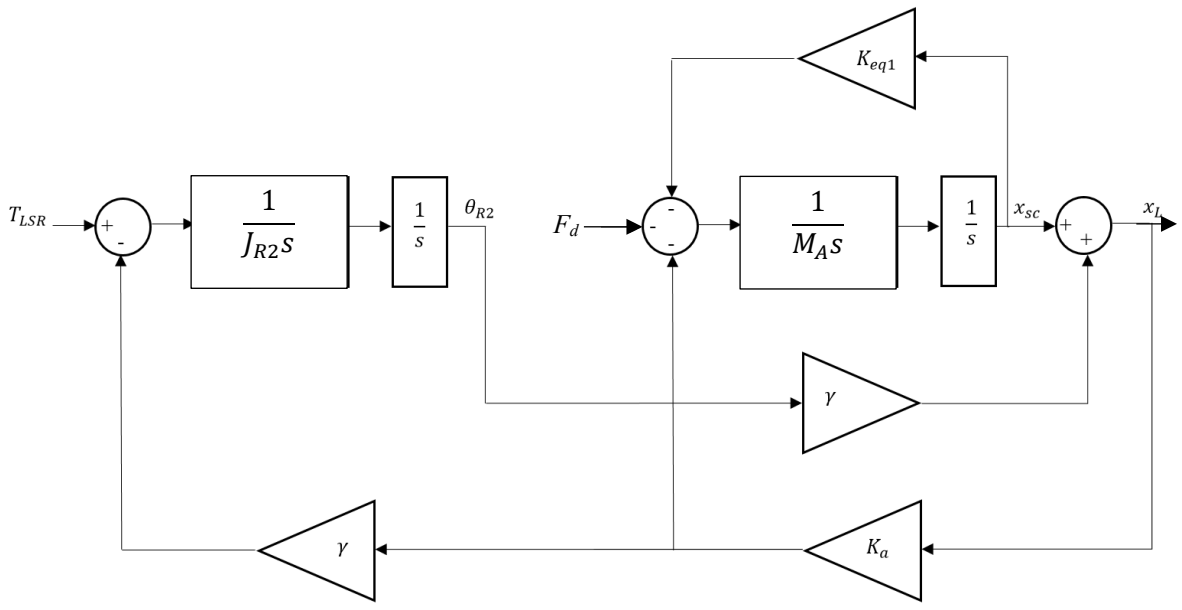

Figure 73. Two-degree of freedom model Simulink implementation

Response model is obtained by taking the frequency response from the PDD LSR torque to load position and plotted in Figure 74.

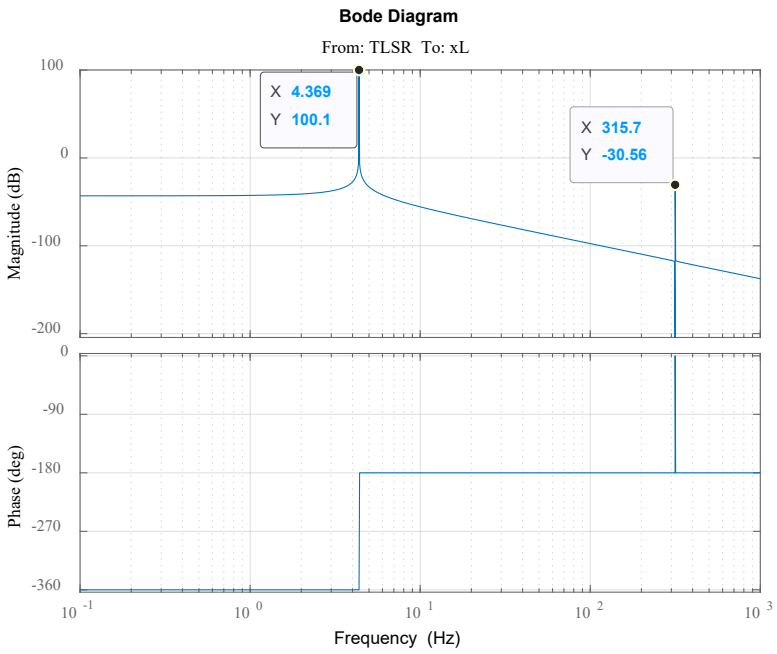

Figure 74. Bode plot (x_L/T_{LSR})

Resonant frequencies of the two-degree of freedom model are indicated in the bode plot shown in Figure 74. For the first resonance, which results from the aerodynamic stiffness, the two-degree of freedom model shows agreement with the six-degree of freedom model. Also, both models seem to agree with Equation (73). For the second resonance, good match between both models and Equation (76) can also be seen.

Table 10 provides a summary of results, which indicates that the simplified models are good approximations of the relevant resonance frequencies. Figures are in Hertz.

Table 10. Comparisons of results

Resonance	*6-DOF model*	*3-DOF model*	*2-DOF model*	*Simple equations*
$f_1\ (Hz)$	*4.37*	*4.37*	*4.37*	*4.37*
$f_2\ (Hz)$	*323*	*339*	*316*	*318.3*
$f_3\ (Hz)$	*3664*	-	-	*4607*
$f_4\ (Hz)$	*4950*	*4999*	-	*4972.2*
$f_5\ (Hz)$	*24401*	-	-	-
$f_6\ (Hz)$	*33438*	-	-	-

Anti-resonance

The analysis carried out above focuses on determination of resonant frequencies, which are the system poles. It is reported in [54] [53] that a dramatic shift in phase is expected due to anti-resonance. If this is accompanied with a magnitude zero crossing, caused either by bandwidth or the resonant frequency,

instability will occur. Therefore, it is important to consider anti-resonance, which is the system zero. The frequency response function can be described in terms of the system's mass, stiffness and damping elements (**spatial properties**) but the expression is rather complex. However, the frequency response function expression can be highly simplified if **modal properties** are used instead.

The system of the case study has three degrees of freedom. And for such a system, the equations of motion are written in matrix form as

$$M\ddot{q} + Kq = T \tag{138}$$

The system matrices [M] and [K] are referred to as the **Spatial Modal**.

If torque is set to zero, the free vibration solution can be determined to give the natural **modal properties**, which is expressed in two matrices, $[e_i]$ and $[v_v]$.

where $[e_i]$ is the eigenvalue matrix and it contains diagonal elements of natural frequency squared, as given by Equation (59), and $[v_v]$ is the eigenvector matrix and it gives the corresponding mode shape. Both matrices make up the **Modal Model**. It is important to remember that the natural frequencies are fixed values whereas the mode shape amplitude may differ with respect to certain factors such as excitation torque amplitude. However, the shape of the mode remains unvaried.

In addition, the modal model possesses some very important properties - known as Orthogonality properties – which, concisely stated, are as follows:

$$[v_v]^T[M][v_v] = [m_i] \tag{139}$$

$$[v_v]^T[K][v_v] = [k_i] \tag{140}$$

Also,

$$\left[\omega_i^2\right] = [m_i]^{-1}[k_i] \tag{141}$$

where, m_i and k_i are called generalised mass and stiffness of mode *i*. By implementing Equations (139) and (140), m_i and k_i can be quantified respectively.

$$[m_i] = \begin{bmatrix} 1 & 0 & 0 \\ 0 & 1 & 0 \\ 0 & 0 & 1 \end{bmatrix} \tag{142}$$

$$[k_i] = \begin{bmatrix} 753.2 & 0 & -0 \\ 0 & 4.54 \times 10^6 & -0 \\ -0 & -0 & 9.87 \times 10^8 \end{bmatrix} \tag{143}$$

Since the eigenvector matrix is not unique, m_i and k_i are not unique but the value of (k_i/m_i) is unique. It is recommended, in [53], to use mass-normalisation as a scaling factor.

$$[v_{vn}] = \frac{1}{\sqrt{m_i}}[v_v] \tag{144}$$

Specific properties are associated with the mass-normalised eigenvectors, $[v_{vn}]$, which are shown in Equation (145) and Equation (146).

$$[v_{vn}]^T[M][v_{vn}] = [I_u] \tag{145}$$

$$[v_{vn}]^T[K][v_{vn}] = \left[\omega_i^2\right] \tag{146}$$

where I_u is the unity matrix.

Now it is possible to proceed to the response analysis to determine the **response model**.

Following the analysis presented in [53], to determine the unknown response, equation of motion is rearranged as;

$$\{q\} = ([K] - \omega_i^2[M])^{-1}\{T\} \tag{147}$$

This can be rewritten;

$$\{q\} = [\alpha(\omega)]^{-1}\{T\} \tag{148}$$

$[\alpha(\omega)]$ is the system $N_d \times N_d$ receptance matrix and represents the response model. The general element in the receptance FRF matrix, $\alpha_{gk}(\omega)$ is defined as follows [53]:

$$\alpha_{gk}(\omega) = \left(\frac{q_g}{T_k}\right);\ T_m = 0, m = 1, N_d; \neq k \tag{149}$$

It is clear from Equation (147) that it is possible to determine the solution of the expression at any particular frequency but complex mathematical manipulation is involved with respect to inversion of the matrix. This adds complexity especially for higher degrees of freedom. For this reason, FRF expressions are derived based on the modal properties, Thus, it is shown in [53] that,

$$\alpha_{gk}(\omega) = \sum_{i=1}^{N_d} \frac{(v_{n(gi)})(v_{n(ki)})}{\omega_i^2 - \omega^2} = \sum_{i=1}^{N_d} \frac{i^{A_{gk}}}{\omega_i^2 - \omega^2} \tag{150}$$

$i^{A_{gk}}$ is known as Modal Constant and sometimes known as Residue.

Expression shown in Equation (150) shows a direct relationship between **modal properties** and its **response properties**. This suggests that system response can be efficiently predicted by using system modal properties, which can be determined using a free vibration analysis.

Looking at Equation (150), the receptance expression results from addition of individual terms. In this case, the signs of the terms are crucial. The effect of the signs can be appreciated by considering the types of frequency response function (FRF).

Point receptance

$$\alpha_{11}(\omega) = \left(\frac{q_1}{T_1}\right) = \frac{(v_{n(11)})(v_{n(11)})}{\omega_1^2 - \omega^2} + \frac{(v_{n(12)})(v_{n(12)})}{\omega_2^2 - \omega^2} + \frac{(v_{n(13)})(v_{n(13)})}{\omega_3^2 - \omega^2}$$
$$= \frac{81.3^2}{(4.37 \times 2\pi)^2 - \omega^2} + \frac{-30.5^2}{(339 \times 2\pi)^2 - \omega^2} \quad (151)$$
$$+ \frac{-2.52^2}{(4999 \times 2\pi)^2 - \omega^2}$$

Figure 75 illustrates point receptances of the individual terms as well as the total FRF model. The total FRF curve is calculated by summing the three terms. With respect to the individual terms, terms can be positive or negative in sign depending on the value of excitation frequency. However, this cannot be noticed in the figure since the logarithmic log (log|α(ω)|) only shows the modulus. But, when the terms are summed to construct the complete receptance expression, the effects of the signs of the individual terms can be observed, which is reflected by the complete FRF model in the figure.

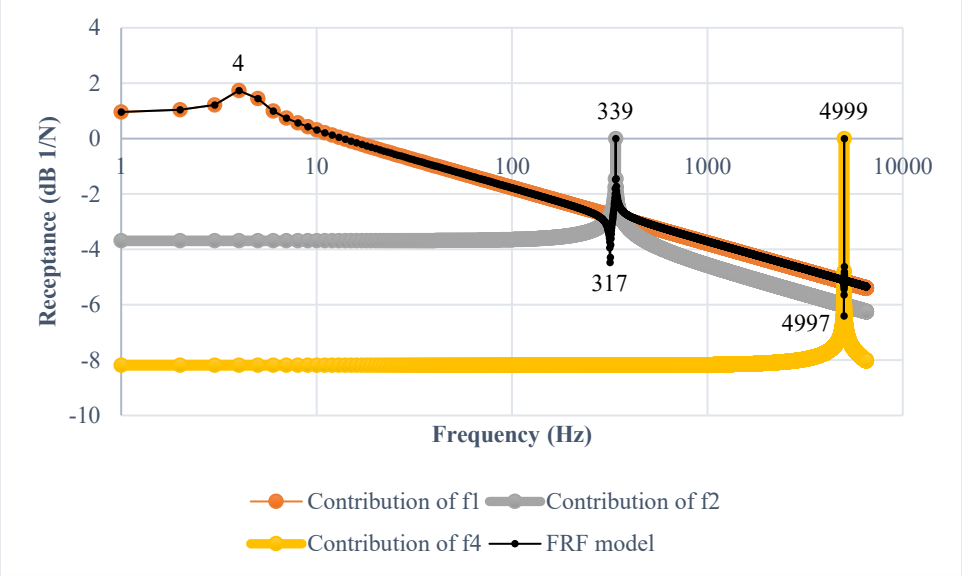

Figure 75. Point receptance plot

A similar figure can be constructed using Matlab, as shown in Figure 76.

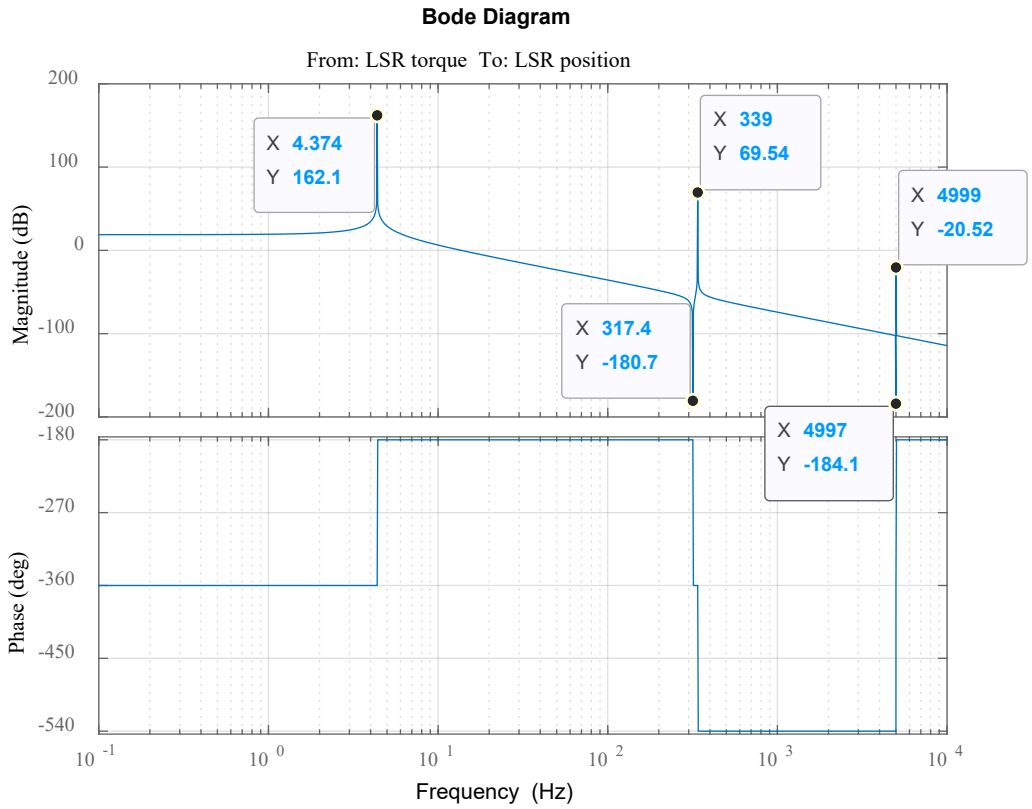

Figure 76. Point receptance plot (Matlab)

Transfer receptance

$$\alpha_{31}(\omega) = \left(\frac{q_3}{T_1}\right) = \frac{(v_{n(31)})(v_{n(11)})}{\omega_1^2 - \omega^2} + \frac{(v_{n(32)})(v_{n(12)})}{\omega_2^2 - \omega^2} + \frac{(v_{n(33)})(v_{n(13)})}{\omega_3^2 - \omega^2}$$
$$= \frac{0.065 \times 81.3}{(4.37 \times 2\pi)^2 - \omega^2} + \frac{0.1714 \times -30.5}{(339 \times 2\pi)^2 - \omega^2} \quad (152)$$
$$+ \frac{0.0141 \times -2.52}{(4999 \times 2\pi)^2 - \omega^2}$$

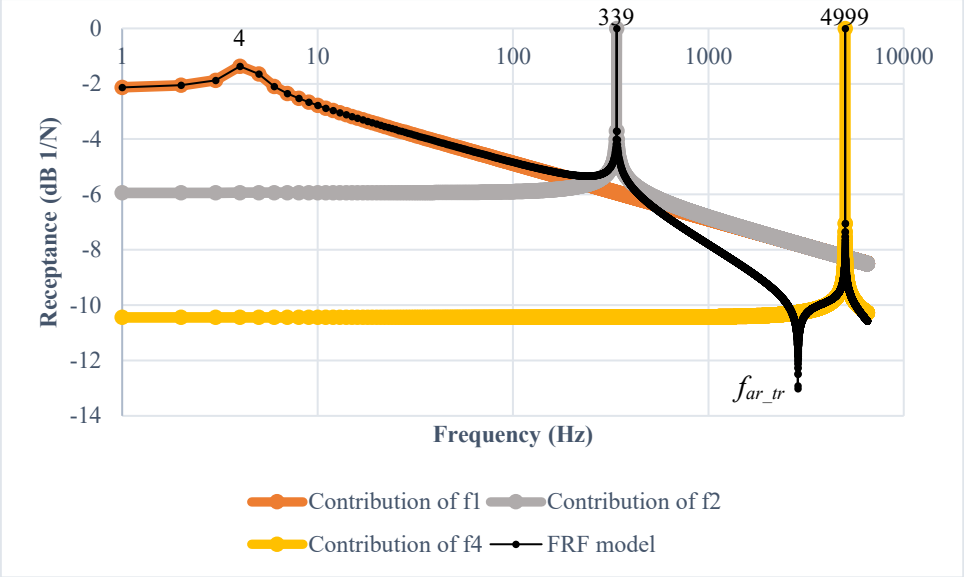

Figure 77. Transfer receptance plot

A similar figure can be constructed using Matlab, as shown in Figure 78.

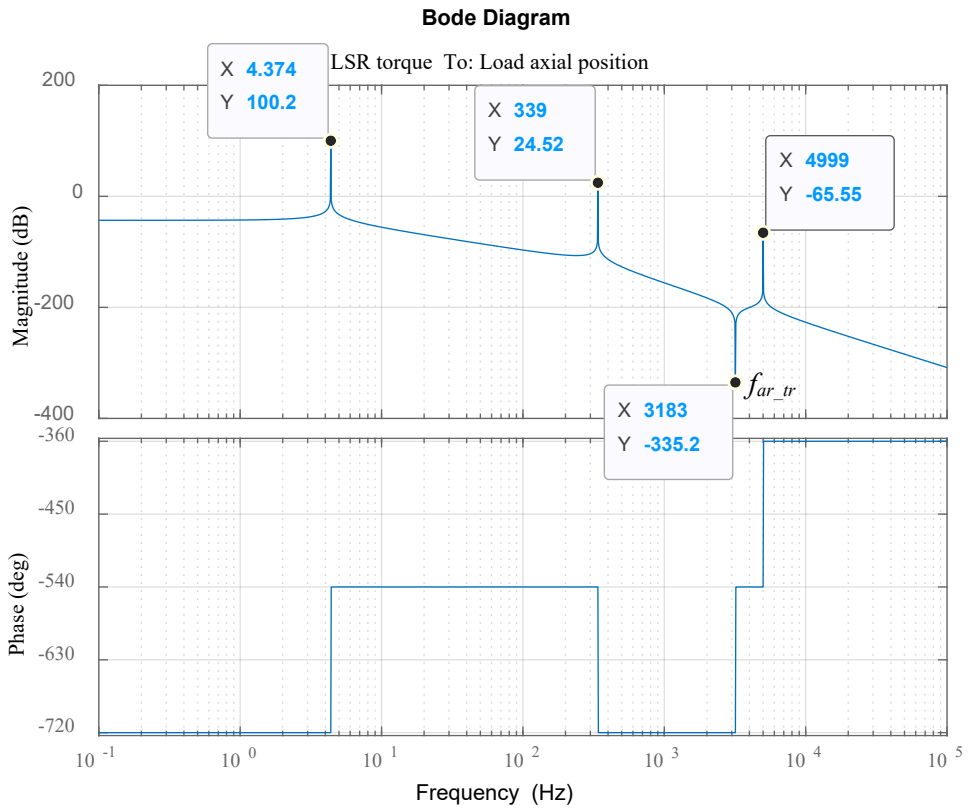

Figure 78. Transfer receptance plot (Matlab)

By observing Equations (151) and (152), a significant difference between the point and transfer receptances is the sign of numerator. When the terms are plotted separately, such sign differences are

unimportant since the curves are plotted after taking the modulus of each term. But when the terms are summed to determine the total FRF, the sign differences become crucial.

Considering the point receptance represented by Equation (151), when the excitation frequency is lower than 4.37 Hz, all terms have a plus sign (+ + +) and therefore terms add making the total FRF greater than each of the individual terms. However, since the logarithmic function is taken for the expression, the contribution of the second and third terms, in case frequency is lower than 4.37 Hz, is insignificant. That is why at a certain natural frequency, vibration occurs with the dominated mode shape whilst other mode shapes have insignificant influence. Similarly, when excitation frequency is greater than 4999 Hz, all the terms have a negative sign (- - -) and hence they add.

On the other hand, when excitation frequency is between f_1 and f_2, terms have different signs (- + +) so at frequency 317 Hz terms cross and hence the sum becomes equal to zero. As a result, anti-resonance occurs, as shown in Figure 75. After such a point, the most influential term is the term whose frequency is the closest (f_2), which is the second term in this case.

In the case of the Transfer receptance, Equation (152), signs of terms are different (+ - -). Hence, at frequencies lower than 4.37 Hz and higher than 5 kHz, the total sum of the terms is lower than the first term and the third term respectively. For an exciting frequency ranging between f_1 and f_2, the terms have the same sign (- - -) and so terms cannot cancel to produce anti-resonance the same way it did in the point receptance. Instead, when the first and the second terms have the same magnitude, the total curve's magnitude is doubled.

The same argument can be made to discuss the result of the FRF function for any frequency, which give rise to another anti resonance in Figure 75 at around 5 kHz and also anti resonance at around 3 kHz in Figure 77. A general rule can be concluded of which the sign of the modal constants can be used as an indicator. That is, like signs of modal constants of two adjacent modes means that an anti-resonance exists somewhere between these two modes. In contrary, an anti-resonance will not be spotted if signs of modal constants are different. Instead, there will be a minima. Therefore, for a point FRF (point receptance), there must be an anti-resonance between each two consecutive modes. On the other hand, for a transfer FRF, the situation is different meaning that between each two modes, a minima or an anti-resonance can be there [53].

Figure 75 and Figure 76 will be important for the speed loop, but Figure 77 and Figure 78 will be important for the position loop. Since Figure 77 and Figure 78 have only one anti-resonance, therefore it is easy to analytically determine such anti resonance in terms of its spatial properties to see what components compose such a frequency. This can be found out by simply calculating the zero of such a transfer function.

$$q = [\theta_R \quad x_{sc} \quad x_L]^T \tag{153}$$

$$M = \begin{bmatrix} J_R & 0 & 0 \\ 0 & M_{sc} & 0 \\ 0 & 0 & M_L \end{bmatrix} \tag{154}$$

$$K = \begin{bmatrix} \gamma^2 K_n & \gamma K_n & -\gamma K_n \\ \gamma K_n & K_b + K_n & -K_n \\ -\gamma K_n & -K_n & K_n + K_a \end{bmatrix} \tag{155}$$

$$T = [T_{LSR} \quad 0 \quad 0]^T \tag{156}$$

Transfer function analysis is carried out. Equations (125), (126), (127) and (128) can be expressed in a more compact form using Laplace transform with an assumption that all initial conditions are set to zero, as presented in Equation (157).

$$\begin{bmatrix} J_R s^2 + \gamma^2 K_n & \gamma K_n & -\gamma K_n \\ \gamma K_n & M_{sc} s^2 + K_b + K_n & -K_n \\ -\gamma K_n & -K_n & M_L s^2 + K_n + K_a \end{bmatrix} \begin{bmatrix} \theta_R \\ x_{sc} \\ x_L \end{bmatrix} = \begin{bmatrix} T_{LSR} \\ 0 \\ 0 \end{bmatrix} \tag{157}$$

Equation (157) can be written symbolically in the way shown in Equation (158).

$$A_u q = T \tag{158}$$

where A_u is the matrix which includes the mass and stiffness matrices as shown in Equation (157).

This can be rearranged as shown in Equations (159) and (160).

$$A_u^{-1} = \frac{1}{\det A_u} adj(A_u) \tag{159}$$

$$A_u^{-1} A_u q = A_u^{-1} T \rightarrow q = A_u^{-1} T = \frac{1}{\det A_u} adj(A_u) T \tag{160}$$

The details of such calculations are presented in Appendix D from which the following non-collocated transfer function can be deduced.

$$\frac{x_L}{T_{LSR}} = \frac{1}{\det A_u} \times (-\gamma K_n^2 + (M_{sc} s^2 + K_b + K_n) \gamma K_n) \tag{161}$$

By rearranging Equation (161), the complex frequency operator, *s*, is shown in Equation (162).

$$s = \mp j \sqrt{\frac{K_b}{M_{sc}}} \tag{162}$$

Therefore, the anti-resonant frequency, f_{ar_tr}, can be estimated using Equation (163).

$$f_{ar\_tr} = \frac{1}{2\pi} \sqrt{\frac{K_b}{M_{sc}}} = 3183 \; Hz \tag{163}$$

2.5 Conclusion

A literature review on ball-screw drive resonance shapes and dependency of resonance frequencies on certain parameters is introduced, and the three approaches to model ball-screw assemblies are discussed. A hybrid model, which combines accuracy and simplicity is selected.

Torsional and axial flexibilities of the screw are investigated. It is shown that such flexibilities contribute mainly towards high frequency resonances and hence the screw can be assumed rigid. Making it possible to use a discrete model to predict system dynamics over the frequency range of interest.

Eigenvalue and eigenvector analysis is carried out on the six-degree of freedom model and results are compared with simple natural frequency equations, derived to represent the dominant motions. Results show good agreement between model and simple equations and only two frequencies are found to be relevant for control purposes. Thus, a four-degree of freedom model, a further reduced two-degree of freedom model and a three-degree of freedom model are proposed, and their predictions of the relevant frequencies are in good agreement with predictions from the six-degree model and the simplified equations.

The reduced order model is also used to adequately predict antiresonance, which is found to be related to the bandwidth of the controller. Anti-resonance is found using resonant frequencies and eigenvectors; rather than spatial properties of the system.

Chapter 3 Resonant frequencies for actuators of different sizes

3.1 Introduction

In chapter 2, ball-screw assembly models are implemented and mode shapes and associated frequencies are discussed with respect to their influential parameters. It is concluded, and as would be expected, frequencies and mode shapes are dependent on physical parameters and operating conditions. However, the analysis was undertaken for a specific actuation system, a rudder surface of a business jet.

The purpose of this chapter is to make sure that the EMA model, obtained in Chapter 2, is generic and can be used for a wide range of aircraft. In this chapter, the effects of the sizes of the actuation system on the mode shapes and frequencies will be investigated, and the applicability of the models adopted in Chapter 2, and their derived simplifications, will be assessed when actuation system sizes vary from the one assumed in prior analysis. Therefore, sensitivity analyses are undertaken, with particular emphasis on selected larger aircraft, whose parameters are approximated using available public domain information. The parameters required to apply the resonant analysis are developed. The resonant analysis is applied to the different aircraft and the light business jet is used as an example.

3.2 Change of size effect on parameters

An increase in aircraft maximum take-off weight (*MTOW*) and aircraft size lead to the use of larger control surfaces and hence higher actuation forces. Figure 79 summarised the *MTOWs* for different types of aircraft. Up to *2005*, the heaviest commercial Airbus aircraft was A340-600 until the A380 came about with *52%* increase in the *MTOW* [55]. Data are extracted from *AIRBUS* website [56].

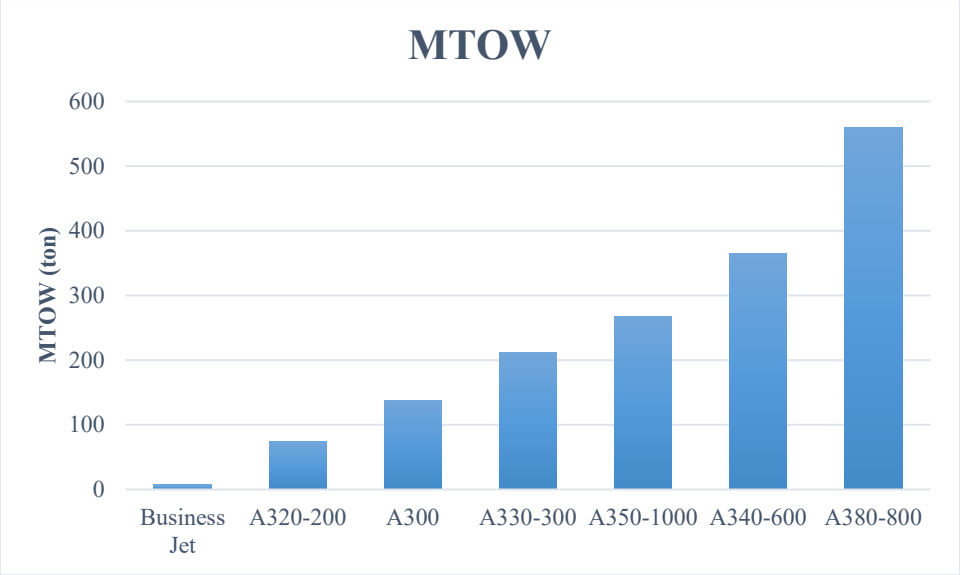

Figure 79. MTOW for different aircraft

With a size increase, many components will increase such as engines power ratings, sizes of control surfaces and force ratings of control surfaces actuators. For this study, and to be consistent with the study undertaken in Chapter 2, the rudder surface is selected.

3.2.1 Load

The aircraft whose parameters are employed in this chapter, is a small business jet with *MTOW* around *7000 kg*. The load is sized based on guidance in [57] [58]. Figure 80 shows a brief structure of one of the rudders surfaces.

Figure 80. Structure of one rudder of the light aircraft

Rudder surface dimensions and material specifications are given for the EMMAS project, and summarised in Table 11.

Table 11. Rudder parameters for business jet

Rudder parameter	Symbol	Value	Unit
Material		Aluminium	
Density	ρ_A	2700	kg/m^3
Overall height	$\frac{1}{2}h$	1	m
Overall length	a or b	0.385	m
Overall width		0.085	m
Rib thickness		0.005	m
Number of ribs		5	
Surface thickness	$\frac{1}{2}T_R$	0.003	m

3.2.1.1 Number of rudder surfaces and actuators

For the aircraft types highlighted in Figure 79, some have only one rudder whereas others have two rudders. Furthermore, for each rudder, the number of actuators depends of aircraft types and the level of required redundancy. According to [55], the *A380* has two actuators per rudder; one is active and the other one is a stand-by. Further, other airbus aircraft have three actuators per rudder [55]. [59] gives more clarifications and states that out of the three actuators, one is operational in the active mode whilst the other two are functioning in the damping mode. Figure 81 summarises this point.

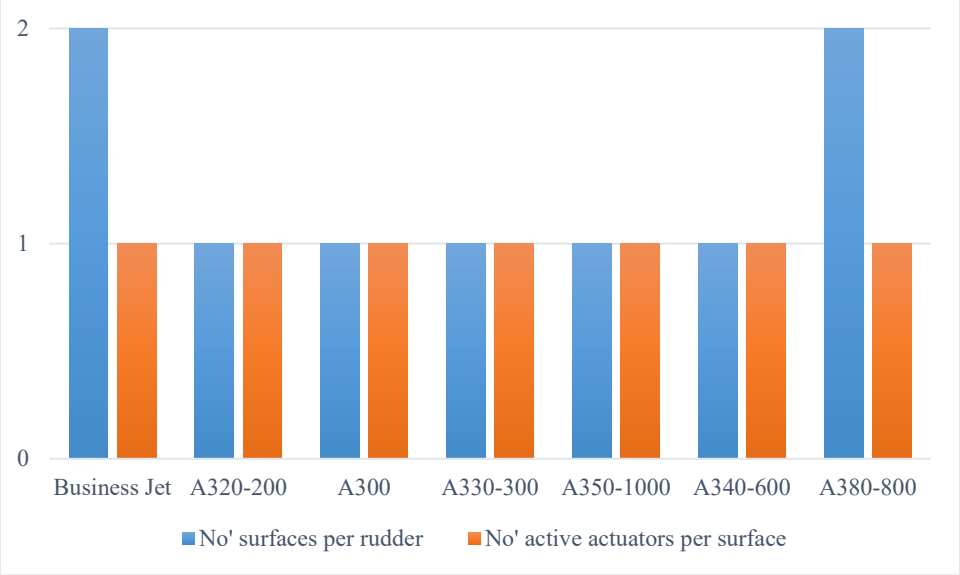

Figure 81. Number of actuators and rudder surfaces

3.2.1.2 Tail dimensions

The vertical tail consists of two parts; a stationary part called the fin and a moving part known as the rudder [58].

The tail dimensions including upper side, *N*, lower side, *P*, and height, *h*, are shown in Figure 82. The tail shape shown in Figure 82 (a) represents tail in most airbus aircraft, whereas aircraft of the case study shape is shown in Figure 82 (b). It is worth noting that the tail in (a) is not a perfect trapezoid but it will be assumed so.

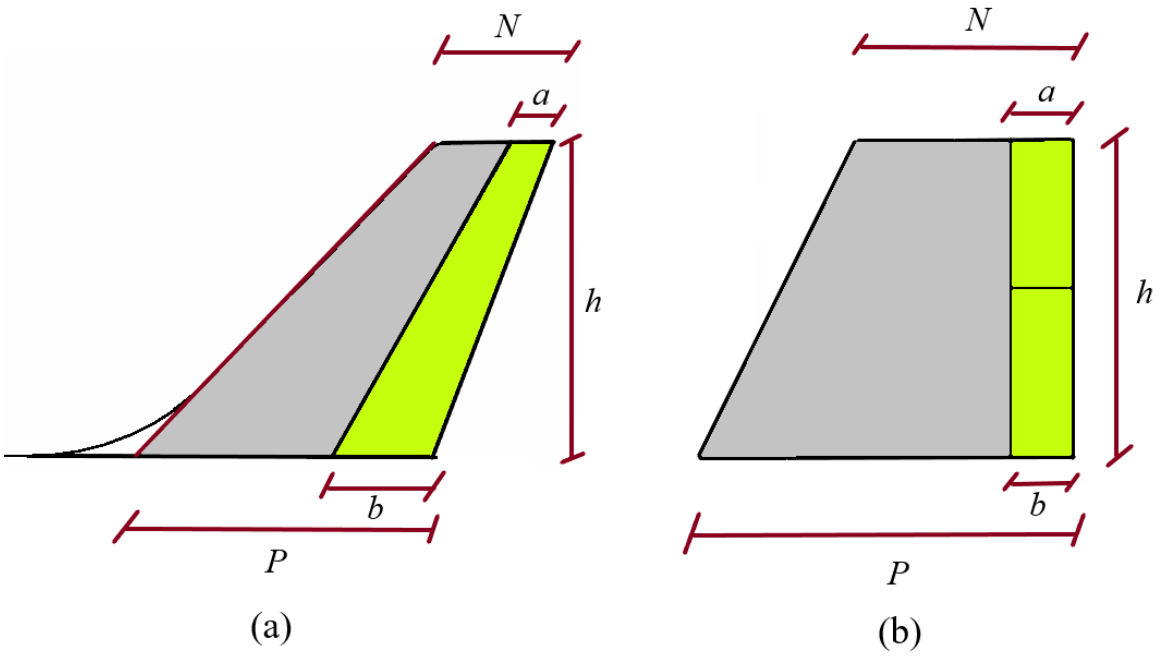

Figure 82. Tail dimensions: (a) Airbus aircraft (b) aircraft of the case study

Tail dimensions for other aircraft are summarised in Table 12. Data are collected from AIRBUS website [56].

Table 12. Tail dimensions

aircraft type	*h (m)*	*N (m)*	*P (m)*
Business jet	2	1.62	2.7
A320-200	5.87	1.73	5.58
A300	8.4	2.97	7.717
A330-300	8.3	3.1	7.79
A350-1000	9.42	3.04	7.79
A340-600	8.8	3.1	8.58
A380-800	14.59	4.7	12.06

3.2.1.3 Taper ratio (T_{ra})

Taper ratio, T_{ra}, is the ratio between the top to bottom dimensions of the tail. Dimensions are summarised in Table 12. Taper ratio is preferred to be in a certain range ($0.3 \leq T_{ra} \leq 0.6$) to improve the wing efficiency [58]. For the business jet, the taper ratio is calculated as [58]:

$$T_{ra} = \frac{N}{P} = 0.6 \tag{164}$$

The taper ratio is shown in Figure 83 for a range of aircraft types.

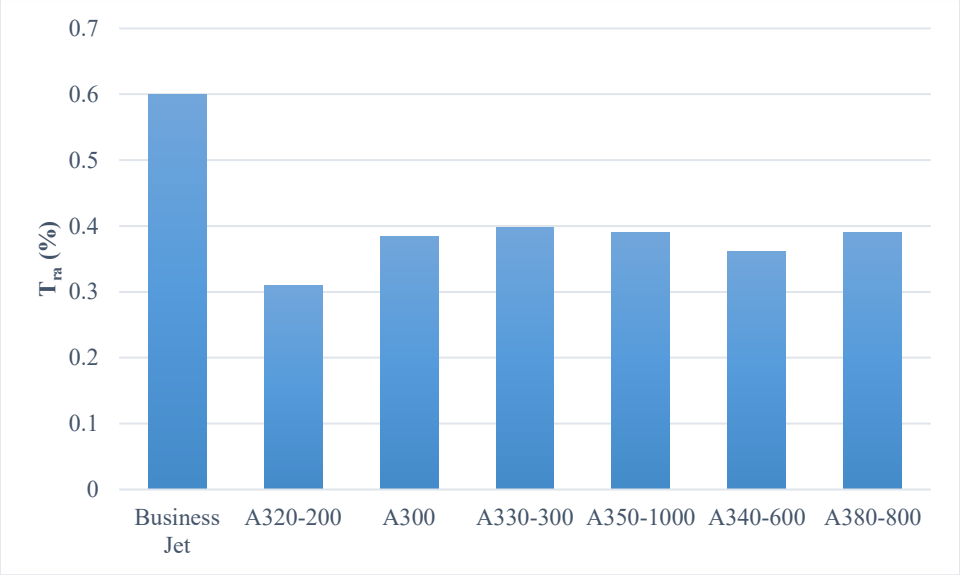

Figure 83. Taper ratio

3.2.1.4 Tail area (A_t)

The vertical tail area, A_t, is calculated as:

$$A_t = \frac{N+P}{2} h = 4.32\, m^2 \tag{165}$$

Figure 84 summarises tail areas for various aircraft types.

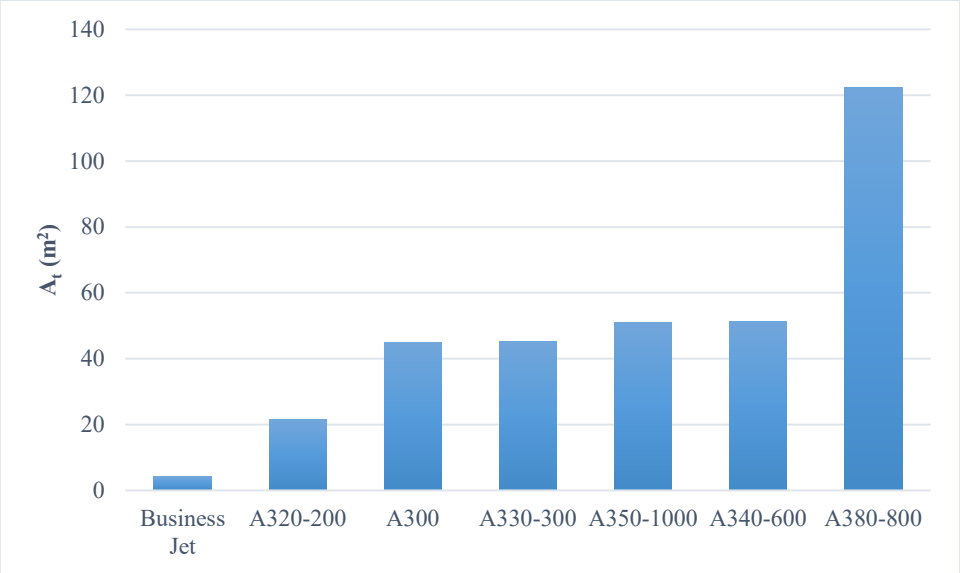

Figure 84. Tail area

3.2.1.5 Rudder dimensions

Figure 82 shows the dimensions of the rudder of the business jet; as can be seen, it is assumed to be rectangular. For the other types of aircraft, the rudder seems almost trapezoidal. Dimensions, including upper side, *a*, lower side, *b*, and height, *h*, are summarised in Table 13 [56].

Table 13. Rudder dimensions

aircraft type	*h (m)*	*a (m)*	*b (m)*
Business jet	2	0.38	0.38
A320-200	5.87	0.5774	1.78
A300	8.4	0.99	2.276
A330-300	8.3	1.0387	2.366
A350-1000	9.42	1.02972	2.5171
A340-600	8.8	1.129	2.785
A380-800 (UR)	9.627	1.289	2.88
A380-800 (LR)	5	2.88	3.563

3.2.1.6 Rudder surface area (A_R)

Figure 82 (b) shows dimensions of rudder for aircraft under study. A_R can be calculated using Equation (166).

$$A_R = h \times a = 0.76\, m^2 \tag{166}$$

The area of one rudder is therefore calculated as:

$$\frac{A_R}{2} = 0.38\, m^2 \tag{167}$$

For the type of rudder shown in Figure 82 (a), area can be calculated using Equation (168).

$$A_R = \frac{a+b}{2} h \tag{168}$$

Figure 85 summarises the rudder surface area for each aircraft type.

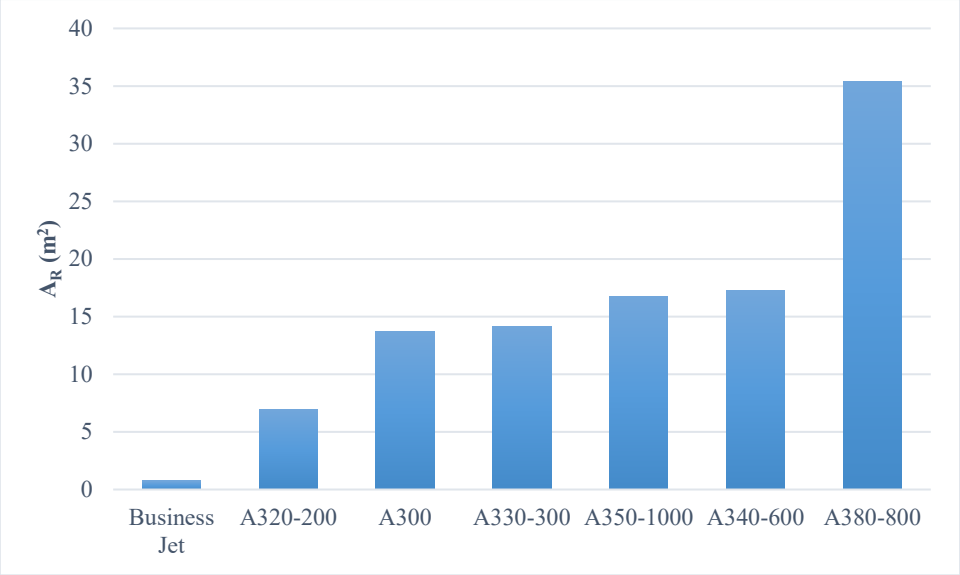

Figure 85. Rudder surface area

3.2.1.7 Ratio of rudder surface area to tail area (R_{Rt})

Rudder composes a certain ratio of the tail. For this specific aircraft, the rudder area is 18% of the total vertical tail area, as approximated in Equation (169).

$$R_{Rt} = \frac{A_R}{A_t} \times 100 \approx 18\% \tag{169}$$

For a range of aircraft, this ratio may reach to just below 35%. Figure 86 gives a summary.

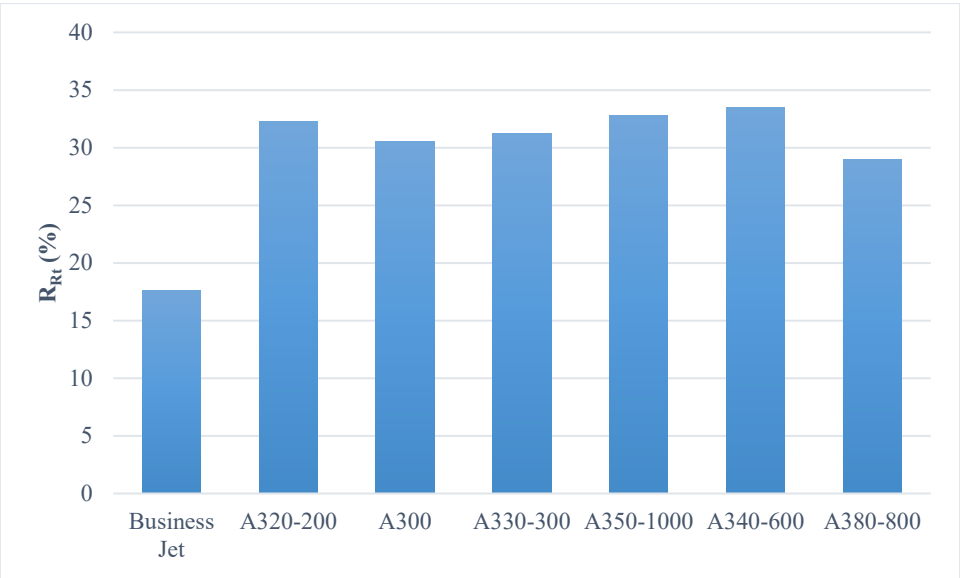

Figure 86. Rudder to tail ratio

3.2.1.8 Surface thickness (T_R)

For the light business jet presented in this project, the rudder is constructed from a spar, four horizontal rips and a pair of Aluminium sheets, as seen in Figure 80. The thickness of one sheet is given as 3 mm.

The rudder practically is hollow, therefore, it can be considered as two surfaces beside each other and hence the total thickness, T_R, is 6 mm, as illustrated in Figure 87.

The density of the rudder aluminium sheets, ρ_A, is assumed to be equal to $2700\ kg/m^3$.

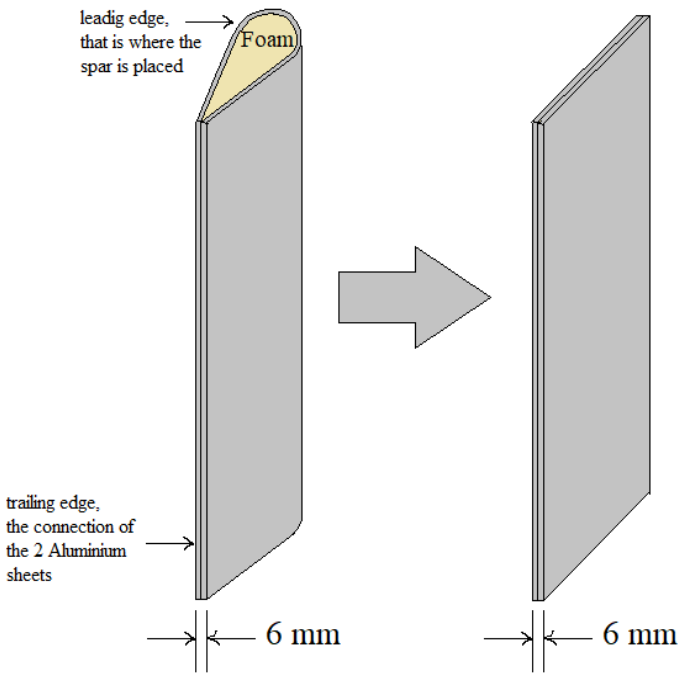

Figure 87. Thickness of rudder surface

On the other hand, a report, provided by The Transportation Safety Board of Canada [60], gives details of rudder design used for *A310*, *A300-600*, *A330* and *A340*. Many details can be found in [60], but the relevant information shall be mentioned here. The rudder consists of a single spar, top and bottom rips (2 rips), and two side panels. In a similar manner to Figure 80 and Figure 87, the spar is located at the leading edge, whereas the two side panels are connected at the trailing edge.

A single side panel is composite composed of a non-metallic honeycomb core, covered with a glass fibre-reinforced plastic and then with CFRP face sheets, as detailed in Figure 88.

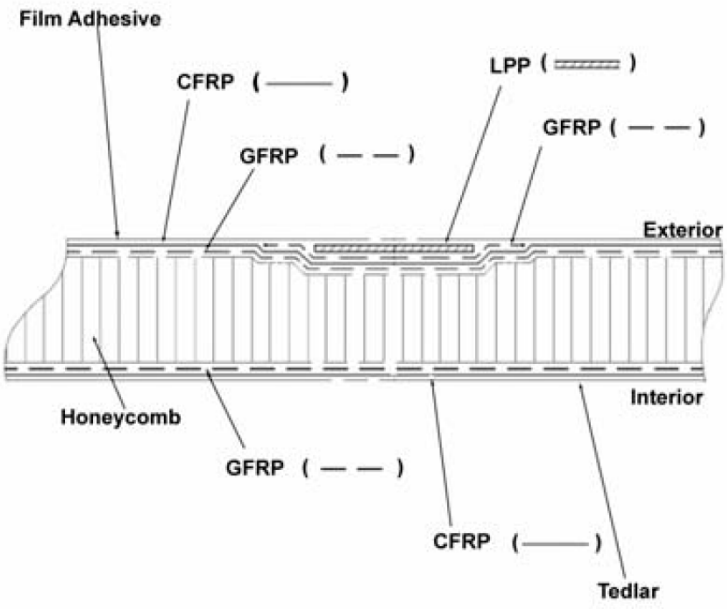

Figure 88. Construction of a rudder single side panel [60]

Density and thickness of the honeycomb is a function of location so they may react to applicable loads [60]. However, a single side panel, presented in [60], has honeycomb core that is *40 mm* thick and has a density, ρ_A, of *32 kg/m*^{3}, on average. Therefore, this will be assumed the case for all Airbus aircraft, to make calculations simpler. Thus, by considering the two side panels together, as shown in Figure 87, T_R can be assumed to be equal to *80 mm*.

3.2.1.9 Rudder mass (M_R)

The mass of one rudder, for the business jet, can be calculated using Equation (170).

$$M_R = \frac{A_R}{2} \times T_R \times \rho_A = 6.156\ kg \tag{170}$$

Note that the value of ρ_A can be found in Table 11 for the business jet. For the other aircraft types, ρ_A is equal to *32 kg/m*^{3}, as mentioned in the previous section. Figure 89 shows rudder mass for various aircraft types.

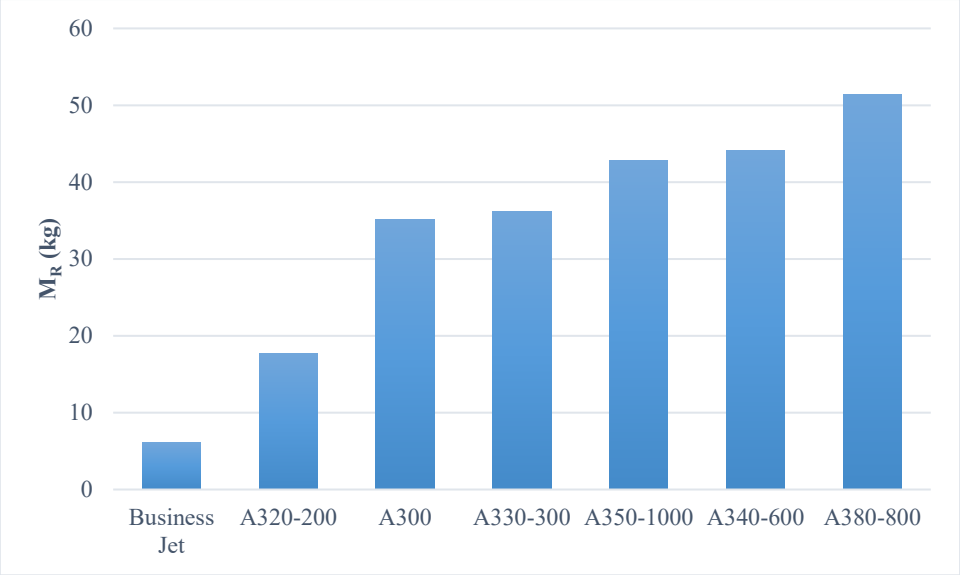

Figure 89. Rudder mass

3.2.1.10 Surface inertia (J_r)

For the business jet, rudder is a perfect rectangle as can be seen in Figure 82 (b). However, in most aircraft, rudder is trapezium (Figure 82 (a)). In the case of the business jet, the rudder can be considered as a rectangular thin plate, as shown in Figure 90. Therefore, the equation used to calculate inertia of a thin rectangular plate can be used to calculate rudder inertia.

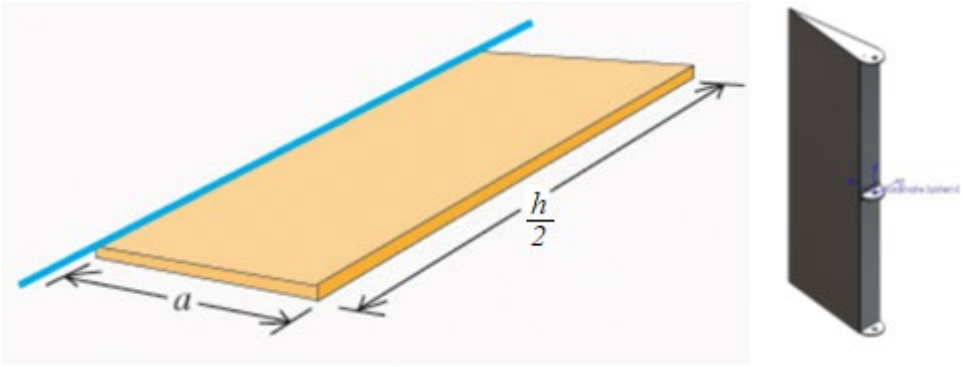

Figure 90. Inertia of surface around an axis

The formula used in this context is as follows:

$$J_r = \frac{1}{3} M_R \times a^2 = 0.296\ kg.m^2 \tag{171}$$

On the other hand, the rudder of the other aircraft can be considered as trapezoidal plate so inertia is calculated using a different approach. The trapezoidal plate can be extended to form a triangular plate; with its base, w, and height, u, as shown in Figure 91.

The inertia of the extended triangular plate, J_e, is calculated as follows [61]:

$$J_e = \frac{1}{12}\rho_A w T_R u^3 = \frac{1}{6} M_R u^2 \tag{172}$$

The inertia of the virtual part, J_v, is calculated in the same manner as J_e since both shapes are similar triangles. The inertia of the rudder, J_r, is calculated as follows:

$$J_r = J_e - J_v \tag{173}$$

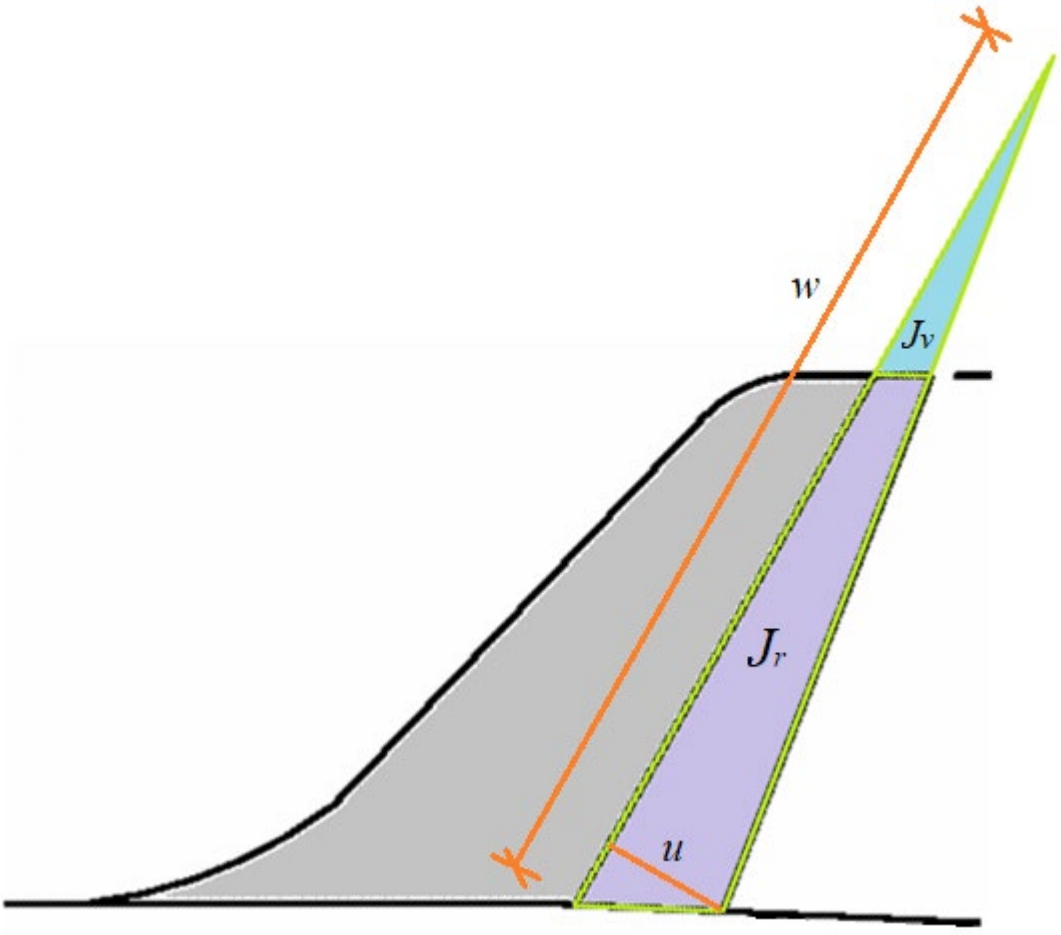

Figure 91. Shapes used to calculate inertia of a trapezoidal rudder

Figure 92 summarises the surface inertias for the mentioned aircraft types.

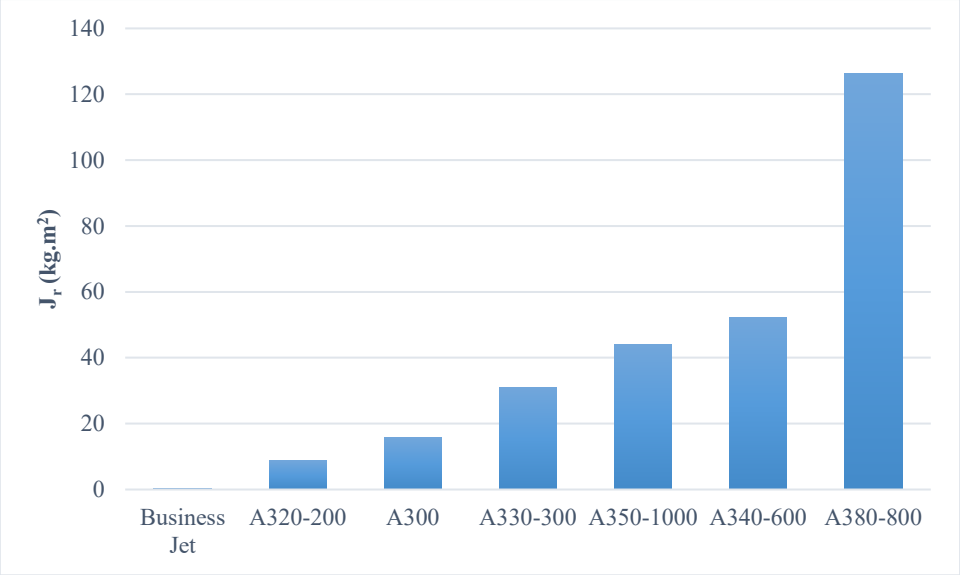

Figure 92. Rudder inertia

3.2.1.11 Deflection angle (α_d)

For the business jet, the rudder is allowed to deflect up to *30°* upon the full deployment, which represents maximum load, as illustrated in Figure 93. For A320, maximum rudder deflection angle is *25°* [62]. Deflection angles for other aircraft are difficult to find so in this study it is assumed to be *25°* for all apart from the business jet.

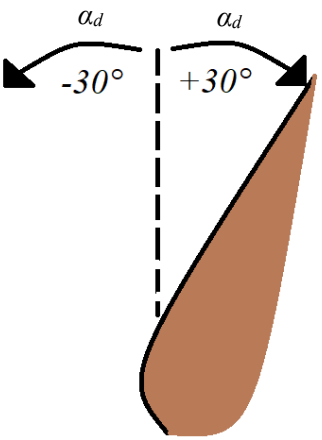

Figure 93. Deflection angle

3.2.1.12 Actuation force (F_{sc})

Although all geometrical dimensions of aircraft rudders can be found in [56], data for actuation force can only be found for certain aircraft. Hence, some actuation forces are to be approximated. Approximation will be done based on data for Airbus aircraft that have only one operational rudder, since they have a similar structure. *MTOW* is plotted against force and a straight line is constructed for known actuation forces. Unknown actuation forces can be fitted into the graph, as detailed in Figure 94.

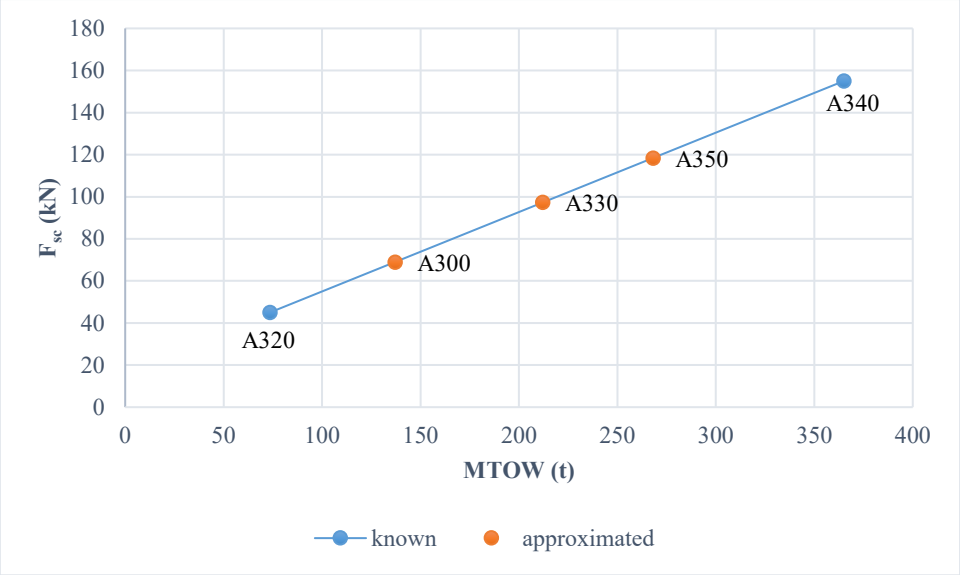

Figure 94. Approximating actuation force from known data

Figure 95 is a summary of rudder actuation forces needed for different aircraft. The forces marked in blue are found in the literature [55] [62] [7]. The data highlighted in orange is approximated.

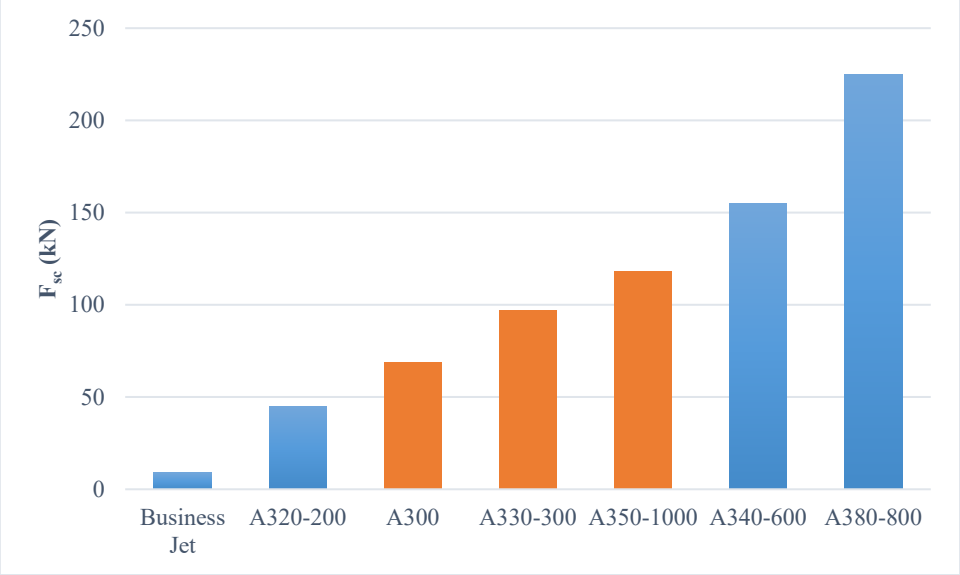

Figure 95. Actuator force with respect to aircraft type (orange = approximated) (blue = known)

3.2.1.13 Stroke (S)

Beside the screw stroke given for the light business jet, some screw strokes can be found in the literature; such as those for *A320*, *A330* and *A340*. It is important to mention that stroke for *A330* and *A340* are equal [7]. It is possible to estimate strokes for other aircraft considering some assumptions. For example, since strokes used in *A330* and *A340* are equal, it is possible to assign the same value for the one used in *A350* since the latter size is within the former two.

As for *A300*, stroke is assumed to be between those of *A320* and *A330*. Similarly, for *A380*, stroke is assumed to linearly increase, from *A340* to *A380*, with force in the same pattern that is between *A300* and *A330*, for example (Figure 96).

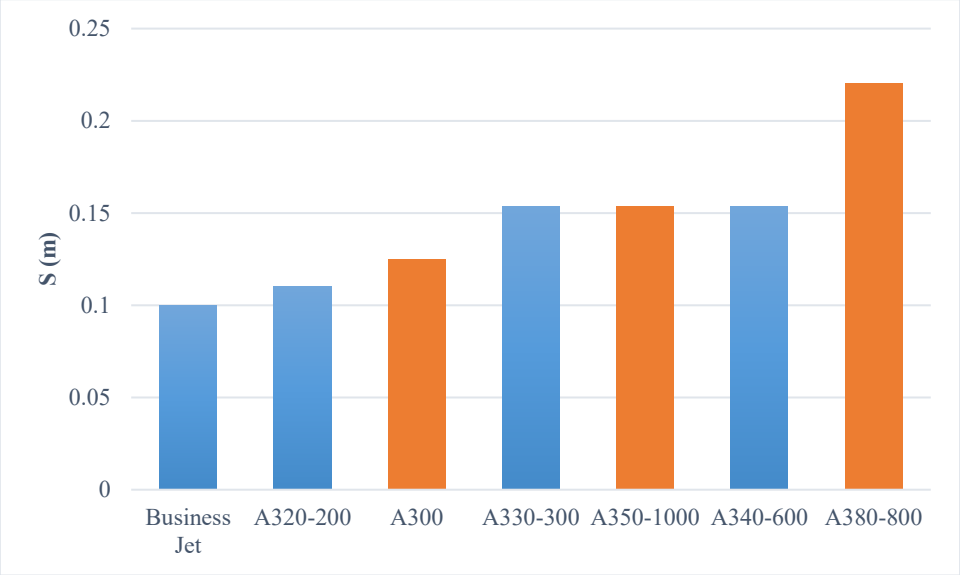

Figure 96. Screw stroke (data in orange is approximated)

3.2.1.14 Link arm length (L_a)

Link arm connects the screw with the rudder hinge to convert screw force into a torque, as described in Figure 97.

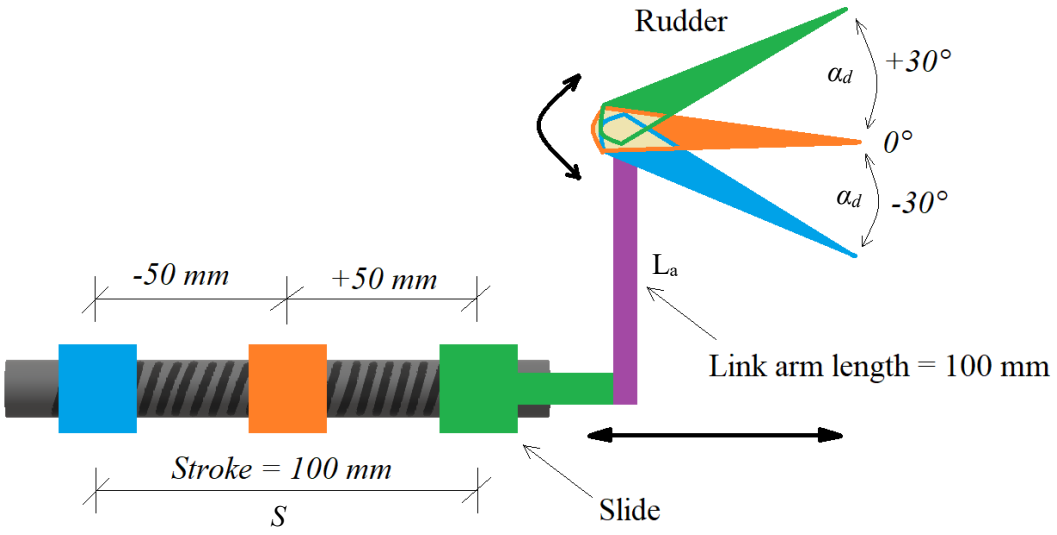

Figure 97. Link arm connecting screw slide with rudder

Limited data is available in literature about the link arm length. In fact, one value is given for the business jet and another is found for *A320* [62]. In [62], it is stated that the link arm length, L_a, can be related to the actuator stroke, S as follows:

$$L_a = \frac{\frac{1}{2}S}{\sin \alpha_d} \tag{174}$$

where α_d is the deflection angle of the rudder explained previously.

Using the stroke values in the preceding subsection, it is possible to plug the values of the strokes into Equation (174).

Figure 98 shows variation of estimated arm lengths for various aircraft types.

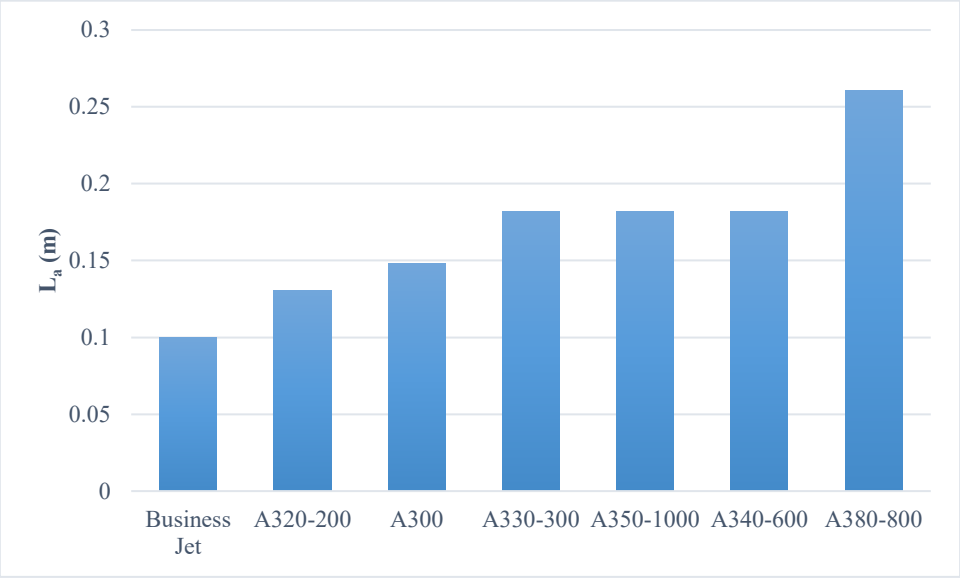

Figure 98. Link arm length

3.2.1.15 Moment at hinge (M_h)

Estimation of the arm length makes it possible to estimate the moment at hinge using Equation (175).

$$M_h = F_{sc} \times L_a \tag{175}$$

Figure 99 shows the variation of moment at hinge for the selected aircraft.

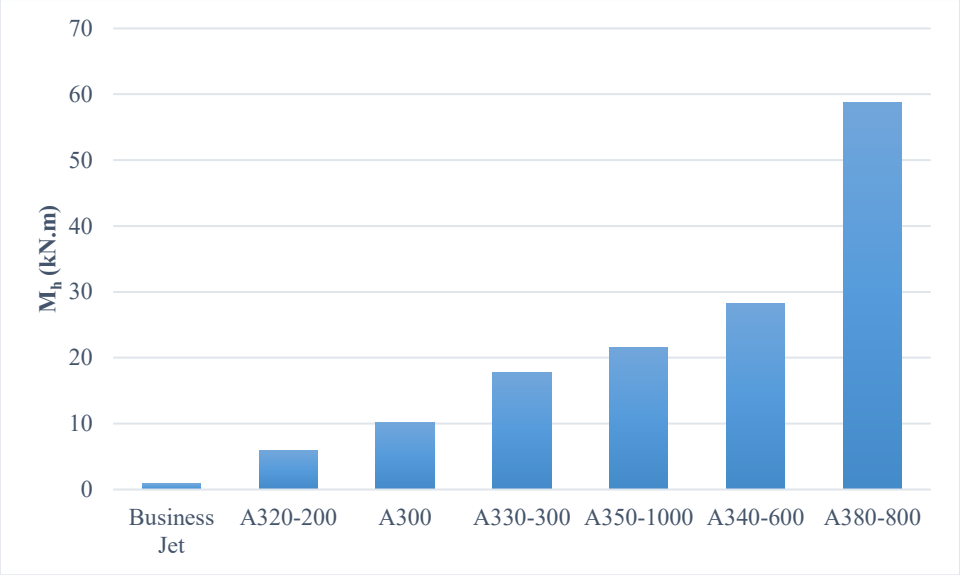

Figure 99. Moment at hinge

3.2.1.16 Equivalent load mass (M_L)

Again, using the estimated arm lengths and surface inertias calculated by Equation (171), load equivalent masses can be determined as follows:

$$M_L = \frac{J_r}{(L_a)^2} \tag{176}$$

Figure 100 gives the equivalent mass seen by the actuator for different aircraft, where the mass is measured in tonne (t)

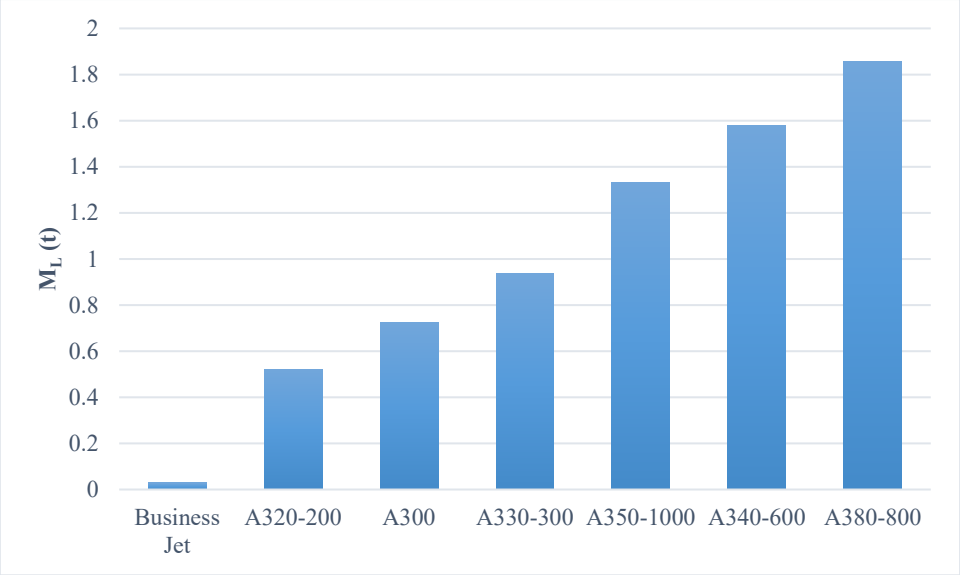

Figure 100. Equivalent load mass

3.2.1.17 Aerodynamic stiffness (K_a)

As mentioned above, for full deployment, the rudder is allowed to deflect up to *30°* for the business jet. As the rudder angle increases, the aerodynamic pressure on the rudder increases, and the relationship is fairly linear.

Half of screw stroke corresponds to full rudder deployment towards one direction. Further, since screw stroke increases for larger aircraft, K_a is always calculated with respect to half of stroke. For a certain displacement on the screw, say *50 mm* in the case of the business jet, aerodynamic stiffness can be estimated as follows.

Thus, the aerodynamic stiffness, K_a, may be calculated:

$$K_a = \frac{F_{sc}}{\frac{1}{2}S} = 180000\ N/m \tag{177}$$

Figure 101 shows the estimated aerodynamic stiffness for the selected set of aircraft.

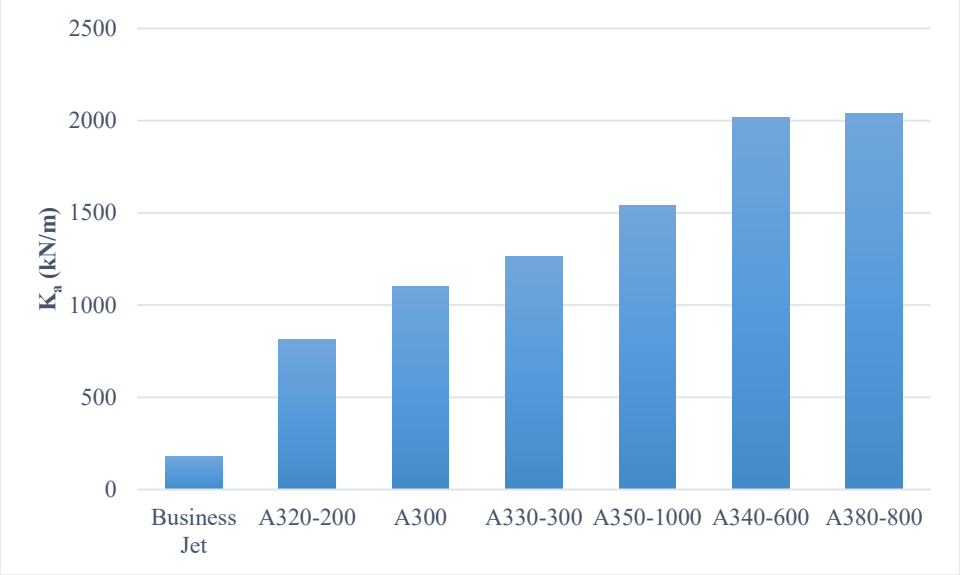

Figure 101. Aerodynamic stiffness

3.2.2 Screw-nut assembly

Screw shaft is a crucial part that has different characteristics according to application and amount of loading. According to [26], physical dimensions such as diameter and length of the ball-screw determine the rigidity of the system and hence have influence on the system dynamical behaviour and structural vibration modes. In calculating screw parameters, screw shaft is assumed a solid cylinder and hence solid cylinder equations are applied.

3.2.2.1 Screw diameter (D_{sc})

To estimate how screw size changes with respect to force, various commercial screws from *SKF* website are investigated to observe the relationship between rated force and screw nominal diameter [63].

Figure 102 shows the variation of screw diameter with rated force for a lead of *5 mm*. The screw diameter is sized using curve fitting as shown in Equation (178).

$$D_{sc} = 1.19 \times 10^{-6} F_{sc} + 0.009433 \quad (178)$$

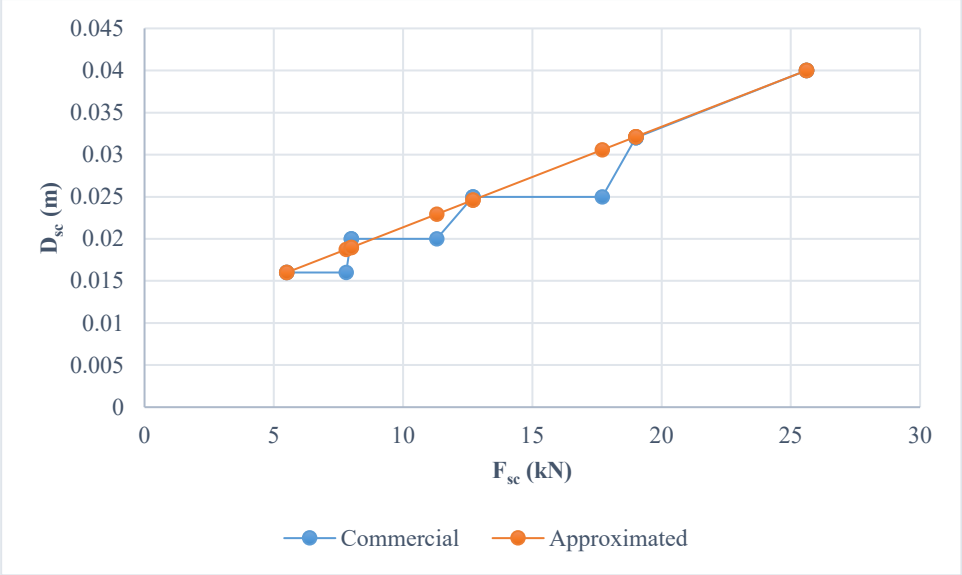

Figure 102. Variation of screw diameter with rated force (lead = 5 mm)

Figure 103 shows the variation of screw diameter with rated force lead of *10 mm* [63]. The screw diameter is sized using curve fitting as shown in Equation (179).

$$D_{sc} = 6.64 \times 10^{-7} F_{sc} + 0.0089 \quad (179)$$

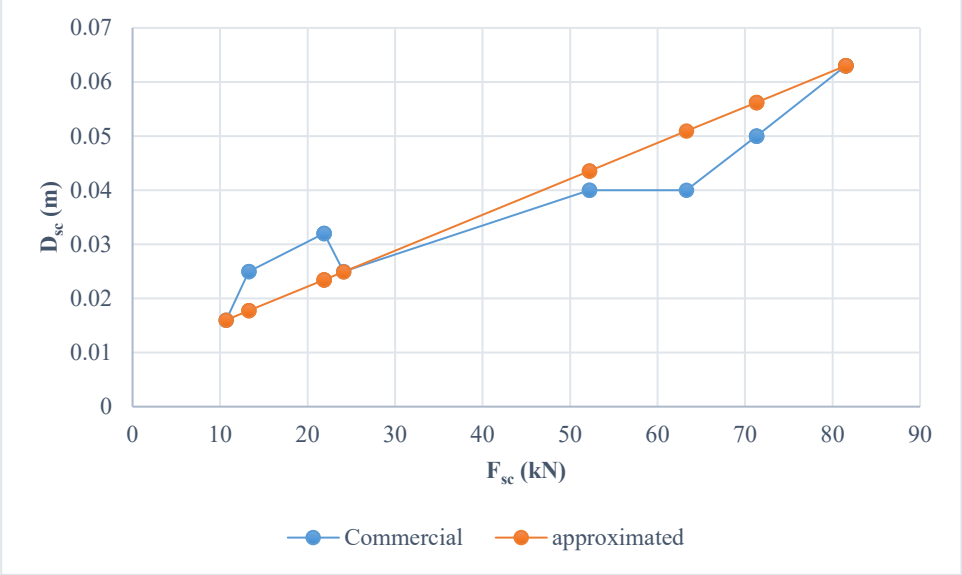

Figure 103. Variation of screw diameter with rated force (lead = 10 mm)

From the two figures above, it can be seen that screw diameter can be assumed to be changing linearly with force. Figure 104 gives the variation of screw diameters with the range of forces encountered required to actuate the rudder of the aircraft under consideration. As can be seen, the screws with smaller lead requires larger diameter.

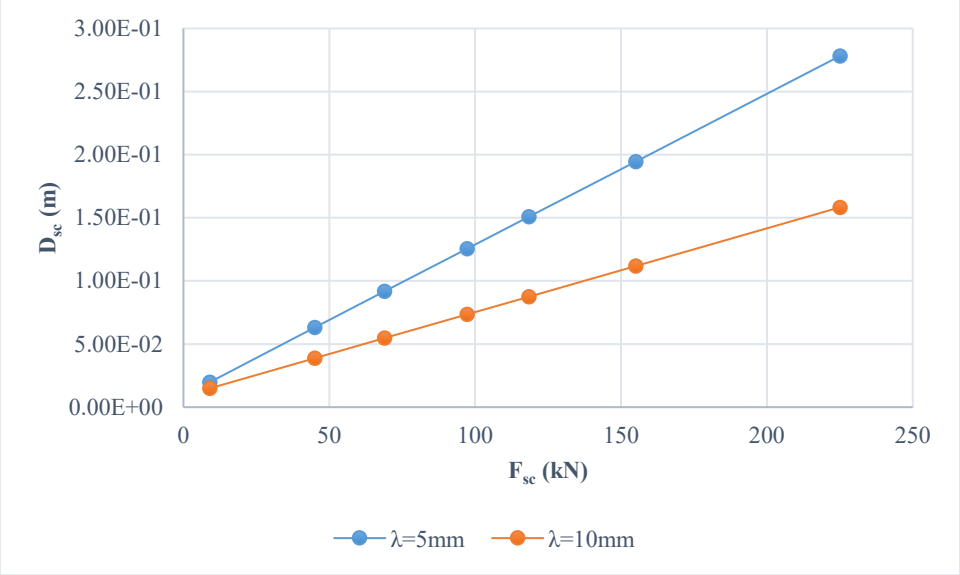

Figure 104. Variation of screw diameter with rated force for different leads

3.2.2.2 Length (L_{sc})

For the light business jet, the stroke, *S*, is *0.1 m* and the screw shaft length is *213 mm*. So around *113 mm* of length is added to the screw shaft on top of the required stroke. If the same amount is added to other strokes, the screw shaft length can be varied with actuation force in the manner depicted in Figure 105.

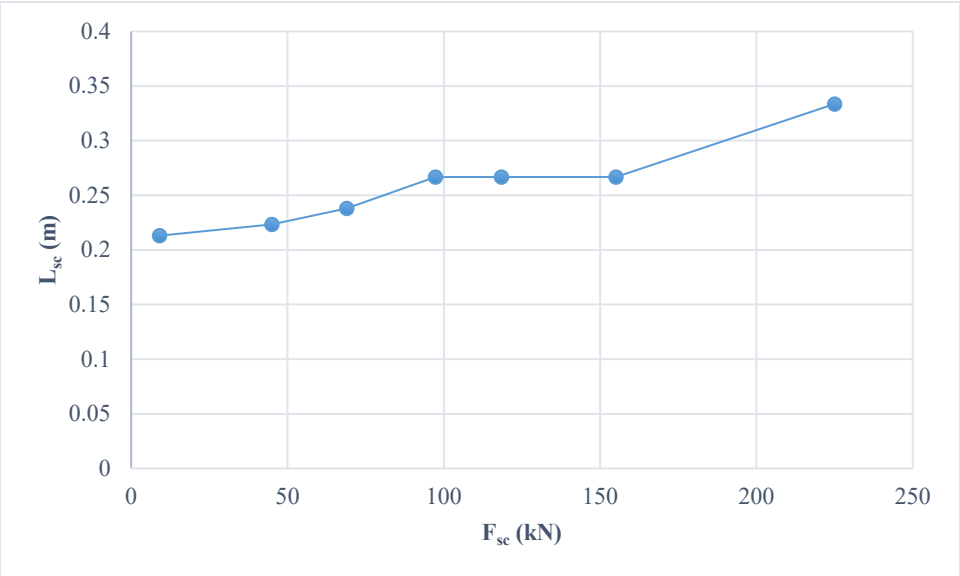

Figure 105. Screw length

3.2.2.3 Screw torsional stiffness (K_{st})

Screw torsional stiffness is given by:

$$K_{st} = \frac{T_{sc}}{\Delta\theta_{sc}} = \frac{G_{sc}I_{sc}}{L_{sc}} \tag{180}$$

where G_{sc} is shear modulus of screw material, I_{sc} is area moment of inertia of screw, and T_{sc} is torque applied on the screw as shown in Figure 106.

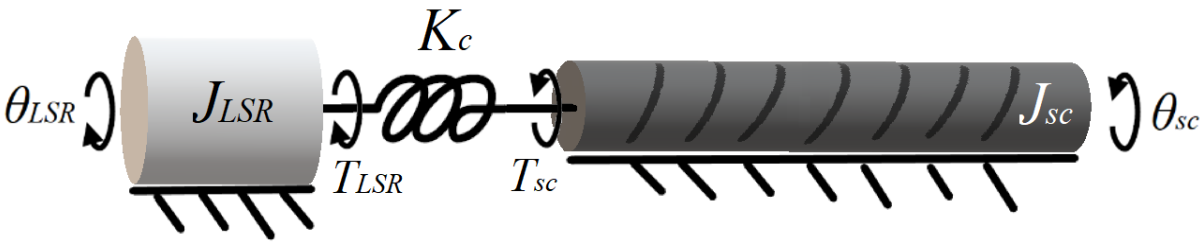

Figure 106. Torque applied on the screw, T_{sc}

Figure 107 shows variation of screw torsional stiffness with actuator force for different lead lengths. As screw with smaller lead is stiffer and hence it is more resistive to torsion.

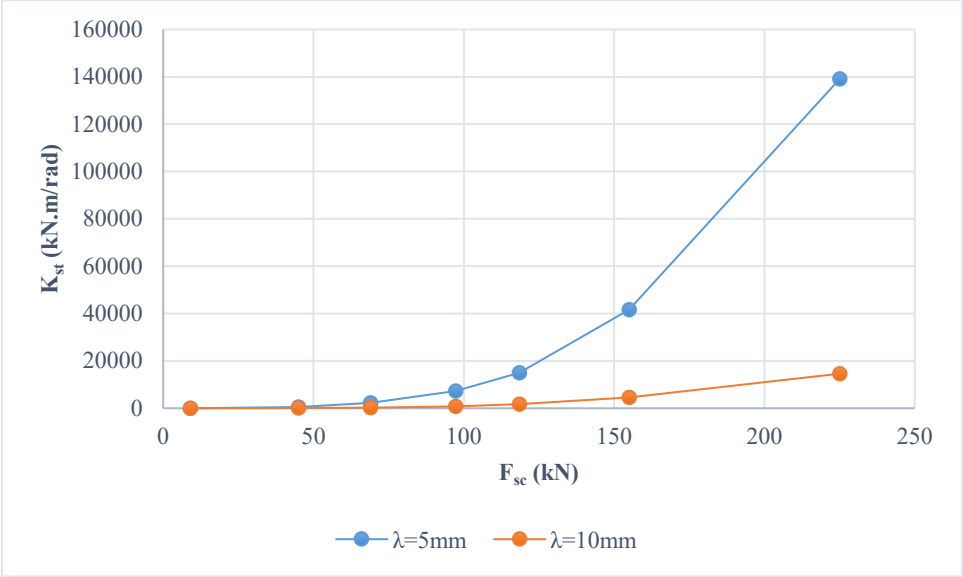

Figure 107. Screw torsional stiffness

3.2.2.4 Screw axial stiffness (K_{sa})

Screw axial stiffness, K_{sa}, is calculated as shown in Equation (181).

$$K_{sa} = \frac{F_{sc}}{\Delta x_{sc}} = \frac{E_{sc}A_{sc}}{L_{sc}} \tag{181}$$

where E_{sc} is Young's modulus of screw material, and A_{sc} is cross sectional area of screw shaft.

Figure 108 shows the variation of the screw axial stiffness with actuator force. Smaller lead cases show a higher stiffness due to larger cross-sectional area.

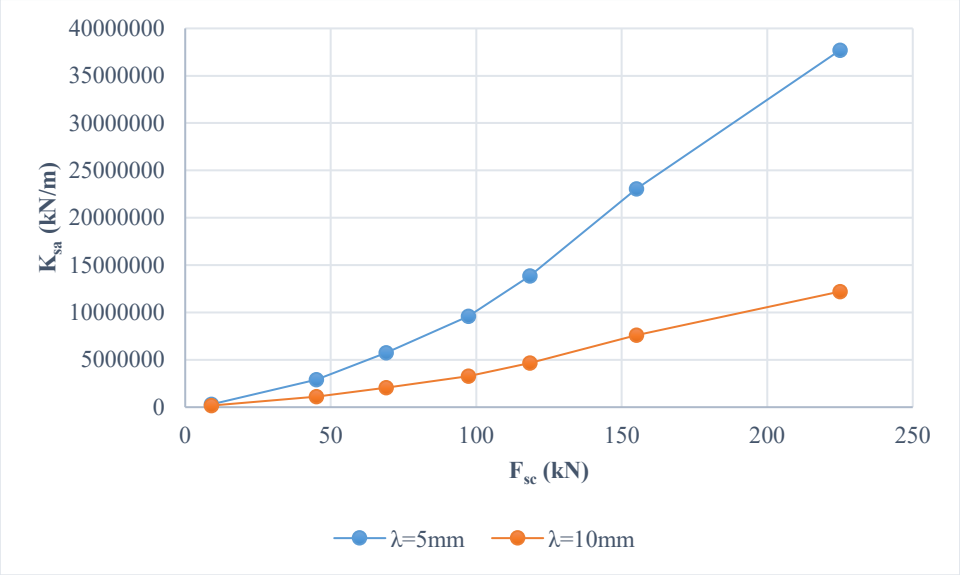

Figure 108. Screw axial stiffness

3.2.2.5 Screw mass (M_{sc})

Screw mass can be calculated using Equation (182).

$$M_{sc} = \rho_{st} A_{sc} L_{sc} \tag{182}$$

where ρ_{st} is the steel density and it is assumed to be $7700\ kg.m^{-3}$.

Figure 109 shows screw mass for the different aircraft.

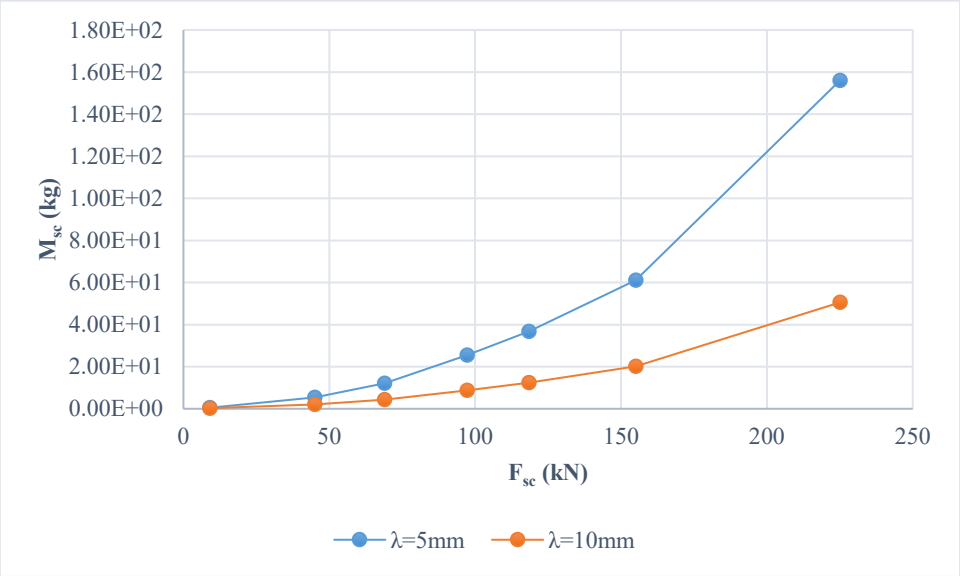

Figure 109. Screw mass

3.2.2.6 Screw inertia (J_{sc})

If a cylinder is spinning around its centre axis, moment of inertia is given in the formula shown in Equation (183).

$$J_{sc} = \frac{1}{8} M_{sc} D_{sc}^2 = 2.44 \times 10^{-5}\ kg.m^2 \tag{183}$$

Various screw inertias are shown in Figure 110.

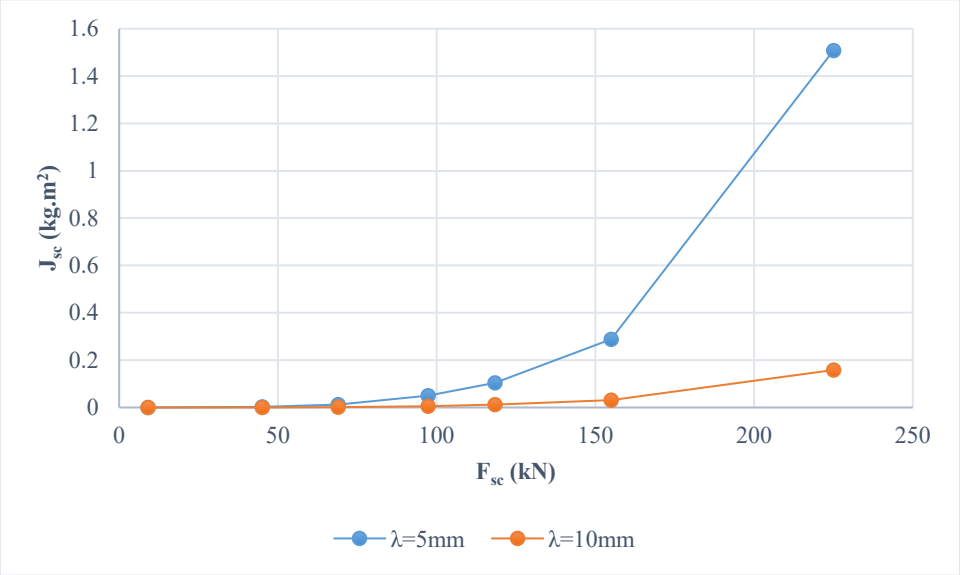

Figure 110. Screw inertia

3.2.2.7 Screw-nut interface stiffness (K_n)

Nut stiffness, K_n, can also be investigated by looking at data provided for commercial screws by the *SKF* website [63]. Figure 111 is a plot of stiffness with respect to force, using curve fits shown in Equation (184) for the 5 mm lead screw and Equation (185) for the 10 mm lead screw. It can be seen that nut stiffness almost linearly changes with respect to force.

$$K_n = 40845.8\, F_{sc} - 77651741.3 \tag{184}$$

$$K_n = 16737.28814\, F_{sc} + 83911016.95 \tag{185}$$

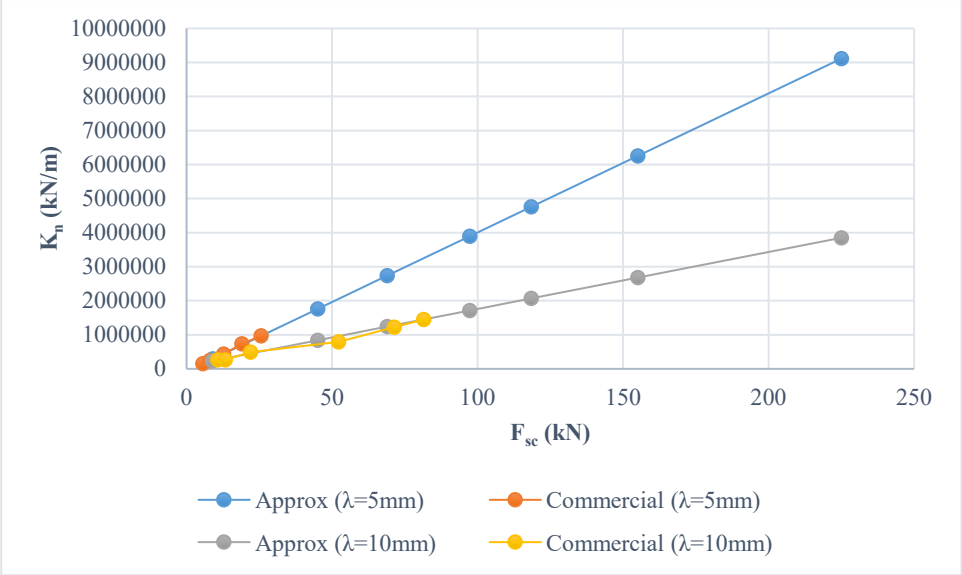

Figure 111. Screw-nut interface stiffness

3.2.2.8 Spline coupling stiffness (K_c)

Spline coupling is a type of coupling that transmit motion by the function of teeth meshing with each other [64]. Information about commercial spline coupling stiffness is not available as much as stiffness of flex coupling. However, it is useful to look at how flexible coupling stiffness changes with rated torque. Also, some information about certain spline coupling can be found in the literature that shows typical stiffness values for a certain type of torques. [65] shows a range of flexible coupling stiffness with respect to rated torque. Figure 112 summarises findings in the *SKF* coupling catalogue. It can be seen below that the stiffness is increased almost linearly with respect to rated torque increase. For this type of flexible coupling, the deflection angle is kept almost constant and equal to roughly *5°*.

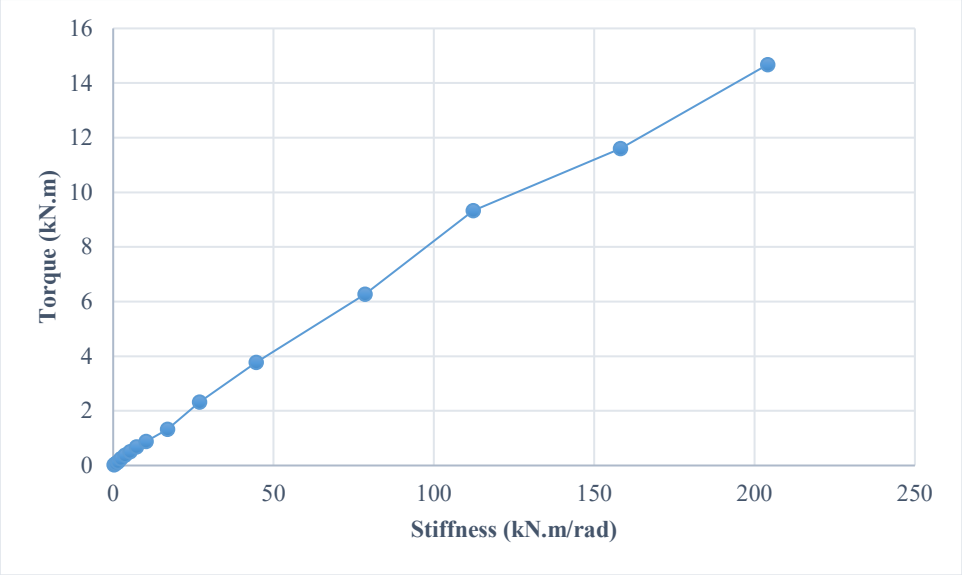

Figure 112. Flex coupling stiffness

The spline coupling stiffness in this project is 1.67×10^4 *N.m/rad* whereas peak torque is 8.6 N.m. At these figures, the deflection angle is *0.03°*. It is clearly evident that spline coupling stiffness is significantly higher than that of the flexible coupling. [64] presents experimental data of measured spline stiffness under a range of torques. The stiffness of the spline coupling used in [64] reaches 9.3×10^4 *N.m/rad*. In [66], spline stiffness is evaluated in four different ways. The spline coupling under study in [66] carries an operational load of *57000 N.m*. The stiffness is evaluated to be 13.4×10^6 *N.m/rad*.

Since the spline coupling is available with significantly high stiffness, it is sensible to keep the deflection angle constant at *0.03°* and increase the stiffness linearly with respect to operational torque increase. Stiffness can be plotted with force as shown in Figure 113.

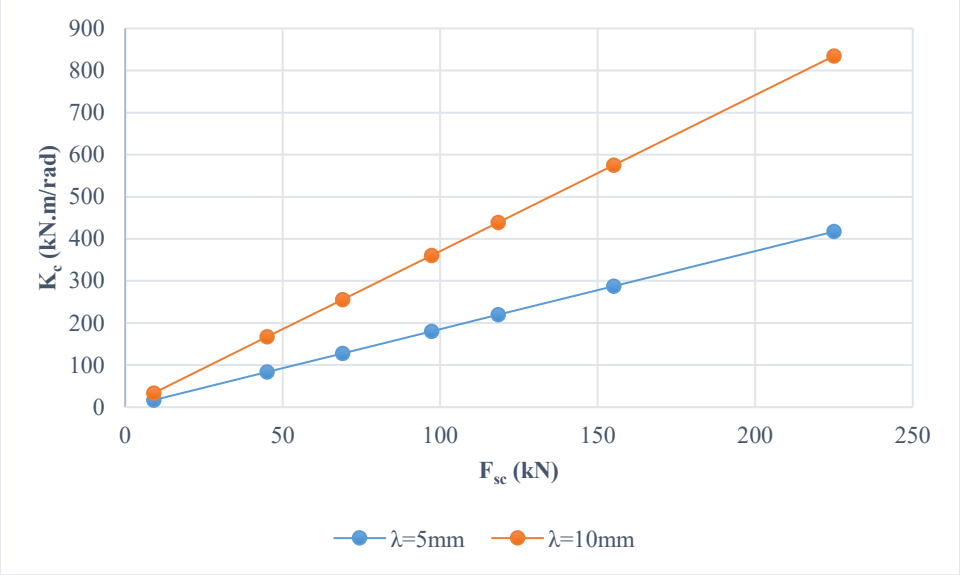

Figure 113. Spline coupling stiffness with force

3.2.2.9 Thrust bearing stiffness (K_b)

Two types of bearings are on the sides of the screw; thrust bearing and support bearing. The thrust bearing is placed at the edge close to the motor and it is there to prevent the screw from pushing towards the motor as a result of load and external forces. On the other hand, the support bearing allows the screw to move freely axially. This is important because during operation, the friction between the screw and nut generates heat that cause an expansion in the screw [11].

Three important parameters are associated with the double direction thrust bearing; load ratings, speed ratings and stiffness. Figure 114 is a graph that shows stiffness with respect to load ratings for commercial thrust bearings (*SKF* website) [67]. Stiffness of bearing is sized according to the pattern shown for the commercial bearing, using curve fitting as shown in Equation (186).

$$K_b = \ln F_{sc} \times 600000000 - 5480000000 \quad (186)$$

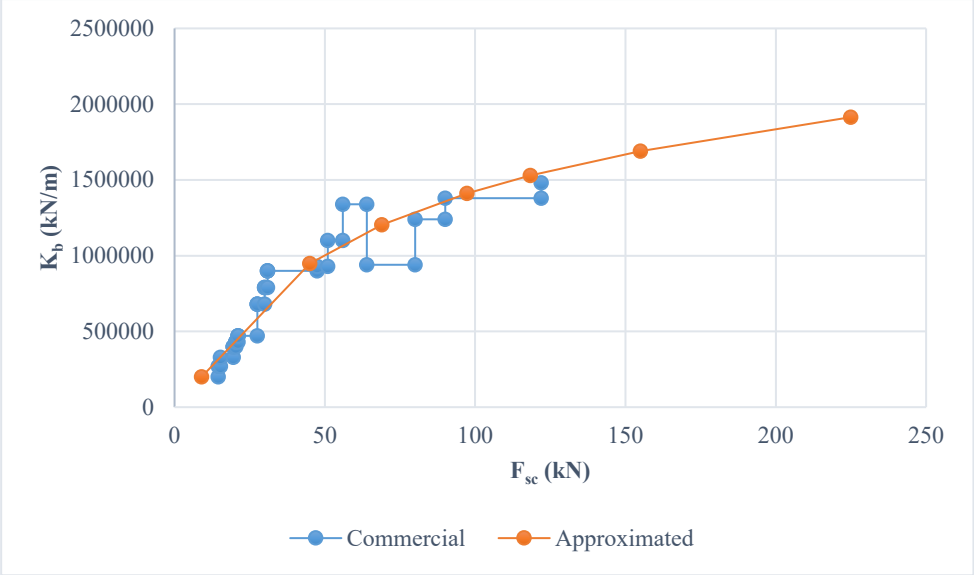

Figure 114. Stiffness of the bearing

3.2.3 Motor sizing

In this section, motor parameters are estimated to be applied in resonant analysis. The most important parameter is the PDD LSR inertia. For such a reason, inertia is estimated after estimating the LSR dimensions.

3.2.3.1 Torque required (T_{LSR})

In PDD, torque is produced by interaction between stator current and the inner HSR PM flux. The torque is transmitted into the LSR via magnetic transmission.

The motor torque, T_{LSR}, required is a function of the screw lead, γ. Therefore, based on a required force, F_{sc}, the torque of the PDD can be determined as follows:

$$T_{LSR} = F_{sc} \times \gamma \tag{187}$$

Figure 115 shows the variation of required motor torque with force.

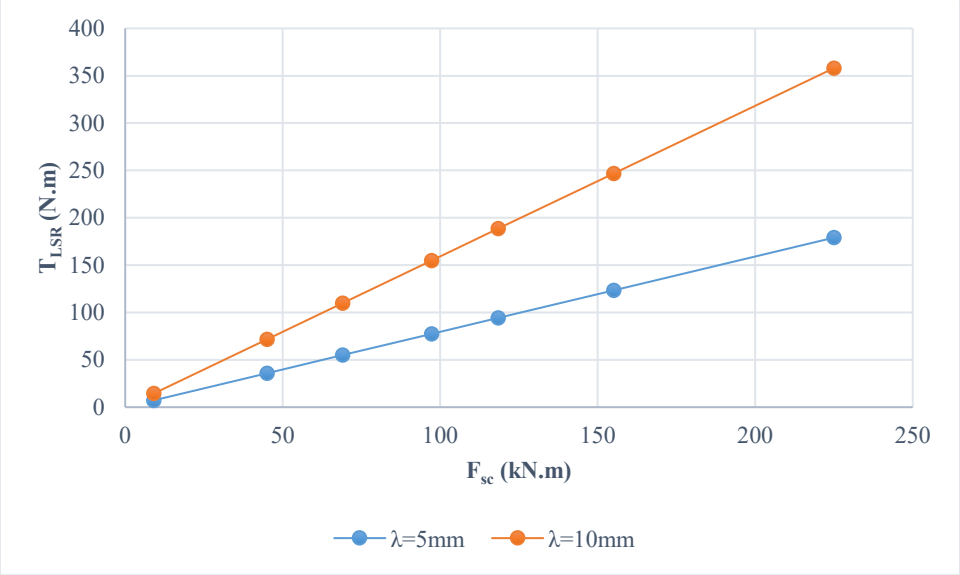

Figure 115. PDD LSR torque

3.2.3.2 Shear stress (σ_{LSR})

For electrical machines including PDDs, airgap shear stress is a characteristic fairly independent of size. Thus, it enables the estimation of output torques for given rotor dimensions, such as dimeter and axial length, as shown in Equation (188) [68].

According to [68], a high-performance industrial servo can have a shear stress between *10.3-20.7 kPa*. Further, airgap shear stress of a conventional surface mount PM machine can reach *13 kPa* [34]. For the PDD employed for the realisation of the business jet actuation system, the shear stress value reaches *52 kPa* [34].

$$\sigma_{LSR} = \frac{2T_{LSR}}{\pi D_o^2 L_{ax}} = 52\ kN.m^{-2} \tag{188}$$

where, L_{ax} and D_o are *PDD* axial length and *LSR* outer diameter, respectively.

3.2.3.3 Aspect ratio (AR)

Aspect ratio is ratio between axial length, L_{ax}, to rotor outer diameter, D_o, as depicted in Figure 116.

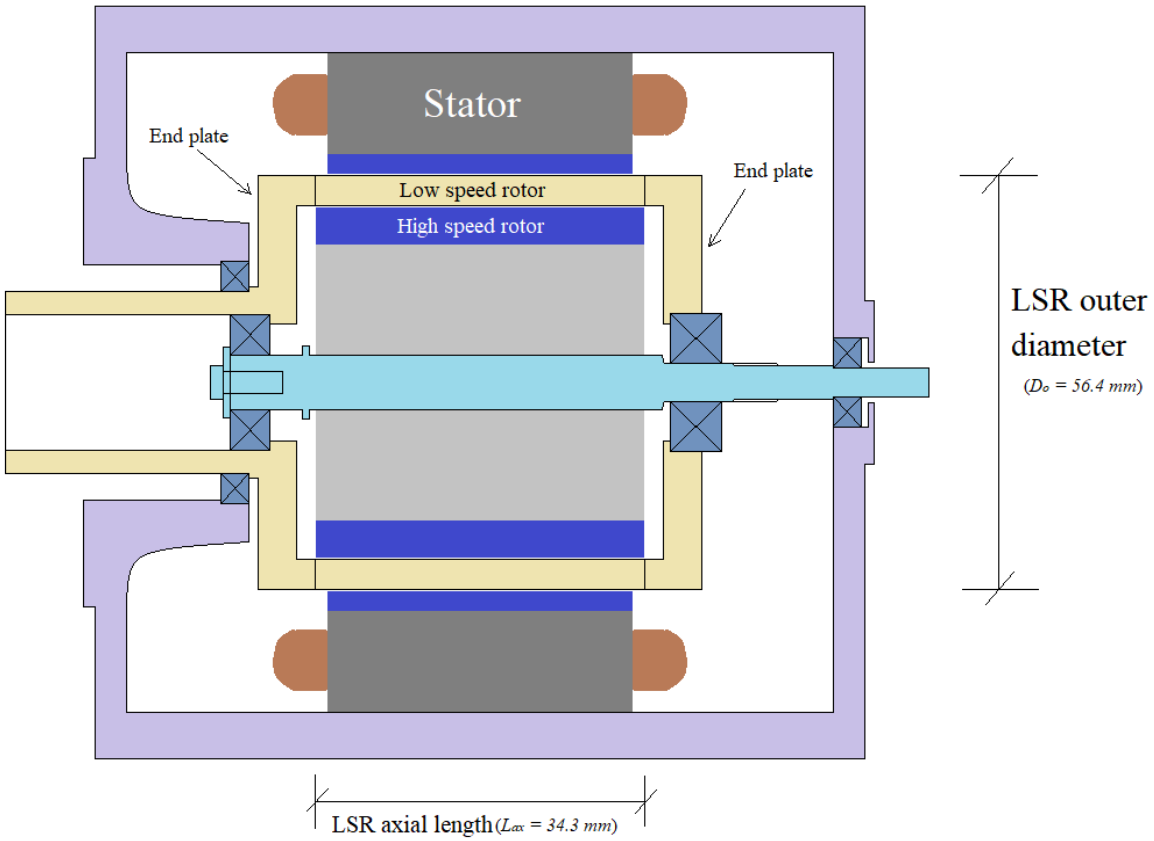

Figure 116. LSR outer diameter and axial length

By using Equation (189), aspect ratio can be evaluated.

$$AR = \frac{L_{ax}}{D_o} = 0.607 \tag{189}$$

This value of aspect ratio is going to be assumed constant for all PDD sizes.

3.2.3.4 LSR outer diameter (D_o)

The axial length can be substituted into Equation (188).

$$\sigma_{LSR} = \frac{2T_{LSR}}{\pi D_o^2 (D_o AR)} = \frac{2T_{LSR}}{\pi D_o^3 AR} \tag{190}$$

which can be re-arranged for *LSR* outer diameter:

$$D_o = \sqrt[3]{\frac{2T_{LSR}}{\pi \sigma_{LSR} AR}} \tag{191}$$

Figure 117 shows the variation of LSR diameter with actuation force.

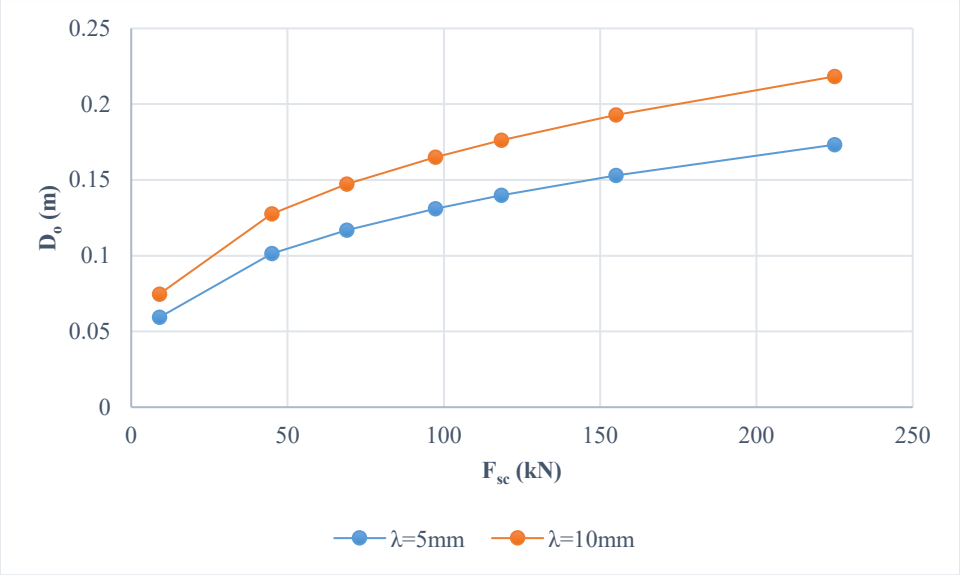

Figure 117. LSR outer diameter

3.2.3.5 LSR axial length (L_{ax})

Using the aspect ratio in Equation (189), and having determined the LSR outer diameter, it is possible to estimate the LSR axial length, as shown in Equation (192).

$$L_{ax} = D_o \times AR \tag{192}$$

Figure 118 shows the variation of LSR axial length with actuator force.

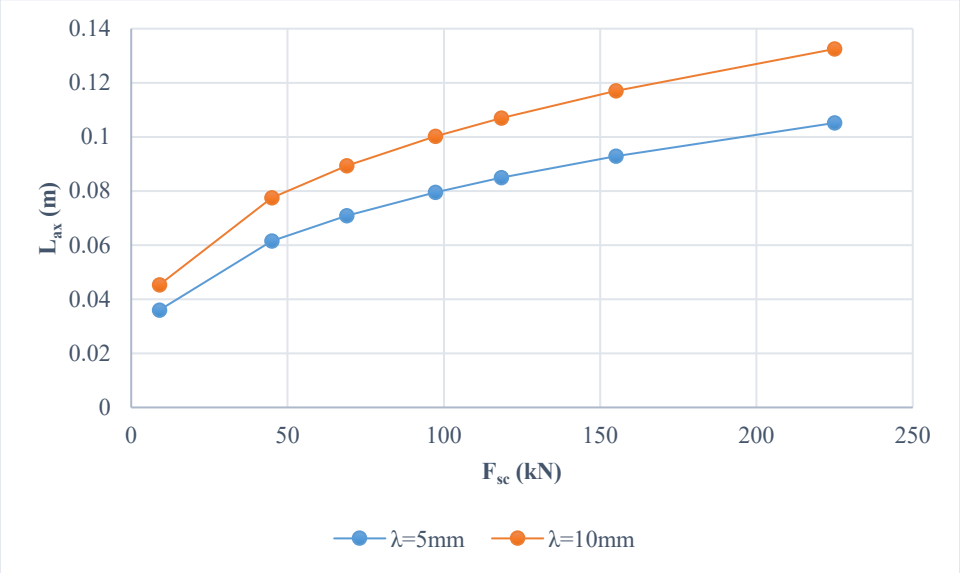

Figure 118. Variation of LSR axial length with actuation force

3.2.3.6 LSR radial thickness (T_r)

The radial thickness of the LSR, T_r, is a function of how many pole-pieces, n_s, are needed, which is a function of the gear ratio, G_r. The pole-pieces are distributed evenly and separated by fibre glass, as illustrated in Figure 119. Let us assume that a pole-piece and a fibre glass have identical square bases.

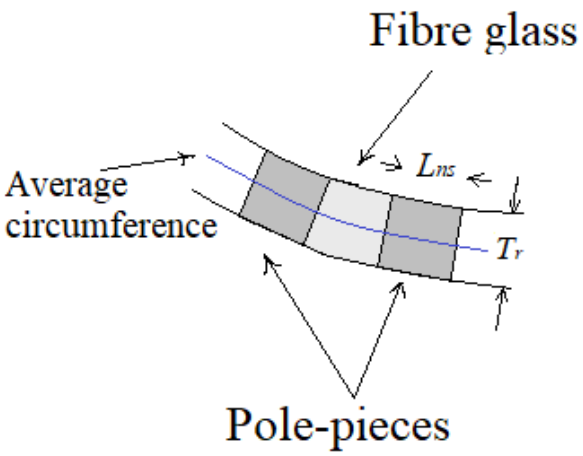

Figure 119. LSR radial thickness

Therefore, it is possible to assume that the length of a side of such a square is equal to the LSR radial thickness, as shown in Equation (193).

$$T_r = L_{ns} \tag{193}$$

where L_{ns} is the length of the side of the pole-pieces square shape.

The average circumference of the LSR , C_{LSR}, can be estimated as shown in Equation (194).

$$C_{LSR} = 2L_{ns}n_s \tag{194}$$

From Equation (193), Equation (194) can be written as shown in Equation (195).

$$2T_r n_s \tag{195}$$

Furthermore, the average circumference of the LSR can be written as a function of LSR outer diameter.

$$C_{LSR} = 2\pi(\frac{1}{2}D_o - \frac{1}{2}T_r) \tag{196}$$

Equating Equation (194) to Equation (196),

$$2T_r n_s = 2\pi(\frac{1}{2}D_o - \frac{1}{2}T_r) \tag{197}$$

Solving Equation (197) for T_r,

$$T_r = \frac{\pi D_o}{2n_s + \pi} \tag{198}$$

Figure 120 shows the variation of radial thickness for PDD LSR with actuator force for various aircraft sizes.

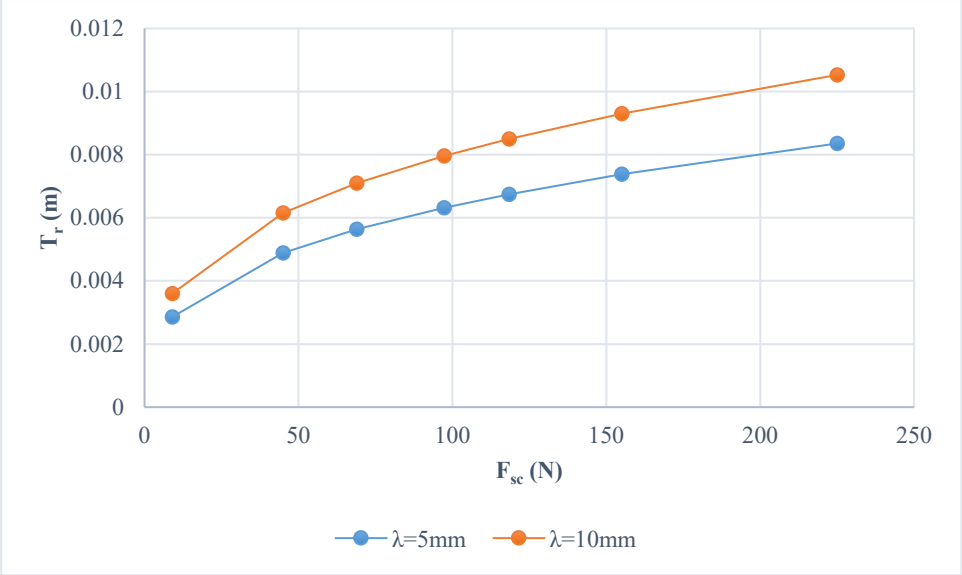

Figure 120. LSR radial thickness

3.2.3.7 LSR inner diameter (D_i)

LSR inner diameter, D_i, can be calculated using Equation (199**Error! Reference source not found.Error! Reference source not found.**).

$$D_i = D_o - 2T_r \tag{199}$$

3.2.3.8 Pole-pieces-fibre-glass inertia (J_{pp})

Equation (200) shows how the pole-pieces-fibre-glass rotor inertia is calculated.

$$J_{pp} = \frac{\pi \rho_{LSR} L_{ax} (D_o^4 - D_i^4)}{32} \tag{200}$$

where, ρ_{LSR} is the average density of the pole-pieces rotor equalling to 4725 kg/m^3, considering steel and glass fibre. Figure 121 shows the variation of the rotor inertia, J_{pp}, with actuator force for different aircraft sizes.

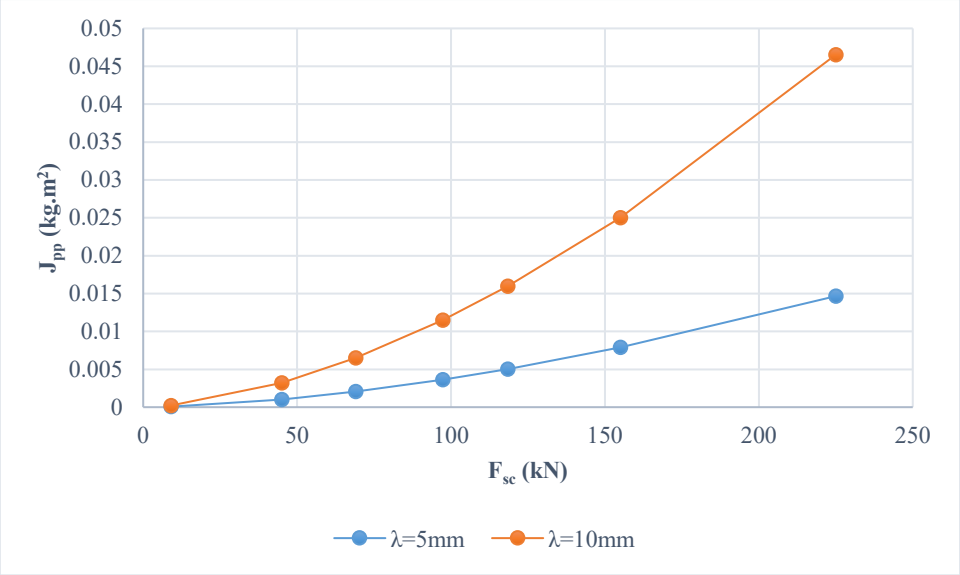

Figure 121. Pole-pieces & fibre glass inertia

3.2.3.9 End plates thickness (T_{ep})

End plates are two plates placed at both sides of the LSR, as shown in Figure 116. The end plate thickness, T_{ep}, of the *LSR* in use is *0.005 m*. It is not known how this parameter would change with PDD size. Further, these are usually made of Aluminium so contribution of overall *LSR* inertia is small if compared with contribution of pole-pieces inertia. Therefore, it is possible to assume this parameter to be fixed.

3.2.3.10 End plates inertias (J_{ep})

End plates can be thought of as two disks at both ends of the *LSR* as shown in Figure 116. Hence the sum of both disks inertias can be given by:

$$J_{ep} = \frac{1}{16}\pi\rho_{ep}T_{ep}D_o^4 \tag{201}$$

where ρ_{ep} is the density of the end plate material equalling to 2710 kg/m^3.

Figure 122 shows the variation of the inertias of both plates, J_{ep}, with the actuation force, for different aircraft sizes.

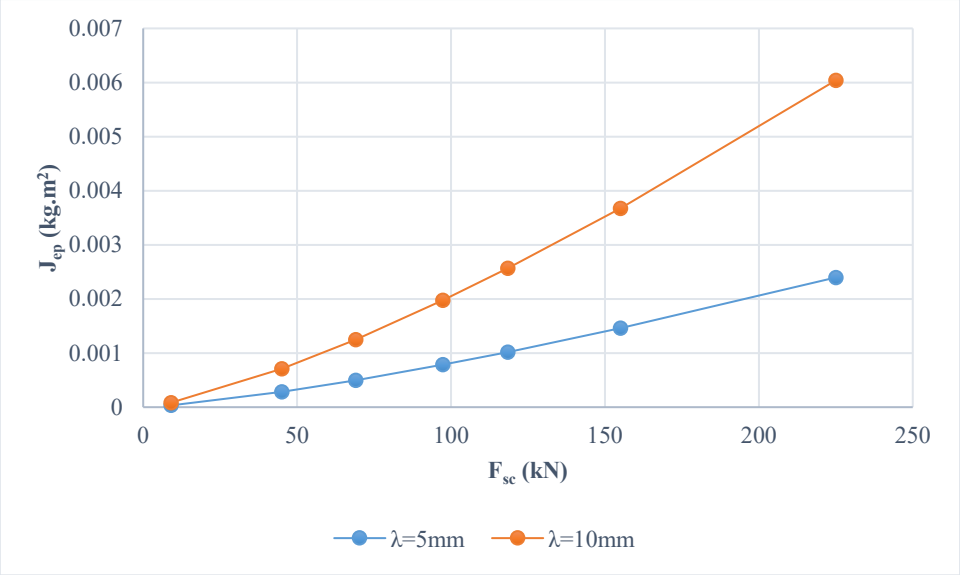

Figure 122. Variation of inertia of LSR end plates with force

3.2.3.11 LSR inertia (J_{LSR})

LSR inertia comprises of the pole-pieces and fibre glass plus the end plate disks; one of the disks is attached to the *LSR* whereas the other is attached to the *LSR* and the load. Therefore, the total inertia of *LSR* is given by:

$$J_{LSR} = J_{pp} + J_{ep} \tag{202}$$

Figure 123 shows the variation of the *LSR* inertia with actuator force, for different aircraft sizes.

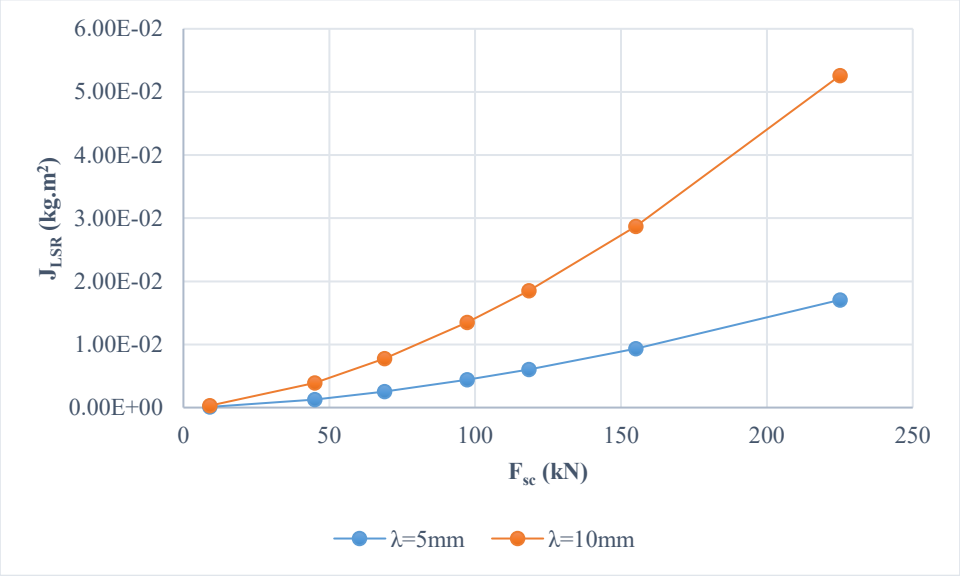

Figure 123. Variation of inertia of LSR with force

3.3 Resonance estimation for various aircraft sizes

Having sized electromechanical actuator for various aircraft sizes, it is crucial to examine dynamics of the actuation system, and compare it with that of the business jet.

In Chapter 2, three models of various degrees of freedom were introduced; namely, six-DOF model, three-DOF model, and two-DOF model. In this subsection, the three models are to be compared.

3.3.1 Deformation motions ($\Delta\theta_{sc}$ & Δx_{sc})

By implementing the six-DOF model, introduced in Chapter 2, eigenvalue and eigenvector analysis is used to show how the highest frequencies change with respect to actuators of different aircraft sizes. To subject screw shaft under operational point of maximum compliance, rudder is assumed at *0°*. The eigenvectors prove that the highest frequencies are mainly dominated by the torsional and translational deformations of the screw shaft. Such deformations depend on the properties of the ball screw. As aircraft size increases, the frequencies associated with the mentioned flexibilities decrease. The resonance associated with axial flexibility decreases to *15 kHz* for both investigated screw leads. On the other hand, the resonance resulting from torsional compliance may decrease to just below *10 kHz* for both leads, as shown in Figure 124.

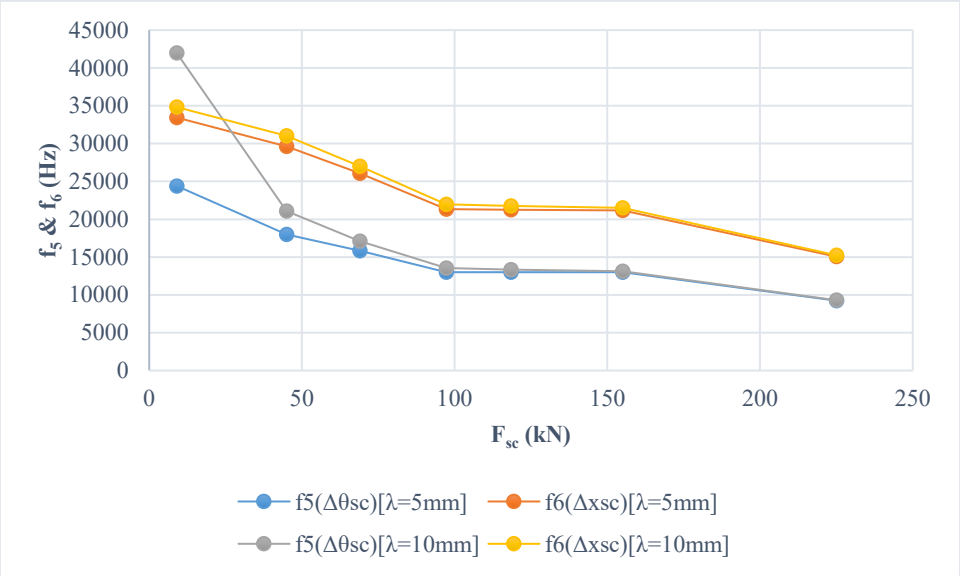

Figure 124. f_5 and f_6 variation with respect to aircraft size

Furthermore, the effects of these two motions, screw torsional and axial deformations, are insignificant on the significant frequencies highlighted, f_1 & f_2. Figure 125 shows a percentage of deformation motions at f_1 and f_2, which proves that the contributions of screw deformations are small. From this it can be deduced that torsional and translational compliances can be neglected and hence the screw shaft can be assumed and modelled as a rigid element. Therefore, the simplified models proposed can work for a big range of aircraft sizes.

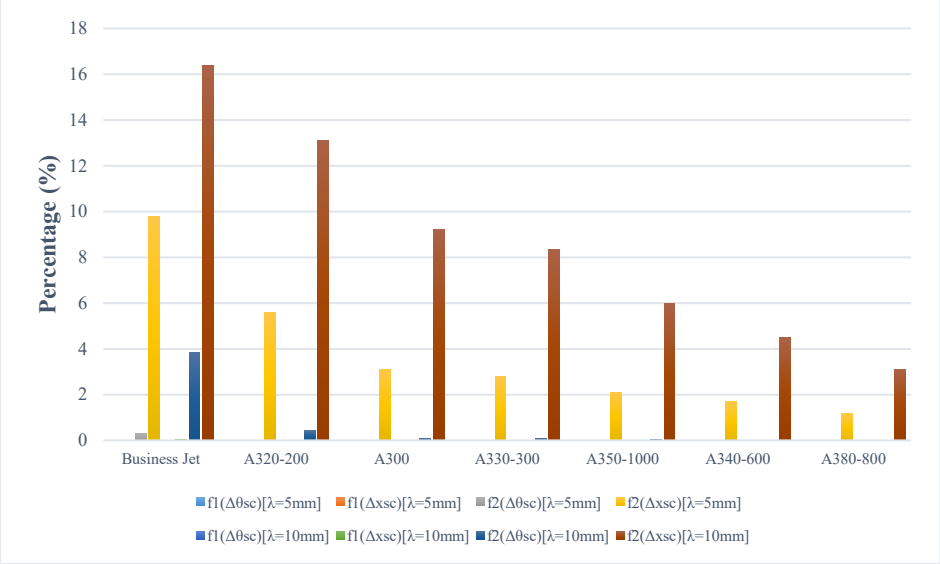

Figure 125. Percentage of deformation mode shapes in f_1 and f_2

Figure 125 is a summary of eigenvectors data presented in Appendix I.

3.3.2 Rigid motions

Four rigid motions are investigated in this test. By implementing the six-DOF model, introduced in Chapter 2, eigenvalue and eigenvector analysis is used to show how the highest frequencies change with respect to actuators of different aircraft sizes. Rudder is assumed at *-30°* to reflect full deployment.

3.3.2.1 f_1 variation for different aircraft sizes

This mode is due to the aerodynamic stiffness. Figure 126 and Figure 127 show the variation of this resonant frequency with actuator force, for leads of *5 mm* and *10 mm* respectively. It can be seen, that this frequency reduces significantly with increased size of the aircraft. It can also be seen that larger transmission ratios, result in larger first resonant frequency, due to the larger screw inertia equivalent mass at lower transmission ratios. For both transmission ratios, the aerodynamics stiffness and load mass are kept unchanged.

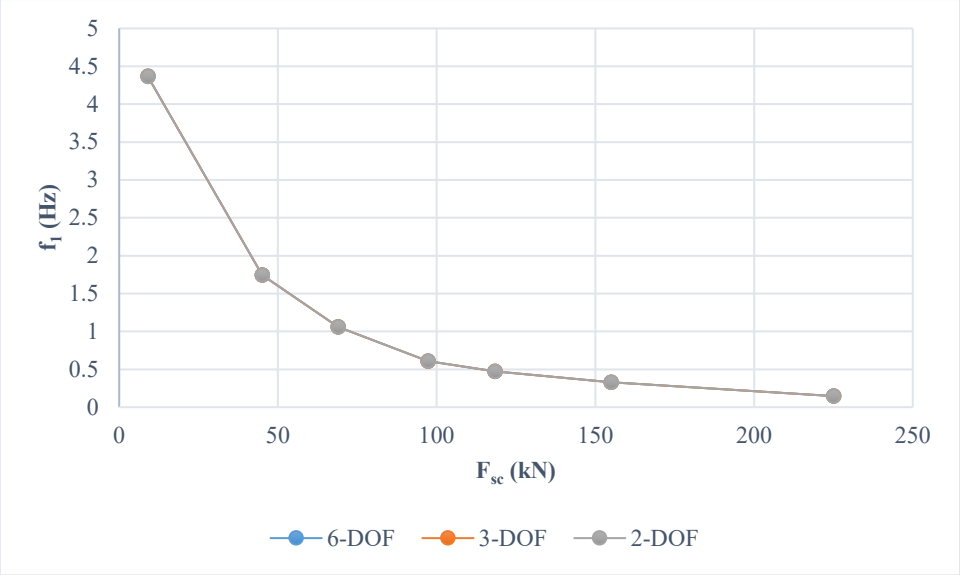

Figure 126. Variation of f_1 variation with aircraft size (λ=5mm)

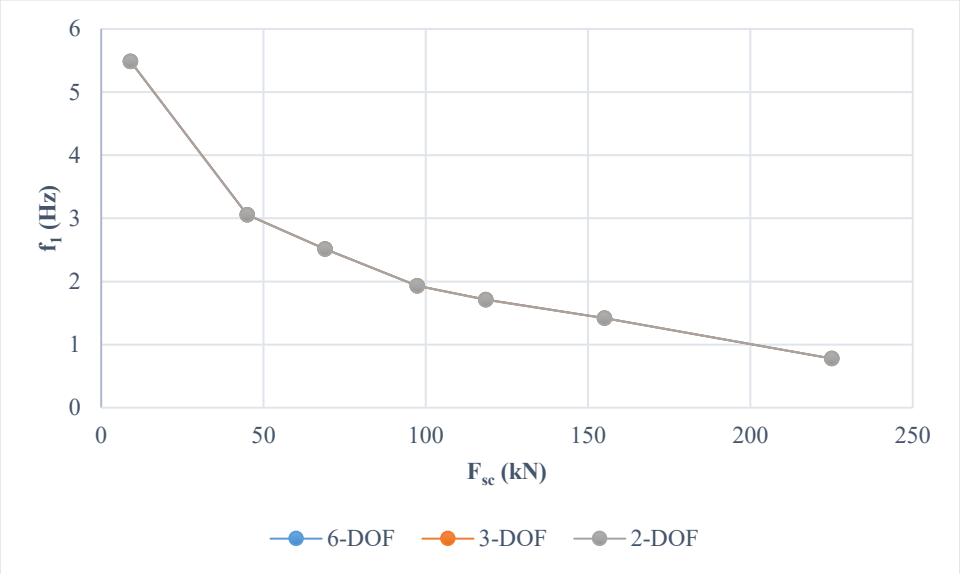

Figure 127. Variation of f_1 variation with aircraft size (λ=10mm)

3.3.2.2 f_2 variation for different aircraft sizes

The second frequency is mainly translational mode and the dominant motion is mainly associated with the load mass, which is moving in the same direction as the screw mass, hence the bearing and the screw-nut interface are the elastic elements. The amplitude of motion at this mode is significant.

Figure 128 and Figure 129 show the variation of f_2 with the actuator force for different aircraft sizes, considering two different screw leads; *5 mm* and *10 mm*, respectively. It can be seen that resonant frequencies are generally lower in the case of the higher transmission ratio. The reason for this difference is due to the change in the screw-nut interface stiffness (see Equation (203)). This is because as screw lead increases, the screw-nut interface is reduced. However, from a practical point of view, the

difference, in f_2 in both graphs, is not considerably large and it can be said that, overall, this frequency is essentially independent of the transmission ratio.

On that account, according to the findings in this section, whether screw lead is *5 mm* or *10 mm* shall not have any serious impact on this frequency since similar results are obtained for both transmission ratios.

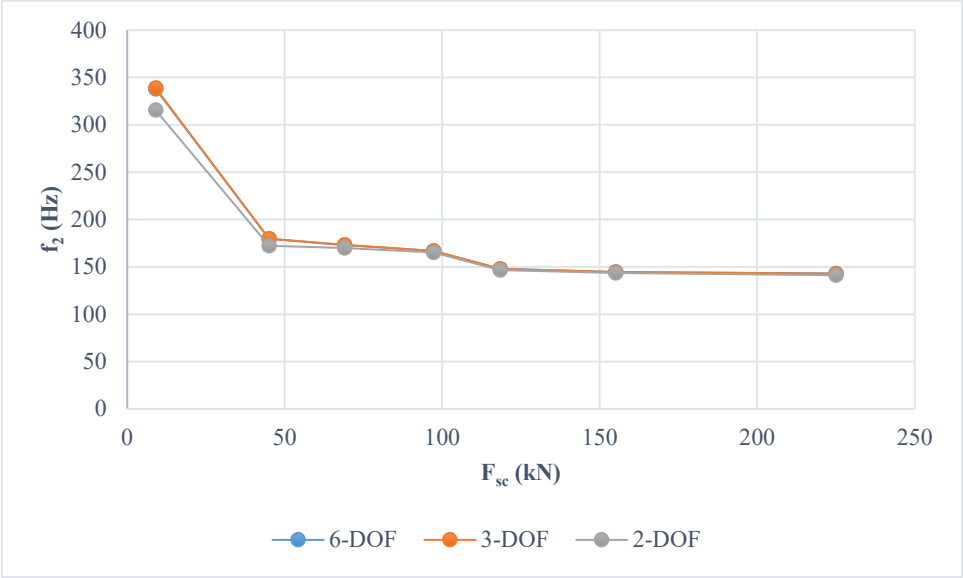

Figure 128. f_2 variation with respect to aircraft size (λ=5mm)

Figure 128 and Figure 129 present the variation of f_2 using three different models. It is evident that the 6-DOF model and the 3-DOF model are in extreme concordance. Yet, the 2-DOF model shows a difference; especially for the lighter aircraft and even especially for the higher transmission ratio. This represents a limitation which is associated with the 2-DOF model.

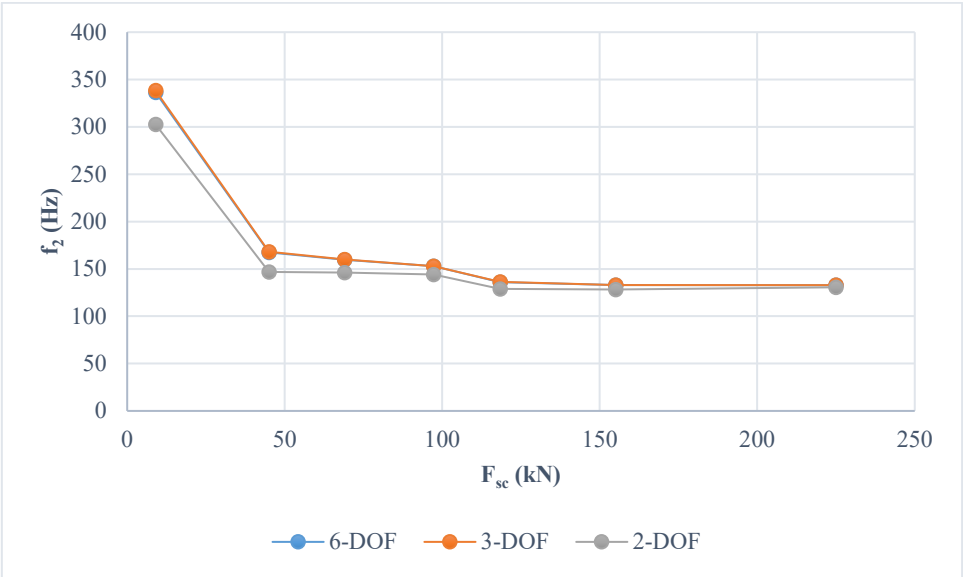

Figure 129. f_2 variation with respect to aircraft size (λ=10 mm)

It is useful to recap that the line representing the 2-DOF model, in Figure 128 and Figure 129, can be analytically determined using Equation (203).

$$f_2 = \frac{1}{2\pi}\sqrt{\frac{\frac{K_b K_n}{K_b + K_n} + K_a}{M_L + M_{sc}}} \tag{203}$$

This represents a decoupled fixed-free system; that is, it represents a purely translational motion of the equivalent mass against the equivalent stiffness. So, it can be said that f_2, determined by the other two models, have a rotary component.

Such a rotary component may arise from the relationship between the screw inertia and the equivalent inertia of the load mass; since they are coupled by K_n. If inertia of load mass is significant in comparison to the screw inertia, this mode will have a significant rotary component. Therefore, it is expected that for a given screw inertia, the inertia of the load mass is more significant in the case of a higher screw lead (Equation (204)).

$$J_L = M_L \gamma^2 \tag{204}$$

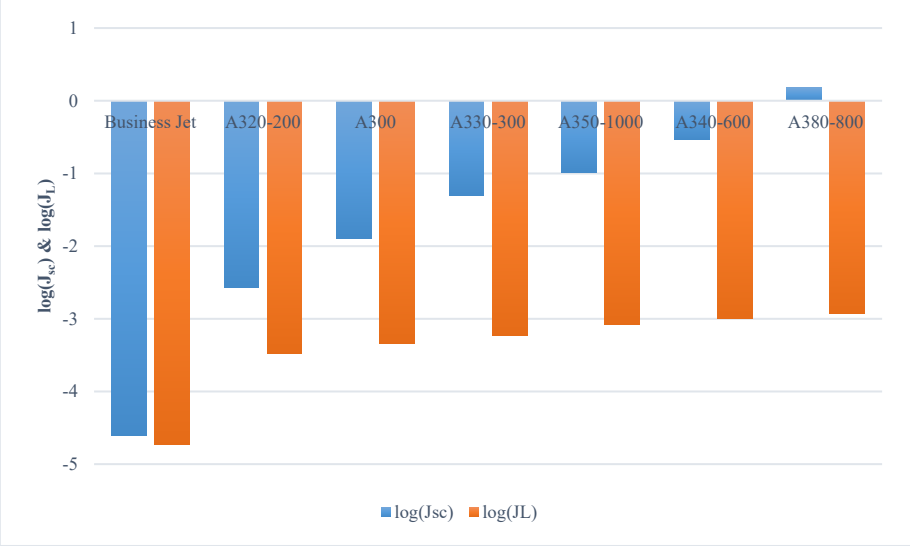

Figure 130. log inertias of load mass and screw (λ = 5 mm)

Figure 130 and Figure 131 show log scales of screw inertia and load mass equivalent inertia, for a screw lead of 5 and 10 mm respectively. It can be seen, in Figure 130 for the business jet, that the inertia of the load mass is significant with respect to J_{sc}. For A320, such significance is less. As aircraft size increases, the inertia of the load mass becomes less significant with respect to J_{sc}, and hence this mode has less rotary component for larger aircrafts. This is proved by the increased similarity between the 3-DOF and the 2-DOF model as aircraft size increases (Figure 128). In Figure 131, however, inertia of load mass is significant, with respect to J_{sc}, for a bigger range of aircraft. For such a reason, dissimilarity between the 3-DOF and 2-DOF models can be seen, in Figure 129, for the first three aircraft. Therefore,

it can be said that the 2-DOF has a limitation and hence will not be accurate if screw transmission ratio is high.

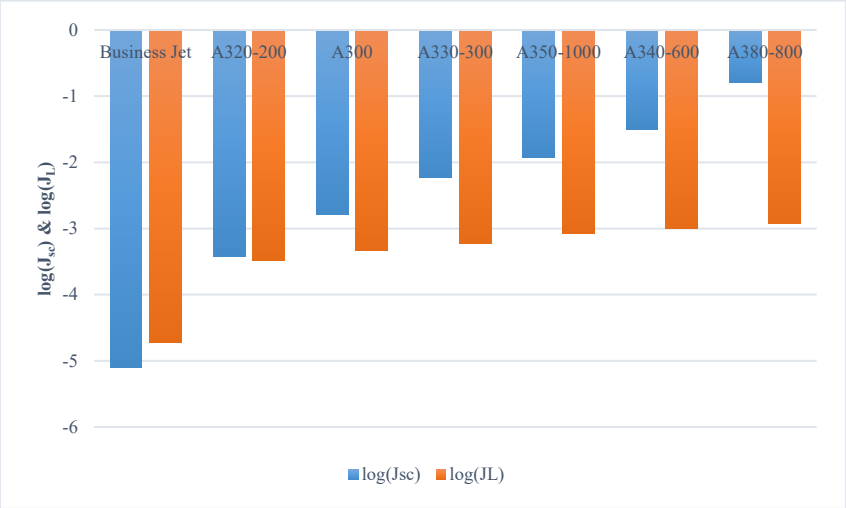

Figure 131. log inertias of load mass and screw (λ = 10 mm)

Figure 128 and Figure 129 show that for larger aircraft sizes, and hence larger rudder, f_2 seems to decrease in a way that resembles a negative exponential until the curve flattens out. This can be interpreted by considering Equation (203), Figure 100 and Figure 114. In Figure 114, K_b increases in a way similar to logarithmic function, and for largest aircraft K_b increases slowly. On the other hand, M_L, in Figure 100, increases in a similar proportion to the increase of the K_b. Therefore, in Equation (203), for largest aircraft, such as A340 and A380, K_b increases and M_L decreases in a similar proportion, which makes f_2 more flattened out at the end of the graph.

It is stated in [28] that the vibrational mode (f_2) will have a strong influence on the bandwidth if the control loop is closed with the direct carriage position. In such a case, adaptive control strategies must be used to achieve a high bandwidth closed loop.

3.3.2.3 f_3 variation for different aircraft sizes

At this frequency, the motor and screw inertias are moving opposite to each other, thus the coupling compliance stiffness is dominant.

Figure 132 shows the variation of the frequency with actuator force for different sizes of aircraft considering two different screw leads; *5 mm* and *10 mm*. For both cases, the frequency seems to drop as aircraft size increases. For the small aircraft, this mode occurs at over *4 kHz* for a smaller lead but it can reach over *10 kHz* for the larger lead. For the largest aircraft, the lowest frequency is just below *800 Hz*. The reason for this decrease is that as the aircraft size increases, the motor and screw inertia increase at a higher rate than the increase in the coupling stiffness.

Since f_3 is neither considered in the 3-DOF model or the 2-DOF model, the 6-DOF model is compared with Equation (205).

$$f_3 = \frac{1}{2\pi}\sqrt{\frac{K_c(J_{LSR} + J_{sc})}{(J_{LSR} \cdot J_{sc})}} \tag{205}$$

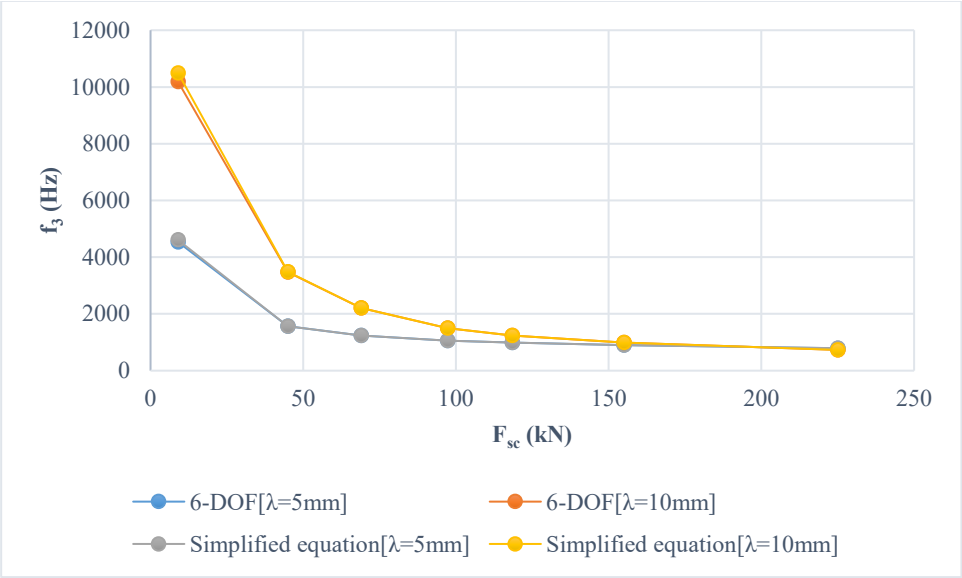

Figure 132. f_3 variation with respect to aircraft size

3.3.2.4 f_4 variation for different aircraft sizes

This is the highest frequency for rigid motions. At this frequency, the screw mass moves against the load mass and also against the stiffness of the bearing. Therefore, the oscillation occurs due to screw-nut compliance as well as bearing compliance. Figure 133 shows the variation of f_4 with actuator force for different aircraft. It can be seen that the transmission ratio has an effect on the frequency, with lower transmission ratios causing lower frequencies.

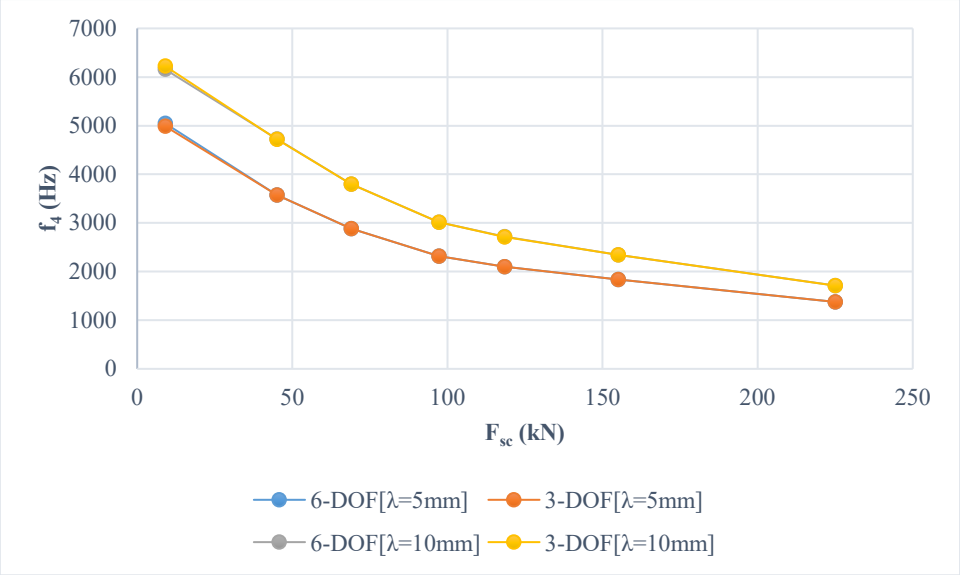

Figure 133. f_4 variation with respect to aircraft size

3.4 Conclusion

An attempt to obtain realistic dependency on transmission ratios, aircraft and parameters are sized upon assigned assumptions for two various transmission ratios. Having sized all parameters, the six-degree of freedom model (hybrid model) is again used to confirm the validity of negation of screw axial and torsional compliances. Then the six-degree of freedom model, the three-degree of freedom model and the two-degree of freedom models are used beside analytical equations for actuators of different aircraft sizes.

f_2 drops as aircraft size becomes larger due to increase of equivalent load. Two transmission ratios show similar values at this resonance. For f_3, frequency drops for the largest aircraft due to increase in screw and motor inertias. For a certain range of aircraft sizes, higher transmission ratio show a higher frequency due to lower values of screw inertia and higher value of coupling stiffness.

To sum up, for EMAs used to actuate rudder in MEAs, screw compliance can be neglected and three-degree of freedom model is adequate for all sizes of aircraft. Two-degree of freedom model can also be used in case load mass equivalent inertia is insignificant with respect to screw inertia. Relevant frequency drops in the case of larger aircraft, which represent a challenge in considering the bandwidth of the controller.

One output from this chapter is the curve fitting equations, employed for aircraft EMA sizing, which could be used in other research studies.

Chapter 4 Analysis of electromechanical interaction

4.1 Introduction

For the studied EMA system, electrical power is converted into mechanical power by means of the PDD. Hence the PDD represents the interface that couples the electrical network with the mechanical system, which is found to have resonance modes. Besides the useful power used in actuation mechanism, disturbance can also pass along. If this occurs, it becomes possible for resonant frequencies to be excited. This leads to electromechanical interaction, which has a serious impact on electrical power system stability and also could cause mechanical components to wear. Resonance excitation could be caused by internal or external means. For instance, internal excitation may come from the acceleration and control signal [29] [27]. On the other hand, external excitation may be a result of load forces (external disturbances); such as cutting forces or unpredicted friction transients. In the application of this project, external excitation may result from disturbance in the aerodynamic load. No matter what the source of excitation is, if occurs will lead to undesired vibrations and compromise stability.

In the literature review, electromechanical interaction is reported in different applications. For example, for aero generation system, it is concluded that transients in the electrical network can excite resonances of the drivetrain driving the generator [39]. Also, propeller movement and manoeuvring, which act like a disturbance load with varying frequencies on marine electric propulsion system, can be capable of causing oscillations in the electrical power system [43].

Moreover, in Chapter 2, a conventional model for aero EMA is presented and it is proved that such oversimplified model is incapable of showing any reactions to a varying frequency load. A more detailed model of EMA implemented and a simplification is made upon justifiable arguments. In this chapter, the obtained simplified model is integrated with the full electromechanical system. The entire system is subjected to sensitivity analysis to demonstrate stability issues. Eigenvalue sensitivity and participation factor are used to evaluate the dependence of system stability upon certain parameters and operating conditions. Time domain model is used to verify stability limits obtained from analysis. Further, time domain tests are also performed to observe interaction resulting from exciting resonant modes by an external disturbance force.

4.2 Integration of the full EMA system

System configuration and parameters are detailed in Figure 134. Note: symbols are defined in the table of notation.

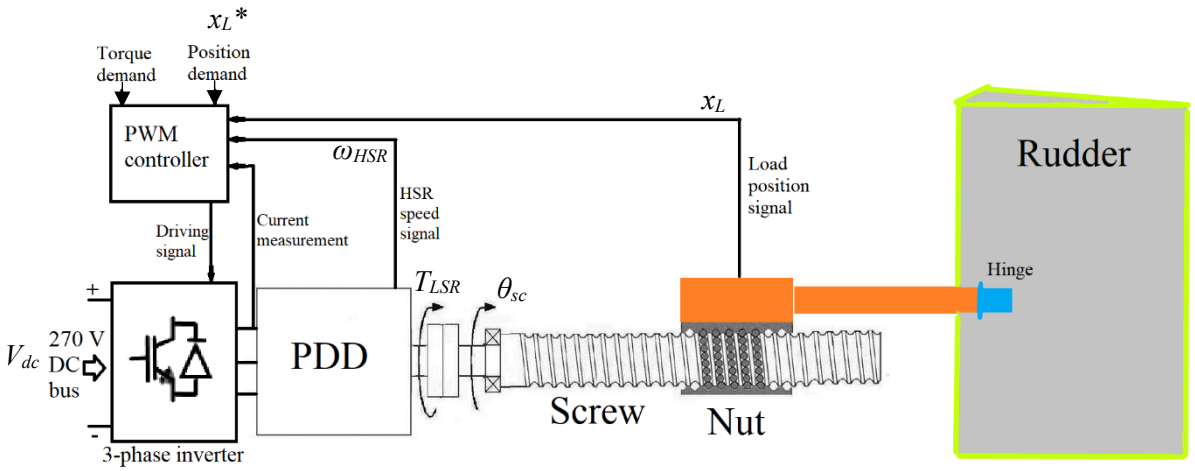

Figure 134. EMA drive system and aerodynamic load

Current loop bandwidth, f_c, is chosen in Chapter 2 to be 500 Hz. This value is selected by considering reasonable bandwidths for speed loop, f_s, and position loop, f_p, to be 50 Hz and 5 Hz respectively. However, due to limitations of the laboratory test rig used in experimental validation (Chapter 5), bandwidths for the control loops are selected accordingly so analysis can be closely compared with laboratory results. Bandwidths are summarised in Table 14.

Table 14. Control loops BWs

	Symbol	Value	Unit
Current loop BW	f_c	500	*Hz*
Speed loop BW	f_s	1.6	*Hz*
Position loop BW	f_p	0.6	*Hz*

4.2.1 Modelling

The three-degree of freedom model, for the ball-screw, simplified in chapter 2 is used here. As mentioned previously, the screw is assumed to be perfectly coupled with the PDD LSR. In this subsection, the model of the ball-screw and aerodynamic load is added to the PDD model. The switching model explained in Chapter 2 is used to verify points of instability, which are identified through analysis. The model implemented can be divided into electrical and mechanical parts.

4.2.1.1 Control scheme

Control scheme implemented is illustrated in Figure 135. It consists of an inner current loop in the *dq* reference frame, an outer loop for speed control, and an utmost loop for position control. Speed control feedback is taken from PDD HSR whereas position control feedback is taken from the screw-nut position. The control scheme design is explained in [50]. Also, control scheme model and PDD model are extensively explained in Chapter 2.

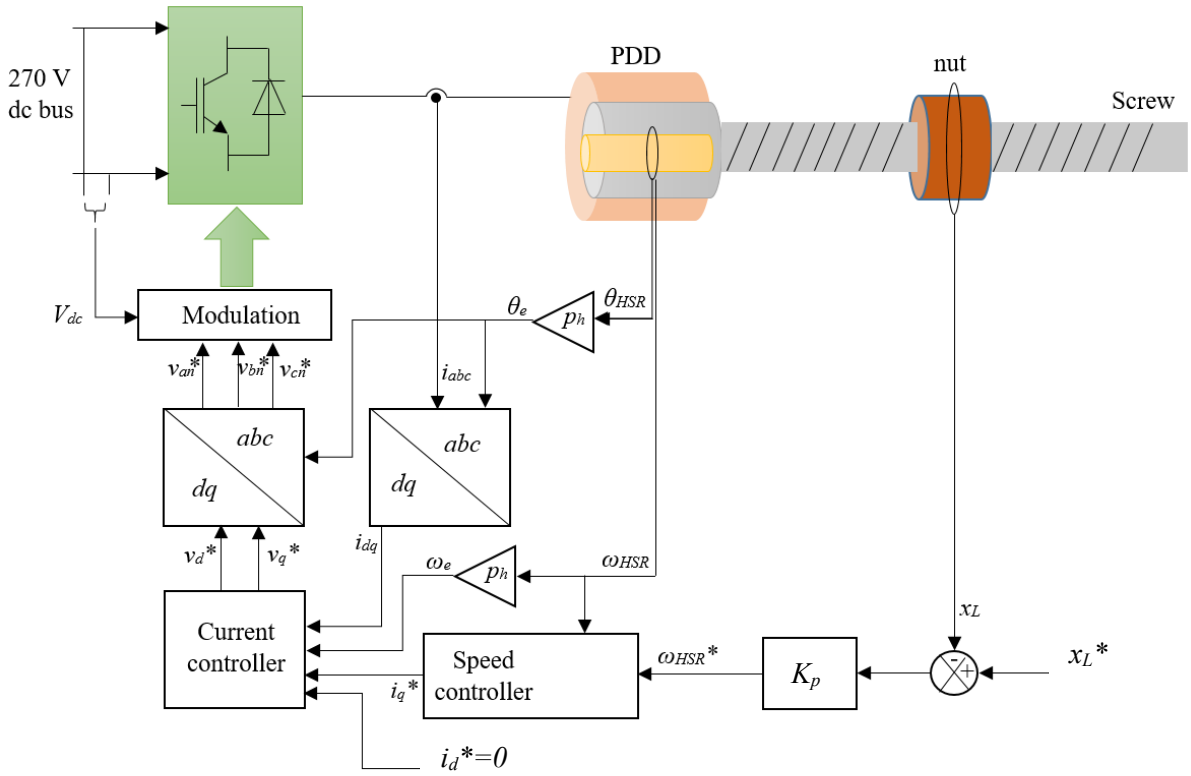

Figure 135. Control scheme implemented

Note: symbols are defined in the table of notation.

4.2.1.2 Electrical parts

For each phase, the phase voltage is divided into three main terms, a voltage drop on the resistor, a voltage drop on the inductance, and back emf, which shows the useful power that is to be converted into mechanical power. More information can be found in Appendix A.

$$v_{an} = R_s i_a + L_s \frac{di_a}{dt} + e_a \tag{206}$$

$$v_{bn} = R_s i_b + L_s \frac{di_b}{dt} + e_b \tag{207}$$

$$v_{cn} = R_s i_c + L_s \frac{di_c}{dt} + e_c \tag{208}$$

4.2.1.3 Mechanical parts

The equations describing the mechanical system are shown as follows [17]:

$$\underbrace{\theta_r}$$

$$T_e - \frac{T_{max}}{G_r}\sin(p_h\theta_{HSR} - n_s\theta_R) = J_{HSR}\ddot{\theta}_{HSR} \tag{209}$$

$$T_{max}\sin(\overbrace{p_h\theta_{HSR} - n_s\theta_R}^{\theta_r}) - K_n((\gamma^2\theta_R + \gamma x_{sc}) - \gamma x_L) = J_R\ddot{\theta}_R \tag{210}$$

$$-K_b x_{sc} - K_n((\gamma\theta_R + x_{sc}) - x_L) = M_{sc}\ddot{x}_{sc} \tag{211}$$

$$K_n((\gamma\theta_R + x_{sc}) - x_L) - K_a x_L = M_L\ddot{x}_L \tag{212}$$

Note that θ_R represents θ_{LSR} and θ_{sc} since in the three-DOF model the screw inertia, J_{sc}, is lumped with the PDD LSR inertia, J_{LSR}, to form the only rotary inertia, J_R. Equation (120) defines θ_R for this particular model.

4.3 Simplification and Linearisation

To be able to perform analysis methods on the system, a linear model should be developed. The integrated model, explained above, contains some non-linear terms such as equations (209) and (210), which contain sine function terms. Also, Equations (206), (207) and (208) are voltage equations for PDD stator and they contain the variable back emf, e_a, and this contain a non-linear function as shown in Equation (213).

$$e_a = \omega_e\Psi_m\sin(\omega_e t) \tag{213}$$

where Ψ_m is the flux linkage of phase A.

Stator voltages (v_{an}, v_{bn}, and v_{cn}) are transformed into their DC equivalents, which are in *dq* frame, as d-axis voltage, v_d, and q-axis voltage, v_q. Stator current (i_a, i_b, and i_c) are also transformed into their DC equivalents, as d-axis current, i_d, and q-axis current, i_q. More information about the derivation of the transformation can be found in Appendix A.

When transforming the three-phase voltages on three-phase stationary reference into a two-phase rotating reference frame, coupling terms are observed, as shown in Equations (214) and (215).

$$v_d = R_s i_d + L_d\frac{di_d}{dt} - \omega_e L_q i_q \tag{214}$$

$$v_q = R_s i_q + L_q\frac{di_q}{dt} + \omega_e L_d i_d + K_e\omega_m \tag{215}$$

i_d and i_q are decoupled. A typical field oriented current control scheme with PI controllers and decoupling can be designed separately for i_d and i_q. If the controller achieves ideal decoupling and

current control over a wide speed range, then the motor dynamics with the closed-loop current controller can be simplified as illustrated in Figure 136.

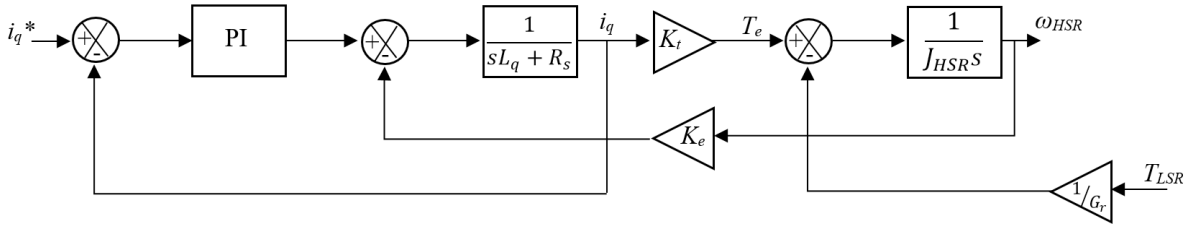

Figure 136. q-axis current loop

i_q^* is the q-axis current demand, T_e is the electromagnetic toque produced by the q-axis current, i_q, and it is given by:

$$T_e = K_t i_q \tag{216}$$

The torque constant, K_t, is related to the back-emf constant, K_e, by:

$$K_t = \frac{3}{2} K_e \tag{217}$$

K_e is a function of the flux linkage and the number of pole-pairs.

$$K_e = p_h \Psi_m \tag{218}$$

In the model composing of the three-DOFs coupled with the PDD, Equation (209) and Equation (210), there is one term that is non-linear, which is $sin(\theta_r)$. The term is shown in Equation (219).

$$T_{max} \sin(p_h \theta_{HSR} - n_s \theta_R) = T_{max} \sin(\theta_r) \tag{219}$$

It is possible to linearise this term by considering Figure 34, where it can be noticed from the Figure that a good stability point exists at 45°. As shown in Figure 137, a linear relationship can be obtained around 45° and hence the term in Equation (219) is linearised based on θ_r = 45°. Therefore, the slope of line, drawn in Figure 137, can be obtained as follows.

$$T_{LSR} = T_{max} \sin(\theta_r) \rightarrow \frac{dT_{LSR}}{d(\theta_r)} = T_{max} \cos(\theta_r) = 10.3 \cos(45^\circ) \tag{220}$$
$$= 7.28\ N.m.rad^{-1} = K_g$$

where K_g can be defined as magnetic stiffness of the PDD.

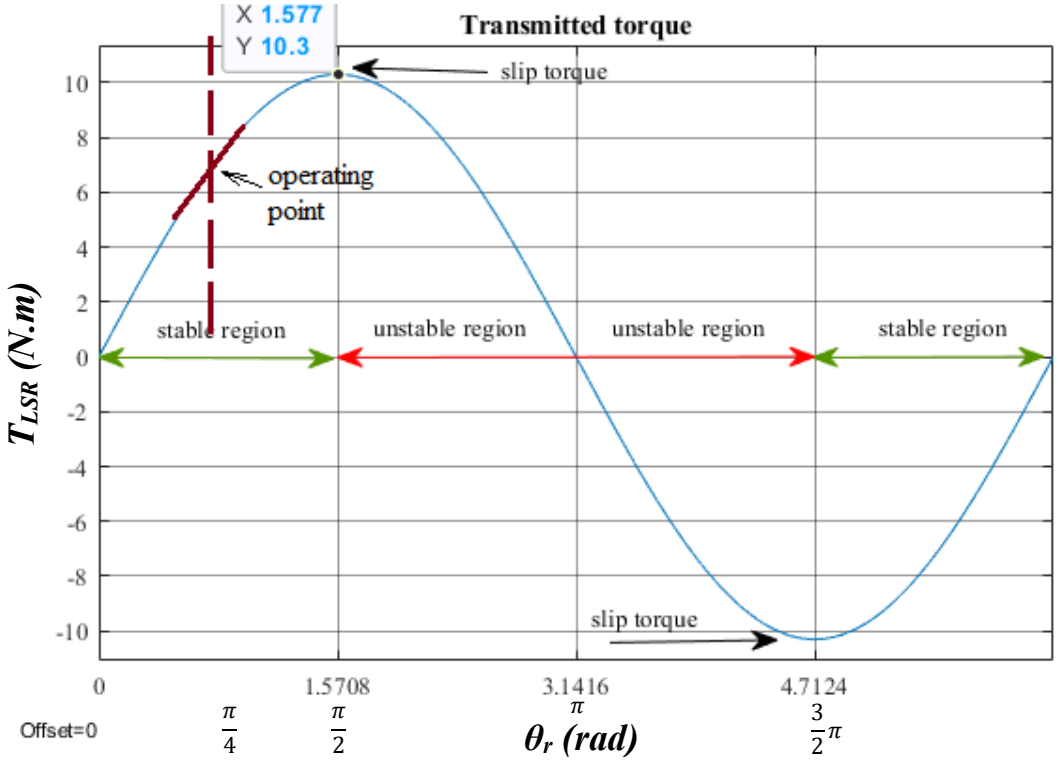

Figure 137. Good stability point at 45°

Using a magnetic stiffness term, Equation (209) and Equation (210) are linearised to become Equations (221) and (222), respectively.

$$T_e - \frac{(p_h\theta_{HSR} - n_s\theta_R)K_g}{G_r} = J_{HSR}\ddot{\theta}_{HSR} \tag{221}$$

$$(p_h\theta_{HSR} - n_s\theta_R)K_g - K_n((\gamma^2\theta_R + \gamma x_{sc}) - \gamma x_L) = J_R\ddot{\theta}_R \tag{222}$$

Combining the block diagrams for the ball-screw, PDD yields the system that is presented by the block diagram shown in Figure 138.

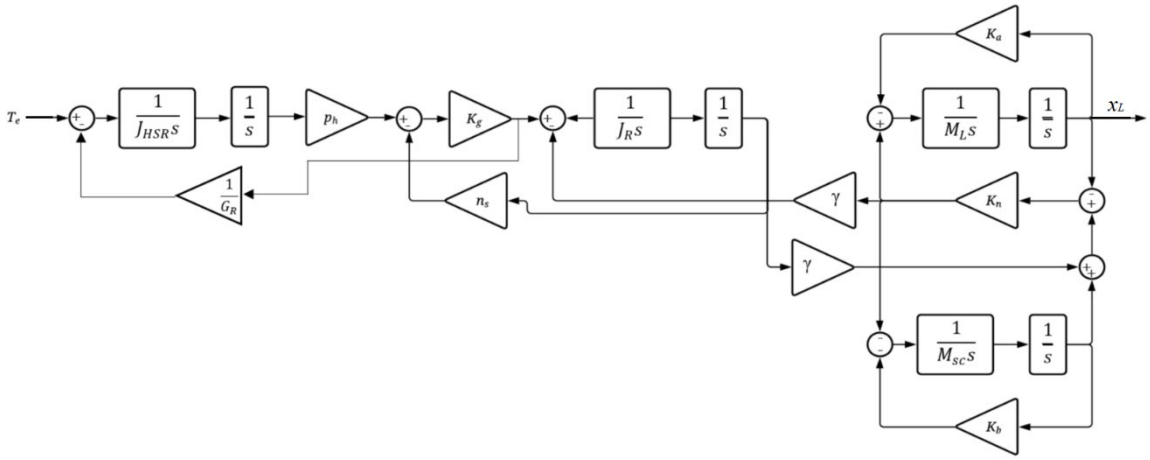

Figure 138. Actuation system model

Frequency domain analysis

The bode plot, presented in Figure 139, shows the frequency response of the linearised system. The load position, x_L, is considered as the output whereas electromagnetic torque, T_e, is considered as the input.

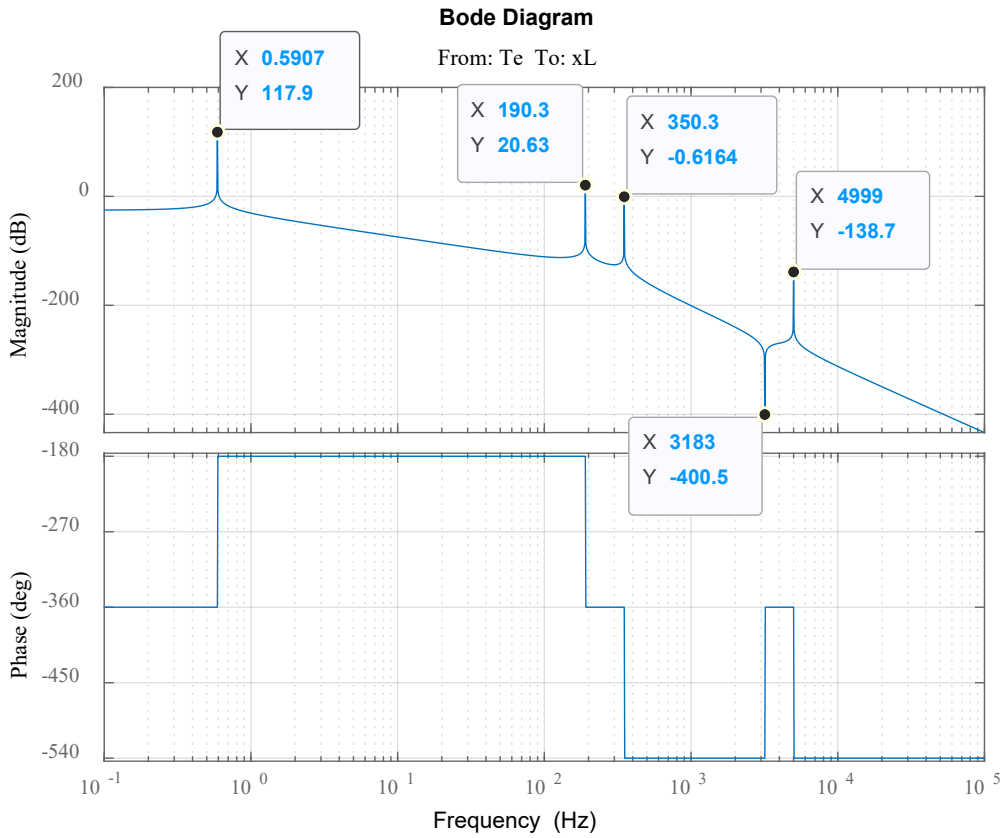

Figure 139. Bode plot (x_L/T_e)

Table 15 summarises the relevant frequencies observed in the bode plot above.

Table 15. Summary of bode plot

	Resonance frequency (*Hz*)	rad.s^{-1}	Significant stiffness
$f_{1\_reflected}$	0.59	*3.7*	K_a
f_g	190	*1200*	K_g
f_2	350	*2200*	K_b and K_n

The three frequencies summarised in Table 15 are highlighted in Chapter 2. $f_{1\_reflected}$, at *0.59 Hz*, is clearly due to the aerodynamic stiffness. It is worth mentioning that this value is related to f_1 in Chapter 2 through the gear ratio, G_r. See equation (223).

$$f_{1\_reflected} = \frac{f_1}{G_r} = \frac{4.37}{7.75} = 0.564\ Hz \tag{223}$$

f_g, at *190 Hz*, occurs due to the PDD magnetic stiffness. f_g can be analytically approximated using Equation (224). This frequency varies and it is a function of relative angle between HSR and LSR. This explains the difference between the value estimated in Figure 139 and the value approximated by Equation (224).

$$f_g = \frac{1}{2\pi}\sqrt{K_g \frac{J_{HSR} + \frac{J_s}{G_r^2}}{J_{HSR}\frac{J_s}{G_r^2}}} = 273\ Hz \tag{224}$$

f_2, at *350 Hz*, is mainly translational mode; the load mass moves against the equivalent stiffness of screw-nut interface and the bearing. Note that in Chapter 2 this value is calculated to be equal to *338 Hz*. The addition of the PDD causes this difference, which is insignificant (+3%).

Linearised full model

The linearised model is rewritten in state space form so modal analysis can be performed. The system is of order 11 and the state variables are:

$$q_l = [x_L, v_L, x_{sc}, v_{sc}, \theta_R, \omega_R, \theta_{HSR}, \omega_{HSR}, i_q, v_q, i_q^*]^T \tag{225}$$

Systems equations are shown below and system matrices are shown in the Appendix E.

$$v_L = \dot{x_L} \tag{226}$$

$$\left(\frac{-K_n - K_a}{M_L}\right)x_L + \frac{K_n}{M_L}x_{sc} + \frac{K_n}{M_L}\gamma\theta_R - \frac{F_d}{M_L} = \dot{v_L} \tag{227}$$

$$v_{sc} = \dot{x_{sc}} \tag{228}$$

$$\frac{K_n}{M_{sc}}x_L + \left(\frac{-K_n - K_b}{M_{sc}}\right)x_{sc} - \frac{K_n}{M_{sc}}\gamma\theta_R = \dot{v_{sc}} \tag{229}$$

$$\omega_R = \dot{\theta_R} \tag{230}$$

$$\frac{\gamma K_n}{J_R}x_L - \frac{\gamma K_n}{J_R}x_{sc} + \left(\frac{-n_s K_g - K_n\gamma^2}{J_R}\right)\theta_R + \frac{p_h K_g}{J_R}\theta_{HSR} = \dot{\omega_R} \tag{231}$$

$$\omega_{HSR} = \dot{\theta_{HSR}} \tag{232}$$

$$\frac{n_s K_g}{G_r J_{HSR}}\theta_R - \frac{p_h K_g}{G_r J_{HSR}}\theta_{HSR} + \frac{K_t}{J_{HSR}} i_q = \dot{\omega_{HSR}} \tag{233}$$

$$-\frac{K_e}{L_q}\omega_{HSR} - \frac{R_s}{L_q} i_q + \frac{1}{L_q} v_q = \dot{\imath_q} \tag{234}$$

$$\begin{aligned} -\left(K_{pc}K_pK_{is}\right)x_L - \frac{K_{pc}K_{ps}K_g n_s}{G_r J_{HSR}}\theta_R + \frac{K_{pc}K_{ps}K_g p_h}{G_r J_{HSR}}\theta_{HSR} \\ + \left(\frac{K_{pc}K_e}{L_q} - K_{pc}K_{is}\right)\omega_{HSR} + \left(\frac{K_{pc}R_s}{L_q} - K_{ic} - \frac{K_{pc}K_{ps}K_t}{J_h}\right) i_q \\ - \frac{K_{pc}}{L_q} v_q + K_{ic} i_q^* + \left(K_{pc}K_pK_{is}\right)x_L^* = \dot{v_q} \end{aligned} \tag{235}$$

$$\begin{aligned} -\left(K_pK_{is}\right)x_L - \frac{K_{ps}K_g n_s}{G_r J_{HSR}}\theta_R + \frac{K_{ps}K_g p_h}{G_r J_{HSR}}\theta_{HSR} - K_{is}\omega_{HSR} - \frac{K_{ps}K_t}{J_{HSR}} i_q + \left(K_pK_{is}\right)x_L^* \\ = \dot{\imath_q^*} \end{aligned} \tag{236}$$

Note: symbols are defined in the table of notation.

The system is implemented in Matlab and it is shown in Figure 140.

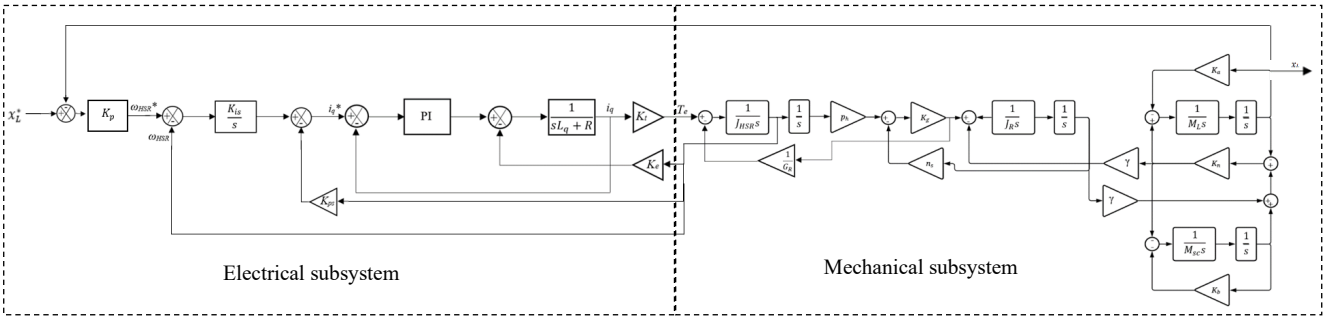

Figure 140. Matlab representation

Comparison between the linearised model and the switching model

Computation time of the switching model is considerably longer than the linearised transfer function model. On that account, it is convenient to use the linearised model to verify the analysis carried out in case the model is needed to be simulated for a longer time. For that purpose, the linearised model is put into comparison with the switching model.

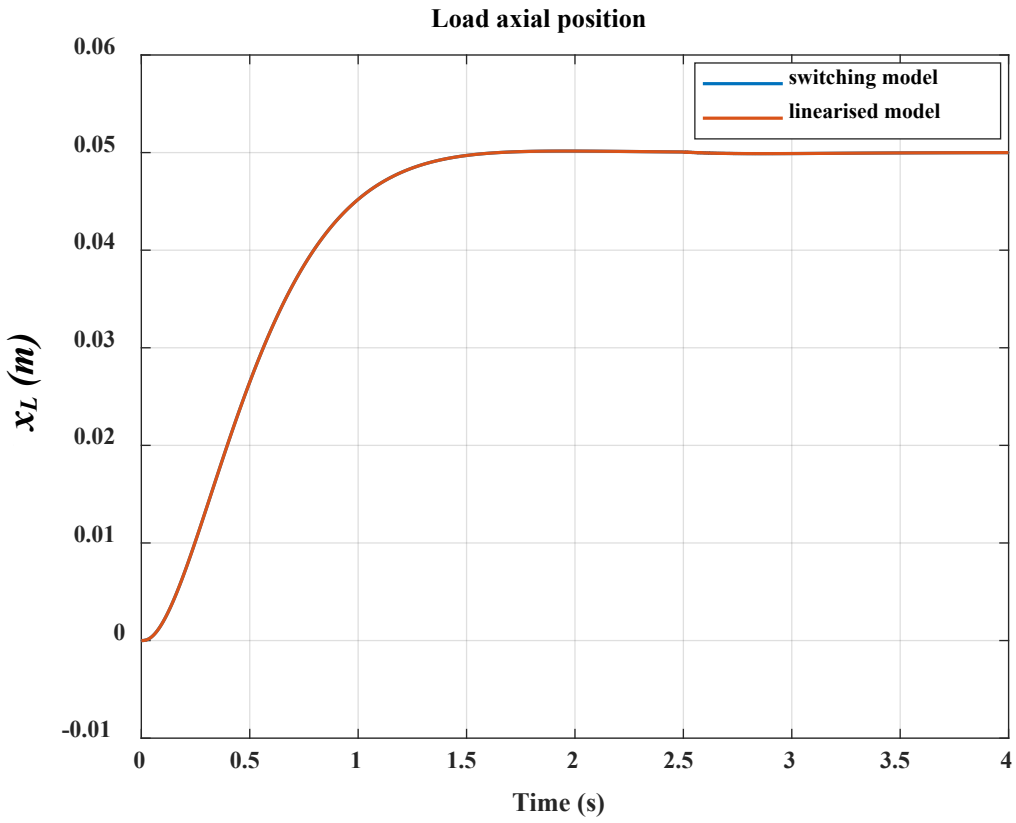

Figure 141. Load axial position

Figure 141 shows the load axial position using the switching model and the average model. At 2.5 seconds, a step disturbance force, equalling to 13% of the operational force, is applied. The application of the step disturbance force demands more current, which can be seen in Figure 142. From Figure 141 and Figure 142, both models show acceptable concordance, and thus the linearised model can be used to verify findings as well.

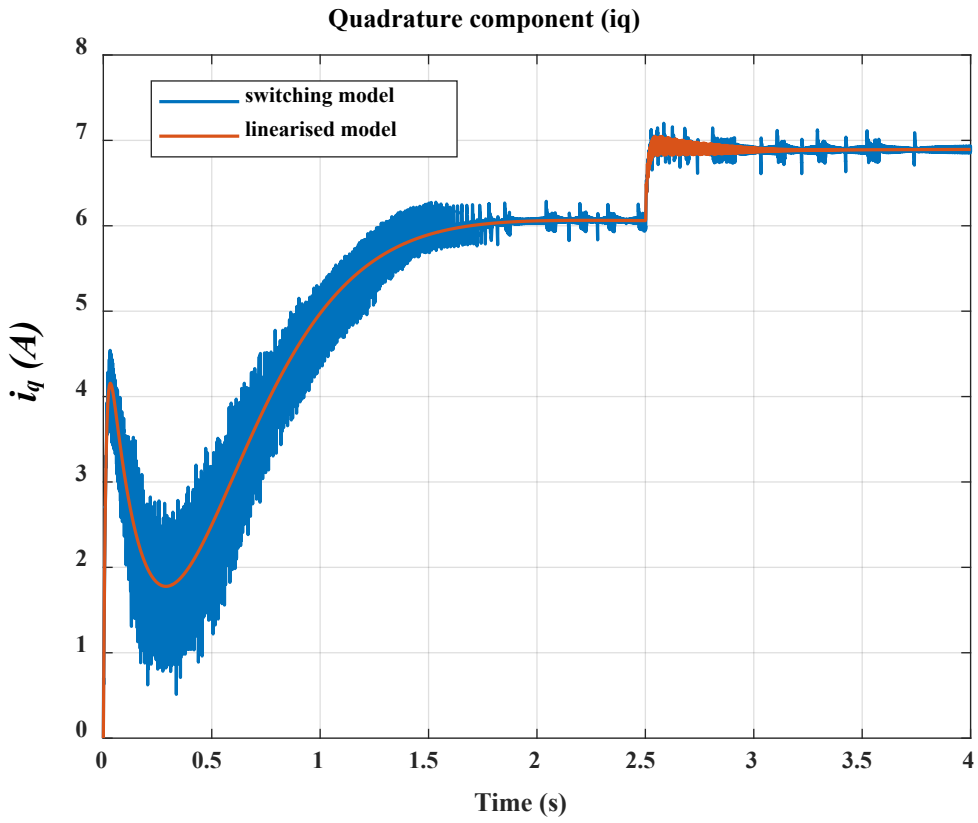

Figure 142. i_q current component

4.4 Modal analysis

This section deals with a comprehensive modal analysis including participation factor and eigenvalue sensitivity. The mechanical part of the EMA consists of several components; namely, motor rotor, ball-screw assembly and load. Several parameters are associated with aforementioned components. For instance, inertia of motor rotor is a crucial element. Further, load equivalent mass is an important parameter that is related to the load. Most significantly, many parameters are associated with ball-screw assembly; such as screw inertia, screw nut interface stiffness, stiffness of the bearing. The modal analysis is carried out in similar methodology followed in [69].

4.4.1 Eigenvalue analysis

Analysing state matrix yields Eigenvalues, which may be real or complex; the latter may be expressed in conjugate pairs. See Equation (237).

$$s_z = -\sigma_z \pm j\omega_z \tag{237}$$

where s_z is the z-th root of the linearised system, σ_z is the real part and it refers to the system stability, and ω_z is the imaginary part and it represents the frequency of oscillation.

The damping ratio, ζ_z, of root s_z can be estimated as,

$$\zeta_z = \frac{\sigma_z}{\sqrt{\sigma_z^2 + \omega_z^2}} \tag{238}$$

Oscillation frequency, f_z, of mode s_z may be calculated as,

$$f_z = \frac{|\omega_z|}{2\pi} \tag{239}$$

Table 16 lists the eigenvalues of the studied system and the corresponding damping ratio and oscillation frequency for each mode.

Table 16. Eigenvalues, damping ratios and oscillation frequencies

Mode	eigenvalue	damping ratio	oscillation frequency (Hz)
$s_{1,2}$	$-2.56\times10^{-11}\pm 31409.6j$	8.14×10^{-16}	4998.998
s_3	-3013.16	1	0
$s_{4,5}$	$-0.023 \pm 2202.232j$	1.05×10^{-5}	350.5
$s_{6,7}$	$-0.99 \pm 1203.75j$	8.21×10^{-4}	191.6
s_8	-398.67	1	0
s_9	-86.4	1	0
$s_{10,11}$	$-4.9 \pm 1.69702j$	9.451×10^{-1}	0.27

4.4.2 Participation factor

To identify how each state variable influences a certain mode, participation factor can be considered. It is a measurement of contribution of the *kth* state variable in the *ith* mode. Table 17 illustrates the participation factor of the state variables.

Table 17. Participation factor of the state variables

	$s_{1,2}$	s_3	$s_{4,5}$	$s_{6,7}$	s_8	s_9	$s_{10,11}$
x_L	2.23×10^{-19}	9.4×10^{-11}	1.95×10^{-10}	1.01×10^{-10}	1.33×10^{-7}	8.7×10^{-7}	1.3×10^{-5}
v_L	0.0036	2.83×10^{-7}	0.0034	0.00105	5.29×10^{-5}	7.5×10^{-5}	7.1×10^{-5}
x_{sc}	2.22×10^{-17}	1.24×10^{-10}	1.2×10^{-10}	3.3×10^{-10}	3.3×10^{-9}	1.9×10^{-9}	1.4×10^{-8}
v_{sc}	0.357	3.724×10^{-7}	0.0025	0.000224	1.3×10^{-6}	1.64×10^{-7}	7.7×10^{-8}
θ_R	1.7×10^{-20}	3.83×10^{-7}	4.5×10^{-9}	5.7×10^{-7}	0.0002	0.0011	0.0163
ω_R	0.64	0.0012	0.9	0.84	0.07	0.1	0.09
θ_{HSR}	1.75×10^{-13}	1.92×10^{-5}	7.6×10^{-7}	9.91×10^{-6}	0.0015	0.009	0.13
ω_{HSR}	0.000142	0.06	0.044	0.1325	0.6	0.74	0.7
i_q	1.53×10^{-7}	0.15435	0.003242	0.0128	0.2	0.06	0.005
v_q	7.51×10^{-5}	0.8	0.006	0.0025	0.073	0.044	0.07
i_q*	1.3×10^{-5}	0.0052	0.004	0.012	0.052	0.06	0.0051

From Table 17, the state variables ω_R, v_{sc}, v_L and ω_{HSR} participate in the modes $s_{1,2}$ whereas other variables have insignificant contributions. Also, the state variables ω_R, ω_{HSR}, v_q, i_q^*, i_q, v_q and v_{sc} participate substantially in modes $s_{4,5}$. Moreover, the state variables ω_R, ω_{HSR}, i_q, i_q^*, v_q, v_L and v_{sc} have

significant participations in mode $s_{6,7}$. Furthermore, the state variables ω_{HSR}, θ_{HSR}, ω_R, v_q, θ_R, i_q^* and i_q exhibit contributions in mode $s_{10,11}$.

It is shown from the participation factor that critical modes are highly dependent on mechanical state variables; such as v_L, v_{sc}, ω_{HSR}, θ_{HSR}, ω_R and θ_R. Parameters of the mechanical system will significantly affect the mechanical state variables. The effect of the mechanical components parameters are assessed in the following section.

4.4.3 Small signal stability due to parametric uncertainties

It is important to carry out small signal sensitivity analysis to observe how system stability is affected by such uncertainties. Parameters are associated with properties of mechanical components such as stiffness. Looking at the state matrix presented in Appendix E, it contains many parameters. In reality, some parameters might change during operation; such as mass and operating conditions. Also, there might be some uncertainties in some parameters such as stiffness. Any variation of such parameters clearly will affect the system eigenvalues. To help estimate the rate and direction of the mode movement due to variations in system parameters, sensitivity analysis is performed.

4.4.3.1 Effect of uncertainties in stiffness of the bearing K_b

The bearing is said to have uncertainties that are affected by certain factors. For example, friction behaviour under operational conditions can be affected by wear period, changing operating load, preload conditions, and temperature. The preload is decided by two main factors; bearing stiffness and a defined deflection. The stiffness is decided by the rolling contact but the deformation refers to the gap between the inner rings [70]. The real deformation is determined by the size and tolerance of such a gap. The manufacturing tolerance of the gap for the case presented in [70] is around ±11%. K_b can be assumed to have an uncertainty up to ±20%. Nominal value of stiffness of bearing is 2×10^8 N/m. Only K_b is changed to include values less than and greater than the value assigned in this project.

Figure 143 shows sensitivity to K_b uncertainties. The real part of the pole seems to become less negative when stiffness K_b is incremented by 20%. In contrary, the value of the imaginary part increases with K_b. Note that only the complex frequencies $s_{4,5}$ in Table 16 are the ones which are changing the most; all other frequencies remain either unchanged or experience insignificant changes showing no sensitivity to such variation in K_b.

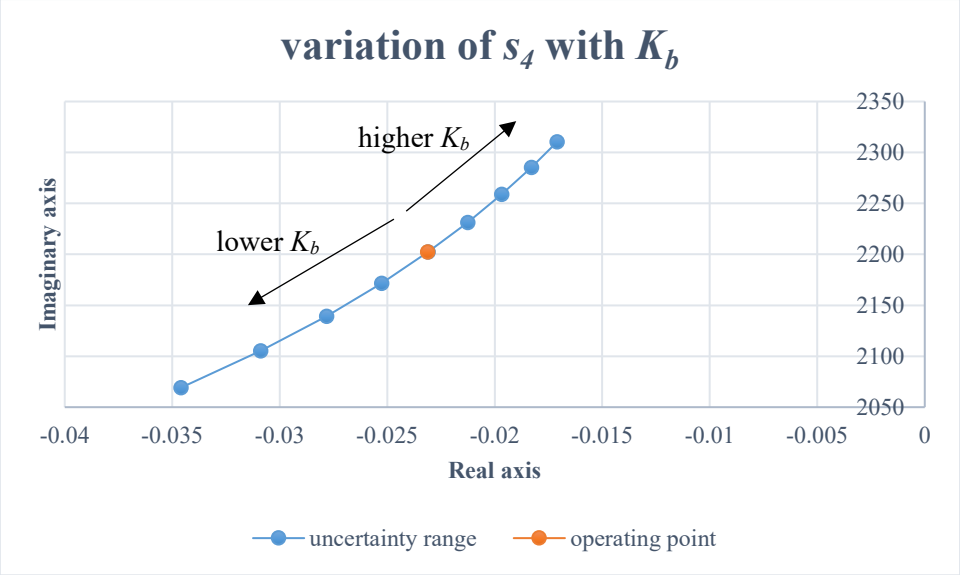

Figure 143. Variation of $s_{4,5}$ with K_b

It is clear from Figure 143 that uncertainty in K_b by 20% will have influence on the stability of the system since it contributes towards moving the real part of the pole. It is true that the uncertainty variation in K_b does not lead to system instability but it is worth observing the response of the entire system with respect to a wide range of change in K_b.

The eigenvalue sensitivities of modes s_4 and s_6 with regard to a variation between 2×10^{01} N/m and 2×10^{12} N/m of K_b are shown in Figure 144. The arrows correspond to poles of lower K_b.

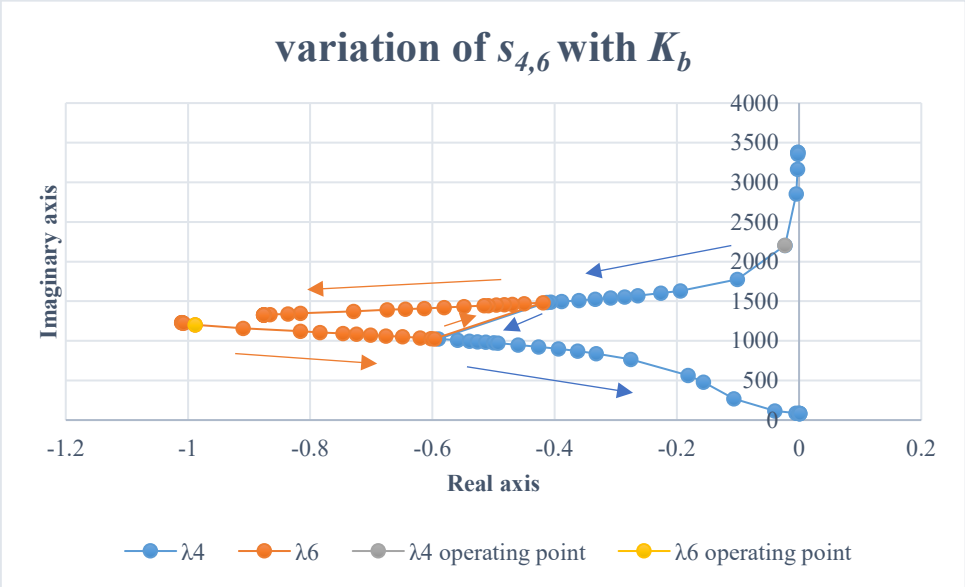

Figure 144. Variation of s_4 and s_6 with K_b

The modes $s_{4,5}$ and $s_{6,7}$ of the operating points are marked in grey and yellow respectively in Figure 144. With an increase in K_b above the operating point, $s_{4,5}$ will move toward the imaginary axis with the imaginary part of the pole moving upwards. Further, $s_{6,7}$ will not be affected by such increase.

Upon a decrease in K_b below the operating point, $s_{4,5}$ will move away from the imaginary axis whereas $s_{6,7}$ will move towards the imaginary axis with a little decrease in the imaginary part of $s_{6,7}$. $s_{4,5}$ are changing with a faster rate until a range that becomes close to $s_{6,7}$. After this range, $s_{4,5}$ starts to move towards the imaginary axis whereas $s_{6,7}$ starts to move in the other direction.

When K_b is decreased to below 3600 N/m, $s_{4,5}$ moves to the RHS and thus system becomes unstable. Therefore, K_b has an adverse impact on stability. Hence, decreasing stiffness to lower than a certain range will compromise stability.

Variation of K_b has the main influence on $s_{4,5}$. Little movement of $s_{6,7}$ can be observed (Figure 144) but this variation is not dominant in the system. Hence it can be said that mechanical system affects power system stability and therefore mechanical elements must be carefully chosen to obtain better damping and required stability.

Time domain, using switching model, can be also used to verify instability under the same conditions (Figure 145 and Figure 146). Nominal value of K_b is used and system is seen stable. Past 2.20 second, K_b is reduced using a slider gain and some oscillations can be seen, which corresponds to $\tau_{4,5}$ yet the system remains stable. When K_b is further reduced to lower than 3600 N/m, system becomes unstable and the critical value of K_b that destabilises the system is the one determined in the analysis.

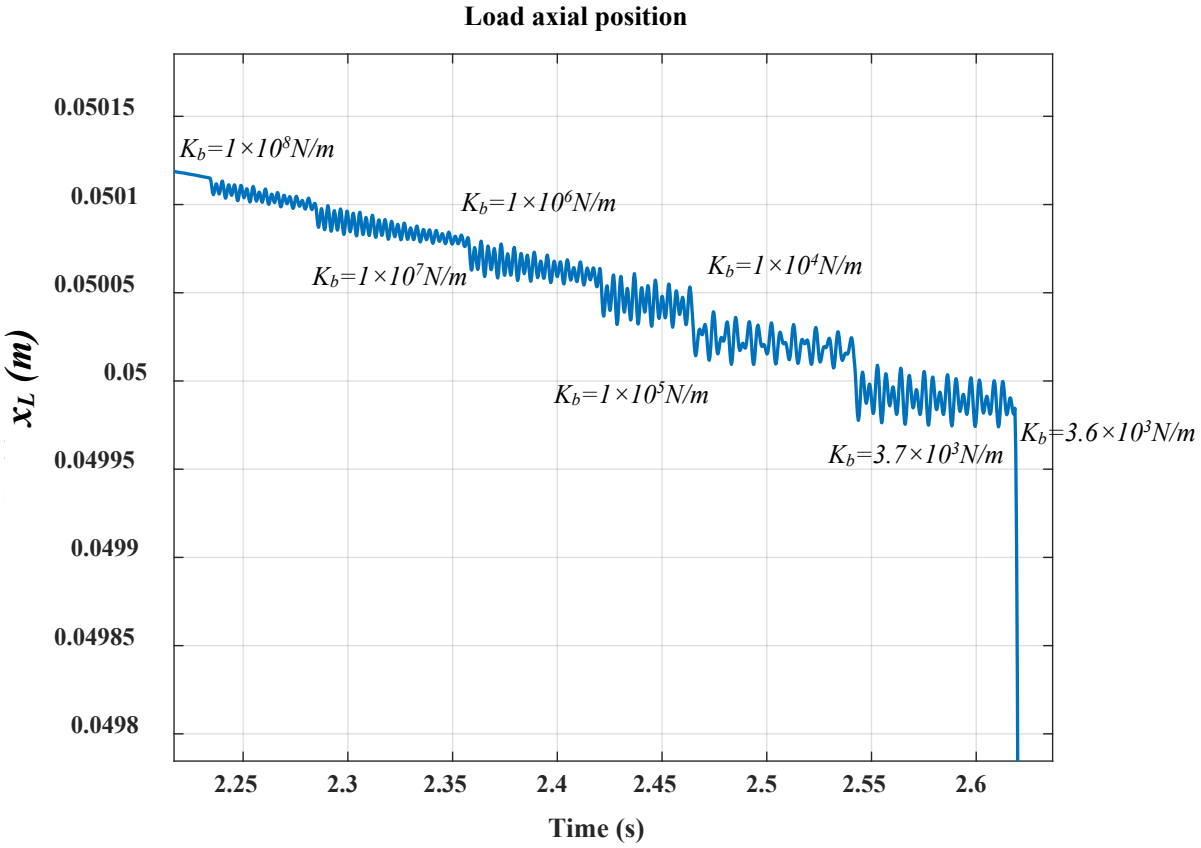

Figure 145. Load axial position (unstable operation) [variation of x_L due to varying K_b]

It is important to mention that oscillations do correspond to $\tau_{4,5}$. During instability, rudder oscillates back and forth between both deflection angles with the frequency 12.4 Hz. This can be seen in Figure

146 when nut oscillates between ±50 mm, which corresponds to ±30° of rudder deflection. It is important to mention that the controller was tuned using trial and error technique for the nominal values. Therefore, instablity situation, occurring in Figure 146, can be improved by retuning the controller. Optimally, the speed loop control BW can be reduced to regain stability.

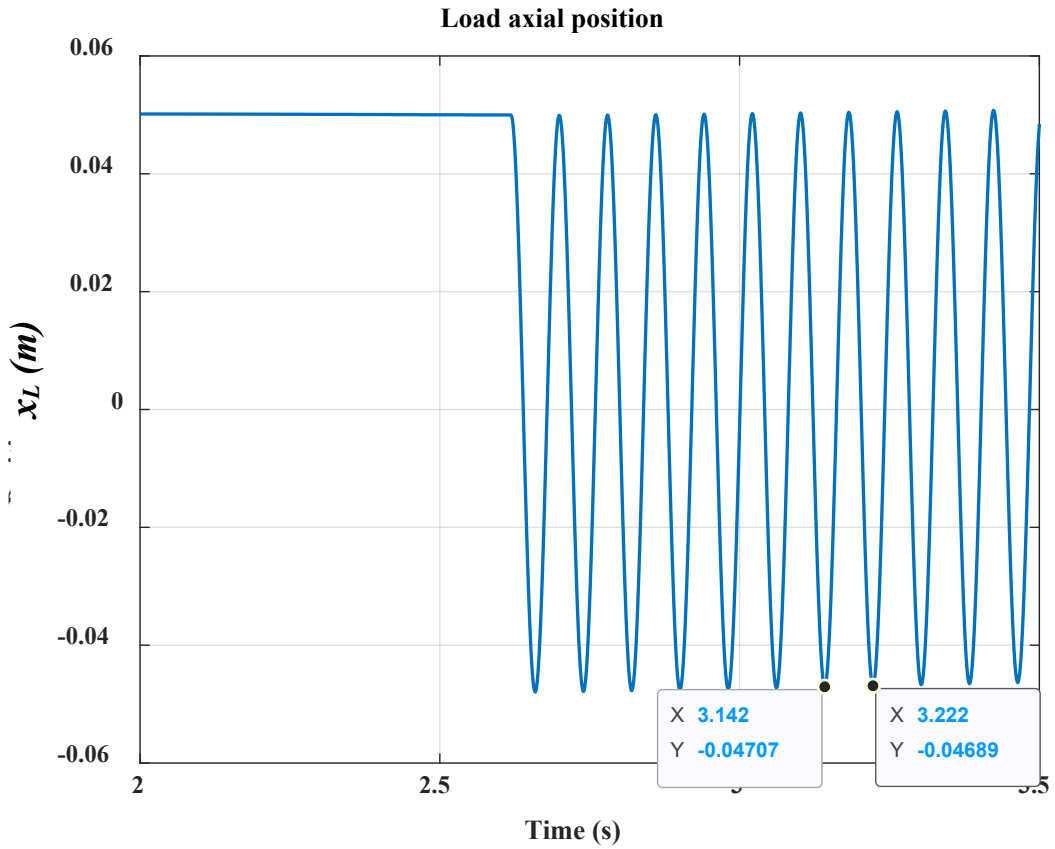

Figure 146. Load axial position (unstable operation) [frequency of oscillations = 12.4 Hz]

To prove instability in power system, phase A current is shown in Figure 147, which shows excessive growth in stator current.

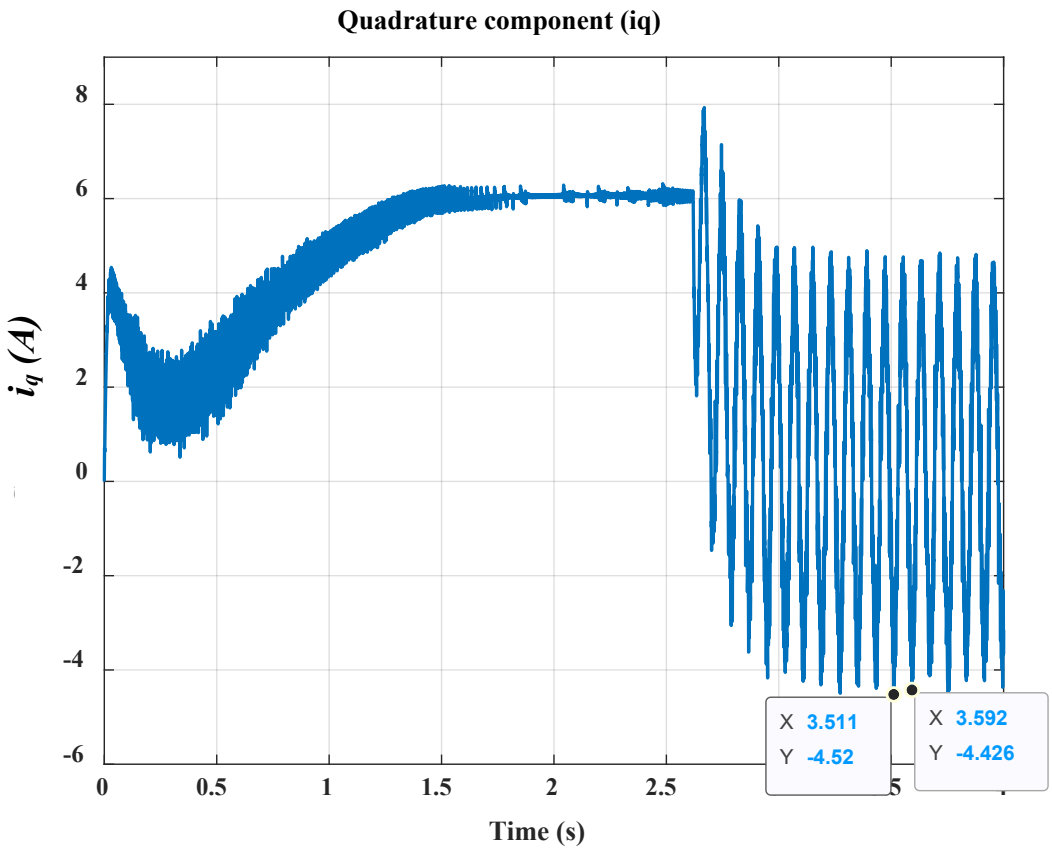

Figure 147. Phase A current (unstable operation) [frequency of oscillations = 12.4 Hz]

The mode that is created due to the mechanical system, $s_{4,5}$, is passed into the electrical network since the current in Figure 147 oscillates with the frequency 12.4 Hz. Additionally, when K_b starts to be varied, current experiences some disturbance as a result as shown in Figure 148.

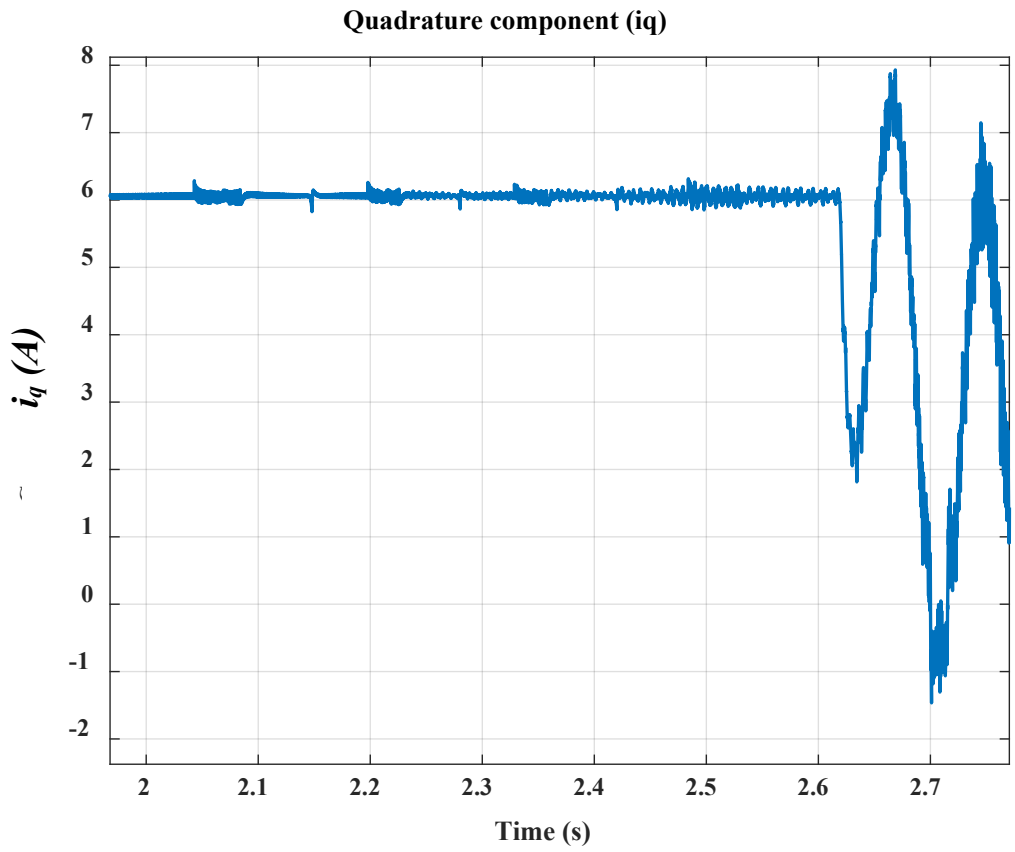

Figure 148. i_q current reaction to variation in K_b

4.4.3.2 Effect of uncertainties in stiffness of the screw-nut interface K_n

For simplicity, properties of stiffness of bearing, K_b, and screw nut interface, K_n, can have uncertainties due to the same effects. So, both parameters can be assumed to have an uncertainty up to ±20%.

It is mentioned in Chapter 3 that K_n has a significant contribution in determining τ_4 so this should have an influence on s_4. Figure 149 shows how the uncertainty in K_n could cause a variation in s_4.

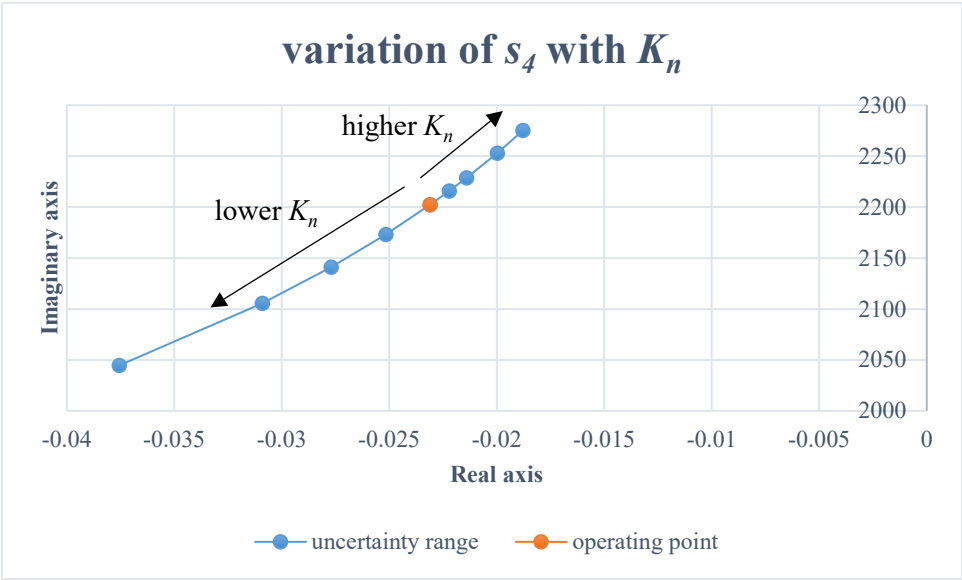

Figure 149. Variation of s_4 with K_n

Insignificant variation in s_6 can be observed as a result of an uncertainty in K_n. Figure 150 shows this.

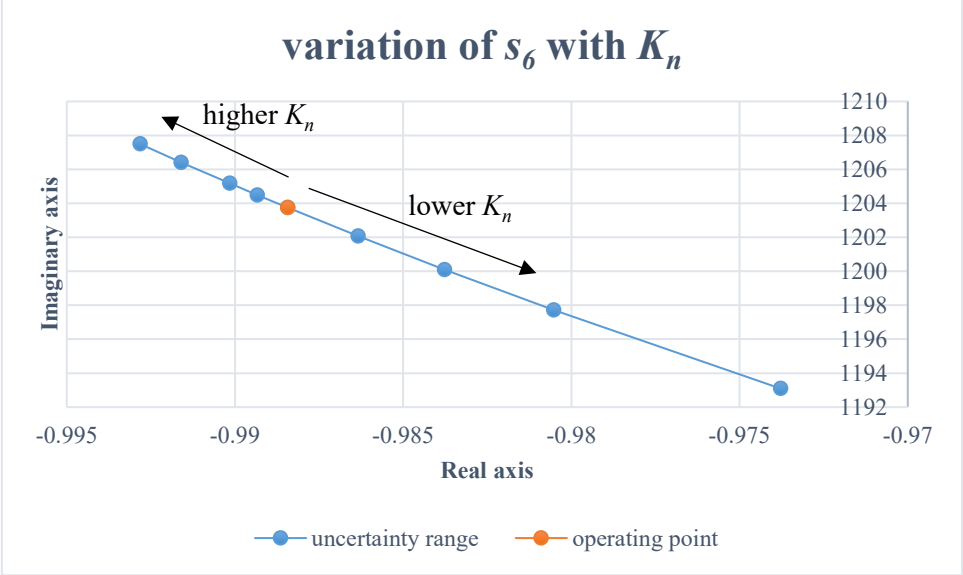

Figure 150. Variation of s_6 with K_n

4.4.3.3 Effect of uncertainties in load equivalent mass M_L

Practically, changing the load mass will change the equivalent inertia of the load mass, and that has a significant change on modes $s_{6,7}$. Further, τ_4 effectively is the oscillation of the load mass against the equivalent stiffness of K_b and K_n. Consequently, M_L will have a significant effect on $s_{4,5}$.

A similar test to the tests performed previously is also carried out here. Load mass is assumed to have an uncertainty of ±20%. All parameters are kept unchanged whereas M_L is varied to see how sensitive system's poles to such parameter.

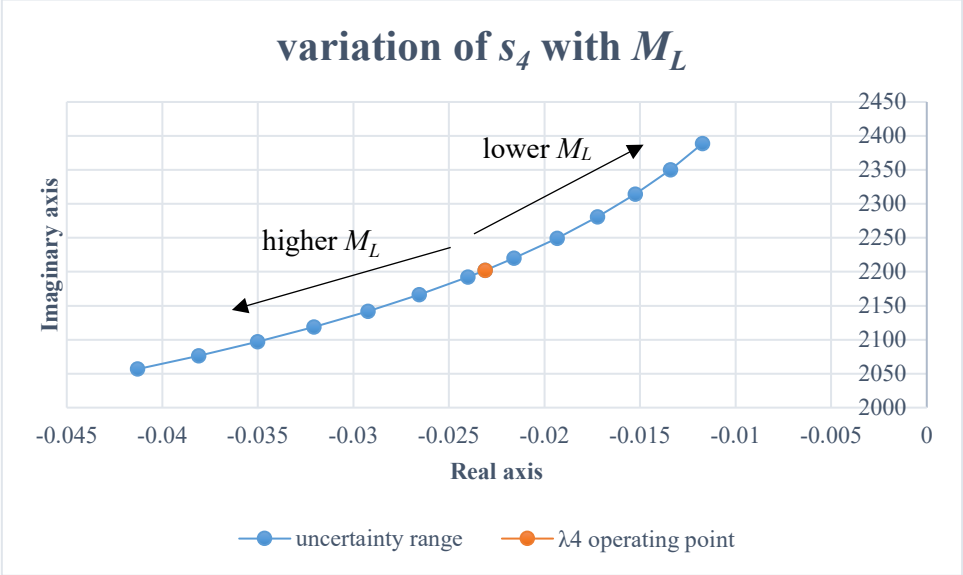

Figure 151. Variation of s_4 with M_L

Sensitivity of modes $s_{4,5}$ and $s_{6,7}$ are shown in Figure 151 and Figure 152 respectively. Only $s_{4,5}$ and $s_{6,7}$ are sensitive to load equivalent mass. Therefore, it can be said that uncertainty in M_L by 20% will have influence on the stability of the system.

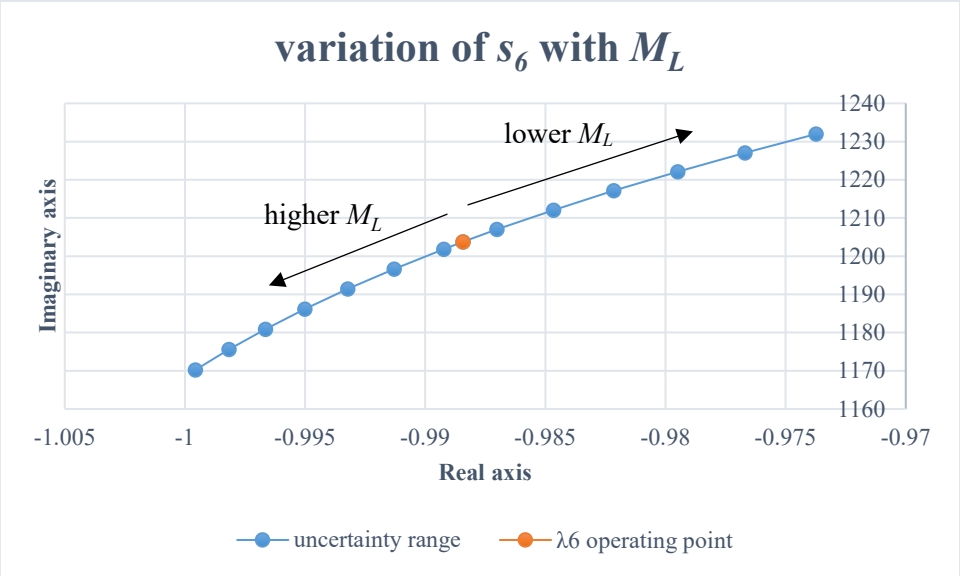

Figure 152. Variation of $s_{5,6}$ with M_L

4.4.4 Effect of speed loop bandwidth

The following simulation is carried out to briefly see how system stability margin changes with respect to resonant frequency for two different control bandwidths. For each control bandwidth, Stiffness of bearing, K_b, is varied since this is seen it affects the resonant frequency. The findings are summarised in Figure 153, which shows that for higher bandwidth the stability margin is reduced. Therefore, stability margin is improved by reducing speed loop bandwidth. The following section presents a comprehensive study regarding the relation between control loop bandwidth and resonant frequencies, which explains the decrease in stability margin in case of a higher bandwidth that is shown in Figure 153.

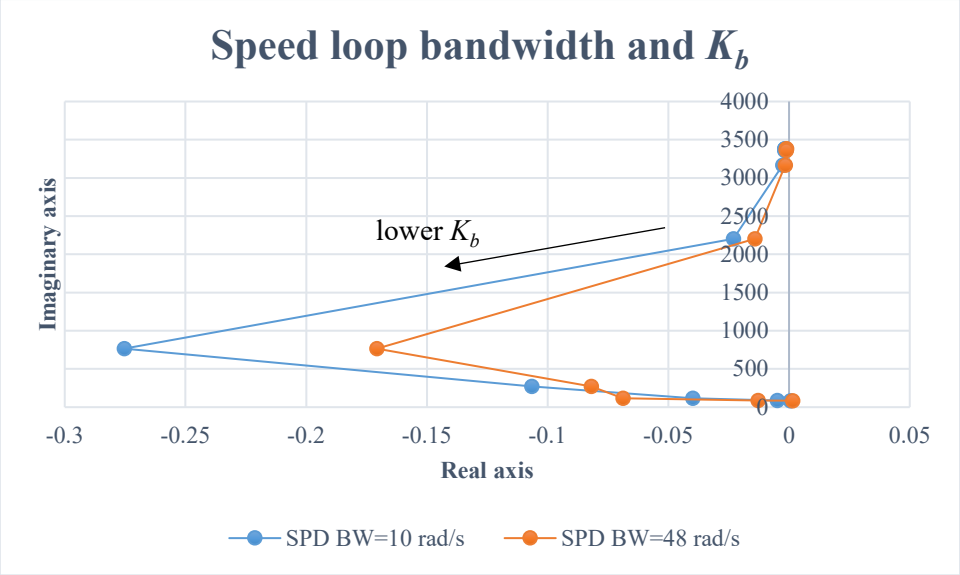

Figure 153. Variation of K_b for two different speed loop bandwidths

4.5 Selection of control loop bandwidths

Speed loop

This section is based on many details expressed in Section (2.4.1). The largest bandwidth of the speed loop can never be more than the anti-resonant frequency [71]. Therefore, it is crucial to note how structure resonance of the system under study may limit the speed loop bandwidth. This serves to identify interaction between both domains to avoid resonance excitation.

It is proved that f_2 is a function of K_b, so K_b is altered to represent the variation in the structure resonance value. The speed loop bandwidth is chosen to be 12.5 Hz. Also, it is proved in Section (2.4.1) that K_a restrains the decrease of f_2 lower than a certain value, which is *12.4 Hz*, as shown in Equation (240).

$$f_2 = \frac{1}{2\pi}\sqrt{\frac{K_{eq1}}{M_L}} \approx \frac{1}{2\pi}\sqrt{\frac{K_a}{M_L}} = 12.4\ Hz \qquad (240)$$

To allow f_2 to decrease further than *12.4 Hz*, K_a is reduced to 2×10^4 N/m, hence, the lowest limit of f_2 may reach to *4 Hz*. Frequency response is measured for the speed loop at three values of K_b, as shown in Figure 154. It can be seen that f_g changes insignificantly. However, f_2 considerably changes. Also, once f_2 becomes below than the speed loop bandwidth, system becomes unstable. Unstable case is shown in Figure 154 and represented by the yellow line.

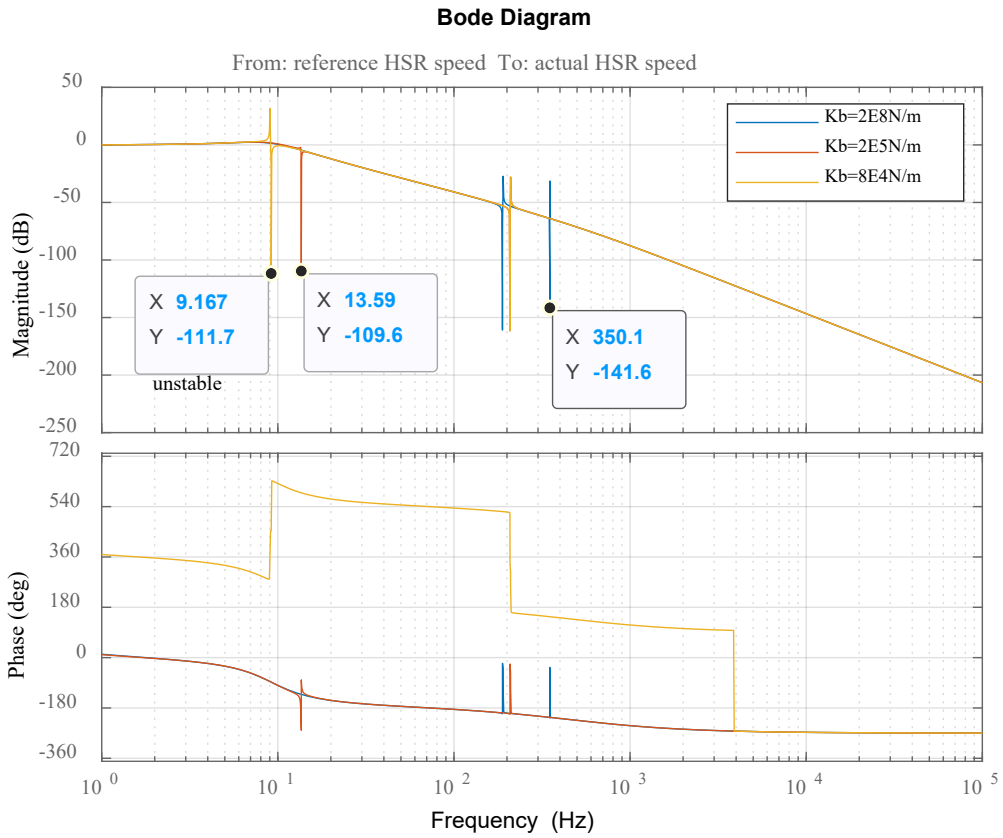

Figure 154. Bode plot (BW = 12.5 Hz) [input: ω_{HSR}^*, output: ω_{HSR}]

The unstable case can be verified using the time-domain switching model. Growing oscillations can be seen in Figure 155. It is important to note that the frequency of oscillation is *9 Hz*, which is the value of f_2.

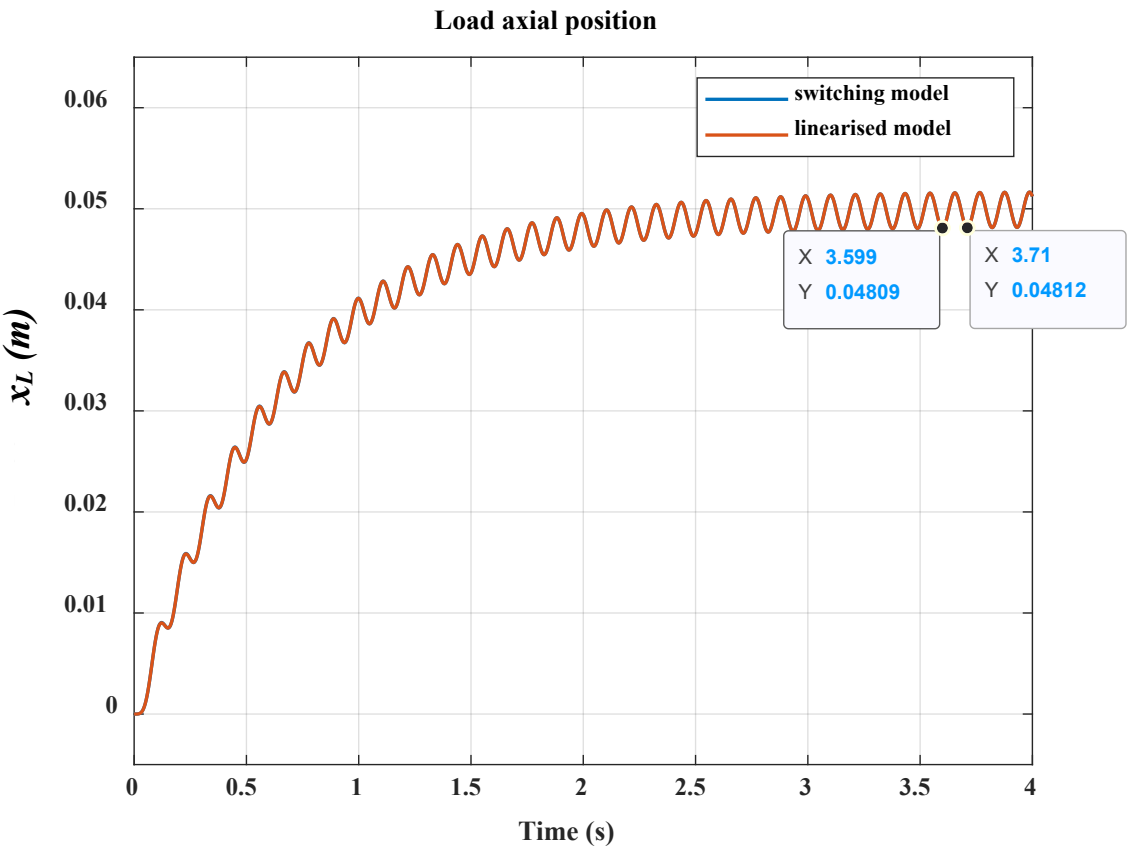

Figure 155. Load axial position (frequency of oscillations = 9 Hz))

Since the switching model takes quite long for computations, Figure 156 shows load axial position using the linear model.

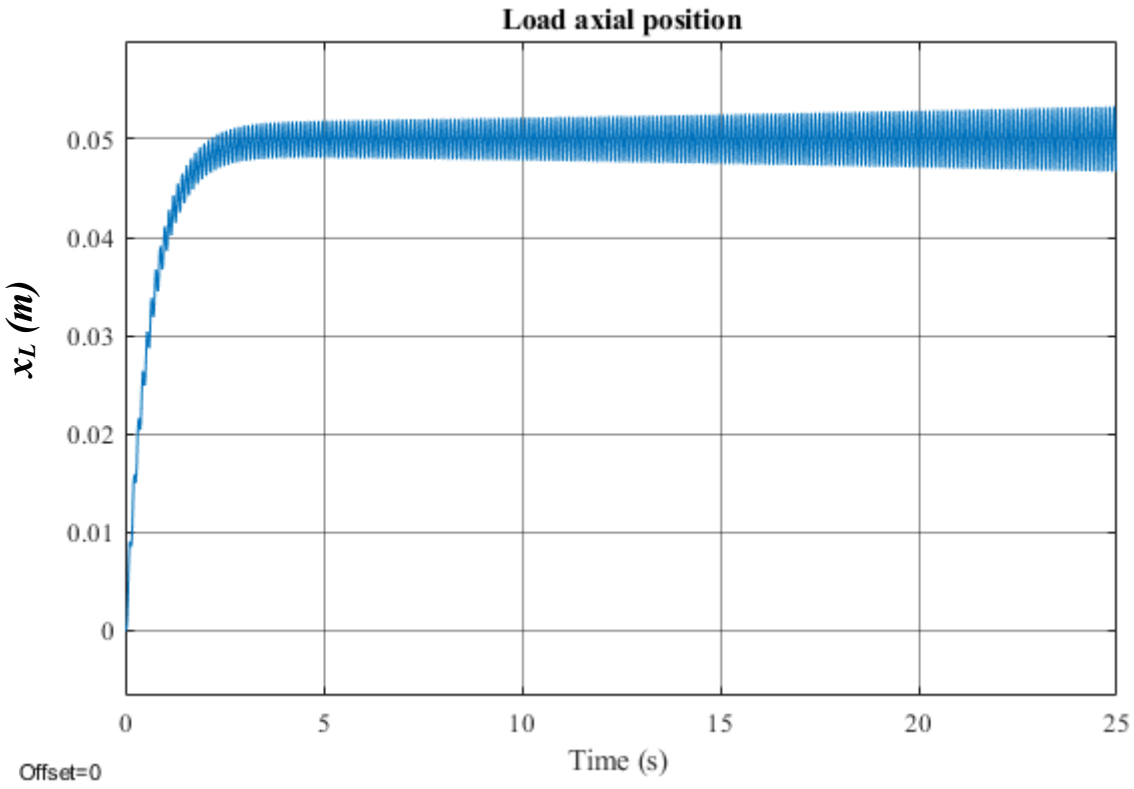

Figure 156. Load axial speed (linear model)

The oscillations with f_2 is also passed into the electrical system. Figure 157 shows i_q current, which is converted from the stator three-phase current for the purpose of field-oriented control. i_q is also simulated for a longer time using the linear model (Figure 158).

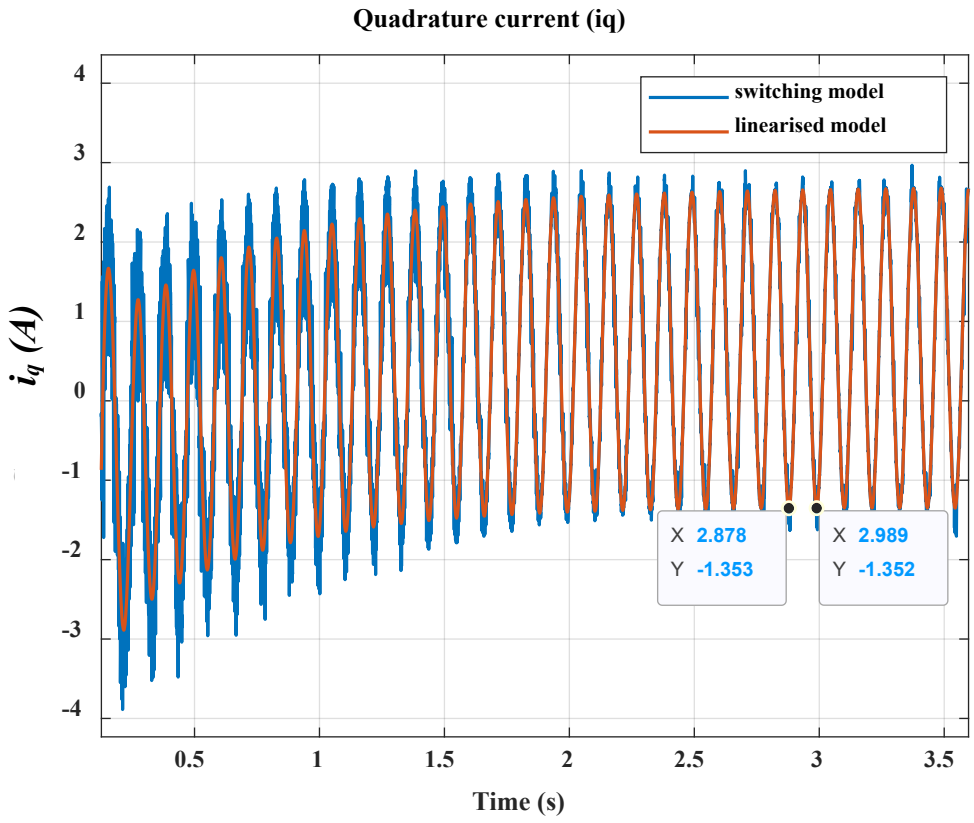

Figure 157. i_q (switching model)

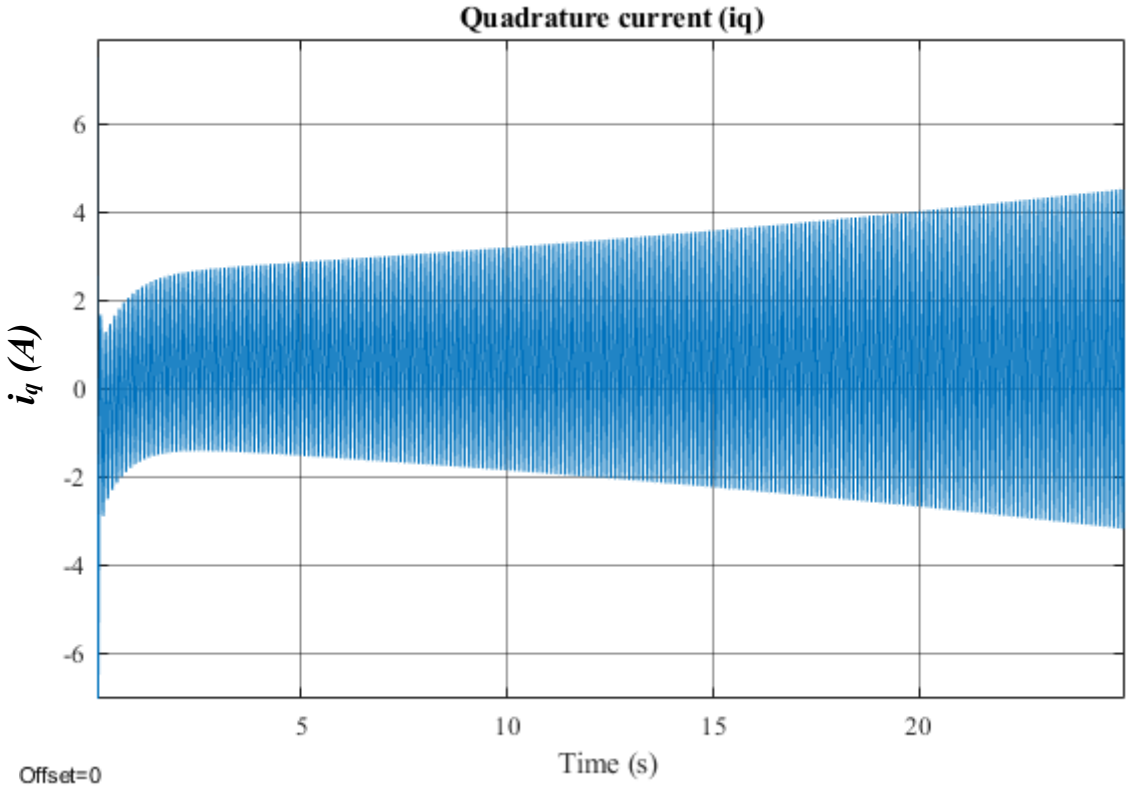

Figure 158. i_q (linear model)

For the unstable case presented in Figure 154, if speed loop BW is reduced, say to *7 Hz*, system regains stability. To destabilise the system, K_b is further reduced to 2.7×10^4 N/m. Bode plot is measured and shown in Figure 159.

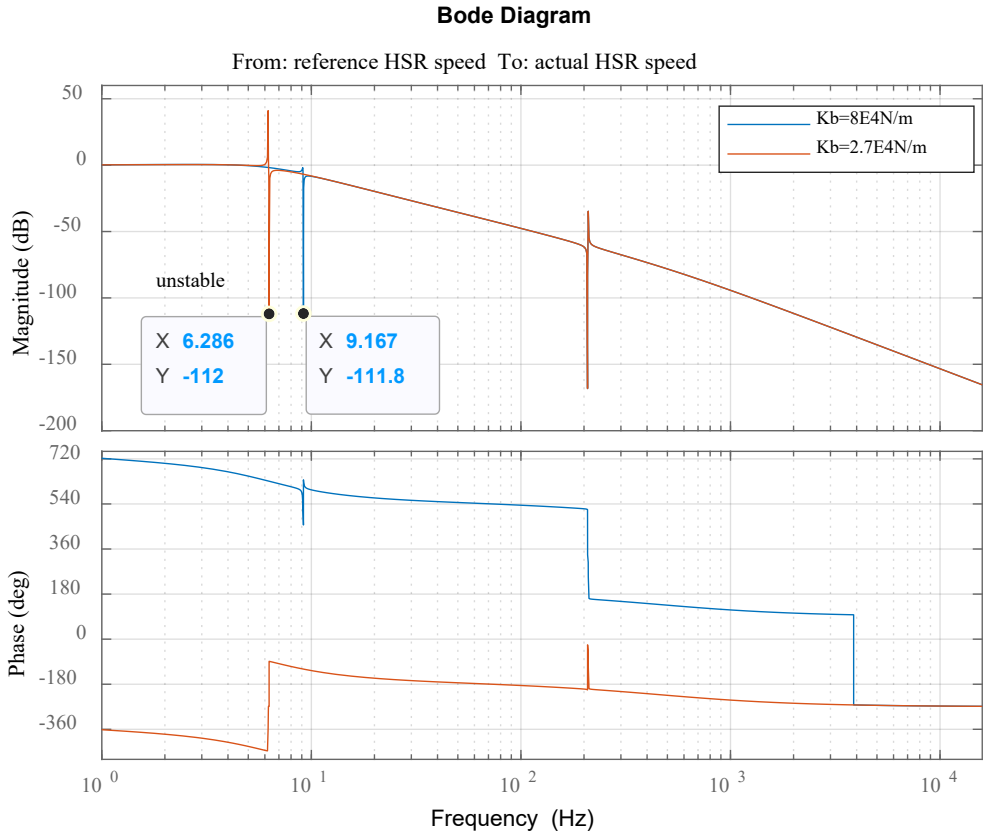

Figure 159. Bode plot (BW = 7 Hz) [input: ω_{HSR}^*, output: ω_{HSR}]

For the point mobility FRFs shown in Figure 154 and Figure 159, f_2 is always combined with an anti-resonant frequency. The reason is extensively explained in Section (2.4.1). Also, another relevant point to recap here is that at the anti-resonance a dramatic drop in the gain magnitude can be seen with a π variation in the phase. This is reported in [54] [53] and a simple example is explained, which shows that at anti-resonance, phase sharply decreases from π/2 to -π/2.

For the case of the unstable systems, the phase dramatic shift, accompanying the anti-resonance, coincides with the 0 dB gain crossing (BW of the speed loop). This is a sign for instability and reported in [72] [73], which states that at the gain crossover frequency, system destabilises if phase falls below –π rad. In contrast, gain crossover frequencies of the stable cases does not show a fall of phase below -π rad. In the case of Figure 154, the spike of f_2 amplitude crossing the 0 dB gain coincides with a phase of +540°, which indicates lack of gain and phase margins. Similarly, in case of Figure 159, the spike of f_2 amplitude crossing the 0 dB gain coincides with a phase of -180°, which also indicates lack of gain and phase margins. Summary of interaction between speed loop BW and aero actuator structure resonance is introduced in Table 18.

Table 18. Interaction between speed loop BW and f_2 (summary)

f_2 (Hz)	f_s = 12.5 Hz	f_s = 7 Hz
350	stable	stable
13.6	stable	stable
9	unstable	stable
6.2	unstable	unstable

From above, it can be said that instability occurs due to interaction between the **speed loop BW** and the resonance structure of the mechanical system. It can be deduced that speed loop bandwidth is restrained by structure resonance of the screw assembly system. This point is mentioned in the literature and verified using frequency-domain and time-domain analysis.

Figure 128 and Figure 129 summarise how this particular frequency may change with respect to aircraft size. From both figures, f_2 is seen to decrease to around *130 Hz* in the case of AIRBUS A380. This makes f_2 have more impact on the system stability since it will be closer to speed loop bandwidth.

Position loop

Again, since f_2 is highly dependent on K_b, then K_b is varied to represent the variation of the actuator mechanical system structure resonance. Speed loop bandwidth is *7 Hz*. In the nominal case, f_2 can never go below 12.4 Hz. This is because of the nature of the mode shape, which is depicted in Figure 59. More details about this particular point can be found in Section (2.4.1). See also Equation (240).

Figure 160 shows the position loop frequency response. In the first case, $K_b = 2\times10^8$ *N/m*, which represents the nominal case. In this nominal case, f_g is lower than f_2; the first spike shows f_g (*190 Hz*) whereas the second peak shows f_2 (*350 Hz*). It is crucial to note the anti-resonant frequency, which is the zero at *3183 Hz*. For the nominal case, the system is stable. Afterwards, K_b is reduced to 2×10^5 *N/m* but system remains stable. K_b is further reduced to 3.1×10^3 *N/m* and here is when the system destabilises.

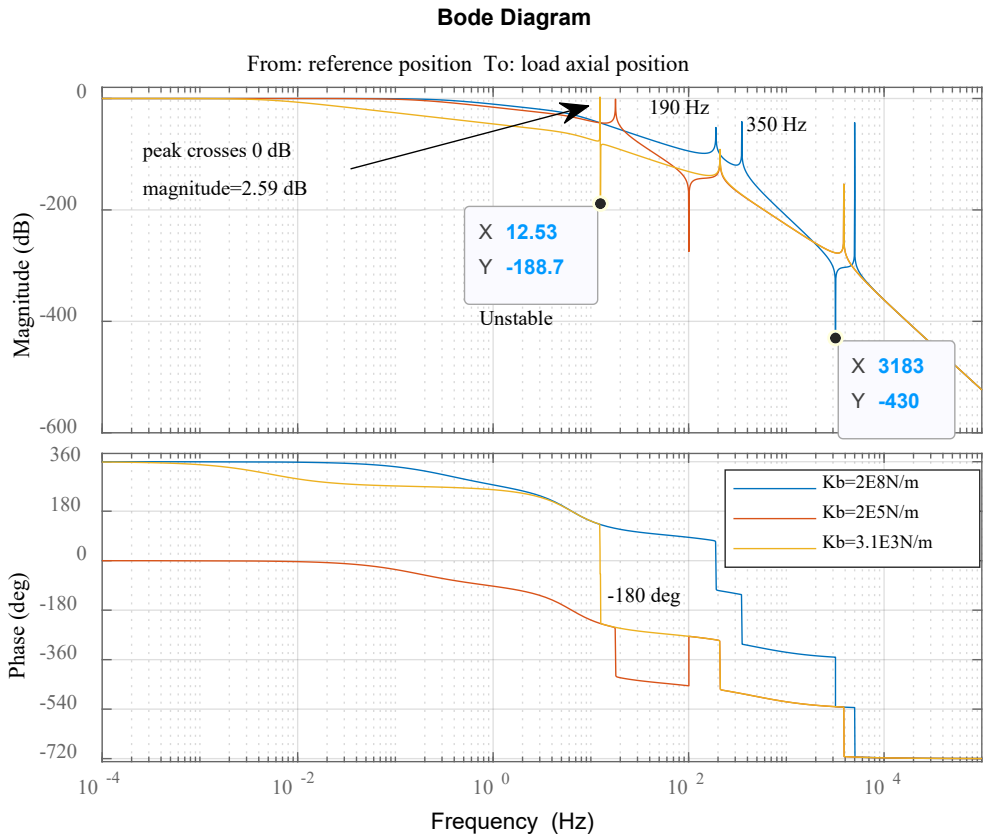

Figure 160. Frequency response (input: x_r, output: x_L)

In Figure 160, Bode plot shown is taken for the closed position loop. When the anti-resonant frequency of the mechanical system comes close to f_2, the system destabilises. Instability in this case is not due to bandwidth of the position loop. That means at the gain crossover frequency, the phase does not go below -π rad even for the unstable cases. As K_b is decreased, f_2 decreases down to a certain point (12.4 Hz), which is restricted by K_a. At this frequency, the resonant frequency, f_2, peak crosses *0 dB*, as illustrated in Figure 160. Simultaneously, the anti-resonant, f_{ar}, causes a dramatic phase shift crossing *-180 deg*. So, the occurrence of *0 dB* crossing by the resonant peak and phase shift (crossing -180 deg), which is caused by the anti-resonant, is the reason for the instability. Equation (240) and Equation (241) are important here.

$$f_{ar\_tr} = \sqrt{\frac{K_b}{M_{sc}}} \tag{241}$$

Following the aircraft sizing data and results obtained in Chapter 3, such an anti-resonant frequency can be estimated for the range of aircraft, as shown in Figure 161.

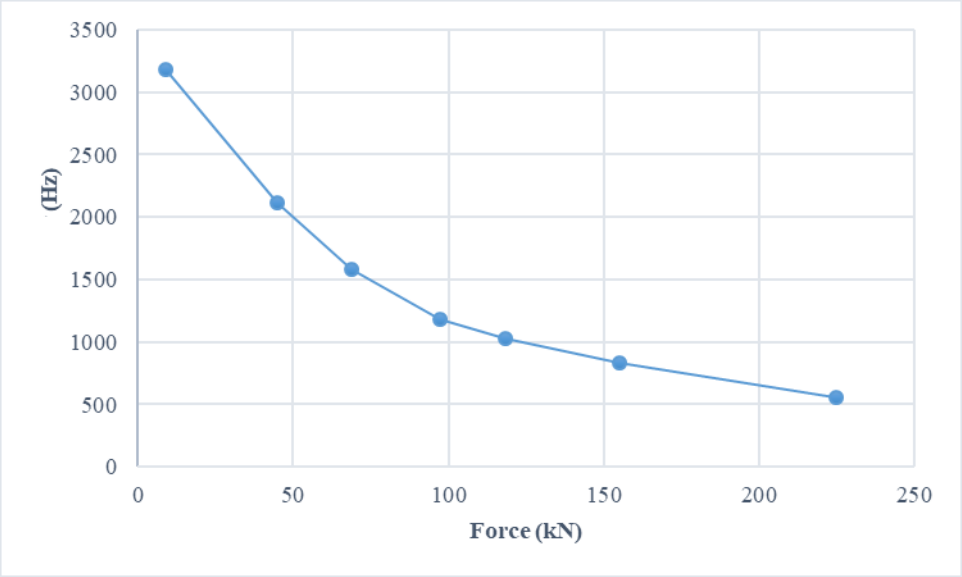

Figure 161. Anti-resonant frequency variation for a range of aircraft

Selecting control bandwidth with respect to the resonant frequencies of the mechanical system

Speed loop bandwidth must be designed to be less than structure resonance. The further is better to keep a reasonable stability margin. This is because it is proved that at the speed loop bandwidth denoting the gain zero crossing, if the anti-resonance, which occurs with a severe phase shift, comes close, stability margin will vanish.

Also, considering the position loop, the anti-resonance shown should be ensured to be separated from the resonant frequency, f_2. This is because it is proved that if the spike of f_2 coincides with the phase drop accompanying the anti-resonance, there will be no stability margin.

4.6 Loads with certain conditions

The switching model used to verify instability points in previous sections is the model used in this section. The PDD drive model is combined with the ball-screw model. Similar tests to those carried out in chapter 2 are performed here. Different load conditions are tested to see the response of the inter-connected system to various loading conditions. The main focus is to prove whether mechanical loading is capable of exciting resonances.

It is found in chapter 3 that there are critical frequencies which are associated with the aero actuation system. Such frequencies can also be seen in Table 15, which summarises three moderately low frequencies that can be within the range of the current controller bandwidth.

4.6.1 A step disturbance force

In this test, a reference position demand to a maximum displacement is set at 0 second. A small fixed step disturbance force of 13% of the actuator rated force is applied at 2.5 second.

At the moment of applying the disturbance step force, little vibration can be observed (Figure 162). The frequency of such vibration matches f_2 summarised in Table 15.

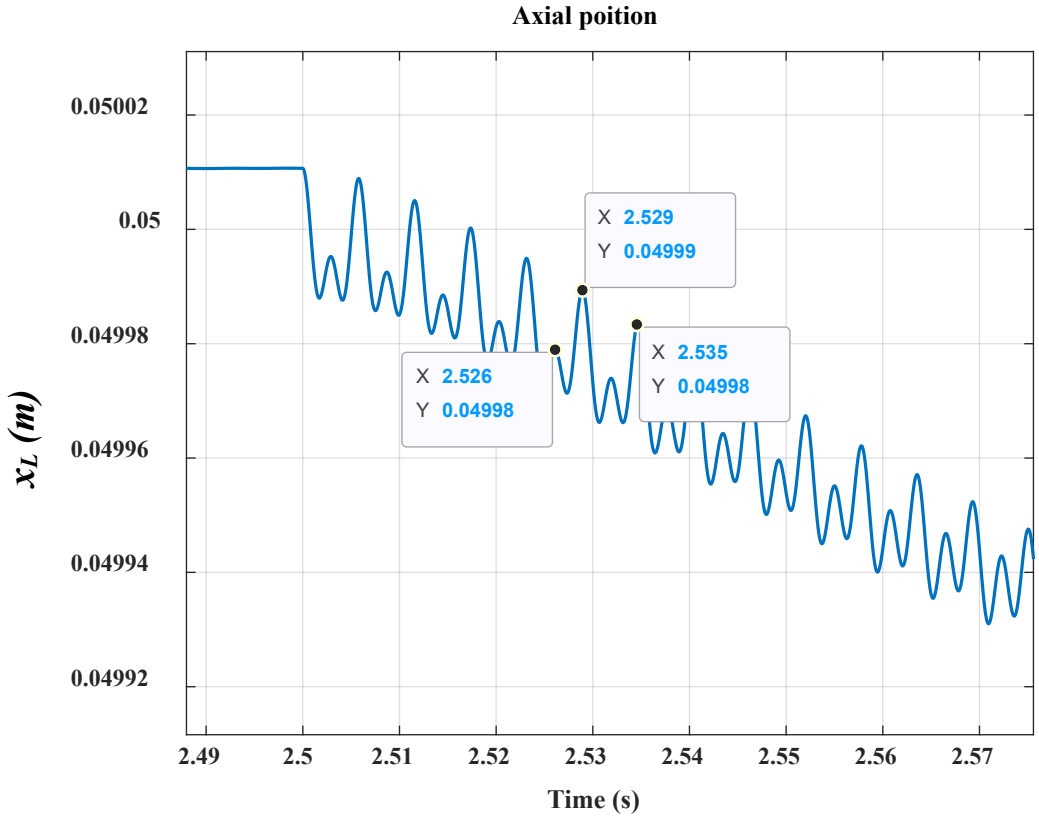

Figure 162. Load position

These oscillations decay away gradually, as shown in Figure 163.

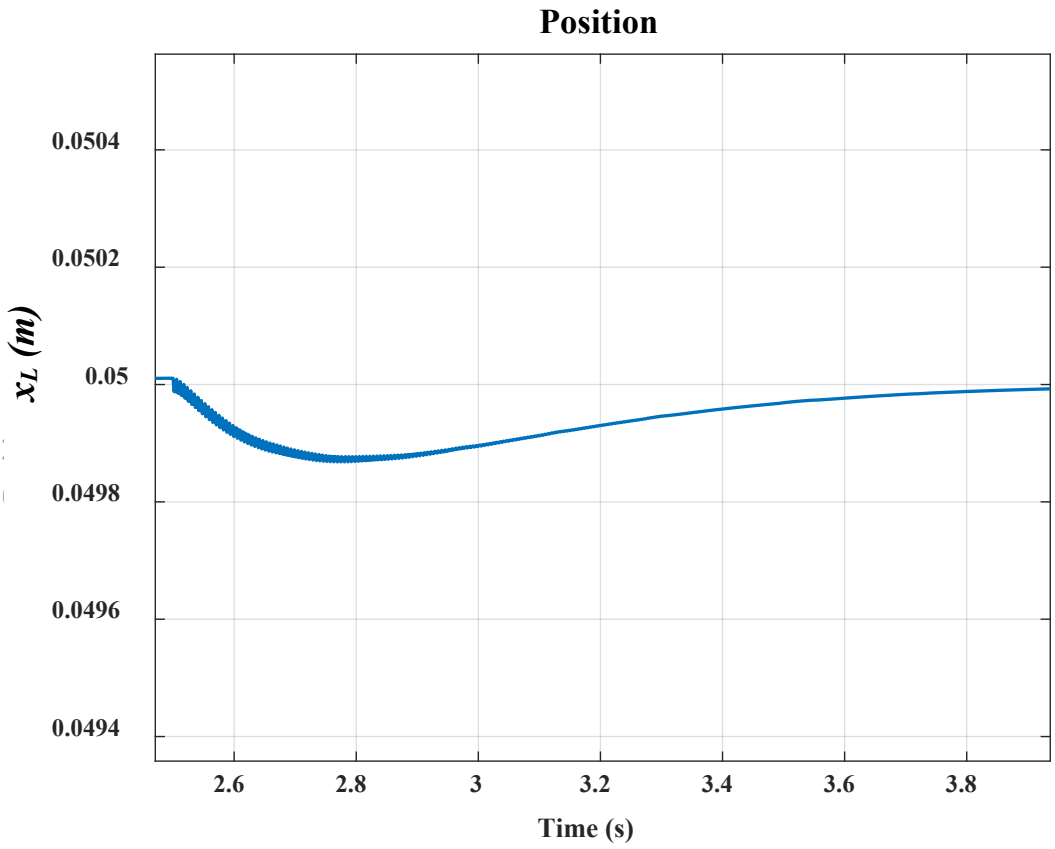

Figure 163. Load position (oscillations decay away with time)

4.6.2 Disturbance torque with certain frequencies

A position demand of maximum displacement is applied at 0 second. A chirp signal is applied to represent a frequency variant disturbance force. The amplitude of the disturbance is 10% of the actuator rated force. The frequency ranges from 200 to 400 Hz.

A steady load position is first seen. When the applied load frequency becomes close to f_2, load position starts to oscillate between its maximum displacements limits (Figure 164). This oscillation, which is with frequency of 4.7 Hz, is certainly not acceptable and it indicates a loss in actuation control. Also, oscillating in this manner will eventually lead to wears in mechanical components. Note that a similar test is carried out in chapter 2 but no dynamics are shown there due to model being over simplified.

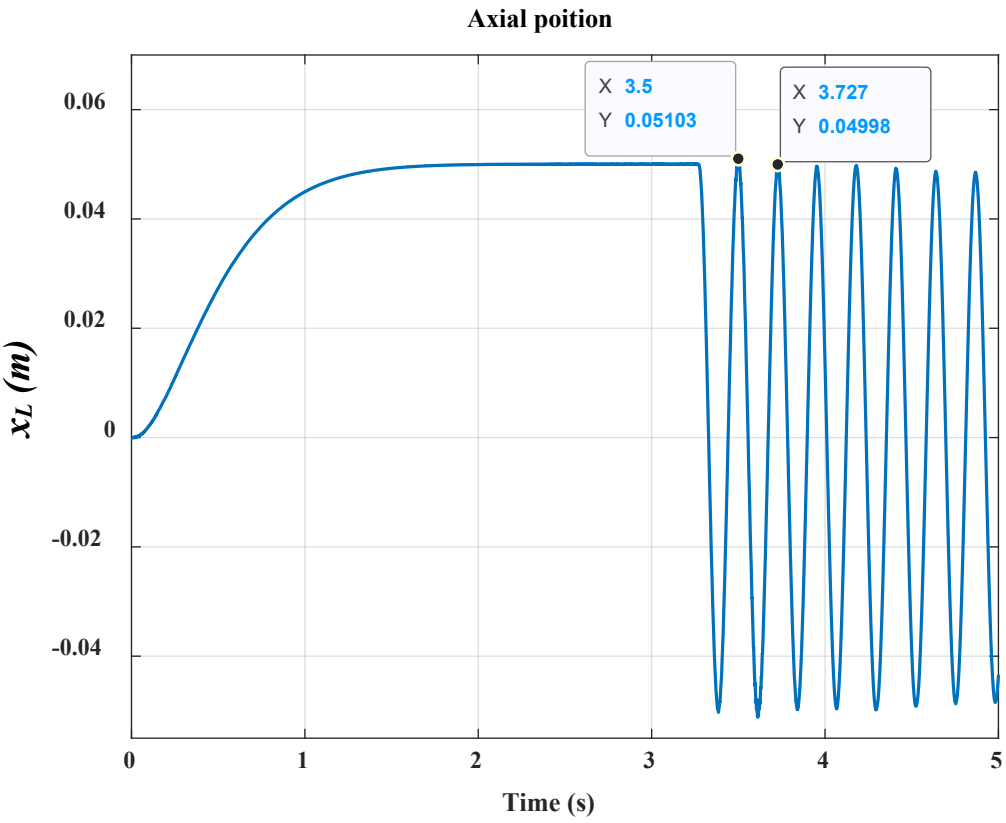

Figure 164. Load position (frequency of oscillations = 4.7 Hz)

As mentioned previously, the amplitude of oscillation is 10% of the maximum rated force. Before the disturbance frequency becomes close to frequency of interest, insignificant vibration (equalling to f_2) is seen as shown in Figure 165 but this can be negligible since it has no effect on any part.

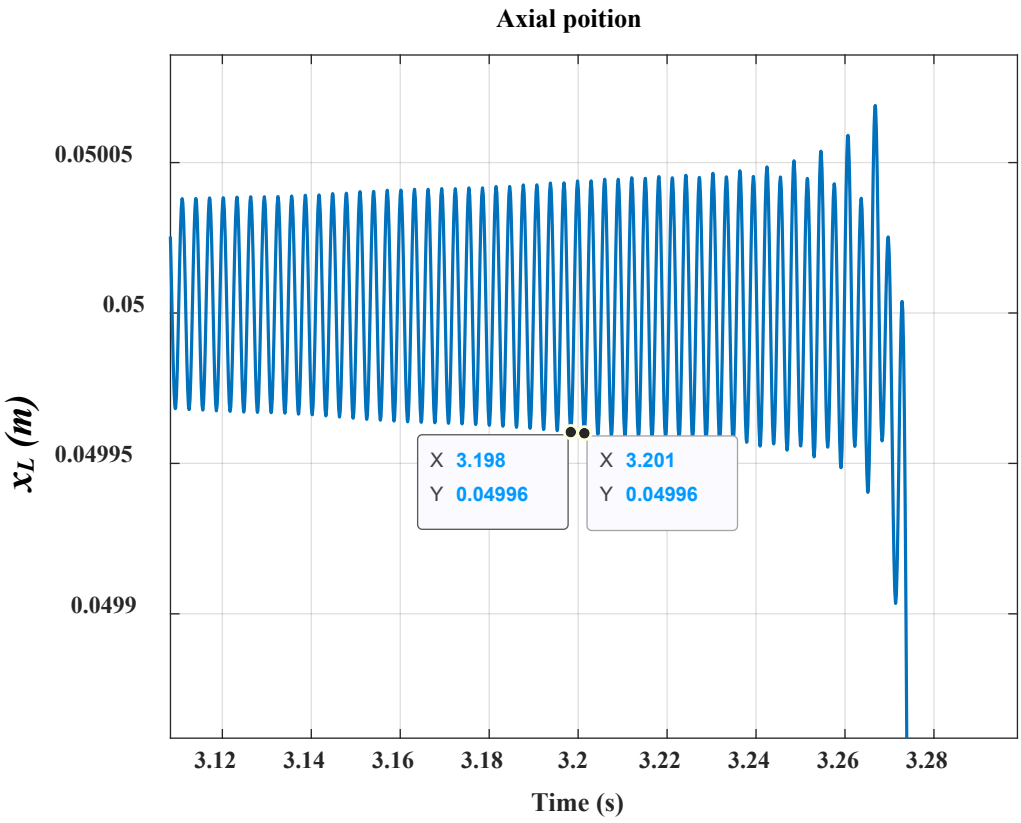

Figure 165. Load position

The frequency of oscillation is 4.7 Hz but there is another frequency component, which is 350 Hz as shown in Figure 166.

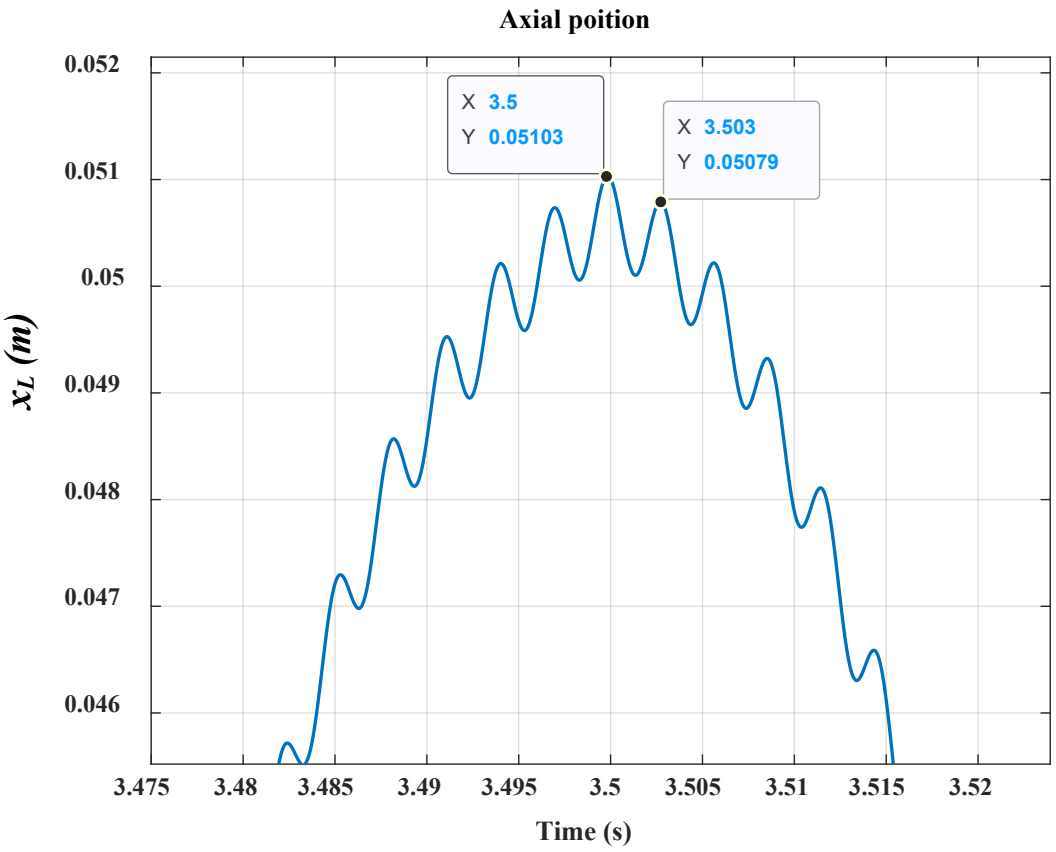

Figure 166. Load position

Figure 164, Figure 165 and Figure 166 show that the little varying frequency disturbance applied, which is of low amplitude, is able to trigger a significant mode in the mechanical system. Also, such vibration is passed into the electrical network. As a result, the PDD winding current is altered in the way shown in Figure 167. High currents may indeed have an impact on the PDD windings and could cause temperature rising and even faults. Subsequently and more significantly, electrical network may become unstable. This local instability could cause a wider instability in the aircraft electrical system, as established in [1] [39] [48]. Note that in Figure 51 and Figure 52 in Chapter 2, i_a is not respondent to any of such frequency varying disturbance due to neglecting significant dynamics in the model.

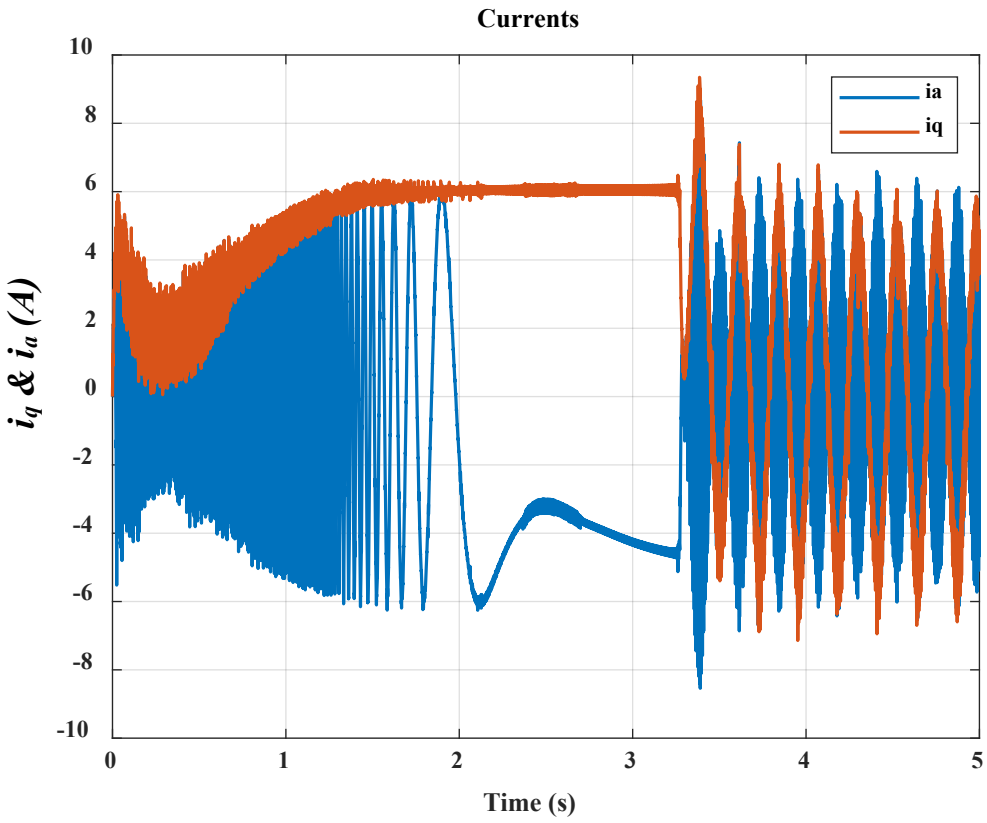

Figure 167. i_a and i_q currents

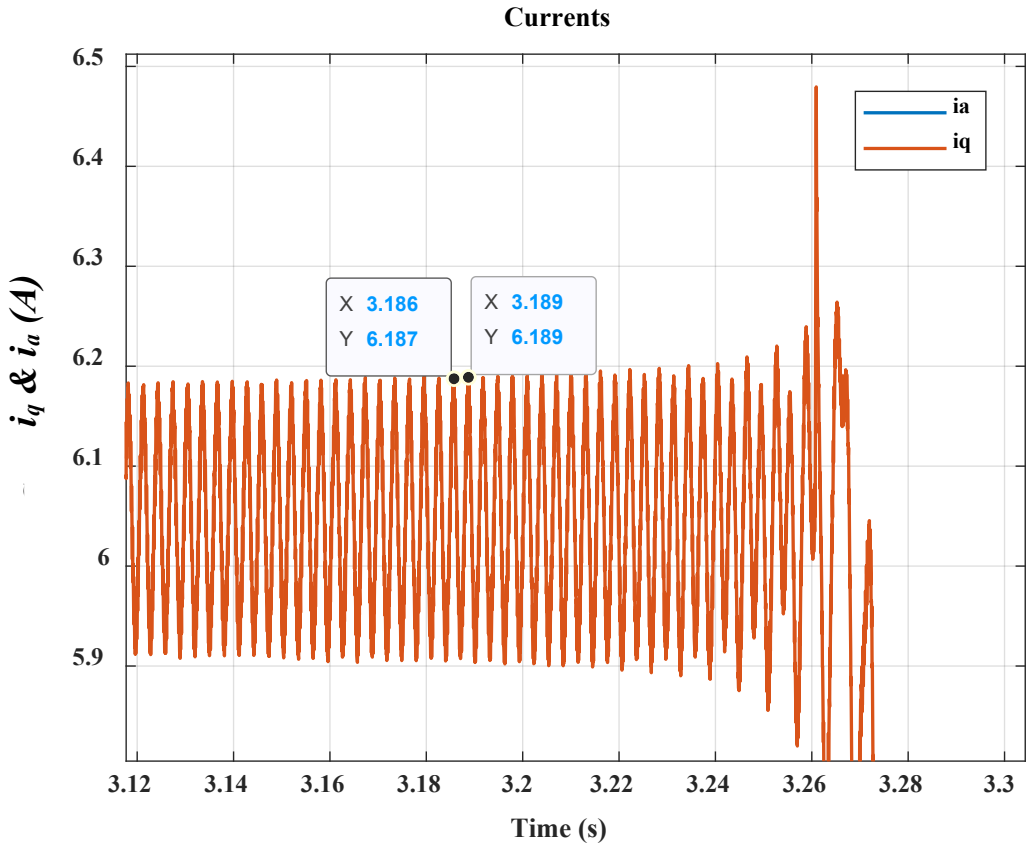

Figure 168. i_a and i_q with f_2 induced

The time domain analysis in this section proves that for the studied EMA system, disturbance from load side could excite the resonance structure of the EMA system, which leads to instability in the electrical system.

4.7 Conclusion

The current bandwidth selected is 500 Hz. Frequency domain analysis of the proposed three-degree of freedom model highlights a resonant mode that happens to be 338 Hz. The proposed three-degree of freedom model replicates the key modes of their higher-order model equivalent values. Also, the proposed reduced order model is able to predict electromechanical interaction. In contrast, the counterpart conventional MEA EMA model, which lumps the mechanical system in one inertia, is therefore inadequate.

Eigenvalue sensitivity to uncertainties in mechanical components show that system stability can be affected by variations in mechanical components' variables although system remains stable if uncertainties are within a close range of the operational values. However, mechanical components can cause instability if crucial component such as K_b is lowered to an extremely low value. Simulation show interaction in that case and oscillations occur corresponding to resonant frequencies.

Broadly, electromechanical interaction is recorded to occur due to two major cases; interaction between mechanical structure resonance and controller, and due to disturbance force on load side. For the first case, it is found that speed loop is strongly related to the structure resonance since anti-resonance brings a severe phase shift that decreases the stability margin. Therefore, it is crucial to ensure that the speed loop bandwidth is designed away from the resonant frequency.

For the second case, natural frequencies, within current loop BW, associated with mechanical system are susceptible to disturbance of frequencies close to resonant frequencies. Time domain tests are carried out to observe performance under various load conditions. Mechanical load variation of low amplitude is shown to induce mechanical vibrations that are clearly identifiable at 338 Hz. In addition, a frequency variant disturbance force, of low amplitude, is applied to represent extreme loading conditions. When disturbance force frequency becomes close to 338 Hz, high oscillation can be observed in the load position. This is capable of degrading mechanical components although disturbance is of low amplitude. Additionally, load position oscillation is passed into the electrical network and can be seen in the PDD winding current. Winding current starts to oscillate with an amplitude that is triple the rated current, which might lead to faults in the PDD windings. Local instability in the EMA system may lead to wide instability in the aircraft electrical network that passes back to the generators. This instability also may be directed back and excite resonances of the mechanical drivetrain transferring power from the gas turbine to the generators. This, indeed could compromise the entire flight stability and hence reliability.

Chapter 5 Experimental validation

5.1 Introduction

To validate results experimentally with minimised cost and maximised safety, a hardware in the loop (HIL) technique is used to emulate complex mechanical systems. A complex mechanical system can compose of many parts and may have various dynamics. HIL technique consists of two main parts; emulator and a real time platform (RTP). An emulator is essentially an electrical drive system that operates to emulate dynamic behaviour of a certain mechanical system. The emulator is controlled by a real time platform that contains a model of the complex mechanical system under study [74].

This chapter presents the test rig used to validate the simulated results. The prototype PDD was built at University of Sheffield. The test rig, shown in Figure 169, is in use to replicate the behaviour of the EMA utilised in rudder actuation.

Figure 169. Test rig as a whole

5.2 Test rig description

The test rig was developed by another researcher as a part of the Electro-Mechanical Magnetic Actuator System (EMMAS) project, which is a project of which the University of Sheffield has carried out in cooperation with Magnomatics Ltd and Triumph Group.

Figure 170 displays the test rig. It consist of a PDD machine drive and a servo machine drive. The LSR on PDD is coupled to the servo motor through membrane couplings. Also, a torque transducer is in between so the torque on the shaft can be measured.

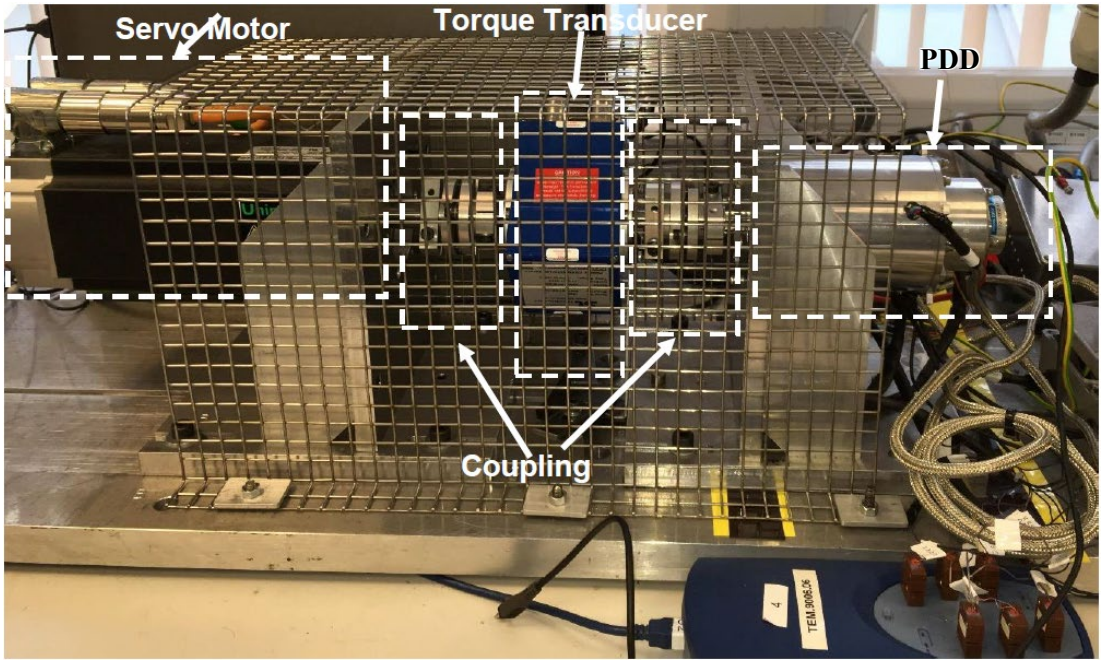

Figure 170. PDD, servo motor, transducer and coupling

5.2.1 PDD drive

The PDD drive was developed by another researcher as a part of the Electro-Mechanical Magnetic Actuator System (EMMAS) project, which is a project of which the University of Sheffield has carried out in cooperation with Magnomatics Ltd and Triumph Group.

5.2.1.1 PDD

PDD construction is described in Chapter 2. The PDD windings star connections can be seen in Figure 171. It is clear that there are two independent three-phase lanes since this machine is fault tolerant (Appendix B). Lane 1 contains 54 turns per phase. Similarly, lane 2 contains 54 turns per phase but in one of the phases, winding is divided into three coils; 26 turns, 1 turn and 27 turns. This is to facilitate tests to observe machine performance under fault conditions. However, this is not the scope of this research.

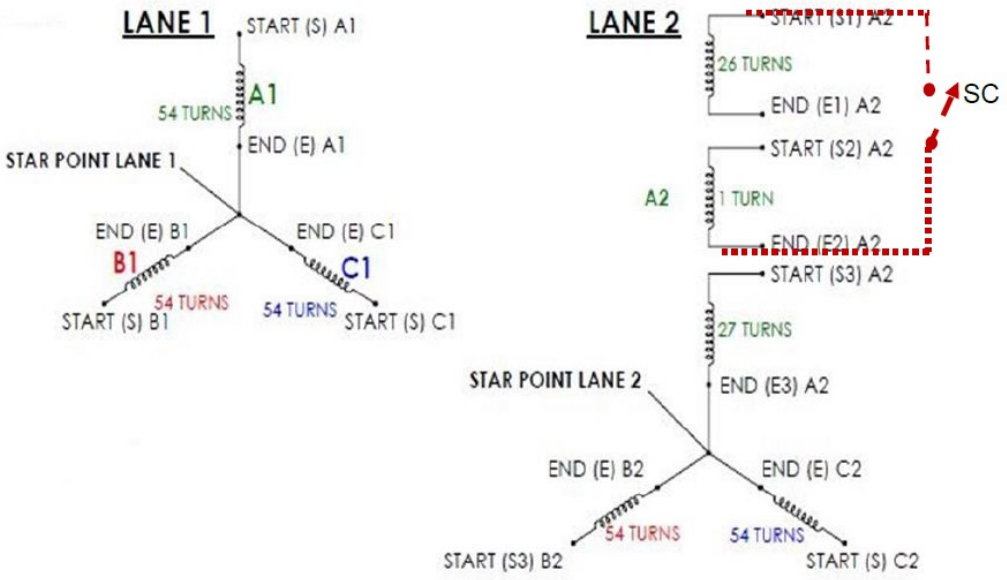

Figure 171. PDD winding sets connection

Each lane contains a search coil (Figure 172), which is used to estimate how magnetic field distribution, within the machine, is affected by an occurring fault.

Figure 172. Search coils

The parameters of the PDD under test are the same as the ones used for simulation in previous chapters. Important parameters are highlighted in Table 19. The parameters were given by the manufacturer. Some of the parameters were verified in the laboratory; such as gear ratio, G_r, PDD torque constants, K_t and K_{t_LSR}, PDD back EMF constant, K_e, motor phase resistance, R_s.

Table 19. PDD parameters

Parameter	*symbol*	*Value*	*Unit*
Moment of inertia on HSR	J_{HSR}	1.35×10^{-4}	$kg.m^2$

Moment of inertia on LSR	J_{LSR}	1.08×10^{-4}	$kg.m^2$
LSR peak speed	n_{LSR_MAX}	*1200*	*rpm*
HSR peak speed	n_{HSR_MAX}	*9300*	*RPM*
Pole pairs	p_h	*4*	*-*
Number of pole pieces	n_s	*31*	*-*
Gear ratio	G_r	*7.75*	*-*
Pull out torque	T_{max}	*10.3*	*N.m*
Viscous damping of the HSR	c_{HSR}	8.20×10^{-5}	*N.m/rad/s*
Viscous damping of the LSR	c_{LSR}	3.10×10^{-4}	*N.m/rad/s*
Viscous damping between HSR and LSR	c_{HSR_LSR}	1.20×10^{-4}	*N.m/rad/s*
PDD torque constant	K_t	*0.148*	*N.m/A*
PDD Torque constant from LSR side	K_{t_LSR}	*1.145*	*N.m/A*
PDD phase resistance	R_s	*0.7*	*Ω*
PDD phase inductance	L_s	1.90×10^{-3}	*H*
Number of turns	N_t	*54*	*turns*
Peak AC phase voltage demand (Limit)	$V_{dc}/2$	*135*	*V*
Peak torque demand (Limit)	T_{LSR_MAX}	*8.6*	*N.m*
Switching frequency	f_{sw}	*10*	*kHz*
Base voltage	V_{base}	*135*	*V*
Base current	I_{base}	*8*	*A*
Base frequency	f_{base}	*620*	*Hz*

5.2.1.2 PDD control

PDD current and speed are constantly regulated to ensure operating speed and torque are according to demand. Since the fault tolerant PDD consists of two independent, three-phase, windings (Appendix B), both windings are controlled independently using separate drives. Each drive utilises Taxes Instruments TMDSHVMTRPFCKIT. Figure 173 shows the TI board used for each lane. Only one lane is tested in this project since fault tolerance testing is out of this study scope.

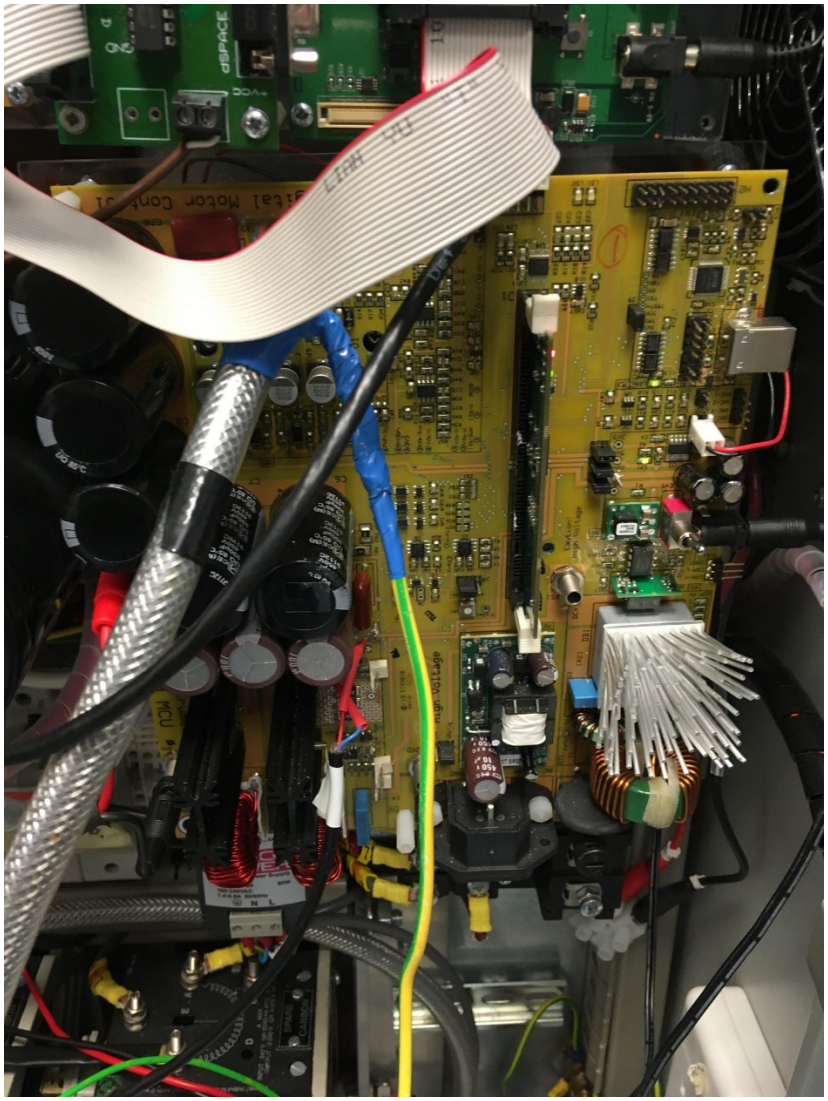

Figure 173. PDD drive

The High Voltage Motor Control and PFC (Power Factor Correction) kit contains the following features:

- AC rectifier stage rated for 750W. This rectifier can accept 110V AC or 220V AC input from mains. The rectified output voltage can be used for input of the PFC stage or, by help of capacitor bank present at the inverter input, used directly as a DC bus for the inverter.
- Power factor correction (PFC) stage rated for 750W. It takes the rectified AC input and can produce a voltage output of up to 400V DC. This module is there to increase efficiency of operation.
- Aux power supply module. This module takes the rectified AC voltage or the PFC output and generates 15V and 5V DC. This 15V DC can be used to power the board in case the DC power entry (see the next point) is not used. The input of this module can be up to 400V DC.

- DC power entry powered by a 15V DC 1 Amp power supply is used to power the microcontroller and the logic circuit present on the board via a DC-jack. Also, from this 15V DC, 15V, 5V and 3.3V points are generated.
- Three-phase voltage source inverter that is capable of sensorless and sensored field oriented control (FOC) of high voltage PMSM motor. The input of this inverter may be 350V DC and output maximum load can be 1kW/1.5kW. Since at rectifier and PFC stages power rating is 750W, a high voltage external power supply is used directly at inverter's terminals via Banana jacks for higher power tests. This will be the case since the under test PDD's power rating is over 1kW.
- Over-current protection for PFC stage and also for the inverter stage.
- QEP (Quadrature Encoder Pulse) input used to receive motor speed and position measurements.
- High precision low-side current sensing using the C2000's highest performance ADC.
- Isolated CAN, SCI and JTAG. On the board, there is an isolated JTAG connection that is connected to the host via USB.
- Instrumentation: four DAC's to observe system variables on an oscilloscope.
- Control card socket, which accepts any of the 32-bit C2000 control cards (Piccolo F28035 control card in this case).
- Open source software available through controlSUITE for each type of motor so it can be modified to tune and run any motor.

All actuation signals, PWMs, and sense signals, ADCs, have designated test points on the board. Figure 174 shows a brief overview of the board and some of the features explained.

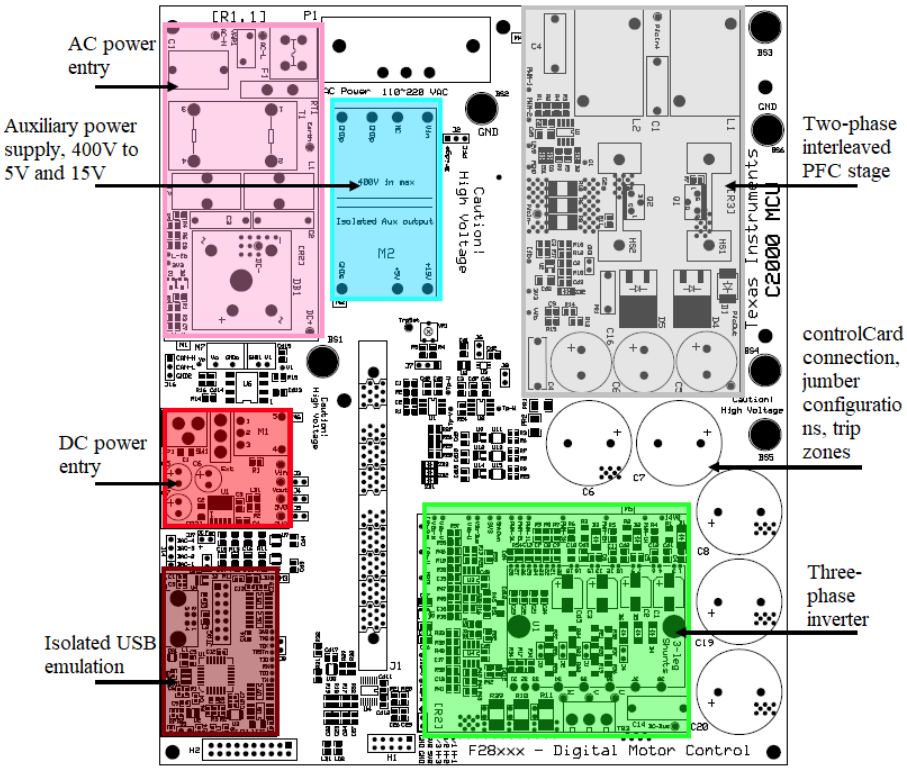

Figure 174. HVMOTORCTRL+PFC [75]

The relevant parameters specified for the board are summarised in Table 20.

Table 20. TMDSHVMTRPFCKIT parameters

Parameter	*symbol*	*Value*	*Unit*
ADC's resolution in bits	N_{bits}	*12*	*bit*
ADC voltage reference	V_{ref_MAX}	*3.3*	*V*

The different stages on the board explained above can be illustrated in a block diagram format as shown in Figure 175. As reasoned above, since this project involves a power rating over 750W, therefore rectifier and PFC stages are bypassed. Instead, V_{dc}, 270V DC, is directly applied at the inverter input terminals (BS5 and BS6) by an external DC power supply.

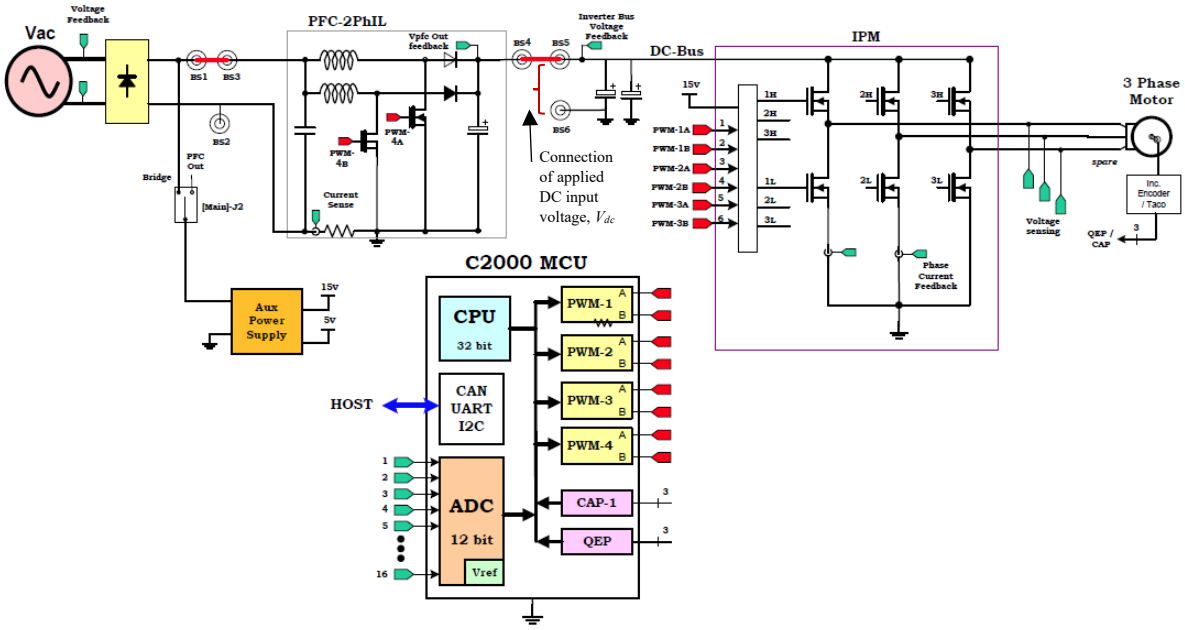

Figure 175. Schematic diagram of the HVDMC + PFC board with C2000 MCU [75]

Hardware is set up according to manufacturer's guide. Code Composer Studio (v9) and controlSUITE are installed and set up with respect to instructions. Various motor control projects are available but the one picked is HVPM_Sensored_Servo.

To be able to make the available project suitable for the PDD in use, certain settings are firstly modified; such as defining the PDD parameters, base quantities and QEP (Quadrature Encoder Pulse) specifications. Table 21 shows a brief of such defined parameters. More information can be found in Appendix G.

Table 21. Setting up parameters

Parameter	*Symbol*	*Base value*	*Unit*
Switching frequency	*ISR_FREQUENCY*	*10*	*kHz*
Stator resistance	*RS*	*0.7*	Ω
Stator inductance	*LS*	1.9×10^{-3}	*H*
Number of poles	*POLES*	*8*	
Base voltage	*BASE_VOLTAGE*	*135*	*V*
Base current	*BASE_CURRENT*	*9.5*	*A*
Base electrical frequency	*BASE_FREQ*	*620*	*Hz*

Number of pulses per channel	*QEP_PULSE_PER_CHNL*	*1024*	*pulse/revolution*

Symbols in Table 21 are related to some of the parameters defined in Table 19. To avoid discrepancy, Table 22 relates symbols of both tables.

Table 22. Symbols used in the code and equations

Symbol used in the code	*Symbols used in the thesis equations*
ISR_FREQUENCY	f_{sw}
RS	R_s
LS	L_s
POLES	$2\times p_h$
BASE_VOLTAGE	V_{base}
BASE_CURRENT	I_{base}
BASE_FREQ	f_{base}
T	$T_{sampling}$

Based on the values defined in the settings file, some other parameters are calculated. For instance, sampling period, $T_{sampling}$, can be computed in Equation (242).

$$T_{sampling} = \frac{0.001}{ISR\_FREQUENCY} = \frac{0.001}{10} = 0.0001\ s \tag{242}$$

It is clearly shown in Figure 175 that there are 16 12-bit ADC inputs. So for each ADC input, the number of voltage intervals, N_{int_MAX}, are calculated in Equation (243).

$$N_{int\_MAX} = 2^{N_{bits}} = 2^{12} = 4096\ levels \tag{243}$$

The maximum voltage reference (span), V_{ref_MAX}, for each ADC input is 3.3 V, which represents the full scale voltage range allowed for analogue input values. However, I have chosen the reference voltage, V_{ref}, value to be 3 V to make sure all signal components are inputted. Otherwise, some components may be clamped due to saturation. For example, to send a speed demand, ω_{HSR}^*, from any real time platform to the TI board, ω_{HSR}^* is firstly converted into per unit value, $\omega_{p.u.}^*$, as follows:

$$\omega_{p.u.}^* = \frac{\omega_{HSR}^*}{\frac{2\pi f_{base}}{p_h}} = \frac{\omega_{HSR}^*}{\omega_{base}} = \frac{1}{973.9}\omega_{HSR}^* \tag{244}$$

where ω_{base}, is the base speed. The per unit speed demand signal, $\omega_{p.u.}^*$, has a maximum value of 1 and hence when sent out, as voltage demand, its maximum value will be equal to 1V. To convert $\omega_{p.u.}^*$ to voltage demand within the chosen scale voltage range allowed for analogue input values, v_ω^*, Equation (245) can be used.

$$v_\omega^* = G_2\omega_{p.u.}^* = \frac{1}{0.3333}\omega_{p.u.}^* \tag{245}$$

where G_2 is the gain used to scale 1 per unit value of the speed demand to 3 V analogue input of the TI board ADC. v_ω^* is shown in Figure 176 with respect $\omega_{p.u.}^*$. Figure 210 is also useful to explain calculations presented in this section.

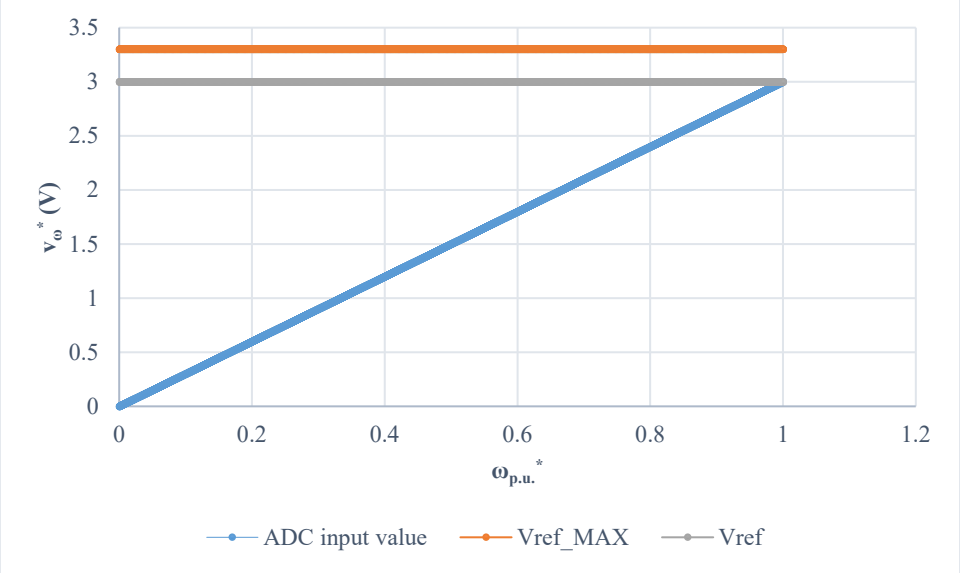

Figure 176. ADC input values in comparison with reference voltages

Thus the number of voltage intervals, $N_{v\_interval}$, that reflects the chosen voltage reference, V_{ref}, can be calculated using Equation (246).

$$N_{v\_interval} = V_{ref} \times \frac{N_{int\_MAX}}{V_{ref\_MAX}} = 3 \times \frac{4096}{3.3} = 3723.64 \tag{246}$$

v_ω^* is fed to an ADC input, and then converted into per unit speed demand used by the code, $\omega_{p.u.\_code}^*$, as shown in Equation (247).

$$\omega_{p.u.\_code}^* = \frac{1}{V_{ref\_MAX}} \times \frac{N_{int\_MAX}}{N_{v\_interval}} v_\omega^* = \frac{1}{3.3} \times \frac{4096}{3723.64} v_\omega^* = 3723.64 \tag{247}$$

$\omega_{p.u.\_code}^*$ is shown in Figure 177 with respect to v_ω^*. Practically, Equation (247) is implemented in the code by adding the following line.

Speedref=_IQ(AdcResult.ADCRESULT8/3723.636);

where Speedref reflects $\omega_{p.u.\_code}^*$.

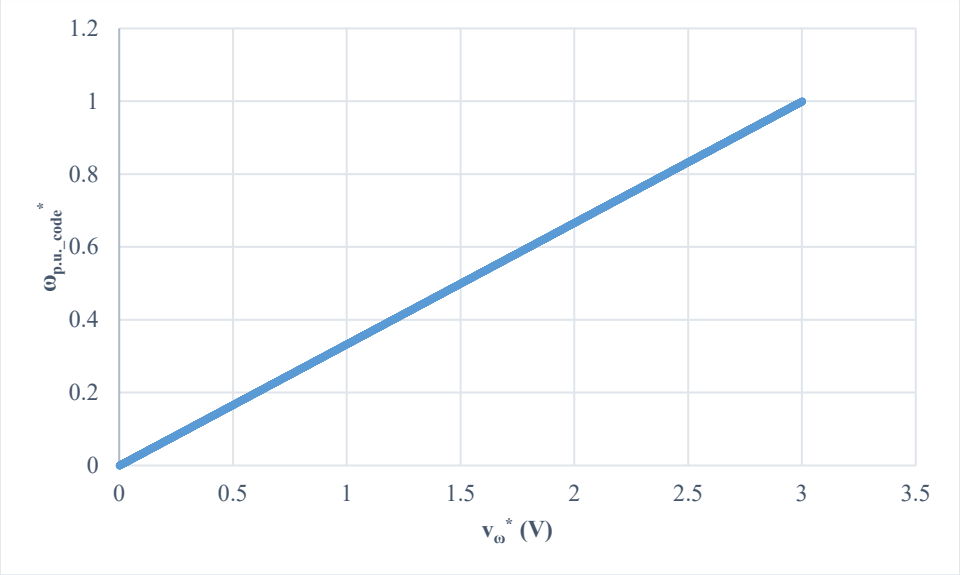

Figure 177. Per unit reference speed received by the µcontroller

Furthermore, in the project algorithm used, the decoupling term (explained in Section (2.3.1) and shown in Figure 30) is not added so it is added below.

```
q_dcoupl=_IQmpy(speed1.Speed,_IQ(0.434));

ipark1.Ds=pi_id.Out-_IQmpy(pi_iq.Fbk,q_dcoupl);

ipark1.Qs=pi_iq.Out+_IQmpy(pi_id.Fbk,q_dcoupl);
```

The number 0.434 reflects the per unit reactance, $XL_{p.u}$, and it is calculated as shown in Equation (248) and Equation (249).

$$Z_{base} = \frac{V_{base}}{I_{base}} = \frac{135}{8} = 16.9\ \Omega \tag{248}$$

$$XL_{p.u.} = \frac{2\pi \times f_{base} * L_s}{Z_{base}} = \frac{2\pi \times 620 * 1.88 * 0.001}{16.9} = 0.434 \tag{249}$$

where V_{base} is PDD base voltage, I_{base} is PDD base current, Z_{base} is PDD base impedance, and f_{base} is base frequency.

The control scheme implemented is FOC (Field Oriented Control) and it is explained in Chapter 2. The PWM three-phase inverter switching signals are obtained by the TI SVPWM algorithm (Appendix C).

5.2.1.3 PDD position sensing

Resolvers can work effectively over a wide temperature range. Also, resolvers are robust against vibrations since they have no electronic components. This is different to encoders, which are less robust [76]. For such reasons, PDD is equipped with a resolver that is attached to the HSR.

The resolver is made up of two components; rotor and stator. Both must be perfectly aligned to avoid any eccentricity that might be introduced to measurements. The rotor consists of a winding known as reference winding whereas stator consists of primary windings and secondary windings. The primary windings are excited with a high frequency sine wave, which is transmitted to the rotor windings [76]. Resolver basic construction is shown in Figure 178.

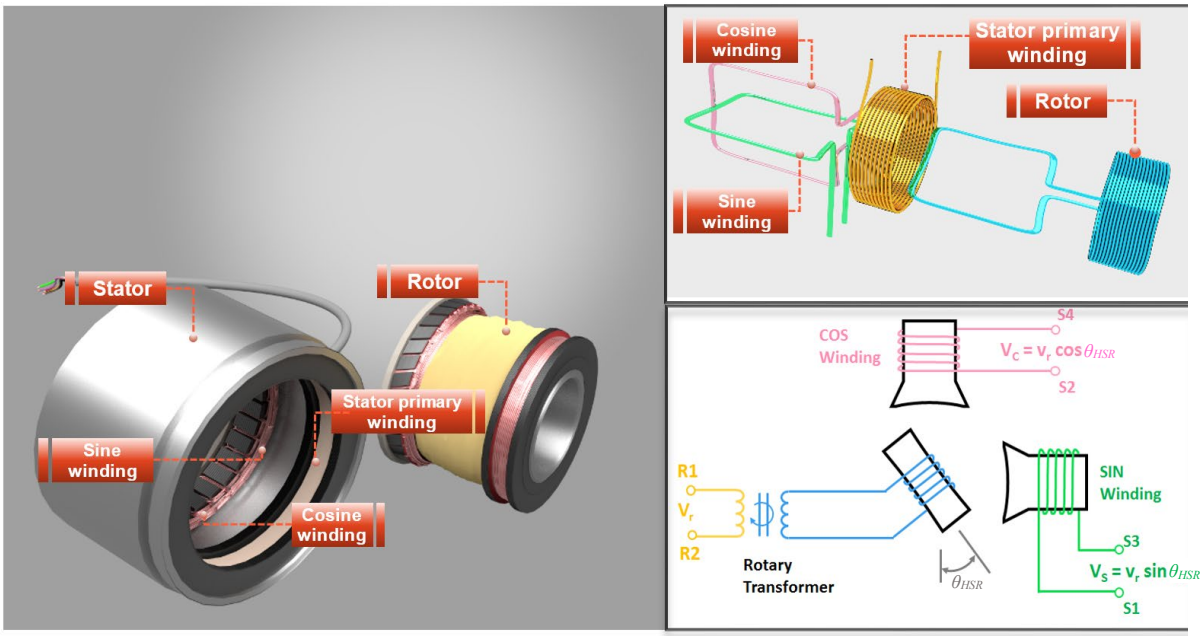

Figure 178. Resolver [76]

During rotation of PDD HSR, resolver is excited with a high frequency sine wave, V_r, and outputs two main outputs; sine and cosine. Each position within a turn is represented by a distinctive amplitude and phase relation of sine and cosine [76]. The resolver output signals are clearly analogue. Therefore, in order for the TI microprocessor to interpret rotor position, resolver analogue output signals must be converted into digital signals using an ADC.

An AD2S1200 Resolver-to-Digital converter board (Figure 179) is employed to convert resolver measurements into digital signals readable by the TI board. Many functional blocks are integrated on the board. For example, there is on-chip fault detection to detect loss of resolver signals and loss of position tracking. Furthermore, there is an on-chip programmable sinusoidal oscillator to provide sine wave excitation (EXC and $\overline{EXC}$) for resolver's primary windings. There are four input signals to the board; sin, $\overline{sin}$, cos and $\overline{cos}$.

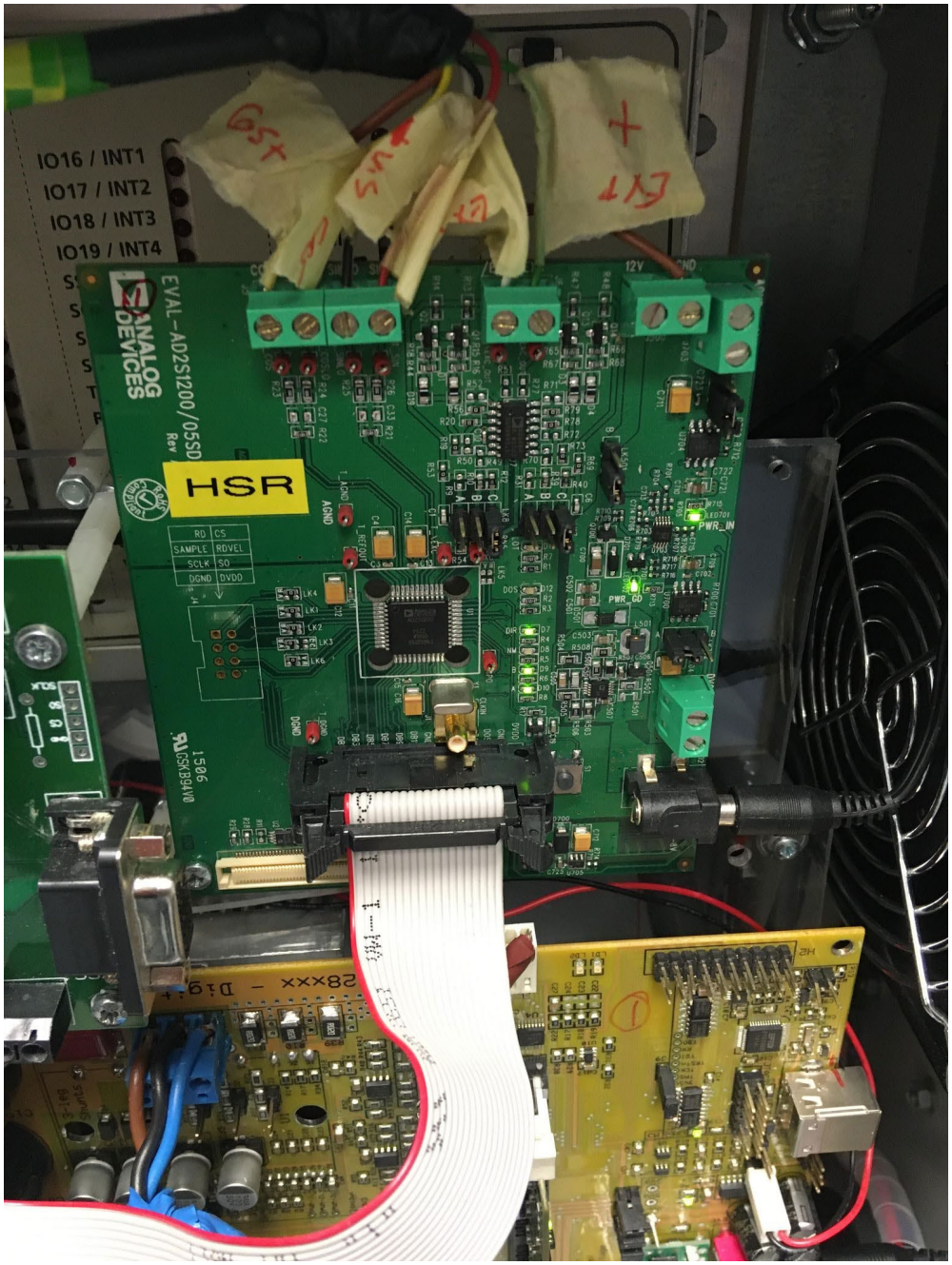

Figure 179. AD2S1200

The board output is a 12-bit angular position, which can be accessed via either a 12-bit parallel port or a 3-wire serial interface. On the board, there is an on-chip incremental encoder emulation with direction output. The resolver-to-digital converter board emulates a 1024-line encoder. The output is produced in a form of three signals; A_{enc}, B_{enc} and Z_{enc}. A_{enc} and B_{enc} carry the designated 1024 pulses per revolution; A_{enc} leads B_{enc} in the forward direction whereas B_{enc} leads A_{enc} in the reverse direction so the direction of rotation is known by the controller. Z_{enc} indicates the index signal, which is only a single pulse per revolution, which marks an end of a revolution so the controller position counter is reset.

5.2.2 Servo drive (mechanical system (rudder, screw, and couplings) emulator)

5.2.2.1 Servo motor

An Emerson Industrial Automation made servo motor (Unimotor HD 089UDC305BFAEA) is employed to load the PDD. The shaft is mechanically coupled with the PDD. Two lines can be seen in Figure 180; one for three-phase power, supplied by the drive, and the other one is for position feedback measurements provided by the resolver installed on the motor shaft.

Figure 180. Servo motor

Industrial servo motor nominal characteristics are summarised in Table 23.

Table 23. Servo motor nominal characteristics

Parameter	*Symbol*	*Value*	*Unit*
Voltage		*400*	*V*
Motor stall torque		*8.00*	*Nm*
Rated torque		*6.90*	*Nm*
Motor peak torque		*24.00*	*Nm*
Rated power		*2.17*	*kW*
Speed		*3000*	*rpm*
Number of poles		*10*	
Maximum coggings		*0*	*Nm*
Inertia	J_{servo}	*2.46*	$kgcm^2$
Drive switching frequency	f_{sw_servo}	*12*	*kHz*
Stall current		*5.00*	*A*

Nominal current		*4.3*	*A*
Maximum current	I_{max}	*15.00*	*A*
Torque constant	K_T	*1.60000*	*Nm/A*
EMF constant	K_E	*98.00*	*V/kmin*$^{-1}$
Phase to phase resistance	$R_{ph\text{-}ph}$	*2.68*	*Ω*
Phase to phase inductance	$L_{ph\text{-}ph}$	*21.72*	*mH*
Weight		*6.50*	*kg*

In addition, a parking brake is installed within the motor for safety. Table 24 relates to the parking brake characteristics.

Table 24. Parking break parameters

Brake	5 – Parking brake	Static torque (N.m)	10
Release time (ms)	50	Backlash (°)	0.75
Brake supply voltage (V)	24	Brake coil power (W)	23.4

5.2.2.2 Servo motor control

The industrial Emerson motor is controlled by a commercial drive (Figure 181) and supplied by three-phase AC. The AC is rectified within the drive cabinet, and three-phase power is supplied to motor through an inverter.

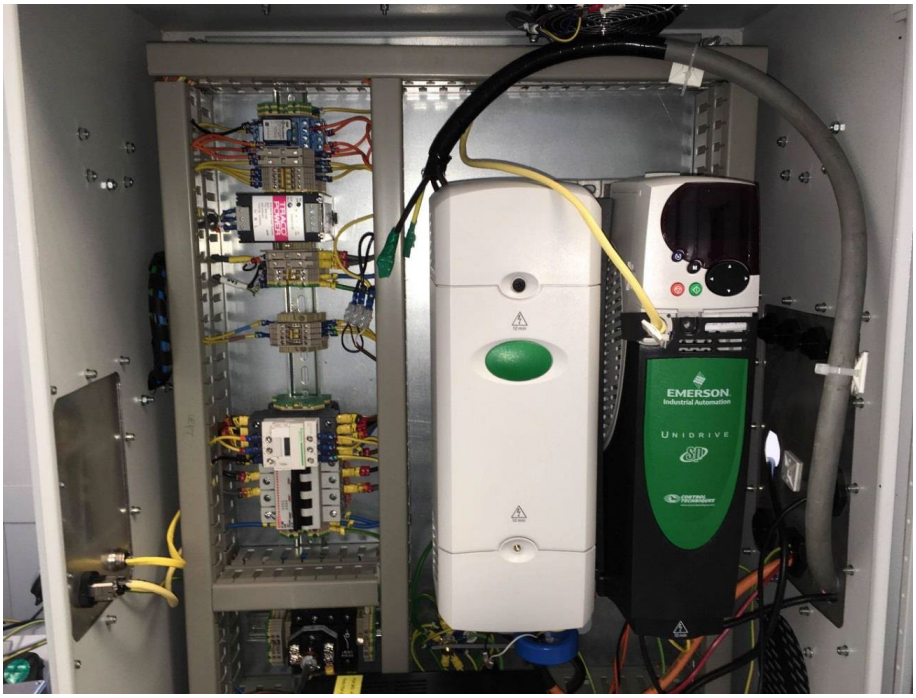

Figure 181. Servo motor drive cabinet

CTsoft software is the platform where the algorithm of servo machine operation is based. After installing CTsoft, the drive number is chosen in the software to match the actual drive in use. Parameter files, within CTsoft, are modified to match the motor and drive used. Many parameter figures can be taken from Table 23. Speed limit is set, within servo drive, to ensure protection against high current. Since this motor is supposed to load the PDD, then the commercial drive, in this case, is supposed to operate under torque control mode. The mode can be easily selected from CTsoft, as indicated by the red line in Figure 182.

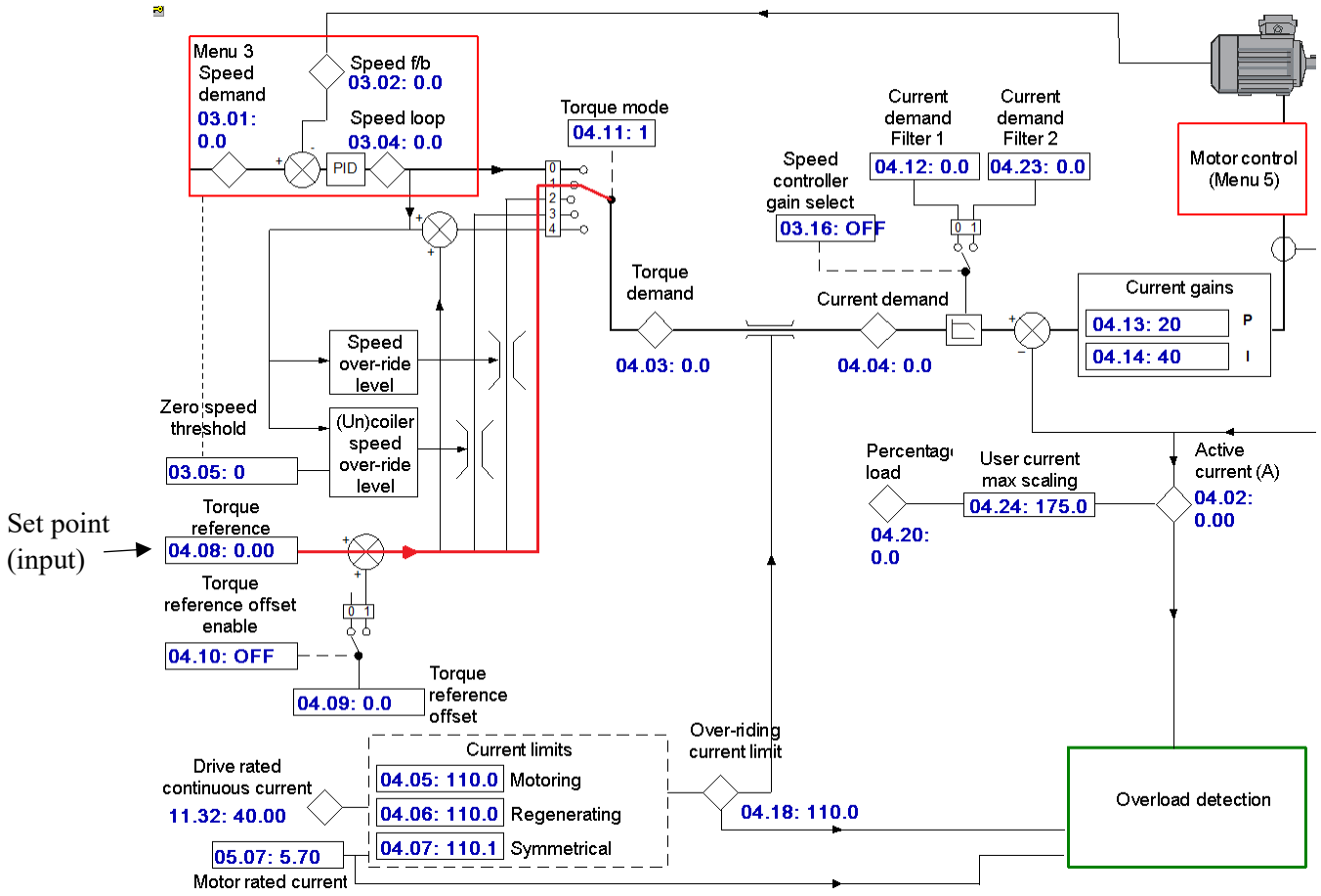

Figure 182. Torque reference selection

Torque input is allowed to be sent from within the software, as a step torque, or to be sent from an external source. The latter option allows for torque to be taken through an analogue input connection available on the Emerson drive. Also, it is important to assign, within CTsoft, the analogue input chosen for the torque demand as shown in Figure 183. The sampling period for this analogue input is 250 µs.

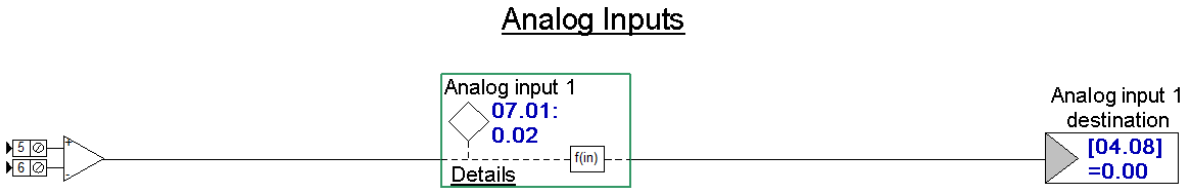

Figure 183. Connecting the torque demand with the analogue input

For example, a torque demand signal can be set by a real time platform; using a model in, say, Matlab/Simulink. This torque demand signal is taken out of the real time controller through a DAC channel. It is then connected to an Emerson drive analogue input, as illustrated in Figure 184.

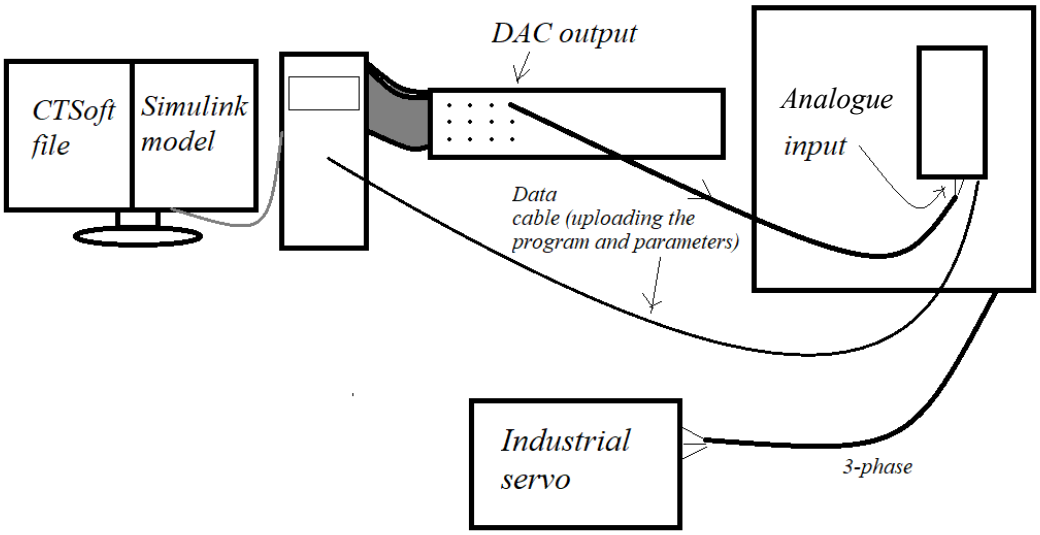

Figure 184. Torque demand

5.2.2.3 Position sensing

The servo motor is equipped with one resolver. An Emerson solutions module (SM-Resolver), depicted in Figure 185, is used to convert resolver analogue output signals (sin, $\overline{sin}$, cos and $\overline{cos}$) into encoder outputs (A_{servo}, $\overline{A_{servo}}$, B_{servo}, $\overline{B_{servo}}$, Z_{servo} and $\overline{Z_{servo}}$) acceptable to the drive. In addition, parameter file within CTsoft is modified to fit module type such as module ID (101) and equivalent lines per revolution (4096) and so on.

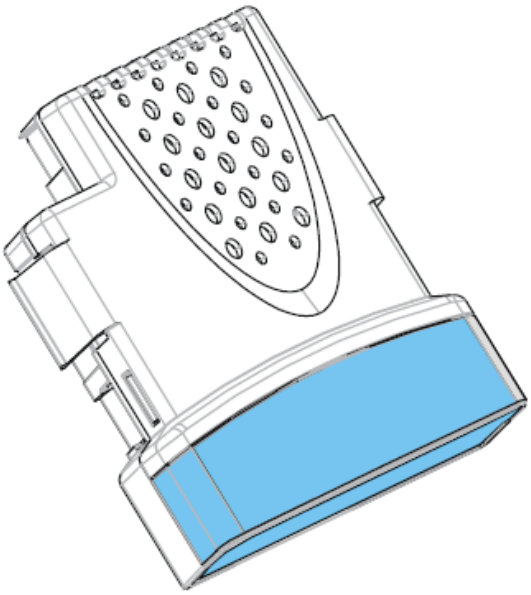

Figure 185. Solutions module (SM-Resolver)

This signal is interpreted by the drive to give rotor position and rotor speed in rad/s and rpm. Such variables can be observed on the CTsoft software as the motor operates. Speed can be taken from the drive by assigning this variable to a DAC output (Figure 186). An analogue output on the drive can be

connected to any real time platform ADC channel so servo motor speed can be used in the real time controller.

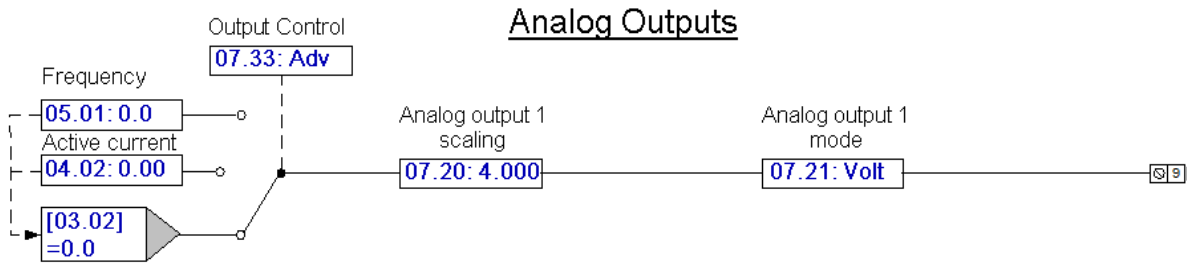

Figure 186. Connecting the speed measurement with the analogue output

5.2.3 Coupling

The servo motor is coupled to the PDD LSR through a coupling. Its commercial name is Huco Dynatork Flex M Coupling and it is shown in Figure 187.

Figure 187. Huco Dynatork Flex M Coupling

Important coupling parameters can be highlighted in Table 25. More parameters can be found in Table 28 in Appendix J.

Table 25. Coupling parameters

Parameter	Symbol	Value	Unit
Torque	$T_{coupling}$	*11.4*	*N.m*
Peak torque	$T_{coupling\_peak}$	*30*	*N.m*
Moment of inertia	$J_{coupling}$	5660×10^{-8}	$kg.m^2$
Torsional stiffness	$K_{coupling}$	*772.5*	*N.m/rad*

5.2.4 Torque transducer

To observe torque, a torque transducer is placed between the PDD and the servo motor. The RWT410/420 Series Transducer can be seen in Figure 188. The transducer is connected to the PC via a

USB connection. The readings can be available using TorqView, which is a software that can be installed and it provides an easy interface to collect measurements data.

Figure 188. RWT410/420 Series Transducer

The important element that is related to the torque transducer is its stiffness, given in Table 26.

Table 26. Transducer stiffness

Parameter	Symbol	Value	Unit
Stiffness	$K_{transducer}$	1.9	kN/m

5.2.5 Real time platform

dSPACE DS1103 is a powerful computation tool and it is used as a real-time controller. Three main relevant parts make up this efficient tool.

5.2.5.1 DS1103

It facilitates an interface with Matlab Simulink. This allows the implementation of control using Matlab Simulink, which is a user-friendly environment. All control code compiling processes are ran automatically in the background.

5.2.5.2 CLP1104 Connecter Panel

The DS1103 Connecter Panel functions as the interface between DS1103 and all other external hardware. The connector panel includes many input and output channels. However, two types of channels are relevant.

- ADC unit, which includes 20 ADC channels. Each is with a 16-bit resolution and an input voltage range of ±10 V.

- DAC unit, which includes 8 DAC channels. Each is with a 16-bit resolution and an output voltage range of ±10 V.

By using dSPACE, it is possible to send speed reference to the PDD drive and torque demand to the servo motor drive simultaneously using DAC channels shown in Figure 189.

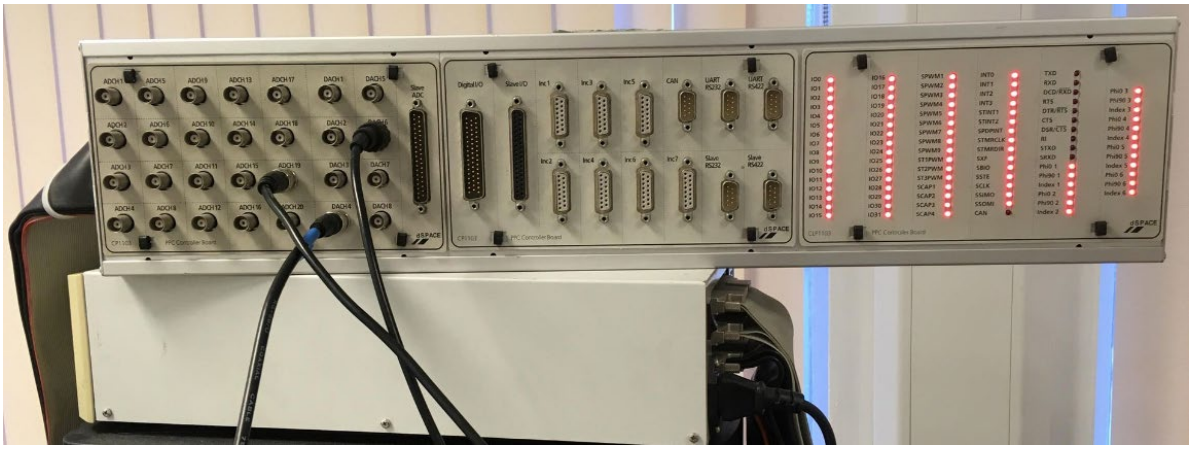

Figure 189. Connecter panel

5.2.5.3 Control desk

A software associated with the dSPACE, known as Control Desk, provides a control panel that has scopes, instruments and to allow real-time management.

5.3 Rig performance and dynamics

5.3.1 Dynamics of the laboratory test rig

As previously mentioned and also depicted in Figure 170, the test rig consists of a PDD, a servo motor which are coupled by two membrane couplings in which a torque transducer is placed in between. Figure 190 summarises the rig construction.

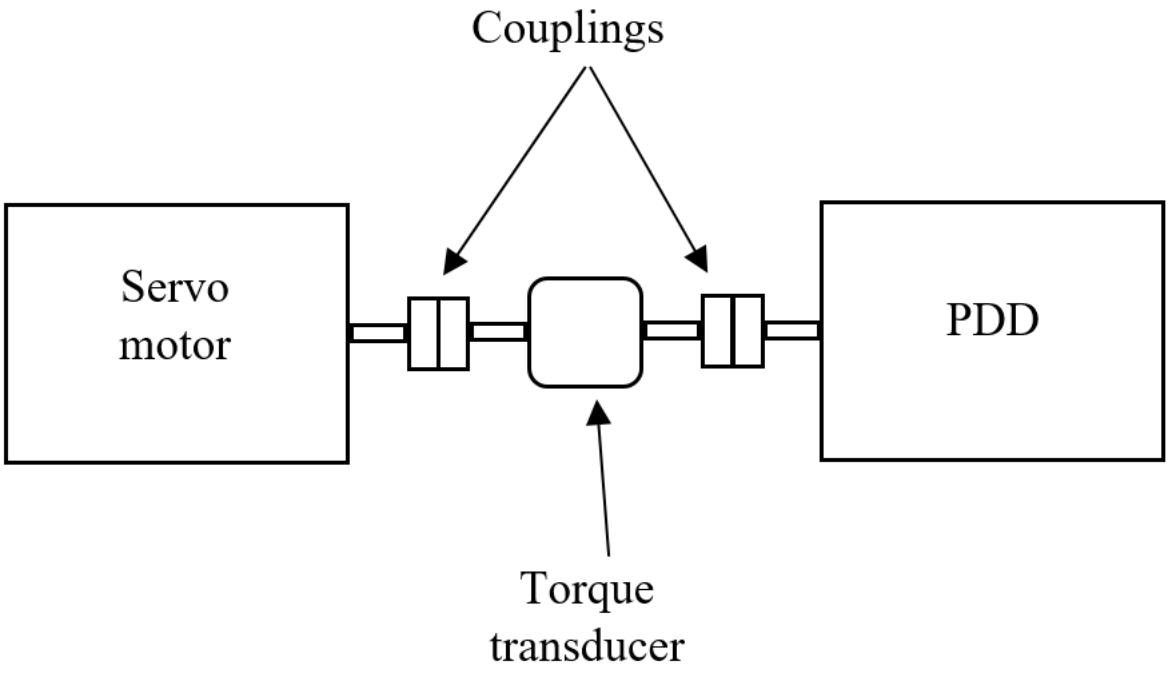

Figure 190. Schematic construction of the test rig

In Figure 190, there are elements with significant inertias; such the PDD HSR, J_{HSR}, LSR, J_{LSR}, and the servo motor, J_{servo}. In addition, other elements are of significant stiffness; such as the two membrane couplings, $K_{coupling}$, and the torque transducer, $K_{transducer}$. To estimate any dynamics which might occur from the test rig, a brief model ought to be presented, as shown in Figure 191.

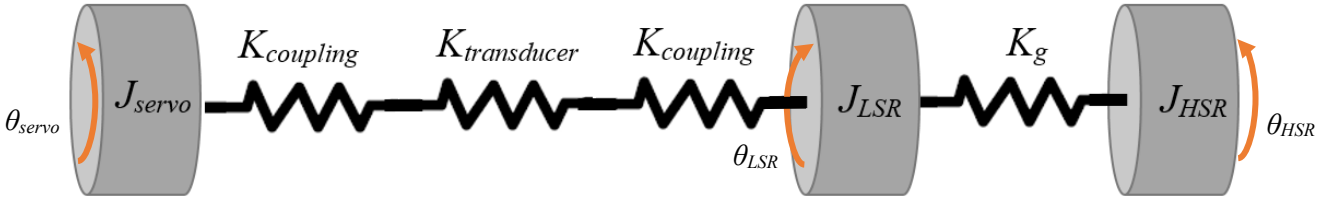

Figure 191. Mechanical model of the test rig

where θ_{servo} is the position of J_{servo}. Also, $K_{coupling}$ and $K_{transducer}$ are defined in Table 25 and Table 26, respectively.

Figure 191 can be simplified considering that the stiffnesses of couplings and transducer are connected in series and thus their sum, K_{rig}, can be calculated as shown in Equation (250).

$$K_{rig} = \frac{1}{\frac{1}{K_{coupling}} + \frac{1}{K_{transducer}} + \frac{1}{K_{coupling}}} = 321\ N/m \tag{250}$$

The more simplified model of the test rig is presented in Figure 192.

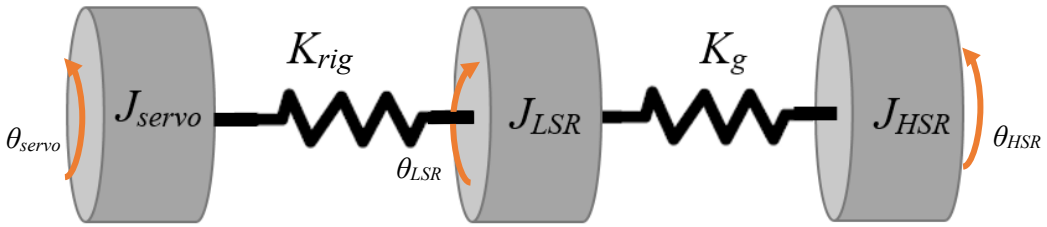

Figure 192. A more simplified mechanical model of the test rig

The model is constructed in Matlab/Simulink and Bode plot is taken from the electromagnetic torque, T_e, to the servo motor speed, ω_{servo}, as shown in Figure 193. Two frequencies are highlighted, 182 Hz is due to the PDD magnetic stiffness. This varies depending on the amount of load exerted on the machine. In the experimental results below, this frequency will turn out to be 142 Hz. The other frequency is shown to be 276 Hz, which is mainly due to the couplings between the PDD and the servo motor.

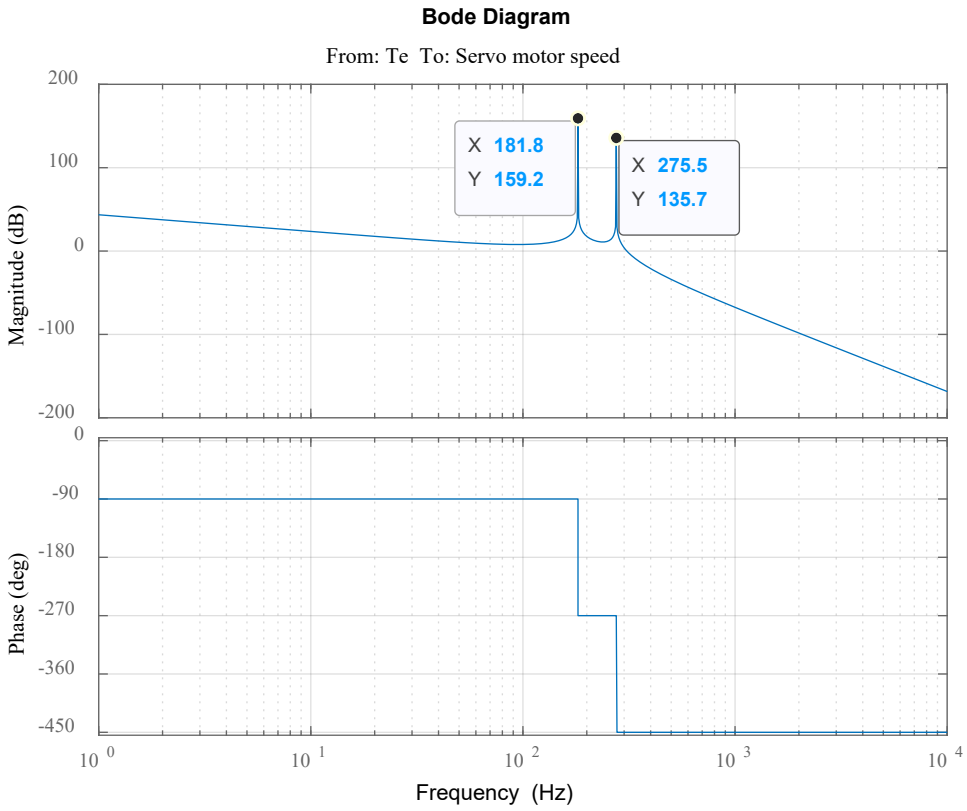

Figure 193. Frequency response of the test rig

To observe any essential dynamics, speed loop simulation is tested for the model. Speed control gains are chosen to make system unstable purposely to see how system behaves, as shown in Figure 194.

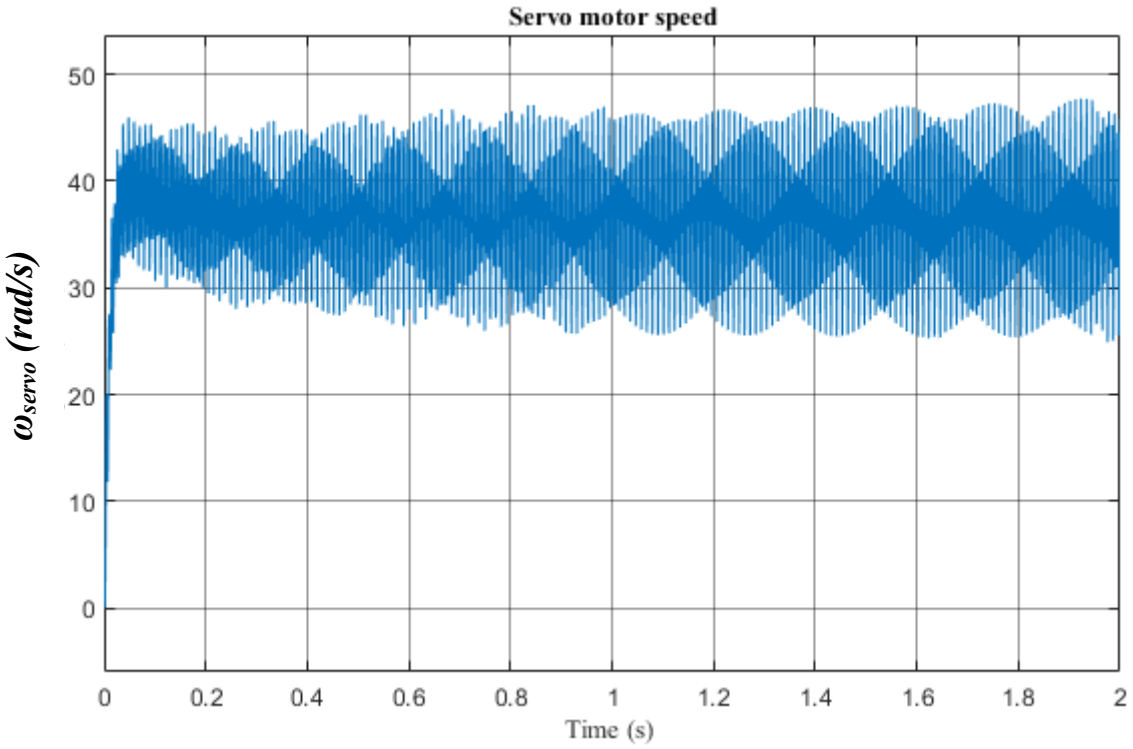

Figure 194. Servo motor speed

In Figure 194, in addition to the higher frequency oscillations, there is another small pattern of frequency that can be observed (Figure 195). It turns out to be equal to 6 Hz. This is important to highlight since this frequency will appear later during rig operation.

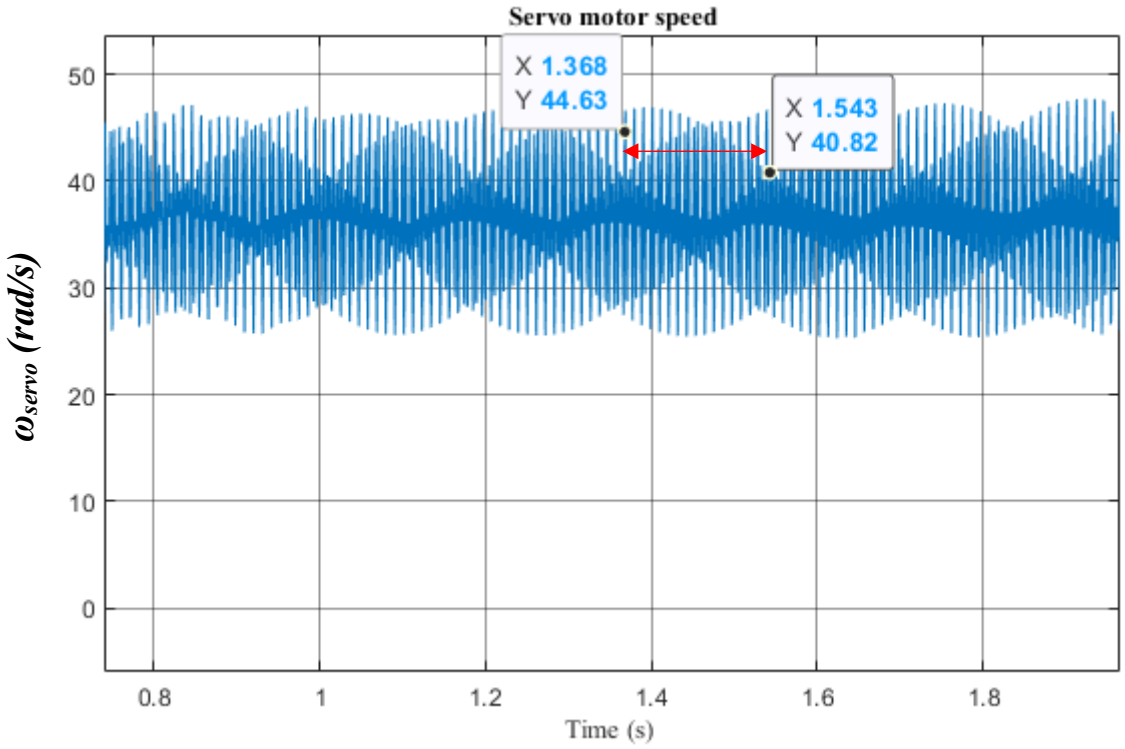

Figure 195. Servo motor speed (a frequency of 6 Hz is highlighted)

5.3.2 Performance under speed control

Speed loop performance is observed by carrying this test. PDD is operated under speed control mode. A reference step speed of 0.3 per unit, equalling 2790 rpm on the HSR side, is sent from dSPACE model to TI. While running, a step torque of 2 N.m is applied, also from dSPCASE, by the servo motor. The torque transducer measurements of torque are shown. Additionally, the servo motor measured speed, which is fed back to dSPACE is also shown. Two control methods are used, conventional PI and also IP control. Beneath each figure in this subsection, there is a figure taken by model simulation to prove matching.

5.3.2.1 Conventional PI

A speed command is set to 0.3 per unit. The control scheme in this case is the conventional PI speed control. The measured speed signal is shown in Figure 196. Notice there is a noticeable dip at instant 3.2s. This is the moment of applying a 2 N.m torque by the servo motor. Further, there is a little spike at instant 5.7s. This is the moment of torque removal.

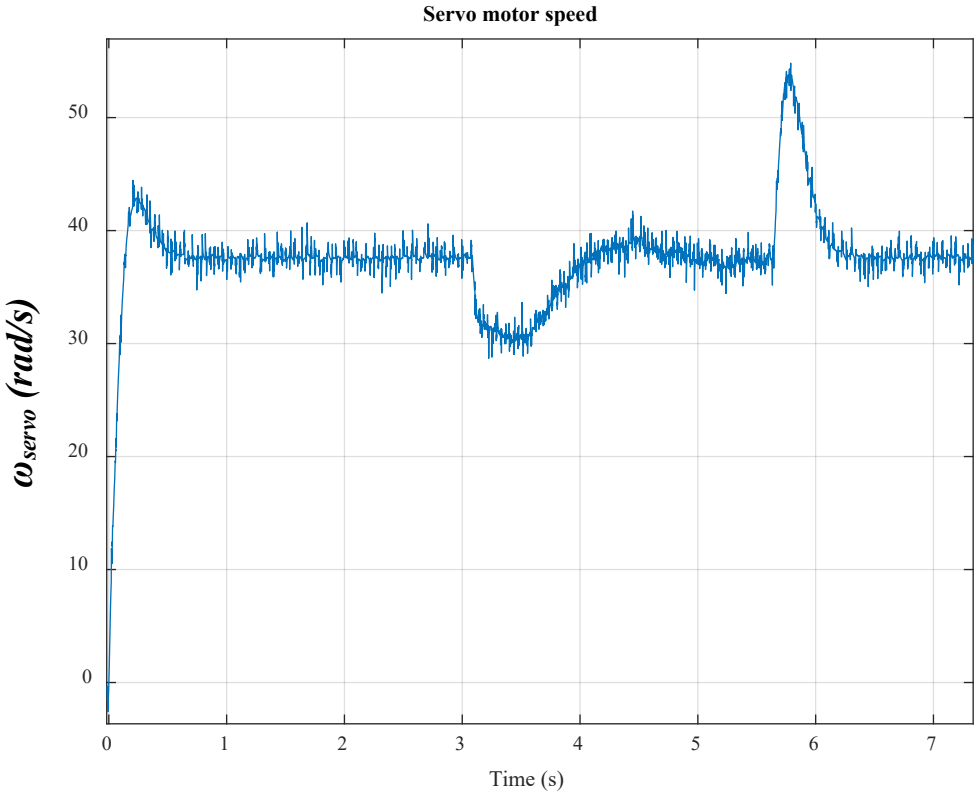

Figure 196. Servo motor (Emerson) speed [speed loop BW = 2.7 Hz]

Simulation is carried out to show similar results shown in Figure 196. It can be seen in Figure 197 that the transfer function shows more oscillatory LSR speed due to lack of damping; unlike the test rig.

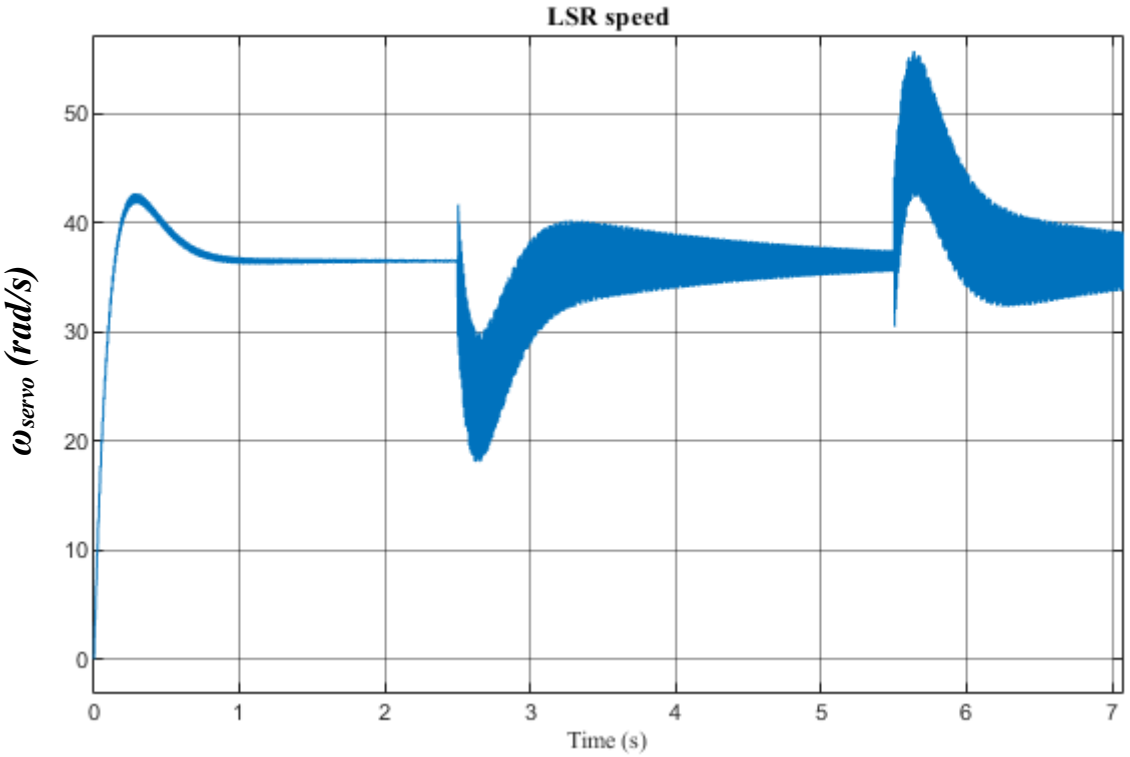

Figure 197. Servo motor speed (simulation)

Figure 198 and Figure 199 show the experimental and simulation speeds respectively. Both show the system response to a step speed command. It is clear that both show acceptable degree of matching.

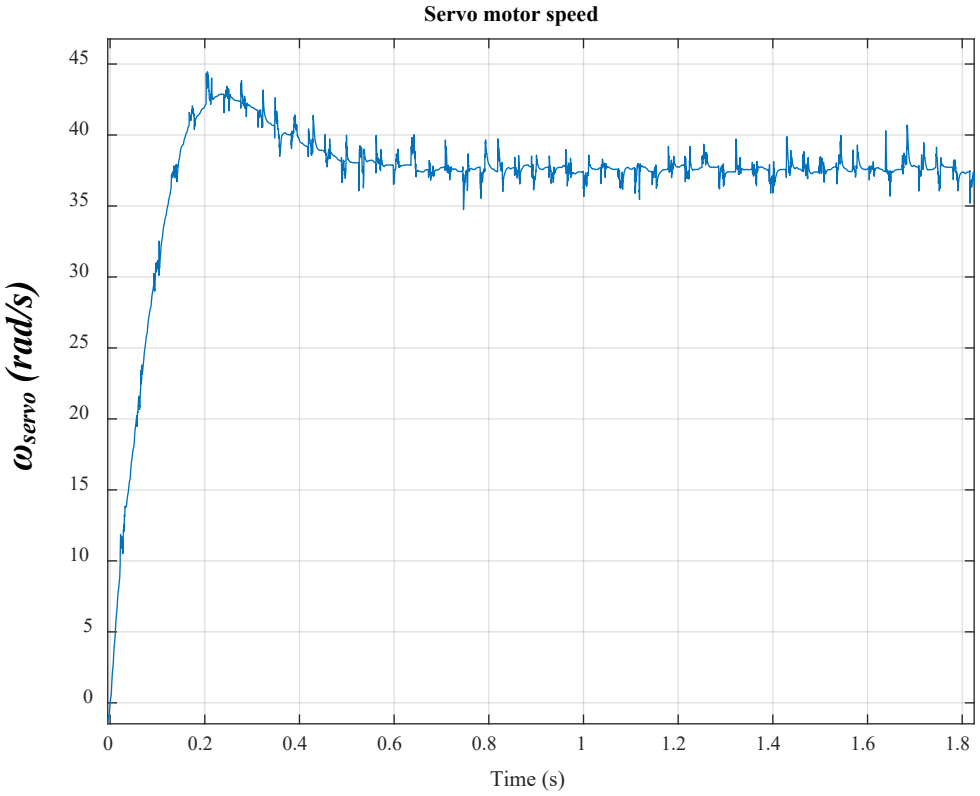

Figure 198. Servo motor speed [speed loop BW = 2.7 Hz]

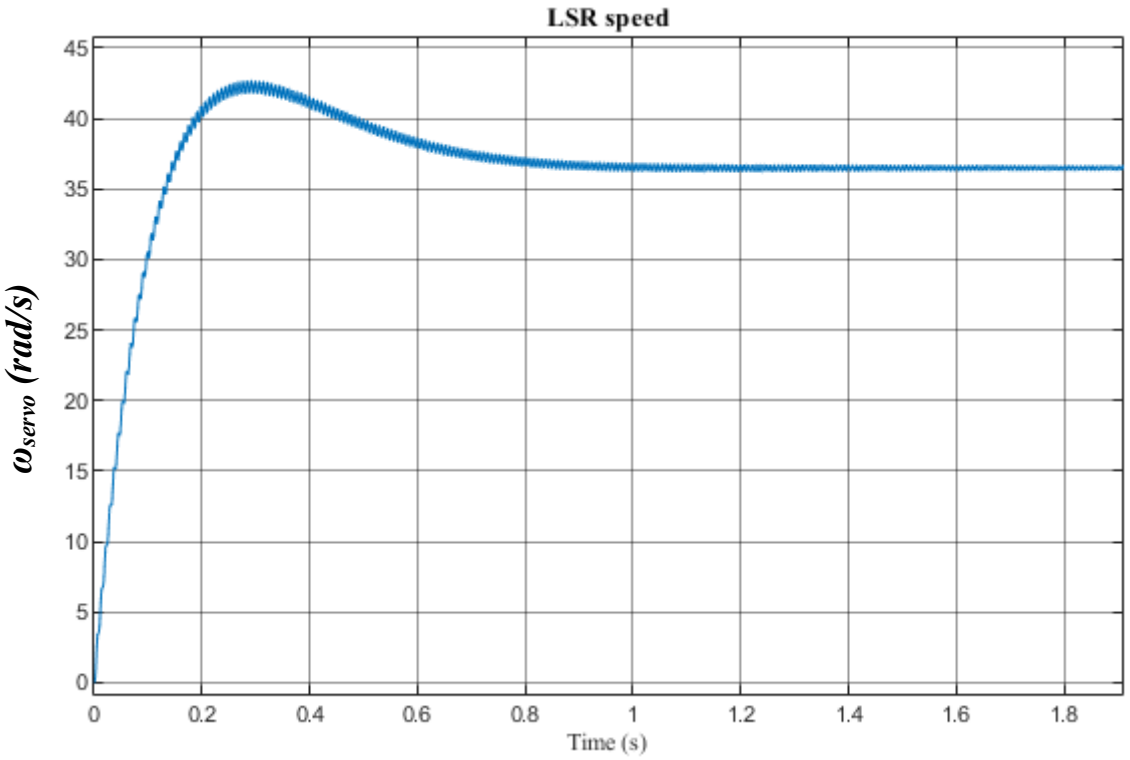

Figure 199. Servo motor speed (simulation)

The torque applied by the servo motor is commanded from dSPACE as a torque step. The torque applied is measured by the torque transducer and shown in Figure 200.

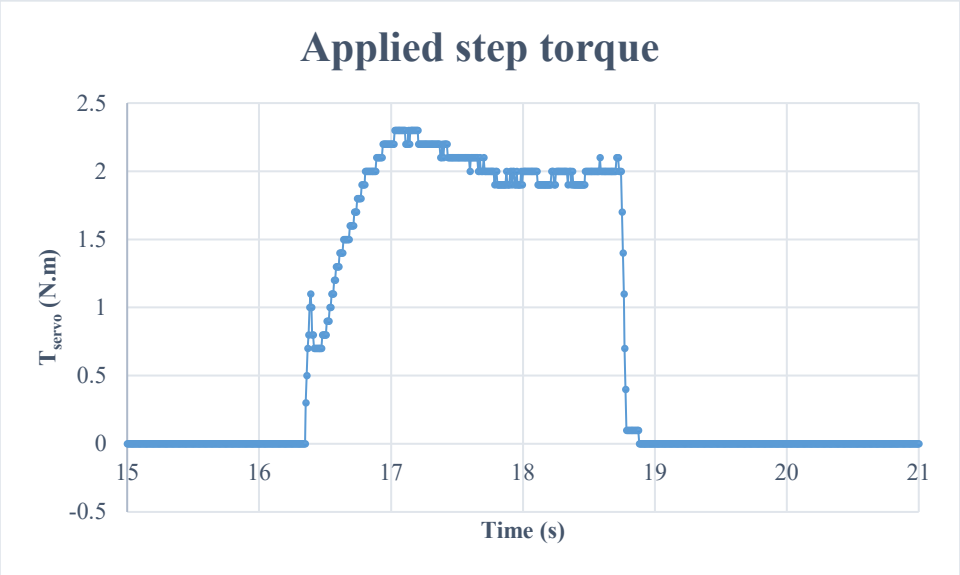

Figure 200. A step torque applied by the servo motor

5.3.2.2 IP speed control

A speed command is set to 0.3 per unit. The control scheme in this case is the IP speed control, which is explained in Chapter 2 and Chapter 4. The measured speed signal is shown in Figure 201. Notice there is a small dip at instant 3.8s. This is the moment of applying a 2 N.m torque by the servo motor. Further, there is a little spike at instant 7s. This is the moment of torque removal. Figure 202 shows the simulation figure, which shows acceptable agreement with Figure 201. In addition, Figure 203 and Figure 204 show the speed response to a step speed command.

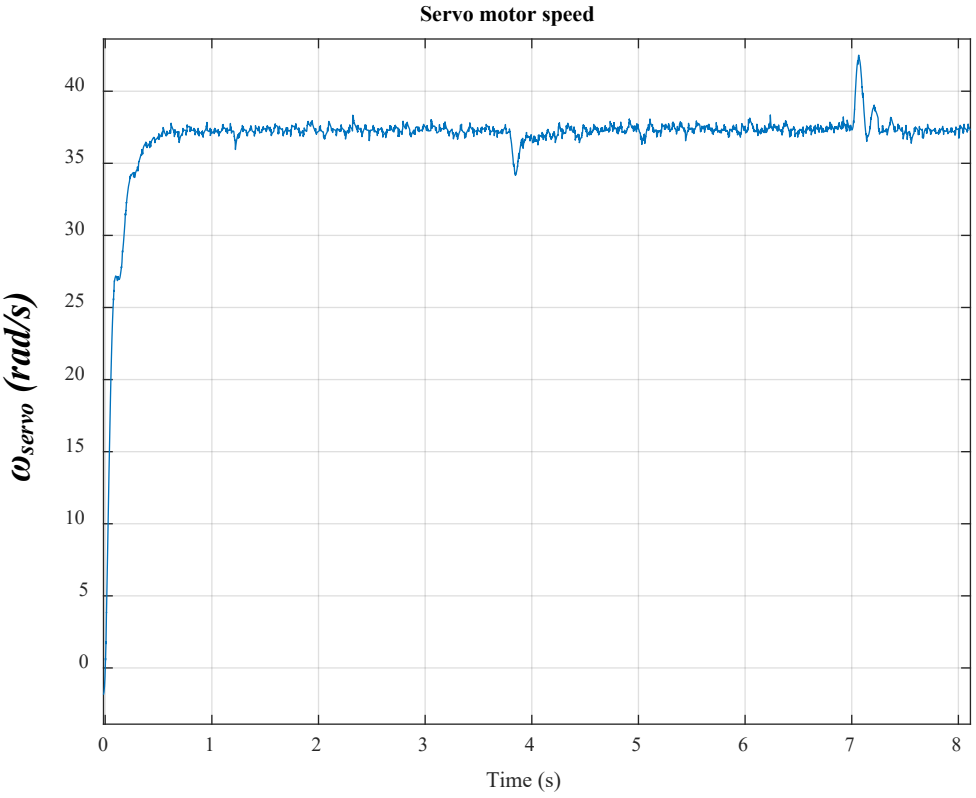

Figure 201. Servo motor speed [speed loop BW = 1.5 Hz]

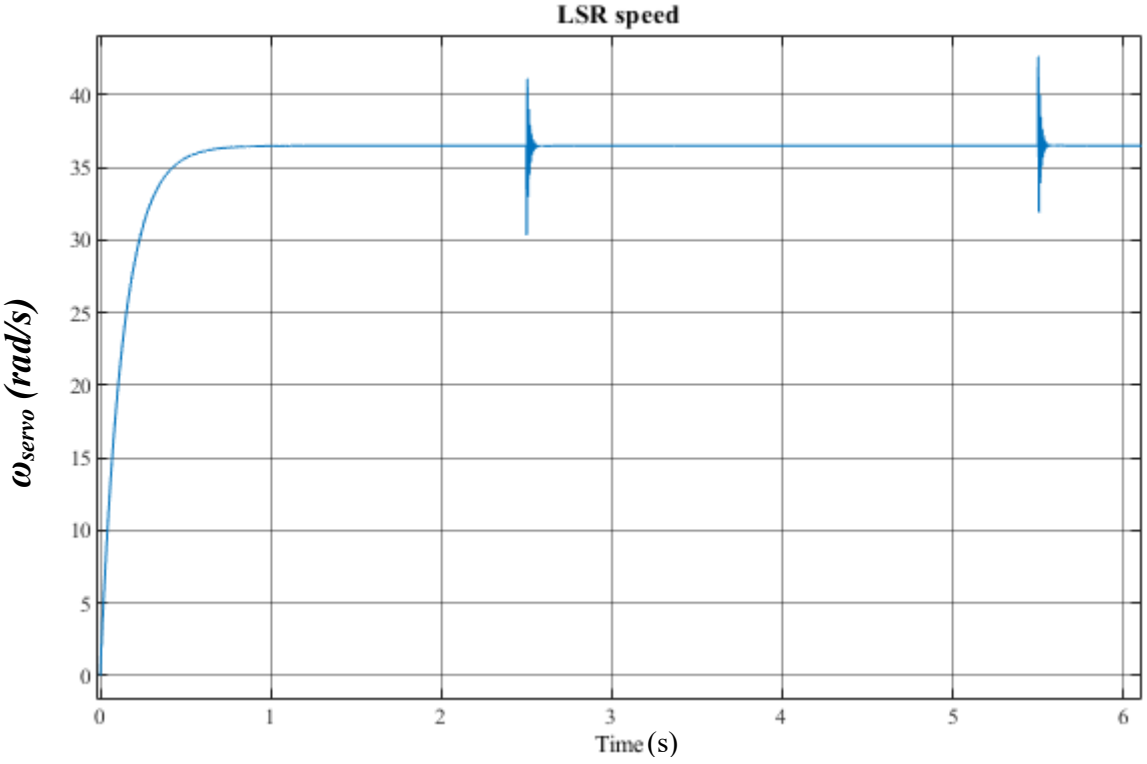

Figure 202. Servo motor speed (simulation)

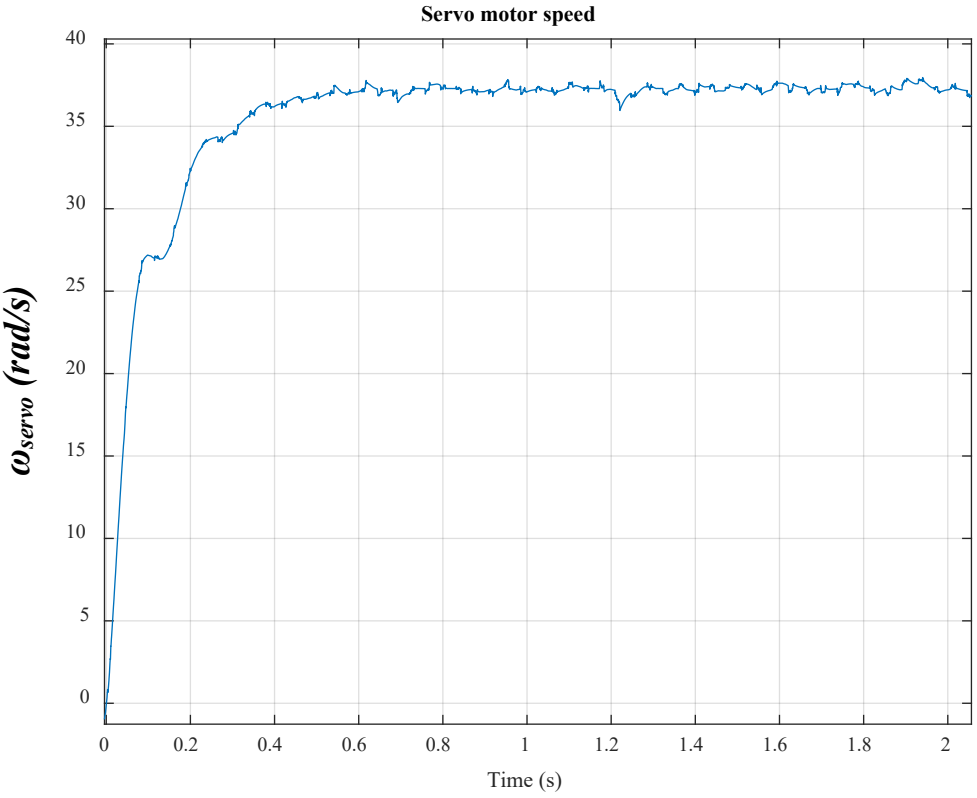

Figure 203. Servo motor speed [speed loop BW = 1.5 Hz]

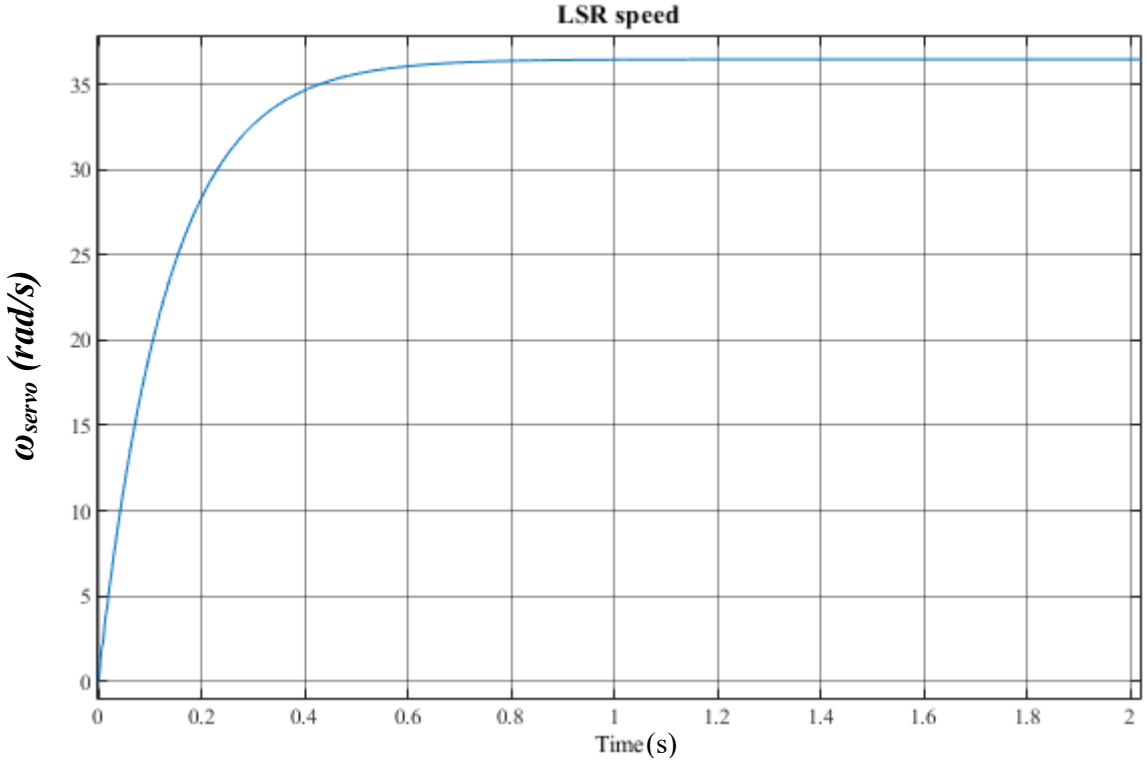

Figure 204. Servo motor speed (simulation)

The torque applied by the servo motor is commanded from dSPACE as a torque step. The torque applied is measured by the torque transducer and shown in Figure 205.

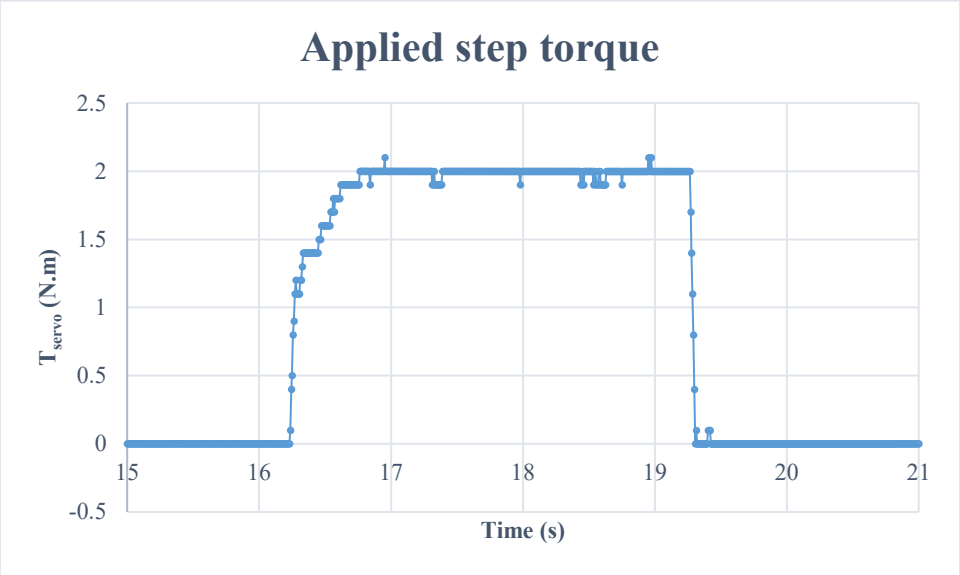

Figure 205. A step torque applied by the servo motor

Phase A winding current, i_a, is measured using a current probe, as shown in Figure 206. The current probe unit used is 5 A/V.

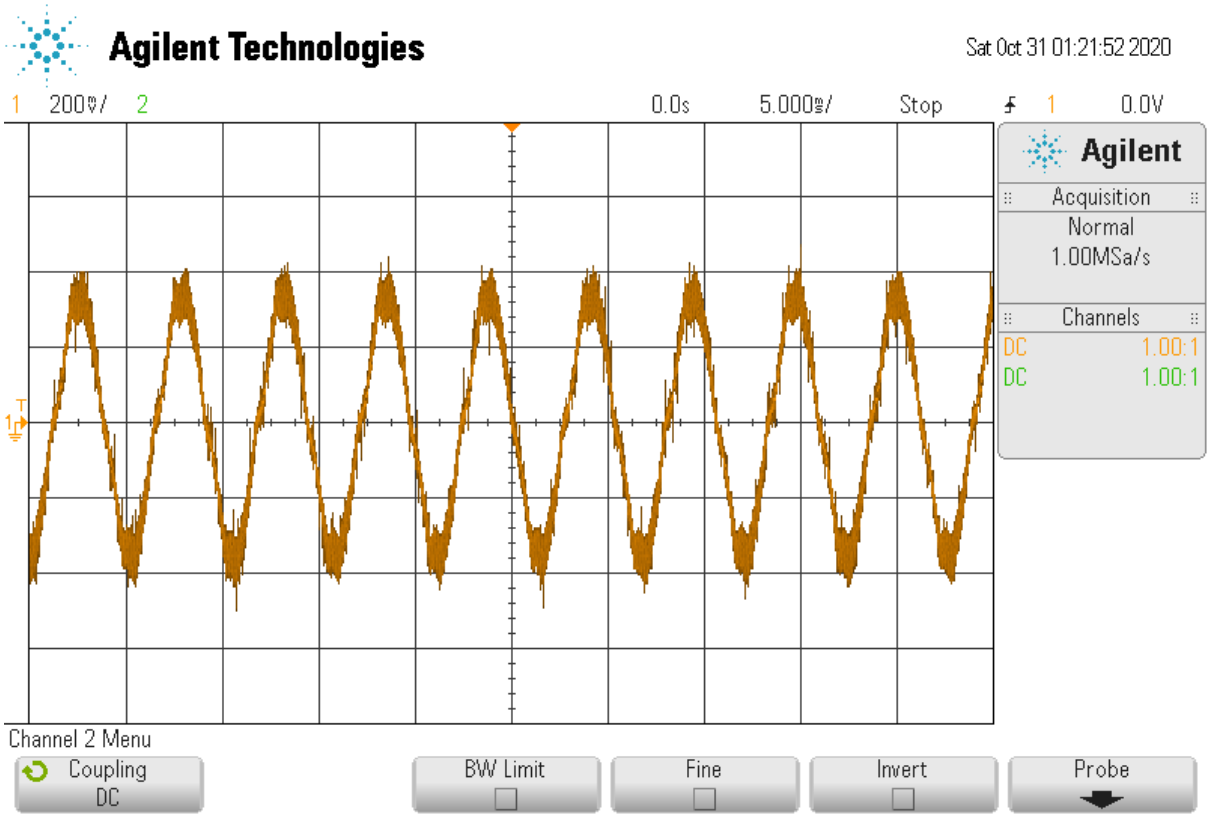

Figure 206. Phase A winding current in a form of voltage [current probe]

To obtain phase A current in Amperes, data in Figure 206 is multiplied by 5, as shown in Figure 207.

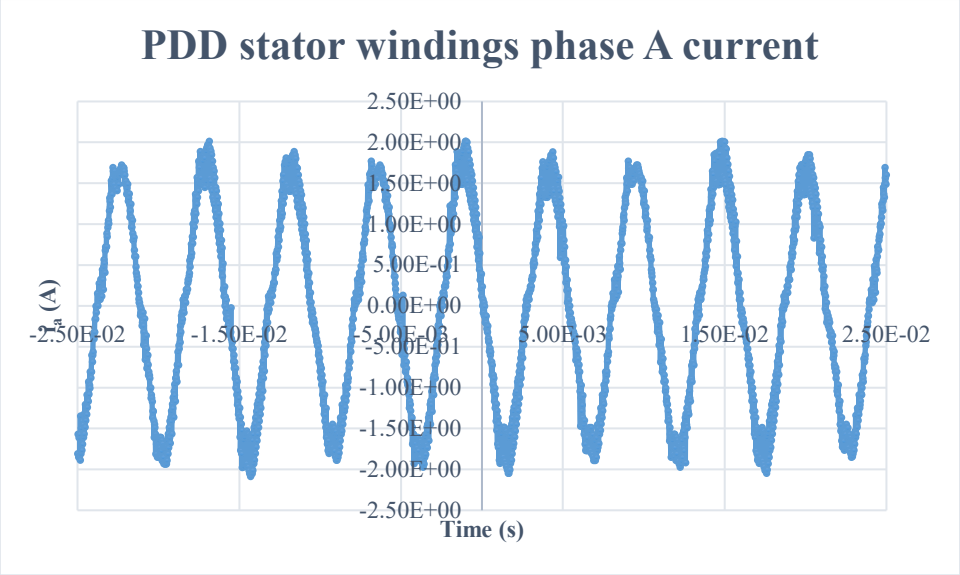

Figure 207. PDD stator windings phase A current [current probe]

5.3.3 PDD machine constants calculation

The peak current, I_p, is around 1.75 A, which corresponds to 2 N.m of demanded torque. This is expected since the torque constant, K_t, given is equal to 0.147 N.m/A.

$$K_t = \frac{T_e}{i_q} = \frac{T_e}{I_p} = \frac{\frac{T_{LSR}}{G_r}}{I_p} = \frac{\frac{2}{7.75}}{1.75} = 0.147\ N.m/A \tag{251}$$

Another torque constant, K_{t_LSR}, is also given to reflect the ratio between the output torque that the PDD can provide, T_{LSR}, to the amount of current supplied, I_p, as follow,

$$K_{t\_LSR} = \frac{T_{LSR}}{i_q} = \frac{T_{LSR}}{I_p} = \frac{2\ N.m}{1.75\ A} = 1.143\ N.m/A \tag{252}$$

The torque constant, K_t, is related to the PDD back EMF constant, K_e, through Equation (253).

$$K_t = \frac{3}{2}K_e \rightarrow K_e = 0.098\ V/rad/s \tag{253}$$

If the PDD LSR is mechanically driven with a speed of 150 rpm (15.71 rad/s), PDD is used as a generator and the HSR speed, ω_{HSR}, is given by,

$$\omega_{HSR} = G_r\omega_{LSR} = 7.75 \times 15.71 = 121.74\ rad.s^{-1} \tag{254}$$

As a result, a voltage is produced at the PDD stator windings (Figure 208). The back-emf constant, K_e, can be obtained using Equation (255).

$$K_e = \frac{E_p}{\omega_{HSR}} = \frac{12}{121.74} = 0.099\, V/rad/s \tag{255}$$

The result in Equation (255) gives the same K_e obtained in Equation (253), using the PDD torques. This confirms the calculations and the acceptable performance of the rig.

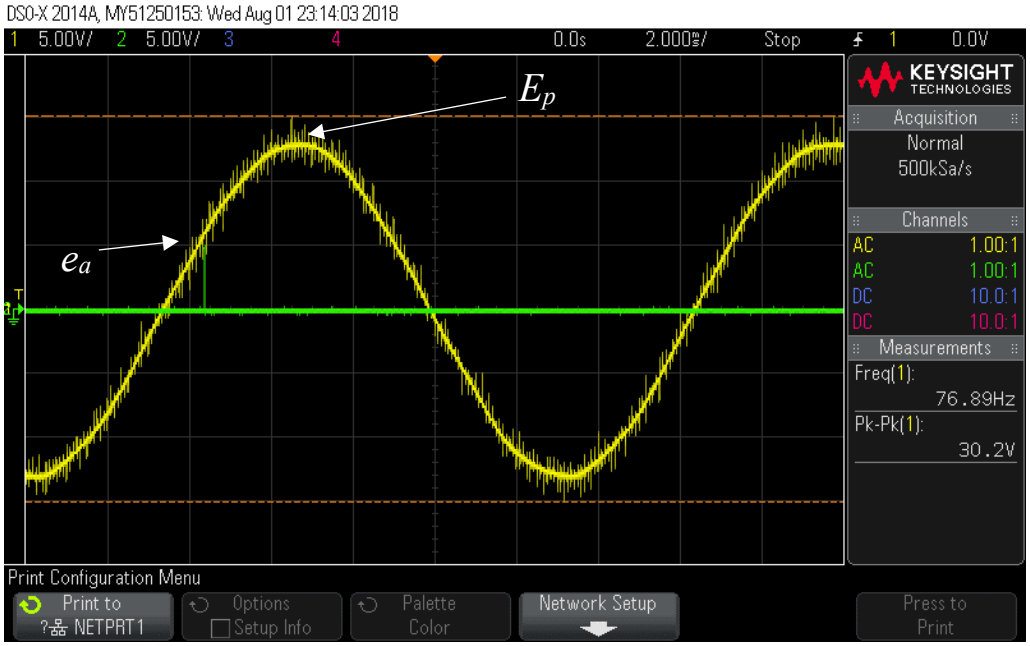

Figure 208. Stator phase A voltage

5.4 Implementing of HIL technique

The PDD machine represents the machine driving the ball-screw. The servo motor drive is set to emulate the behaviour of the ball-screw assembly and aerodynamic load according to a control signal from dSPACE (RTP). Such torque command signal is a function of load position, as explained in Chapter 2. PDD position control is set in the dSPACE and based on that a speed command is sent to PDD drive (Equation (243) to Equation (247)). The current and speed controller of the PDD are performed on the Texas Instrument kit. So, the servo motor operates under torque control mode whereas PDD operates under speed control mode, as shown in Figure 209.

In this set up, the PDD LSR is assumed to be perfectly coupled with the servo machine shaft. The sum of both inertias, J_{rig}, is given in Equation (256).

$$J_{rig} = J_{LSR} + J_{servo} = 3.54 \times 10^{-4} \tag{256}$$

Therefore,

$$\theta_{rig} = \theta_{LSR} = \theta_{servo} \tag{257}$$

where θ_{rig} is the position of J_{rig}. Also,

$$\omega_{rig} = \omega_{LSR} = \omega_{servo} \tag{258}$$

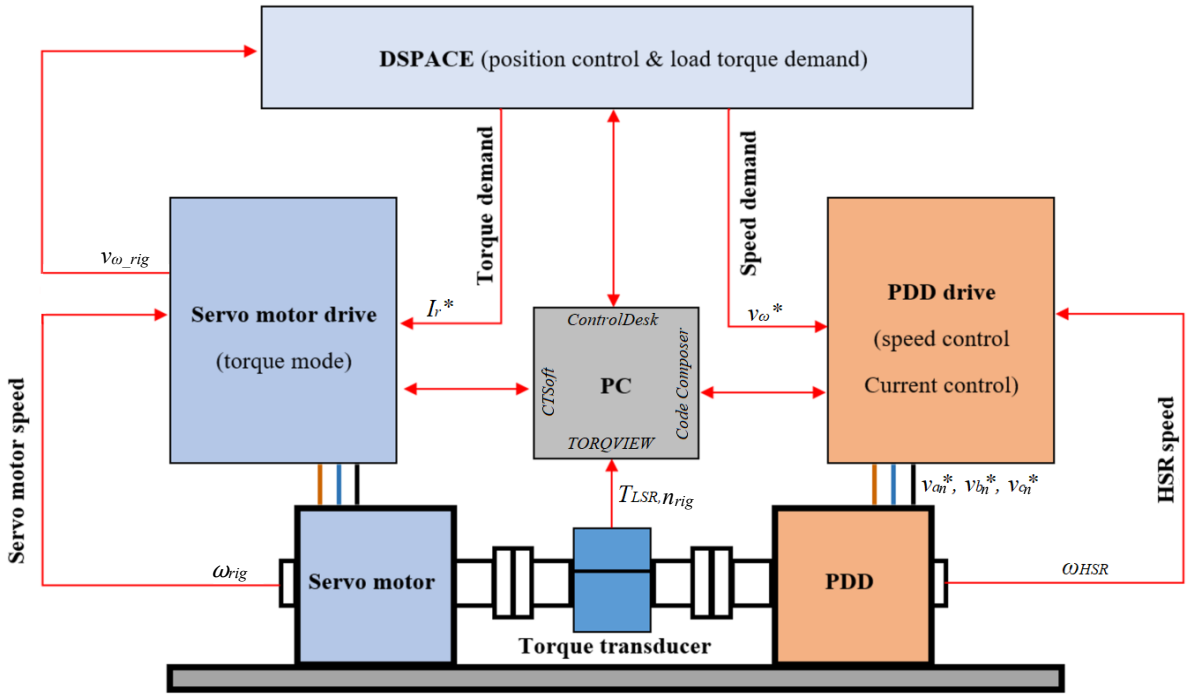

Figure 209. Schematic diagram of the HIL technique

Note: symbols are defined in the table of notation.

Matlab Simulink is used to develop the model control. Figure 210 details how the three-degree of freedom model is implemented using dSPACE. It is evident that there is only one input to the model and two outputs from the model. The only input is the servo motor speed. The first output is the speed demand to the PDD drive whereas the second output is the torque command to the servo drive. This is because, as mentioned earlier, PDD operates under speed control mode while servo motor operates under torque control mode. It is worth mentioning that the torque command is sent to the drive as i_q current demand and it is sampled with a frequency of 4000 Hz.

Further, any signal sent out of the model, using ADC channel, has to be multiplied by 0.1, which is a gain that is part of the dSPACE setup. Also any signal that is sent to the model, using DAC channel, has to be multiplied by 10. Both gains are highlighted in amber in Figure 210.

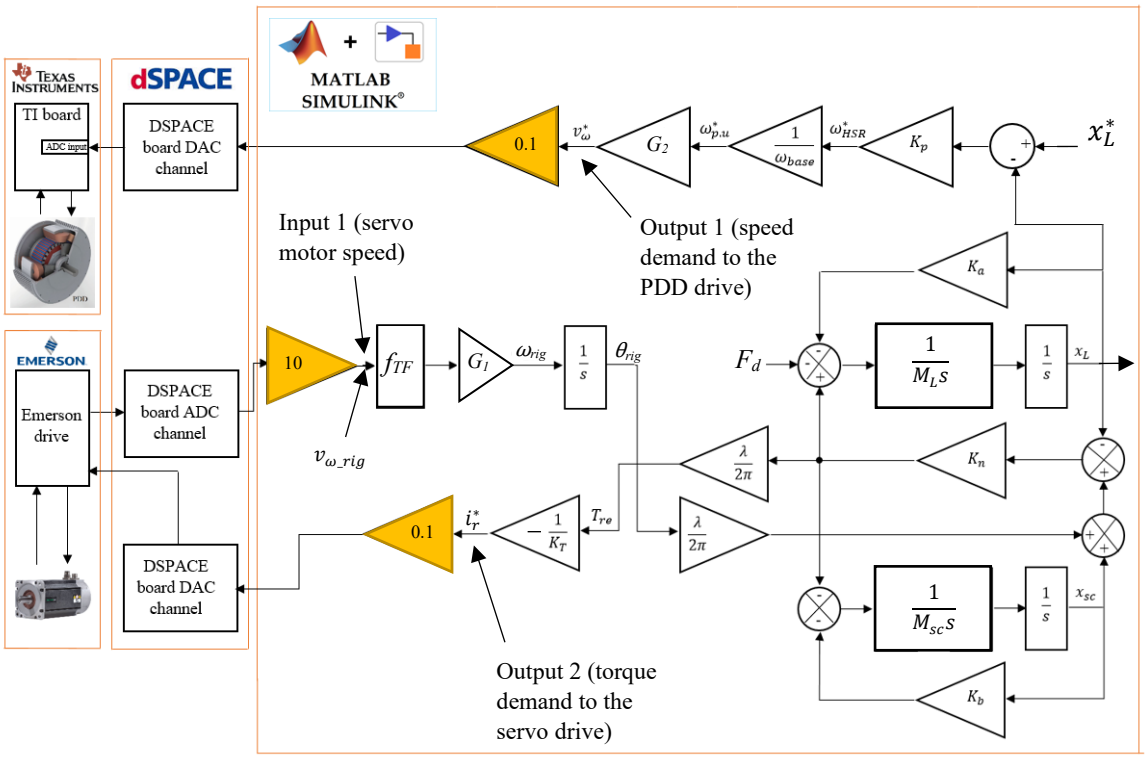

Figure 210. Implementation of the three-DOF model in dSPACE

where ω_{base} is the PDD base speed, ω_{HSR}^* is the HSR mechanical speed demand, $\omega_{p.u.}^*$ is per unit speed demand, v_ω^* is voltage representing the HSR speed demand, T_{re} is reaction torque signal of the screw-load on the PDD and it is actually the torque demand signal, K_T is servo machine torque constant, ω_{rig} is the mechanical speed of J_{rig}, x_L^* is load axial position demand, i_r^* is current demand signal to the servo drive, v_{ω_rig} is voltage representing ω_{rig}, G_1 is the gain used to transfer to v_{ω_rig} to ω_{rig}, and f_{TF} is the transfer of the filter used given in Equation (263).

The equivalent load inertia,J_L, seen by the PDD LSR is equal to 1.88×10^{-5} kg.m^2. Also, the ball-screw inertia (J_{sc}) is equal to 2.44×10^{-5} kg.m^2. The sum of such inertias, J_R, is:

$$J_R = J_{LSR} + J_{sc} = 4.32 \times 10^{-5}\ kg.m^2 \tag{259}$$

On the other hand, the servo motor inertia, J_{servo}, alone is equal to 2.46×10^{-4} kg.m^2. So the rig inertia, J_{rig}, is equal to 3.54×10^{-4} kg.m^2 (Equation (256)). This makes the system of the case study, which is the business jet system, have a considerably lower inertia than that of the laboratory test rig, which is the system used in the laboratory to validate findings. More quantitatively, the business jet system's inertia is equal to 18% of that of the laboratory system's inertia. Therefore, the laboratory test rig is expected to have significantly higher damping than the system of the case study.

Furthermore, in analysing the actuation system structure resonance in Chapter 2, it is clarified that f_1 occurs due to aerodynamic stiffness and it can be analytically calculated using Equation (260).

$$f_1 = \frac{1}{2\pi}\sqrt{\frac{K_a}{M_L + \frac{J_{sc}}{\gamma^2} + \frac{J_{LSR}}{\gamma^2}}} = \frac{1}{2\pi}\sqrt{\frac{K_a}{M_L + \frac{J_R}{\gamma^2}}} = 4.37\ Hz \tag{260}$$

In the case of the experimental test rig, the inertias will be those of LSR, J_{LSR}, and the servo motor, J_{servo}. Consequently, f_1 will drop to 2.6 Hz, as shown in Equation (261).

$$f_{1\_rig} = \frac{1}{2\pi}\sqrt{\frac{K_a}{M_L + \frac{J_{servo}}{\gamma^2} + \frac{J_{LSR}}{\gamma^2}}} = \frac{1}{2\pi}\sqrt{\frac{K_a}{M_L + \frac{J_{rig}}{\gamma^2}}} = 2.6\ Hz \tag{261}$$

5.4.1 Input 1 (servo motor speed)

The resolver on the servo motor produces a signal that goes to Emerson drive through a resolver card, which converts this analogue signal to a digital one. Thus, it is possible for the servo drive to show speed and position on the CTsoft software. Initially, it is crucial to identify the parameter to be fed back. It is chosen to be the measured speed in rpm (parameter 3.02 in CTsoft software (Figure 186)). The measured speed signal is taken out of the drive using a DAC output. It is important to calibrate such speed with respect to output voltage, as shown in Figure 211, which shows that the voltage is related to the speed according to Equation (262).

$$v_{\omega\_rig} = 0.0066 n_{rig} \tag{262}$$

where, n_{rig} is the speed of PDD LSR, which is mechanically coupled with the servo machine shaft.

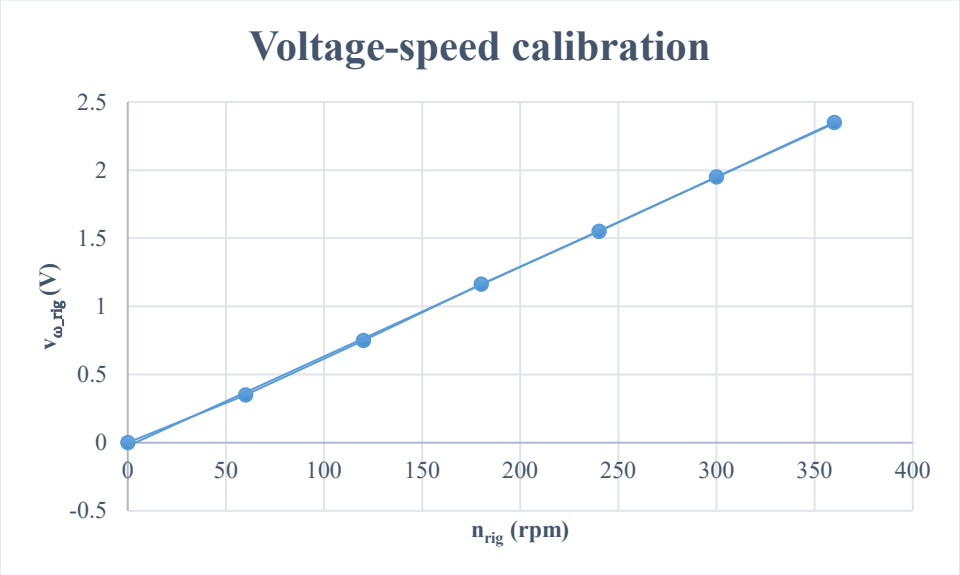

Figure 211. Voltage output with respect to speed

This signal is connected to the dSPACE board through an ADC channel. The signal is multiplied by 10 as required by the dSPACE; a signal coming in must multiplied by 10 whereas a signal coming out is divided by 10.

For various reasons, this signal is associated with noise, which can be cleaned using a filter. Equation (263) is the transfer function of the first order filter used.

$$f_{TF} = \frac{1}{\frac{1}{2\pi f_{co}} s + 1} \tag{263}$$

The voltage signal entering the dSPACE is multiplied by a factor (see Figure 211 and Equation (262)) to reproduce the speed in rpm, as shown in Equation (264).

$$n_{rig} = \frac{1}{0.0066} v_{\omega\_rig} \tag{264}$$

To obtain speed in rad/s, the known ratio can be used. G_1 can be shown in Equation (265).

$$G_1 = \frac{1}{0.0066} \times \frac{2\pi}{60} \tag{265}$$

Therefore, ω_{rig} can be obtained using the following equation.

$$\omega_{rig} = G_1 v_{\omega\_rig} \tag{266}$$

This signal is then integrated to obtain LSR angular position, θ_{LSR}, which represents the angular position of the rotary parts, θ_R, as explained in the three-degree of freedom model described in Chapter 2.

5.4.2 Output 1 (speed demand to the PDD drive)

Position control is carried out within Simulink and as a result a speed command is produced. The speed demand is divided by the base speed to produce the equivalent per unit demand value, as shown in Equation (267).

$$\omega^*_{p.u.} = \frac{\omega_{ref}}{9300 \times \frac{2\pi}{60}} \tag{267}$$

The per unit speed command signal is then converted into a voltage signal. TI board provides ADC inputs where maximum input voltage can be up to 3.3 V. 3 V is decided to represent the 1 per unit speed command. For this reason, the per unit demand speed is divided by 0.33, as shown in Equation (268).

$$v^*_{\omega} = \frac{\omega^*_{p.u.}}{0.333} \tag{268}$$

The voltage signal needs to be divided by 10 as required by dSPACE.

5.4.3 Output 2 (torque demand to the servo drive)

After position control is performed and servo angular position is obtained, the model will produce a reaction torque, T_{re}. This torque emulates the impact of the ball-screw and aerodynamic load on the PDD LSR. However, the way the control scheme in CTsoft is set up is that torque demand is inputted in a form of current demand. For this reason, this reaction torque is divided by the servo motor torque constant, which is *1.6 N.m/A*, to produce the current command.

$$i_r^* = \frac{T_{re}}{1.6} \tag{269}$$

Additionally, the current demand in CTsoft is set up in a form of a percentage of the rated current, according to Equation (270).

$$i_{\%} = \frac{i_r^* \times 100}{I_{servo\_rated}} = \frac{i_r^* \times 100}{5.7} \tag{270}$$

where I_{servo_rated} is the rated current of the servo machine.

In response of the torque demand, which is in a form of current demand, the active current is measured by the Emerson drive and can be shown in the CTsoft software (Figure 182), which can be predicted as shown in Equation (271).

$$i_{active} = \frac{i_{\%} \times I_{servo\_rated}}{100} \tag{271}$$

The torque applied by the servo motor hence is;

$$T_{servo} = K_T \times i_{active} = 1.6 i_{active} \tag{272}$$

This torque is also measured by the torque transducer, which shows great matching with expectations (Figure 200 and Figure 205). Finally, a gain of 0.1 is needed as a requirement of dSPACE.

5.5 Experimental results

In this section, The PDD is tested first to show responses to speed demands. Also, torque loads are applied to show PDD response to torque. Responses are shown under PI speed control and IP speed control. After testing the PDD independently, the whole system is then examined. Similar tests to those performed in Chapter 2 and 4 are carried out experimentally. The current loop bandwidth is chosen to be 500 Hz whereas the speed loop bandwidth is varied and it is specified in the beginning of each test.

Similar tests to those performed by simulation in Chapters 2 and 4 are carried out experimentally. Two models of the actuator are used; the oversimplified one-DOF model and the three-DOF model. Both models are implemented by the emulator. Different load conditions are tested to see the response of the inter-connected system to various loading conditions. Position reference demands are set in forms of step demands. The chosen position loop bandwidth is 0.4 Hz.

5.5.1 Position control with no external disturbance

5.5.1.1 One-DOF model (simplified model)

The first test in this section is carried out by using the single inertia model. In chapter 2, it is mentioned that for this particular model, the following equation is true.

$$\theta_{LSR} = \theta_{sc} \tag{273}$$

The way the single inertia model is impeletened using the HIL technique is shown in Figure 212.

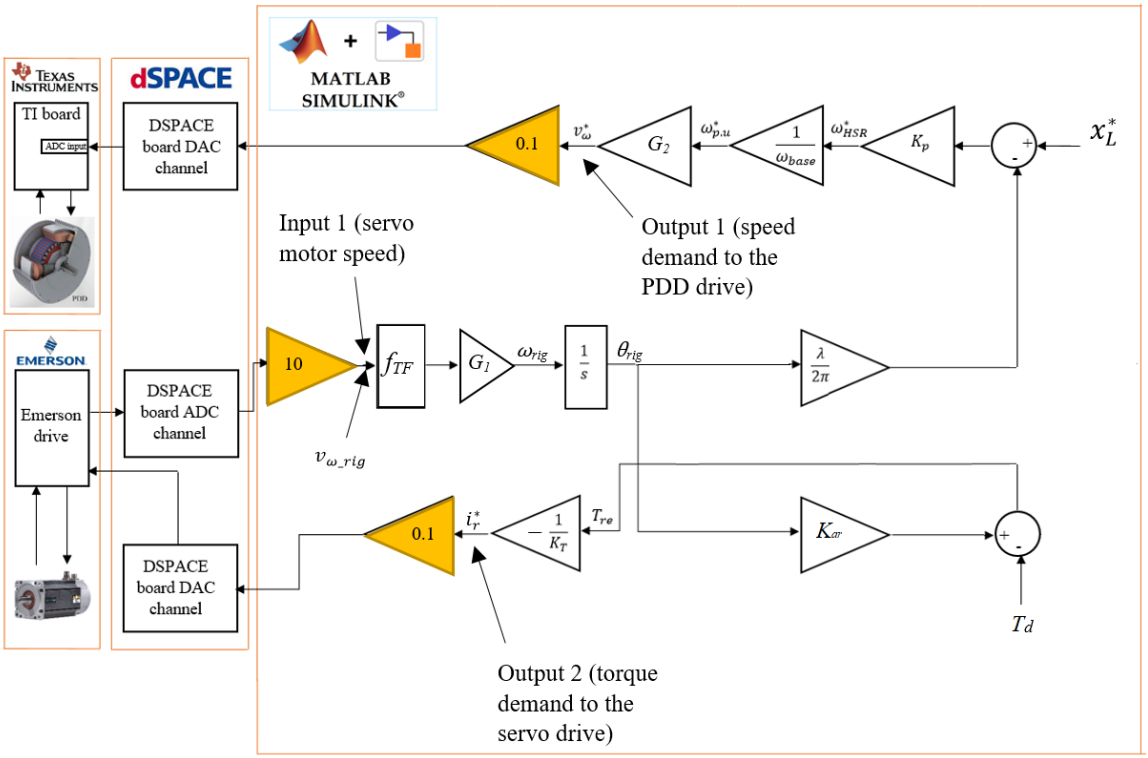

Figure 212. Implementation of the single inertia model in dSPACE

A step rotary load position demand is set to 25 rad. This is equivalent to just less than 4 rotations of the screw. Figure 213 shows the model rotary position.

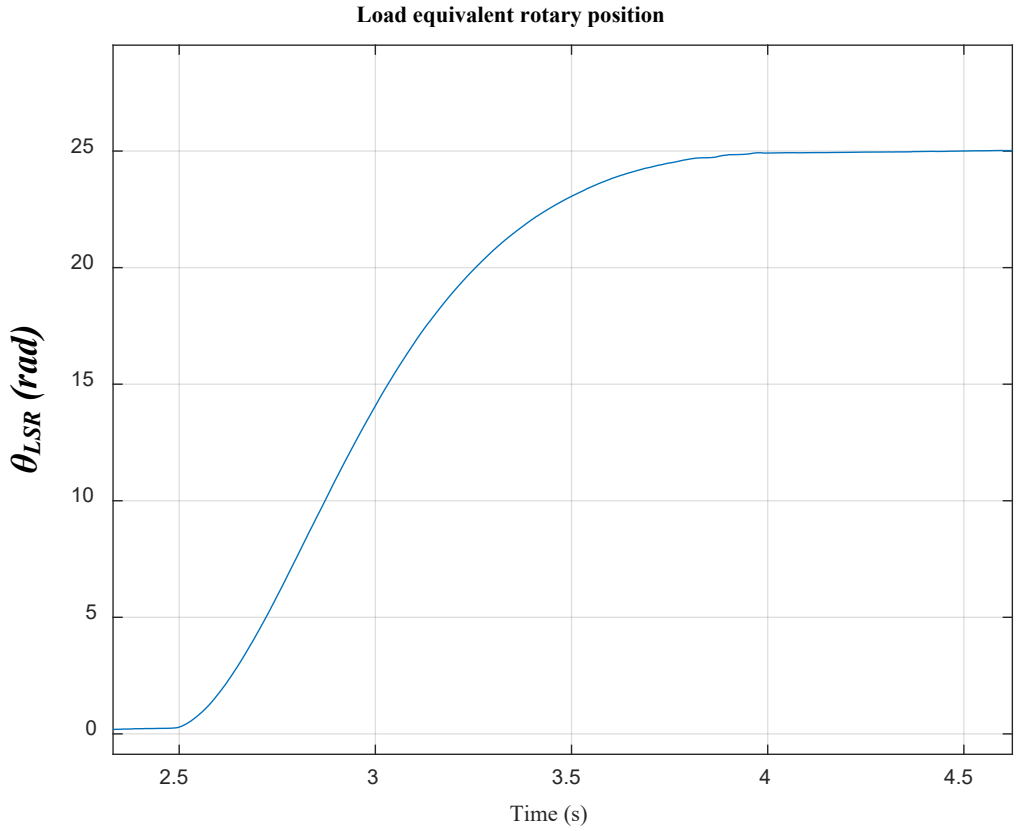

Figure 213. Rotary position

No oscillations can be seen in Figure 213. Figure 213 is magnified to ensure whether any oscillations can be seen, which is proved by Figure 214.

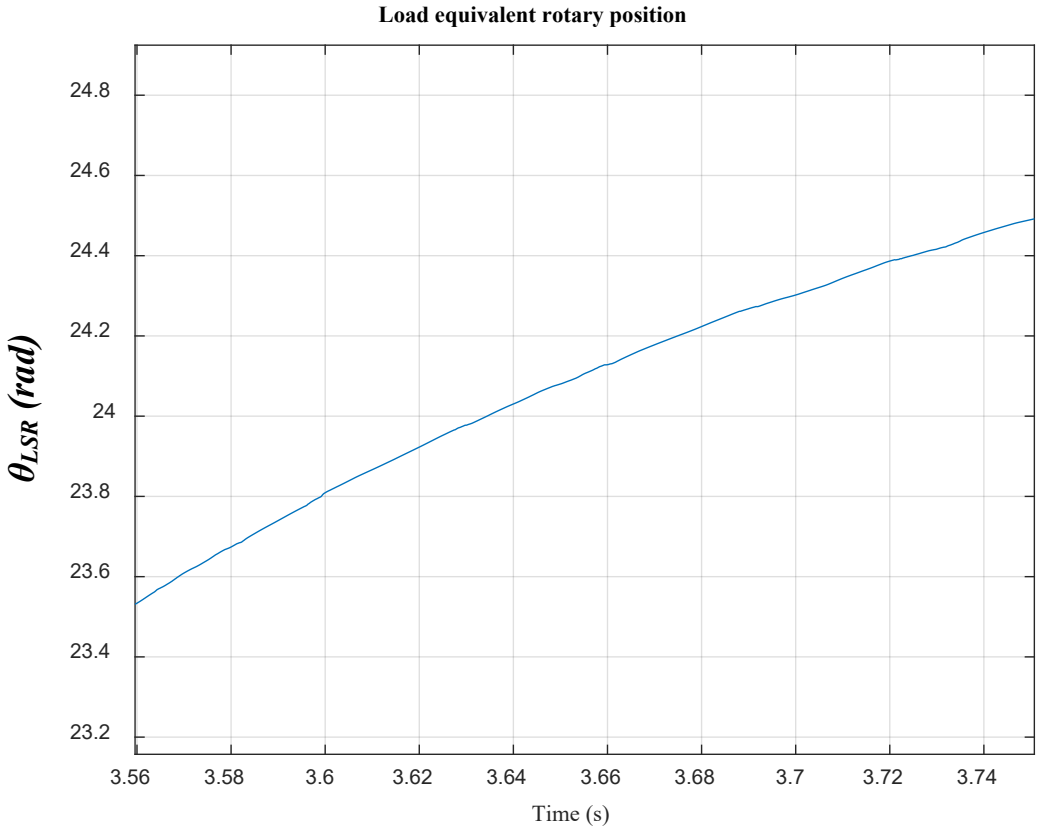

Figure 214. Rotary position

Servo motor speed signal is shown in Figure 215.

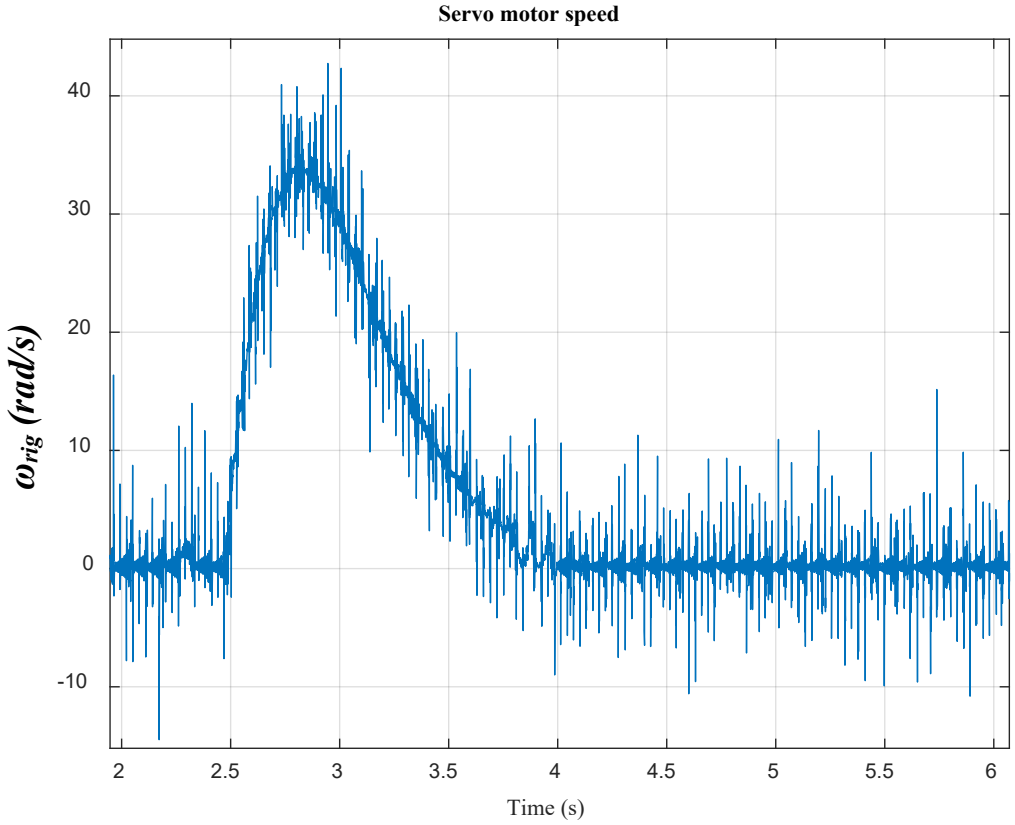

Figure 215. Servo motor speed [speed loop BW = 1 Hz]

With zooming into Figure 215, the only relevant frequency that is seen is 142 Hz, which results from the PDD magnetic stiffness, as illustrated in Figure 216.

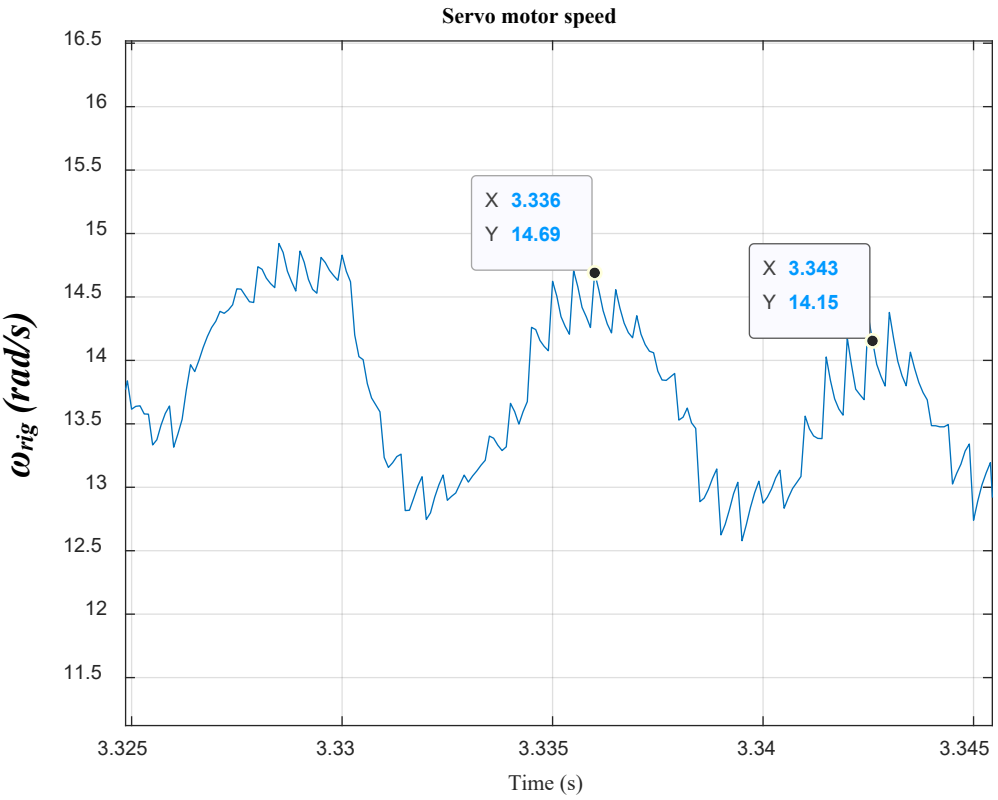

Figure 216. Measured LSR speed (a frequency equal to 142 Hz is highlighted)

The reaction torque applied is depicted in Figure 217. The torque sent to the servo motor is clear of any significant dynamics.

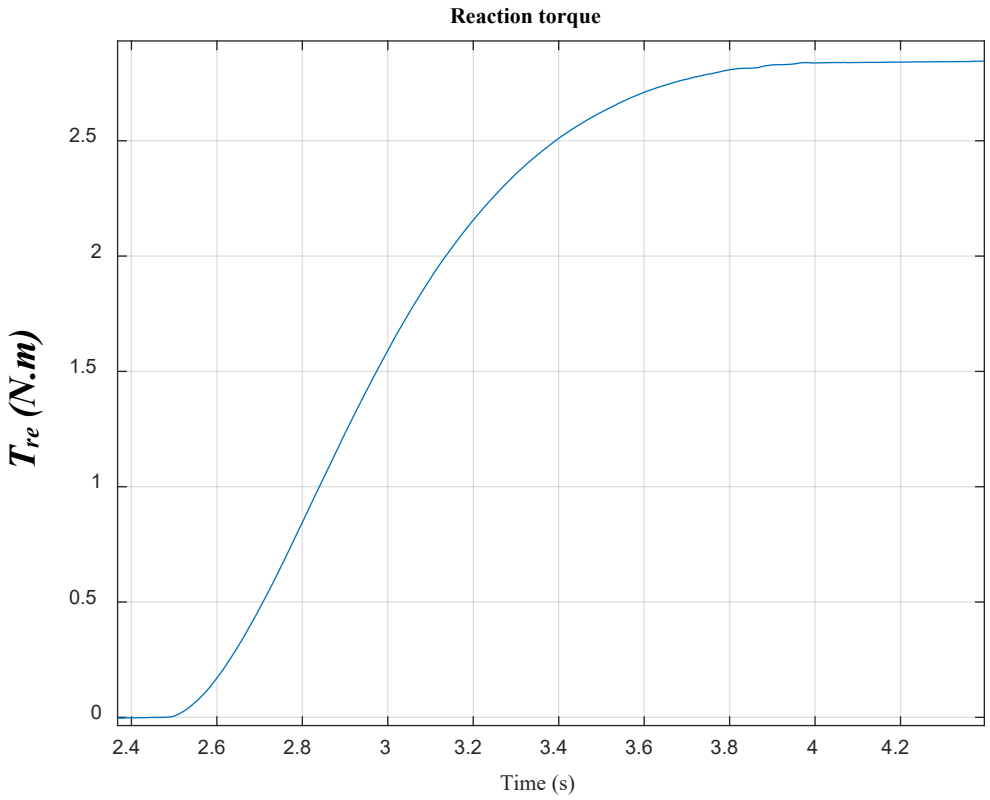

Figure 217. Reaction torque

5.5.1.2 Three-DOF model (Nominal values)

A displacement step of 28 mm is set as an axial position demand. The load axial position follows the demand as shown in Figure 218.

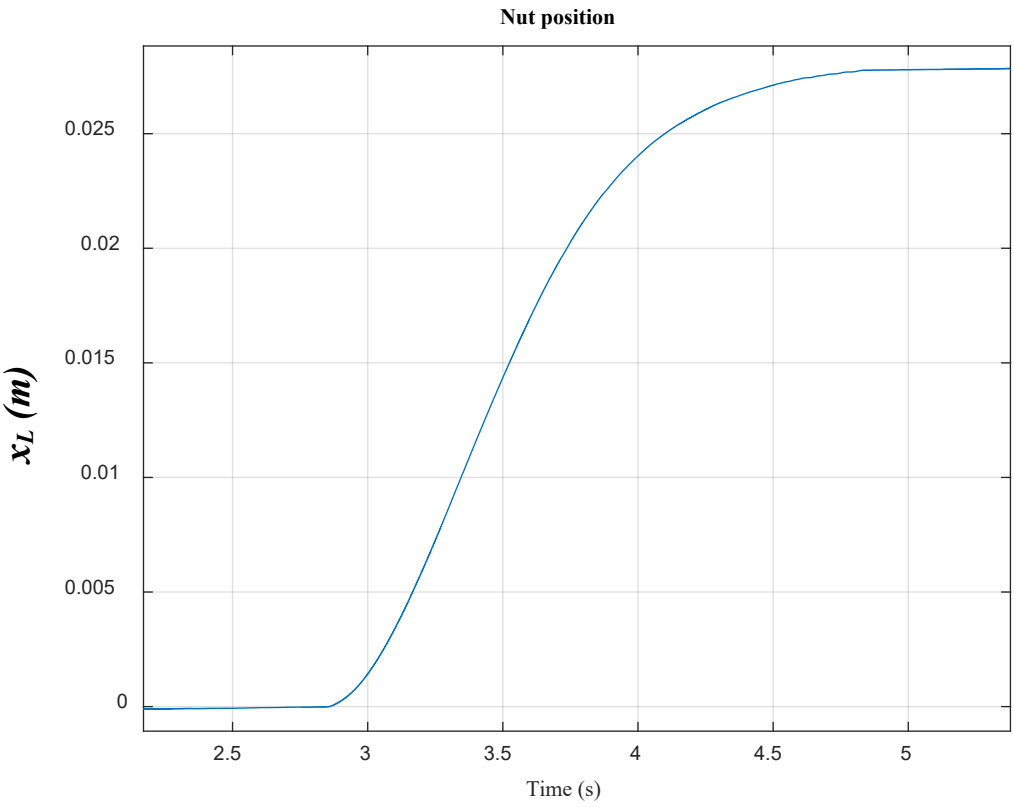

Figure 218. Load axial position

Oscillations with minor amplitude can be seen in the axial position, as illustrated in Figure 219. The frequency identified is 350 Hz, which is the value of f_2.

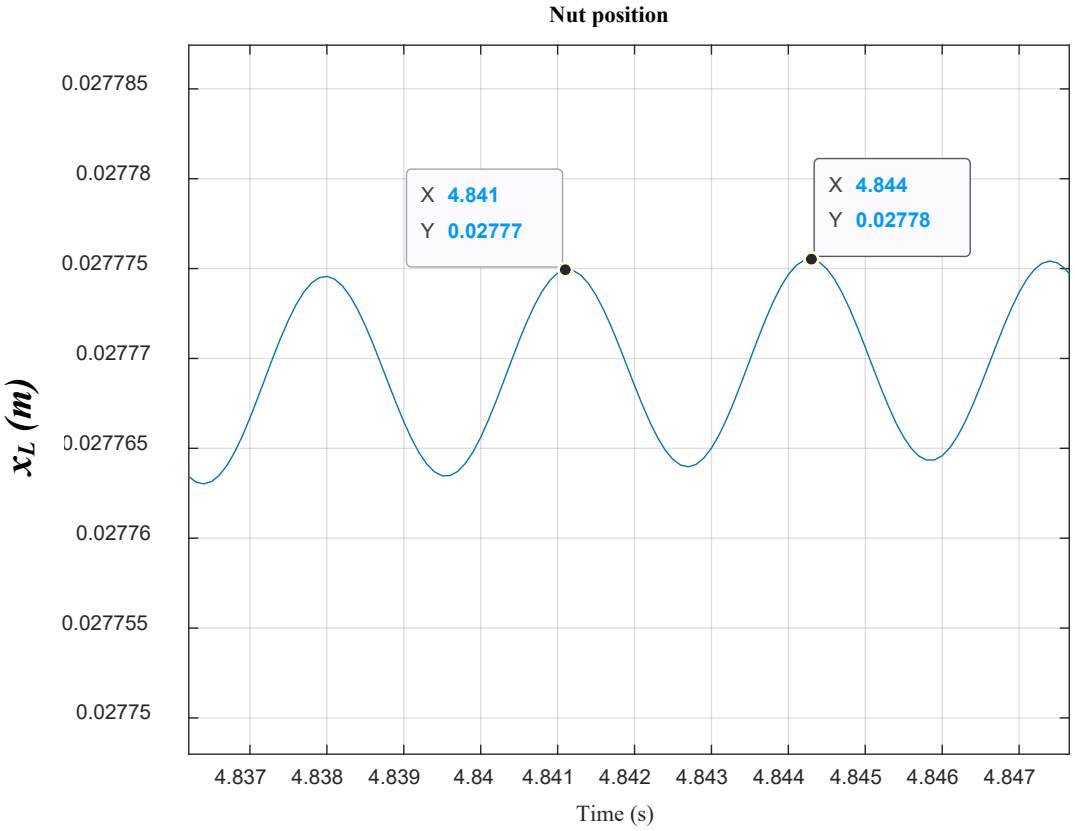

Figure 219. Load axial position (a frequency of 350 Hz is highlighted)

Taking the FFT, the axial position, x_L, response in time domain, shown in Figure 219, is transformed into a response in the frequency domain, as shown in Figure 220. The second resonant frequency, f_2, is located at 350 Hz.

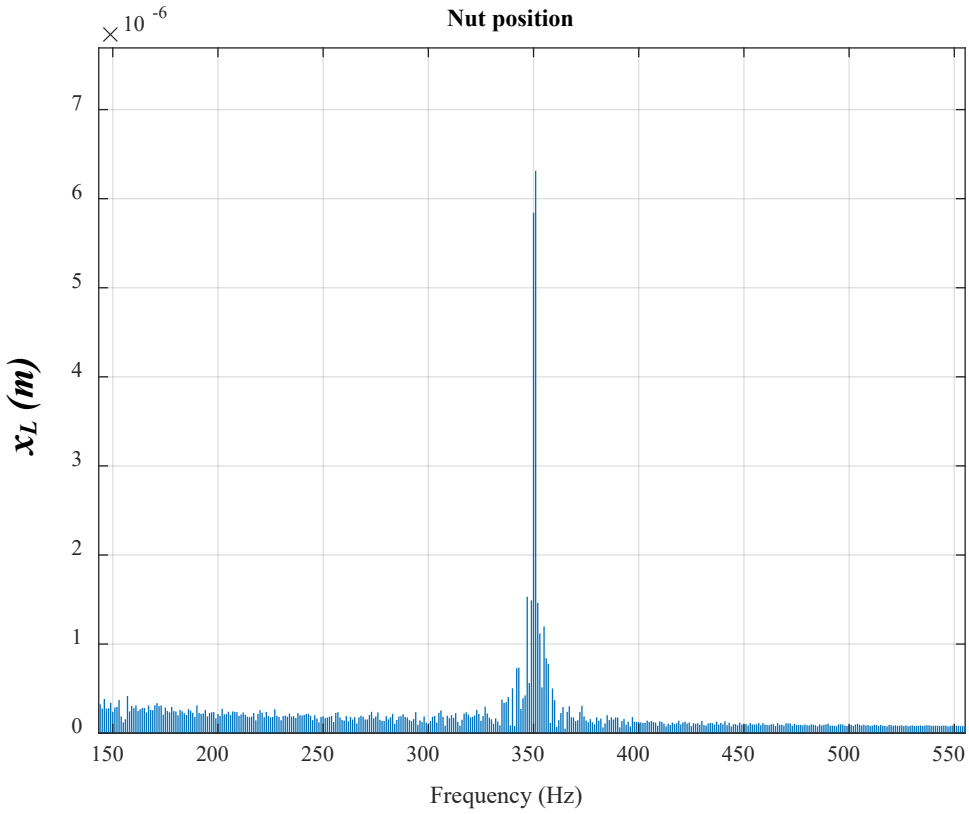

Figure 220. Axial position in the frequency domain

The speed rises to cover demand position and starts to fall as the actual position approaches the commanded value (Figure 221).

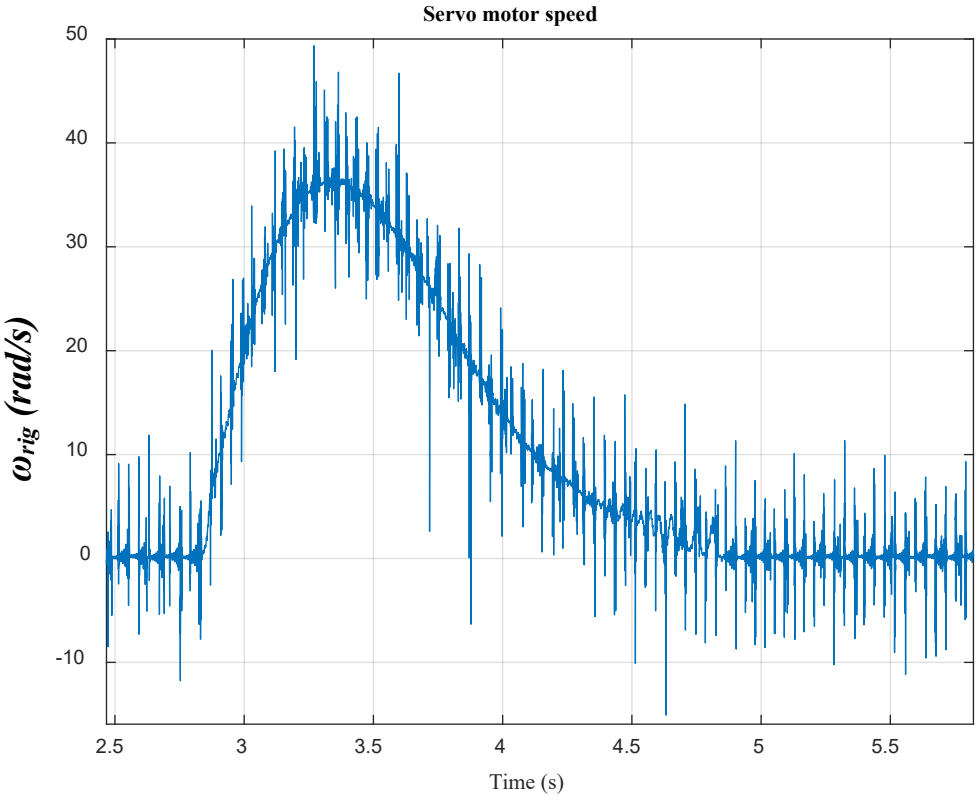

Figure 221. Servo motor speed [speed loop BW = 1 Hz]

The resonant frequency f_2 can be spotted in the measured servo motor speed signal, as illustrated in Figure 222.

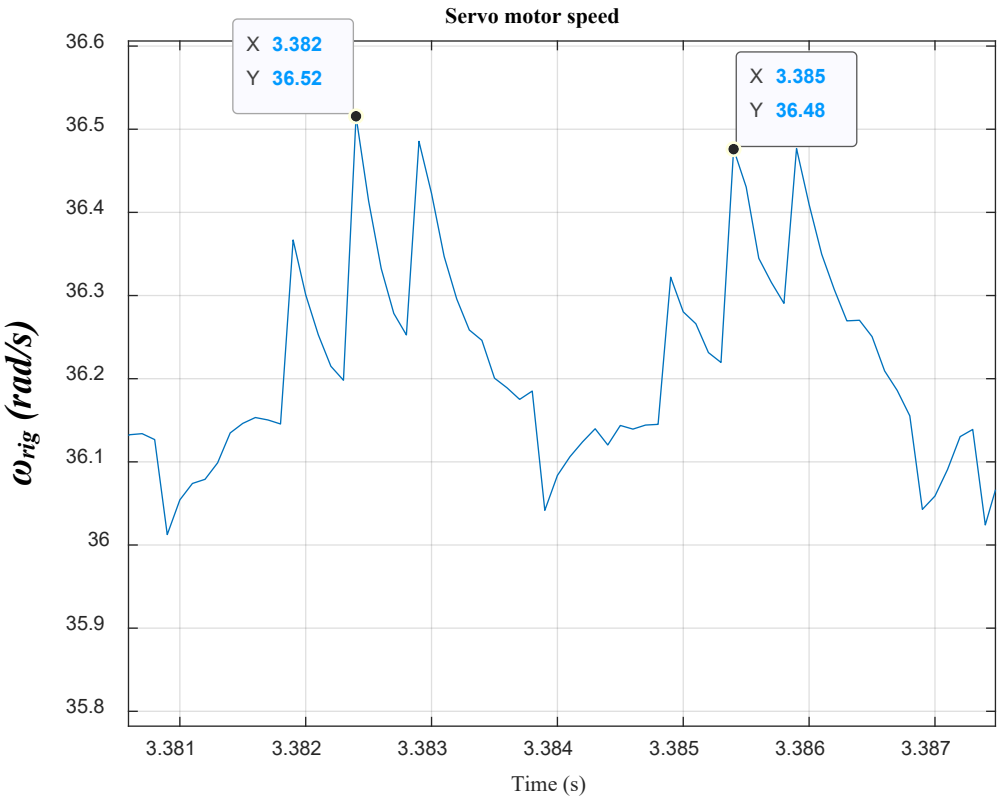

Figure 222. Servo motor speed (a frequency of 350 Hz is identified)

Taking the FFT, the rig speed, ω_{rig}, response in time domain, is transformed into a response in the frequency domain, as shown in Figure 223. The second resonant frequency, f_2, is located at 350 Hz. The signal is associated with noise and this is expected seeing the noise in the time tomain response (Figure 221).

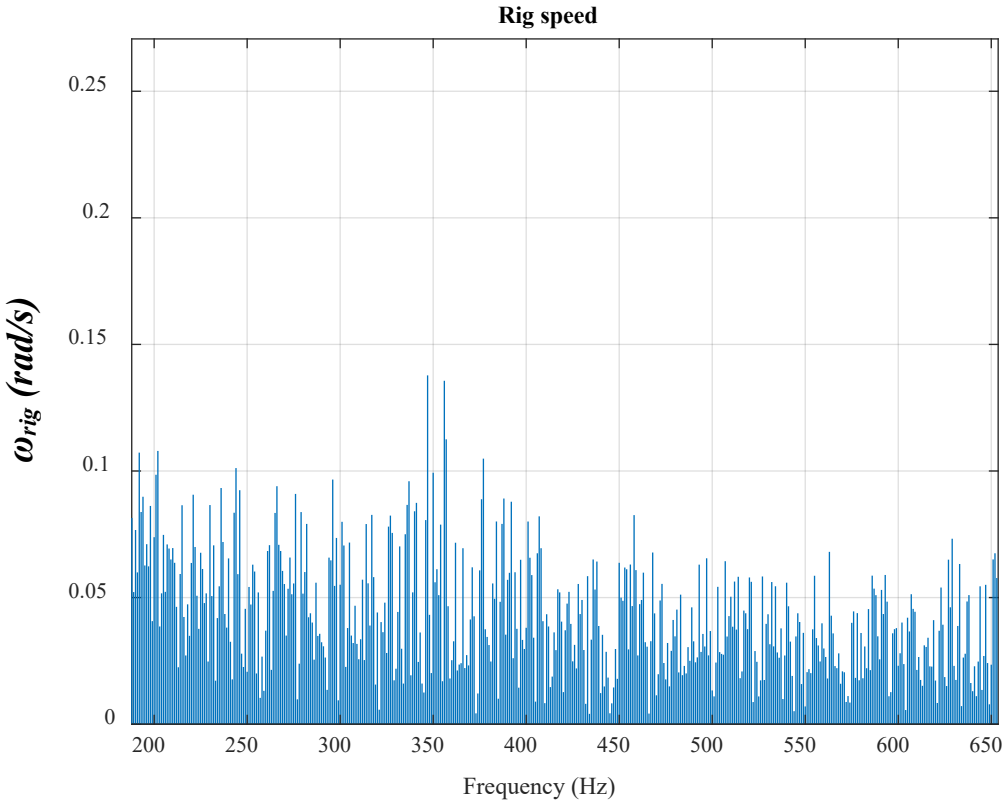

Figure 223. Rig speed in the frequency domain

In addition to f_2, f_g is also identified in the measured speed signal, which can be seen in Figure 224.

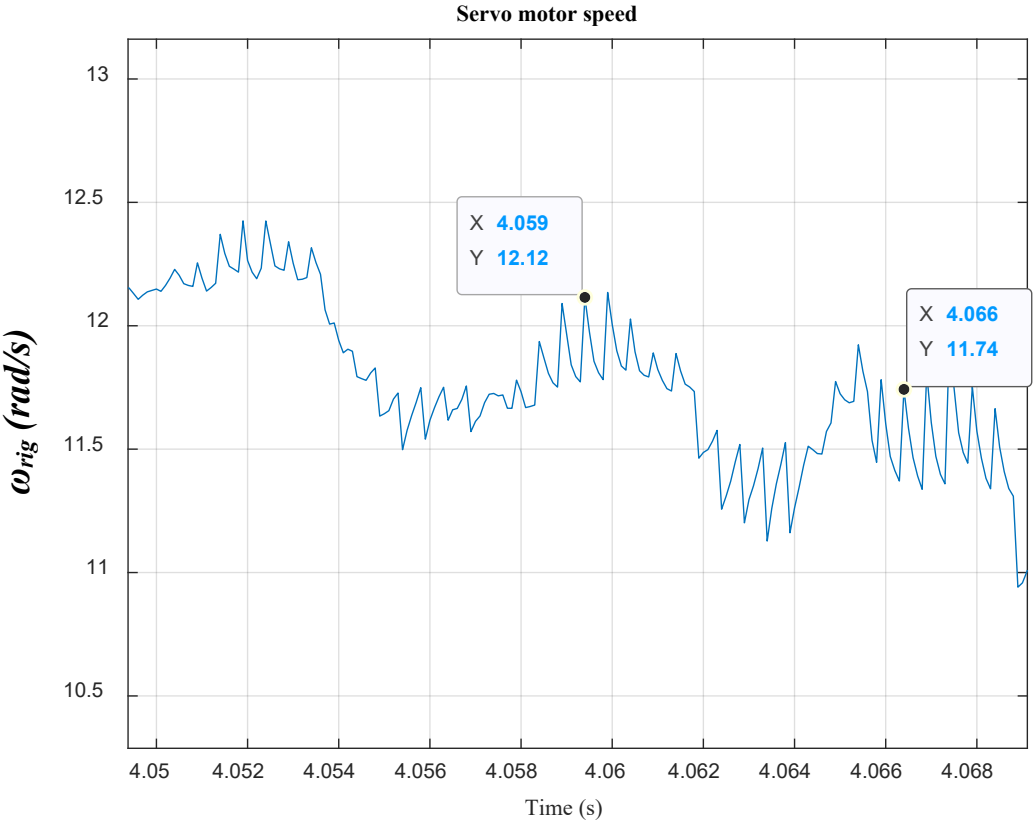

Figure 224. Servo motor speed (f_g =142 Hz is identified)

The servo motor applies the reaction torque, demanded by the model, on the PDD. The torque measured by the torque transducer can be seen in Figure 225.

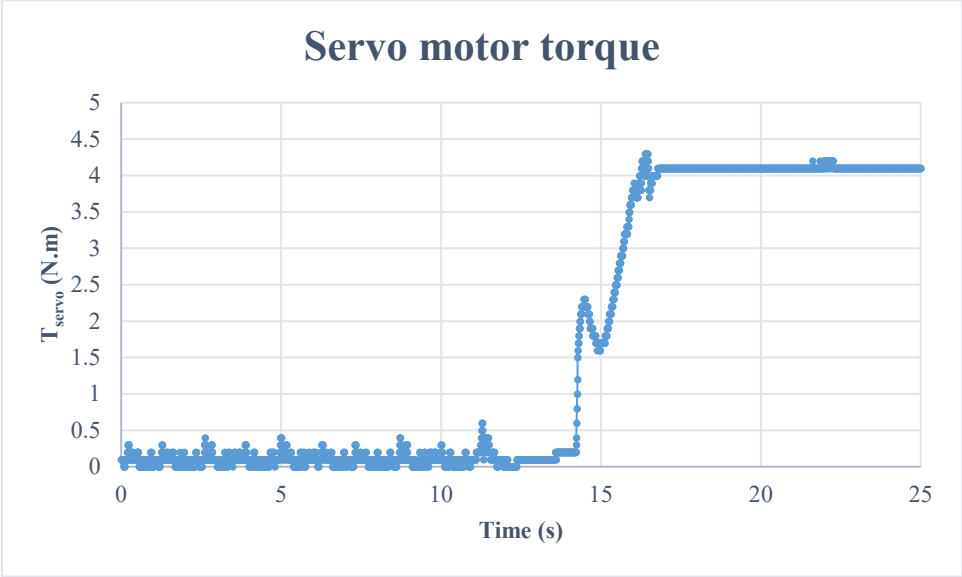

Figure 225. Reaction torque applied on the PDD

When using the nominal values, the structure resonance of mechanical system can actually be seen. However, due to test rig damping, the dynamics are damped to a large extent. This is because the under study system's inertia is equal to 18% of that of the laboratory system's inertia, as mentioned in Section (5.3.1). For this reason, K_b is reduced to make f_2 more noticeable.

5.5.1.3 Three-DOF model ($K_b = 2\times10^6$ N/m)

In this test, the stiffness of the bearing is reduced to lower the value of f_2. The position demand is set to 28 mm. The nut follows the demanded position, as shown in Figure 226.

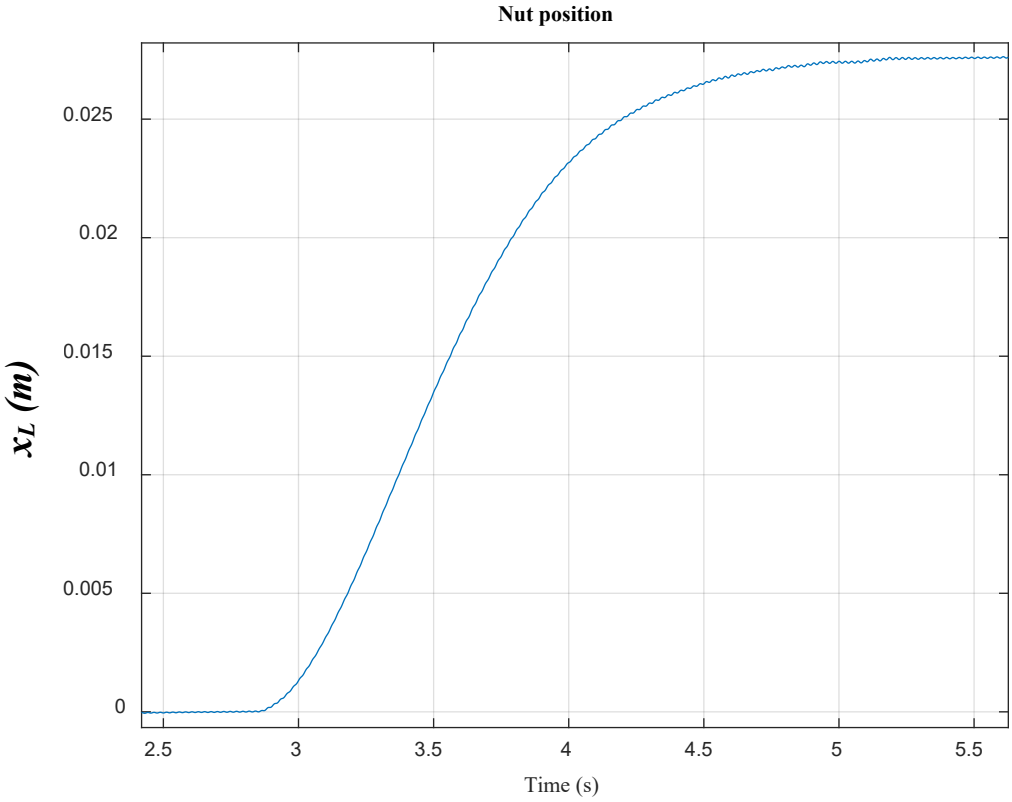

Figure 226. Load axial position [speed loop BW = 1 Hz]

The nut position has slight oscillations yet they are noticeable, as illustrated in Figure 227. Notice that the amplitude of oscillations is higher in this case when compared to the previous case, which is shown in Figure 219.

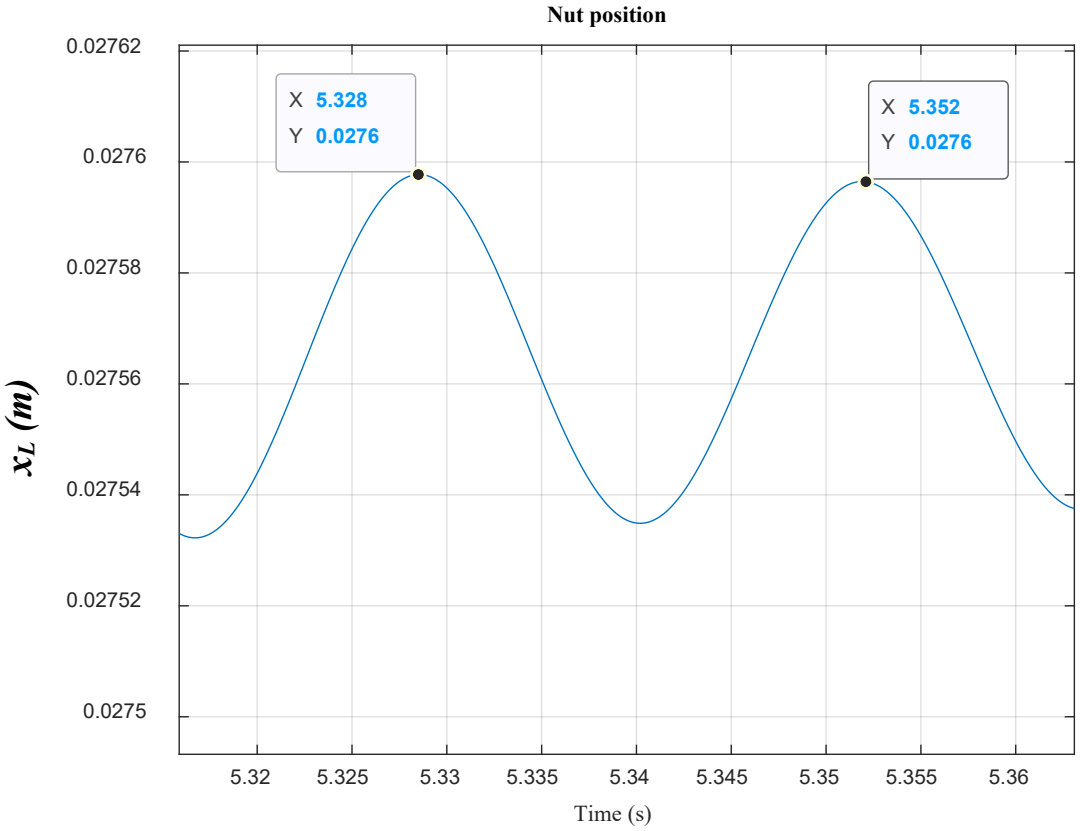

Figure 227. Load axial position (f_2 = 42 Hz is highlighted)

Taking the FFT, the axial position, x_L, response in time domain, shown in Figure 227, is transformed into a response in the frequency domain, as shown in Figure 228. The second resonant frequency, f_2, is located at 42 Hz.

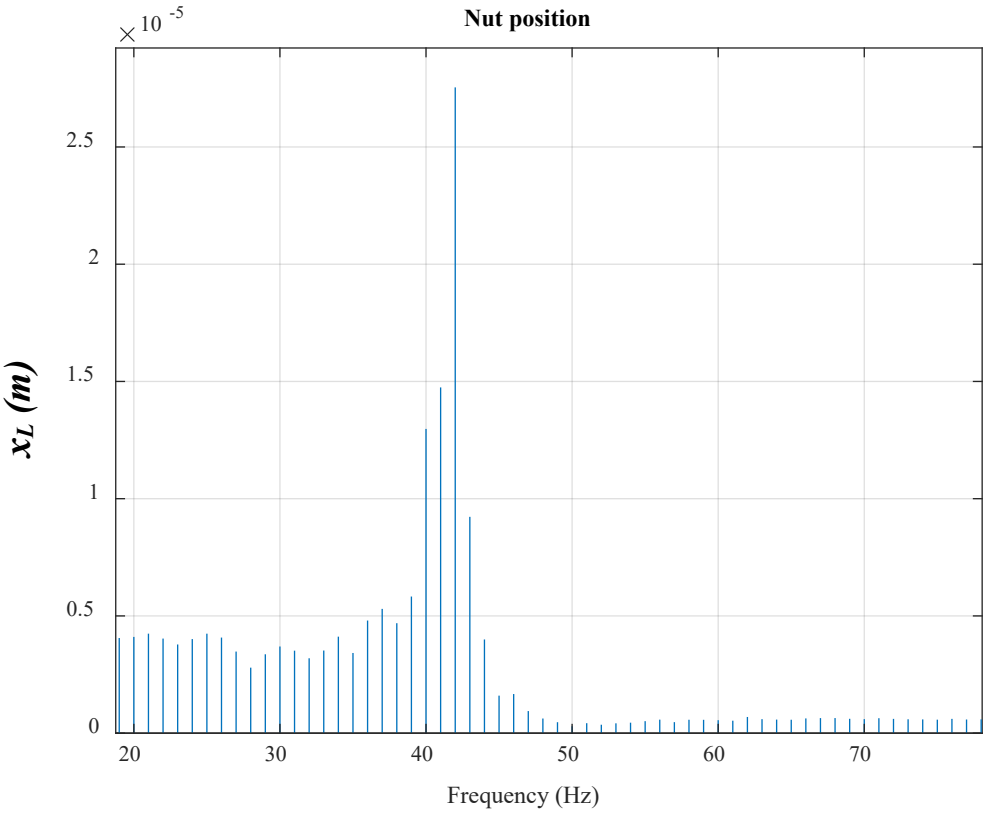

Figure 228. Axial position in the frequency domain

The servo motor speed signal is measured and depicted in Figure 227.

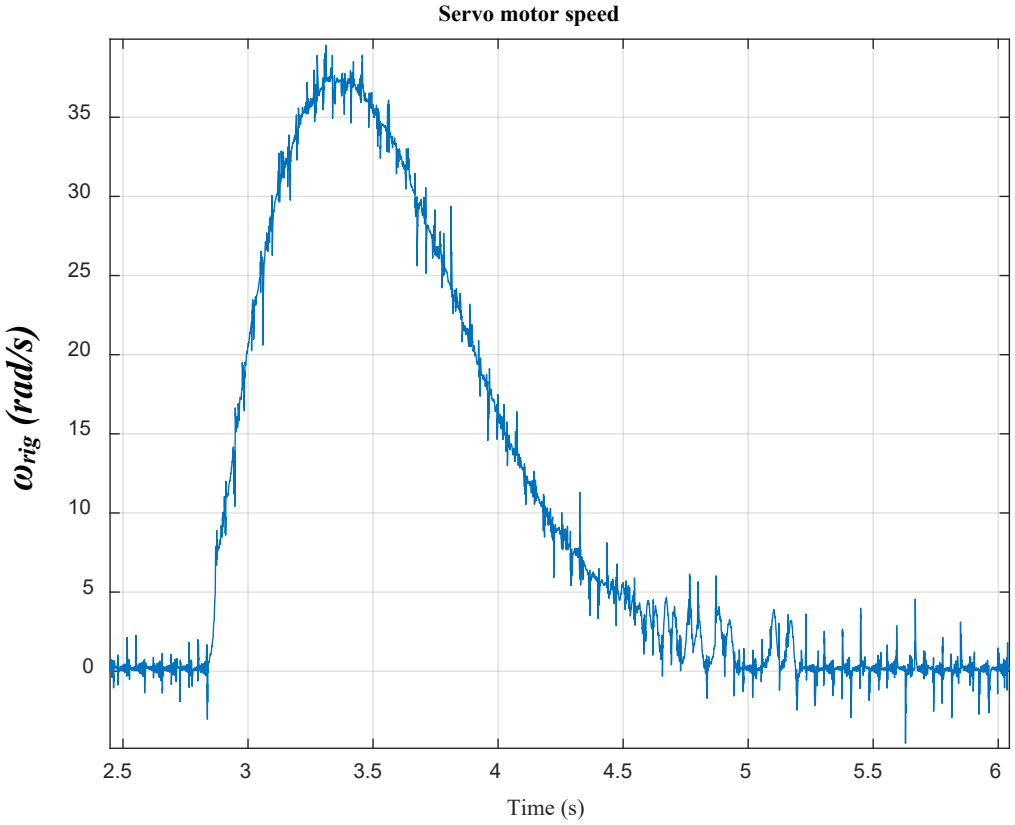

Figure 229. Servo motor speed

The frequency f_2 is observed in the servo motor speed and identified in Figure 230.

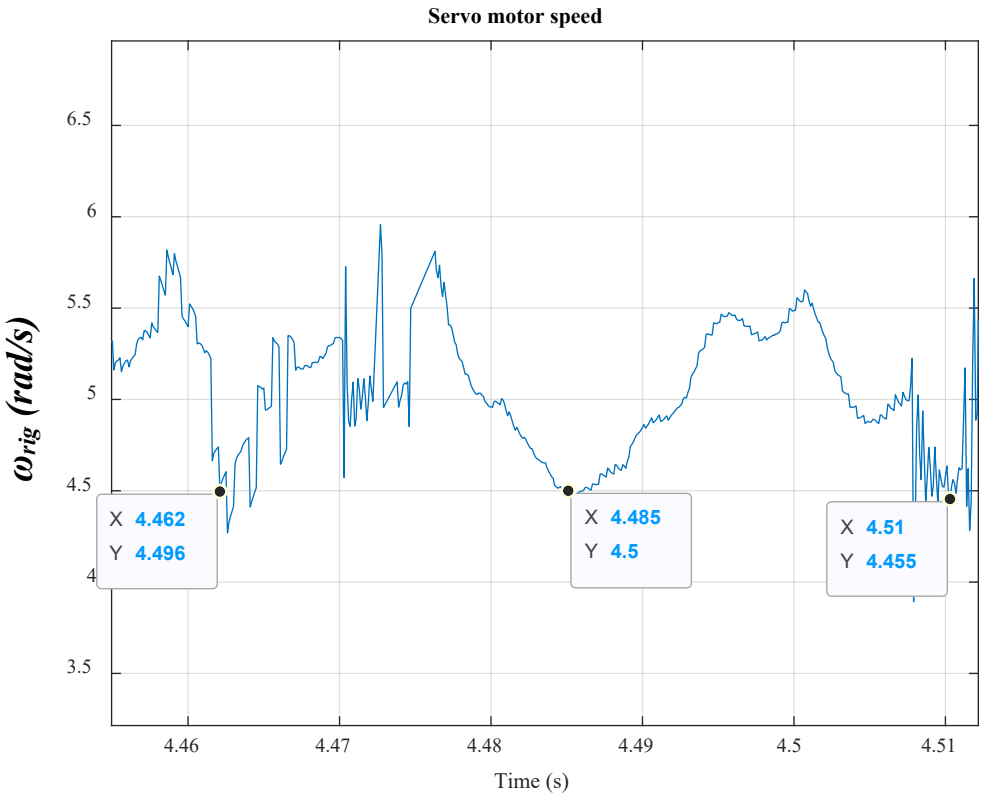

Figure 230. Servo motor speed (a frequency of 42 Hz is identified)

Taking the FFT, the rig speed, ω_{rig}, response in time domain, is transformed into a response in the frequency domain, as shown in Figure 231. The second resonant frequency, f_2, is located at 42 Hz. The signal is associated with noise and this is expected seeing the noise in the time tomain response (Figure 227).

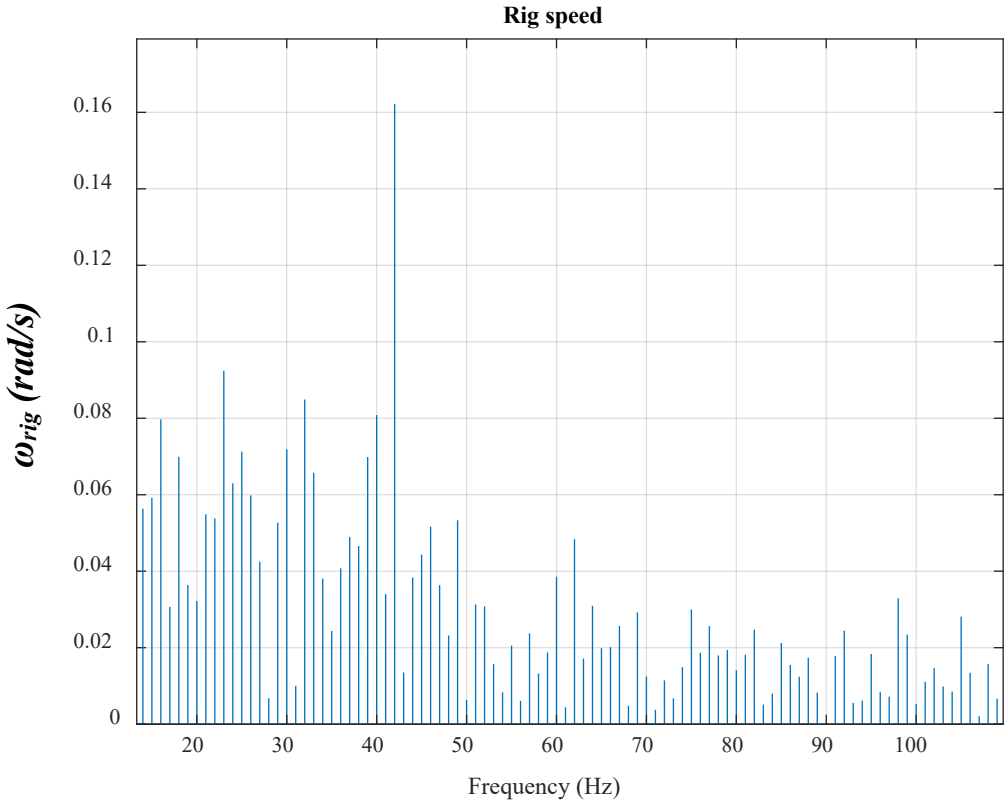

Figure 231. Rig speed in the frequency domain

The torque signal sent to the servo motor represents the reaction torque of the ball-screw system, which is depicted in Figure 232.

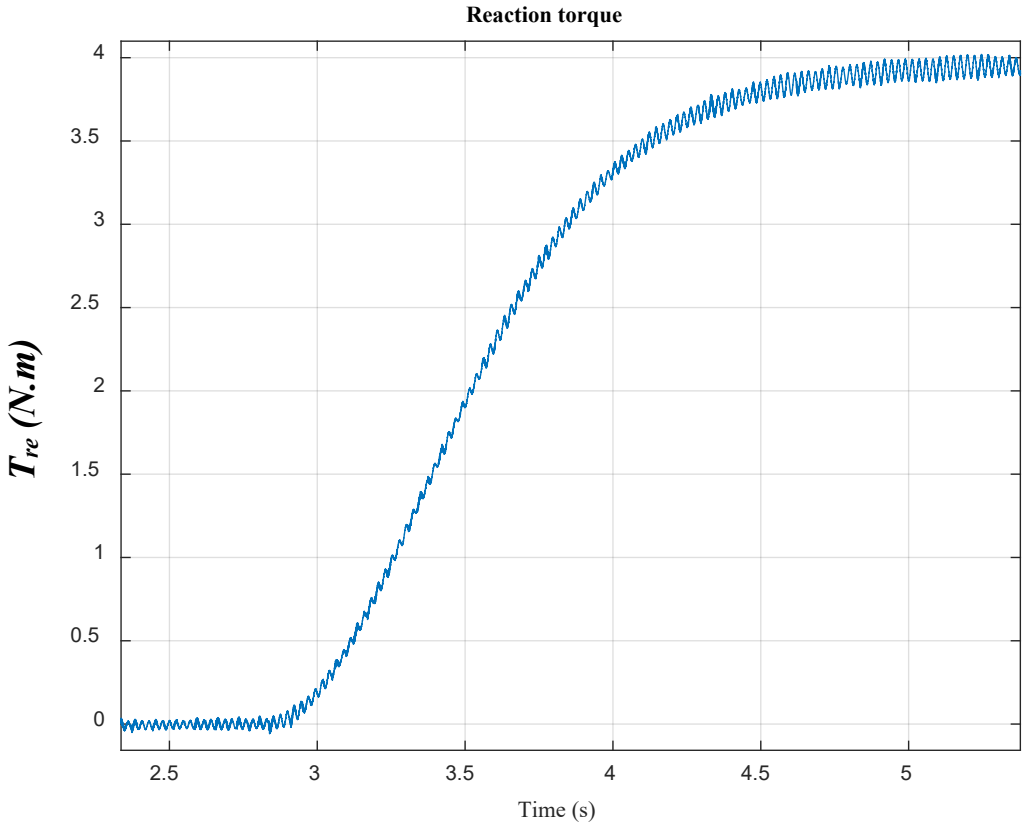

Figure 232. Reaction torque sent to the servo motor to apply on the PDD

The reaction torque shows noticeable oscillations. Their frequency is identified in Figure 233.

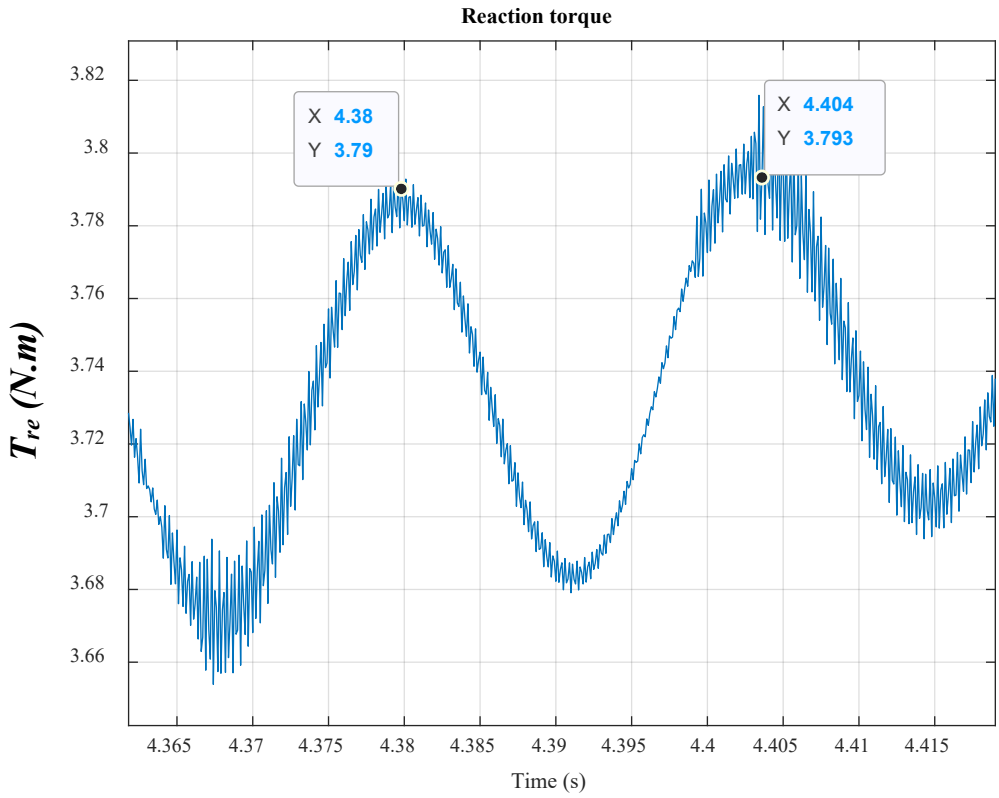

Figure 233. Reaction torque (a frequency of 42 Hz is identified)

Taking the FFT, the reaction torque, T_{re}, in time domain, shown in Figure 233, is transformed into a response in the frequency domain, as shown in Figure 234. The second resonant frequency, f_2, is located at 42 Hz.

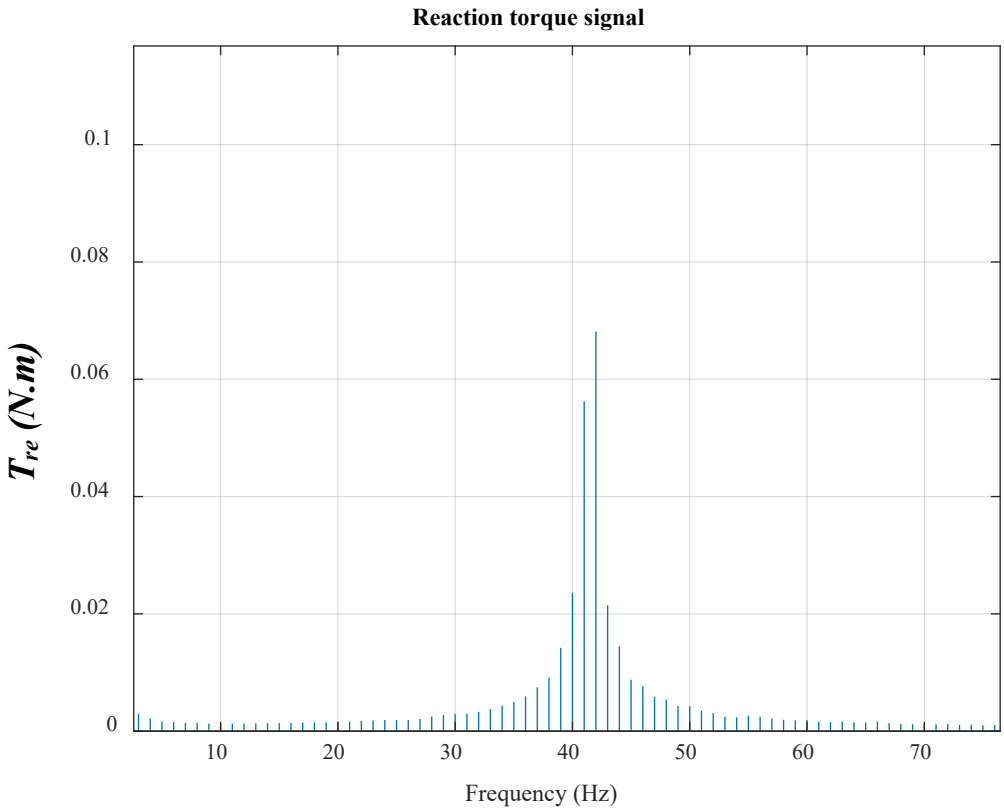

Figure 234. Reaction torque in the frequency domain

The servo motor drive receives the torque demand signal depicted in Figure 232 and applies a torque on the PDD. The measured torque applied is shown in Figure 235.

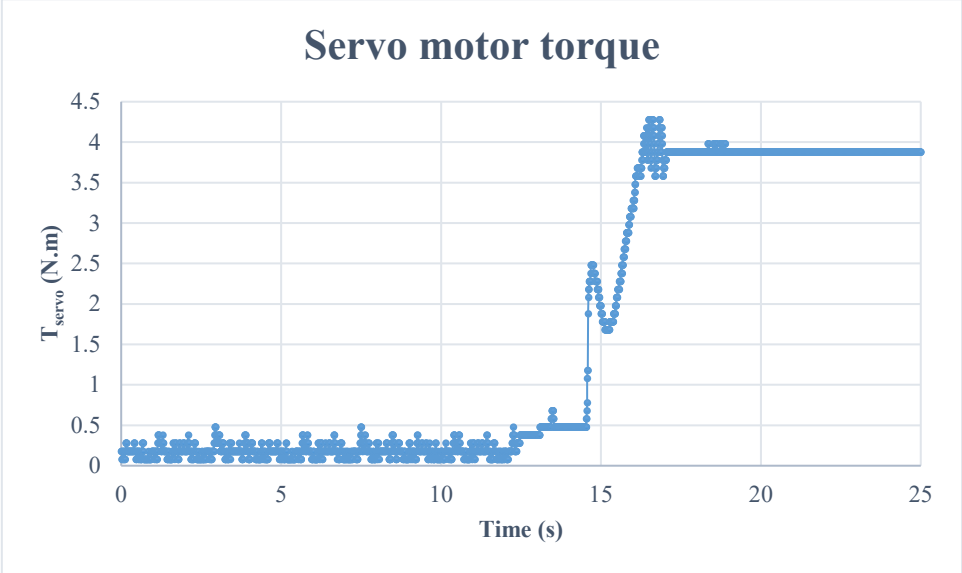

Figure 235. Reaction torque applied to the PDD

5.5.2 Disturbance torque with certain frequencies

Further tests can be done to investigate system reaction to extreme load conditions. Disturbance loads of a certain frequency range, located within the current control bandwidth, are simulated and experimentally tested. The disturbance is applied in a form of a chirp signal with a frequency range of interest. The amplitude of the load reaches *8%* of the rated value.

5.5.2.1 One-DOF model (simplified model)

The first test is carried out by using the single inertia model. A step axial load position demand is set to 24 mm. This is equivalent to a rotary demand position of 30.16 rad. The signal frequency ranges from 1 to 125 Hz.

The system operates like normal except the extra amount of the applied torque is added. The only dynamics that can be seen is due to the PDD magnetic stiffness. No mechanical system dynamics are observed. System seems to operate ordinarily in a similar way shown in Section (5.5.1.1), as shown in Figure 236.

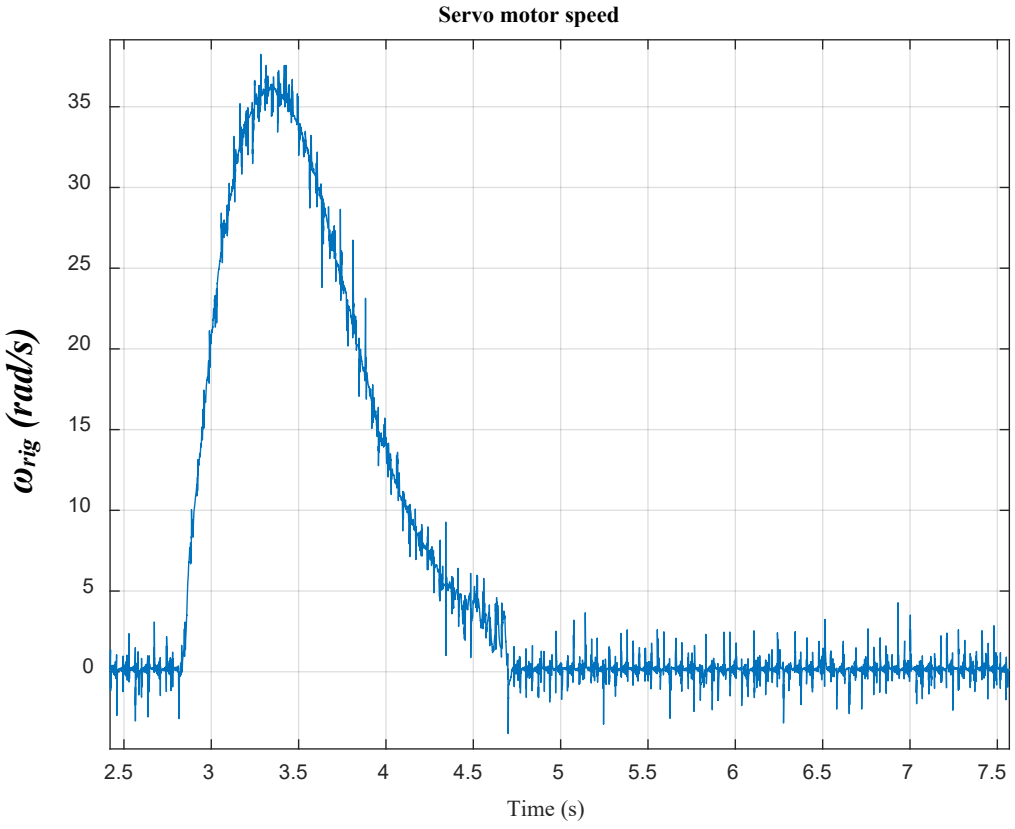

Figure 236. Measured servo motor speed [speed loop BW = 1 Hz]

The model used develops a reaction torque, which is sent to the servo motor as a torque demand. Figure 237 shows the torque applied by the servo motor. This torque is measured by the transducer located between both machines. It is clear that the torque is a function of the position, as previously stated.

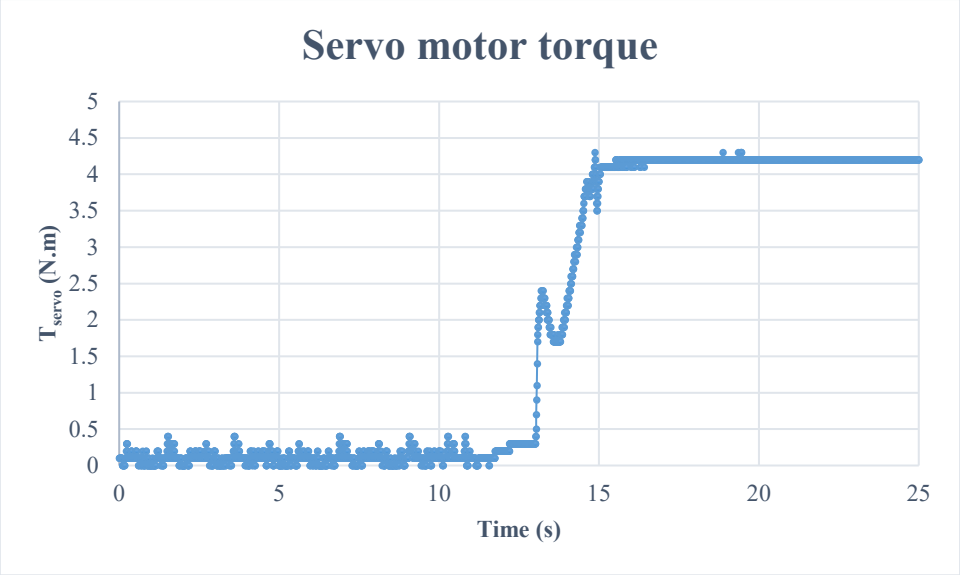

Figure 237. Servo motor torque applied on the PDD

5.5.2.2 Three-DOF model ($K_b = 2\times10^7$ N/m)

It is mentioned in Section (5.3.1) that the laboratory test rig is characterised by its own dynamics. An important frequency is equal to *142 Hz*, which occurs due to the magnetic stiffness of the PDD, and can vary over a certain range depending on the amount of load applied on the machine. Also, another crucial frequency is equal to *275.5 Hz*, which is related to the rest of the rig. The frequency *275.5 Hz* is quite close to *350 Hz* (f_2). So, it is challenging to apply a chirp frequency to excite f_2 since this could also excite the *275.5 Hz* and this frequency is out of interest. Therefore, K_b is reduced, say to 2×10^7 *N/m*, and hence f_2 becomes equal to *122 Hz*. Thus, the applied signal frequency ranges from 50 to 125 Hz.

Figure 238 shows the load axial position. It can be seen that at lower frequencies there is only negligible oscillation. However, as the disturbance frequency becomes close to f_2 oscillations are amplified.

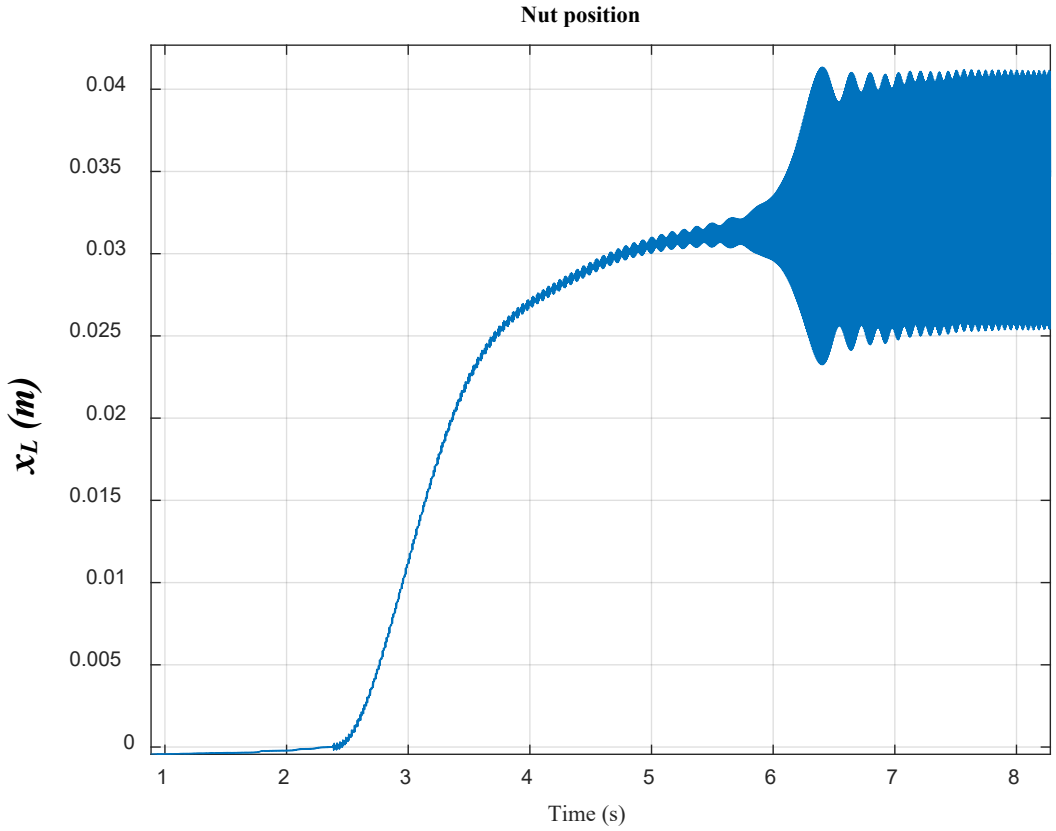

Figure 238. Load axial position

Frequency of oscillations is highlighted in Figure 239, which illustrates a frequency of *122 Hz*.

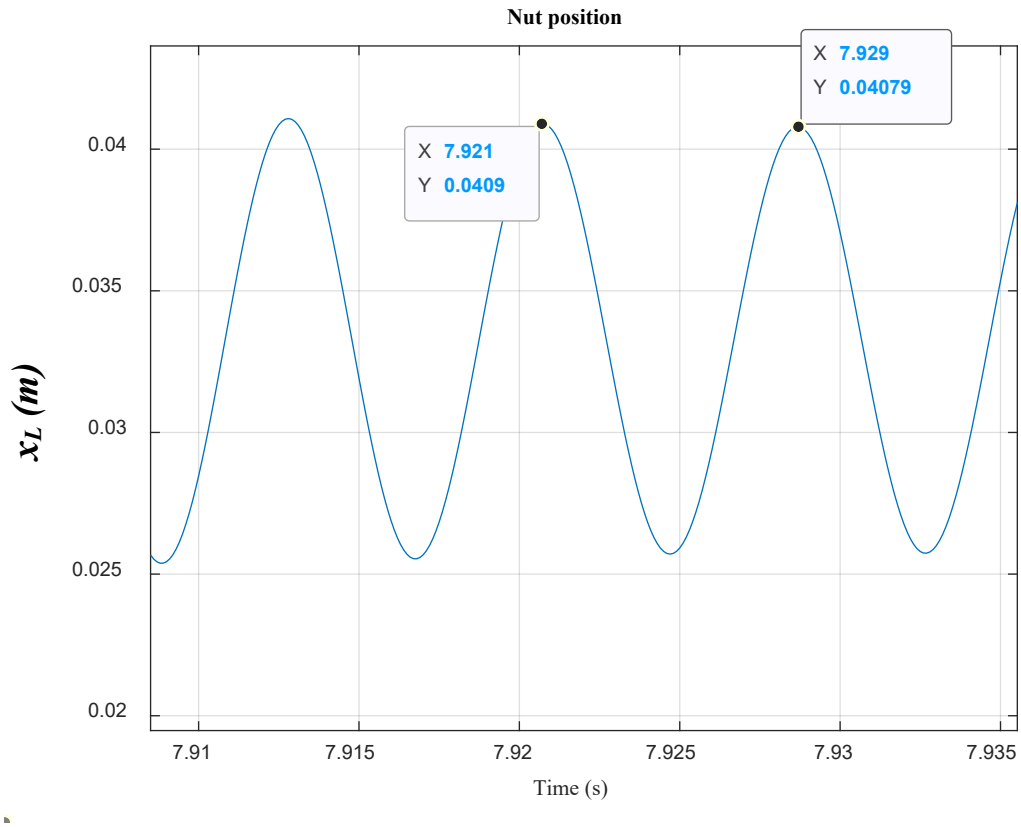

Figure 239. Load axial position (frequency of 122 Hz is highlighted)

Taking the FFT, the axial position, x_L, response in time domain, shown in Figure 239, is transformed into a response in the frequency domain, as shown in Figure 240. The second resonant frequency, f_2, is located at 122 Hz.

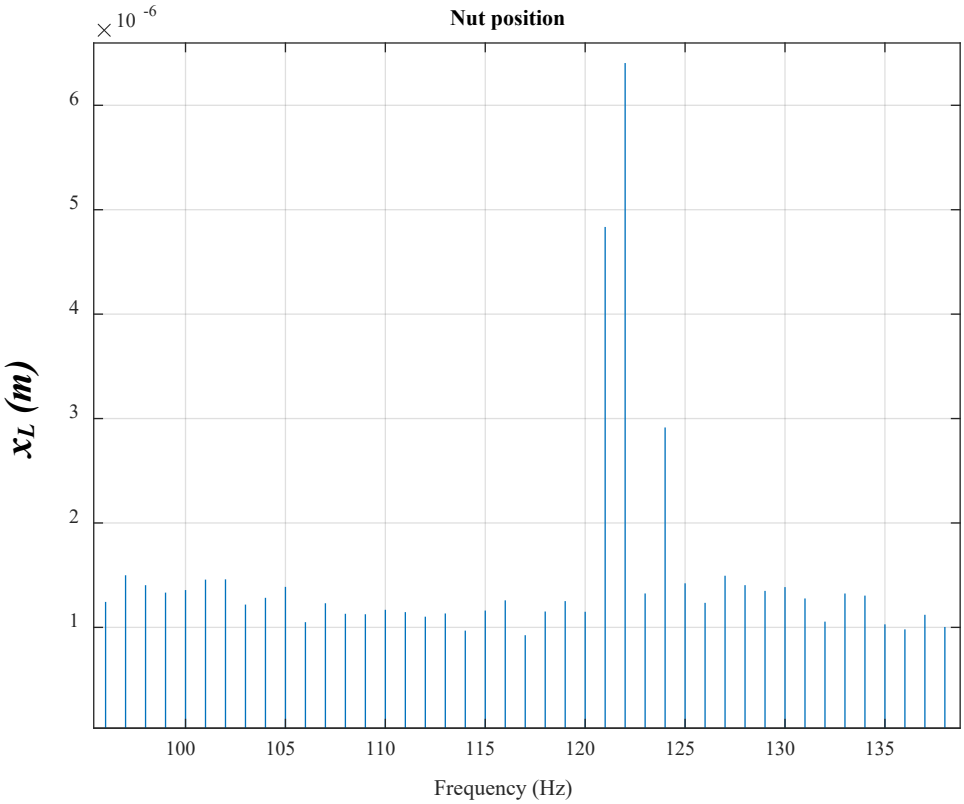

Figure 240. Axial position in the frequency domain

The excited frequency disrupts the operational speed (Figure 241). The control of PDD is lost as a result of this test. At instant 4s, the drive protection is activated to prevent the sudden increase in the current demanded by the amplified reaction torque. Figure 242 shows a simulated speed under the same conditions taken for this test. It is shown that at instant 4s resonance is excited and speed is amplified.

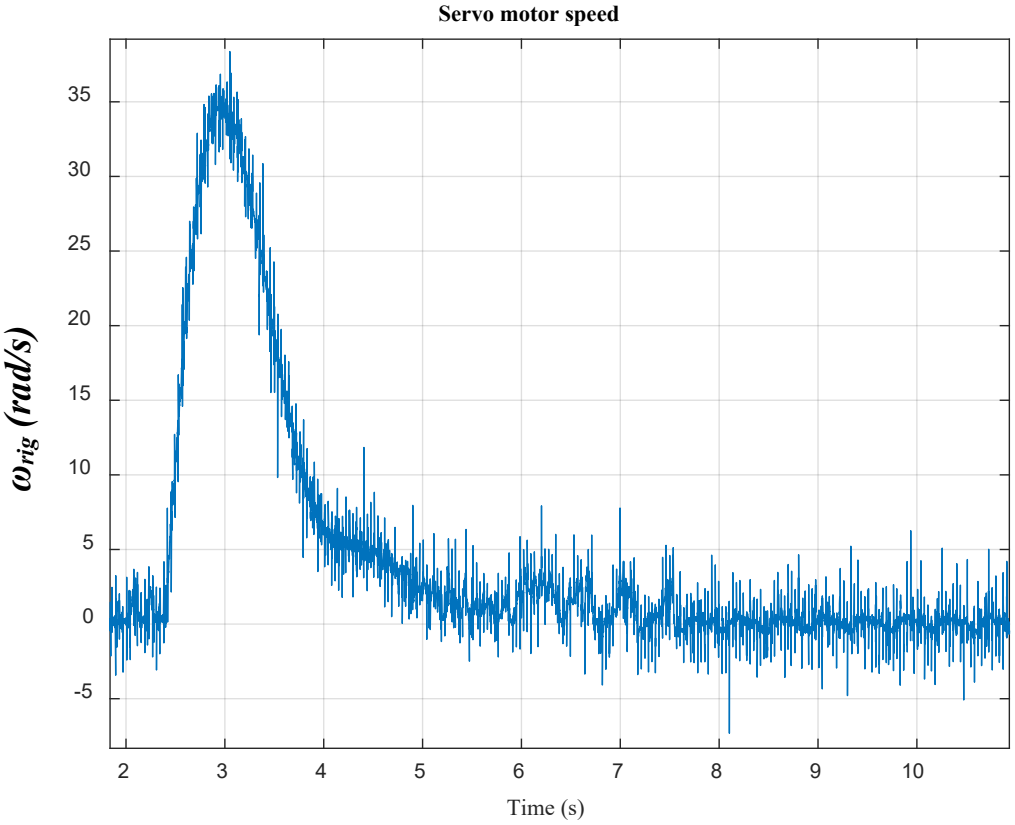

Figure 241. Servo motor speed [speed loop BW = 1 Hz]

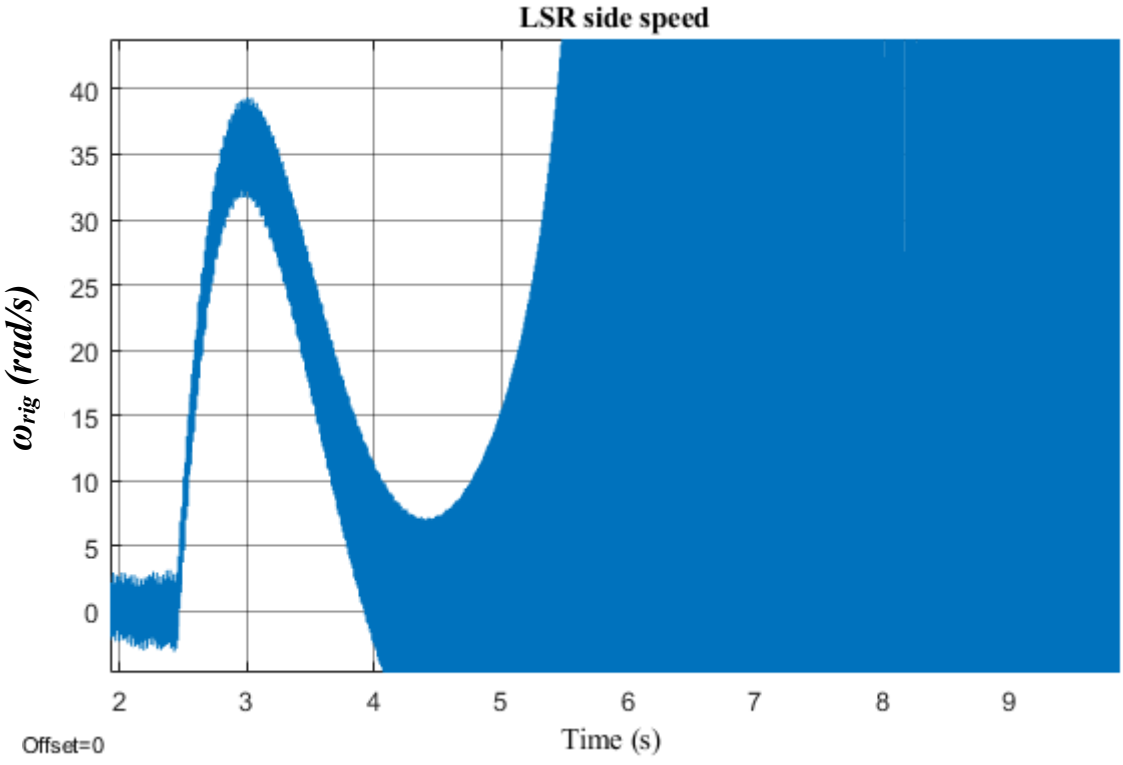

Figure 242. LSR side speed (simulated)

The excited frequency can be observed in the servo motor speed signal, as shown in Figure 243.

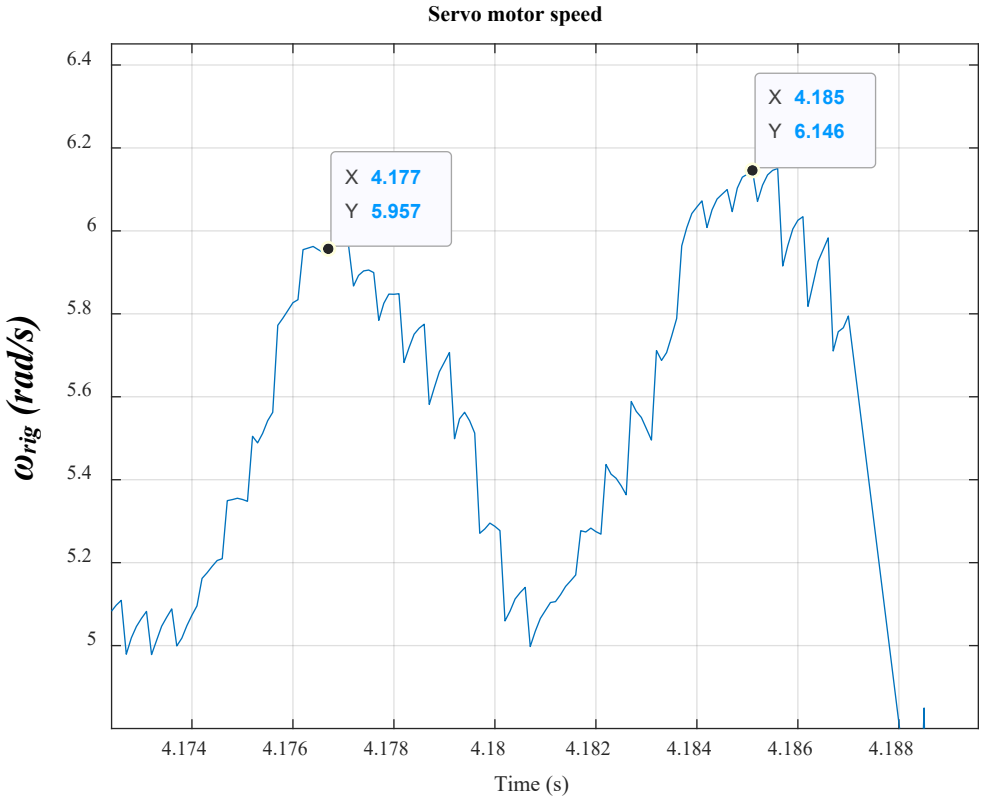

Figure 243. Servo motor speed (Frequency of 122 Hz is highlighted)

Taking the FFT, the rig speed, ω_{rig}, response in time domain, is transformed into a response in the frequency domain, as shown in Figure 244. The second resonant frequency, f_2, is located at 122 Hz. The signal is associated with noise and this is expected seeing the noise in the time tomain response (Figure 241).

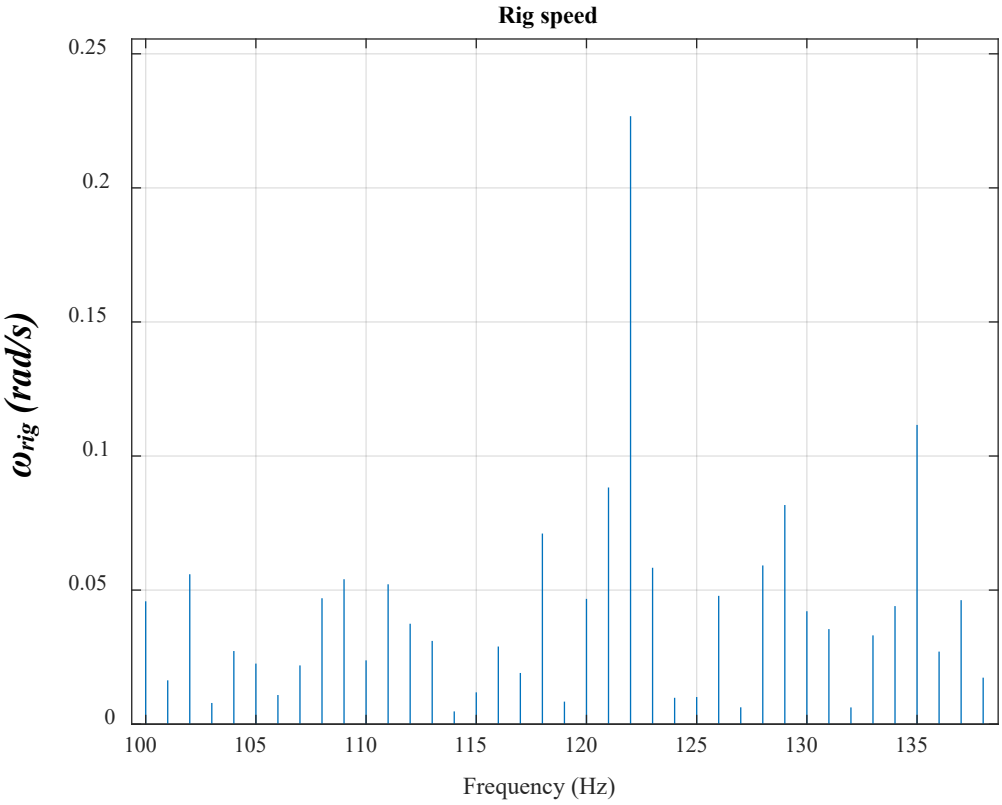

Figure 244. Rig speed in the frequency domain

At the moment of the frequency oscillation, the speed oscillates with f_2 and then system destabilises and loses control. Then the system starts to oscillate with f_1, which occurs due to the aerodynamic stiffness. This can be seen in Figure 241 and also in Figure 245. In Chapter 2, this frequency is determined to be equal to *4.37 Hz*. However, the extra inertia added by the servo motor has the effect of reducing this frequency to around *2.6 Hz*. This is explained in Section (5.3.1).

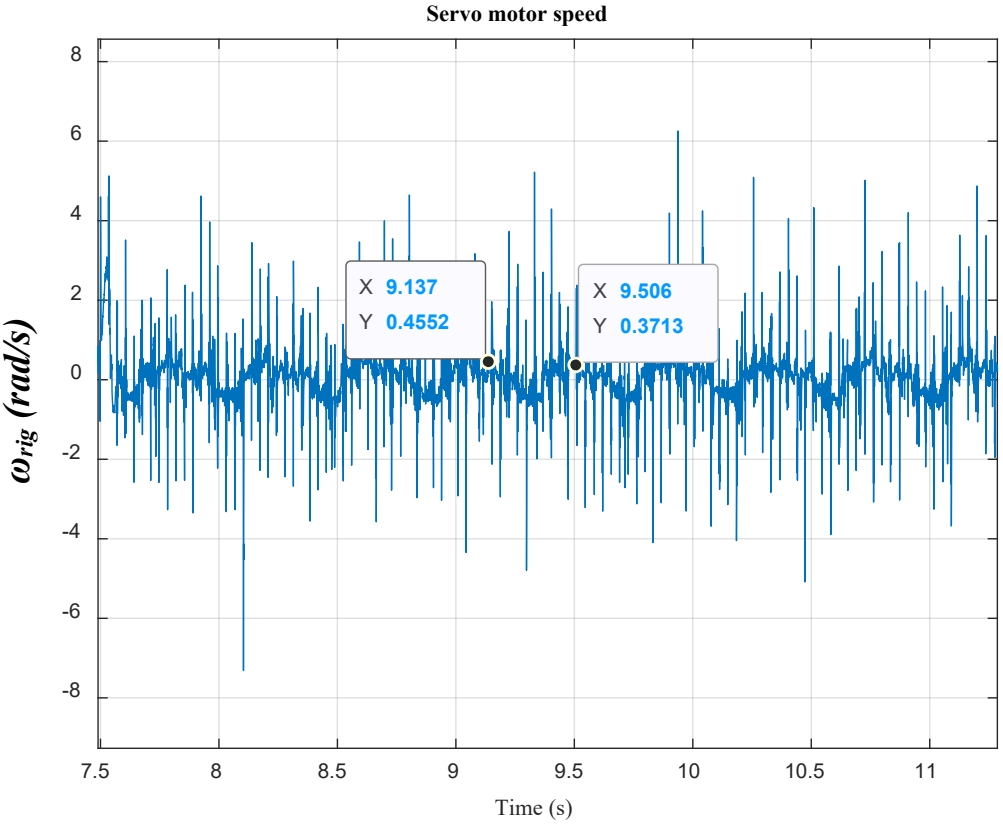

Figure 245. Servo motor speed (a frequency of 2.6 Hz is highlighted)

The reaction torque is emulated by the servo motor. The servo motor torque can be seen in Figure 246. Instability can be evidently observed.

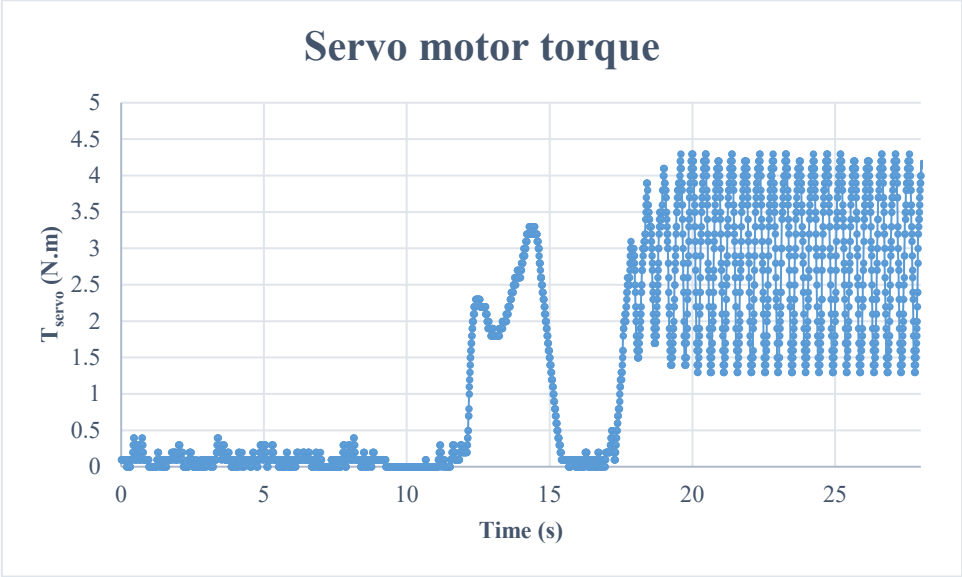

Figure 246. Servo motor applied torque on the PDD

The oscillation of torque occurs with 2.6 Hz, which results from the aerodynamic stiffness. Figure 247 shows the oscillations more clearly.

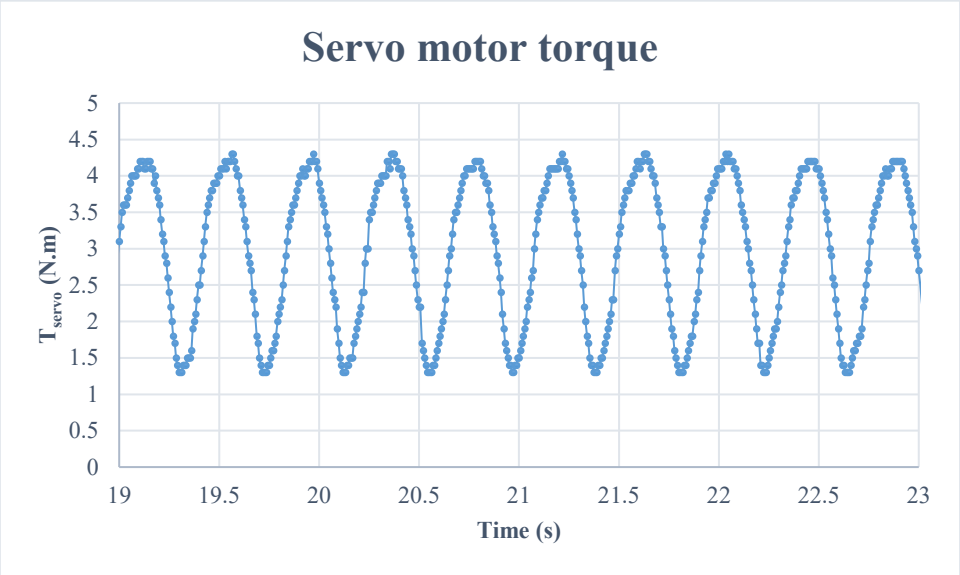

Figure 247. Servo motor applied torque on the PDD (a frequency of 2.6 Hz is highlighted)

5.5.2.3 Three-DOF model ($K_b = 2\times10^6$ N/m)

Reducing the value of K_b will make f_2 even lower, reaching to 42 Hz, and hence the influence of exciting this resonance is more severe. The disturbance in this test is applied from *1 Hz* to *70 Hz* since this is the frequency range of interest.

Figure 248 illustrates that oscillation is easily triggered even with a small frequency since K_b is quite compliant in this case. In addition, as the disturbance frequency approaches 42 Hz, the oscillations are magnificently amplified, which indicates the loss of system stability.

Additionally, when nut position is set at zero, it reflects the rudder at 0º. When rudder moves between -30º to 0º to +30º, the equivalent nut position changes from -50mm to 0mm to +50mm, repectively (Figure 38). This explains the position of the rudder when x_L is negative.

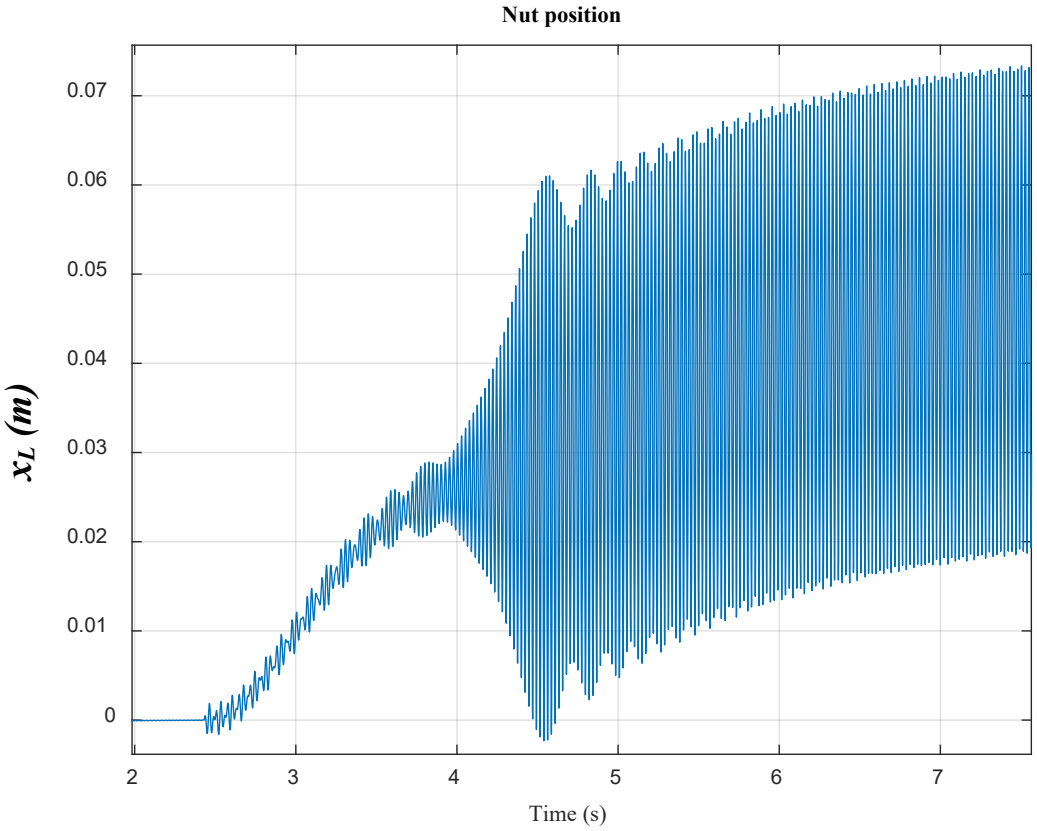

Figure 248. Load axial position

If load axial position is magnified, the frequency that can be seen is 42 Hz, as illustrated in Figure 249.

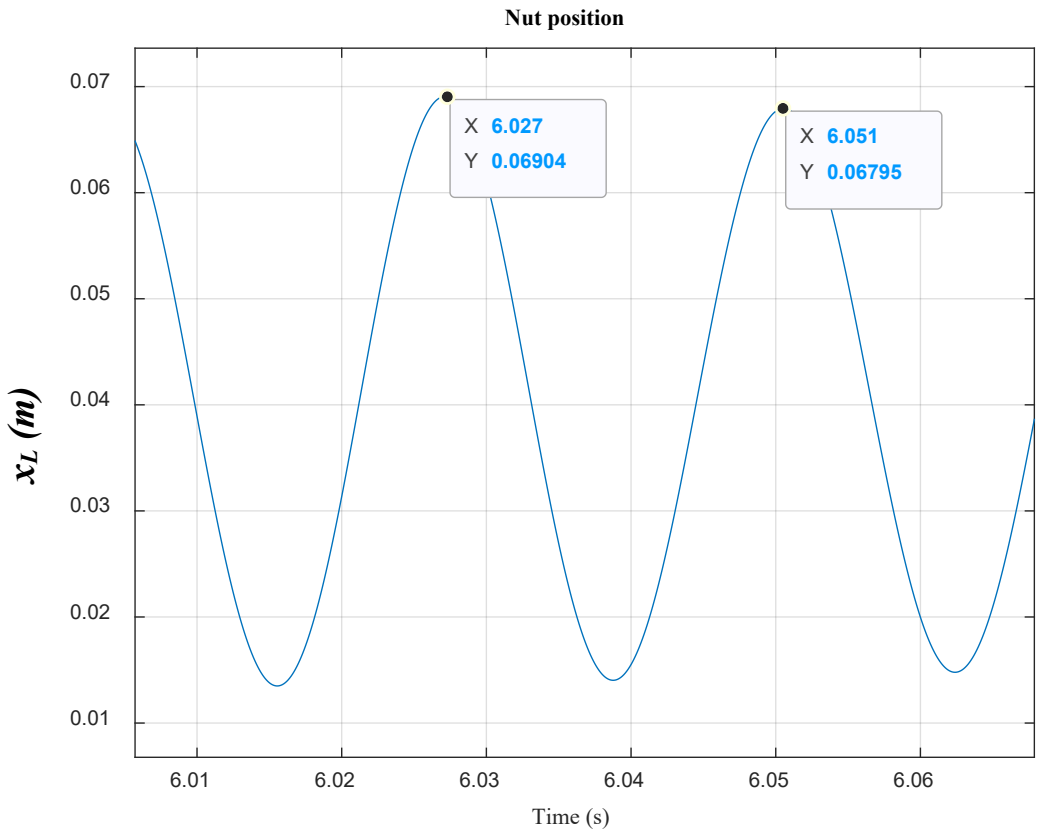

Figure 249. Load axial position (a frequency of 42 Hz is highlighted)

Taking the FFT, the axial position, x_L, response in time domain, shown in Figure 249, is transformed into a response in the frequency domain, as shown in Figure 250. The second resonant frequency, f_2, is located at 42 Hz.

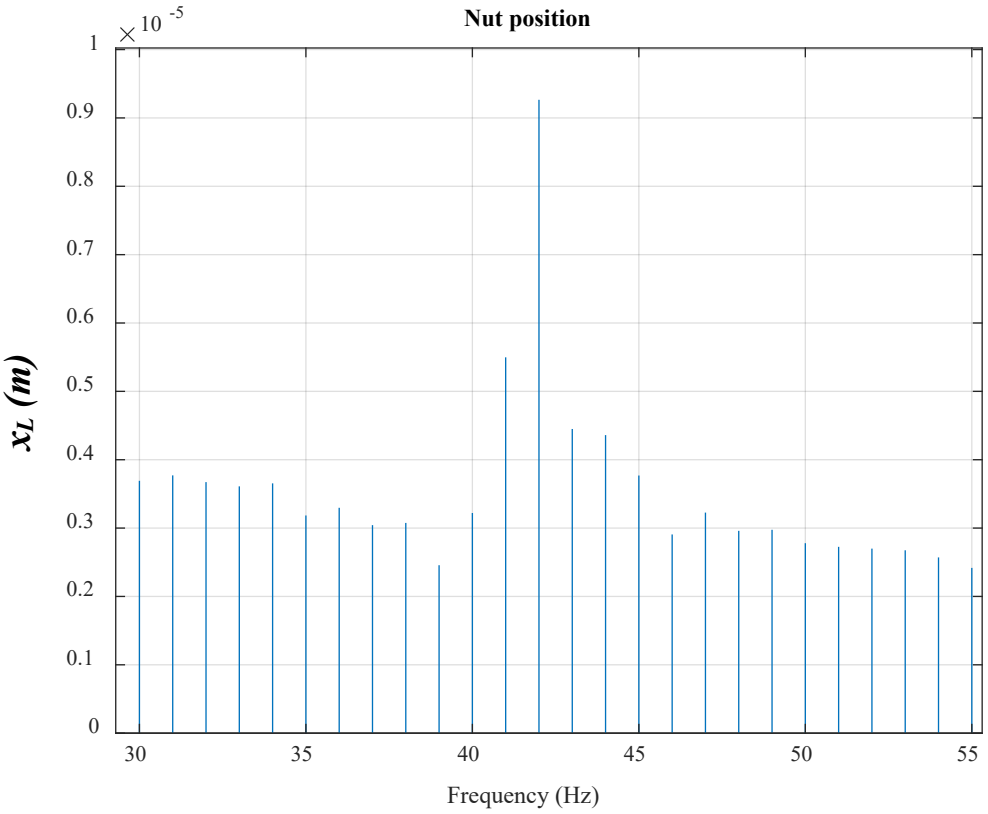

Figure 250. Axial position in the frequency domain

The servo motor speed is shown in Figure 251. It can be seen that the system operates as normal for 1.5 seconds (from instant 2.5s until 4s), which also can be noticed in Figure 248. During this time, the speed rises and then falls as actual position approaches demand. While the speed falls reaching to a value of 6 rad/s, the resonance is excited making the speed rise drifting from command. This, in turn, involves a subsequent rise in current to make up the sudden increase in speed. Instability has clearly happened here. After 0.8 seconds (at 4.8s), drive system protection is activated and speed is forcefully reduced. See the decrease in speed in Figure 251 since the instant 4.8s. Same test under the same conditions is simulated and speed instability is shown in Figure 252.

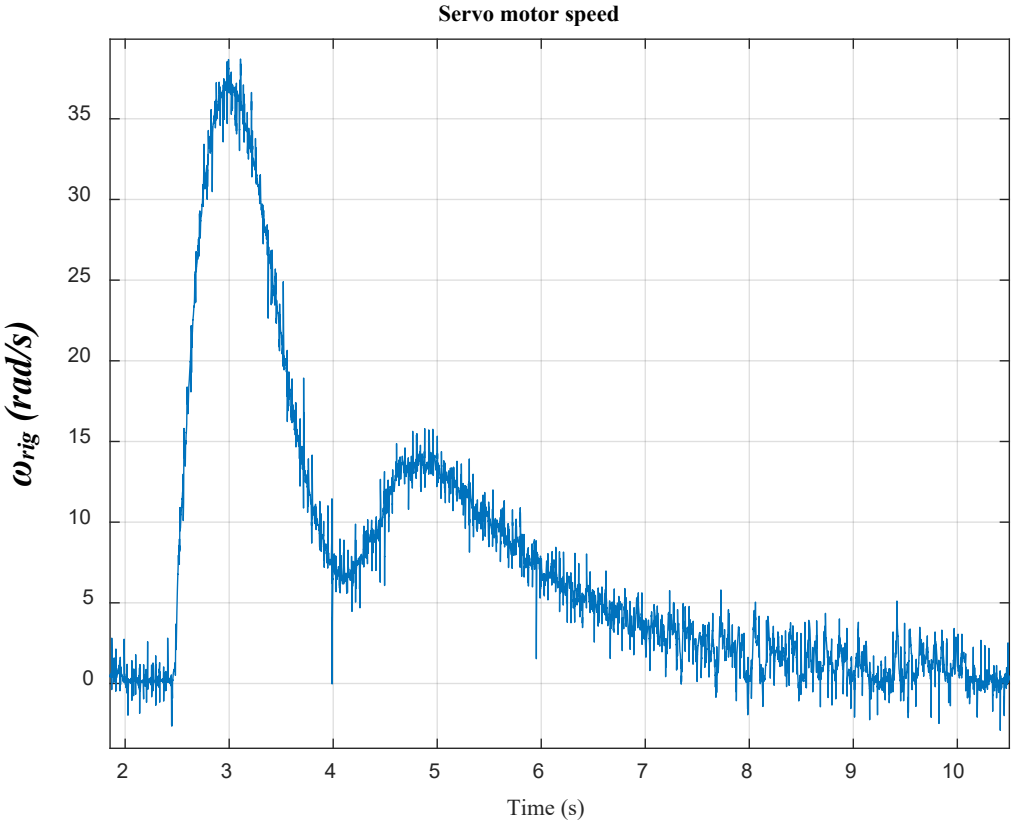

Figure 251. Servo motor speed [speed loop BW = 1 Hz]

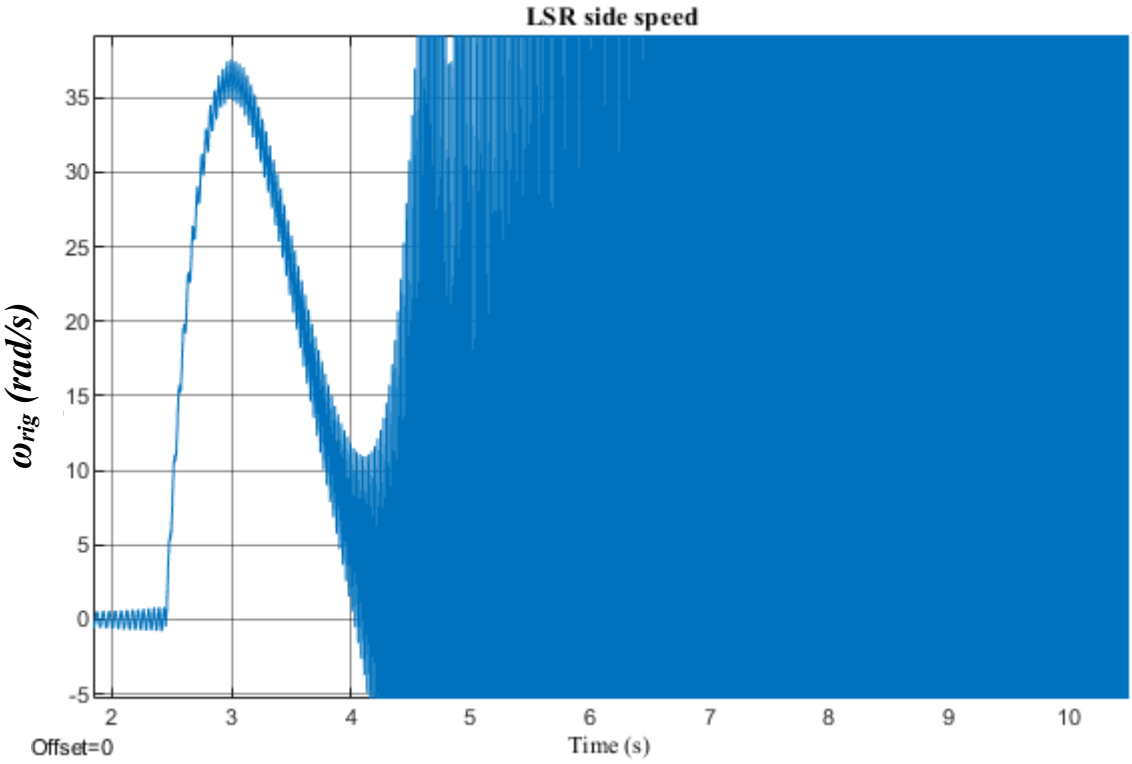

Figure 252. LSR side speed (simulated)

While system is driven to instability, the excited frequency, f_2, can be observed in the servo motor speed signal (Figure 253).

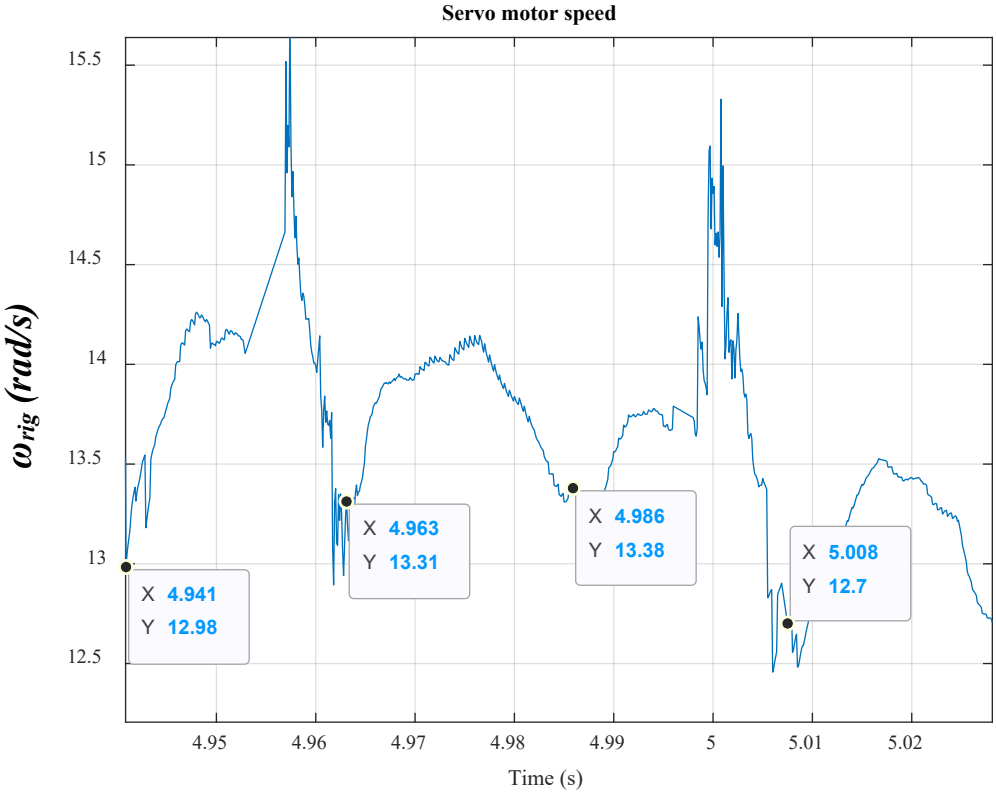

Figure 253. Servo motor speed (a frequency of 42 Hz is highlighted)

Taking the FFT, the rig speed, ω_{rig}, response in time domain, is transformed into a response in the frequency domain, as shown in Figure 254. The second resonant frequency, f_2, is located at 42 Hz. The signal is associated with noise and this is expected seeing the noise in the time tomain response (Figure 251).

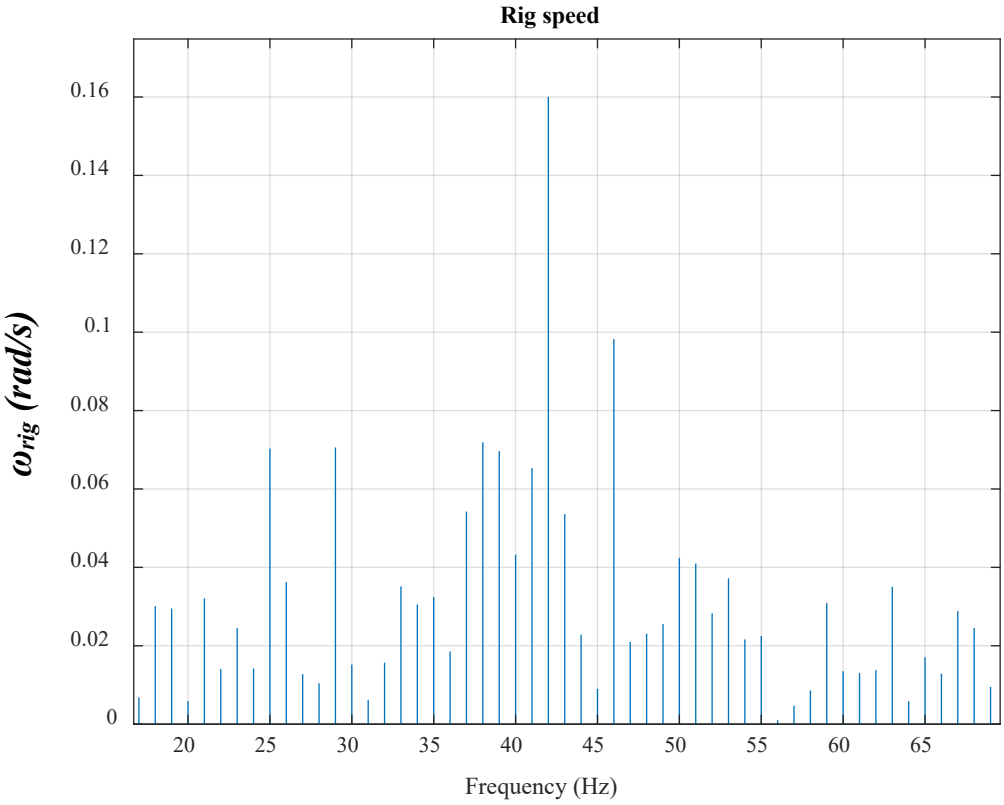

Figure 254. Rig speed in the frequency domain

The system is unstable so it starts to oscillate. Another frequency that can be seen is 6 Hz (Figure 255). This is due to the laboratory test rig and it is explained in Section (5.3.1).

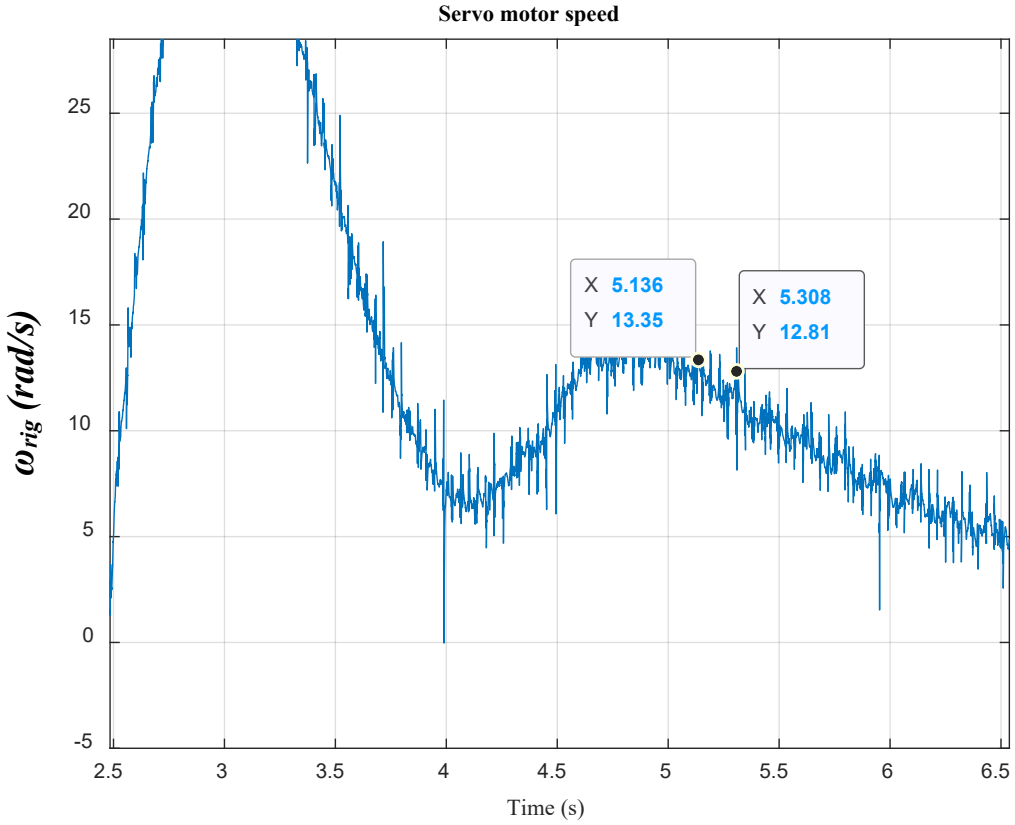

Figure 255. Servo motor speed (a frequency of 6 Hz is highlighted)

The servo motor applies the reaction torque of the mechanical system on the PDD. It can be seen in Figure 256 that the torque increases to supply the demand. However, after around 1.5 seconds of initiating the torque, the torque is stopped from increasing further by the drive protection, which has the effect of reducing the torque significantly. Instability is evident here.

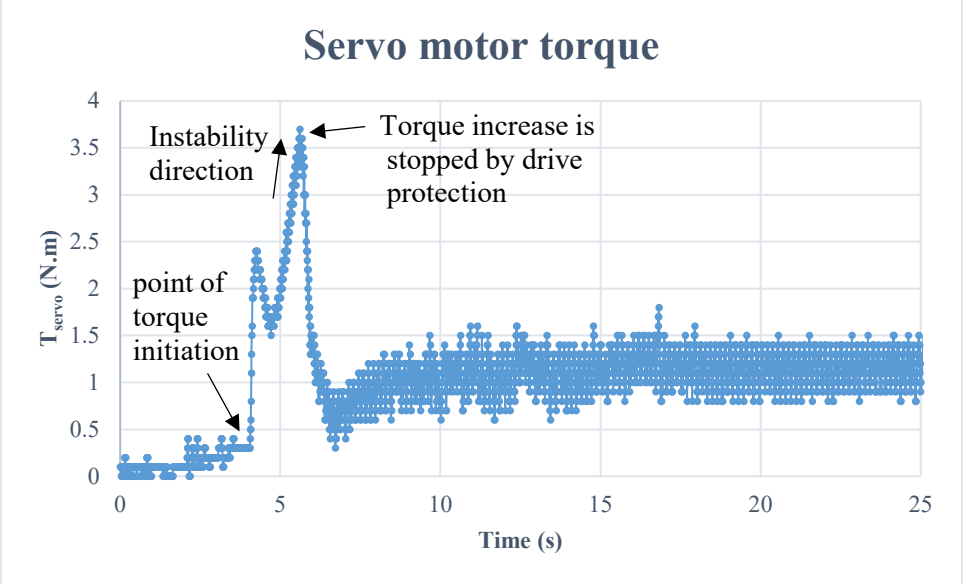

Figure 256. Servo motor applied torque on the PDD

The torque oscillates with a frequency equal to the excited frequency of the actuation system, which is *42 Hz*, as shown in Figure 257.

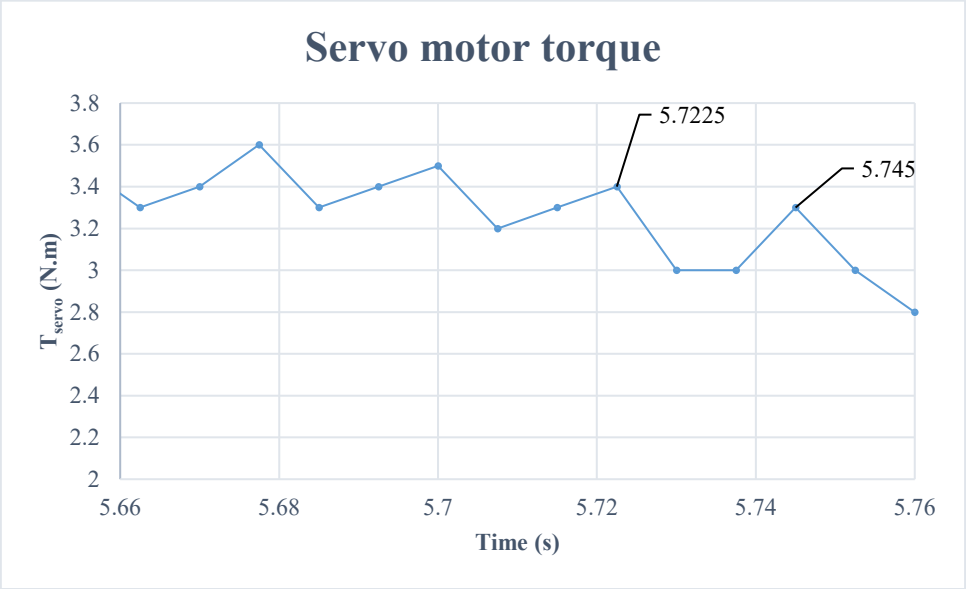

Figure 257. Servo motor applied torque on the PDD (a frequency of 42 Hz is highlighted)

When the system becomes unstable, system inertia starts to oscillate back and forth. There is a frequency that can be observed there (*6 Hz*), which is related to the laboratory test rig. This is explained in Section (5.3.1) and can be seen in Figure 258 (period = 19.56 – 19.3875 = 0.1725s). Additionally, within those broader oscillations, there are other oscillations inside, which are of a frequency equalling to 42 Hz (period = 19.5825 - 19.56 = 0.0225s).

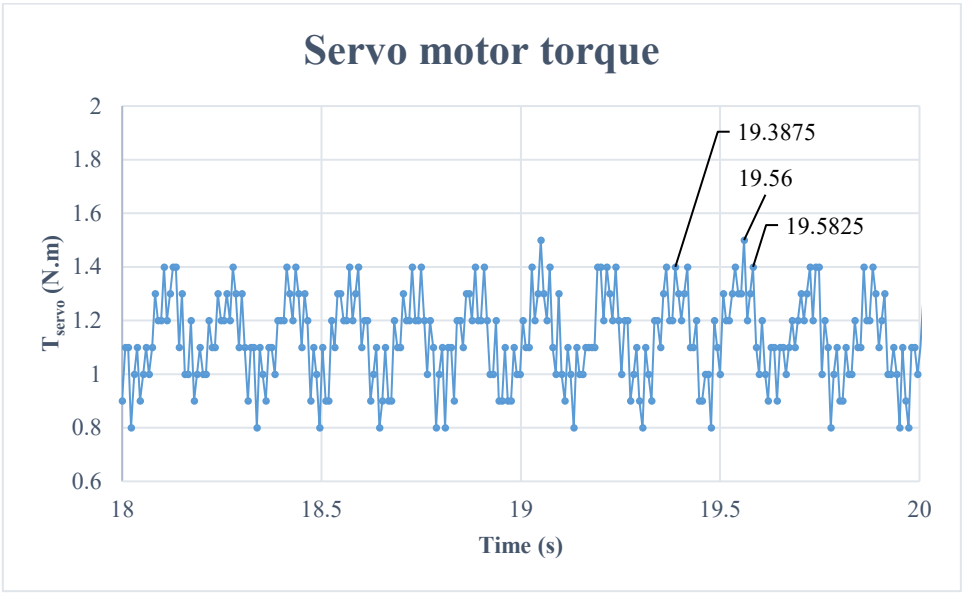

Figure 258. Servo motor applied torque on the PDD (frequencies highlighted = 6 Hz & 42 Hz)

The two mentioned frequencies are passed to the PDD stator windings, which is measured and depicted in Figure 259. The low amplitude of current is because of the torque being minimised and damped by the servo drive protection system. Otherwise, current would have continued to grow, which would lead to a fault in machine and also cause some damage to mechanical components.

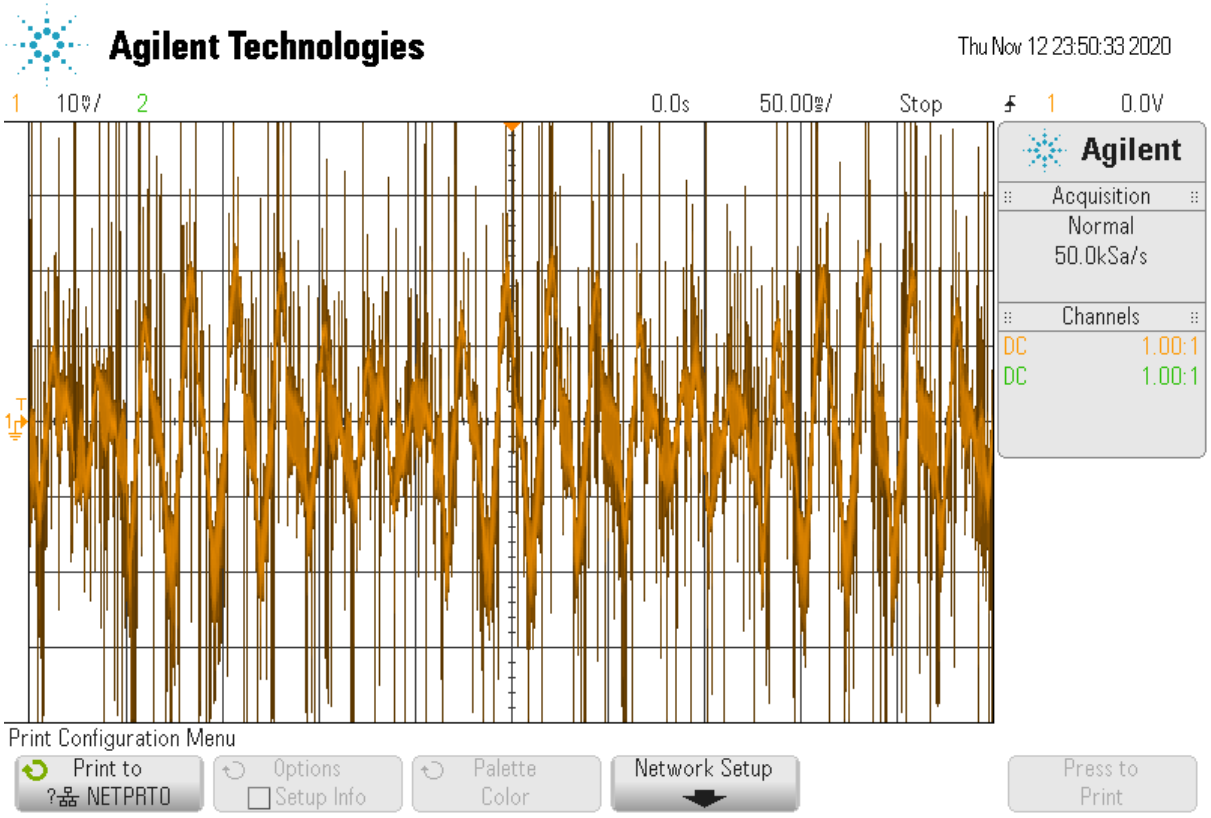

Figure 259. Phase A current by oscilloscope

To observe data more clearly so frequencies can be spotted more evidently, Figure 259 is presented more clearly in Figure 260. Two frequencies can be clearly observed. The first is *42 Hz* (period = 0.185 – 0.162 = 0.023s), which is the value of f_2, and this proves that the dynamics of the aircraft actuation system can propagate into the electrical system and can be shown in the PDD windings current. The other frequency, which is equal to *6 Hz* (period = 0.185 – 0.021 = 0.164s), is due to the laboratory test rig. This frequency is explained in Figure 194 and Figure 195.

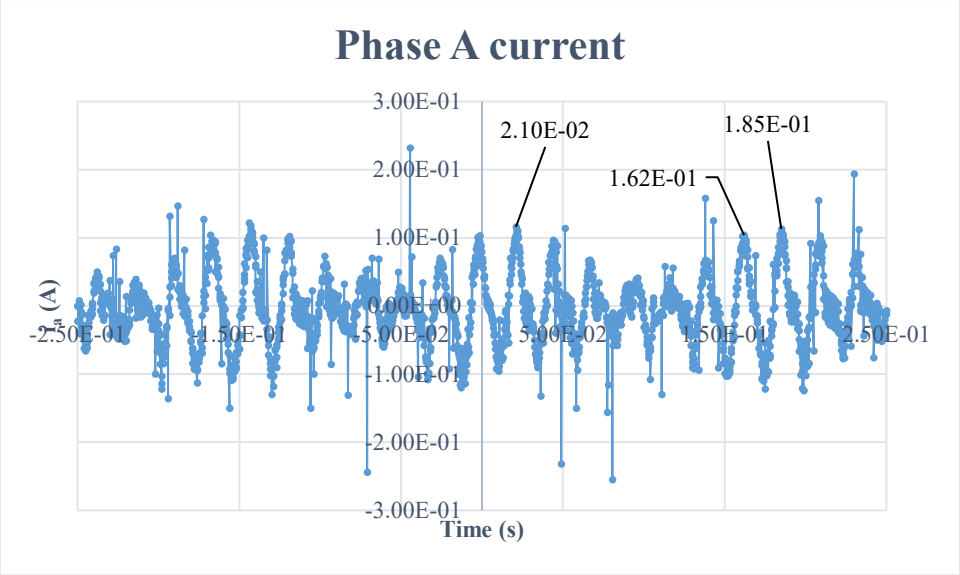

Figure 260. Measured phase A current

5.5.3 Effect of speed loop bandwidths on operation

To examine effect of bandwidth on operation, speed loop bandwidth is reduced to *0.5 Hz* and compared with the shape shown in Figure 251. A chirp signal of a low amplitude and a varying frequency (*1-70 Hz*) is applied in both cases to excite f_2. The comparison is depicted in Figure 261. The chirp signal is capable to destabilise the system but the system drive protection stops the procedure to prevent current increase. Simulated speed is depicted in Figure 262 for the lower BW case. It can be seen from Figure 261 that in the case of higher bandwidth the system is fast whilst the other case is noticeably low. However, the higher BW case is more oscillatory. Also, the frequency f_2 (*42 Hz*) is of higher amplitude in the case of higher BW, as shown in Figure 263 and Figure 264. This agrees with what is stated, in Chapter 4, with respect to the correlation between the mechanical system resonance characteristics and the speed loop bandwidths. The point emphasised here is that for a higher speed loop bandwidth, the stability margin is less.

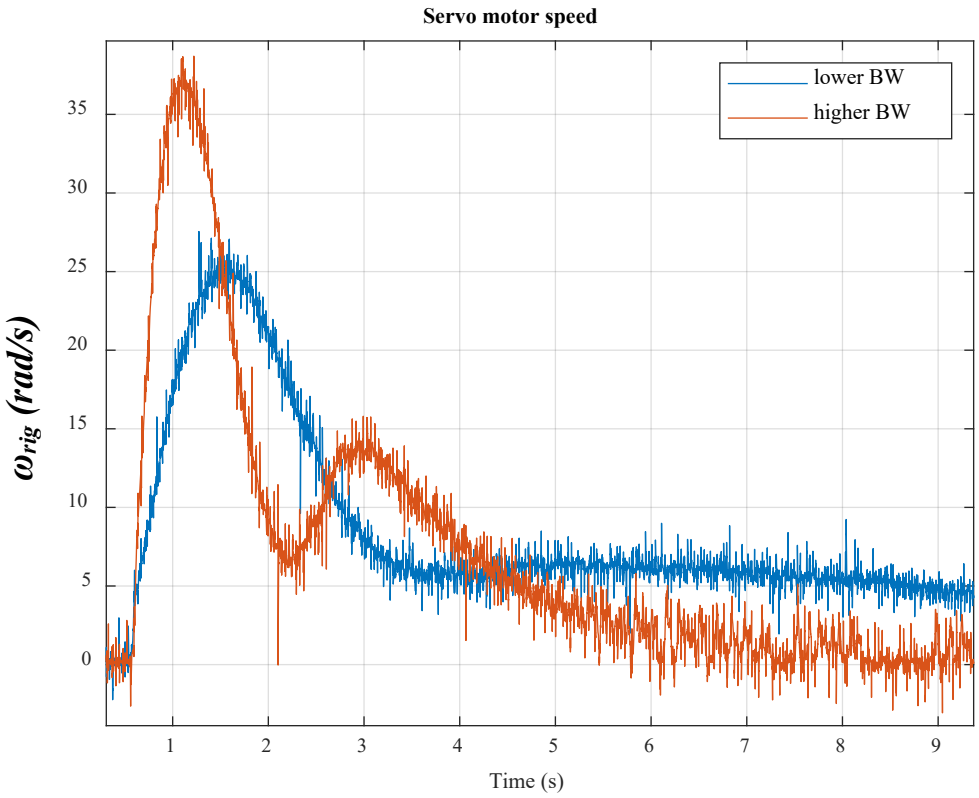

Figure 261. Servo motor speed using two different speed loop bandwidths

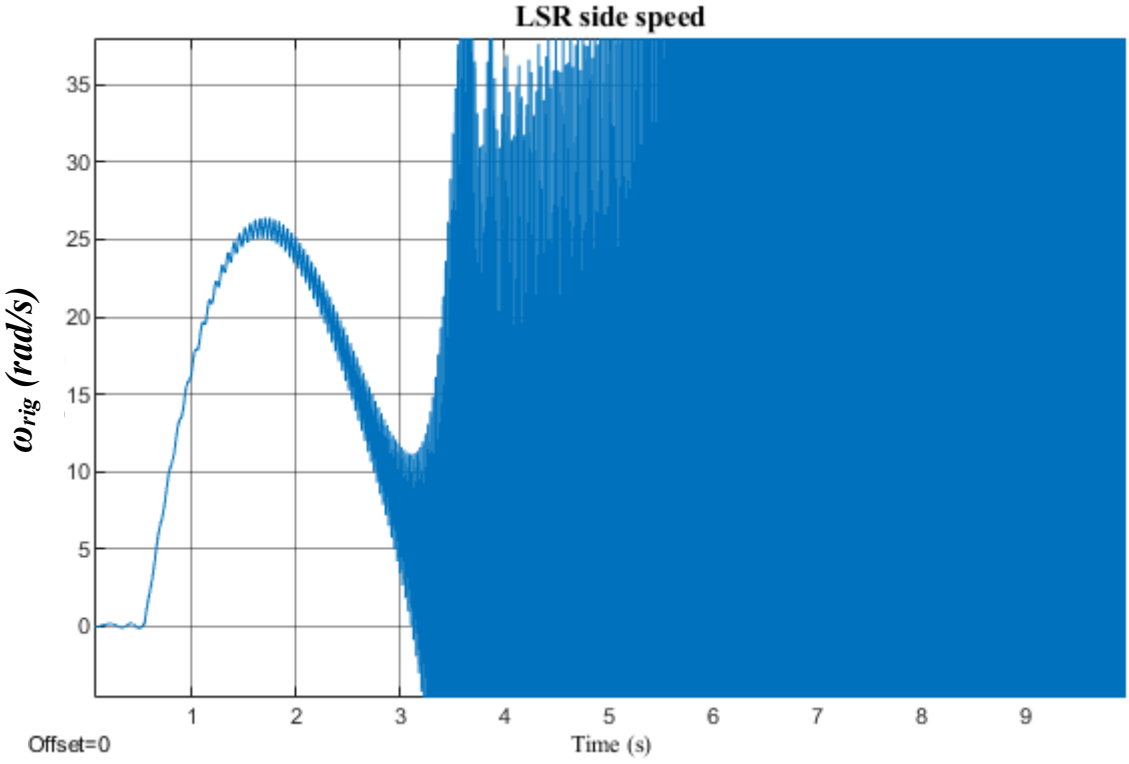

Figure 262. LSR side speed (lower BW case)

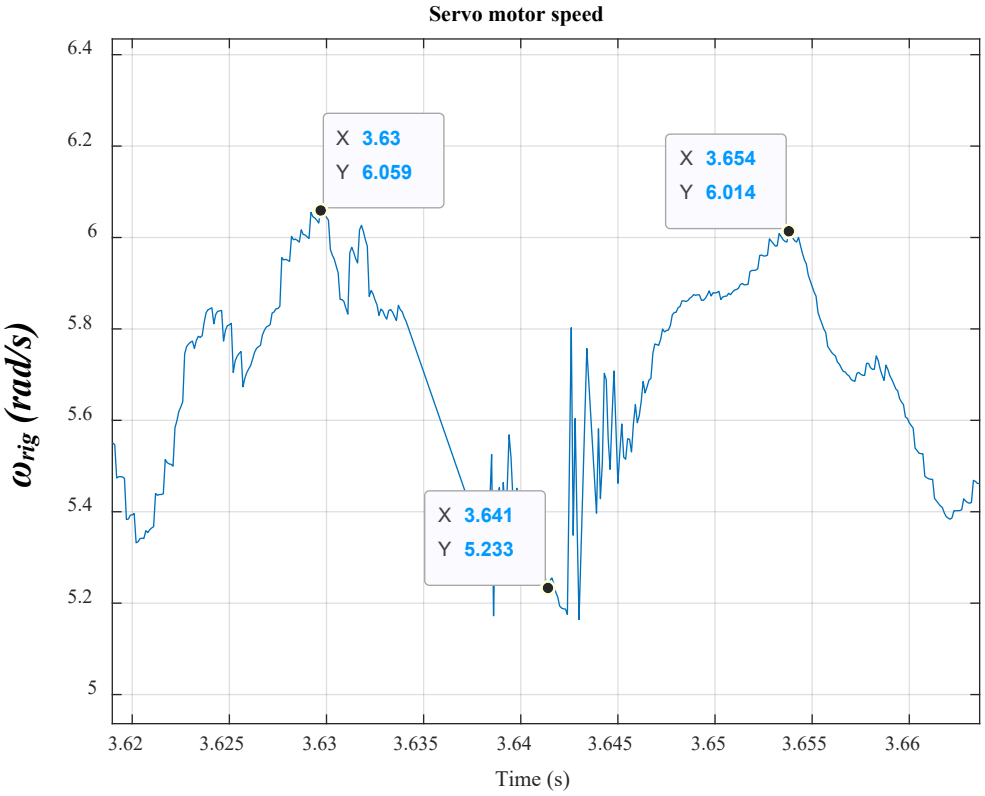

Figure 263. Lower BW case (amplitude of oscillations = 0.78 rad/s)

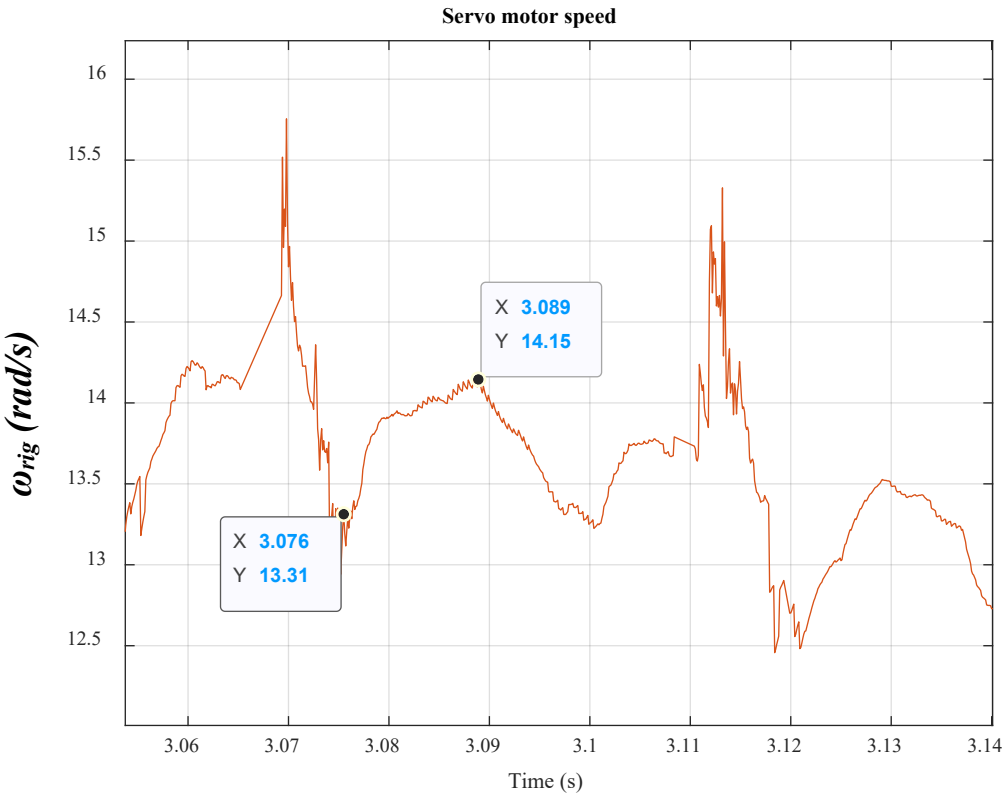

Figure 264. Lower BW case (amplitude of oscillations = 0.84 rad/s)

Looking back at Figure 263 and Figure 264, another frequency can be observed, which equals to 275 Hz. This is induced by the laboratory test rig. This is fully explained in Section (5.3.1). This frequency is clearly identified in Figure 265 and Figure 266. However, if the coordinates are subtracted, the outcome will be 0.004s. This is equivalent to 250 Hz. The correct period of this mechanically induced frequency is 0.00364s. The error is introduced by Matlab figure since it rounds the data tips to four significant figures.

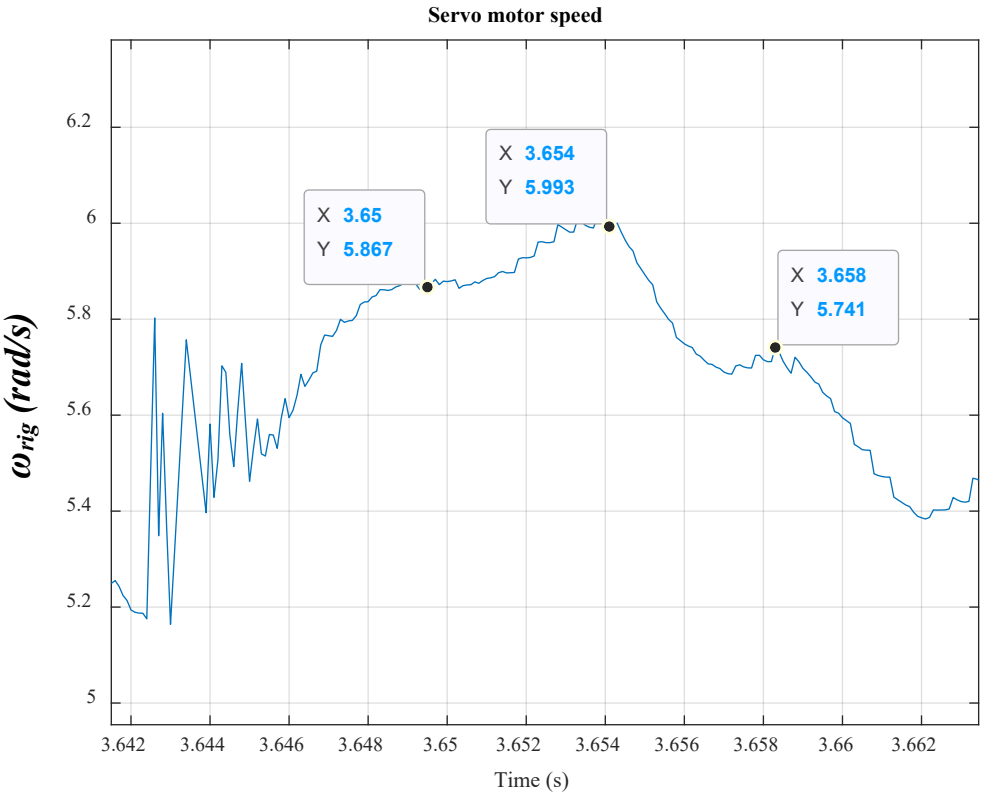

Figure 265. 275 Hz induced by the test rig

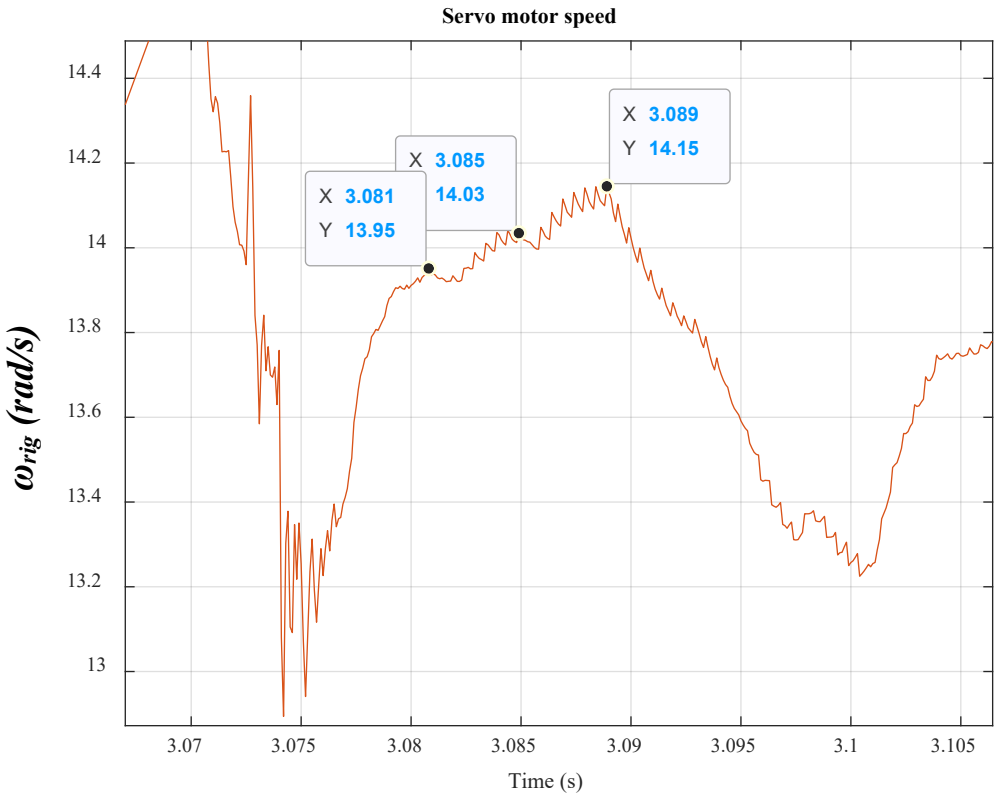

Figure 266. 275 Hz induced by the test rig

In the above tests, the position demand is set to around half of maximum displacement. This means that the torque applied is around half of the rated value. Although the disturbance amplitude is low, yet if it occurs with a frequency that is close to resonance, at this point oscillations develop and grow instantly. Such oscillations will result in degradation of the hardware and instability of the electrical network.

5.6 Conclusion

To sum up, testing of aircraft actuation system is aimed at highlighting the crucial dynamics of such a mechanical system. Hardware in the loop technique is used since it is proved to be an effective method to test complex mechanical systems with low cost and high safety. The common simplified model of aero actuation system is examined and compared with the proposed three-DOF model. During normal operation, the mechanical structure frequencies can be observed despite of high system damping.

As structure frequency is decreased by varying a vital parameter, the frequency becomes more obvious during normal operation. Extreme loading conditions of the system illustrate resonance excitation, which is unseen using the simplified one-DOF model available in the literature. Instability case is shown to be more severe when resonance frequency is lower and also when the speed loop bandwidth is higher. The highlighted frequencies have been shown to propagate to electrical system, which proves the occurrence of electromechanical interaction.

Chapter 6 Conclusion

In this chapter, a summary of work presented, contributions and future improvements are introduced.

6.1 Recap of work presented

In chapter 1, an application background is presented to introduce conventional aircraft and their impact on environment and cost. The need to electrification of aircraft is emphasised. Various electrifiable systems on-board are mentioned. Major electrifiable systems presented are actuators, which is stated that they are used for various systems on-board; such as thrust reversers, landing gear, gear breaks, flight control surfaces and so on. It is pointed out that primary flight control surface (rudder) is the system to be under study. Many types of actuators are mentioned and the electromechanical actuator is highlighted due to many advantages; such as lighter weight of electrical power distribution system, reductions in maintenance and better controllability. Three types of screw mechanism are shown but ball-screw system is the one picked due to high accuracy and low cost. Due to many disadvantages associated with mechanical gearboxes, magnetic gearing is justified to be a better choice for this application.

A comprehensive literature review is given that covered relation of the ongoing research to previous publications. It was established, from previous work, that aircraft power system stability may be vulnerable to actuator dynamics such as load torque. However, other aero actuator dynamics, such as structure resonance, was never reported. It was crucial to investigate this uncovered work because electromechanical actuators were reported to have resonance dynamics. Further, it was reported that electromechanical interaction occurred in many systems such as aero gas turbine, land-based and wind generation systems, as well as systems used in marine and industrial applications. It was argued that to bring advantage to an increased aircraft electrification, the aircraft required an uprated EMA system model to be accountable for stability analysis and control design. It was stated that EMA system must be ensured stable to protect the electrical power network. Indeed, optimised functionality of EMA system is an integral part of a safe flight operation, and this emphasised the need of the research.

In chapter 2, configuration of rudder EMA system, which was proposed under a previous research project, is detailed. Assumptions and control schemes are designated. The conventional aero EMA model, which lumps the entire mechanical system to a single equivalent inertia, is considered. System is simulated under normal position demand to show system operation. Additionally, certain load conditions, such as a varying frequency disturbance, are applied to examine system response. It is shown that the conventional model is irresponsive to the applied varying frequency disturbance. It is then when the addition of a more detailed model becomes essential. Many models and modelling approaches, for ball-screw systems, are out there developed by mechanical engineers. After a careful study, model techniques are classified into three main types; finite elements method, hybrid models, and discrete models. Due to many flaws associated with FEM; such as low speed and high number of resonance

modes, FEM is excluded. A moderately low order hybrid model with adequate details are found to have high accuracy and experimentally validated. Rigid mass motions and screw shaft torsional and axial flexibilities are the dynamics accounted for in this hybrid model, which is taken as a starting point. It turns out that certain dynamics such as screw shaft torsional and axial compliance could be neglected. Consequently, the hybrid model is simplified and the screw shaft is assumed torsionally and axially rigid. From this, a discrete model is obtained, which contains only four degrees of freedom accounting for mass motions.

It is shown that there are two crucial resonances which are low-frequency modes and may have the potential to cause instability. That was why they had to be carefully considered. In contrary, the other two frequencies are found to be high-frequency modes. On those bases, it is possible to reduce the discrete four-DOF model to an equivalent two-DOF model. However, it is not possible to lump the screw-nut interface with any other element since this is the component that composes the interaction between linear and rotary motions. The two-DOF model is proved effective in the case of lower screw lead. This is because, in this case, interaction between rotational and axial motions is lower, and this was established in previous publications. For such a reason, the model is reduced to up to three-DOFs. The latter is compared with the hybrid six-DOF and both models show similar results. Further, in Chapter two, all resonance dynamics of the actuator system are mathematically analysed to highlight the relevant parameters which produce them.

In this research study, the system under examination is an EMA for a small business jet. That was why it was vital to investigate the findings for a range of aircraft sizes. Since parameters of actuation systems for commercial aircraft are not available, actuation systems are sized in Chapter 3. The sizing is based on certain assumptions as well as limited available data. The outcomes of the sizing procedure show reasonable figures, which give the confidence that performed approximation is acceptable. The models shown in Chapter 2 are applied to different aircraft sizes. It is shown that the proposed three-DOF model is adequate and can be usable for any aircraft size. Also, it is shown that the resonant frequencies become lower as aircraft sizes increases, which indicates the severity of structure resonance effects in case of larger aircraft.

In chapter 4, the mechanical system is integrated with the electrical system and analysis is performed to find interactions between both domains. Entire system is linearised to undergo small signal stability analysis. Modal analysis shows that by varying mechanical system parameters, system stability margin varies accordingly. This proves the proposal that mechanical system has to be considered in more details and the traditional simplified model is insufficient. The latter is incapable of highlighting any variation in stability margin coming from mechanical system parameters since all parameters are lumped together. From the frequency response analysis it is proved that mechanical structure resonance is closely related to speed loop bandwidth, which means that the bandwidth is limited by the mechanical

system responses. This is due to the properties of anti-resonance, which causes a phase shift passing through -180º. This coincides with the 0dB gain crossing, represented by the bandwidth limit. According to stability criteria, that effectively compromises system stability. Further, time domain analysis shows that there are some oscillations in the normal operation which are not seen by using the traditional EMA model. Also, time domain analysis shows instability occurrence due to extreme loading conditions, where resonance, located within current controller range, is excited by a disturbance of little amplitude and an equal frequency. The simplified traditional model of aero EMA is subjected to similar loading conditions but no interactions are spotted due to oversimplifications.

In Chapter 5, results are validated by a test rig, which includes detailed mechanical emulator implemented in dSPACE platform. The test rig construction is explained in details. Similar tests carried out in previous chapters are performed in the laboratory. It is concluded that instability could occur under certain loading conditions, which if the traditional model is used no instability is observed. Also, it is proved that instability is more severe in case of higher speed loop bandwidth and lower mechanical resonant frequencies.

6.2 Findings and contribution

6.2.1 Findings

A low order simplified model was obtained based on a validated modelling technique. The simplified model produced matches the high order model. The proposed three-DOF model was compared with the over simplified one-DOF model used in literature. Crucial frequencies have shown to be evident during normal operation and extreme loading conditions whereas the one-DOF model showed no dynamics.

Electromechanical interaction has been identified as a serious problem for aero EMA systems. The issues arise from the actuator structure resonance, certain type of loads, current and speed loops' bandwidths that set the requirements for prompt flight surface actuation. The research was focused on rudder actuation, which is a primary control surface. However, it may also be applicable to other primary control surfaces or any other aircraft system where actuator is utilised.

6.2.2 Contribution

Electromechanical interaction in aircraft electromechanical actuation system is considered in full detail. The electromechanical actuator (EMA) is considered to actuate the rudder. Electromechanical system is simulated using accurate electromechanical actuation models, which led to proposing simplified models. An experimental test rig is used, employing Hardware In the Loop (HIL) technique, to emulate the actuation system. Results validate the modelling techniques and electromechanical interaction analysis. EMA system is sized for a range of common aircraft types; using curve fitting equations,

which could be used in other research studies. Analysis confirmed that the suggested modelling methodology is generic and can be valid for various aircraft sizes.

In this study, contribution is mainly made to knowledge. This means that contribution is essentially focused on the identification of critical parameters, interaction between electrical and mechanical systems and associated conditions. The experimental results validate and confirm the findings. Also, experimental results help in spotting if certain dynamics are neglected in the simulations.

6.3 Future work

1. Active damping must be added to the system in order for it to be operated reliably even in case of extreme load conditions. Active damping should be done through the PDD controller to limit the transfer of disturbances between the mechanical and electrical domains.
2. The thesis covers identifying mechanical system dynamics for a range of aircraft sizes. The study presented in Chapter 4 can also be performed on a range of aircraft sizes. This must be preceded by continuation of sizing process to include properties of PDD airgap, HSR, stator windings.

6.4 Publications

The following three papers are in the preparation:

1- Ali Elmajdub et al., "*Modelling methodology of electro-mechanical actuators for aircraft rudder applications -Part 1*" to be submitted to IEEE Transactions on Aerospace and Electronic Systems.

2- Ali Elmajdub et al., "*Modelling of electro-mechanical actuators for aircraft rudder applications considering different aircraft sizes -Part 1I*" to be submitted to IEEE Transactions on Aerospace and Electronic Systems.

3- Ali Elmajdub et al., "*Investigation of interactions between mechanical and electrical subsystems of an electro-mechanical actuator for aircraft rudder applications"*, to be submitted to IEEE Transactions on Transportation Electrification.

Appendices

Appendix A

PDD modelling & abc to dq axes transformation derivation

$$\begin{bmatrix} v_{an} \\ v_{bn} \\ v_{cn} \end{bmatrix} = \begin{bmatrix} R_s & 0 & 0 \\ 0 & R_s & 0 \\ 0 & 0 & R_s \end{bmatrix} \begin{bmatrix} i_a \\ i_b \\ i_c \end{bmatrix} + \begin{bmatrix} L-M & 0 & 0 \\ 0 & L-M & 0 \\ 0 & 0 & L-M \end{bmatrix} \frac{d}{dt} \begin{bmatrix} i_a \\ i_b \\ i_c \end{bmatrix} + \begin{bmatrix} e_a \\ e_b \\ e_c \end{bmatrix}$$

$$\begin{bmatrix} v_{an} \\ v_{bn} \\ v_{cn} \end{bmatrix} = \begin{bmatrix} R_s & 0 & 0 \\ 0 & R_s & 0 \\ 0 & 0 & R_s \end{bmatrix} \begin{bmatrix} i_a \\ i_b \\ i_c \end{bmatrix} + \frac{3}{2} \begin{bmatrix} L & 0 & 0 \\ 0 & L & 0 \\ 0 & 0 & L \end{bmatrix} \frac{d}{dt} \begin{bmatrix} i_a \\ i_b \\ i_c \end{bmatrix} + \begin{bmatrix} -\omega_e \Psi_m \sin(\omega_e t) \\ -\omega_e \Psi_m \sin\left(\omega_e t - \frac{2\pi}{3}\right) \\ -\omega_e \Psi_m \sin\left(\omega_e t + \frac{2\pi}{3}\right) \end{bmatrix}$$

$$\begin{bmatrix} v_d \\ v_q \end{bmatrix} = \frac{2}{3} \begin{bmatrix} \cos(\omega_e t) & \cos\left(\omega_e t - \frac{2\pi}{3}\right) & \cos\left(\omega_e t + \frac{2\pi}{3}\right) \\ -\sin(\omega_e t) & -\sin\left(\omega_e t - \frac{2\pi}{3}\right) & -\sin\left(\omega_e t + \frac{2\pi}{3}\right) \end{bmatrix} \begin{bmatrix} v_{an} \\ v_{bn} \\ v_{cn} \end{bmatrix}$$

$$\begin{bmatrix} i_a \\ i_b \\ i_c \end{bmatrix} = \begin{bmatrix} \cos(\omega_e t) & -\sin(\omega_e t) \\ \cos\left(\omega_e t - \frac{2\pi}{3}\right) & -\sin\left(\omega_e t - \frac{2\pi}{3}\right) \\ \cos\left(\omega_e t + \frac{2\pi}{3}\right) & -\sin\left(\omega_e t + \frac{2\pi}{3}\right) \end{bmatrix} \begin{bmatrix} i_d \\ i_q \end{bmatrix}$$

$$\frac{d}{dt} \begin{bmatrix} i_a \\ i_b \\ i_c \end{bmatrix} = \frac{d}{dt} \begin{bmatrix} \cos(\omega_e t) & -\sin(\omega_e t) \\ \cos\left(\omega_e t - \frac{2\pi}{3}\right) & -\sin\left(\omega_e t - \frac{2\pi}{3}\right) \\ \cos\left(\omega_e t + \frac{2\pi}{3}\right) & -\sin\left(\omega_e t + \frac{2\pi}{3}\right) \end{bmatrix} \begin{bmatrix} i_d \\ i_q \end{bmatrix}$$

$$\frac{di_a}{dt} = \frac{d(i_d \cos(\omega_e t) - i_q \sin(\omega_e t))}{dt}$$

$$= -\omega_e i_d \sin(\omega_e t) + \cos(\omega_e t) \frac{di_d}{dt} - \omega_e i_q \cos(\omega_e t) - \sin(\omega_e t) \frac{di_q}{dt}$$

$$\frac{di_b}{dt} = \frac{d(i_d \cos\left(\omega_e t - \frac{2\pi}{3}\right) - i_q \sin\left(\omega_e t - \frac{2\pi}{3}\right))}{dt}$$

$$= -\omega_e i_d \sin\left(\omega_e t - \frac{2\pi}{3}\right) + \cos\left(\omega_e t - \frac{2\pi}{3}\right) \frac{di_d}{dt} - \omega_e i_q \cos\left(\omega_e t - \frac{2\pi}{3}\right)$$

$$- \sin\left(\omega_e t - \frac{2\pi}{3}\right) \frac{di_q}{dt}$$

$$\frac{di_c}{dt} = \frac{d(i_d \cos\left(\omega_e t + \frac{2\pi}{3}\right) - i_q \sin\left(\omega_e t + \frac{2\pi}{3}\right))}{dt} =$$

$$= -\omega_e i_d \sin\left(\omega_e t + \frac{2\pi}{3}\right) + \cos(\omega_e t + 2\pi/3) \frac{di_d}{dt} - \omega_e i_q \cos(\omega_e t + 2\pi/3)$$

$$- \sin\left(\omega_e t + \frac{2\pi}{3}\right) \frac{di_q}{dt}$$

$$\frac{d}{dt}\begin{bmatrix} i_a \\ i_b \\ i_c \end{bmatrix} = \omega_e \begin{bmatrix} \cos(\omega_e t) & -\sin(\omega_e t) \\ \cos\left(\omega_e t - \frac{2\pi}{3}\right) & -\sin\left(\omega_e t - \frac{2\pi}{3}\right) \\ \cos\left(\omega_e t + \frac{2\pi}{3}\right) & -\sin\left(\omega_e t + \frac{2\pi}{3}\right) \end{bmatrix} \begin{bmatrix} -i_q \\ i_d \end{bmatrix} + \begin{bmatrix} \cos(\omega_e t) & -\sin(\omega_e t) \\ \cos\left(\omega_e t - \frac{2\pi}{3}\right) & -\sin\left(\omega_e t - \frac{2\pi}{3}\right) \\ \cos\left(\omega_e t + \frac{2\pi}{3}\right) & -\sin\left(\omega_e t + \frac{2\pi}{3}\right) \end{bmatrix} \frac{d}{dt}\begin{bmatrix} i_d \\ i_q \end{bmatrix}$$

$$\begin{bmatrix} v_{an} \\ v_{bn} \\ v_{cn} \end{bmatrix} = \begin{bmatrix} R_s & 0 & 0 \\ 0 & R_s & 0 \\ 0 & 0 & R_s \end{bmatrix} \begin{bmatrix} i_a \\ i_b \\ i_c \end{bmatrix} + \frac{3}{2}\omega_e \begin{bmatrix} L & 0 & 0 \\ 0 & L & 0 \\ 0 & 0 & L \end{bmatrix} \begin{bmatrix} \cos(\omega_e t) & -\sin(\omega_e t) \\ \cos\left(\omega_e t - \frac{2\pi}{3}\right) & -\sin\left(\omega_e t - \frac{2\pi}{3}\right) \\ \cos\left(\omega_e t + \frac{2\pi}{3}\right) & -\sin\left(\omega_e t + \frac{2\pi}{3}\right) \end{bmatrix} \begin{bmatrix} -i_q \\ i_d \end{bmatrix} + \frac{3}{2}\begin{bmatrix} L & 0 & 0 \\ 0 & L & 0 \\ 0 & 0 & L \end{bmatrix} \begin{bmatrix} \cos(\omega_e t) & -\sin(\omega_e t) \\ \cos\left(\omega_e t - \frac{2\pi}{3}\right) & -\sin\left(\omega_e t - \frac{2\pi}{3}\right) \\ \cos\left(\omega_e t + \frac{2\pi}{3}\right) & -\sin\left(\omega_e t + \frac{2\pi}{3}\right) \end{bmatrix} \frac{d}{dt}\begin{bmatrix} i_d \\ i_q \end{bmatrix} + \begin{bmatrix} -\omega_e \Psi_m \sin(\omega_e t) \\ -\omega_e \Psi_m \sin\left(\omega_e t - \frac{2\pi}{3}\right) \\ -\omega_e \Psi_m \sin\left(\omega_e t + \frac{2\pi}{3}\right) \end{bmatrix}$$

Multiply each side by the following transformation matrix:

$$\frac{2}{3}\begin{bmatrix} \cos(\omega_e t) & \cos\left(\omega_e t - \frac{2\pi}{3}\right) & \cos\left(\omega_e t + \frac{2\pi}{3}\right) \\ -\sin(\omega_e t) & -\sin\left(\omega_e t - \frac{2\pi}{3}\right) & -\sin\left(\omega_e t + \frac{2\pi}{3}\right) \end{bmatrix}$$

$$\frac{2}{3}\begin{bmatrix} \cos(\omega_e t) & \cos\left(\omega_e t-\frac{2\pi}{3}\right) & \cos\left(\omega_e t+\frac{2\pi}{3}\right) \\ -\sin(\omega_e t) & -\sin\left(\omega_e t-\frac{2\pi}{3}\right) & -\sin\left(\omega_e t+\frac{2\pi}{3}\right) \end{bmatrix}\begin{bmatrix} v_{an} \\ v_{bn} \\ v_{cn} \end{bmatrix}$$

$$=\frac{2}{3}\begin{bmatrix} \cos(\omega_e t) & \cos\left(\omega_e t-\frac{2\pi}{3}\right) & \cos\left(\omega_e t+\frac{2\pi}{3}\right) \\ -\sin(\omega_e t) & -\sin\left(\omega_e t-\frac{2\pi}{3}\right) & -\sin\left(\omega_e t+\frac{2\pi}{3}\right) \end{bmatrix}\begin{bmatrix} R_s & 0 & 0 \\ 0 & R_s & 0 \\ 0 & 0 & R_s \end{bmatrix}\begin{bmatrix} \cos(\omega_e t) & -\sin(\omega_e t) \\ \cos\left(\omega_e t-\frac{2\pi}{3}\right) & -\sin\left(\omega_e t-\frac{2\pi}{3}\right) \\ \cos\left(\omega_e t+\frac{2\pi}{3}\right) & -\sin\left(\omega_e t+\frac{2\pi}{3}\right) \end{bmatrix}\begin{bmatrix} i_d \\ i_q \end{bmatrix}$$

$$+\left(\frac{3}{2}\right)\left(\frac{2}{3}\right)\omega_e\begin{bmatrix} \cos(\omega_e t) & \cos\left(\omega_e t-\frac{2\pi}{3}\right) & \cos\left(\omega_e t+\frac{2\pi}{3}\right) \\ -\sin(\omega_e t) & -\sin\left(\omega_e t-\frac{2\pi}{3}\right) & -\sin\left(\omega_e t+\frac{2\pi}{3}\right) \end{bmatrix}\begin{bmatrix} L & 0 & 0 \\ 0 & L & 0 \\ 0 & 0 & L \end{bmatrix}\begin{bmatrix} \cos(\omega_e t) & -\sin(\omega_e t) \\ \cos\left(\omega_e t-\frac{2\pi}{3}\right) & -\sin\left(\omega_e t-\frac{2\pi}{3}\right) \\ \cos\left(\omega_e t+\frac{2\pi}{3}\right) & -\sin\left(\omega_e t+\frac{2\pi}{3}\right) \end{bmatrix}\begin{bmatrix} -i_q \\ i_d \end{bmatrix}$$

$$+\left(\frac{3}{2}\right)\left(\frac{2}{3}\right)\begin{bmatrix} \cos(\omega_e t) & \cos\left(\omega_e t-\frac{2\pi}{3}\right) & \cos\left(\omega_e t+\frac{2\pi}{3}\right) \\ -\sin(\omega_e t) & -\sin\left(\omega_e t-\frac{2\pi}{3}\right) & -\sin\left(\omega_e t+\frac{2\pi}{3}\right) \end{bmatrix}\begin{bmatrix} L & 0 & 0 \\ 0 & L & 0 \\ 0 & 0 & L \end{bmatrix}\begin{bmatrix} \cos(\omega_e t) & -\sin(\omega_e t) \\ \cos\left(\omega_e t-\frac{2\pi}{3}\right) & -\sin\left(\omega_e t-\frac{2\pi}{3}\right) \\ \cos\left(\omega_e t+\frac{2\pi}{3}\right) & -\sin\left(\omega_e t+\frac{2\pi}{3}\right) \end{bmatrix}\frac{d}{dt}\begin{bmatrix} i_d \\ i_q \end{bmatrix}$$

$$+\frac{2}{3}\begin{bmatrix} \cos(\omega_e t) & \cos\left(\omega_e t-\frac{2\pi}{3}\right) & \cos\left(\omega_e t+\frac{2\pi}{3}\right) \\ -\sin(\omega_e t) & -\sin\left(\omega_e t-\frac{2\pi}{3}\right) & -\sin\left(\omega_e t+\frac{2\pi}{3}\right) \end{bmatrix}\begin{bmatrix} e_a \\ e_b \\ e_c \end{bmatrix}$$

$$\begin{bmatrix} v_d \\ v_q \end{bmatrix}=R_s\begin{bmatrix} i_d \\ i_q \end{bmatrix}+\frac{3}{2}\omega_e L\begin{bmatrix} -i_q \\ i_d \end{bmatrix}+\frac{3}{2}L\frac{d}{dt}\begin{bmatrix} i_d \\ i_q \end{bmatrix}$$

$$+\frac{2}{3}\begin{bmatrix} \cos(\omega_e t) & \cos\left(\omega_e t-\frac{2\pi}{3}\right) & \cos\left(\omega_e t+\frac{2\pi}{3}\right) \\ -\sin(\omega_e t) & -\sin\left(\omega_e t-\frac{2\pi}{3}\right) & -\sin\left(\omega_e t+\frac{2\pi}{3}\right) \end{bmatrix}\begin{bmatrix} e_a \\ e_b \\ e_c \end{bmatrix}$$

$$\begin{bmatrix} e_d \\ e_q \end{bmatrix}=\frac{2}{3}\begin{bmatrix} \cos(\omega_e t) & \cos\left(\omega_e t-\frac{2\pi}{3}\right) & \cos\left(\omega_e t+\frac{2\pi}{3}\right) \\ -\sin(\omega_e t) & -\sin\left(\omega_e t-\frac{2\pi}{3}\right) & -\sin\left(\omega_e t+\frac{2\pi}{3}\right) \end{bmatrix}\begin{bmatrix} e_a \\ e_b \\ e_c \end{bmatrix}$$

$$=\frac{2}{3}\begin{bmatrix} \cos(\omega_e t) & \cos\left(\omega_e t-\frac{2\pi}{3}\right) & \cos\left(\omega_e t+\frac{2\pi}{3}\right) \\ -\sin(\omega_e t) & -\sin\left(\omega_e t-\frac{2\pi}{3}\right) & -\sin\left(\omega_e t+\frac{2\pi}{3}\right) \end{bmatrix}\begin{bmatrix} -\omega_e\Psi_m\sin(\omega t) \\ -\omega_e\Psi_m\sin\left(\omega_e t-\frac{2\pi}{3}\right) \\ -\omega_e\Psi_m\sin\left(\omega_e t+\frac{2\pi}{3}\right) \end{bmatrix}$$

$$=\frac{2}{3}\begin{bmatrix} -\omega_e\Psi_m(\cos(\omega_e t)\sin(\omega_e t)+\cos\left(\omega_e t-\frac{2\pi}{3}\right)\sin\left(\omega_e t-\frac{2\pi}{3}\right)+\cos\left(\omega_e t+\frac{2\pi}{3}\right)\sin\left(\omega_e t+\frac{2\pi}{3}\right)) \\ \omega_e\Psi_m(\sin^2(\omega_e t)+\sin^2\left(\omega_e t-\frac{2\pi}{3}\right)+\sin^2\left(\omega_e t+\frac{2\pi}{3}\right)) \end{bmatrix}$$

$$\cos(\omega_e t)\sin(\omega_e t)+\cos\left(\omega_e t-\frac{2\pi}{3}\right)\sin\left(\omega_e t-\frac{2\pi}{3}\right)+\cos\left(\omega_e t+\frac{2\pi}{3}\right)\sin\left(\omega_e t+\frac{2\pi}{3}\right)=0$$

$$\sin^2(\omega_e t)+\sin^2\left(\omega_e t-\frac{2\pi}{3}\right)+\sin^2\left(\omega_e t+\frac{2\pi}{3}\right)=\frac{3}{2}$$

$$\begin{bmatrix} e_d \\ e_q \end{bmatrix}=\begin{bmatrix} 0 \\ \omega_e\Psi_m \end{bmatrix}$$

$$\omega_e=p_h\omega_{HSR}$$

$$\begin{bmatrix} e_d \\ e_q \end{bmatrix} = \begin{bmatrix} 0 \\ p_h \omega_{HSR} \Psi_m \end{bmatrix}$$

$$K_e = p_h \Psi_m$$

$$\begin{bmatrix} e_d \\ e_q \end{bmatrix} = \begin{bmatrix} 0 \\ K_e \omega_{HSR} \end{bmatrix}$$

$$L - M = L_d = L_q = \frac{3}{2} L$$

$$\begin{bmatrix} v_d \\ v_q \end{bmatrix} = \begin{bmatrix} R_s & -\omega_e L_q \\ \omega_e L_d & R_s \end{bmatrix} \begin{bmatrix} i_d \\ i_q \end{bmatrix} + \begin{bmatrix} L_d & 0 \\ 0 & L_q \end{bmatrix} \frac{d}{dt} \begin{bmatrix} i_d \\ i_q \end{bmatrix} + \begin{bmatrix} 0 \\ K_e \omega_{HSR} \end{bmatrix}$$

T_e is the electromagnetic toque produced by the q-axis current i_q.

$$T_e = K_t i_q$$

$$K_t = \frac{3}{2} K_e$$

$$T_{LSR} = T_{max} \sin(p_h \theta_{HSR} - n_s \theta_{LSR})$$

T_{LSR} is the transmitted torque to the LSR.

$$\theta_r = p_h \theta_{HSR} - n_s \theta_{LSR}$$

θ_r is the load angle.

The d-q axes components of currents, voltages, resistances and inductances combine to form the dynamics of the SM PMSM. Equations are shown below.

$$v_d = R_s i_d + L_d \frac{di_d}{dt} - \omega_e L_q i_q$$

$$v_q = R_s i_q + L_q \frac{di_q}{dt} + \omega_e L_d i_d + K_e \omega_{HSR}$$

Appendix B

Fault tolerance

According to [8], failure is more probable to occur in the electrical part (power supply, inverter and motor windings) than the mechanical assembly (motor bearings, gearbox and screw). Therefore, extra windings (with various topologies) are added for redundancy to add a degree of fault tolerance. Under normal operation, the motor provides torque that is sufficient for the load. When a fault occurs (winding short circuit), drag torque opposing the motor torque is synthesised; and hence load torque plus the drag torque must be overcome. The principle of fault-tolerant motor is to overcome both torques by means of the remaining unfaulty phases.

Selecting fault tolerant winding configurations depends mainly on two factors; reliability and power losses (motor losses and drive losses). Motor losses comprise copper losses and iron losses. On the other

hand, drive losses comprise power switches conducting losses and also switching losses. [77] indicates that the application of commercial MEA demands primarily the safety of actuator and its drive. [77] refers to two classifications of fault tolerant drives. The first category is a number of isolated single phase winding that is driven by independent H-bridge power converter. The second category is a repetition of three-phase windings provided each three-phase is driven by independent three-phase power converters. Figure 267 summarises such two categories.

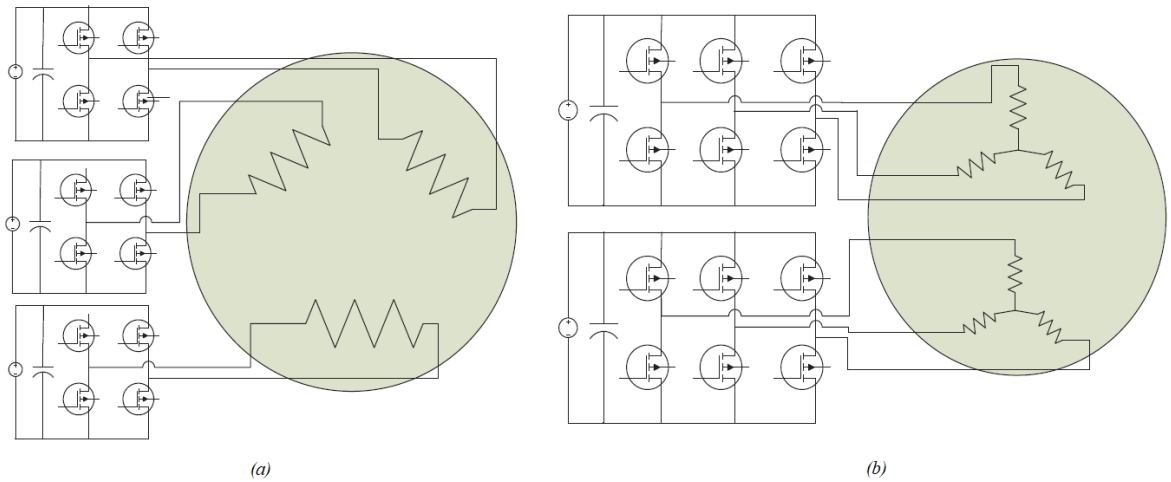

Figure 267. Two configurations for fault tolerant drive (a) triple lane single phase (b) dual 3-phae [78]

A study showing a comparison between various winding configurations are presented in [8]. Dynamic performance is shown in [8] under normal and fault cases. Moreover, since fault is probable to occur, various winding layouts are compared, with respect to reliability, to realise a fault tolerance machine. It is concluded that duplex and independent three-phase configurations introduces the lowest failure rate.

Appendix C

PWM techniques for AC drives

Various methods are used to control the switching in order to supply the PDD with three-phase voltage of a required amplitude and frequency. The method used in this project is SVPWM but it is worth giving an introduction on the SPWM technique.

Sinusoidal PWM method

This is a simple technique to apply. The current controller determines the required amplitude and frequency of the three-phase voltage. Such reference voltages are known as reference modulating signals. The normalised reference modulating signals are compared with a triangle carrier signal with a frequency known as the switching frequency. The intersection between the reference waves and the carrier wave decides the moments of the switching. Each phase is modulated separately [49].

Figure 268 below shows the three-phase reference voltages superimposed on the triangular carrier wave. When the reference phase A voltage is greater than the carrier wave, T_1 will be on and T_4 will be off. But when the reference phase A voltage is less than the carrier wave, T_1 will be off and T_4 will be on. Switching instants for the other two phases are determined in the same manner [49].

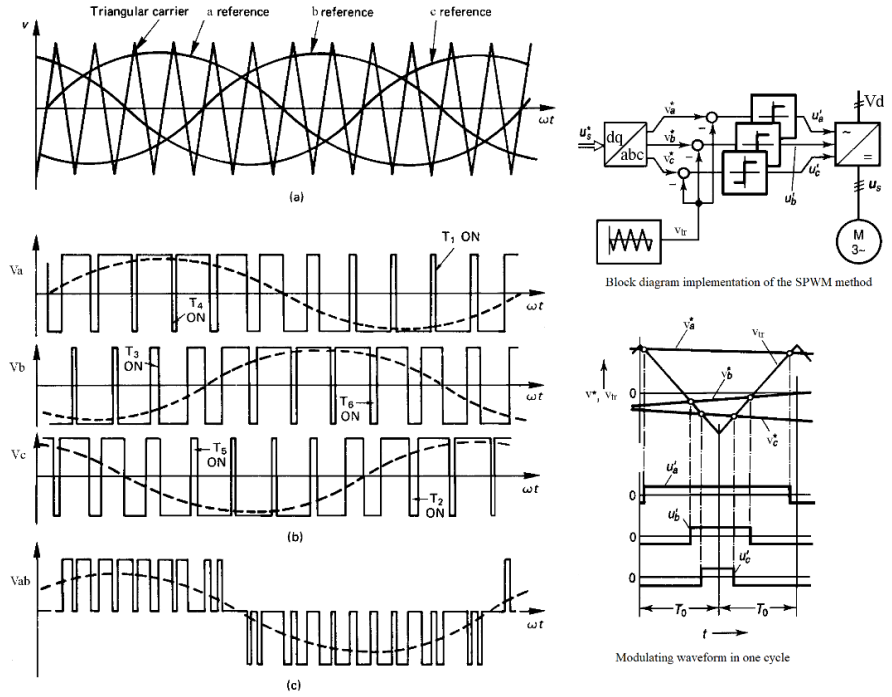

Figure 268. SPWM technique [49]

The amplitude modulation ratio, m_a, is given by Equation (274).

$$m_a = \frac{V_{ref}}{V_{tr}} \tag{274}$$

When the modulation index, m_a, equals *1*, the maximum line to line rms voltage, $V_{L\text{-}L(rms)}$, is given in Equation (275) [49].

$$V_{L-L(rms)} = 0.612 V_{dc} \tag{275}$$

Meanwhile, when *m* equals *1*, the phase voltage amplitude, $V_{ph(peak)}$, is given in Equation (276) [49].

$$V_{ph(peak)} = \frac{1}{2} V_{dc} \tag{276}$$

Space vector PWM (SVPWM) method

The SVPWM is more advanced than SPWM. The principle of this technique lies on combining the switching states of the six switches. In total there are eight switching states; six of them are active states and the other two are zero states. During zero states all phase voltages are equal to zero [79]. Table 27 shows the eight states mentioned.

Table 27. Switching states of the three-phase VSI [49]

a	*b*	*c*	$V_{an}(v_d)$	$V_{bn}(v_d)$	$V_{cn}(v_d)$
0	*0*	*0*	*0*	*0*	*0*
1	*0*	*0*	*2/3*	*-1/3*	*-1/3*
1	*1*	*0*	*1/3*	*1/3*	*-2/3*
0	*1*	*0*	*-1/3*	*2/3*	*-1/3*
0	*1*	*1*	*-2/3*	*1/3*	*1/3*
0	*0*	*1*	*-1/3*	*-1/3*	*2/3*
1	*0*	*1*	*1/3*	*-2/3*	*1/3*
1	*1*	*1*	*0*	*0*	*0*

The primary step is to convert the three-phase voltages into their equivalent v_x and v_y. This can be done by vector summing all the three-phase voltages as expressed in Equation (277) and Equation (278), respectively [79].

$$v_x = \frac{2}{3}(v_{an} + v_{bn}\cos\frac{2\pi}{3} + v_{cn}\cos\frac{4\pi}{3}) \tag{277}$$

$$v_y = \frac{2}{3}(v_{bn}\sin\frac{2\pi}{3} + v_{cn}\sin\frac{4\pi}{3}) \tag{278}$$

Note that the factor 2/3 is to make the voltage vector magnitude equals a phase voltage magnitude.

Then, the magnitude and angle of the voltage phasor can be found out by applying Equation (279) and Equation (280), respectively.

$$|V_{cs}| = \sqrt{{v_x}^2 + {v_y}^2} \tag{279}$$

$$\delta_{cs} = \tan^{-1}(\frac{v_y}{v_x}) \tag{280}$$

According to Table 27, there are eight states; two are zero states and six of them are active states. The six active states map out a hexagon shown in Figure 269, which has six regions (n = 1, 2, …, 6). The zero vectors are represented in the origin of the hexagon. Hence, the switching will depend on where the reference voltage vector in the hexagon is. This is because the switching will involve the two adjacent vectors, plus the zero vectors, confining the reference voltage vector.

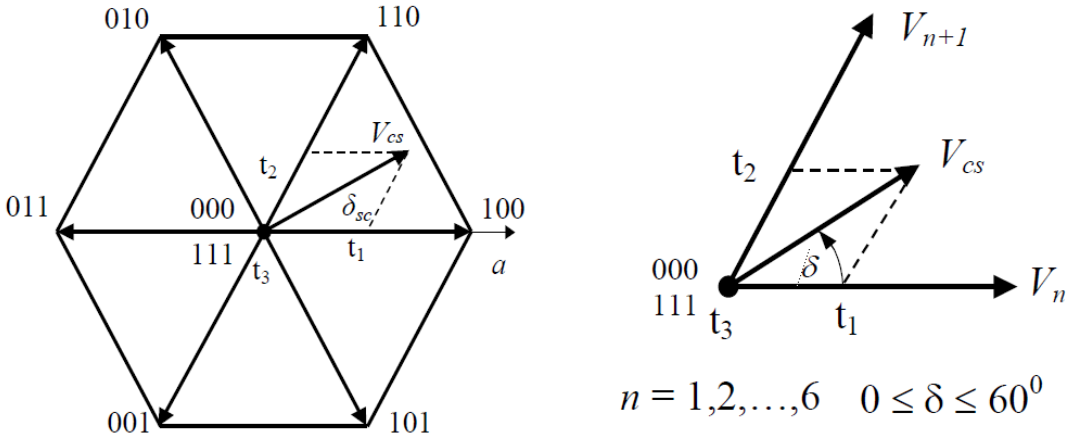

Figure 269. SVPWM technique hexagon [49]

For instance, say the vector V_{cs} is in the region *1*, such a vector can be obtained by switching between V1 (100), V2 (110) and zeros (000 & 111) with a certain interval for each state. All of the switching states with their corresponding intervals will make up one period of the PWM cycle.

Equation (281) will be manipulated in order to determine the time interval for each state. Let us state that the period is *T*.

$$TV_{cs} = t_1 V_n + t_2 V_{n+1} + t_3(0_{000\ or\ 111}) \tag{281}$$

If the vector, located in region *1*, is analysed to its *x* and *y* components, Equation (282) and Equation (283) can represent the *x* and *y* components, respectively.

$$TV_{cs}\cos\delta_{cs} = |V_n|t_1 + 0.5|V_{n+1}|t_2 = \frac{2}{3}V_{dc}(t_1 + 0.5t_2) \tag{282}$$

$$TV_{cs}\sin\delta_{cs} = \frac{\sqrt{3}}{2}|V_{n+1}|t_2 = \frac{1}{\sqrt{3}}V_{dc}t_2 \tag{283}$$

Equation (283) is rearranged for t_2 as shown in Equation (284).

$$t_2 = \sqrt{3}\frac{V_{cs}}{V_{dc}}T\sin\delta_{cs} = mT\sin\delta_{cs} \tag{284}$$

Where *m* is given by;

$$m = \sqrt{3}\frac{V_{cs}}{V_{dc}} \tag{285}$$

Equation (284) is substituted in Equation (282) and rearranged for t_1 as shown in Equation (286).

$$t_1 = \frac{3}{2}\frac{V_{cs}}{V_{dc}}T\cos\delta_{cs} - \frac{\sqrt{3}}{2}\frac{V_{cs}}{V_{dc}}T\sin\delta_{cs} = mT\sin(\frac{\pi}{3} - \delta_{cs}) \tag{286}$$

The intervals of the zero vectors (000 & 111) are t_0 and t_7, respectively. Also, both of these are equal.

$$t_0 + t_7 = T - (t_1 + t_2) \tag{287}$$

$$t_0 = t_7 = \frac{1}{2}(T - (t_1 + t_2)) \tag{288}$$

Figure 270 illustrates the technique when the voltage vector is located in region *1*. a, b and c correspond to the top switches in leg 1, 2 and 3, respectively. 0 denotes the top switch is off whilst the bottom switch on the same inverter leg is on. Similarly, *1* denotes the top switch is on whilst the bottom switch on the same leg is off. It can be seen than the zero vector 000 is placed at the edges of the cycle whereas the zero vector 111 is inserted in the middle. The order of the switching sequence is sorted to accomplish the minimum amount of switching [49].

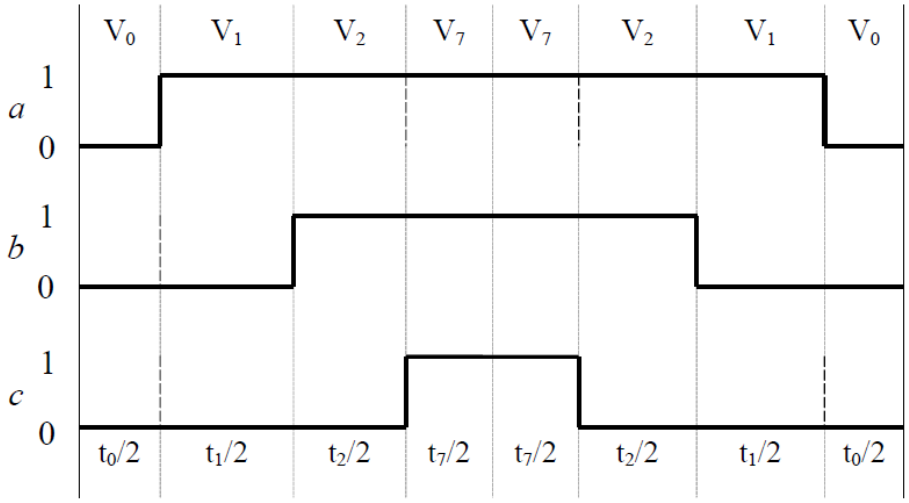

Figure 270. Voltage vector in region 1 [49]

The output of the SVPWM is linearly proportional with the modulation signal *m* provided that the reference voltage is no longer than the radius of the circle inserted inside the hexagon. When the modulation signal *m* equals *1*, the peak phase voltage reaches its maximum value.

$$V_{L-L(rms)} = \frac{\sqrt{3}}{\sqrt{2}}\frac{1}{\sqrt{3}}V_{dc} = \frac{1}{\sqrt{2}}V_{dc} = 0.707V_{dc} \tag{289}$$

$$V_{ph(peak)} = \frac{1}{\sqrt{3}}V_{dc} = 0.5774V_{dc} \tag{290}$$

Equation (289) and Equation (290) can be compared to Equation (275) and Equation (276), respectively. It can be seen that SVPWM methods provides over 15% higher output voltage than SPWM method.

One more step is essential to perform, which is detecting whether the magnitude of the voltage vector (V_{cs}) is outside the hexagon. If it is, voltage limiting is applied using one of the various four methods mentioned in [17]. The four methods mentioned in [17] are circular limit method (CL), minimum

amplitude error method (MAE), space vector limit method (SVL) and Dynamic vector method (DVL). Therefore, prior to calculating the intervals associated to the switching states, it is crucial to ensure the voltage vector is maintained within the hexagon.

Appendix D

Calculation of anti-resonant frequency, f_{ar}

$$q = [\theta_R \quad x_{sc} \quad x_L]^T \tag{291}$$

$$M = \begin{bmatrix} J_R & 0 & 0 \\ 0 & M_{sc} & 0 \\ 0 & 0 & M_L \end{bmatrix} \tag{292}$$

$$K = \begin{bmatrix} \gamma^2 K_n & \gamma K_n & -\gamma K_n \\ \gamma K_n & K_b + K_n & -K_n \\ -\gamma K_n & -K_n & K_n + K_a \end{bmatrix} \tag{293}$$

$$T = [T_{LSR} \quad 0 \quad 0]^T \tag{294}$$

$$\begin{bmatrix} J_R s^2 + \gamma^2 K_n & \gamma K_n & -\gamma K_n \\ \gamma K_n & M_{sc} s^2 + K_b + K_n & -K_n \\ -\gamma K_n & -K_n & M_L s^2 + K_n + K_a \end{bmatrix} \begin{bmatrix} \theta_R \\ x_{sc} \\ x_L \end{bmatrix} = \begin{bmatrix} T_{LSR} \\ 0 \\ 0 \end{bmatrix} \tag{295}$$

Equation (157) can be written symbolically in the way shown in Equation (158).

$$AX = T \tag{296}$$

This can be rearranged as shown in Equations (159) and (160).

$$A^{-1} = \frac{1}{\det A} adj(A) \tag{297}$$

$$A^{-1}AX = A^{-1}T \rightarrow X = A^{-1}T = \frac{1}{\det A} adj(A)T \tag{298}$$

$$adj(A) = \begin{bmatrix} (M_L s^2 + K_n + K_a)(M_{sc} s^2 + K_b + K_n) - K_n^2 & -\gamma K_n (M_L s^2 + K_n + K_a) + \gamma K_n^2 & -\gamma K_n^2 + \gamma K_n (M_{sc} s^2 + K_b + K_n) \\ -(M_L s^2 + K_n + K_a)\gamma K_n + \gamma K_n^2 & (M_L S^2 + K_n + K_a)(J_R s^2 + \gamma^2 K_n) - \gamma^2 K_n^2 & K_n (J_R s^2 + \gamma^2 K_n) - \gamma^2 K_n^2 \\ -\gamma K_n^2 + (M_{sc} s^2 + K_b + K_n)\gamma K_n & K_n (J_R s^2 + \gamma^2 K_n) - \gamma^2 K_n^2 & (M_{sc} s^2 + K_b + K_n)(J_R s^2 + \gamma^2 K_n) - \gamma^2 K_n^2 \end{bmatrix} \tag{299}$$

$$\frac{x_L}{T_{LSR}} = \frac{1}{\det A} \times (-\gamma K_n^2 + (M_{sc} s^2 + K_b + K_n)\gamma K_n) \tag{300}$$

$$-\gamma K_n^2 + (M_{sc} s^2 + K_b + K_n)\gamma K_n = 0 \tag{301}$$

$$-\gamma K_n^2 + \gamma K_n M_{sc} s^2 + \gamma K_n K_b + \gamma K_n^2 = 0 \tag{302}$$

$$\gamma K_n M_{sc} s^2 + \gamma K_n K_b = 0 \tag{303}$$

$$\gamma K_n M_{sc} s^2 = -\gamma K_n K_b \tag{304}$$

$$M_{sc} s^2 = -K_b \tag{305}$$

$$s^2 = \frac{-K_b}{M_{sc}} \tag{306}$$

By rearranging Equation (161), the complex frequency operator, *s*, is shown in Equation (162).

$$s = \mp j\sqrt{\frac{K_b}{M_{sc}}} \tag{307}$$

Therefore, the anti-resonant frequency, f_{ar}, can be estimated using Equation (163).

$$f_{ar} = \frac{1}{2\pi}\sqrt{\frac{K_b}{M_{sc}}} = 3183\ Hz \tag{308}$$

Appendix E

Linearised system state space matrices

$$X_c = [x_L, v_L, x_{sc}, v_{sc}, \theta_R, \omega_R, \theta_{HSR}, \omega_{HSR}, i_q, v_q, i_q^*]^T \tag{309}$$

System matrices are shown below.

$$\boldsymbol{A} = \begin{bmatrix}
0 & 1 & 0 & 0 & 0 & 0 & 0 & 0 & 0 & 0 & 0 \\
\left(\frac{-K_n - K_a}{M_L}\right) & 0 & \frac{K_n}{M_L} & 0 & \frac{K_n}{M_L}\gamma & 0 & 0 & 0 & 0 & 0 & 0 \\
0 & 0 & 0 & 1 & 0 & 0 & 0 & 0 & 0 & 0 & 0 \\
\frac{K_n}{M_{sc}} & 0 & \left(\frac{-K_n - K_b}{M_{sc}}\right) & 0 & -\frac{K_n}{M_{sc}}\gamma & 0 & 0 & 0 & 0 & 0 & 0 \\
0 & 0 & 0 & 0 & 0 & 1 & 0 & 0 & 0 & 0 & 0 \\
\frac{\gamma K_n}{J_R} & 0 & -\frac{\gamma K_n}{J_R} & 0 & \left(\frac{-n_s K_g - K_n \gamma^2}{J_R}\right) & 0 & \frac{p_h K_g}{J_R} & 0 & 0 & 0 & 0 \\
0 & 0 & 0 & 0 & 0 & 0 & 0 & 1 & 0 & 0 & 0 \\
0 & 0 & 0 & 0 & \frac{n_s K_g}{G_r J_{HSR}} & 0 & -\frac{p_h K_g}{G_r J_{HSR}} & 0 & \frac{K_t}{J_{HSR}} & 0 & 0 \\
0 & 0 & 0 & 0 & 0 & 0 & 0 & -\frac{K_e}{L_q} & -\frac{R_s}{L_q} & \frac{1}{L_q} & 0 \\
-(K_{pc}K_pK_{is}) & 0 & 0 & 0 & -\frac{K_{pc}K_{ps}K_g n_s}{G_r J_{HSR}} & 0 & \frac{K_{pc}K_{ps}K_g p_h}{G_r J_{HSR}} & \left(\frac{K_{pc}K_e}{L_q} - K_{pc}K_{is}\right) & \left(\frac{K_{pc}R_s}{L_q} - K_{ic} - \frac{K_{pc}K_{ps}K_t}{J_{HSR}}\right) & -\frac{K_{pc}}{L_q} & K_{ic} \\
-(K_pK_{is}) & 0 & 0 & 0 & -\frac{K_{ps}K_g n_s}{G_r J_{HSR}} & 0 & \frac{K_{ps}K_g p_h}{G_r J_{HSR}} & -K_{is} & -\frac{K_{ps}Kt}{J_{HSR}} & 0 & 0
\end{bmatrix}$$

$$\boldsymbol{B} = \begin{bmatrix}
0 & 0 \\
0 & -\frac{1}{M_L} \\
0 & 0 \\
0 & 0 \\
0 & 0 \\
0 & 0 \\
0 & 0 \\
0 & 0 \\
0 & 0 \\
(K_{pc}K_pK_{is}) & 0 \\
(K_pK_{is}) & 0
\end{bmatrix}$$

$$\boldsymbol{C} = [1 \quad 0 \quad 0 \quad 0 \quad 0 \quad 0 \quad 0 \quad 0 \quad 0 \quad 0 \quad 0]$$

$$\boldsymbol{D} = [0 \quad 0]$$

Appendix F

Matlab code

Six-DOF model

```
ML = 29.63;
xs = 0.05;
Dsc = 1.97E-02;
rsc = Dsc/2;
Asc = pi*(rsc^2);
Isc = 1.49E-08;
Lsc = 0.213;
Ka = 180000;
JLSR = 1.08E-04;
Kc = 16700;
Kb = 200000000;
Kn = 289960199;
Jc = 0;
Gsc = 7.9E10;
Esc = 2.07E11;
Rhost = 7700;
Msl = 0;
Lambda = 0.005;
Y = Lambda/(2*pi);
M = [JLSR+(Jc/2) 0 0 0 0 0;
    0 Msl+ML 0 0 0 0;
    0 0 Rhost*Isc*Lsc+(Jc/2) Rhost*Isc*(Lsc-(xs/2)) 0 0;
    0 0 Rhost*Isc*(Lsc-(xs/2)) Rhost*Isc*(Lsc-(2*xs/3)) 0 0;
    0 0 0 0 Rhost*Asc*Lsc Rhost*Asc*(Lsc-(xs/2));
    0 0 0 0 Rhost*Asc*(Lsc-(xs/2)) Rhost*Asc*(Lsc-(2*xs/3))];
K1 = [Kc 0 -Kc 0 0 0;
    0 0 0 0 0 0;
    -Kc 0 Kc 0 0 0;
    0 0 0 ((Gsc*Isc)/xs) 0 0;
    0 0 0 0 Kb 0;
    0 0 0 0 0 (Asc*Esc/xs)];
K2 = [0 0 0 0 0 0;
    0 Kn+Ka -Y*Kn -Y*Kn -Kn -Kn;
    0 -Y*Kn Y*Y*Kn Y*Y*Kn Y*Kn Y*Kn;
    0 -Y*Kn Y*Y*Kn Y*Y*Kn Y*Kn Y*Kn;
    0 -Kn Y*Kn Y*Kn Kn Kn;
```

```
    0 -Kn Y*Kn Y*Kn Kn Kn];
K = K1+K2;
[V,D] = eig(K,M);
O= (sqrt(D))/(2*pi);
```

Three-DOF model

```
clear all;
close all;
clc;
format long
Lambda = 0.005;
Y = Lambda/(2*pi);
Kn = 289960199;
Kb = 200000000;
JLSR = 1.08E-04;
Ka = 180000;
Jsc = 2.44375E-05;
Msc = 5.02E-01;
ML = 29.63088;
JR = Jsc+JLSR;
syms Fr;
K = [Y*Y*Kn Y*Kn -Y*Kn;
    Y*Kn (Kb+Kn) (-Kn);
    -Kn*Y (-Kn) (Kn+Ka)];
M = [JR 0 0;
     0 Msc 0
     0 0 ML];
[V,D] = eig(K,M);
N = (sqrt(D))/(2*pi);
```

Origin of anti-resonance

```
clear all;
close all;
clc;
format long
Lambda = 0.005;
Y = Lambda/(2*pi);
Kn = 289960199;
```

```
Kb = 200000000;
JLSR = 1.08E-04;
Ka = 180000;
Jsc = 2.44375E-05;
Msc = 5.02E-01;
ML = 29.63088;
JR = Jsc+JLSR;
syms Fr;
K = [Y*Y*Kn Y*Kn -Y*Kn;
    Y*Kn (Kb+Kn) (-Kn);
    -Kn*Y (-Kn) (Kn+Ka)];
M = [JR 0 0;
     0 Msc 0
     0 0 ML];
[V,D] = eig(K,M);
N = (sqrt(D))/(2*pi);
F = V.';
mi= F*M*V;
ki= F*K*V;
H = (sqrtm(mi));
P = inv(H);
Q = V*P;
I = (Q.')*M*Q;
W = (Q.')*K*Q;
G = (sqrt(W))/(2*pi);
```

Speed loop

```
Jsc = 2.43507E-5;
JLSR = 1.08E-04;
Kps = 0.5;
Kis = 0.08;
Kpc = 5.969026042;
Kic = 2199.114858;
Lq = 0.0019;
Rs = 0.7;
Kt = 0.108*sqrt(2);
Ke = 0.072*sqrt(2);
JHSR = 1.35e-4;
```

```
ph = 4;
ns = 31;
Kg = 10.3*0.7187;
Gr = 7.75;
A=[0 1 0 0 0 0 0;
(-Kg*ns)/JR 0 Kg*ph/JR 0 0 0 0;
0 0 0 1 0 0 0;
(Kg*ns)/(Gr*JHSR) 0 -(Kg*ph)/(Gr*JHSR) 0 Kt/JHSR 0  0;
0 0 0 -Ke/Lq -Rs/Lq 1/Lq 0;
-(Kpc*Kps*Kg*ns/(Gr*JHSR)) 0 +Kpc*Kps*Kg*ph/(Gr*JHSR) (Kpc*Ke/Lq)-
(Kpc*Kis) (Kpc*Rs/Lq)-Kic-(Kpc*Kps*Kt/JHSR) -Kpc/Lq Kic;
(-Kps*Kg*ns/(Gr*JHSR)) 0 +Kps*Kg*ph/(Gr*JHSR) -Kis -Kps*Kt/JHSR 0
0];
B=[0 0;
0 -1/JR;
0 0;
0 0;
0 0;
Kpc*Kis 0;
Kis 0];
C=[0 0 0 1 0 0 0];
D=[0 0];
[V,D] = eig(A);
```

1-DOF

```
Lambda = 0.005;
Y = Lambda/(2*pi);
ML = 29.63;
Msc = 5.00E-01;
Jsc = 2.43507E-5;
Ka = 0.137;
JLSR = 1.08E-04;
Kb = 2e8;
Kn = 289960199;
JL = Y^(2)*ML;
Js = JLSR+Jsc+JL;
Kp = 15;
Kps = 0.5;
```

```
Kis = 0.08;
Kpc = 5.969026042;
Kic = 2199.114858;
Lq = 0.0019;
Rs = 0.7;
Kt = 0.108*sqrt(2);
Ke = 0.072*sqrt(2);
JHSR = 1.35e-4;
ph = 4;
ns = 31;
Kg = 10.3*0.7187;
Gr = 7.75;
A=[0 1 0 0 0 0 0;
(-Kg*ns-Ka)/Js 0 Kg*ph/Js 0 0 0 0;
0 0 0 1 0 0 0;
(Kg*ns)/(Gr*JHSR) 0 -(Kg*ph)/(Gr*JHSR) 0 Kt/JHSR 0  0;
0 0 0 -Ke/Lq -Rs/Lq 1/Lq 0;
(-Kpc*Kp*Kis)-(Kpc*Kps*Kg*ns/(Gr*JHSR)) 0 +Kpc*Kps*Kg*ph/(Gr*JHSR)
(Kpc*Ke/Lq)-(Kpc*Kis) (Kpc*Rs/Lq)-Kic-(Kpc*Kps*Kt/JHSR) -Kpc/Lq
Kic;
(-Kps*Kg*ns/(Gr*JHSR))-Kp*Kis 0 +Kps*Kg*ph/(Gr*JHSR) -Kis -
Kps*Kt/JHSR 0 0];
B=[0 0;
0 -1/Js;
0 0;
0 0;
0 0;
Kpc*Kis*Kp 0;
Kis*Kp 0];
C=[1 0 0 0 0 0 0];
D=[0 0];
[V,D] = eig(A);
```

3-DOF

```
lambda = 0.005;
Y = lambda/(2*pi);
ML = 29.63;
Msc = 5.00E-01;
```

```
Jsc = 2.44375E-05;
Ka = 180000;
JLSR = 1.08E-04;
JR = JLSR+Jsc;
Kb = 200000000;
Kn = 289960199;
Kc = 1.67e4;
Kp = 15*2*pi/0.005;
Kps = 0.08;
Kis = 0.5;
Kpc = 5.969026042;
Kic = 2199.114858;
Lq = 0.0019;
Rs = 0.7;
Kt = 0.108*sqrt(2);
Ke = 0.072*sqrt(2);
JHSR = 1.35e-4;
ph = 4;
ns = 31;
Kg = 10.3*0.7187;
Gr = 7.75;
A=[0 1 0 0 0 0 0 0 0 0 0;
((-Kn-Ka)/ML) 0 Kn/ML 0 Y*Kn/ML 0 0 0 0 0 0;
0 0 0 1 0 0 0 0 0 0 0;
Kn/Msc 0 (-Kn-Kb)/Msc 0 -Kn*Y/Msc 0 0 0 0 0 0;
0 0 0 0 0 1 0 0 0 0 0;
Y*Kn/JR 0 -Y*Kn/JR 0 (-Kg*ns-(Kn*Y^2))/JR 0 Kg*ph/JR 0 0 0 0;
0 0 0 0 0 0 0 1 0 0 0;
0 0 0 0 (Kg*ns)/(Gr*JHSR) 0 -(Kg*ph)/(Gr*JHSR) 0 Kt/JHSR 0  0;
0 0 0 0 0 0 0 -Ke/Lq -Rs/Lq 1/Lq 0;
-Kpc*Kp*Kis 0 0 0 -Kpc*Kps*Kg*ns/(Gr*JHSR) 0 Kpc*Kps*Kg*ph/(Gr*JHSR)
(Kpc*Ke/Lq)-(Kpc*Kis) (Kpc*Rs/Lq)-Kic-(Kpc*Kps*Kt/JHSR) -Kpc/Lq
Kic;
-Kp*Kis 0 0 0 -Kps*Kg*ns/(Gr*JHSR) 0 Kps*Kg*ph/(Gr*JHSR) -Kis -
Kps*Kt/JHSR 0 0];
B=[0 0;
0 -1/ML;
```

```
0 0;
0 0;
0 0;
0 0;
0 0;
0 0;
0 0;
Kpc*Kis*Kp 0;
Kis*Kp 0];
C=[1 0 0 0 0 0 0 0 0 0 0];
D=[0 0];
[V,D] = eig(A);
```

Appendix G

Texas instrument code

Settings code

```
/*
============================================================================
File name:  HVPM_Sensored_Servo-Settings.H

Description: Incremental Build Level control file.
============================================================================
*/
#ifndef PROJ_SETTINGS_H

/*----------------------------------------------------------------------------
Following is the list of the Build Level choices.
-----------------------------------------------------------------------------*/
#define LEVEL1  1               // Module check out (do not connect the motors)
#define LEVEL2  2           // Verify ADC, park/clarke, calibrate the offset
#define LEVEL3  3           // Verify closed current(torque) loop, QEP and speed
meas.
#define LEVEL4  4           // Verify close speed loop and speed PID
#define LEVEL5  5           // verify position control with QEP
#define LEVEL6  6           // verify position control with position f/b using SPI
/*----------------------------------------------------------------------------
This line sets the BUILDLEVEL to one of the available choices.
-----------------------------------------------------------------------------*/
```

```
#define   BUILDLEVEL LEVEL4


#ifndef BUILDLEVEL
#error  Critical: BUILDLEVEL must be defined !!
#endif  // BUILDLEVEL
//---------------------------------------------------------------------------


#ifndef TRUE
#define FALSE 0
#define TRUE  1
#endif

#define PI 3.14159265358979

// Define the system frequency (MHz)
#if (DSP2803x_DEVICE_H==1)
#define SYSTEM_FREQUENCY 60
#elif (DSP280x_DEVICE_H==1)
#define SYSTEM_FREQUENCY 100
#endif

// Define the ISR frequency (kHz)
#define ISR_FREQUENCY 10

//// Define the electrical motor parametes (Estun Servomotor)
//#define RS       2.35                   // Stator resistance (ohm)
//#define RR                                      // Rotor resistance (ohm)
//#define LS       0.0065                         // Stator inductance (H)
//#define LR                                             // Rotor inductance (H)
//#define LM                                             // Magnatizing
inductance (H)
//#define POLES    8                                     // Number of poles
//
//// Define the base quantites
//#define BASE_VOLTAGE    236.140        // Base peak phase voltage (volt)
//#define BASE_CURRENT    20             // Base peak phase current (amp)
//#define BASE_TORQUE                   // Base torque (N.m)
//#define BASE_FLUX                     // Base flux linkage (volt.sec/rad)
```

```
//#define BASE_FREQ       200            // Base electrical frequency (Hz)

// Define the electrical motor parametes (Teco Servomotor)
#define RS          0.7                     // Stator resistance (ohm)
#define RR                                    // Rotor resistance (ohm)
#define LS   0.00188                                // Stator inductance (H)
#define LR                                          // Rotor inductance (H)
#define LM                                          // Magnatizing inductance (H)
#define POLES       8                                     // Number of poles

// Define the base quantites
#define BASE_VOLTAGE    135        // Base peak phase voltage (volt)
#define BASE_CURRENT    8             // Base peak phase current (amp)
#define BASE_TORQUE     7              // Base torque (N.m)
#define BASE_FLUX       0.07                 // Base flux linkage (volt.sec/rad)
#define BASE_FREQ         620            // Base electrical frequency (Hz)

// QEP specs
#define QEP_PULSE_PER_CHNL         1024       // QEP's pulse per channel
#define QEP_PULSE_PER_POLEPAIR    (QEP_PULSE_PER_CHNL*4/(POLES/2))

// RESOLVER specs
#define RESOLVER_STEPS_PER_TURN         4096       // Resolver's discrete
steps/turn
#define RESOLVER_STEPS_PER_POLEPAIR    (RESOLVER_STEPS_PER_TURN/(POLES/2))
#define REF_PULSE_PER_REV              10000


#endif
```

Main code

```
/* ======================================================================
System Name:    HVPM_Sensored_Servo

File Name:      HVPM_Sensored_Servo.C

Description:    Primary system file for the Real Implementation of Sensored
                Field Orientation Control for Three Phase Permanent-Magnet
                Synchronous Motor (PMSM)
```

```
Originator:     Digital control systems Group - Texas Instruments

Note: In this software, the default inverter is supposed to be HVDMC board.
================================================================================
===
 History:
--------------------------------------------------------------------------------
---
 10-9-2010  Version 1.1: Supports F2803x
 10-17-2012 Version 4.1: Includes position control build levels with
                              - QEP interface
                              - position f/b from SPI interface (such as an
external
                                resolver interface can send out position data on
SPI)
================================================================================
*/

// Include header files used in the main function

#include "PeripheralHeaderIncludes.h"
#define   MATH_TYPE      IQ_MATH
#include "IQmathLib.h"
#include "HVPM_Sensored_Servo.h"
#include "HVPM_Sensored_Servo-Settings.h"
#include <math.h>

#ifdef FLASH
#pragma CODE_SECTION(MainISR,"ramfuncs");
#pragma CODE_SECTION(OffsetISR,"ramfuncs");
#endif

// =====================================================
// ---------- SPI i/f for resolver ---------------------
#define  SPIPORT             SpiaRegs                  /* SpiaRegs  <-> SpibRegs
*/
#define  PIEVECT_SPIRXINT    PieVectTable.SPIRXINTA    /* SPIRXINTA <-> SPIRXINTB
*/

#define  POS_KI_LOW_SPD    _IQ(0.0001)
```

```
#define  POS_KI_MED_SPD    _IQ(0.001)
#define  POS_KI_HI_SPD     _IQ(0.01)
// =================================================================

// Prototype statements for functions found within this file.
interrupt void MainISR(void);
interrupt void OffsetISR(void);
void DeviceInit();
void MemCopy();
void InitFlash();
void HVDMC_Protection(void);
void SPI_slave_init(void);
interrupt void SpiRxISR(void);

// State Machine function prototypes
//-----------------------------------
// Alpha states
void A0(void);  //state A0
void B0(void);  //state B0
void C0(void);  //state C0

// A branch states
void A1(void);  //state A1
void A2(void);  //state A2
void A3(void);  //state A3

// B branch states
void B1(void);  //state B1
void B2(void);  //state B2
void B3(void);  //state B3

// C branch states
void C1(void);  //state C1
void C2(void);  //state C2
void C3(void);  //state C3

// Variable declarations
void (*Alpha_State_Ptr)(void);  // Base States pointer
void (*A_Task_Ptr)(void);       // State pointer A branch
void (*B_Task_Ptr)(void);       // State pointer B branch
```

```
void (*C_Task_Ptr)(void);       // State pointer C branch

// Used for running BackGround in flash, and ISR in RAM
extern Uint16 *RamfuncsLoadStart, *RamfuncsLoadEnd, *RamfuncsRunStart;


int16   VTimer0[4];         // Virtual Timers slaved off CPU Timer 0 (A events)
int16   VTimer1[4];         // Virtual Timers slaved off CPU Timer 1 (B events)
int16   VTimer2[4];         // Virtual Timers slaved off CPU Timer 2 (C events)
int16   SerialCommsTimer;

// Global variables used in this system

Uint16 OffsetFlag=0;
_iq offsetA=0;
_iq offsetB=0;
_iq offsetC=0;
_iq K1=_IQ(0.998);      //Offset filter coefficient K1: 0.05/(T+0.05);
_iq K2=_IQ(0.001999);   //Offset filter coefficient K2: T/(T+0.05);
extern _iq IQsinTable[];
extern _iq IQcosTable[];


_iq VdTesting = _IQ(0.0);           // Vd reference (pu)
_iq VqTesting = _IQ(0.15);          // Vq reference (pu)
_iq IdRef = _IQ(0.0);               // Id reference (pu)
_iq IqRef = _IQ(0.15);              // Iq reference (pu)
_iq q_dcoupl = _IQ(0.0);              // Iq reference (pu)
_iq new_prop_gain;
_iq new_scheme;
_iq pure_integral;


#if (BUILDLEVEL<LEVEL3)             // Speed reference (pu)
_iq  SpeedRef = _IQ(0.15);          // For Open Loop tests
#else
_iq  SpeedRef = _IQ(0.3);           // For Closed Loop tests
_iq  Speedref = _IQ(0.0);
#endif
```

```
float32 T = 0.001/ISR_FREQUENCY;    // Samping period (sec), see parameter.h

Uint32 IsrTicker = 0;
Uint16 BackTicker = 0;
Uint16 lsw=0;
Uint16 TripFlagDMC=0;               //Trip status
Uint16 Init_IFlag=0;

// Default ADC initialization
int ChSel[16]   = {0,0,0,0,0,0,0,0,0,0,0,0,0,0,0,0};
int TrigSel[16] = {5,5,5,5,5,5,5,5,5,5,5,5,5,5,5,5};
int ACQPS[16]   = {8,8,8,8,8,8,8,8,8,8,8,8,8,8,8,8};

int16 DlogCh1 = 0;
int16 DlogCh2 = 0;
int16 DlogCh3 = 0;
int16 DlogCh4 = 0;


volatile Uint16 EnableFlag = FALSE;
Uint16 RunMotor = FALSE;

Uint16 SpeedLoopPrescaler = 10;      // Speed loop prescaler
Uint16 SpeedLoopCount = 1;           // Speed loop counter


// Instance a few transform objects
CLARKE clarke1 = CLARKE_DEFAULTS;
PARK park1 = PARK_DEFAULTS;
IPARK ipark1 = IPARK_DEFAULTS;

// Instance PI regulators to regulate the d and q  axis currents, and speed
PI_CONTROLLER pi_spd = PI_CONTROLLER_DEFAULTS;
PI_CONTROLLER pi_id  = PI_CONTROLLER_DEFAULTS;
PI_CONTROLLER pi_iq  = PI_CONTROLLER_DEFAULTS;
PI_CONTROLLER pi_pos = PI_CONTROLLER_DEFAULTS;

// Instance a PWM driver instance
PWMGEN pwm1 = PWMGEN_DEFAULTS;
```

```
// Instance a PWM DAC driver instance
PWMDAC pwmdac1 = PWMDAC_DEFAULTS;

// Instance a Space Vector PWM modulator. This modulator generates a, b and c
// phases based on the d and q stationery reference frame inputs
SVGEN svgen1 = SVGEN_DEFAULTS;

// Instance a ramp controller to smoothly ramp the frequency
RMPCNTL rc1 = RMPCNTL_DEFAULTS;

//  Instance a ramp generator to simulate an Anglele
RAMPGEN rg1 = RAMPGEN_DEFAULTS;

// Instance a speed calculator based on QEP
SPEED_MEAS_QEP speed1 = SPEED_MEAS_QEP_DEFAULTS;

// Instance a QEP interface driver
QEP qep1 = QEP_DEFAULTS;

// Create an instance of DATALOG Module
DLOG_4CH dlog = DLOG_4CH_DEFAULTS;

// ===========================================================================

// ---------------------------------------------------
// variables specific for position loop implementation
// ---------------------------------------------------
#if (BUILDLEVEL!=LEVEL6)
  Uint32  cntr=0, alignCnt = 5000;
#else
  // Instance a RESOLVER interface driver
  RESOLVER resolver1 = RESOLVER_DEFAULTS;

  Uint32  cntr=0, alignCnt = 20000, spiReady=0;
  int32 tmp;
  _iq ref1 = _IQ(0.1), ref2 = _IQ(0.6);
#endif

_iq IdRef_start = _IQ(0.1), IdRef_run = _IQ(0.0);
```

```
// ===========================================
// slew programmable ramper
// ===========================================
_iq ramper(_iq in, _iq out, _iq rampDelta) {
    _iq err;

    err = in - out;
    if (err > rampDelta)        return(out + rampDelta);
    else if (err < -rampDelta)  return(out - rampDelta);
    else                        return(in);
}

// ===========================================
// position reference generation test module
// ===========================================
int32 posArray[8] = { _IQ(1.5), _IQ(-1.5), _IQ(2.5), _IQ(-2.5) },
        ptrMax = 2, cntr1=0, ptr1=0, posSlewRate = _IQ(0.001);
int32 refPosGen(int32 out)
{
    int32 in = posArray[ptr1];

    out = ramper(in, out, posSlewRate);

    if (in == out)
    if (++cntr1 > 1000)
    {
        cntr1 = 0;
        if (++ptr1 >= ptrMax)
            ptr1 = 0;
    }
    return (out);
}

#if (BUILDLEVEL==LEVEL6)
// =======================================================
// SPI interrupt to receive position data (slave mode)
// =======================================================
interrupt void SpiRxISR(void)
{
```

```
    resolver1.RawTheta = SPIPORT.SPIRXBUF;
    resolver1.Speed    = (int16)SPIPORT.SPIRXBUF;

    SPIPORT.SPIFFRX.bit.RXFFOVFCLR = 1;               // Clear Overflow flag
    SPIPORT.SPIFFRX.bit.RXFFINTCLR = 1;               // Clear Interrupt flag
    PieCtrlRegs.PIEACK.all         = PIEACK_GROUP6;    // Issue PIE ack

    spiReady = 4;
    return;
}

// ===========================================================================
// Initialize SPI in slave mode to receive position data from resolver
// ===========================================================================
void SPI_slave_init(void)
{
    // Initialize SPI FIFO registers
    SPIPORT.SPIFFTX.bit.SPIRST     = 1;       // enable fifo - 0xE040;
    SPIPORT.SPIFFTX.bit.SPIFFENA   = 1;       // enable fifo enhancements
    SPIPORT.SPIFFTX.bit.TXFIFO     = 1;       // re-enable tx fifo
    SPIPORT.SPIFFTX.bit.TXFFIENA   = 0;       // disable tx fifo int based txffil
match
    SPIPORT.SPIFFTX.bit.TXFFINTCLR = 1;       // clr TXFFINT flag in SPIFFTX

    //SPIPORT.SPIFFRX.bit.RXFFOVFCLR = 1;     // clr RXFFOVF flag in SPIFFRX -
0x2042;
    SPIPORT.SPIFFRX.bit.RXFIFORESET = 1;      // re-enable rx fifo
    SPIPORT.SPIFFRX.bit.RXFFINTCLR  = 1;      // clr RXFFINT flag in SPIFFRX
    SPIPORT.SPIFFRX.bit.RXFFIENA    = 0;      // disable rx fifo int based rxffil
match
    SPIPORT.SPIFFRX.bit.RXFFIL      = 2;      // two rx data

    SPIPORT.SPIFFCT.all=0x0;                  // no time space between consecutive
words in a packet

    // Initialize SPI
    SPIPORT.SPICCR.bit.SPISWRESET  = 0;       // reset SPI - 0x000F
    SPIPORT.SPICCR.bit.SPILBK      = 0;       // no loop back
    SPIPORT.SPICCR.bit.CLKPOLARITY = 0;       // clk polarity is rising edge
    SPIPORT.SPICCR.bit.SPICHAR     = 0xf;     // data length = 16b
```

```
    SPIPORT.SPICTL.bit.CLK_PHASE     = 0;     // Enable normal phase - 0x0002
    SPIPORT.SPICTL.bit.MASTER_SLAVE  = 0;     // slave mode
    SPIPORT.SPICTL.bit.OVERRUNINTENA = 0;     // disable rx overrun flag bit
interrupts (SPISTS.7)
    SPIPORT.SPICTL.bit.TALK          = 1;     // enable talk
    SPIPORT.SPICTL.bit.SPIINTENA     = 0;     // SPI int disable

    //SPIPORT.SPIBRR =0x00F;                    // Baud rate

    SPIPORT.SPICCR.bit.SPISWRESET    = 1;       // Relinquish SPI from Reset

    SPIPORT.SPIPRI.bit.FREE    = 1;             // Set so breakpoints don't
disturb xmission
    SPIPORT.SPIPRI.bit.STEINV  = 0;             // SPISTE pin in normal mode (no
inversion)
    SPIPORT.SPIPRI.bit.TRIWIRE = 0;             // 4 wire SPI
}
#endif

// ********************************************************************
// main function coded here
// ********************************************************************
void main(void)
{

    DeviceInit();   // Device Life support & GPIO

// Only used if running from FLASH
// Note that the variable FLASH is defined by the compiler

#ifdef FLASH
// Copy time critical code and Flash setup code to RAM
// The  RamfuncsLoadStart, RamfuncsLoadEnd, and RamfuncsRunStart
// symbols are created by the linker. Refer to the linker files.
    MemCopy(&RamfuncsLoadStart, &RamfuncsLoadEnd, &RamfuncsRunStart);

// Call Flash Initialization to setup flash waitstates
// This function must reside in RAM
    InitFlash();    // Call the flash wrapper init function
```

```
#endif //(FLASH)

   // Waiting for enable flag set
   while (EnableFlag==FALSE)
    {
      BackTicker++;
    }

// Timing sync for background loops
// Timer period definitions found in device specific PeripheralHeaderIncludes.h
    CpuTimer0Regs.PRD.all =  mSec1;     // A tasks
    CpuTimer1Regs.PRD.all =  mSec5;     // B tasks
    CpuTimer2Regs.PRD.all =  mSec50;    // C tasks

// Tasks State-machine init
    Alpha_State_Ptr = &A0;
    A_Task_Ptr = &A1;
    B_Task_Ptr = &B1;
    C_Task_Ptr = &C1;

// Initialize PWM module
    pwm1.PeriodMax = SYSTEM_FREQUENCY*1000000*T/2;  // Prescaler X1 (T1), ISR
period = T x 1
    pwm1.HalfPerMax=pwm1.PeriodMax/2;
    pwm1.Deadband  = 2.0*SYSTEM_FREQUENCY;          // 120 counts -> 2.0 usec for
TBCLK = SYSCLK/1
    PWM_INIT_MACRO(1,2,3,pwm1)

// Initialize PWMDAC module
    pwmdac1.PeriodMax=500;          // @60Mhz, 1500->20kHz, 1000-> 30kHz, 500-
>60kHz
    pwmdac1.HalfPerMax=pwmdac1.PeriodMax/2;
    PWMDAC_INIT_MACRO(6,pwmdac1)    // PWM 6A,6B
    PWMDAC_INIT_MACRO(7,pwmdac1)    // PWM 7A,7B

// Initialize DATALOG module
    dlog.iptr1 = &DlogCh1;
    dlog.iptr2 = &DlogCh2;
    dlog.iptr3 = &DlogCh3;
    dlog.iptr4 = &DlogCh4;
```

```
    dlog.trig_value = 0x1;
    dlog.size = 0x0c8;
    dlog.prescalar = 5;
    dlog.init(&dlog);


// Initialize ADC for DMC Kit Rev 1.1
    ChSel[0]=1;     // Dummy meas. avoid 1st sample issue Rev0 Picollo*/
    ChSel[1]=1;     // ChSelect: ADC A1-> Phase A Current
    ChSel[2]=9;     // ChSelect: ADC B1-> Phase B Current
    ChSel[3]=3;     // ChSelect: ADC A3-> Phase C Current
    ChSel[4]=15;    // ChSelect: ADC B7-> Phase A Voltage
    ChSel[5]=14;    // ChSelect: ADC B6-> Phase B Voltage
    ChSel[6]=12;    // ChSelect: ADC B4-> Phase C Voltage
    ChSel[7]=7;     // ChSelect: ADC A7-> DC Bus  Voltage
    ChSel[9]=6;     // ChSelect: ADC A6-> Speed reference from dSPACE
    ChSel[8]=4;     // ChSelect: ADC A4-> Speed reference from dSPACE

    ADC_MACRO_INIT(ChSel,TrigSel,ACQPS)

// Initialize QEP module
#if (BUILDLEVEL!=LEVEL6)
    qep1.LineEncoder = QEP_PULSE_PER_CHNL;
    qep1.MechScaler = _IQ30(0.25/qep1.LineEncoder);
    qep1.PolePairs = POLES/2;
    qep1.CalibratedAngle = 855;
    QEP_INIT_MACRO(1,qep1)

// Initialize RESOLVER module
#else
    resolver1.StepsPerTurn = RESOLVER_STEPS_PER_TURN;
    resolver1.MechScaler   = _IQ30(1.0/resolver1.StepsPerTurn);
    resolver1.PolePairs    = POLES/2;
#endif

// Initialize the Speed module for QEP based speed calculation
    speed1.K1 = _IQ21(1/(BASE_FREQ*T));
    speed1.K2 = _IQ(1/(1+T*2*PI*5));  // Low-pass cut-off frequency
    speed1.K3 = _IQ(1)-speed1.K2;
    speed1.BaseRpm = 120*(BASE_FREQ/POLES);
```

```
// Initialize the RAMPGEN module
    rg1.StepAngleMax = _IQ(BASE_FREQ*T);

// ************** QEP demo PI values *****************
#if (BUILDLEVEL!=LEVEL6)
// Initialize the PI module for position
    pi_pos.Kp = _IQ(50.0);            //_IQ(10.0);
    pi_pos.Ki = _IQ(0.001);          //_IQ(T*SpeedLoopPrescaler/0.3);
    pi_pos.Umax = _IQ(1.0);
    pi_pos.Umin = _IQ(-1.0);

// Initialize the PI module for speed
    pi_spd.Kp=_IQ(1.0);
    pi_spd.Ki=_IQ(0.0005);
    //pi_spd.Ki=_IQ(T*SpeedLoopPrescaler/0.2);
    pi_spd.Umax =_IQ(3.0);
    pi_spd.Umin =_IQ(-3.0);

// Initialize the PI module for Id
    pi_id.Kp=_IQ(0.35);   //1.0);
    pi_id.Ki=_IQ(0.0022);   //T/0.04);
    pi_id.Umax =_IQ(3.0);
    pi_id.Umin =_IQ(-3.0);

// Initialize the PI module for Iq
    pi_iq.Kp=_IQ(0.35);   //1.0);
    pi_iq.Ki=_IQ(0.0022);   //T/0.04);
    pi_iq.Umax =_IQ(3.0);
    pi_iq.Umin =_IQ(-3.0);

// ************** resolver demo PI values *****************
#else
// Initialize the PI module for position
    pi_pos.Kp = _IQ(10.0);            //_IQ(10.0);
    pi_pos.Ki = POS_KI_LOW_SPD;       //_IQ(0.001);
//_IQ(T*SpeedLoopPrescaler/0.3);
    pi_pos.Umax = _IQ(1.0);
    pi_pos.Umin = _IQ(-1.0);
```

```
// Initialize the PI module for speed
    pi_iq.Kp=_IQ(0.3);   //1.0);
    pi_iq.Ki=_IQ(0.0003);   //T/0.04);
    pi_iq.Umax =_IQ(0.95);   //0.8);
    pi_iq.Umin =_IQ(-0.95);  //-0.8);

// Initialize the PI module for Id
    pi_spd.Kp=_IQ(1.0);
    pi_spd.Ki=_IQ(T*SpeedLoopPrescaler/0.2);
    pi_spd.Umax =_IQ(0.95);
    pi_spd.Umin =_IQ(-0.95);

// Initialize the PI module for Iq
    pi_id.Kp=_IQ(0.3);   //1.0);
    pi_id.Ki=_IQ(0.0003);   //T/0.04);
    pi_id.Umax =_IQ(0.6);   //0.3);
    pi_id.Umin =_IQ(-0.6);  //-0.3);
#endif
// =====================================================

//  Note that the vectorial sum of d-q PI outputs should be less than 1.0 which
refers to maximum duty cycle for SVGEN.
//  Another duty cycle limiting factor is current sense through shunt resistors
which depends on hardware/software implementation.
//  Depending on the application requirements 3,2 or a single shunt resistor can
be used for current waveform reconstruction.
//  The higher number of shunt resistors allow the higher duty cycle operation and
better dc bus utilization.
//  The users should adjust the PI saturation levels carefully during open loop
tests (i.e pi_id.Umax, pi_iq.Umax and Umins) as in project manuals.
//  Violation of this procedure yields distorted current waveforms and unstable
closed loop operations which may damage the inverter.

//Call HVDMC Protection function
    HVDMC_Protection();

// Reassign ISRs.

    EALLOW; // This is needed to write to EALLOW protected registers
```

```
    PieVectTable.ADCINT1 = &OffsetISR;

// Enable PIE group 1 interrupt 1 for ADC1_INT
    PieCtrlRegs.PIEIER1.bit.INTx1 = 1;

// Enable EOC interrupt(after the 4th conversion)

    AdcRegs.ADCINTOVFCLR.bit.ADCINT1=1;
    AdcRegs.ADCINTFLGCLR.bit.ADCINT1=1;
    AdcRegs.INTSEL1N2.bit.INT1CONT=1;  //
    AdcRegs.INTSEL1N2.bit.INT1SEL=4;
    AdcRegs.INTSEL1N2.bit.INT1E=1;

// Enable CPU INT1 for ADC1_INT:
    IER |= M_INT1;

//===========================================================
#if (BUILDLEVEL==LEVEL6)
    // SPIB slave config for resolver interface
    SPI_slave_init();
    SPIPORT.SPIFFRX.bit.RXFFIENA = 1;     // enable rx fifo int based rxffil match
    SPIPORT.SPICTL.bit.SPIINTENA = 1;     // SPI int disable

// SPIB Rx interrupt settings
    EALLOW; // This is needed to write to EALLOW protected registers
    PIEVECT_SPIRXINT = &SpiRxISR;  // PieVectTable.SPIRXINT(A/B)
    EDIS;

// Enable PIE group 6 interrupt 1 for SPIB_RX_INT
    PieCtrlRegs.PIEIER6.bit.INTx1 = 1;   // SPIA_RX - INTx1,   SPIB_RX - INTx3

// Enable CPU INT6 for SPIA(B)_RX_INT:
    IER |= M_INT6;
#endif
//===========================================================

// Enable global Interrupts and higher priority real-time debug events:
    EINT;   // Enable Global interrupt INTM
    ERTM;   // Enable Global realtime interrupt DBGM
```

```
    EDIS;



// IDLE loop. Just sit and loop forever:
    for(;;)  //infinite loop
    {
        // State machine entry & exit point
        //===========================================================
        (*Alpha_State_Ptr)();   // jump to an Alpha state (A0,B0,...)
        //===========================================================

    }
} //END MAIN CODE



//===========================================================================
=
//  STATE-MACHINE SEQUENCING AND SYNCRONIZATION FOR SLOW BACKGROUND TASKS
//===========================================================================
=

//--------------------------------- FRAMEWORK ----------------------------------
-
void A0(void)
{
    // loop rate synchronizer for A-tasks
    if(CpuTimer0Regs.TCR.bit.TIF == 1)
    {
        CpuTimer0Regs.TCR.bit.TIF = 1;  // clear flag

        //-----------------------------------------------------------
        (*A_Task_Ptr)();        // jump to an A Task (A1,A2,A3,...)
        //-----------------------------------------------------------

        VTimer0[0]++;           // virtual timer 0, instance 0 (spare)
        SerialCommsTimer++;
    }
```

```
    Alpha_State_Ptr = &B0;      // Comment out to allow only A tasks
}

void B0(void)
{
    // loop rate synchronizer for B-tasks
    if(CpuTimer1Regs.TCR.bit.TIF == 1)
    {
        CpuTimer1Regs.TCR.bit.TIF = 1;              // clear flag

        //--------------------------------------------------------------
        (*B_Task_Ptr)();        // jump to a B Task (B1,B2,B3,...)
        //--------------------------------------------------------------
        VTimer1[0]++;           // virtual timer 1, instance 0 (spare)
    }

    Alpha_State_Ptr = &C0;      // Allow C state tasks
}

void C0(void)
{
    // loop rate synchronizer for C-tasks
    if(CpuTimer2Regs.TCR.bit.TIF == 1)
    {
        CpuTimer2Regs.TCR.bit.TIF = 1;              // clear flag

        //--------------------------------------------------------------
        (*C_Task_Ptr)();        // jump to a C Task (C1,C2,C3,...)
        //--------------------------------------------------------------
        VTimer2[0]++;           //virtual timer 2, instance 0 (spare)
    }

    Alpha_State_Ptr = &A0;  // Back to State A0
}


//===========================================================================
=
//  A - TASKS (executed in every 1 msec)
```

```
//===========================================================================
=
//-----------------------------------------------------------
void A1(void) // SPARE (not used)
//-----------------------------------------------------------
{
        if(EPwm1Regs.TZFLG.bit.OST==0x1)
        TripFlagDMC=1;      // Trip on DMC (halt and IPM fault trip )

    //-------------------
    //the next time CpuTimer0 'counter' reaches Period value go to A2
    A_Task_Ptr = &A2;
    //-------------------
}

//-----------------------------------------------------------------
void A2(void) // SPARE (not used)
//-----------------------------------------------------------------
{

    //-------------------
    //the next time CpuTimer0 'counter' reaches Period value go to A3
    A_Task_Ptr = &A3;
    //-------------------
}

//---------------------------------------
void A3(void) // SPARE (not used)
//---------------------------------------
{

    //-----------------
    //the next time CpuTimer0 'counter' reaches Period value go to A1
    A_Task_Ptr = &A1;
    //-----------------
}
```

```
//===========================================================================
=
//  B - TASKS (executed in every 5 msec)
//===========================================================================
=

//---------------------------------- USER -------------------------------------
-

//-----------------------------------------
void B1(void) // Toggle GPIO-00
//-----------------------------------------
{

    //-----------------
    //the next time CpuTimer1 'counter' reaches Period value go to B2
    B_Task_Ptr = &B2;
    //-----------------
}

//-----------------------------------------
void B2(void) //  SPARE
//-----------------------------------------
{

    //-----------------
    //the next time CpuTimer1 'counter' reaches Period value go to B3
    B_Task_Ptr = &B3;
    //-----------------
}

//-----------------------------------------
void B3(void) //  SPARE
//-----------------------------------------
{

    //-----------------
    //the next time CpuTimer1 'counter' reaches Period value go to B1
    B_Task_Ptr = &B1;
    //-----------------
```

```
}


//===========================================================================
=
//  C - TASKS (executed in every 50 msec)
//===========================================================================
=

//--------------------------------- USER -----------------------------------
-

//---------------------------------------
void C1(void)   // Toggle GPIO-34
//---------------------------------------
{

    if(EPwm1Regs.TZFLG.bit.OST==0x1)            // TripZ for PWMs is low (fault
trip)
      { TripFlagDMC=1;
      GpioDataRegs.GPBTOGGLE.bit.GPIO42 = 1;
      }

    if(GpioDataRegs.GPADAT.bit.GPIO15 == 1)     // Over Current Prot. for
Integrated Power Module is high (fault trip)
      { TripFlagDMC=1;
      GpioDataRegs.GPBTOGGLE.bit.GPIO44 = 1;
      }

    GpioDataRegs.GPBTOGGLE.bit.GPIO34 = 1;     // Turn on/off LD3 on the
controlCARD
    //-----------------
    //the next time CpuTimer2 'counter' reaches Period value go to C2
    C_Task_Ptr = &C2;
    //-----------------

}

//---------------------------------------
void C2(void) //  SPARE
```

```
//---------------------------------------
{

    //-----------------
    //the next time CpuTimer2 'counter' reaches Period value go to C3
    C_Task_Ptr = &C3;
    //-----------------
}


//---------------------------------------
void C3(void) //  SPARE
//---------------------------------------
{

    //-----------------
    //the next time CpuTimer2 'counter' reaches Period value go to C1
    C_Task_Ptr = &C1;
    //-----------------
}
// ===========================================================================




// MainISR
interrupt void MainISR(void)
{

// Verifying the ISR
    IsrTicker++;

// ============================== LEVEL 4 ====================================
//    Level 4 verifies the speed regulator performed by PI module.
//    The system speed loop is closed by using the measured speed as a feedback.
// ===========================================================================
//    lsw=0: lock the rotor of the motor,
//    lsw=1: close the current loop,
//    lsw=2: close the speed loop (sensored FOC).
```

```
#if (BUILDLEVEL==LEVEL4)


    Speedref=_IQ(AdcResult.ADCRESULT8/3723.636);
// ---------------------------------------------------------------------------
//  Connect inputs of the RMP module and call the ramp control macro
// ---------------------------------------------------------------------------
    if(lsw==0)rc1.TargetValue = 0;
    else rc1.TargetValue = SpeedRef;
    RC_MACRO(rc1)

// ---------------------------------------------------------------------------
//  Connect inputs of the RAMP GEN module and call the ramp generator macro
// ---------------------------------------------------------------------------
    rg1.Freq = rc1.SetpointValue;
    RG_MACRO(rg1)

// ---------------------------------------------------------------------------
//  Measure phase currents, subtract the offset and normalize from (-0.5,+0.5) to
(-1,+1).
//  Connect inputs of the CLARKE module and call the clarke transformation macro
// ---------------------------------------------------------------------------
    clarke1.As = _IQmpy2(_IQ12toIQ(AdcResult.ADCRESULT1)-offsetA); // Phase A
curr.
    clarke1.Bs = _IQmpy2(_IQ12toIQ(AdcResult.ADCRESULT2)-offsetB); // Phase B
curr.
    CLARKE_MACRO(clarke1)

// ---------------------------------------------------------------------------
//  Connect inputs of the PARK module and call the park trans. macro
// ---------------------------------------------------------------------------
    park1.Alpha = clarke1.Alpha;
    park1.Beta = clarke1.Beta;

    if(lsw==0) park1.Angle = 0;
    else if(lsw==1) park1.Angle = rg1.Out;
    else park1.Angle = qep1.ElecTheta;

    park1.Sine = _IQsinPU(park1.Angle);
    park1.Cosine = _IQcosPU(park1.Angle);
```

```
    PARK_MACRO(park1)

// ------------------------------------------------------------------------
//    Connect inputs of the PI module and call the PID speed controller macro
// ------------------------------------------------------------------------
   if (SpeedLoopCount==SpeedLoopPrescaler)
     {
      //pi_spd.Ref = rc1.SetpointValue;
      pi_spd.Ref = Speedref;
      pi_spd.Fbk = speed1.Speed;
      //pure_integral = pi_spd.v1-pi_spd.up;
      PI_MACRO(pi_spd);
      new_prop_gain = _IQmpy(pi_spd.Fbk, _IQ(0.08));
      //new_scheme = pure_integral - new_prop_gain;
      new_scheme = pi_spd.ui-new_prop_gain;
      SpeedLoopCount=1;
     }
    else SpeedLoopCount++;

    if(lsw!=2)  {pi_spd.ui=0; pi_spd.i1=0;}

// ------------------------------------------------------------------------
//    Connect inputs of the PI module and call the PID IQ controller macro
// ------------------------------------------------------------------------
//  if(lsw==0) pi_iq.Ref = 0;
//    else if(lsw==1) pi_iq.Ref = IqRef;
//    else pi_iq.Ref =  pi_spd.Out;
//  pi_iq.Fbk = park1.Qs;
//  PI_MACRO(pi_iq)

// ------------------------------------------------------------------------
//    Connect inputs of the PI module and call the PID IQ controller macro
// ------------------------------------------------------------------------
    if(lsw==0) pi_iq.Ref = 0;
    else if(lsw==1) pi_iq.Ref = IqRef;
    else pi_iq.Ref = new_scheme;
    pi_iq.Fbk = park1.Qs;
    PI_MACRO(pi_iq)
```

```
// ---------------------------------------------------------------------------
//    Connect inputs of the PI module and call the PID ID controller macro
// ---------------------------------------------------------------------------
    if(lsw==0) pi_id.Ref = _IQ(0.05);
    else pi_id.Ref = IdRef;
    pi_id.Fbk = park1.Ds;
    PI_MACRO(pi_id)

// ---------------------------------------------------------------------------
//  Connect inputs of the INV_PARK module and call the inverse park trans. macro
// ---------------------------------------------------------------------------
    q_dcoupl=_IQmpy(speed1.Speed,_IQ(0.434));
    ipark1.Ds =pi_id.Out-_IQmpy(pi_iq.Fbk,q_dcoupl);
    ipark1.Qs =pi_iq.Out+_IQmpy(pi_id.Fbk,q_dcoupl);
    ipark1.Sine=park1.Sine;
    ipark1.Cosine=park1.Cosine;
    IPARK_MACRO(ipark1)

// ---------------------------------------------------------------------------
//  Connect inputs of the INV_PARK module and call the inverse park trans. macro
// ---------------------------------------------------------------------------
    //ipark1.Ds = pi_id.Out;
    //ipark1.Qs = pi_iq.Out;
    //ipark1.Sine=park1.Sine;
    //ipark1.Cosine=park1.Cosine;
    //IPARK_MACRO(ipark1)

// ---------------------------------------------------------------------------
//    Detect calibration angle (optional) and call the QEP module
// ---------------------------------------------------------------------------
    if (lsw==0) {EQep1Regs.QPOSCNT=0; EQep1Regs.QCLR.bit.IEL = 1;} // Reset
position cnt.

    if ((EQep1Regs.QFLG.bit.IEL==1) && Init_IFlag==0)             // Check the
first index occurrence
       {qep1.CalibratedAngle= EQep1Regs.QPOSILAT; Init_IFlag++;}   // Keep the
latched position

    if (lsw!=0) QEP_MACRO(1,qep1);
```

```
// ---------------------------------------------------------------------------
//    Connect inputs of the SPEED_FR module and call the speed calculation macro
// ---------------------------------------------------------------------------
    speed1.ElecTheta = _IQ24toIQ((int32)qep1.ElecTheta);
    speed1.DirectionQep = (int32)(qep1.DirectionQep);
    SPEED_FR_MACRO(speed1)

// ---------------------------------------------------------------------------
//  Connect inputs of the SVGEN_DQ module and call the space-vector gen. macro
// ---------------------------------------------------------------------------
    svgen1.Ualpha = ipark1.Alpha;
    svgen1.Ubeta  = ipark1.Beta;
    SVGENDQ_MACRO(svgen1)
// ---------------------------------------------------------------------------
//  Connect inputs of the PWM_DRV module and call the PWM signal generation macro
// ---------------------------------------------------------------------------
    pwm1.MfuncC1 = svgen1.Ta;
    pwm1.MfuncC2 = svgen1.Tb;
    pwm1.MfuncC3 = svgen1.Tc;
    PWM_MACRO(1,2,3,pwm1)                          // Calculate the new PWM
compare values

// ---------------------------------------------------------------------------
//    Connect inputs of the PWMDAC module
// ---------------------------------------------------------------------------
    pwmdac1.MfuncC1 = clarke1.As;
    pwmdac1.MfuncC2 = clarke1.Bs;
    PWMDAC_MACRO(6,pwmdac1)                        // PWMDAC 6A, 6B

    pwmdac1.MfuncC1 = rg1.Out;
    pwmdac1.MfuncC2 = speed1.ElecTheta ;
    PWMDAC_MACRO(7,pwmdac1)

// ---------------------------------------------------------------------------
//    Connect inputs of the DATALOG module
// ---------------------------------------------------------------------------
    DlogCh1 = (int16)_IQtoIQ15(qep1.ElecTheta);
    DlogCh2 = (int16)_IQtoIQ15(rg1.Out);
    DlogCh3 = (int16)_IQtoIQ15(clarke1.As);
    DlogCh4 = (int16)_IQtoIQ15(clarke1.Bs);
```

```
#endif // (BUILDLEVEL==LEVEL4)

// ---------------------------------------------------------------------------
//    Call the DATALOG update function.
// ---------------------------------------------------------------------------
    dlog.update(&dlog);


// Enable more interrupts from this timer
    AdcRegs.ADCINTFLG.bit.ADCINT1=1;

// Acknowledge interrupt to recieve more interrupts from PIE group 3
    PieCtrlRegs.PIEACK.all = PIEACK_GROUP1;


}// MainISR Ends Here



/*********************************************************/
/*******************Offset Compensation*******************/
/*********************************************************/

interrupt void OffsetISR(void)
{
// Verifying the ISR
    IsrTicker++;

// DC offset measurement for ADC

    if (IsrTicker>=5000)
        {
            offsetA=
_IQmpy(K1,offsetA)+_IQmpy(K2,_IQ12toIQ(AdcResult.ADCRESULT1));         //Phase A
offset
            offsetB=
_IQmpy(K1,offsetB)+_IQmpy(K2,_IQ12toIQ(AdcResult.ADCRESULT2));         //Phase B
offset
```

```
            offsetC=
_IQmpy(K1,offsetC)+_IQmpy(K2,_IQ12toIQ(AdcResult.ADCRESULT3));         //Phase C
offset
        }

    if (IsrTicker > 20000)
    {
        EALLOW;
        PieVectTable.ADCINT1=&MainISR;
        EDIS;
    }

// Enable more interrupts from this timer
    AdcRegs.ADCINTFLG.bit.ADCINT1=1;

// Acknowledge interrupt to recieve more interrupts from PIE group 1
    PieCtrlRegs.PIEACK.all = PIEACK_GROUP1;

}

//*************** End of Offset Comp. ********************//


/*********************************************************/
/***************Protection Configuration******************/
/*********************************************************/

void HVDMC_Protection(void)
{

// Configure Trip Mechanism for the Motor control software
// -Cycle by cycle trip on CPU halt
// -One shot IPM trip zone trip
// These trips need to be repeated for EPWM1 ,2 & 3

//=========================================================================
//Motor Control Trip Config, EPwm1,2,3
//=========================================================================
      EALLOW;
// CPU Halt Trip
```

```
      EPwm1Regs.TZSEL.bit.CBC6=0x1;
      EPwm2Regs.TZSEL.bit.CBC6=0x1;
      EPwm3Regs.TZSEL.bit.CBC6=0x1;


      EPwm1Regs.TZSEL.bit.OSHT1   = 1;  //enable TZ1 for OSHT
      EPwm2Regs.TZSEL.bit.OSHT1   = 1;  //enable TZ1 for OSHT
      EPwm3Regs.TZSEL.bit.OSHT1   = 1;  //enable TZ1 for OSHT

// What do we want the OST/CBC events to do?
// TZA events can force EPWMxA
// TZB events can force EPWMxB

      EPwm1Regs.TZCTL.bit.TZA = TZ_FORCE_LO; // EPWMxA will go low
      EPwm1Regs.TZCTL.bit.TZB = TZ_FORCE_LO; // EPWMxB will go low

      EPwm2Regs.TZCTL.bit.TZA = TZ_FORCE_LO; // EPWMxA will go low
      EPwm2Regs.TZCTL.bit.TZB = TZ_FORCE_LO; // EPWMxB will go low

      EPwm3Regs.TZCTL.bit.TZA = TZ_FORCE_LO; // EPWMxA will go low
      EPwm3Regs.TZCTL.bit.TZB = TZ_FORCE_LO; // EPWMxB will go low


      EDIS;

     // Clear any spurious OV trip
      EPwm1Regs.TZCLR.bit.OST = 1;
      EPwm2Regs.TZCLR.bit.OST = 1;
      EPwm3Regs.TZCLR.bit.OST = 1;

//************************* End of Prot. Conf. *************************//
}

//===========================================================================
// No more.
//===========================================================================
```

Appendix H

Matlab switching model

Entire model

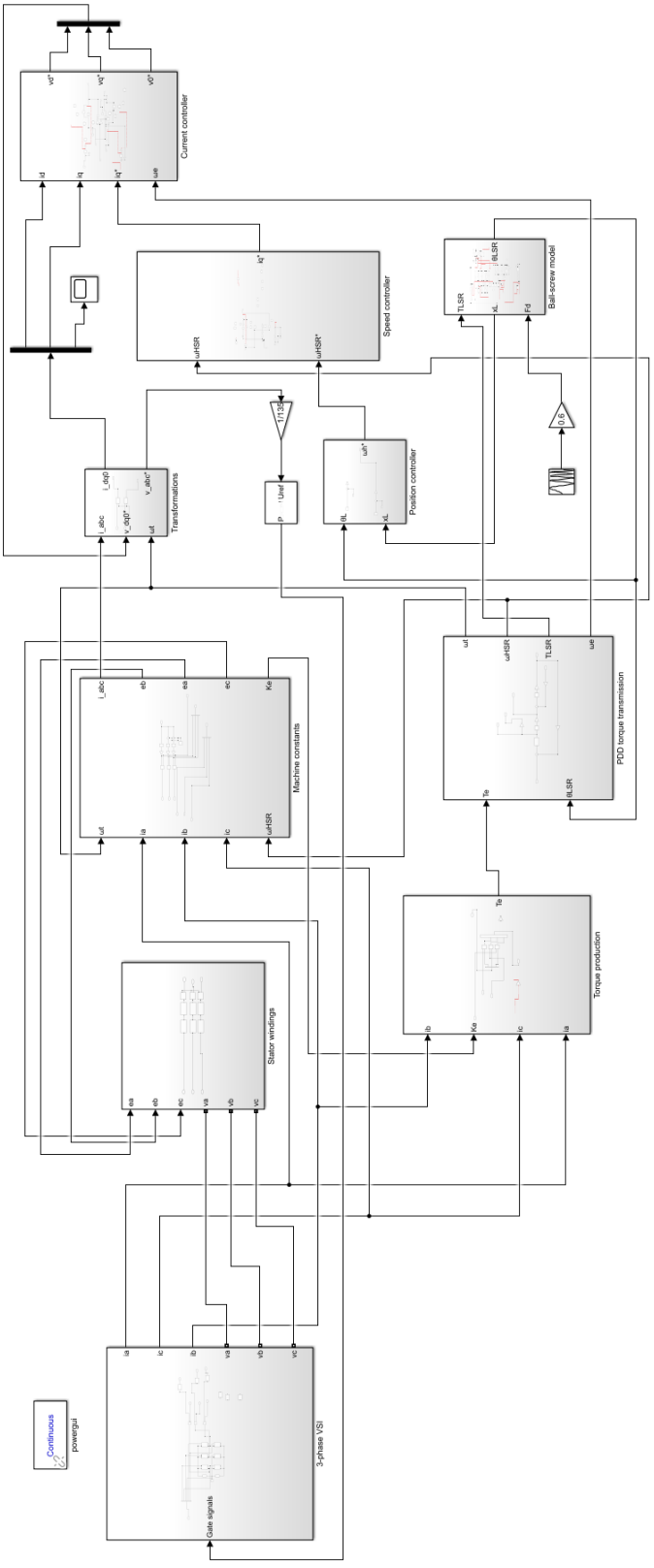

Three-phase VSI

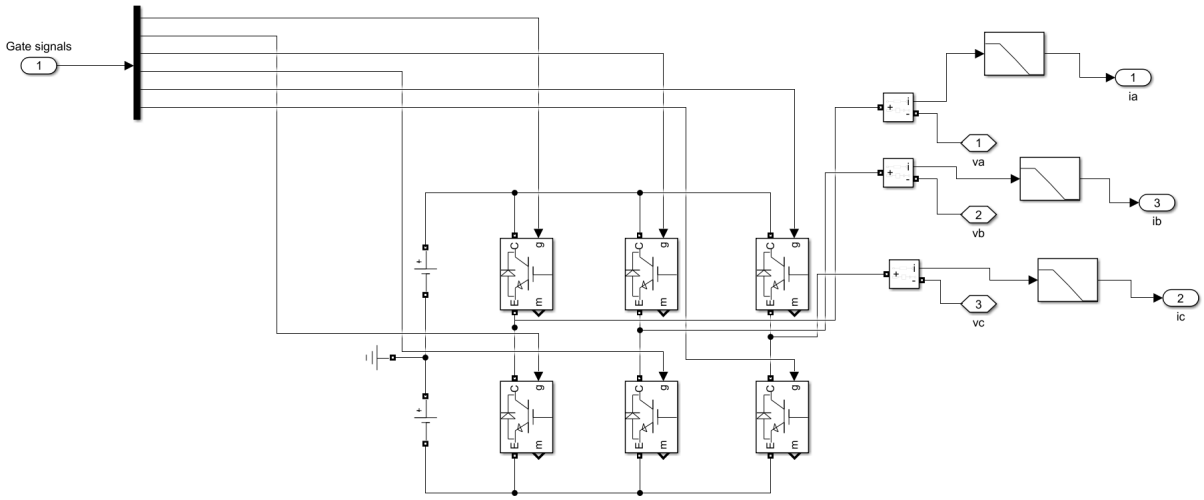

Stator windings

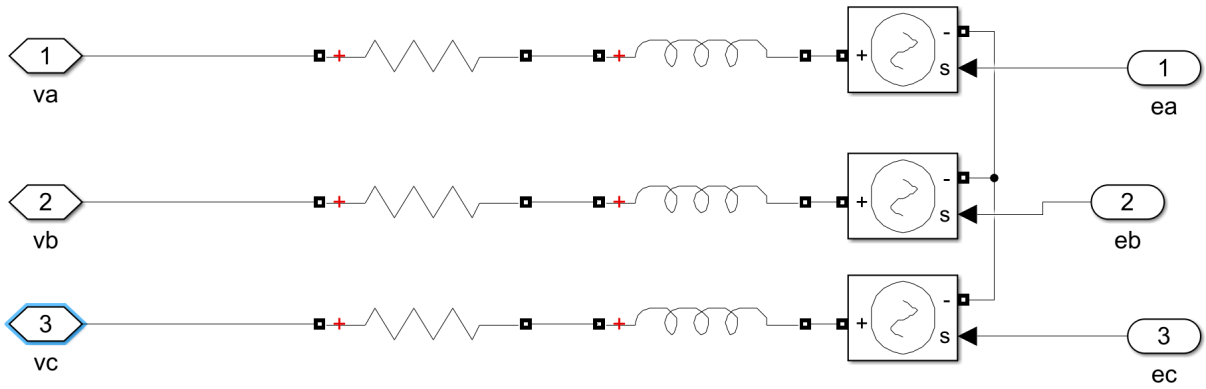

Machine constant

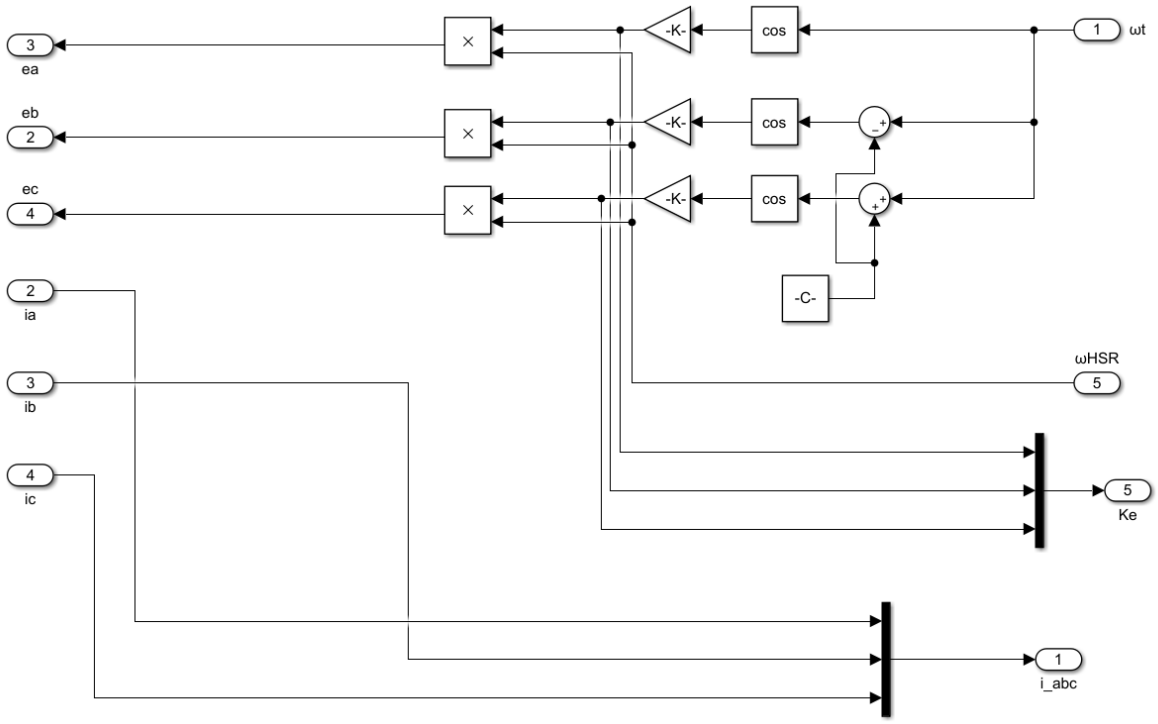

Transformations

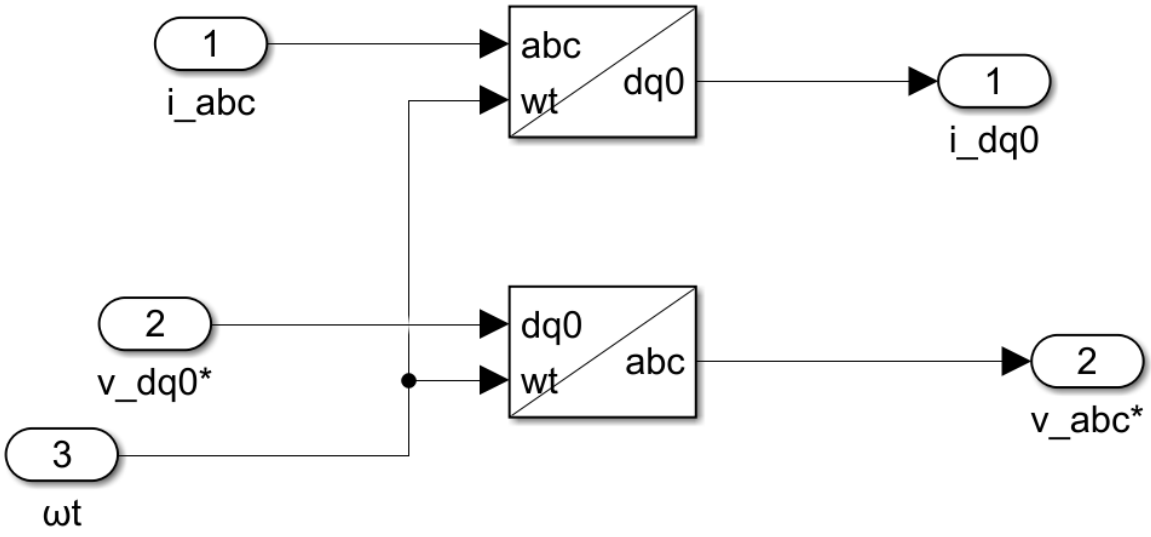

Torque production

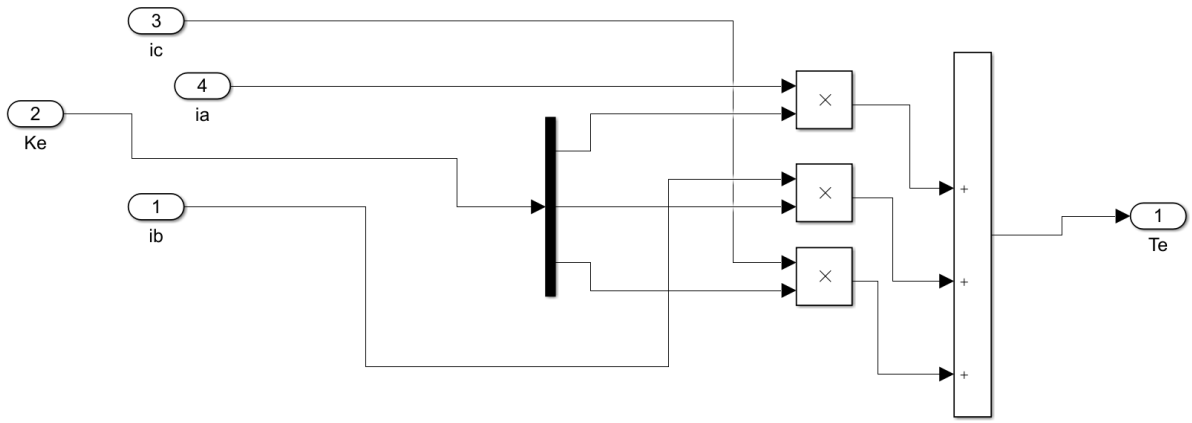

Appendix I

Mode shapes of the system

Business Jet (Lead = 5 mm)

	v_1	v_2	v_3	v_4	v_5	v_6
θ_{LSR}	81.33948	30.70782	40.81006	3.466293	-4.76463	0.000947
x_L	81.22044	-215.303	-1.43675	18.41904	0.030553	-0.17191
θ_{sc}	81.33909	29.88871	-99.0546	-18.2206	719.5345	-0.26924
$\Delta\theta_{sc}$	-0.00029	-0.59598	-90.8647	-12.736	-791.387	0.449859
x_{sc}	-0.06404	-132.937	235.0796	-1593.37	-4.78542	-6222.26
Δx_{sc}	-0.01015	-21.0427	31.20922	-178.189	3.277746	6997.342

A320-200 (Lead = 5 mm)

	v_1	v_2	v_3	v_4	v_5	v_6
θ_{LSR}	15.25605	4.441955	22.99247	0.075628	-0.33569	8.75E-06
x_L	15.23643	-52.7653	0.071944	3.700867	0.002448	-0.0245
θ_{sc}	15.25602	4.359352	-10.0079	-0.50398	65.43263	-0.00464
$\Delta\theta_{sc}$	-1.3E-06	-0.00386	-1.08658	0.015353	-74.4706	0.008722
x_{sc}	-0.0121	-35.3575	8.531602	-516.402	-0.44446	-1838.79
Δx_{sc}	-0.00098	-2.85018	0.642018	-26.8077	0.230022	2089.926

A300 (Lead = 5 mm)

	v_1	v_2	v_3	v_4	v_5	v_6
θ_{LSR}	7.965655	1.396401	18.1184	0.029968	-0.14808	2.63E-06
x_L	7.955073	-45.8787	0.0315	4.242896	0.001699	-0.02485
θ_{sc}	7.965648	1.364761	-3.36971	-0.16431	29.02969	-0.0014
$\Delta\theta_{sc}$	-1.7E-07	-0.00076	-0.2728	0.007237	-33.3836	0.002633

x_{sc}	-0.00707	-31.7181	3.02502	-349.922	-0.19333	-1185.4
Δx_{sc}	-0.00039	-1.74146	0.152998	-10.8585	0.103778	1361.217

A330-300 (Lead = 5 mm)

	v_1	v_2	v_3	v_4	v_5	v_6
θ_{LSR}	4.258479	0.451486	-14.4365	-0.01513	-0.08589	1.29E-06
x_L	4.25318	-40.5078	-0.00703	-4.97417	0.001484	-0.02992
θ_{sc}	4.258477	0.439695	1.186939	0.062995	13.9359	-0.00057
$\Delta\theta_{sc}$	-2.9E-08	-0.00022	0.096821	-0.00321	-16.2736	0.001077
x_{sc}	-0.00377	-29.3056	-1.17201	243.3347	-0.10607	-778.349
Δx_{sc}	-0.00016	-1.23696	-0.04383	4.611857	0.058957	907.888

A350-1000 (Lead = 5 mm)

	v_1	v_2	v_3	v_4	v_5	v_6
θ_{LSR}	2.998942	0.265571	-12.4989	-0.00974	-0.05291	5.76E-07
x_L	2.994891	-34.0374	-0.00126	-4.32744	0.000886	-0.02168
θ_{sc}	2.998941	0.259402	0.684143	0.036934	9.660436	-0.00028
$\Delta\theta_{sc}$	-1.1E-08	-8.9E-05	0.047766	-0.00163	-11.2834	0.000535
x_{sc}	-0.00299	-25.4733	-0.70039	203.6037	-0.06283	-647.765
Δx_{sc}	-9.5E-05	-0.80771	-0.0193	2.564925	0.035388	755.9845

A340-600 (Lead = 5 mm)

	v_1	v_2	v_3	v_4	v_5	v_6
θ_{LSR}	1.828801	0.107277	-10.1894	-0.00529	-0.02702	1.85E-07
x_L	1.825998	-31.1909	0.001872	-4.87259	0.000589	-0.01883
θ_{sc}	1.8288	0.104445	0.31393	0.017583	5.805843	-0.00011
$\Delta\theta_{sc}$	-2.8E-09	-3E-05	0.017983	-0.00062	-6.78239	0.0002
x_{sc}	-0.00217	-24.386	-0.33908	158.0413	-0.03007	-501.949
Δx_{sc}	-4.6E-05	-0.51324	-0.00598	1.019734	0.017174	586.1167

A380-800 (Lead = 5 mm)

	v_1	v_2	v_3	v_4	v_5	v_6
θ_{LSR}	0.809478	-0.02255	-7.60417	0.002702	-0.01723	1.13E-07
x_L	0.808421	28.33206	0.004477	6.867248	0.000692	-0.03171
θ_{sc}	0.809478	-0.02181	0.080883	-0.00558	2.361418	-4.1E-05
$\Delta\theta_{sc}$	-4.3E-10	1.1E-05	0.006409	0.000236	-2.82883	7.91E-05
x_{sc}	-0.00086	23.37755	-0.10414	-97.7954	-0.01645	-291.757
Δx_{sc}	-1.4E-05	0.388245	-0.00117	0.012197	0.009774	349.5075

Business Jet *(Lead = 10 mm)*

	v_1	v_2	v_3	v_4	v_5	v_6
θ_{LSR}	51.11821	25.25667	8.490104	2.457257	0.003723	-2.05969
x_L	51.03658	-103.325	-1.72994	6.291021	0.08128	0.009533
θ_{sc}	51.11766	24.39586	-59.0804	-32.1884	-1.598	1285.873
$\Delta\theta_{sc}$	-0.00241	-3.79759	-280.787	-137.502	0.772246	-1368.08
x_{sc}	-0.03694	-58.3494	431.3001	-892.835	4132.151	3.71033
Δx_{sc}	-0.01023	-16.1548	100.3588	-177.916	-4622.78	-5.28056

A320-200 (Lead = 10 mm)

	v_1	v_2	v_3	v_4	v_5	v_6
θ_{LSR}	13.37807	7.443704	4.739111	0.202696	-0.43329	5.64E-05
x_L	13.35729	-24.0485	0.029345	0.871503	0.001859	-0.00818
θ_{sc}	13.37795	7.26895	-32.8414	-3.7313	176.9782	-0.04988
$\Delta\theta_{sc}$	-6.1E-05	-0.0929	-17.7887	-1.54265	-196.882	0.088554
x_{sc}	-0.00878	-13.3203	37.24376	-382.823	-1.03679	-1506.52
Δx_{sc}	-0.00188	-2.84733	7.20006	-62.8259	0.607742	1700.103

A300 (Lead = 10 mm)

	v_1	v_2	v_3	v_4	v_5	v_6
θ_{LSR}	9.465308	4.203307	4.694909	0.086964	-0.23774	1.78E-05
x_L	9.449817	-21.3613	0.055174	0.963944	0.0017	-0.00843
θ_{sc}	9.465237	4.084862	-18.5246	-1.35456	82.74528	-0.01549
$\Delta\theta_{sc}$	-1.7E-05	-0.02804	-4.72833	-0.18457	-93.9387	0.028768
x_{sc}	-0.00724	-11.9665	15.79298	-274.755	-0.55774	-999.947
Δx_{sc}	-0.00112	-1.8515	2.248005	-31.1688	0.298225	1141.535

A330-300 (Lead = 10 mm)

	v_1	v_2	v_3	v_4	v_5	v_6
θ_{LSR}	6.781751	2.393085	4.725465	0.044724	-0.15182	9.33E-06
x_L	6.771175	-19.3342	0.063066	1.124213	0.001678	-0.01027
θ_{sc}	6.781714	2.315796	-9.58251	-0.54316	41.01972	-0.00664
$\Delta\theta_{sc}$	-4.9E-06	-0.01006	-1.52147	-0.01665	-47.5196	0.012585
x_{sc}	-0.00541	-11.1379	7.512859	-198.046	-0.34578	-668.198
Δx_{sc}	-0.00067	-1.37492	0.858776	-16.604	0.183955	775.3599

A350-1000 (Lead = 10 mm)

	v_1	v_2	v_3	v_4	v_5	v_6
θ_{LSR}	5.449042	1.833238	4.581568	0.029297	-0.09802	4.38E-06
x_L	5.439967	-16.3098	0.049873	0.978147	0.001058	-0.00757
θ_{sc}	5.449016	1.779722	-6.57382	-0.32544	28.83615	-0.00344
$\Delta\theta_{sc}$	-2.2E-06	-0.00433	-0.71528	0.000581	-33.5125	0.006536
x_{sc}	-0.00493	-9.88162	5.038496	-169.331	-0.21849	-560.401
Δx_{sc}	-0.00047	-0.93264	0.442975	-10.5325	0.117516	651.3671

A340-600 (Lead = 10 mm)

	v_1	v_2	v_3	v_4	v_5	v_6
θ_{LSR}	3.947159	1.031571	4.265682	0.016361	-0.0519	1.49E-06
x_L	3.939676	-15.2716	0.043377	1.114248	0.000737	-0.00668
θ_{sc}	3.947143	0.997038	-3.67854	-0.15931	17.61902	-0.00136
$\Delta\theta_{sc}$	-6.6E-07	-0.00145	-0.24945	0.003392	-20.5305	0.002575
x_{sc}	-0.0044	-9.62774	2.847687	-134.67	-0.11099	-437.058
Δx_{sc}	-0.00028	-0.61302	0.169621	-5.35774	0.060932	508.9191

A380-800 (Lead = 10 mm)

	v_1	v_2	v_3	v_4	v_5	v_6
θ_{LSR}	2.154371	0.33001	3.776235	0.008424	-0.03412	9.63E-07
x_L	2.150893	-14.3314	0.021738	1.616735	0.000888	-0.01136
θ_{sc}	2.154368	0.316015	-1.19061	-0.05288	7.301523	-0.00056
$\Delta\theta_{sc}$	-9.2E-08	-0.00039	-0.07888	0.002403	-8.73391	0.00107
x_{sc}	-0.00224	-9.51153	1.024141	-86.1329	-0.06404	-257.377
Δx_{sc}	-0.00012	-0.4932	0.048355	-2.21186	0.036643	307.569

Appendix J

Membrane coupling parameters

Table 28. Coupling parameters

Torque (N.m)	Moment of inertia ($kg.m^2$)	Mass (kg)	Peak torque (N.m)	Flexural stiffness		
				Torsional×103 (N.m/rad)	Angular (N/deg)	Axial (N/mm)
11.4	5660×10^{-8}	0.164	30	7.5	10	<9

References

[1] T. Feehally, “Electro-Mechanical Interaction in Aero Gas Turbine-Generator Systems,” Ph.D. dissertation, School of Electrical and Electronic Engineering., The University of Manchester, Manchester, 2012.

[2] K. Areerak *et al*., "The stability analysis of AC-DC systems including actuator dynamics for aircraft power systems," *2009 13th European Conference on Power Electronics and Applications*, 2009, pp. 1-10.

[3] N. Nagel, "Actuation Challenges in the More Electric Aircraft: Overcoming Hurdles in the Electrification of Actuation Systems," in *IEEE Electrification Magazine*, vol. 5, no. 4, pp. 38-45, Dec. 2017, doi: 10.1109/MELE.2017.2755266.

[4] O. Bennouna and N. Langlois, "Modeling and simulation of electromechanical actuators for aircraft nacelles," *2013 9th International Symposium on Mechatronics and its Applications (ISMA)*, 2013, pp. 1-5, doi: 10.1109/ISMA.2013.6547389.

[5] S.-P. Wang, M. Tomovic, and H. Liu, *Commercial Aircraft Hydraulic Systems: Shanghai Jiao Tong University Press Aerospace Series*. Elsevier Science, 2016.

[6] A. O. Onche, “Electric Machine with Integrated Torque Limiter,” MSc. Dissertation, Department of Electronic & Electrical Engineering., The University of Sheffield, Sheffield, 2014.

[7] M. Fanliang, “Actuation system design with electrically powered actuators,” MSc. Dissertation, School Of Engineering., Cranfield University, Bedford, 2011.

[8] E. K. Hussain, K. Atallah, M. Odavic, R. S. Dragan and R. E. Clark, "Pseudo Direct Drive electrical machines for flight control surface actuation," *8th IET International Conference on Power Electronics, Machines and Drives (PEMD 2016)*, 2016, pp. 1-6, doi: 10.1049/cp.2016.0237.

[9] G. Qiao, G. Liu, Z. Shi, Y. Wang, S. Ma, and T. C. Lim, “A review of electromechanical actuators for More/All Electric aircraft systems,” in Proc. Institution Mech. Eng., Part C: J. Mech. Eng. Sci., Nov. 2017, pp. 4128–4151.

[10] L. EITEL. (2019, Mar. 23). *Update on roller-screw actuator design and applications (with video and image galleries)* [Online]. Available: https://www.linearmotiontips.com/update-on-roller-screw-actuator-design-and-applications-with-video-and-image-galleries/

[11] K. K. Varanasi, “On the Design of a Precision Machine for Closed-Loop Performance,” MSc. Dissertation, Department of Mechanical Engineering and the Department of Electrical Engineering and Computer Science., Massachusetts Institute of Technology, Cambridge, MA, 2002.

[12] S. Prathibha and S. Amritha, "Control of ball-screw drive systems," *2017 International Conference on Intelligent Computing, Instrumentation and Control Technologies (ICICICT)*, 2017, pp. 80-84, doi: 10.1109/ICICICT1.2017.8342538.

[13] G. Pritschow and N. Croon, "Ball screw drives with enhanced bandwidth by modification of the axial bearing," *CIRP Ann. - Manuf. Technol.*, vol. 62, no. 1, pp. 383–386, 2013.

[14] D. Maloney. (2018, Nov. 13). *Mechanisms: Lead screws and ball screws* [Online]. Available: https://hackaday.com/2018/11/13/mechanisms-lead-screws-and-ball-screws/

[15] ABSSAC Ltd. (2012, Aug. 01). *Abssac's leadscrew and plastic nut animation* [Online]. Available: https://www.youtube.com/watch?v=l4i4FOa_WF8

[16] K. Atallah, J. Rens, S. Mezani and D. Howe, "A Novel "Pseudo" Direct-Drive Brushless Permanent Magnet Machine," in *IEEE Transactions on Magnetics*, vol. 44, no. 11, pp. 4349-4352, Nov. 2008, doi: 10.1109/TMAG.2008.2001509.

[17] M. Bouheraoua, "Control of Pseudo Direct Drive," Ph.D. dissertation, Department of Electronic and Electrical Engineering., The University of Sheffield, Sheffield, 2013.

[18] K. Atallah and D. Howe, "A novel high-performance magnetic gear," in *IEEE Transactions on Magnetics*, vol. 37, no. 4, pp. 2844-2846, July 2001, doi: 10.1109/20.951324.

[19] R. G. Montague, C. M. Bingham and K. Atallah, "Magnetic gear dynamics for servo control," *Melecon 2010 - 2010 15th IEEE Mediterranean Electrotechnical Conference*, 2010, pp. 1192-1197, doi: 10.1109/MELCON.2010.5475900.

[20] C. G. C. Neves and A. F. F. Filho, "Magnetic Gearing Electromagnetic Concepts," *J. Microwaves, Optoelectron. Electromagn. Appl.*, vol. 16, no. 1, pp. 108–119, 2017.

[21] K. Areerak, "Modelling and Stability Analysis of Aircraft Power Systems," Ph.D. dissertation, Department of Electrical and Electronic Engineering., The University of Nottingham, Nottingham, 2009.

[22] B. Henke, O. Sawodny and R. Neumann, "Distributed Parameter Modeling of Flexible Ball Screw Drives Using Ritz Series Discretization," in *IEEE/ASME Transactions on Mechatronics*, vol. 20, no. 3, pp. 1226-1235, June 2015, doi: 10.1109/TMECH.2014.2333775.

[23] J. Kasberg. (2015, Jul. 30). *The Fundamentals of Ball Screws* [Online]. Available: https://www.machinedesign.com/mechanical-motion-systems/linear-motion/article/21834347/the-fundamentals-of-ball-screws.

[24] Thomson Linear Motion. *What is the difference between pitch and lead when referring to a screw?* [Online]. Available: https://www.thomsonlinear.com/en/support/tips/what-is-the-difference-

between-pitch-and-lead-when-referring-to-a-screw.

[25] K. K. Varanasi and S. A. Nayfeh, “The Dynamics of Lead-Screw Drives: Low-Order Modeling and Experiments,” *ASME*, vol. 126, pp. 388–396, 2004.

[26] S. Frey, A. Dadalau, and A. Verl, “Expedient modeling of ball screw feed drives,” *Prod. Eng. - Res. Dev.*, vol. 6, pp. 205–211, 2012.

[27] D. A. Vicente, R. L. Hecker, and G. M. Flores, “Ball Screw Drive Systems: Evaluation of Axial and Torsional Deformations,” *Mecánica Computacional*, vol. XXVIII, no. 38, pp. 3265-3277, 2009.

[28] D. A. Vicente, R. L. Hecker, F. J. Villegas, and G. M. Flores, “Modeling and vibration mode analysis of a ball screw drive,” *Int. J. Adv. Manuf. Technol.*, vol. 58, no. 1-4, pp. 257-265, Jan. 2012.

[29] K. Erkorkmaz and A. Kamalzadeh, "High bandwidth control of ball screw drives", *CIRP Ann. - Manuf. Technol.*, vol. 55, no. 1, pp. 393-398, 2006.

[30] A. Hatwesh, S. Fletcher, A. Longstaff, W. Pan and F. Gu, "Expedient identification of the dynamics of ball-screw drives using online-validation," *2017 23rd International Conference on Automation and Computing (ICAC)*, 2017, pp. 1-6, doi: 10.23919/IConAC.2017.8082054.

[31] S. Sumsurooah, M. Odavic and S. Bozhko, "A Modeling Methodology for Robust Stability Analysis of Nonlinear Electrical Power Systems Under Parameter Uncertainties," in *IEEE Transactions on Industry Applications*, vol. 52, no. 5, pp. 4416-4425, Sept.-Oct. 2016, doi: 10.1109/TIA.2016.2581151.

[32] S. Sumsurooah, M. Odavic and S. Bozhko, "Development of LFT-based models for robust stability analysis of a generic electrical power system over all operating conditions," *2015 International Conference on Electrical Systems for Aircraft, Railway, Ship Propulsion and Road Vehicles (ESARS)*, 2015, pp. 1-6, doi: 10.1109/ESARS.2015.7101478.

[33] T. Wu, S. Bozhko, G. Asher, P. Wheeler, and D. Thomas, “Fast Reduced Functional Models of Electromechanical Actuators for More-Electric Aircraft Power System Study,” *SAE Tech. Pap.*, 2008, doi: 10.4271/2008-01-2859.

[34] R. S. Dragan, R. E. Clark, E. K. Hussain, K. Atallah and M. Odavic, "Magnetically Geared Pseudo Direct Drive for Safety Critical Applications," in *IEEE Transactions on Industry Applications*, vol. 55, no. 2, pp. 1239-1249, March-April 2019, doi: 10.1109/TIA.2018.2873511.

[35] C. Pislaru, D. G. Ford, and G. Holroyd, “Hybrid modelling and simulation of a computer numerical control machine tool feed drive,” *Proc. Inst. Mech. Eng. I, J. Syst. Control Eng.*, vol. 218, no. 2,

pp. 111–120, 2004.

[36] G. Holroyd, C. Pislaru, and D. G. Ford, “Modelling the dynamic behaviour of a ball-screw system taking into account the changing position of the ball-screw nut,” in *Laser Metrology and Machine Performance VI*. Southampton, U.K.: WIT Press, 2003, pp. 337–347.

[37] M. F. Zaeh, T. Oertli, and J. Milberg, “Finite element modelling of ball screw feed drive systems,” *CIRP Ann., Manuf. Technol.*, vol. 53, no. 1, pp. 289–292, 2004.

[38] R. Whalley, M. Ebrahimi, and A. A. Abdul-Ameer, “Hybrid modelling of machine tool axis drives,” *Int. J. Mach. Tool Manuf.*, vol. 45, no. 14, pp. 1560–1576, 2005.

[39] T. Feehally and J. Apsley, "Analysis of electro-mechanical interaction in aircraft generator systems," *2015 IEEE Energy Conversion Congress and Exposition (ECCE)*, 2015, pp. 5417-5424, doi: 10.1109/ECCE.2015.7310422.

[40] S. Goldberg and W. R. Schmus, "Subsynchronous Resonance and Torsional Stresses in Turbine-Generator Shafts," in *IEEE Transactions on Power Apparatus and Systems*, vol. PAS-98, no. 4, pp. 1233-1237, July 1979, doi: 10.1109/TPAS.1979.319322.

[41] L. Ran, D. Xiang and J. L. Kirtley Jr., "Analysis of Electromechanical Interactions in a Flywheel System with a Doubly Fed Induction Machine," *2010 IEEE Industry Applications Society Annual Meeting*, 2010, pp. 1-8, doi: 10.1109/IAS.2010.5615696.

[42] L. Ran, D. Xiang and J. L. Kirtley, "Analysis of Electromechanical Interactions in a Flywheel System With a Doubly Fed Induction Machine," in *IEEE Transactions on Industry Applications*, vol. 47, no. 3, pp. 1498-1506, May-June 2011, doi: 10.1109/TIA.2011.2127436.

[43] I. M. Elders *et al*., "Modelling and Analysis of Electro-Mechanical Interactions between Prime-Mover and Load in a Marine IFEP System," *2007 IEEE Electric Ship Technologies Symposium*, 2007, pp. 77-84, doi: 10.1109/ESTS.2007.372067.

[44] M. A. Valenzuela, J. M. Bentley and R. D. Lorenz, "Evaluation of torsional oscillations in paper machine sections," in *IEEE Transactions on Industry Applications*, vol. 41, no. 2, pp. 493-501, March-April 2005, doi: 10.1109/TIA.2005.844383.

[45] M. A. Valenzuela, J. M. Bentley and R. D. Lorenz, "Evaluation of torsional oscillations in paper machine sections," *Conference Record of 2004 Annual Pulp and Paper Industry Technical Conference (IEEE Cat. No.04CH37523)*, 2004, pp. 15-22, doi: 10.1109/PAPCON.2004.1338357.

[46] C. B. Mayer, "Torsional Vibration Problems and Analyses of Cement Industry Drives," in *IEEE Transactions on Industry Applications*, vol. IA-17, no. 1, pp. 81-89, Jan. 1981, doi:

10.1109/TIA.1981.4503903.

[47] H. Takahashi, T. Yuki, and K. Suzuki, “Modeling of ball screw driven stage for drilling machines with lumped parameter system model and FEM model,” *Mech. Eng. J.*, vol. 3, no. 4, pp. 16–00068, 2016.

[48] T. Feehally, I. E. Damián and J. M. Apsley, "Analysis of Electromechanical Interaction in Aircraft Generator Systems," in *IEEE Transactions on Industry Applications*, vol. 52, no. 5, pp. 4327-4336, Sept.-Oct. 2016, doi: 10.1109/TIA.2016.2585088.

[49] J. Wang, Class Lecture, Topic: "4-Voltage Source Inverter (VSI) and PWM techniques for AC drives." EEE6203, Dept. of Electronic & Electrical Engineering, University of Sheffield, Sheffield, 2016.

[50] J. Wang, Class Lecture, Topic: "3- Synchronous Permanent Magnet Motor Drives." EEE6203, Dept. of Electronic & Electrical Engineering, University of Sheffield, Sheffield, 2016.

[51] T. M. O'Sullivan, C. M. Bingham and N. Schofield, "High-Performance Control of Dual-Inertia Servo-Drive Systems Using Low-Cost Integrated SAW Torque Transducers," in *IEEE Transactions on Industrial Electronics*, vol. 53, no. 4, pp. 1226-1237, June 2006, doi: 10.1109/TIE.2006.878311.

[52] Jiabin Wang and Kais Atallah, "Modeling and control of ‘pseudo’ direct-drive brushless permanent magnet machines," *2009 IEEE International Electric Machines and Drives Conference*, 2009, pp. 870-875, doi: 10.1109/IEMDC.2009.5075306.

[53] D. J. Ewins, *Modal Testing: Theory and Practice*, First Edit. Letchworth: Research Studies Press Ltd, 1984.

[54] J. W. Rao *et al.*, “Level attraction and level repulsion of magnon coupled with a cavity anti-resonance,” *New J. Phys.*, vol. 21, no. 6, p. 065001, 2019.

[55] J.-C. Maré, *Aerospace Actuators 3: European Commercial Aircraft and Tiltrotor Aircraft*, 3rd ed. John Wiley & Sons, 2018.

[56] Airbus. *Aircraft Characterisitcs Aircraft and Maintenance Planning* [Online]. Available: https://www.airbus.com/aircraft/support-services/airport-operations-and-technical-data/aircraft-characteristics.html

[57] D. P. Raymer, *Aircraft Design: A Conceptual Approach*, 4th ed. American Institute of Aeronautics and Astronautics, 2006.

[58] A. K. Kundu, *Aircraft Design*. Cambridge: Cambridge University Press, 2010.

[59] Hursts. *Airbus Technical Notes* [Online]. Available: https://hursts.org.uk/airbus-technical/notes.pdf.

[60] "Loss of Rudder in Flight," The Transportation Safety Board of Canada (TSB), 2007.

[61] M. Negahban, Class Lecture, Topic: "19- Mass moment of inertia." MECH 223, College of Engineering, University of Nebraska-Lincoln, Lincoln, 2003.

[62] X. Longxian, "Actuation Technology for Flight Control System on Civil Aircraft," MSc. Dissertation, School of Engineering., Cranfield University, Bedford, 2009.

[63] EWELLIX. *Precision rolled ball screws catalogue* [Online]. Available: https://medialibrary.ewellix.com/Products/Ball and roller screws/Precision ball screws/2_PUBLICATIONS/IL-05004-EN-precision-rolled-ball-screws-catalogue.pdf.

[64] F. Curà and A. Mura, "Experimental procedure for the evaluation of tooth stiffness in spline coupling including angular misalignment," *Mech. Syst. Signal Process.*, vol. 40, no. 2, pp. 545–555, 2013.

[65] SKF. *SKF Couplings* [Online]. Available: https://www.skf.com/binaries/pub20/Images/0901d196806fd7be-SKF-Couplings---15822_2-EN_tcm_20-317965.pdf.

[66] Y. Guo, J. Keller, R. Errichello, and Chris Halse, "Gearbox Reliability Collaborative Analytic Formulation for the Evaluation of Spline Couplings," NREL, Golden, CO, 2013.

[67] SKF. *Angular Contact Thrust Ball Bearings* [Online]. Available: https://www.skf.com/uk/products/super-precision-bearings/angular-contact-thrust-ball-bearings-for-screw-drives.

[68] T. J. E. Miller, Brushless Permanent Magnet And Reluctance Motor Drives, New York:Oxford University Press, 1989.

[69] F. Gao, X. Zheng, S. Bozhko, C. I. Hill and G. Asher, "Modal Analysis of a PMSG-Based DC Electrical Power System in the More Electric Aircraft Using Eigenvalues Sensitivity," in *IEEE Transactions on Transportation Electrification*, vol. 1, no. 1, pp. 65-76, June 2015, doi: 10.1109/TTE.2015.2427312.

[70] B. Kauschinger and S. Schroeder, "Uncertainties in Heat Loss Models of Rolling Bearings of Machine Tools," in *Procedia CIRP*, vol. 46, pp. 107–110, 2016.

[71] G. Zhang and J. Furusho, "Speed control of two-inertia system by PI/PID control," in *IEEE Transactions on Industrial Electronics*, vol. 47, no. 3, pp. 603-609, June 2000, doi: 10.1109/41.847901.

[72] K. Webb, Class Lecture, Topic: "8- Frequency Response Design." MAE 4421, College of Engineering, Oregon State University, Corvallis.

[73] Mathworks. *Assessing Gain and Phase Margins* [Online]. Available: https://www.mathworks.com/help/control/ug/assessing-gain-and-phase-margins.html#d120e3035.

[74] C. Gan, R. Todd and J. M. Apsley, "Drive System Dynamics Compensator for a Mechanical System Emulator," in *IEEE Transactions on Industrial Electronics*, vol. 62, no. 1, pp. 70-78, Jan. 2015, doi: 10.1109/TIE.2014.2327581.

[75] Texas Instruments, "High Voltage Motor Control and PFC (R1.1) Kit Hardware Reference Guide," TMDSHVMTRPFCKIT datasheet, Oct. 2010.

[76] Learnchannel-TV. (2018, Feb. 20). *How does a resolver work* [Online]. Available: http://learnchannel-tv.com/drives/servomotor/resolver/.

[77] J. W. Bennett, B. C. Mecrow, D. J. Atkinson and G. J. Atkinson, "Safety-critical design of electromechanical actuation systems in commercial aircraft", *IET Electr. Power Appl.*, vol. 5, no. 1, pp. 37-47, 2011.

[78] S. Zhu, T. Cox, Z. Xu, C. Gerada and C. Li, "Design Considerations of Fault-Tolerant Electromechanical Actuator Systems for More Electric Aircraft (MEA)," *2018 IEEE Energy Conversion Congress and Exposition (ECCE)*, 2018, pp. 4607-4613, doi: 10.1109/ECCE.2018.8557426.

[79] A. Iqbal, A. Lamine, I. Ashraf and Mohibullah, "Matlab/Simulink Model of Space Vector PWM for Three-Phase Voltage Source Inverter," *Proceedings of the 41st International Universities Power Engineering Conference*, 2006, pp. 1096-1100, doi: 10.1109/UPEC.2006.367646.